5-2016

A Computational Evaluation of Transonic Wind Tunnel Wall Interference on High Aspect Ratio Models in the Arnold Engineering Development Complex 16 Foot Transonic Tunnel

William Calain Schuman
University of Tennessee - Knoxville, wschuman@vols.utk.edu

To the Graduate Council:

I am submitting herewith a thesis written by William Calain Schuman entitled "A Computational Evaluation of Transonic Wind Tunnel Wall Interference on High Aspect Ratio Models in the Arnold Engineering Development Complex 16 Foot Transonic Tunnel." I have examined the final electronic copy of this thesis for form and content and recommend that it be accepted in partial fulfillment of the requirements for the degree of Master of Science, with a major in Aerospace Engineering.

Trevor M. Moeller, Major Professor

We have read this thesis and recommend its acceptance:

William B. Baker Jr., Gregory D. Power

Accepted for the Council:
Carolyn R. Hodges

Vice Provost and Dean of the Graduate School

(Original signatures are on file with official student records.)

A Computational Evaluation of Transonic Wind Tunnel Wall Interference on High Aspect Ratio Models in the Arnold Engineering Development Complex 16 Foot Transonic Tunnel

A Thesis Presented for the

Master of Science

Degree

The University of Tennessee, Knoxville

William Calain Schuman

May 2016

DEDICATION

To my loving wife, Nissa. I told you I would finish my degree eventually!

ACKNOWLEDGEMENTS

First, I would like to thank Mike Mills for the thesis topic. His suggestion that I investigate transonic wall interference led directly to my thesis research. Next, I would like to thank Jared Gudenkauf and Moufid Aboulmouna for their help with learning and applying USM3Dns to wind tunnel simulations. Without their instruction and advice my thesis would not have been possible. I would also like to thank the members of my thesis committee, Dr. Baker, Dr. Power, and Dr. Moeller for their advice. Thanks also to Jean Frantz, the AEDC technical librarian, for her help with background research. This work was made possible by a grant of computing time from the High Performance Computer Modernization Program (HPCMP). This work was approved for public release on April 4, 2016 under AEDC PA number: AEDC2016-084. Distribution is unlimited.

ABSTRACT

One of the inherent difficulties in utilizing a ventilated test section wind tunnel is the interaction of the model flow field and the test section walls. If high quality aerodynamic data is required for the system under test it is necessary to determine the impact of the test section walls on the flow field around the model. A parametric study was undertaken using the CFD code USM3Dns to determine the impact of model size and wingspan on observed transonic wind tunnel wall interference. The study used a simplified model of the Propulsion Wind Tunnel 16T test section as the test facility, and the NASA Common Research Model as the test article. CFD solutions were acquire for both free-stream and wind tunnel simulations, and the difference between the two was the inferred wall interference. Overall, the scale of the model, and thereby the model blockage, had the largest impact on the inferred transonic wall interference for both the lift and pitching moment coefficient.

TABLE OF CONTENTS

LIST OF TABLES

LIST OF FIGURES

NOMENCLATURE

1T	AEDC Model Tunnel 1T, 1 foot cross section transonic model tunnel
4T	AEDC Aerodynamic Tunnel 4T, 4 foot cross section transonic aerodynamic tunnel
16T	AEDC Propulsion Wind Tunnel 16T, 16 foot cross section transonic tunnel
a	Speed of sound
AEDC	Arnold Engineering Development Complex
b	Configuration wingspan in inches
b/w	Configuration wingspan to tunnel width ratio
BC	Boundary condition
c_{break}	Configuration chord at the Yehudi break of the wing in inches
c_{root}	Configuration chord at the root of the wing in inches
c_{tip}	Configuration chord at the tip of the wing in inches
$c_{y/b}$	Configuration chord at non-dimensional span station y/b
$\bar{c}$	Mean aerodynamic chord
$\bar{c}_1$	Mean aerodynamic chord for inboard wing section
$\bar{c}_2$	Mean aerodynamic chord for outboard wing section
CAD	Computer aided drafting
CD	Drag coefficient
CD_{FS}	Free-stream simulation drag coefficient
CD_{Ti}	Wing tunnel simulation drag coefficient, interpolated to free-stream calculated lift coefficient value
CD_V	Viscous component of the drag coefficient
CL	Lift coefficient
CL_{FS}	Free-stream simulation lift coefficient
CL_T	Wind tunnel simulation lift coefficient
CLM	Pitching moment coefficient

CLM_{FS}	Free-stream simulation pitching moment coefficient
CLM_{Ti}	Wind tunnel simulation pitching moment coefficient, interpolated to free-stream calculated lift coefficient value
CLM_V	Viscous component of the pitching moment coefficient
Config	Configuration
Cp	Pressure coefficient
Cp_{FS}	Free-stream simulation pressure coefficient
Cp_{T}	Wind tunnel simulation pressure coefficient
CRM	NASA Common Research Model, a test geometry used for CFD validation cases
D.CD	Difference between free-stream and tunnel simulation drag coefficients
D.CD_V	Difference between free-stream and tunnel simulation viscous portions of the drag coefficients
D.CL	Difference between free-stream and tunnel simulation lift coefficients
D.CLM	Difference between free-stream and tunnel simulation pitching moment coefficients
D.CLM_V	Difference between free-stream and tunnel simulation viscous portions of the pitching moment coefficients
deg	Degrees
DSRC	Department of Defense Supercomputer Resource Center
FS	Free-stream
HAAS	High angle automated sting test cart, commonly called Cart 1
HPCMP	High Performance Computer Modernization Program
M	Mach number
MAC	Mean aerodynamic chord
P_s	Static pressure
s	Configuration reference area
s_1	Inboard wing section planform area, semi-span

$s_{\acute{2}}$	Outboard wing section planform area, semi-span
T	Tunnel
V	Velocity
x	Stream-wise test section coordinate, positive downstream, in inches
x_{MRC}	X coordinate of configuration moment reference center, in inches
x_{grid}	X coordinate in grid coordinates for calculations, in inches
$(x_{LE})_{y/b}$	X coordinate of the wing leading edge at non-dimensional span location y/b
$(x/c)_{y/b}$	Non-dimensional length, referenced to wing chord at non-dimensional span location y/b
y	Span-wise test section coordinate, positive left when facing downstream, in inches
y+	non-dimensional distance from a viscous wall for CFD calculations, used to calculate necessary grid spacing near a viscous surface
y_{MRC}	Y coordinate of configuration moment reference center, in inches
y/b	Non-dimensional span, referenced to wing half-span
z	Normal test section coordinate, positive upwards, in inches
z_{MRC}	Z coordinate of configuration moment reference center, in inches
α	Angle of attack, degrees
β	Angle of sideslip, degrees
∆Cp	Difference between free-stream and wind tunnel simulation pressure coefficient
γ	Ratio of specific heats, 1.4 for air
λ_1	Taper ratio of wing from root to Yehudi break
λ_2	Taper ratio of wing from Yehudi break to wingtip

CHAPTER I
INTRODUCTION AND MOTIVATION

Since their introduction in the 1940s ventilated test section transonic wind tunnels have been the primary aerodynamic data source for nearly every military aircraft that flies in that regime [1]. One of the inherent difficulties in utilizing a ventilated test section is the interaction of the model flow field and the test section walls [2]. If high quality aerodynamic data is required for the system under test it is necessary to determine the impact of the test section walls on the flow field around the model. This problem has been extensively studied since the introduction of ventilated wall test facilities, and several techniques exist to calculate and /or correct for wall interference [3], [4], [5], [6].

The techniques used for correcting wall interference broadly fall into two categories. The first technique, mechanical wall interference reduction, is the use of a non-solid wall boundary to cancel wave reflections off the wall. This correction methodology includes perforated ventilated wall, porous ventilated wall, slotted ventilated wall, and adaptive wall wind tunnels. These tunnels employ plenum suction with open walls to reduce the thickness of the boundary layer, control Mach number, and attempt to eliminate wall interference in the test section. The second technique used for wall corrections is computational. This technique has increased in fidelity as computational capability has increased, from simple source and sink modeling methods to full computational fluid dynamics simulations of the test cell with viscous effects [3], [4], [5], [6]. Even when utilizing complex ventilated walls, no wall configuration has been shown to completely eliminate interference in the transonic regime from all model types [7]. Thus, a combination of the two techniques provides the best opportunity for removing wall interference from test data.

The 16 foot transonic propulsion wind tunnel (16T) of the Arnold Engineering Development Complex (AEDC) utilizes a ventilated test section with perforated walls of 6% porosity, inclined stream-wise 60 deg, as presented in Figure 1 [8]. The wall configuration was based upon the results of wall interference experiments in the 1 ft. transonic model tunnel (1T) at AEDC [9]. Virtually every fixed wing aircraft in service with the Department of Defense that operates in the transonic regime has been tested at AEDC [1].

With the increased utilization of onboard aerodynamic models in aircraft, highly accurate transonic wind tunnel data is becoming even more important. This will be especially true for the next generation of high altitude / long endurance ISR and bomber aircraft, which are expected to fly through the transonic speed range and utilize mid to high aspect ratio wings for aerodynamic efficiency, based upon legacy systems [10], [11]. The requirement for large model sizes, driven by the need to more closely match flight

Reynolds number, is directly opposed to the need for smaller models to reduce transonic wall interference [12]. A firm understanding of the interference caused by the tunnel boundary conditions will be necessary for precise calculations of aircraft system performance. The purpose of this study is to use computational tools to evaluate the impact of wind tunnel wall interference on a high aspect ratio model in the transonic regime when tested in a simulation of the AEDC Propulsion Wind Tunnel 16T.

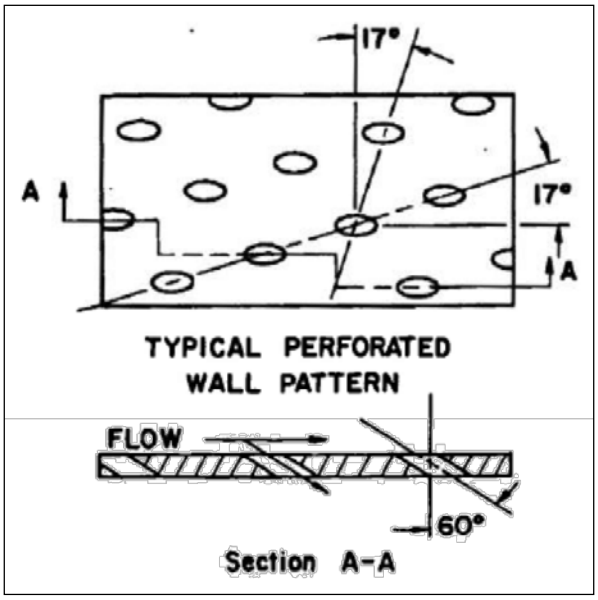

Figure 1. Tunnel 16T Porous Wall Schematic

CHAPTER II
LITERATURE REVIEW

Test Facility Descriptions

Propulsion Wind Tunnel 16T

AEDC Propulsion Wind Tunnel 16T is a closed-loop, continuous-flow, variable-density tunnel capable of being operated at Mach numbers from 0.06 to 1.60 and stagnation pressures from 120 to 4,000 psfa. The tunnel stagnation temperature can be varied from approximately 60 to 160 deg F depending upon the available cooling water temperature. The tunnel is equipped with a scavenging system that removes combustion products when testing rocket motors or turbine engines. The test section is 16-ft. square by 40-ft. long and enclosed by 60-deg inclined-hole perforated walls of six percent porosity. The side wall angle is variable from 1.5 deg convergence to 1-deg divergence. Two test section carts are used in 16T. Both may be used for large-scale aerodynamic, inlet, and afterbody model testing and one cart is configurable to perform captive trajectory sting (CTS) testing [13]. The general arrangement of the Tunnel 16T is presented in Figure 2 [14]. The layout of Cart 1, the test cart typically used for aerodynamic testing, is presented in Figure 3 with the centerline pipe calibration equipment [15].

Aerodynamic Wind Tunnel 4T

Transonic Wind Tunnel 4T is a mid-size (48- by 48-in. cross section) continuous-flow test facility designed for high productivity. The tunnel is primarily used to investigate static/dynamic stability and weapons separation control parameters for flight vehicles, and it provides high-quality, uniform airflow from Mach 0.05 to 2.46. This tunnel can be operated from an independent drive compressor up to Mach 1.3 or use the PWT Plenum Evacuation System (PES) for variable density capability operations up to Mach 2.46. 4T has a unit Reynolds number range of 0.02-7.1 million / ft., depending upon test conditions [16].

The 4T test section is 4-ft square and 12.5 ft. long, enclosed by 60-deg inclined-hole perforated walls. Porosity is variable from approximately 0- to 10-percent open. The two sidewalls are fixed, and the top and bottom walls are movable up to 1/2 deg from a position parallel to the test section centerline. The test section is enclosed by a 14-ft-square plenum chamber that can be evacuated, allowing part of the tunnel main flow to be removed through the test section walls to both generate supersonic flow and to alleviate wall interference. A schedule of wall porosity and wall angle is used as a function of Mach number [13]. The general arrangement of Tunnel 4T is shown in Figure 4 [17].

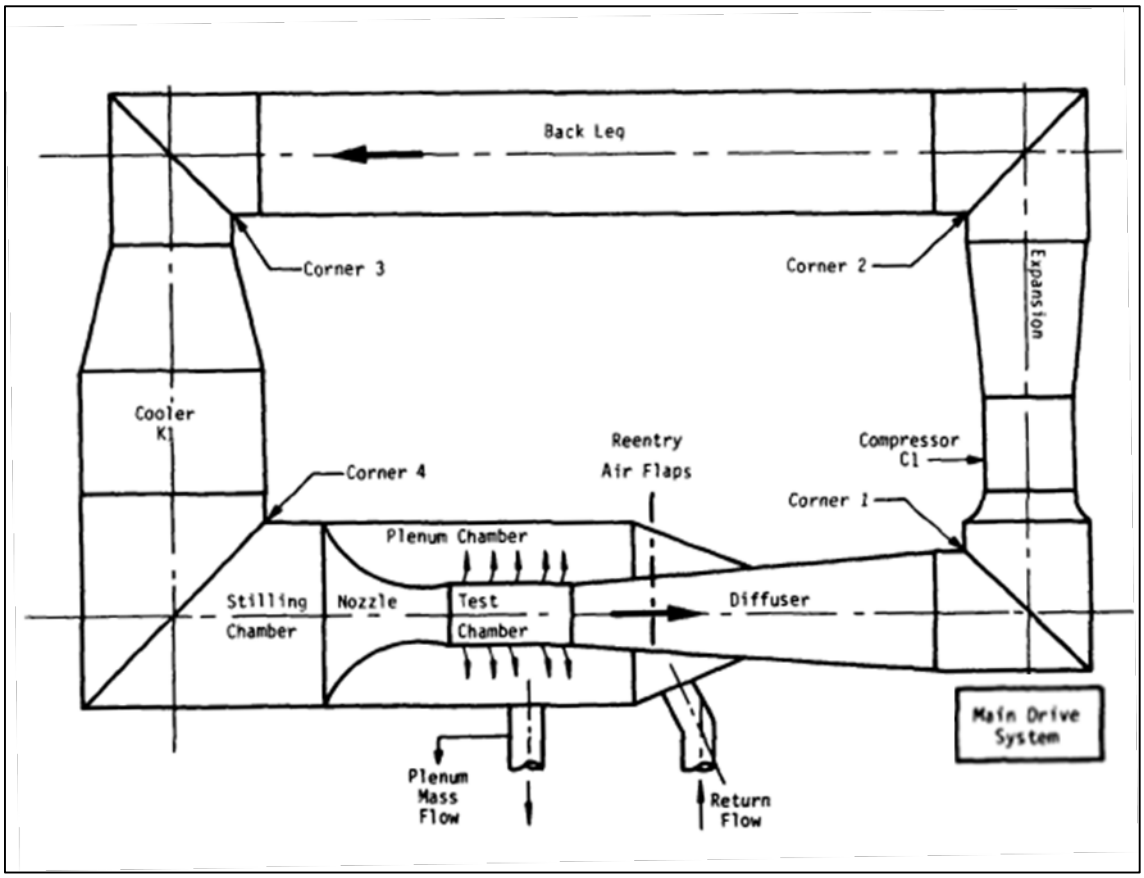

Figure 2. General Layout of Propulsion Wind Tunnel 16T

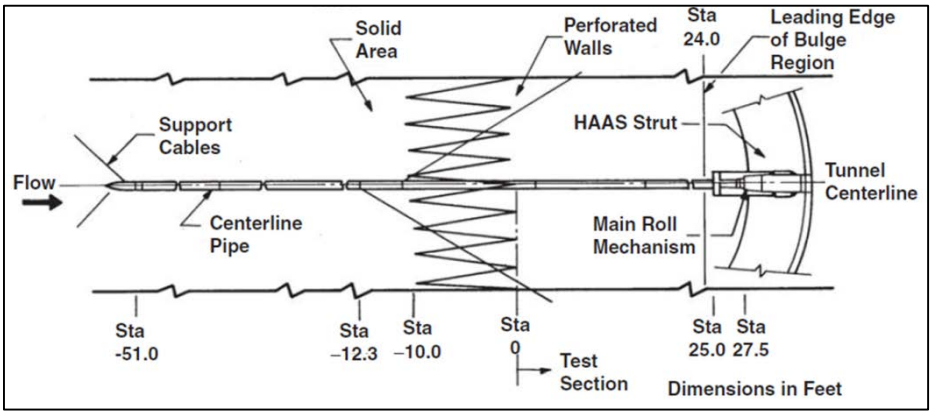

Figure 3. Layout of the High Angle Automated Sting (HAAS) Test Cart (Pictured with Centerline Pipe Calibration Test Article)

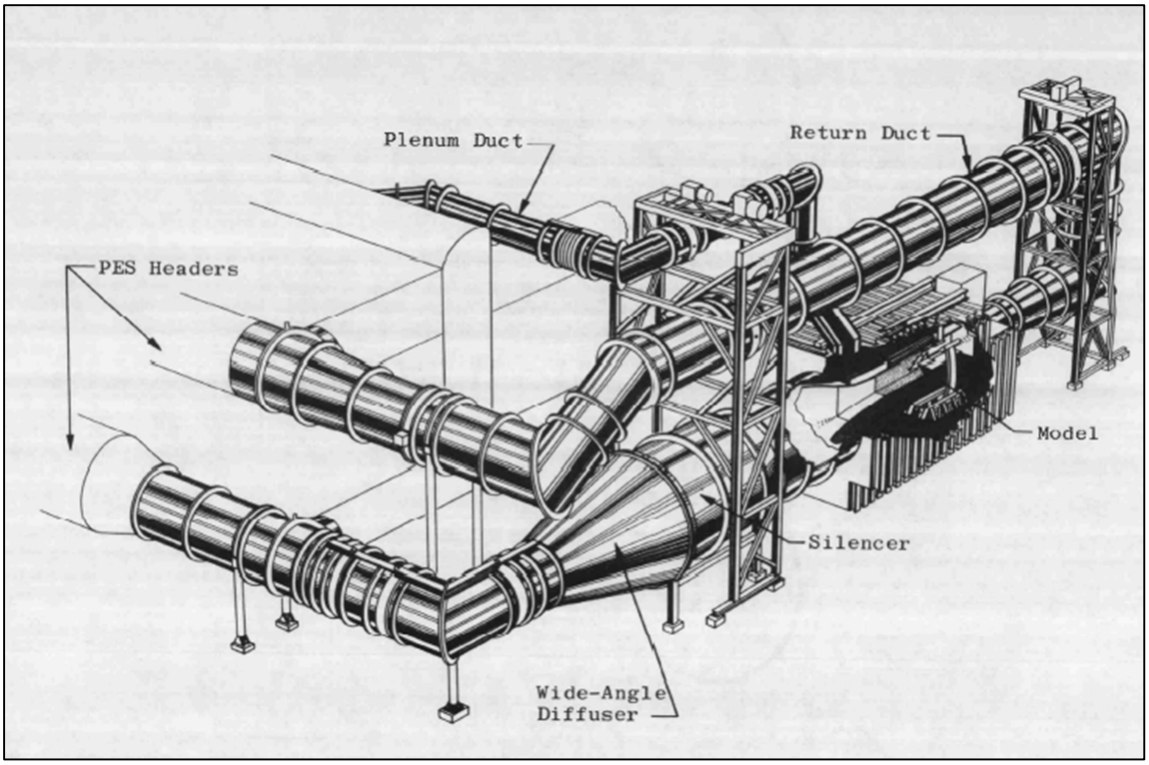

Figure 4. Layout of PWT Aerodynamic Wind Tunnel 4T

Transonic Model Tunnel 1T

Numerous wall interference experiments conducted at AEDC were conducted in the Transonic Model Wind Tunnel (1T), which was a continuous-flow, non-return wind tunnel equipped with a two-dimensional, flexible nozzle and an auxiliary plenum evacuation system. 1T was capable of testing from Mach 0.2 to 1.5. The test section was of square cross section nominally 12 in. square and 37.5 in. long. The tunnel was operated at a total pressure of approximately 2,850 psfa. The stagnation temperature could be varied from 80 to 120°F above ambient temperature to prevent visible condensation from occurring in the test section [18]. The tunnel arrangement is shown in Figure 5 [19]. Tunnel 1T is currently not in an operational state.

Drivers of Transonic Wall Interference

The major driver of wall interference in transonic wind tunnel testing is the reflection off of the wall boundary of expansion and compression waves [7]. This reflection becomes important once the model under test reaches its critical Mach number, and areas of supercritical flow begin to appear on the model's surface, as presented in Figure 6 [20].

As the waves from the model impact the tunnel boundary, they reflect back towards the model as compression or expansion waves, depending upon the characteristics of the wind tunnel wall [21], [22]. Figure 7 illustrates the onset of transonic flow in a constrained environment; a closed-wall wind tunnel in this case [20].

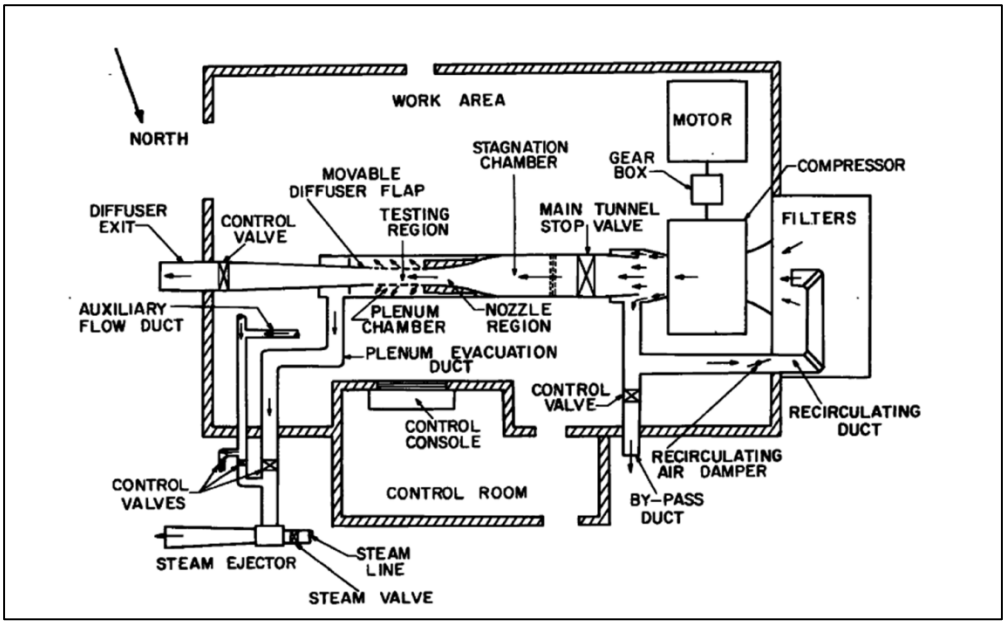

Figure 5. Layout of PWT Model Tunnel 1T

The three main drivers of ventilated wall characteristics are the test section Mach number, the wall boundary layer thickness, and the wall geometry. In general, a 6% inclined porous wall of the type employed in 16T reduces the magnitude of the lift and drag interference of the tunnel at subsonic Mach numbers for models of less than 2% blockage [23]. It was also found that walls of varied or fixed 6% porosity minimized the supersonic wall interference where other wall types failed to do so [23]. These results did not show that the wall interference was eliminated, but that it was reduced when compared to test facilities with other wall configurations.

As the wall boundary condition is dependent upon the thickness of the boundary layer, unit Reynolds number is a primary driver of the wall interference characteristics of a wind tunnel test section [2]. This is especially true in perforated wall wind tunnels, where the wall characteristics are tied very closely to the boundary layer thickness [24]. Operationally these tunnels rely upon plenum suction to remove a portion of the boundary layer from the wind tunnel wall, in addition to relieving blockage.

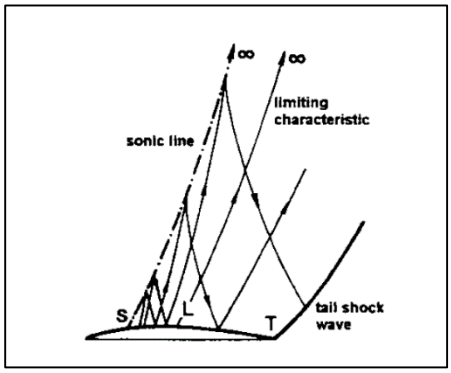

Figure 6. Onset of Transonic Flow over a Generic Airfoil [23]

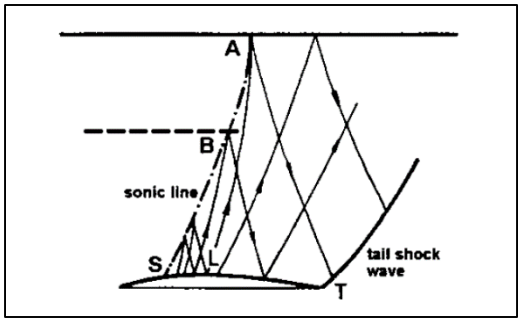

Figure 7. Onset of Transonic Flow over a Generic Airfoil in a Constrained Environment [23]

Another major driver of transonic wall interference is model geometry. Early tests at AEDC demonstrated that for an axisymmetric cone-cylinder model increasing blockage up to 4% did not have a major impact on wall interference in a test section with 6% porosity, 60 deg inclined holes [8]. When lifting models of different aspect ratios were tested, however, it showed that both model aspect ratio and wingspan had large impacts on the observed wall interference [25].

Often, aerodynamic data from transonic tunnels is used in incremental form rather than absolute form. Test customers have built their stability and control effectiveness databases on increments between configurations tested in the wind tunnel [2]. One of the inherent assumptions used in this procedure is that the tunnel induced effects are constant across configurations [2]. Tests of the same model between 16T and 4T have shown this to not be the case, and that wall interference can also be influenced by configurations

changes on the same model [2]. These results did not suggest that all types of incremental data were suspect, but that configurations that caused major changes in the model's pressure signature at the wall would change the interference characteristics [2].

Ventilated Wall Wind Tunnel Development

Development of Fixed Perforated Walls for Transonic Wind Tunnels at AEDC

The design of ventilated wall transonic wind tunnels can be traced back to experiments carried out in the 1940s and 1950s. The attainable speed of manned aircraft was increasingly approaching the transonic regime and adequate test facilities did not exist that were capable of simulating that speed range. Using standard solid-wall tunnels was not possible, since the testable model size became impracticably small as the sonic limit was approached [7].

This shortfall in test facilities led to an investigation by NACA of ventilated test sections for use in the transonic speed regime [26]. According to Goethert, "since solid boundaries and open-jet boundaries produce wave reflections with opposite characteristics, the possibility exists of eliminating wave reflection by means of suitable mixing of open and solid boundaries" [27]. The early NACA tunnel utilized longitudinal slots to decrease the magnitude of the required subsonic velocity correction and during early testing discovered that the ventilated slots also relieved choking phenomena [7]. This study also indicated that, in addition to reducing wall interference, it would be possible to use the same wind tunnel for testing in the subsonic, transonic, and supersonic regimes [26]. The AEDC transonic tunnel 16T was designed to utilize this discovery and test from the subsonic through the supersonic speed range.

Once it became possible to use the same wind tunnel for testing from the subsonic through the supersonic speed range, wall interference in these test facilities began to be investigated. Early ventilated test sections generally used longitudinally slotted test section walls. Experiments at AEDC determined that slotted wall wind tunnels had poor shock cancellation characteristics, and were generally limited to Mach numbers less than 1.05 [7], [27]. Goethert noted that, based upon tests in a 10 ft. transonic tunnel, "the reflected-wave system of slotted walls extends over a considerably larger area than for perforated walls" [27]. Since 16T was intended to test up to Mach 1.60, other wall configurations were investigated.

In the 1950s porous walls began to be investigated. Theoretical work at Cornell Aeronautical Laboratory showed that "small grain" porous walls would be necessary to effectively cancel shocks from a wind tunnel model [7], [9]. Addition work at Ohio State University and AEDC confirmed the Cornell results, and demonstrated that a 22% porosity wall with holes normal to the flow was effective in cancelling out the bow shock from a 3-

dimensional model [9]. The results of the Ohio State and AEDC studies were the basis for the design of the first set of walls for 16T. For normally inclined perforated walls, the required porosities for shock cancellation and expansion wave cancellation were different at every Mach number tested , so another series of tests were undertaken in 1T to try and determine a more advantageous wall configuration for 16T [9]. These studies included slotted walls, perforated walls, and porous walls of various open area ratios and porosities [7], [8]. Goethert concluded that, “On the basis of comparative tests with a 1.1% blockage model and as a result of a large number of other tests, it can be stated that the greater potential for testing compete airplane models through the transonic Mach number range lies with suitably shaped perforated test sections, particularly when special emphasis is to be placed on the supersonic Mach number range” [7]. At this point inclined porous walls began to be investigated at AEDC.

Differential resistance walls are perforated walls with the ventilation holes inclined in the flow direction. The driving force behind the development of the differential resistance wall was to reduce the amount of inflow into the test section from the plenum area [7]. Figure 1 presents a cross section of the differential resistance type wall used in the 16T test section. This wall configuration was selected after a parametric study of several different hole inclination angles, wall thicknesses, and open area ratios [7], [22]. The 6% open area ratio, 60 deg inclined hole wall configuration was selected for 16T because it matched the compression wave cancellation properties of the 22% porosity normal inclination hole wall while also providing excellent resistance to inflow (a significant problem with using normal hole inclination walls) and better cancellation of expansion waves emanating from a model [7], [21]. These studies varied Mach number from 0.75 to 1.4, but focused on Mach 1.2 [7], [21], [22].

All of the initial studies used to design the test section walls of 16T used axisymmetric models to ascertain wall interference [7], [8], [21], [27]. These were generally cone-cylinder type models of different blockage ratios, since analytic solutions were readily available for cone-cylinder aerodynamics in supersonic and subsonic flow. Further testing on perforated wall configurations determined that the 16T wall configuration could not completely cancel the wall interference effects in the Mach range of 0.95 – 1.10 [8]. Despite this, no other wall configuration tested during this time frame was able to produce interference free results in the Mach range of 0.95 – 1.10 [8]. Estabrooks also showed that the 60 deg inclined, 6% porosity wall configuration used in 16T produced representative forebody drag results for a 0.5% blockage cone-cylinder model over the entire Mach number range tested and produced representative data for a 2% blockage cone-cylinder model over the entire Mach number range excluding Mach 1.0-1.10 [8]. The Estabrooks study concluded that although the fixed porosity wall did a good job cancelling out wall interference, the open-area ratio required for minimum interference changed with Mach number [7], [8].

Variable Porosity Test Sections

After 16T became operational, variable porosity walls became of interest. Estabrooks had demonstrated that the required porosity for the greatest reduction in test section wall interference was a function of Mach number [8]. This led to studies in 1T of variable porosity wind tunnel walls. The variable porosity test section showed promise in reducing wall interference effects in the Mach number range of 1.05-1.10 [19]. These interference studies also used the AEDC 20 deg cone-cylinder model mentioned previously. The results of this test series was used to develop the variable porosity test section walls used in PWT aerodynamic wind tunnel 4T [28].

In the early 1970s AEDC began to investigate interference effects on lifting models in transonic test cells [29]. The first test to attempt to evaluate interference on lifting models used a modified F-111 test article with fixed wings. This test article was used in both 16T and 4T, and the results compared against one another to evaluate wall interference effects in 4T [29]. This test series put forward a recommended porosity schedule for the tunnel based upon observed interference in the model lift coefficient and pitching moment [29]. At the conclusion of the study, it was thought that interference free data could be obtained between Mach 0.7 and 1.2 using the recommended porosity schedule for 4T [29]. Tests of the AGARD Calibration Model B in 16T and 4T the same year concluded that between Mach 0.2 and 1.0 there were no indications of wall interference in the 4T data [30]. Both studies did note differences in pitching moment and lift coefficient between the two facilities, but they were attributed to other causes.

In 1974 an investigation was launched to determine causes of three-dimensional wall interference in 4T [31]. The purpose of the test was to identify the causes of pitching moment and axial force differences in the F-111 test from 1970 [31]. This test series used 16T as an interference free database while evaluating wall interference in 4T. The test model was a straight wing aircraft model with large planform wings. It was instrumented with pressure orifices on the centerline of the fuselage, mid-span of the wing, and the mid-span of the tail. All forces and moment were calculated by integrating the pressures from these orifices [31]. This study concluded that for supercritical flow over the wing, “the compressive disturbance on the upper surface (of the wing) was never completely eliminated by porosity changes” [31].

Tests of the ONERA calibration models in 16T, 4T, and the NASA Ames 11 foot transonic wind tunnel (11TWT) were designed to use ‘interference free’ data from 16T and 11TWT to determine wall interference effects in smaller wind tunnels. This was part of a wind tunnel wall interference study between the Office National d’Etudes et de Recherches Aerospatiales (ONERA), NASA Ames, and AEDC. The purpose of the study was to evaluate theoretical correction procedures and to establish and confirm guidelines for model sizing in transonic tunnels [32]. Two of the three models tested during this study

were geometrically scaled versions of a wing / body / tail transport aircraft configuration. This allowed scale and span effects to be evaluated on a high aspect ratio lifting model. Based on the test data, no value of porosity in 4T was able to completely eliminate the wall interference from the test cell [32]. The ONERA model had slightly higher blockage and aspect ratios than the F-111 and AGARD models. At this point in time, the adaptive wall wind tunnel began to be studied in earnest.

Adaptive Wall Wind Tunnels

The adaptive wall concept combined evolving computational techniques with more advanced variable porosity walls to try and reduce wall interference online on a test-by-test basis [33]. As noted previously, the optimum porosity for zero-interference in a perforated wall wind tunnel is a function of Mach number [33]. Thus the ideal wall for wind tunnel testing would have to be adjusted for different Mach numbers and model configurations [34]. The wall configuration required to reduce the interference would have to be based upon both measurements of the wall and aerodynamic predictions of the unrestricted flow field about the model [18], [34]. Walls of this type, using longitudinally variable porosity and longitudinally variable plenum suction, came close to matching “free flight’ computational results in an AEDC study on two-dimensional adaptive wall concepts [18].

The adaptive wall methodology provides better wall interference characteristics than a fixed porosity or variable porosity wind tunnel. By varying the wall characteristics based upon the model geometry and expected flow field, the theoretical interference can be reduced for any specific application. This requires, however, significant computing resources and a much more complicated test cell arrangement. The adaptive wall tunnel had to calculate a new CFD-type solution for each angle of attack, changed the wall characteristics, and then acquired the model aerodynamic data after the wall characteristics were set. This made it much less productive than the current continuous sweep test technique used in the transonic test cells at AEDC. In addition, it became accepted that adaptive wall technology would be unable to provide interference-free flow field conditions [35]. The lower test cell productivity, the high cost of retrofitting existing facilities, and the remaining wall interference were enough to justify not employ adaptive walls in the production transonic test cells (4T, 16T) at AEDC. This established the need for computational assessments of the magnitude of wall interference in 16T.

Computational Correction Routines

Global and Incremental Corrections

Computational correction routines for transonic wind tunnel tests can be broadly grouped into two categories, global and incremental corrections [20]. A global correction to transonic wind tunnel data uses measurements from near the wall boundary and tries

to correlate that measurement with a free stream condition that would cause those boundary conditions [4], [20], [36]. This can be very difficult, and is very sensitive to the measured boundary conditions in the wind tunnel [37]. The global corrections are a spiritual descendant of the linear subsonic correction methodologies proposed by AGARD [20].

Incremental correction routines are more common for transonic facilities, since they do not require any additional test cell instrumentation. This routine uses a confined CFD solution of the model, with the proper porous wall boundary condition, and a CFD solution of the model in an unconfined environment. The difference between the two solutions is the interference due to the wind tunnel wall boundary [4]. The incremental wall interference analysis technique was selected for use in the current study.

A Brief History of Transonic Wind Tunnel Wall Correction Methods

The first analytic solutions for perforated wall boundary interference in wind tunnels were presented by Lo and Oliver in 1970 at AEDC [38]. They presented a model based upon the inviscid, irrotational field equation for subsonic flow, and adjusted it for the porous wall boundary condition. In this model, a horseshoe vortex was used as the model for the disturbance potential in the calculation of lift interference [39]. Solid blockage interference was modeled using a three-dimensional doublet, with the strength of the doublet proportional to the volume of the wind tunnel model. Wake blockage interference was modeled with a point source, with the strength of the source held proportional to the value of the wind tunnel drag coefficient [38]. Other than the correction for the wall boundary condition, the methods presented in Lo's report were typical of subsonic wall interference calculations made at the time.

The subsonic corrections were applied to transonic flow by using the linear subsonic theory outlined previously with compressibility effects accounted for by using the Prandtl-Glauert scaling factor [40]. In the mid-1970s AEDC began to apply linear transonic theory to the wall interference problem [40]. This theory still relied upon the assumption that the flow field was inviscid and irrotational. The transonic small perturbation equations were then employed to calculate the blockage interference due to the wind tunnel model in the perforated test section [40].

Soon after linear transonic theory had been investigated at AEDC, research began into using integral equation methods to calculate wall and blockage interference in ventilated transonic tunnels [12]. One of the advantages inherent in using the integral equation method is that it can be applied to the nonlinear transonic integral equations, and then be applied to supercritical flow [12]. The linear transonic equations do not always provide satisfactory simulation of the physics of transonic flow when supercritical flow has appeared on a wind tunnel model [3]. This study demonstrated that applying the integral

equation method to transonic flow was an accurate and efficient method for analyzing wall effects on a two-dimensional, non-lifting airfoil [12].

In the early 1980s, global transonic wind tunnel corrections began to be investigated [41]. Early attempts at global corrections for three-dimensional models corrected the test section Mach number and angle of attack using solutions of the potential equations around simplified representations of test articles [41]. Pressure measurements outside of the wall boundary layer were necessary for utilization of this technique. Since this was an inviscid method, it could not be applied when significant amounts of shock-boundary layer interaction occurred.

AEDC first employed modern computational fluid dynamics to try and correct for transonic wall interference in 1987. During this study, Donnegan and Benek solved the Euler equations using a computation routine with an improved porous boundary simulation of the wind tunnel wall [5]. This was one of the first applications of a Chimera grid mesh routine for wall boundary interference studies. The solutions were in good agreement with the measured wall characteristics, and the pressure distribution trends agreed on the test article surface. One of the shortcomings of this solution methodology was the lack of any simulation of viscous effects, which are what were thought to have caused the discrepancies between the CFD solutions and the wind tunnel data [5].

During this same time frame, engineers at NASA Langley began to modify their aerodynamic analysis code to calculate wall interference at transonic speeds. Instead of using the linear transonic equations or early CFD methods, the researchers at Langley used a small disturbance flow solver with a homogenous boundary condition representative of solid, open, porous, or slotted walls [42]. This code solved a non-conservative form of the transonic small disturbance equations. This derivation was similar to the linear transonic equations employed previously by AEDC, in that it was based upon an approximation of the potential flow equations [42]. This caused the Langley correction routine to have some of the same drawbacks as the AEDC linear transonic routine, namely a lack of fidelity when shock-boundary layer interactions were prevalent.

Further research at AEDC in the late 1980s suggested that for “Group 1” transonic flows (flows that are subcritical) experimental three-dimensional wind tunnel data could be corrected for wall effects using an inviscid methodology [3], [43]. This was another application of the ‘global’ correction type. This research used several inviscid Euler solvers, along with wall boundary conditions measurements from wind tunnel tests, to calculate the magnitude of the wall interference correction necessary to the wind tunnel test data [43]. Once the flow became supercritical, however, viscous effects began to significantly impact the wall interference and the inviscid correction routines performed poorly [3]. It was suggested by Sickles that viscous thin-layer Navier-Stokes (TNS) solutions could be used for efficient calculations of transonic wall interference effects while

taking into account viscosity, such as shock-boundary layer interaction [3], [43]. The TNS solutions were not employed for the Sickles AEDC study due to the high computational load required (for the time period) [43].

In the early 1990s AEDC performed a computational investigation of transonic wall interference on the Space Shuttle Launch Vehicle in 16T. For this study, the AEDC perforated wall boundary condition was incorporated into the NASA Ames Overflow CFD solver to study the impact of wall interference on a 3% scale model [44]. Overflow is a structured grid Navier-Stokes code developed by NASA, which included viscous effects through various turbulence models. This study was an application of the incremental correction routine, where a free air and simulated wind tunnel solutions were calculated and the difference between the two was the interference. Wall interference was greatest for this configuration at the mid-section of the vehicle. Computations were performed with and without the porous wall boundary condition; including the boundary condition improved correlations between the CFD and test data in both pressure distributions and coefficient data [44].

Wall interference assessment and correction research became a lower priority at AEDC in the late 1990s and early 2000s. During this time frame CFD codes were becoming more capable as computer processing power increased exponentially, and wall interference research continued at other facilities. At the German-Dutch wind tunnel DNW-HST, the wall interference models were based entirely upon ENFLOW CFD solutions [45]. Maseland concluded that, “comparisons of sectional pressure distributions obtained in free air and tunnel simulations for the test article showed consistent wall interference effects with increasing model size” [45]. Hashimoto simulated the ONERA M5 model in the JAXA 2x2 m transonic wind tunnel using CFD. His research indicated that increasing grid density while faithfully reproducing the test section geometry brought the computations into good agreement with test data [6].

CHAPTER III
MATERIALS AND METHODOLOGY

Computational Codes and Methods

The USM3Dns unstructured computational fluid dynamics code was applied for this study. USM3Dns is a three-dimensional, unstructured CFD code developed by NASA that employs a tetrahedral cell-centered finite volume Navier-Stokes flow solver [46]. AEDC previously validated a porous wall boundary condition in USM3Dns, so that it could be applied to model porous wall AEDC test cells [47]. The Spalart-Allmaras (S-A) one equation turbulence model was employed to model viscous flow for this study [48]. All solutions were run fully turbulent for both the free-stream and wind tunnel cases. Unstructured grids for USM3Dns were prepared using the Pointwise™ software suite [49]. Tetrahedral cells were extruded off of the model and wind tunnel wall surface grids using the Pointwise ™ T-Rex tool to model the viscous layer.

Models & Geometry

The NASA Common Research Model (CRM) CAD geometry was used as the test article. The CRM was developed and built by NASA in order to create a modern experimental database for CFD code validation [50]. It was a high aspect ratio transport type configuration, with a design cruise Mach number of 0.85 and cruise lift coefficient of 0.5 [50]. In addition, the geometry for the CRM was Distribution A (publically available). These considerations made the CRM a good candidate for a transonic wall interference study. Figure 8 presents a three-view and an isometric view of the baseline semi-span CRM geometry, as used for this study. The standard CRM CAD geometry included flow-through engine nacelles; they were omitted for this study for simplicity. In addition, only the starboard half of the CRM was used for computations to reduce the processing load of running a large CFD grid.

The original CRM CAD geometry was provided in an IGES file at flight scale, thus it had to be scaled to a reasonable wind tunnel model size to be used for the current study. Goethert recommended a model span no larger than 50% of the test section width if quality drag data were desired at transonic speeds [7]. NASA recommends a model span to tunnel width ratio of no larger than 0.5-0.7 for testing at transonic speeds in the Unitary Plan Wind Tunnel [51]. Based upon these recommendations several modified CRM geometries were created, ranging in wind tunnel model scale from three to six percent and ranging in the span to tunnel width ratio from 0.33 to 0.77. Table 1 presents the configuration number for each CRM model investigated, the model scale tested for each configuration, each configuration's reference area (S), wing span (b), mean aerodynamic chord (MAC), aspect ratio (AR), tunnel width to model span ratio (b/w), and model blockage percentage.

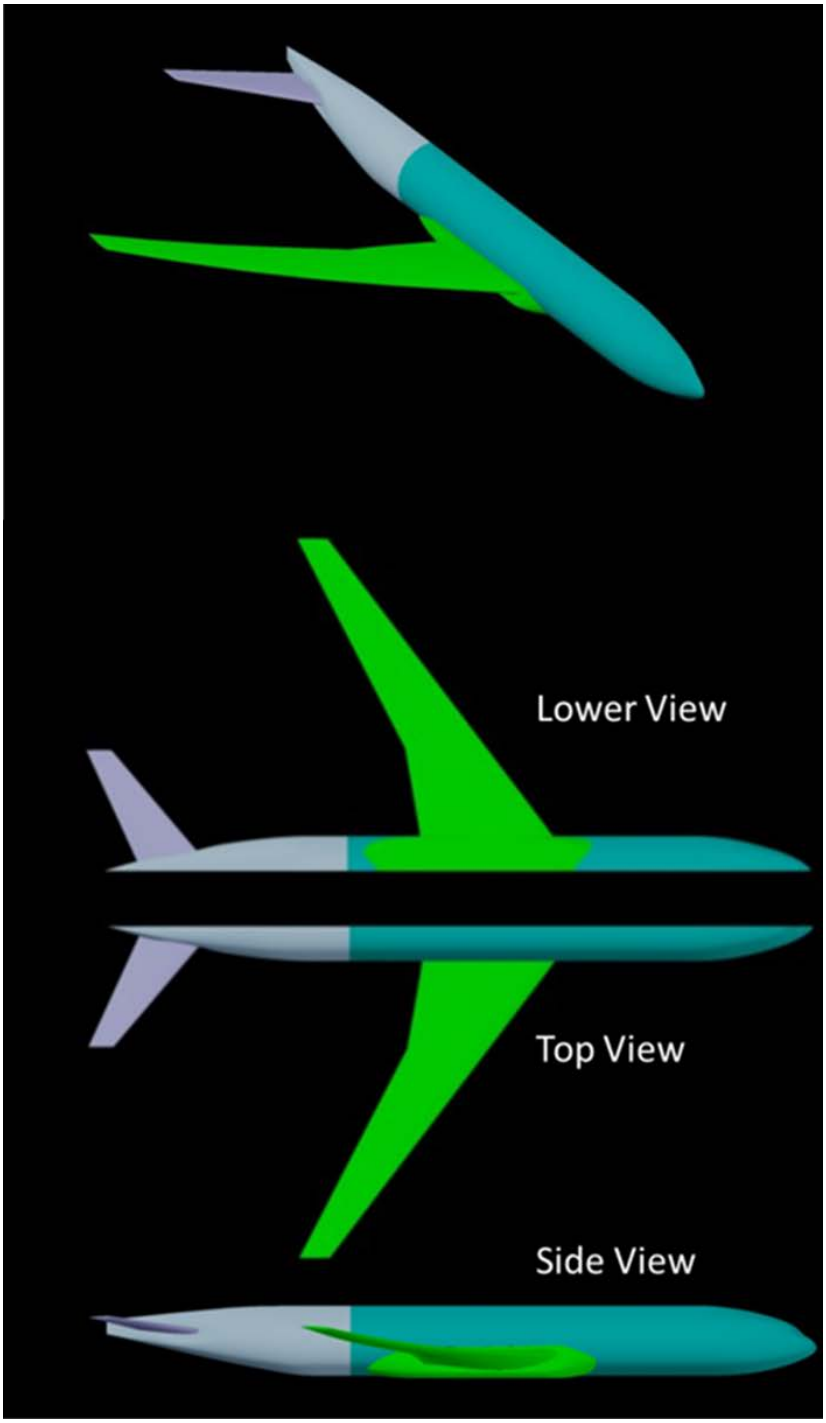

Figure 8. CRM Model Geometry

Table 1. CRM Model Geometries

Configuration	1	2	3	1.1	1.2	2.1	3.1	4
Description	4% CRM model	5% CRM model	6% CRM model	4% CRM model, 10% increased wingspan	4% CRM model, 20% increased wingspan	5% CRM model, 10% increased wingspan	6% CRM model, 10% increased wingspan	3% CRM model
Scale	4.15%	4.98%	5.81%	4.15%	4.15%	4.98%	5.81%	2.70%
S (in^2)	1099.24	1582.91	2154.51	1209.16	1319.09	1741.20	2369.96	465.32
S / 2 (in^2)	549.62	791.45	1077.26	604.58	659.54	870.60	1184.98	232.66
b (in)	96	115.2	134.4	105.6	115.2	126.72	147.84	62.46
b/2 (in)	48	57.6	67.2	52.8	57.6	63.36	73.92	31.23
MAC (in)	13.59	16.31	19.02	13.59	13.59	16.31	19.02	8.84
b/w	0.5	0.6	0.7	0.55	0.6	0.66	0.77	0.33
Blockage, %, α=0	0.63%	0.91%	1.24%	0.68%	0.85%	0.98%	1.33%	0.27%
Blockage, %, α=5	0.71%	1.02%	1.40%	0.84%	0.88%	1.21%	1.64%	0.30%
x_{MRC} (in)*	55.02	66.02	77.03	55.02	55.02	66.02	77.03	35.80
y_{MRC} (in)*	0.00	0.00	0.00	0.00	0.00	0.00	0.00	0.00
z_{MRC} (in)*	7.38	8.86	10.34	7.38	7.38	8.86	10.34	4.80

* The moment reference center was measured in the body axis of the model, positive x aft, positive y span-wise, and positive z upwards. It was measured from a reference point just off the nose of the model.

Initially, AutoCAD was used to scale the provided IGES geometry down to Configuration 1, the 4% CRM model. The 4% geometry was then output as an IGES file and imported into the Pointwise software suite. The geometry at this point existed as a database within the Pointwise software. One of the utilities included in Pointwise was a scaling tool that could be used on databases, and applied in any combination of the three dimensions. The scaling tool was used to scale the 4% geometry to 5%, 6%, and 3% of full scale as Configurations 2, 3, and 4 respectively.

To determine the impact of increased wingspan on wind tunnel wall interference nearly independent of scale, extended wingspan geometry was required. The pointwise scaling utility was employed to extend the wingspan of Configurations 1, 2, and 3. The wingspan was extended by scaling the wing IGES database only in the span-wise plane. This left the root and tip chords of the wing unchanged, but extended the wingspan by the desired amount. Configurations 1.1, 2.1, and 3.1 were versions of Configurations 1, 2, and 3 respectively with their wingspans extended 10%. Configuration 1.2 was Configuration 1 with the wingspan extended 20%.

Figure 9 presents a planform view of the CRM wing with the salient geometric features called out [50]. Equations 1-8 were used to calculate the reference area and mean aerodynamic chord for all models. This approach was used in lieu of simply scaling the reference quantities provided for the CRM in reference [50], so that the calculation of reference areas and MACs for the extended wing configurations was consistent with the linearly scaled configurations. The wing was split for mean aerodynamic chord and reference area calculations at the Yehudi break, which was located at 37% of the semi-span. This made it possible to treat the wing geometry as a combination of two trapezoids, simplifying the reference calculations. The wing reference area was the sum of the two trapezoidal areas, and the mean aerodynamic chord was the weighted average of the mean aerodynamic chord of the two trapezoidal wing sections.

$$\lambda_1 = {c_{break}}/{c_{root}} \quad (1)$$

$$\lambda_2 = {c_{tip}}/{c_{break}} \quad (2)$$

$$\bar{c}_1 = {2}/{3} * c_{root} * \frac{1+\lambda_1+\lambda_1^2}{1+\lambda_1} \quad (3)$$

$$\bar{c}_2 = {2}/{3} * c_{break} * \frac{1+\lambda_2+\lambda_2^2}{1+\lambda_2} \quad (4)$$

$$s_1' = {1}/{2} * (c_{root} + c_{break}) * {b}/{2} * 0.37 \quad (5)$$

$$s_2' = {1}/{2} * (c_{break} + c_{tip}) * {b}/{2} * 0.63 \quad (6)$$

$$s_{ref} = 2 * (s_{\acute{1}} + s_{\acute{2}}) \quad (7)$$

$$\bar{c} = \frac{((\bar{c}_1 * s_{\acute{1}}) + (\bar{c}_2 * s_{\acute{2}}))}{s} \quad (8)$$

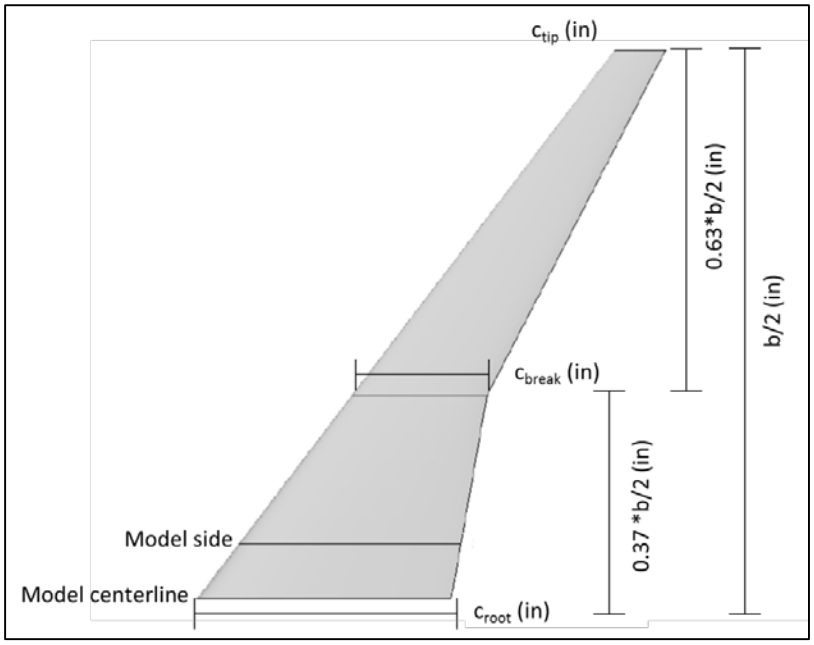

Figure 9. CRM Wing Geometry [50]

Grid Generation

All grid generation was performed in Pointwise. Grid spacing on the model's surface (geometry) was set to 0.1 inches for all configurations. The surface grid spacing for the far-field boundary of the free-stream cases was 10 inches. The far-field boundaries were 580 inches (+/- 5.5 fuselage lengths of Configuration 1) from station 0, just off the nose of the model. The far-field boundary for the free-stream cases was modeled as a hemisphere. The cell width adjacent to the viscous wall was set to a value of 0.000104 for all configurations but Configuration 4, to set an average y+ of 1 or less for these configurations. Configuration 4 used a cell width adjacent to the viscous wall of 0.0000745, to set an average y+ of 1. Pointwise's TREX grid utility was employed to create the viscous layer of cells using the given cell width value, a growth rate of 1.3, the minimum number of cells set to 1, and the maximum number of TREX cells set to 40. After creating the viscous layer cells TREX then finished gridding the volume with isotropic cells. Figure 10 presents an image of a typical free-stream grid for Configuration 1. A

single free-stream grid was created for each configuration, which USM3Dns would then rotate to set angle of attack [46]. To reduce computational workload, all grids were created half-span, with the x-z plane set as the plane of symmetry.

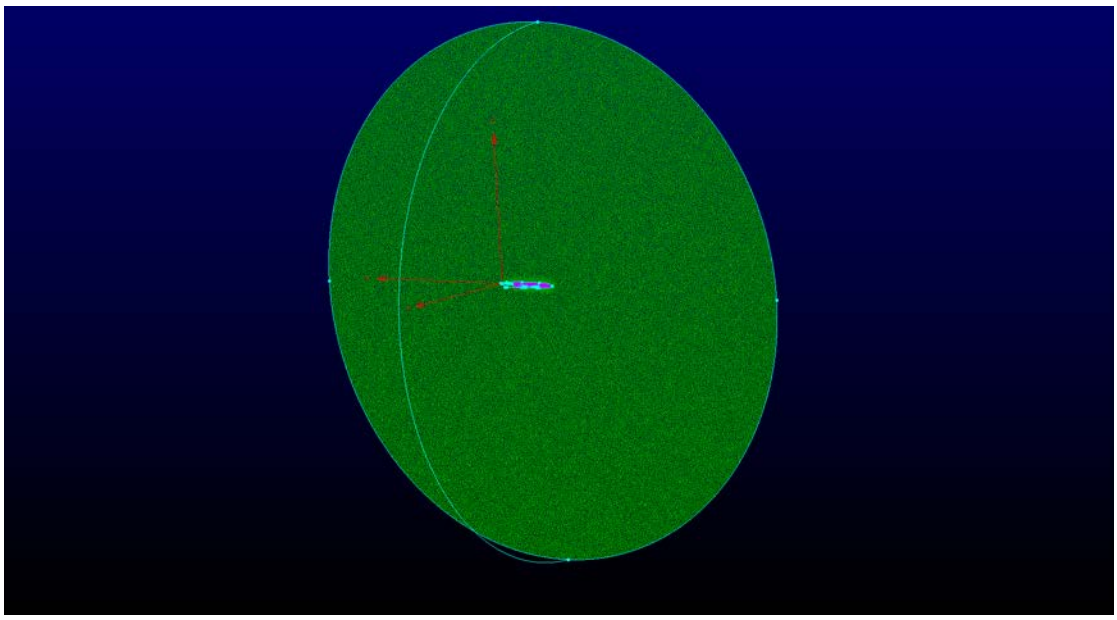

Figure 10. Free-stream Grid for Configuration 1

The wind tunnel simulation grids were built to be mirrored around the symmetry plane, much like the free-stream grids. The 16T test section was simulated as an 8 ft. x 16 ft. x 40 ft. volume. Since the purpose of the study was to evaluate the impact of the test section walls on the test article, no provision was made to model the HAAS strut or a sting assembly. Since the bulge in the aft test section was designed to relieve the blockage of the HAAS strut, it also was not modeled for this study. The wall boundaries of the test section were grid with a stream-wise spacing of 4 inches. The viscous layer for the walls was created using the same settings as the configuration under test, with the cell spacing at the wall set to 0.000104. A unique grid was created for each configuration at each angle of attack tested in the wind tunnel simulation. Figure 11 presents a typical wind tunnel simulation grid for Configuration 1. Average grid sizes were between 70 and 75 million cells for both the free-stream and wind tunnel simulations.

Flow Conditions and USM3Dns Solver Settings

All solutions were run at Mach 0.85 and a unit Reynolds number of 3 million / ft. These conditions were selected because Mach 0.85 is solidly in the transonic speed range while being the design cruise point for the CRM, and a unit Reynolds number of 3 million / ft. is near the center of the 16T test envelope at Mach 0.85 [13], [50]. Total temperature was set to 100 deg F for all solutions, which is typical of 16T at Mach 0.85. Solutions were run every one degree of angle of attack from zero to five degrees. This angle of attack range was chosen for study to bracket the cruise lift coefficient of the CRM of 0.50 and provide a sufficient range of points to identify trends with angle of attack in the wall interference [50]. All solutions were acquired at zero angle of sideslip. USM3Dns required an individual input card for each case run. An example input card for a free-stream case was included as Appendix 1. The input card included provisions for all of the flow solver settings, in addition to the simulation initial conditions and model specific geometry.

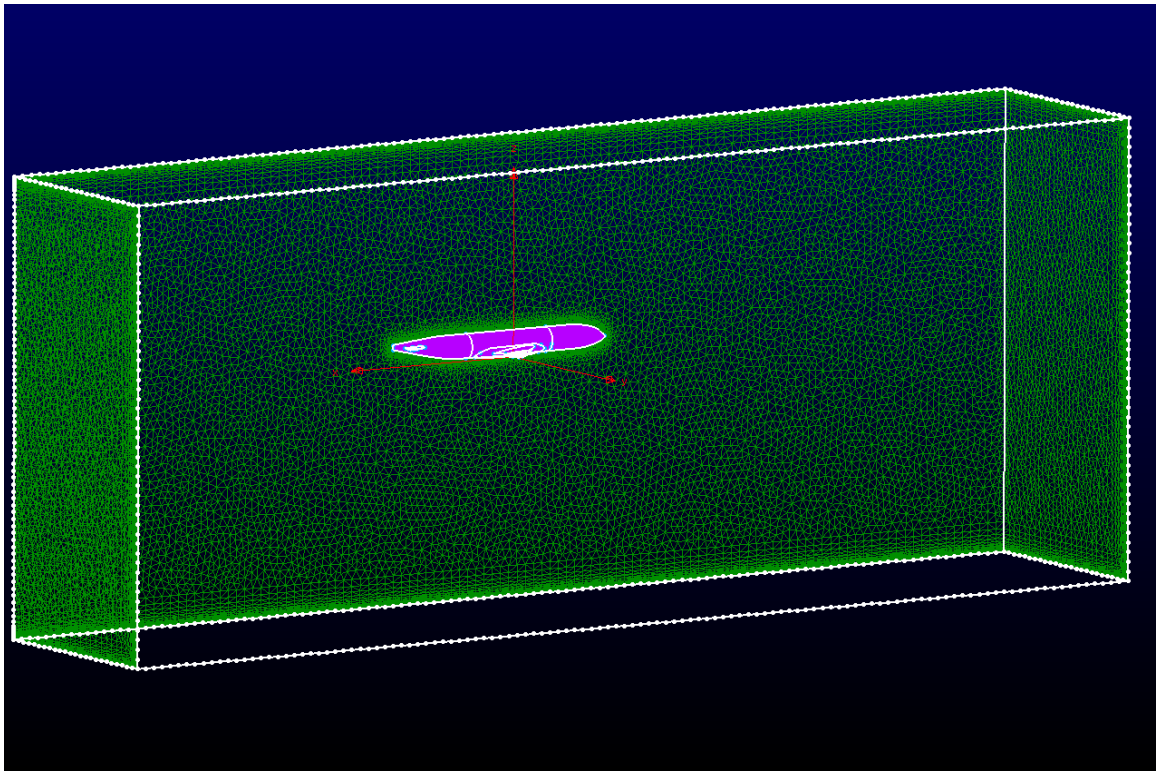

Figure 11. Typical Wind Tunnel Grid for Configuration 1

For the current study USM3Dns was run in steady state mode. For most solver settings, the recommended settings from the USM3Dns user manual were employed [52]. The MINMOD limiter was applied, since supersonic flow was expected to be observed on the upper surface of the wing [52]. Fully viscous solutions were specified with the S-A one equation turbulence model [48], [52]. All solutions were run for 8000 iterations on the Navy DSRC Shepard, which provided sufficient convergence for all cases, as determined from the solution residuals. Shepard is a Cray XC30 supercomputer, rated for 817 TFLOPS [53]. Solution times were on the order of 4 hours per case, with each case run on 480 processors. Figure 12 presents a typical convergence plot for a free-stream case.

USM3Dns Boundary Conditions

The boundary conditions for the free-stream simulation were relatively straightforward. The two halves of the hemisphere were set to characteristic inflow and outflow (boundary condition 3), which was designed for subsonic cases. The CRM model was set to be a viscous surface, so the no-slip boundary condition was applied (USM3Dns boundary condition 4). The tangent flow boundary condition was applied to the symmetry plane. After observing post-processed flow simulation images, it was clear that the using these boundaries on the free-stream cases provided a good simulation of Mach 0.85 flow [52]. This was determined by observing the change in Mach number as the freestream flow approached the model. If the change in Mach number was less than 0.005 outside the zone of influence of the model, the Mach number of the simulation was considered good.

The boundary conditions for the tunnel simulations were, by necessity, more complex than the free-stream cases. For the test section inflow, several boundary conditions were used to set the desired flow conditions. Based upon test volume Mach number distributions, the characteristic inflow boundary condition (BC 3) was selected for all the wind tunnel flow cases. This provided the best flow quality throughout the test section while still providing reasonable viscous forces on the model. The test section exit was modeled with a fixed pressure boundary condition (BC 1002), which was set equal to static pressure for this study. The static pressure was calculated by USM3Dns based upon the input Mach number, Reynolds number, and total temperature. The CRM model was set to be a viscous surface, so the no-slip boundary condition was applied (USM3Dns boundary condition 4). The walls of the wind tunnel test section were modeled using the methods outline in Reference [47], which allowed for modeling porous boundaries without having to grid and model a plenum. The porous boundary condition (BC 2400) required that a porosity and back pressure be set for each porous region. The back pressure and porosity had to be set in both a boundary conditions file and porosity file. Appendix 2 presents a typical wind tunnel test case boundary condition file, and Appendix 3 presents a typical porosity file.

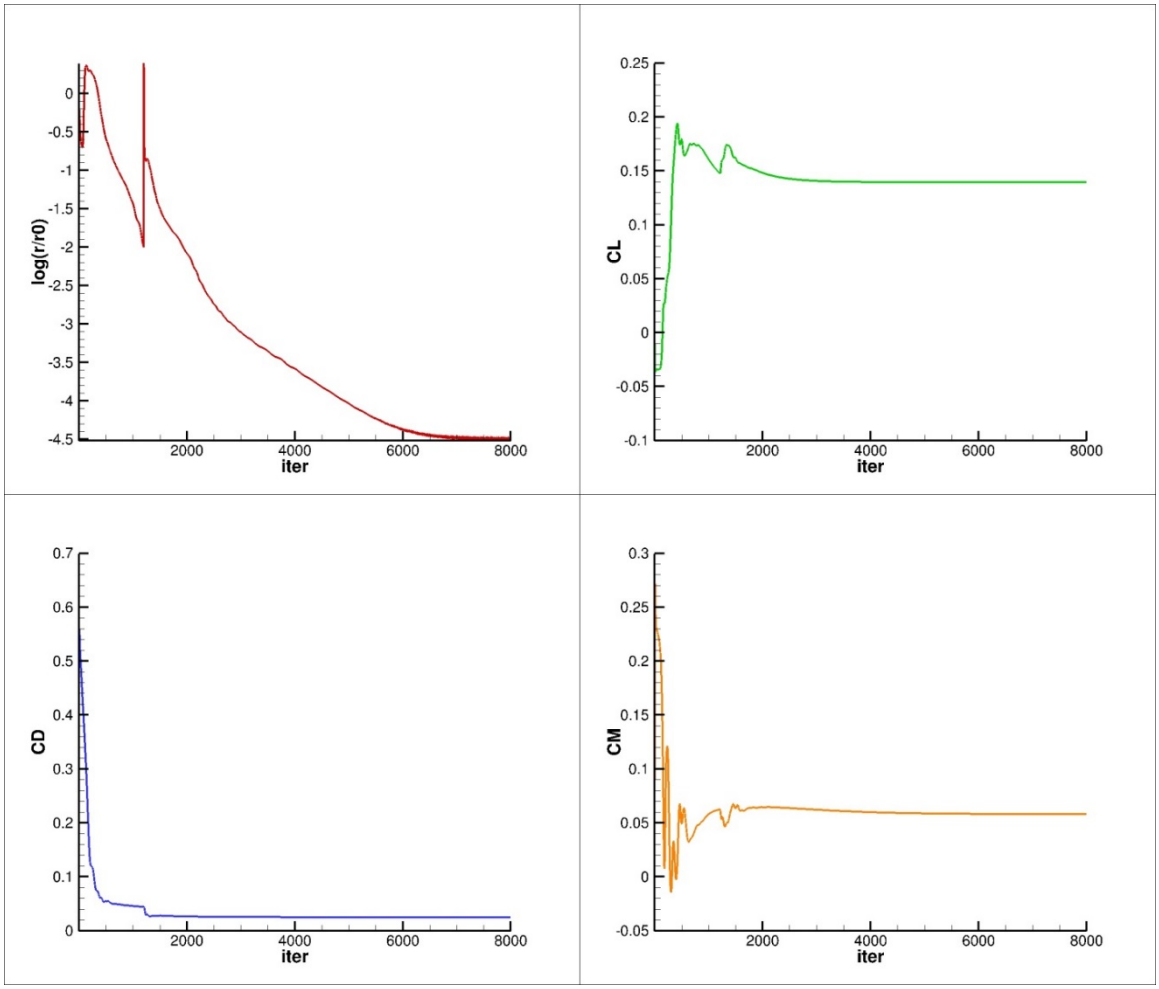

Figure 12. Convergence Plot for Configuration 1, 0 deg Angle of Attack, Free-stream Simulation

Data Reduction and Analysis

USM3Dns includes a module to calculate force and moment coefficient internal to the code. The force and moment coefficients are non-dimensionalised using the input Mach number, reference dimensions, and Reynolds number. The lift, drag, and pitching moment coefficient were analyzed for wall interference in this study. The lift coefficient was studied as a function of angle of attack. The drag and pitching moment coefficients were analyzed as a function of lift coefficient. All force and moment coefficient plots were created using the AEDC developed Datamine software, due the ease with which it could create large numbers of plots [54]. Interference from the tunnel walls was inferred from the difference between the free-stream and tunnel solutions in lift coefficient at fixed angle of attack and in pitching moment and drag coefficient at fixed lift coefficients using Equations 9 - 11.

$$\boldsymbol{D.CL = (CL_{FS} - CL_{T})\ @\alpha} \quad \textbf{(9)}$$

$$\boldsymbol{D.CD = (CD_{FS} - CD_{T_i})\ @CL} \quad \textbf{(10)}$$

$$\boldsymbol{D.CLM = (CLM_{FS} - CLM_{T_i})\ @CL} \quad \textbf{(11)}$$

Some level of interference was expected on the lift coefficient for the tunnel simulation cases. In order to compare the tunnel and free-stream simulations at the same lift coefficient, some form of data interpolation had to be employed. Akima splines were used to interpolate the calculated tunnel simulation pitching moment coefficient and drag coefficient data from the values for the tunnel case to the CFD calculated values of life coefficient from the free-stream simulations [55]. The difference in the drag and pitching moment coefficient between the two simulations was then presented as a function of lift coefficient.

USM3Dns produced a flow field file for every solution. This file contained the grid, x, y, and z coordinates for every cell, the fluid density at every cell, the total energy of every cell, and the three components of momentum at every cell. Tecplot 360™ was used to post-process the USM3Dns flow files and calculate velocity, static pressure, sonic speed, Mach number, and pressure coefficient for the flow field using Equations 12--18.These equations were applied to both the free-stream and wind tunnel simulations. The difference between the pressure coefficients over the model from a free-stream and tunnel simulation at a single angle of attack was calculated using Equation 19.

After calculating the flow parameters, Tecplot™ macros were coded to create ΔCp images overlaid on the model geometry and Cp profiles as a function of the fraction of the local chord length. Equation 20 was used to calculate the fraction of the local chord length. Cp contours were taken at 25%, 50%, 75%, and 95% of the wing semi-span to determine any trends with span location. All Cp contour plots presented both the free-stream and

wind tunnel simulation data. Table 2 presents the wingspan locations pressure profiles were taken at for each configuration. Figure 13 presents an example of the span-wise locations Cp profiles were extracted from for Configuration 1.

$$\gamma = 1.4 \tag{12}$$

$$M_{\infty} = 0.85 \tag{13}$$

$$V = \sqrt{(\rho * u)^2 + (\rho * v)^2 + (\rho * w)^2}/\rho \tag{14}$$

$$P_s = (\gamma - 1) * ((\rho * e) - ((\rho * u)^2 + (\rho * v)^2 + (\rho * w)^2))/(\rho/2) \tag{15}$$

$$a = \sqrt{\gamma * P_s/\rho} \tag{16}$$

$$M = V/a \tag{17}$$

$$C_p = (P_s - 1/\gamma) * (2/M_{\infty}^2) \tag{18}$$

$$\Delta C_p = C_{p_{FS}} - C_{p_T} \tag{19}$$

$$(x/c)_{\frac{y}{b}} = \frac{x_{grid} - (x_{LE})_{\frac{y}{b}}}{(c)_{\frac{y}{b}}} \tag{20}$$

Table 2. Span-wise Locations of Pressure Profile Plots

Config.	25% b/2 (in.)	50% b/2 (in.)	75% b/2 (in.)	95% b/2 (in.)	b/2 (in.)
1	12	24	36	45.6	48
1.1	13.2	26.4	39.6	50.16	52.8
1.2	14.4	28.8	43.2	54.72	57.6
2	14.4	28.8	43.2	54.72	57.6
2.1	15.84	31.68	47.52	60.192	63.36
3	16.8	33.6	50.4	63.84	67.2
3.1	18.48	36.96	55.44	70.224	73.92
4	7.81	15.62	23.42	29.67	31.23

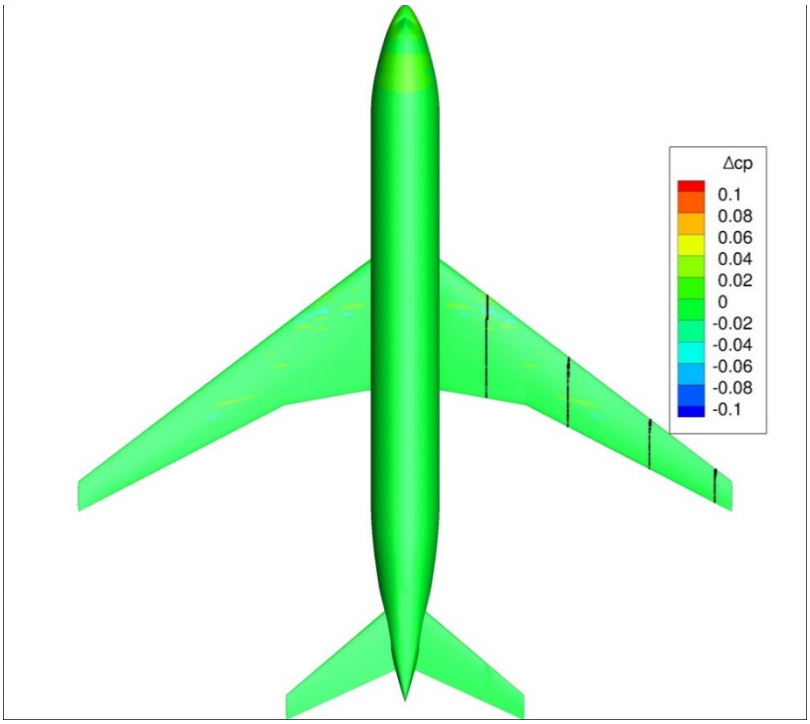

Figure 13. Pressure Profile Plot Span-wise Locations for Configuration 1

Sensitivity of Solutions to Inlet Boundary Conditions

The wind tunnel simulation cases proved to be extremely sensitive to the test section inlet boundary condition. Initially, the jet boundary condition was used to model the test section inlet, based upon the recommendations of USM3Dns users at AEDC. For this boundary condition the free-stream pressure ratio, temperature ratio, and specific heat ratio were set in the input card. Figure 14 presents the Mach number distribution down the symmetry plane of the tunnel for a Configuration 1 case where the jet boundary condition (BC 101) was employed for the inflow plane. The Mach number distribution down the length of the tunnel was very good. Figure 15 presents the difference in the viscous and total drag coefficient between a free-stream and tunnel simulation for the 4% model. The majority of the difference between the two cases was due to the viscous forces from the wind tunnel simulation. This seemed unrealistic, since the Reynolds numbers set in the free-stream and wind tunnel simulations were the same at 3 million / ft. Since the point of the study was to infer wall interference from the difference between free-stream and wind tunnel simulations, this was not an acceptable result.

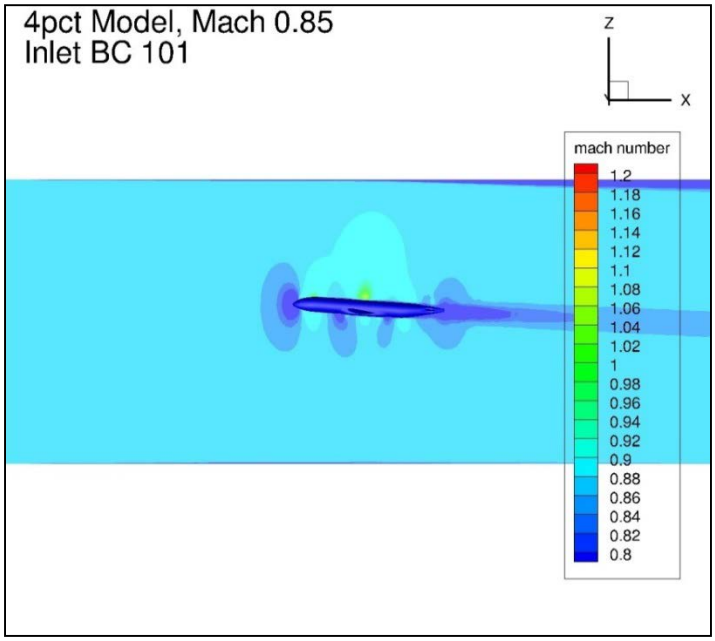

Figure 14. Configuration 1 Symmetry Plane Mach Number Distribution, 4 deg Angle of Attack, Inlet BC 101, Tunnel Simulation

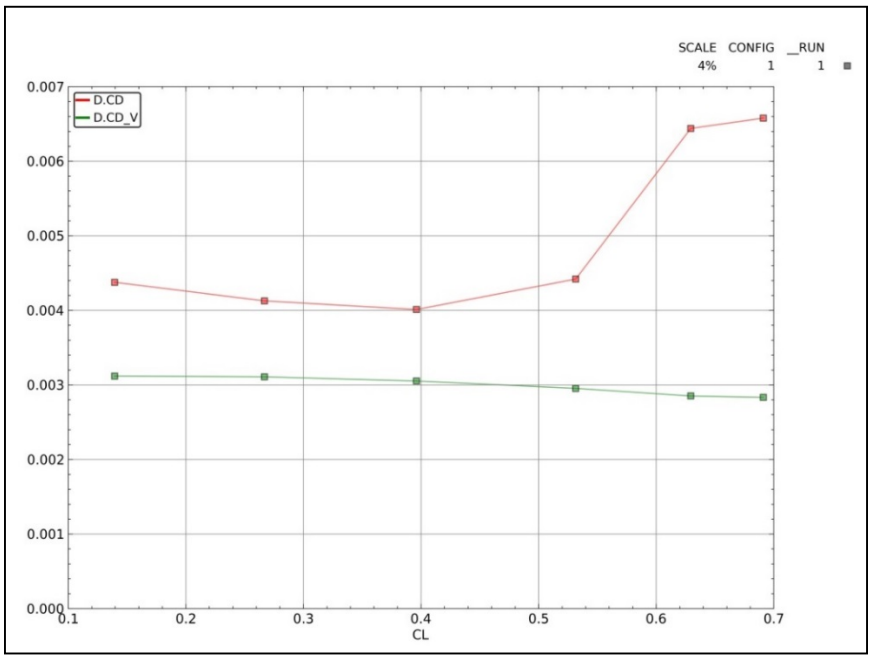

Figure 15. Difference in Viscous and Total Drag Coefficient Between Free-stream and Tunnel Simulations for Configuration 1, Inlet BC 101

After conferring with other USM3Dns users at AEDC about the viscous forces problem, it was recommended that the special inflow boundary condition (BC 1001) be used. BC 1001 was developed to be an inflow condition for internal flow problems, and as such was suggested for some wind tunnel simulations [52]. It enforces a constant free-stream entropy and total pressure while extrapolating velocity from downstream to set the static pressure at the boundary. After re-running all the tunnel simulations with BC 1001 as the inflow boundary condition, problems were noted with some of the solutions. Figure 16 presents the symmetry plane Mach number distribution for all six angles of attack for Configuration 2.1 tunnel simulations with BC 1001 as the inlet boundary. Note the streams of low Mach number extending from the nose of the model upstream to the inlet boundary at several angles of attack. These streams of low Mach and high pressure ended up causing major differences in the force and moment coefficients due to the uneven Mach number distribution throughout the test volume. This also was not acceptable for the current study, since it would not be possible to separate the impact of the wind tunnel walls from the uneven Mach number distribution for the limited number of cases where the low Mach regions existed.

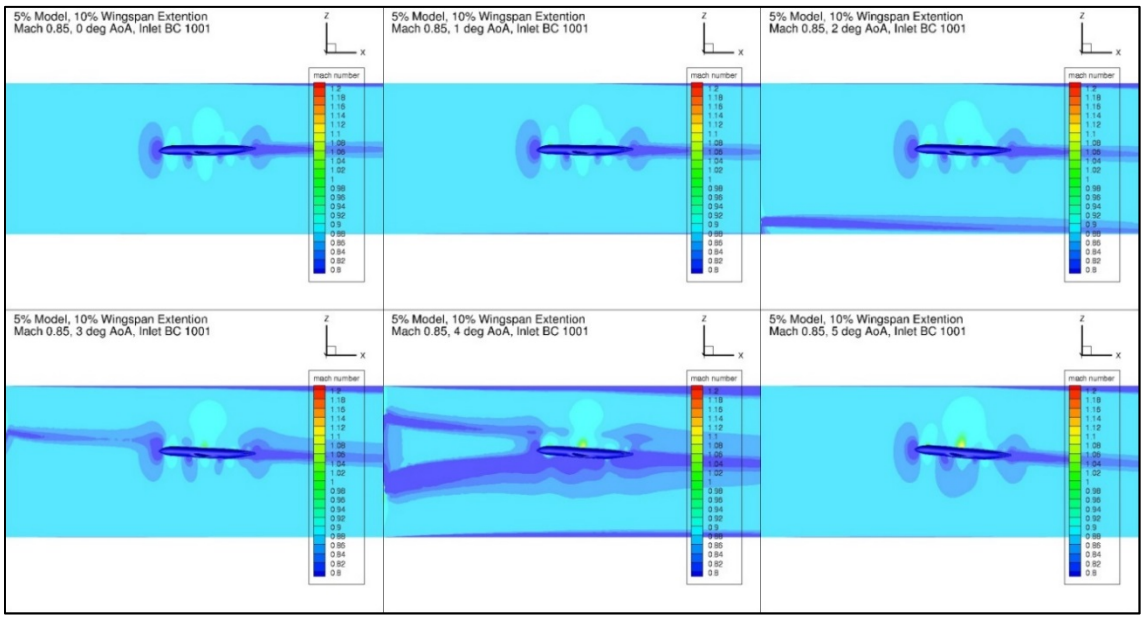

Figure 16. Configuration 2.1 Symmetry Plane Mach Number Distribution, Inflow BC 1001, Tunnel Simulation

After viewing the results from BC 1001, it became apparent that another solution was required for the inlet boundary on the tunnel cases. Two addition boundary conditions

were investigated. A subset of the wind tunnel simulation cases were run with the inlet boundary set to BC 0 and BC 3. Boundary condition 0 enforces free-stream conditions on the inflow boundary based upon the input Mach number, angle of attack, and angle of sideslip [52]. It was recommended for use on supersonic inflow cases. Boundary condition 3 is the characteristic inflow boundary discussed earlier. Configuration 1 and Configuration 3.1 were selected for this subset study, Configuration 1 to give a small model baseline and Configuration 3.1 since most of the errors observed in the BC 1001 runs occurred on the larger models (Configurations 2.1 and 3.1). Figures Figure 17 and Figure 18 present symmetry plane Mach number distributions from all four inlet BCs for Configuration 1 and Configuration 3.1 at 4 degrees angle of attack. Numerically, the force and moment coefficient results from BC 0 and BC 3 were identical. However, at 4 degrees angle of attack both configurations had a small spot at the inlet of high Mach number flow followed by a shock for BC 0. This seemed to be a local phenomenon, and did not propagate downstream for any of the test cases it was observed in. Out of an abundance of caution, BC 3 was selected as the final inlet BC for the wind tunnel simulations, due to its uniform Mach number distribution throughout the test volume and reasonable viscous force and moment coefficient values.

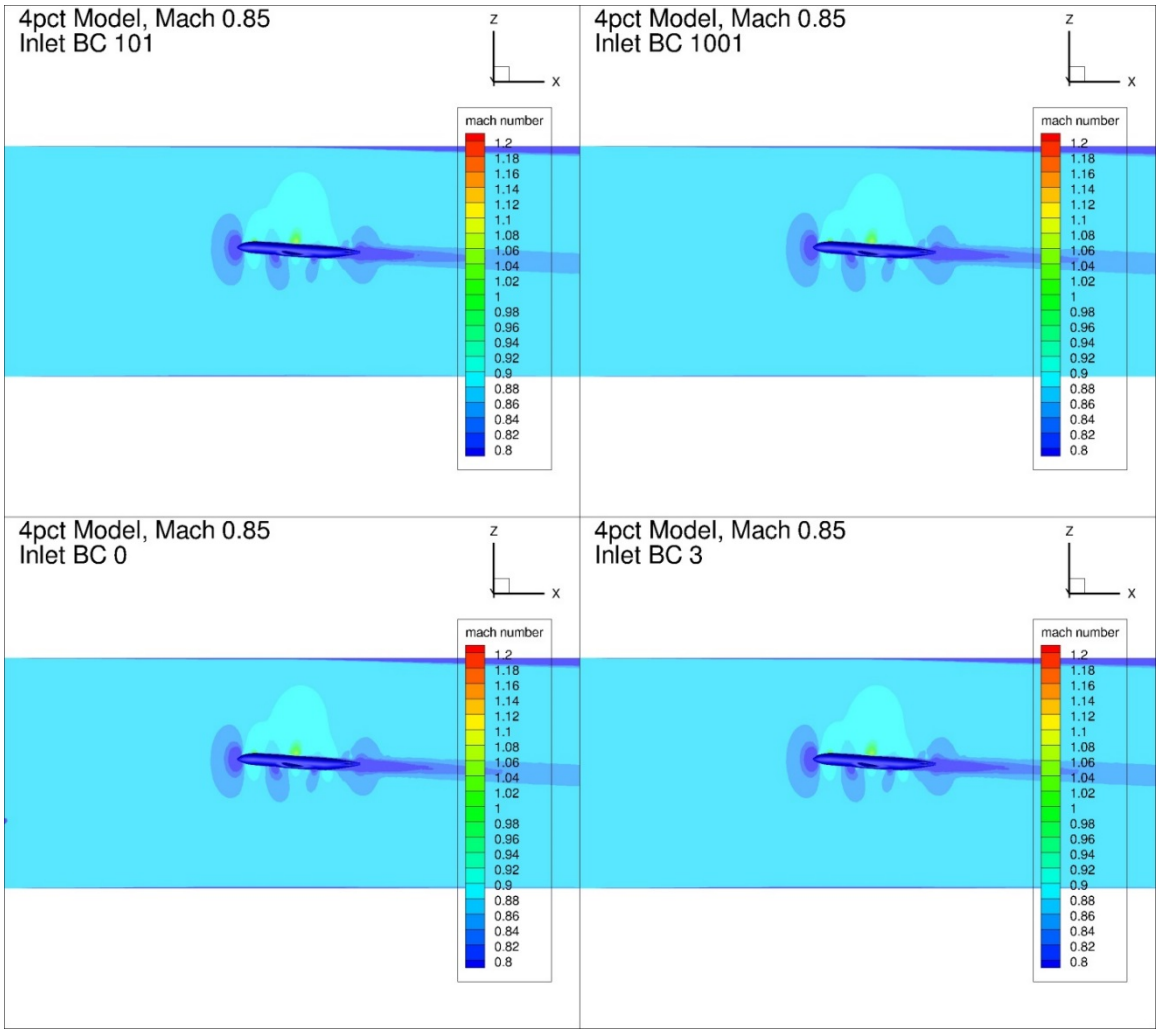

Figure 17. Effect of Inflow BC on Symmetry Plane Mach Number Distribution for Configuration 1, 4 degrees Angle of Attack, Tunnel Simulation

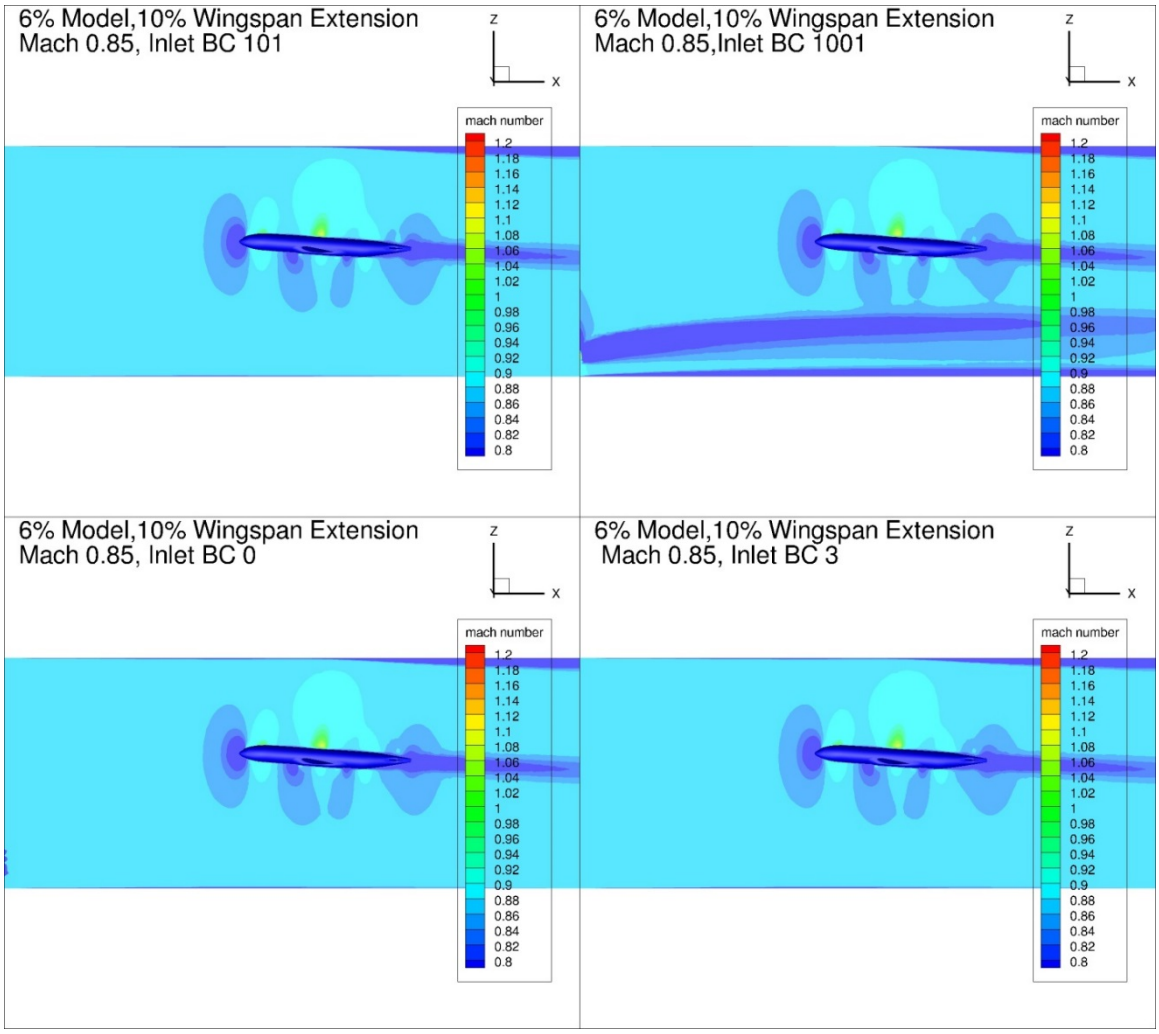

Figure 18. Effect of Inflow BC on Symmetry Plane Mach Number Distribution for Configuration 3.1, 4 degrees Angle of Attack, Tunnel Simulation

CHAPTER IV
RESULTS, DISCUSSION, AND CONCLUSIONS

4% Model with 0%, 10%, and 20% Wingspan Extensions (Configurations 1, 1.1, and 1.2)

Figure 22 in Appendix 4 presents the lift coefficient and the lift coefficient difference between the free-stream and tunnel simulations as a function of angle of attack for all 4% scale configurations. All of the tunnel simulations had a lower lift coefficient as a function of angle of attack when compared against the corresponding free-stream case. For angles of attack lower than 3 degrees, increased wingspan corresponded with higher lift coefficient interference as a function of angle of attack. This trend reversed at 3 degrees angle of attack and above.

Figure 23 – Figure 25 in Appendix 4 present the total and viscous pitching moment and drag coefficient as a function of lift coefficient for Configurations 1, 1.1, and 1.2, respectively. Figure 26 presents the difference between the free-stream and tunnel simulation for the pitching moment and drag coefficient as a function of the lift coefficient for all three configurations. The difference between the tunnel and free-stream simulations in the viscous pitching moment and drag coefficients was very small for all three configurations. The difference in the viscous drag and pitching moment coefficients was less than one count (CD/CLM = 0.0001) across the entire angle of attack range. In addition, the differences between the viscous pitching moment coefficients was two orders of magnitude lower than the difference in the total pitching moment coefficient for all configurations. Increasing model wing span for the 4% model seemed to cause an increase in the pitching moment coefficient interference above a lift coefficient of 0.5. Below CL = 0.5, the interference in the pitching moment coefficient was nearly equivalent between all three 4% models. The difference in the drag coefficient between the wind tunnel and free-stream simulations was within +/- 7 counts across the lift coefficient range investigated. Near the cruise lift coefficient of 0.5, the difference in the drag coefficient between simulations was within +/- 5 drag counts for all the 4% configurations.

Figure 44 and Figure 56 in Appendix 5 present typical ΔCp plots for Configuration 1 at 0 and 4 degrees angle of attack, respectively. Figure 42-- Figure 95 in Appendix 5 present the change in pressure coefficient over the model between the free-stream and tunnel simulations for Configurations 1, 1.1, and 1.2. In general, lower angles of attack exhibited much smaller differences between the free-stream and tunnel simulations in pressure coefficient. As angle of attack increased, large differences (>0.1 ΔCp) were observed between the two solutions. This was most likely the cause of the increasing difference in pitching moment coefficient between the two solutions as the lift coefficient increased. The shift in the pressure coefficient over the wing was likely due to a shift in

the shock location on the upper surface of the wing. These conclusions agree with the experimental observations and conclusions of Refs [25] and [56].

Figure 186 and Figure 190 present pressure profile plots of the Configuration 1 CRM wing at four span-wise locations for both the free-stream and wind tunnel simulations at 0 and 4 degrees angle of attack, respectively. Data are presented for 25%, 50%, 75%, and 95% of the wingspan for each configuration. Figure 186 - Figure 203 in Appendix 6 present the pressure profile plots for all the 4% configurations investigated. The wind tunnel simulation had a lower suction peak and overall lower suction as a function of x/c than the Free-stream case at 4 deg angle of attack. This held true for all of the 4% configurations above 2 degrees angle of attack. At lower angles of attack the free-stream and wind tunnel simulations agreed fairly well at the four span-wise stations investigated for the 4% configurations.

5% Model with 0% and 10% Wingspan Extensions (Configurations 2 and 2.1)

Figure 27 in Appendix 4 presents the lift coefficient and the lift coefficient difference between the free-stream and tunnel simulations as a function of angle of attack for the 5% scale model with 0% and 10% wingspan extensions (Configuration 2 and Configuration 2.1). All of the tunnel simulations had a lower lift coefficient as a function of angle of attack when compared against the corresponding free-stream case. For angles of attack lower than 3 degrees, increased wingspan corresponded with higher lift coefficient interference as a function of angle of attack. This trend reversed at 3 degrees angle of attack and above. These results were similar to those of the 4% configurations.

Figure 28 and Figure 29 in Appendix 4 present the total and viscous pitching moment and drag coefficient as a function of lift coefficient for the tunnel and free-stream simulations of Configurations 2 and 2.1, respectively. Figure 30 presents the difference between the free-stream and tunnel simulation for the pitching moment and drag coefficient as a function of the lift coefficient. The difference between the tunnel and free-stream simulations in the viscous pitching moment and drag coefficients was very small for both configurations. The difference in the viscous drag and pitching moment coefficients was less than one count (CD/CLM = 0.0001) across the entire angle of attack range. This was expected with both the tunnel and free-stream simulations being run at the same Reynolds number. In addition, the differences between the viscous pitching moment coefficients was two orders of magnitude lower than the difference in the total pitching moment coefficient for all configurations. Increasing model wing span for the 5% model did not cause a consistent change in the pitching moment coefficient interference observed. The difference in the drag coefficient between the wind tunnel and free-stream simulations was within +5/-10 counts across the lift coefficient range investigated.

Figure 98 and Figure 110 of Appendix 5 present typical ΔCp plots for Configuration 2 at 0 and 4 degrees angle of attack, respectively. Figure 96 - Figure 131 in Appendix 5 present the change in pressure coefficient over the model between the free-stream and tunnel simulations for Configurations 2 and 2.1 for all conditions investigated In general, lower angles of attack exhibited much smaller differences between the free-stream and tunnel simulations in pressure coefficient. As angle of attack increased, large differences (>0.1 ΔCp) were observed between the two solutions. This was most likely the cause of the increasing difference in pitching moment coefficient between the two solutions as the lift coefficient increased. The shift in the pressure coefficient over the wing was likely due to a shift in the shock location on the upper surface of the wing. These conclusions agree with the experimental observations and conclusions of Refs [25] and [56].

Figure 204 and Figure 208 in Appendix 6 present pressure profile plots of the Configuration 2 CRM wing at four span-wise locations for both the free-stream and wind tunnel simulations at 0 and 4 degrees angle of attack, respectively. Data are presented for 25%, 50%, 75%, and 95% of the wingspan for each configuration. Figure 204 - Figure 215 in Appendix 6 present the pressure profile plots for all the 5% configurations investigated. The wind tunnel simulation had a lower suction peak and overall lower suction as a function of x/c than the free-stream case at both 0 and 4 deg angle of attack. This held true for all of the 5% configurations at all angles of attack. The magnitude of the difference between the two solutions grew as angle of attack, and thereby lift coefficient, increased.

6% Model with 0% and 10% Wingspan Extensions (Configurations 3 and 3.1)

Figure 31 presents the lift coefficient and the lift coefficient difference between the free-stream and tunnel simulations as a function of angle of attack for the 6% scale model with 0% and 10% wingspan extensions (Configuration 3 and Configuration 3.1). All of the tunnel simulations had a lower lift coefficient as a function of angle of attack when compared against the corresponding free-stream case. For angles of attack lower than 3 degrees, increased wingspan corresponded with higher lift coefficient interference as a function of angle of attack. This trend reversed at 3 degrees angle of attack and above. These results were similar to those of the 4% and 5% configurations.

Figure 32 and Figure 33 present the total and viscous pitching moment and drag coefficient as a function of lift coefficient for the tunnel and free-stream simulations of Configurations 3 and 3.1, respectively. Figure 34 presents the difference between the free-stream and tunnel simulation for the pitching moment and drag coefficient as a function of the lift coefficient. The difference between the tunnel and free-stream simulations in the viscous pitching moment and drag coefficients was very small for both configurations. The difference in the viscous drag and pitching moment coefficients was less than one count (CD/CLM = 0.0001) across the entire angle of attack range. This was

expected with both the tunnel and free-stream simulations being run at the same Reynolds number. In addition, the differences between the viscous pitching moment coefficients was two orders of magnitude lower than the difference in the total pitching moment coefficient for all configurations. Increasing model wing span for the 6% model did not cause a consistent change in the pitching moment coefficient interference observed. The difference in the drag coefficient between the wind tunnel and free-stream simulations was within +/- 7 counts across the lift coefficient range investigated.

Figure 134 and Figure 146 in Appendix 5 present typical ΔCp plots for Configuration 3 at 0 and 4 degrees angle of attack, respectively. Figure 132 - Figure 167 in Appendix 5 present the change in pressure coefficient over the model between the free-stream and tunnel simulations for Configurations 3 and 3.1 for all conditions investigated In general, lower angles of attack exhibited much smaller differences between the free-stream and tunnel simulations in pressure coefficient. As angle of attack increased, large differences (>0.1 ΔCp) were observed between the two solutions. This was most likely the cause of the increasing difference in pitching moment coefficient between the two solutions as the lift coefficient increased. The shift in the pressure coefficient over the wing was likely due to a shift in the shock location on the upper surface of the wing. These conclusions agree with the experimental observations and conclusions of Refs [25] and [56].

Figure 216 and Figure 220 in Appendix 6 present pressure profile plots of the Configuration 3 CRM wing at four span-wise locations for both the free-stream and wind tunnel simulations at 0 and 4 degrees angle of attack, respectively. Data are presented for 25%, 50%, 75%, and 95% of the wingspan for each configuration. Figure 216 - Figure 227 in Appendix 6 present the pressure profile plots for all the 6% configurations investigated. The wind tunnel simulation had a lower suction peak and overall lower suction as a function of x/c than the free-stream case at both 0 and 4 deg angle of attack. This held true for all of the 6% configurations at all angles of attack. The magnitude of the difference between the two solutions grew as angle of attack, and thereby lift coefficient, increased.

3% Model, Configuration 4

Figure 35 in Appendix 4 presents the lift coefficient and the lift coefficient difference between the free-stream and tunnel simulations as a function of angle of attack for Configuration 4. All of the tunnel simulations had a lower lift coefficient as a function of angle of attack when compared against the corresponding free-stream case. These results were similar to those of all other configurations studied, however Configuration 4 demonstrated the smallest lift interference of any configuration.

Figure 36 presents the total and viscous pitching moment and drag coefficient as a function of lift coefficient for the tunnel and free-stream simulations of Configurations 4. Figure 37 presents the difference between the free-stream and tunnel simulation for the pitching moment and drag coefficient as a function of the lift coefficient. The difference between the tunnel and free-stream simulations in the viscous pitching moment and drag coefficients was very small for this configuration. The difference in the viscous drag and pitching moment coefficients was less than one count (CD/CLM = 0.0001) across the entire angle of attack range. This was expected with both the tunnel and free-stream simulations being run at the same Reynolds number. In addition, the differences between the viscous pitching moment coefficients was two orders of magnitude lower than the difference in the total pitching moment coefficient for all configurations.

The difference in the drag coefficient between the wind tunnel and free-stream simulations was much larger than any other configuration studied. At this time, no explanation has been found as to why the tunnel drag coefficient was significantly lower than the free-stream simulation. The difference between the two solutions decreased as lift coefficient increased. This would indicate a difference in the zero lift drag coefficient. Since the difference in the viscous portion of the drag coefficient was very small, this leads to the conclusion that the pressure portion of the zero lift drag coefficient may be the cause of the difference.

Figure 170 and Figure 183 in Appendix 5 present typical ΔCp plots for Configuration 4 at 0 and 4 degrees angle of attack, respectively. Figure 168 - Figure 185 in Appendix 5 present the change in pressure coefficient over the model between the free-stream and tunnel simulations for Configuration 4 for all conditions investigated In general, Configuration 4 at all angles of attack exhibited much smaller differences between the free-stream and tunnel simulations in pressure coefficient than the other configurations tested. As the smallest model, it was expected that the amount of pressure interference due to the tunnel boundaries would be smaller than the other configurations tested. The observed differences between the free-stream and wind tunnel simulations did not seem to be large enough to cause the differences noted in the drag coefficient data.

Figure 228 and Figure 232 in Appendix 6 present pressure profile plots of the Configuration 4 CRM wing at four span-wise locations for both the free-stream and wind tunnel simulations at 0 and 4 degrees angle of attack, respectively. Data are presented for 25%, 50%, 75%, and 95% of the wingspan for each configuration. Figure 228 - Figure 233 in Appendix 6 present the pressure profile plots for all the 3% configurations investigated. The two simulations had nearly identical pressure profiles at 0 degrees angle of attack. The wind tunnel simulation had a lower suction peak and overall lower suction as a function of x/c than the free-stream case at 4 degrees angle of attack. The differences between the two solutions were much smaller than the differences observed for the larger

configurations. The magnitude of the difference between the two 3% model solutions grew as angle of attack, and thereby lift coefficient, increased.

Impact of Model Scale and Wingspan on Wall Interference

Figure 38 in Appendix 4 presents the lift coefficient and change in lift coefficient between free-stream and tunnel simulations for Configurations 1, 2, 3, and 4. These were the baseline configurations, without any wingspan extension. The first trend that became immediately obvious was the dependence of the lift coefficient interference on the scale, and thereby blockage, of the model. As would seem intuitive, increased model scale corresponded directly with an increased magnitude of lift coefficient interference. The increase seemed to be nearly linear as a function of model blockage.

Figure 39 presents the change in total and viscous pitching moment and drag coefficient between the free-stream and wind tunnel simulations as a function of lift coefficient for Configurations 1, 2, 3, and 4. As presented in previous sections, the differences between the free-stream and tunnel simulations in the viscous components of the pitching moment coefficient and drag coefficient for all configurations was very small. The interference in the pitching moment increased as scale increased, but it was not as linear as the lift coefficient interference. There was no clear trend in the total drag coefficient interference between model scales.

Figure 22, Figure 27, and Figure 31 presented the impact of increasing the wingspan on the observed lift coefficient interference for Configurations 1, 2, and 3 respectively. Generally, increasing the wingspan increased the lift coefficient interference for the lower portion of the angle of attack envelope, and decreased the observed lift coefficient interference for the higher angles of attack studied when compared against the baseline cases. This may be an effect of the decreased leading edge wing sweep caused by scaling the wingspan only in one dimension.

Figure 26, Figure 30, and Figure 34 presented the impact of increasing the wingspan on the difference between the free-stream and wind tunnel simulation viscous and total pitching moment coefficients and viscous and total drag coefficients. There was no discernible trend with increased wingspan and wall interference in the drag coefficient or the pitching moment coefficient. This held true for all the configurations studied.

Figure 40 presents the lift coefficient and the lift coefficient difference between the free-stream and tunnel simulations as a function of angle of attack for all the configurations investigated. The most important conclusion drawn from this figure is that the wingspan extensions had a much smaller impact on the lift coefficient interference than the model scale and blockage. Figure 41 presents the differences between the free-stream and wind tunnel simulations in the viscous and total pitching moment and drag coefficients for all the configurations studied. The differences in the pitching moment coefficient, much like

the lift coefficient, were much more dependent upon model scale than upon wingspan. There were no readily apparent trends in the drag coefficient interference between model scales and wingspans.

CHAPTER V
RECOMMENDATIONS FOR FUTURE WORK AND SUMMARY OF CONCLUSIONS

Limitations of Current Study and Plans for Future Work

There were several limitations to the current study. First, there was no wind tunnel data from the CRM in 16T to validate the wind tunnel simulations. Changes in testing standards should await a case study with a validation data set. Next, only a single Mach number and Reynolds number were analyzed. For a complete transonic wall interference program, a much larger portion of the testing envelope should be studied. While studying a larger portion of the test envelope, sideslip cases should also be addressed. The current study only used zero angle of sideslip to take advantage of model and test section symmetry to lower the required computational load. In addition, the current study did not model the entire test cell; only the test section was modeled. To get a better understand of wall interference in the test section, the wind tunnel nozzle through the end of the test section should be simulated to better model the boundary layer height at the test section entrance.

There are plans to address most of the current study's limitations in follow-on studies. The study is going to be re-run using a large scale model previously tested in 16T. By necessity, this follow-on study would also include the model sting, HAAS strut, and test section bulge to properly stimulate the test article flow field. In addition, several transonic Mach number / Reynolds number combinations will be investigated at various angles of attack and sideslip. Both wings-level-yaw and pitch-roll sideslip combinations will be studied in a separate investigation. Another follow on study would also model the test section from the nozzle through the aft end of the test section, to determine the solution sensitivity to test section inlet boundary layer thickness. While the current study only used USM3Dns, it has been proposed to recreate the study using NASA's OVERFLOW structured CFD solver and DoD HPCMO's KESTREL CFD code. This would provide a larger database of wall interference results to investigate, and would allow for an evaluation of the available CFD codes to determine which one was best suited for studying wall interference. Additionally, USM3Dns offers an option in free-stream cases to set a desired lift coefficient and the solver will iterate until it converges on that lift coefficient [52]. It would be desirable to re-run this study setting $CL_{FS} = CL_T$. This should provide more accurate results than interpolating calculated drag and pitching moment coefficient data as a function of the lift coefficient from the free-stream case to the measured lift coefficient of the wind tunnel simulation.

Summary

A computational parametric study was performed using NASA's USM3Dns CFD code to determine the impact of wingspan and model scale on transonic wind tunnel wall interference at Mach 0.85 and a unit Reynolds number of 3 million / ft. The NASA Common Research Model was used as the test article, and a simplified model of the AEDC Propulsion Wind Tunnel 16T test section was used as the test facility. Force and moment coefficients, pressure profile plots, and pressure contour plots were post-processed from CFD solutions to evaluate the difference between free-stream and wind tunnel simulations at six angles of attack. Models were created at 3%, 4%, 5%, and 6% of full scale based upon wind tunnel model sizing criteria. Additional models were created with extended wingspans for the 4%, 5% and 6% models to evaluate the impact of wingspan on wall interference. Model blockage ranged from 0.27 – 1.64%. Overall, the scale of the model, and therefore the blockage, had the largest impact on the inferred transonic wall interference for both the lift and pitching moment coefficient. No model size was free of wall interference.

LIST OF REFERENCES

[1] AEDC Public Affairs Office, "AEDC Fact Sheet," 1 July 2012. [Online]. Available: http://www.arnold.af.mil/library/factsheets/factsheet.asp?id=12977. [Accessed 23 February 2015].

[2] E. M. Kraft, A. Ritter and M. L. Laster, "Advances at AEDC in Treating Transonic Wind Tunnel Wall Interference," in *International Council of the Aeronautical Sciences*, London, United Kingdom, 1986. ICAS-86-1.6.1

[3] W. L. Sickles and J. C. Erickson, Jr., "Evaluation of Wall Interference Assessment and Correction Techniques," Arnold Engineering Development Center, Arnold AFB, TN, 1988. AEDC TR-87-45

[4] Advisory Group for Aerospace Research & Development, "Wind Tunnel Wall Corrections," North Atlantic Treaty Organization, Neuilly-Sur-Seine Cedex, France, 1998. AGARD-AG-336

[5] T. L. Donegan, J. A. Benek and J. C. Erickson, "Calculation of Transonic Wall Interference," American Institute of Aeronautics and Astronautics, New York, NY, 1987. AIAA 87-1432

[6] A. Hashimoto, A. Takashi, K. Masataka and K. Yamamoto, "Transonic Wind Tunnel Simulation with Porous Wall and Support Devices," American Institute of Aeronautics and Astronautics, Reston, VA, 2010. AIAA 2010-4201

[7] B. H. Goethert, Transonic Wind Tunnel Testing, Mineola, New York: Dover Publications, Inc, 2007.

[8] B. B. Estabrooks, "Wall-Interference Effects on Axisymmetric Bodies in Transonic Wind Tunnels with Perforated Wall Test Sections," Arnold Engineering Development Center, Arnold AFB, TN, 1959. AEDC-TR-59-12

[9] M. Pindzola and W. L. Chew, "A Summary of Perforated Wall Wind Tunnel Studies at the Arnold Engineering Development Center," Arnold Engineering Development Center, Arnold AFB, TN, 1960. AEDC TR-60-9

[10] U.S. Air Force, "B-2 Spirit Fact Sheet," June 2014. [Online]. Available: http://www.af.mil/AboutUs/FactSheets/Display/tabid/224/Article/104482/b-2-spirit.aspx. [Accessed 25 February 2015].

[11] U.S. Air Force, "RQ-4 Global Hawk Fact Sheet," October 2014. [Online]. Available: http://www.af.mil/AboutUs/FactSheets/Display/tabid/224/Article/104516/rq-4-global-hawk.aspx. [Accessed 25 02 2015].

[12] E. M. Kraft, "An Integral Equation Method for Boundary Interference in a Perforated-wall Wind Tunnel at Transonic Speeds," Arnold Engineering Development Center, Arnold AFB, TN, 1976. AEDC-TR-76-43

[13] D. Veazey and J. Hopf, "Comparison of Aerodynamic Data Obtained in the Arnold Engineering Development Center Wind Tunnels 4T and 16T," American Institute of Aeronautics and Astronautics, Reston, VA, 1998. AIAA 1998-2874

[14] P. B. Stich, "Mathematical modeling of the AEDC Propulsion Wind Tunnel (16T)," Arnold Engineering Development Center, Arnold AFB, TN, 1985. AEDC TR-84-32

[15] American Institute of Aeronautics and Astronautics, "Calibration of Subsonic and Transonic Wind Tunnels," American Institute of Aeronautics and Astronautics, Reston, VA, 2003. AIAA R-093-2003

[16] C. D. Abbott, E. J. Mickle and W. K. Brooks, "Status of AEDC Transonic, Supersonic, and Hypersonic Wind Tunnel improvement Programs," American Institute of Aeronautics and Astronautics, Reston, VA, 2012. AIAA 2012-3172

[17] J. Gunn, "Calibration of the AEDC-PWT Aerodynamic Wind Tunnel (4T) Using Diffuser Flap Plenum Suction," Arnold Engineering Development Center, Arnold AFB, TN, 1970. AEDC TR-70-74

[18] R. L. Parker, Jr. and W. L. Sickles, "Two-Dimensional Adaptive-Wall Experiments," Arnold Engineering Development Center, Arnold AFB, TN, 1981. AEDC TR-80-63

[19] J. L. Jacocks, "Reduction of Wall Interference Effects in the AEDC-PWT 1-ft Transonic Wind Tunnel with Variable Perforated Walls," Arnold Engineering Development Center, Arnold AFB, TN, 1969. AEDC TR-69-86

[20] M. Mokry and M. Khalid, "WIND Study of Transonic Wall Interference in Two-Dimensional Wind Tunnels with Ventilated Walls," American Institute of Aeronautics and Astronautics, Reston, VA, 2000. AIAA 2000-2375

[21] D. J. Gray and H. Gardenier, "Experimental and Theoretical Studies on Three-Dimensional Wave Reflections in Transonic Test Cells," Arnold Engineering Development Center, Arnold AFB, TN, 1955. AEDC TN-55-42

[22] B. Goethert, "Physical Aspects of Three-Dimensional Wave Reflections in Transonic Wind Tunnels at Mach Number 1.20 (Perforated, Slotted, and Combined Slotted-Perforated Walls)," Arnold Engineering Development Center, Arnold AFB, TN, 1956. AEDC TR-55-45

[23] J. L. Grunnet, "Transonic Wind Tunnel Wall Interference Minimization," *Journal of Aircraft,* vol. 21, no. 9, pp. 694-699, 1984.

[24] J. L. Jacocks, "Aerodynamic Characteristics of Perforated Walls for Transonic Wind Tunnels," Arnold Engineering Development Center, Arnold AFB, TN, 1977. AEDC TR-77-61

[25] R. F. Starr, "Experimental Observations of Wall Interference at Transonic Speeds," *Journal of Aircraft,* vol. 15, no. 12, pp. 822-828, 1978.

[26] R. H. Wright and V. G. Ward, "NACA Transonic Wind Tunnel Test Sections," National Advisory Committee for Aeronautics, Washington, DC, 1948. NACA RM-L8J06

[27] B. H. Goethert, "Flow Establishment and Wall Interference in Transonic Wind Tunnels," Arnold Engineering Development Center, Arnold AFB, TN, 1954. AEDC TR-54-44

[28] J. L. Jacocks, "Determination of Optimum Operating Parameters for the AEDC-PWT 4-ft Transonic Tunnel with Variable Porosity Test Section Walls," Arnold Engineering Development Center, Arnold AFB, TN, 1969. AEDC TR-69-164

[29] J. L. Jacocks, "Evaluation of Interference Effects on a Lifting Model in the AEDC-PWT 4-ft Transonic Tunnel," Arnold Engineering Development Center, Arnold AFB, TN, 1970. AEDC TR-70-72

[30] C. Anderson, "An Investigation of the Aerodynamic Characteristics of the AGARD Model B for Mach Numbers from 0.2 to 1.0," Arnold Engineering Development Center, Arnold AFB, TN, 1970. AEDC TR-70-100

[31] T. W. Binion, Jr., "An Investigation of Three-dimensional Wall Interference in a Variable Porosity Transonic Wind Tunnel," Arnold Engineering Development Center, Arnold AFB, TN, 1974. AEDC TR-74-76

[32] J. T. W. Binion, "Tests of the ONERA Calibration Models in Three Transonic Wind Tunnels," Arnold Engineering Development Center, Arnold AFB, TN, 1976. AEDC TR-76-133

[33] E. M. Kraft and R. L. Parker, Jr., "Experiments for the Reduction of Wind Tunnel Wall Interference by Adaptive-Wall Technology," Arnold Engineering Development Center, Arnold AFB, TN, 1979. AEDC TR-79-51

[34] C. Lo, "Wind-Tunnel Wall Interference Reduction by Streamwise Porosity Distribution," *AIAA Journal,* vol. 10, no. 4, pp. 547-551, 1972.

[35] R. Crites and F. W. Steinle, Jr., "Wall Interference Reduction Methods for Subsonic Wind Tunnels," American Institute of Aeronautics and Astronautics, Reston, VA, 1995. AIAA 95-0107

[36] G. Lombardi, M. V. Salvetti and M. Morelli, "Correction of Wall Interference in Wind Tunnels: A Numerical Investigation," *Journal of Aircraft,* vol. 38, no. 5, pp. 944-949, 2001.

[37] C. Lo and N. Ulbrich, "Comparison of One- and Two- Interface Methods for Tunnel Wall Interference Calculations," vol. 27, no. 8, pp. 732-735, 1990.

[38] C. F. Lo and R. H. Oliver, "Boundary Interference in a Rectangular Wind Tunnel with Perforated Walls," Arnold Engineering Development Center, Arnold AFB, TN, 1970. AEDC TR-70-67

[39] E. M. Kraft and C. F. Lo, "A General Solution for Lift Interference in Rectangular Ventilated Wind Tunnels," American Institute of Aeronautics and Astronautics, New York, NY, 1973. AIAA 73-209

[40] C. F. Lo., "Application of Linearized Transonic Theory to Tunnel Blockage Interference," Arnold Engineering Development Center, Arnold AFB, TN, 1974. AEDC TR-74-65

[41] M. H. Rizk, M. Hafez, E. M. Murman and D. Lovell, "Transonic Wind Tunnel Wall Interference Corrections for Three-Dimensional Models," American Institute of Aeronautics and Astronautics, Washington, D.C., 1982. AIAA 82-0588

[42] P. S. Phillips and E. G. Waggoner, "A Transonic Wind Tunnel Wall Interference Prediction Code," American Institute of Aeronautics and Astronautics, Reston, VA, 1988. AIAA 88-2538-CP

[43] W. Sickles and J. Erickson, "Wall Interference Correction for Three-Dimensional Transonic Flows," American Institute of Aeronautics and Astronautics, Washington, D.C., 1990. AIAA 90-1408

[44] F. W. Martin, W. L. Sickles and S. A. Stanley, "Transonic Wind Tunnel Wall Interference Analysis for the Space Shuttle Launch Vehicle," American Institute of Aeronautics and Astronautics, Washington, D.C., 1993. AIAA 93-0420

[45] J. E. Maseland, M. Laban, H. van der Ven and J. W. Kooi, "Development of CFD-based Interference Models for the DNW-HST Transonic Wind Tunnel," American Institute of Aeronautics and Astronautics, Reston, VA, 2006.AIA 2006-3639

[46] N. T. Frink, S. Z. Pirzadeh, P. C. Parikh, M. J. Pandya and M. K. Bhat, "The NASA Tetrahedral Unstructured Software System (TetrUSS)," International Congress of Aeronautical Sciences, Harrogate, United Kingdom, 2000. ICAS Paper No. 0241

[47] N. T. Frink, D. L. Bonhaus, V. N. Vatsa, S. X. S. Bauer and A. F. Tinetti, "A Boundary Condition for Simulation of Flow over Porous Surfaces," American Institute of Aeronautics and Astronautics, Reston, VA, 2001. AIAA 2001-2412

[48] P. Spalart and S. Allmaras, "A One-Equation Turbulence Model for Aerodynamic Flows," American institute of Aeronautics and Astronautics, Washington, D.C., 1992. AIAA 92-0439

[49] Pointwise, Inc. , "Pointwise Grid Generation Software," 2015. [Online]. Available: http://www.pointwise.com/pw/. [Accessed 21 10 2015].

[50] J. C. Vassberg, M. A. DeHaan, S. M. Rivers and R. A. Wahls, "Development of a Common Research model for Applied CFD Validation Studies," American Institute of Aeronautics and Astronautics, Reston, VA, 2008. AIAA 2008-6919

[51] J. Daugherty, *NASA Ames Unitary Plan Wind Tunnel Blockage Rcommendations,* Moffett Field, CA: National Aeronautics and Space Administration, 1984.

[52] N. T. D. Frink, "TetrUSS: USM3Dns Online Manual," August 2003. [Online]. Available: http://tetruss.larc.nasa.gov/. [Accessed 1 September 2015].

[53] Navy DSRC, "Navy DSRC High Performance Computing Systems Hardware," 13 April 2012. [Online]. Available: http://www.navydsrc.hpc.mil/hardware/index.html. [Accessed 21 March 2016].

[54] M. L. Skelley, T. F. Langham and W. L. Peters, "Integrated Test and Evaluation for the 21st Century," AIAA, Reston, VA, 2004. AIAA 2004-6873

[55] H. Akima, "A New Method of Interpolation and Smooth Curve Fitting Based on Local Procedures," *Journal of the Association for Computing machinery,* vol. 17, no. 4, pp. 589-602, October 1970.

[56] J. A. Blackwell Jr. and G. A. Pounds, "Wind-Tunnel Wall Interference Effects on a Supercritical Airfoil at Transonic Speeds," *Journal of Aircraft,* vol. 14, no. 10, pp. 929-935, October 1977.

APPENDICES

Appendix 1: Typical Free-stream Simulation Input Card

Mach	alpha	beta	ReUe	Tinf,dR	itwall	Tw/Tinf	ipwall
0.85000	3.00000	0.00000	0.250E+06	559.67000	0	1.00000	0
sref	cref	bref	xmc	ymc	zmc	gamma	
549.62000	13.58800	48.00000	55.01900	0.00000	7.38400	1.40000	
ioverset	impl	dt/cfl1	iramp	clf2	cflmin	GS_tol	crelax
0	1	-1.00	500	25.00	1.00	0.00000	1.00000
itimeacc	deltat	ntstep	res_step	imvgrd	iravg	nbgnavg	
0	0.00000	1	-3.00	0	0	1500	
irest	mstage	iresmth	dqmax	pbreak	pmin	limiter	ak_lstr
0	3	1	0.50000	0.05000	0.00100	1.00000	0.40000
nupdate	nwrest	nwflo	nwflobgn	ipltqn	idiagnos	nodeypl	lim_frz
1	8000	8000	0	2	0	0	3
iorder	lapl-avg	high-bc	ifds	ivisc	itrip	ev_lim	
-2	1	1	1	2	0	0.000	
ncyc	nengines	nsinkbc	nrotor	compF&M	p_bc1002	cldes	
8000	0	0	0	-12	0.71429	0.00000	

Figure 19. USM3Dns Input Card for Configuration 1 Free-stream Case, 3 deg Angle of Attack

Appendix 2: Typical Wind Tunnel Simulation Boundary Conditions File

Patch #	BC	Family	#surf	surfIDs	Family
#					
1	3	3	0	0	Inflow
2	4	4	0	0	Model
3	1002	1002	0	0	Outflow
4	1	1	0	0	Symmetry
5	2400	0.94	0	0	Tunnel_walls

Figure 20. Typical Wind Tunnel Simulation Boundary Condition File

Appendix 3: Typical Wind Tunnel Simulation Porosity File

```
1
1,5,0.94,0.714444
```

Figure 21. Typical Wind Tunnel Simulation Porosity File

Appendix 4: Force and Moment Coefficient Data

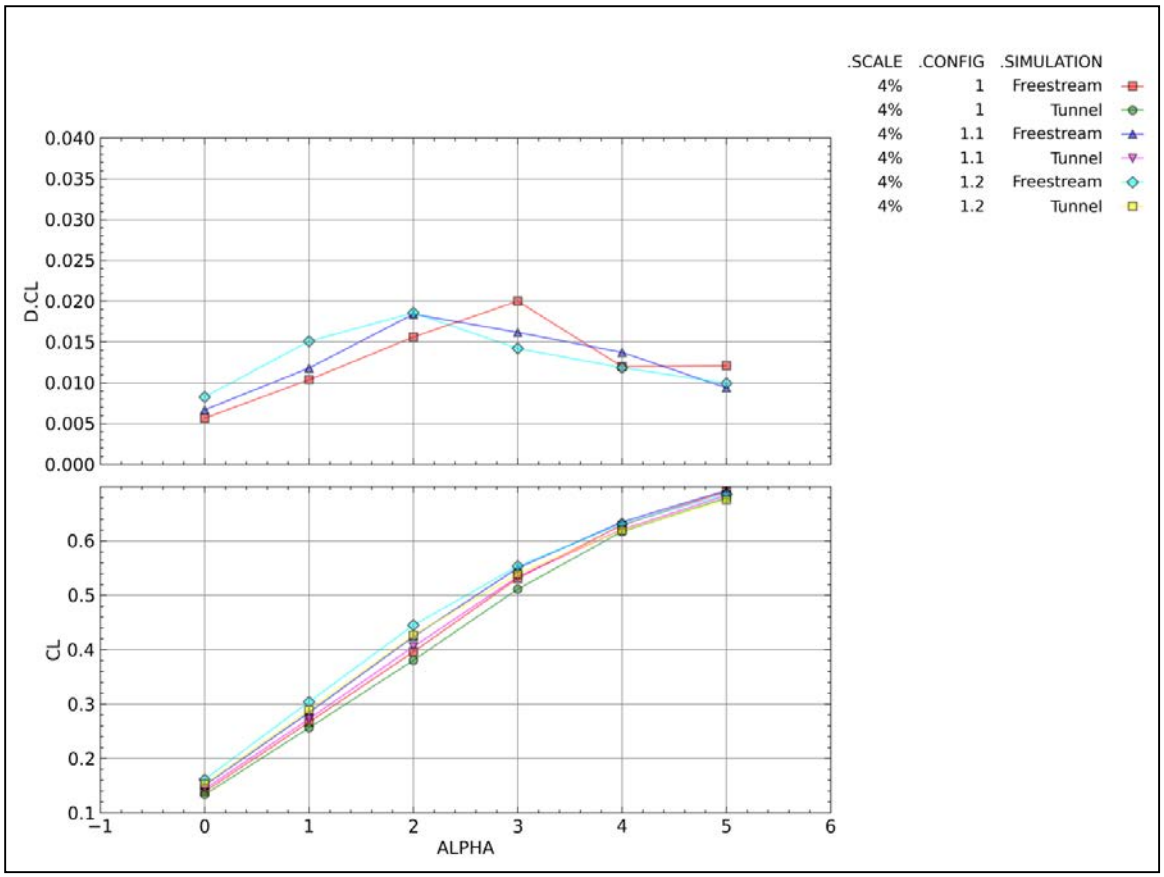

Figure 22. Free-stream and Wind Tunnel Simulation Lift Coefficient and Difference in Lift Coefficient as a Function of Angle of Attack for Configurations 1, 1.1, and 1.2

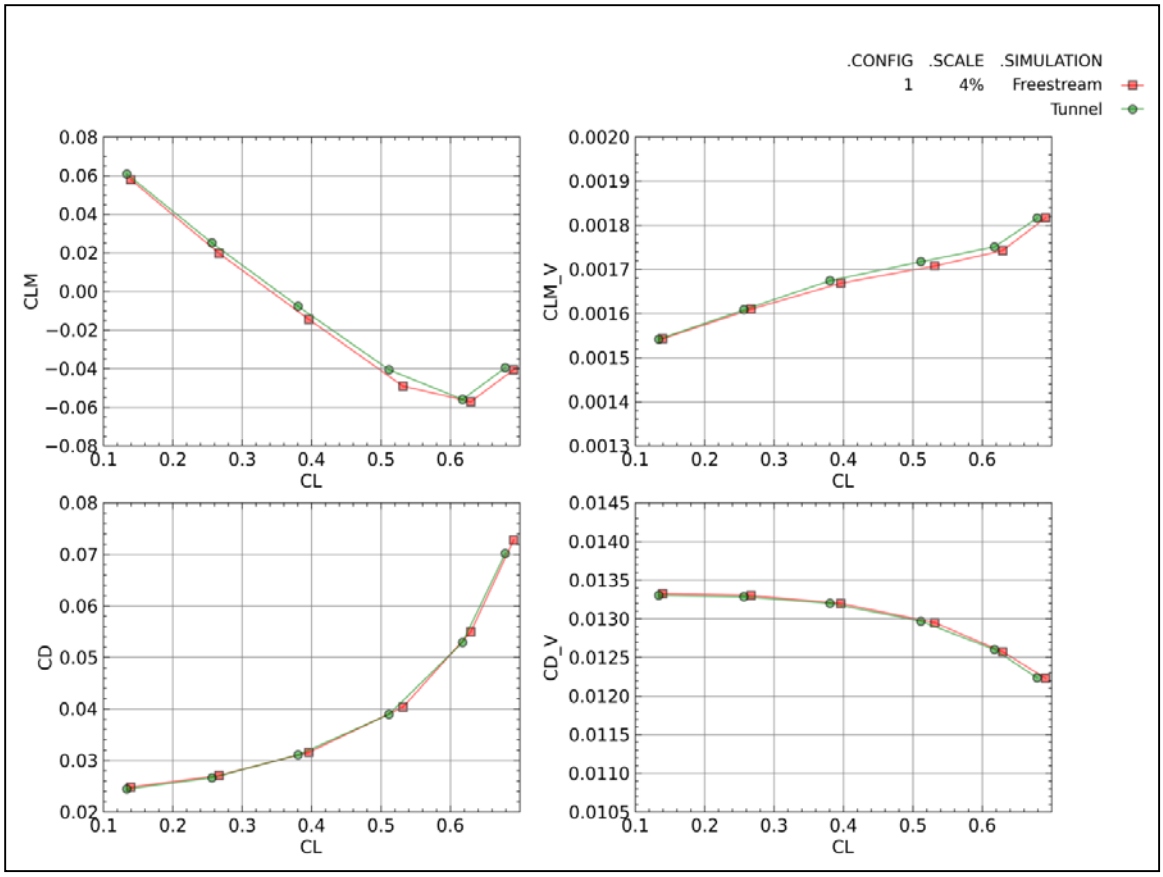

Figure 23. Free-stream and Wind Tunnel Simulation Total and Viscous Pitching Moment and Drag Coefficients for Configuration 1

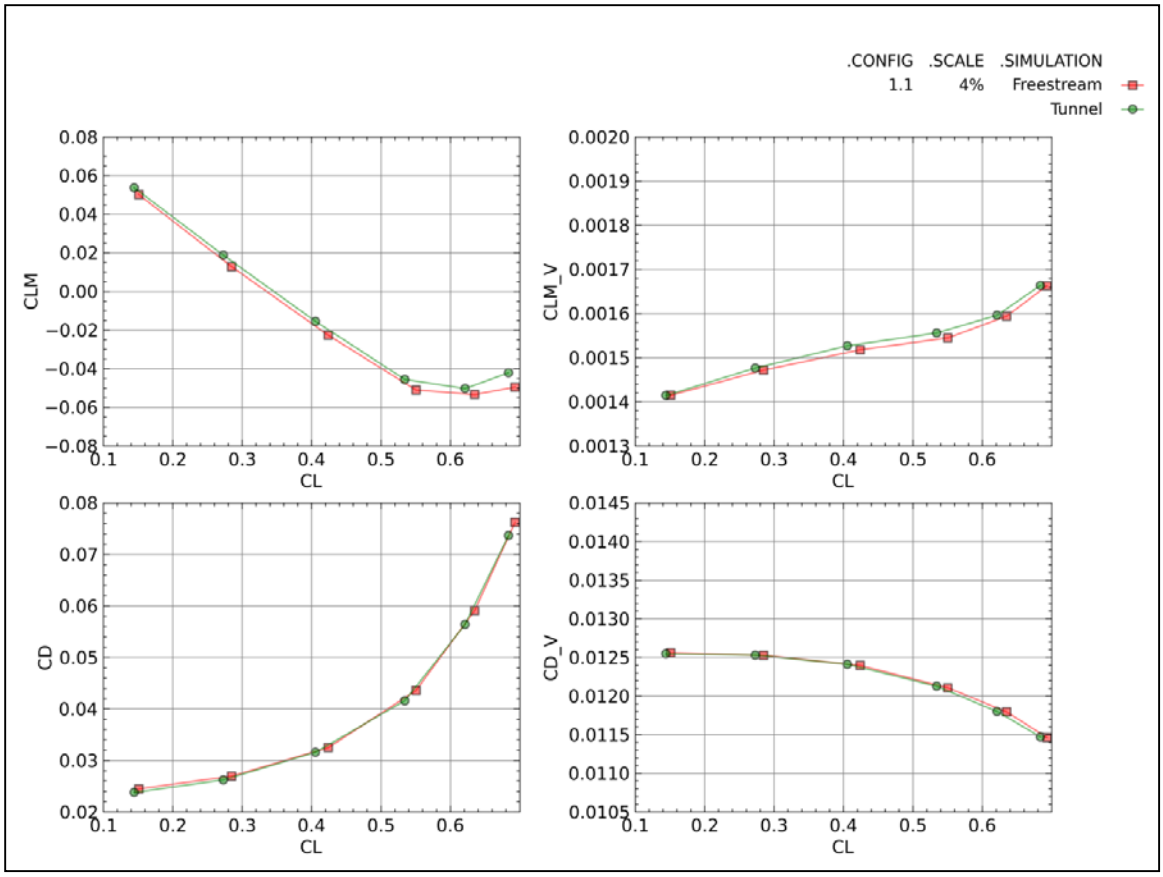

Figure 24. Free-stream and Wind Tunnel Simulation Total and Viscous Pitching Moment and Drag Coefficients for Configuration 1.1

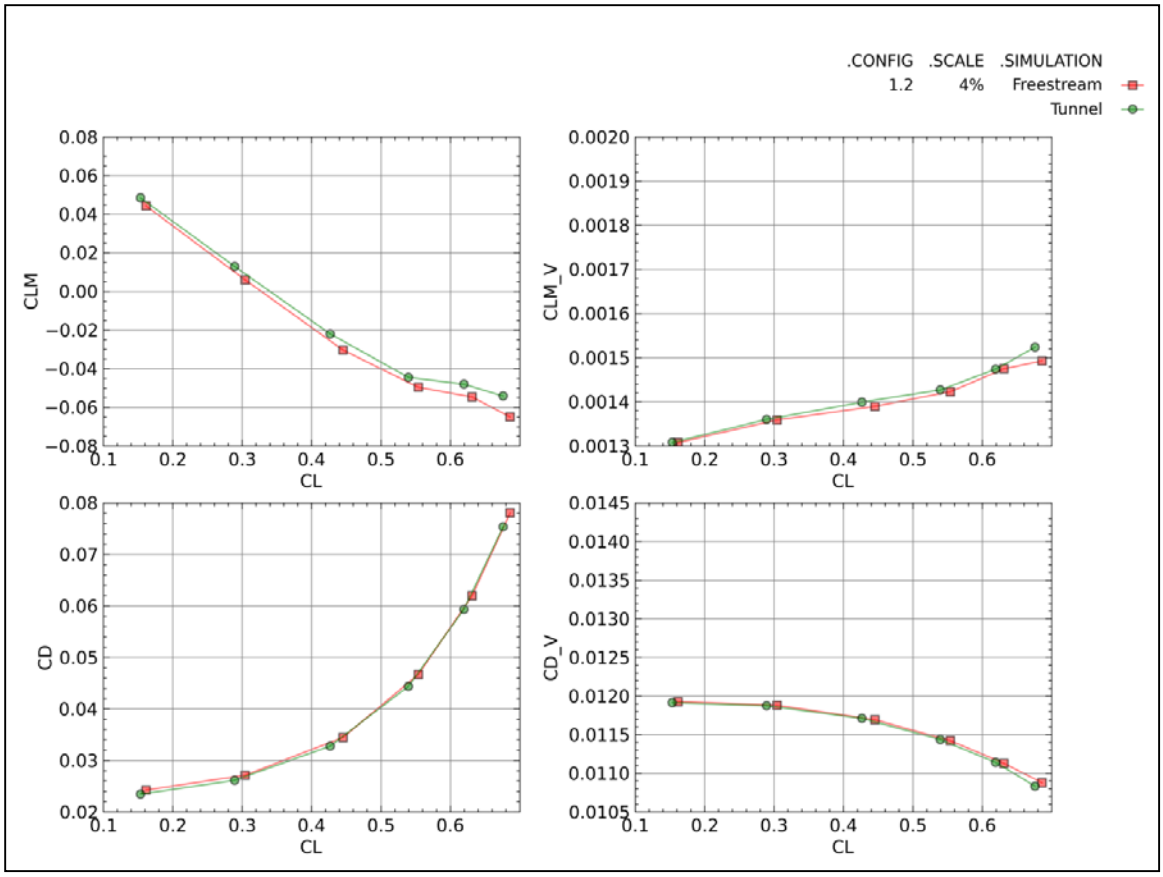

Figure 25. Free-stream and Wind Tunnel Simulation Total and Viscous Pitching Moment and Drag Coefficients for Configuration 1.2

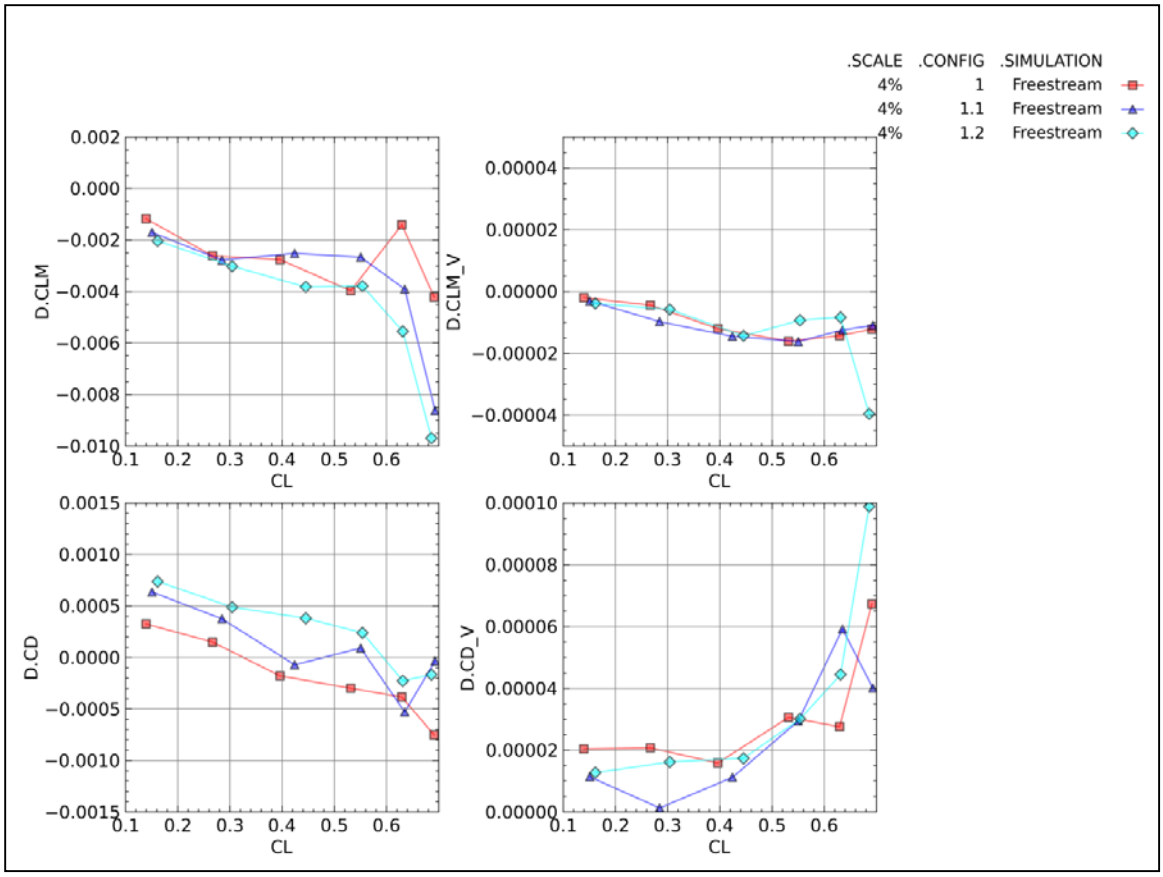

Figure 26. Differences in Free-stream and Wind Tunnel Simulation Total and Viscous Pitching Moment and Drag Coefficients for Configurations 1, 1.1, and 1.2

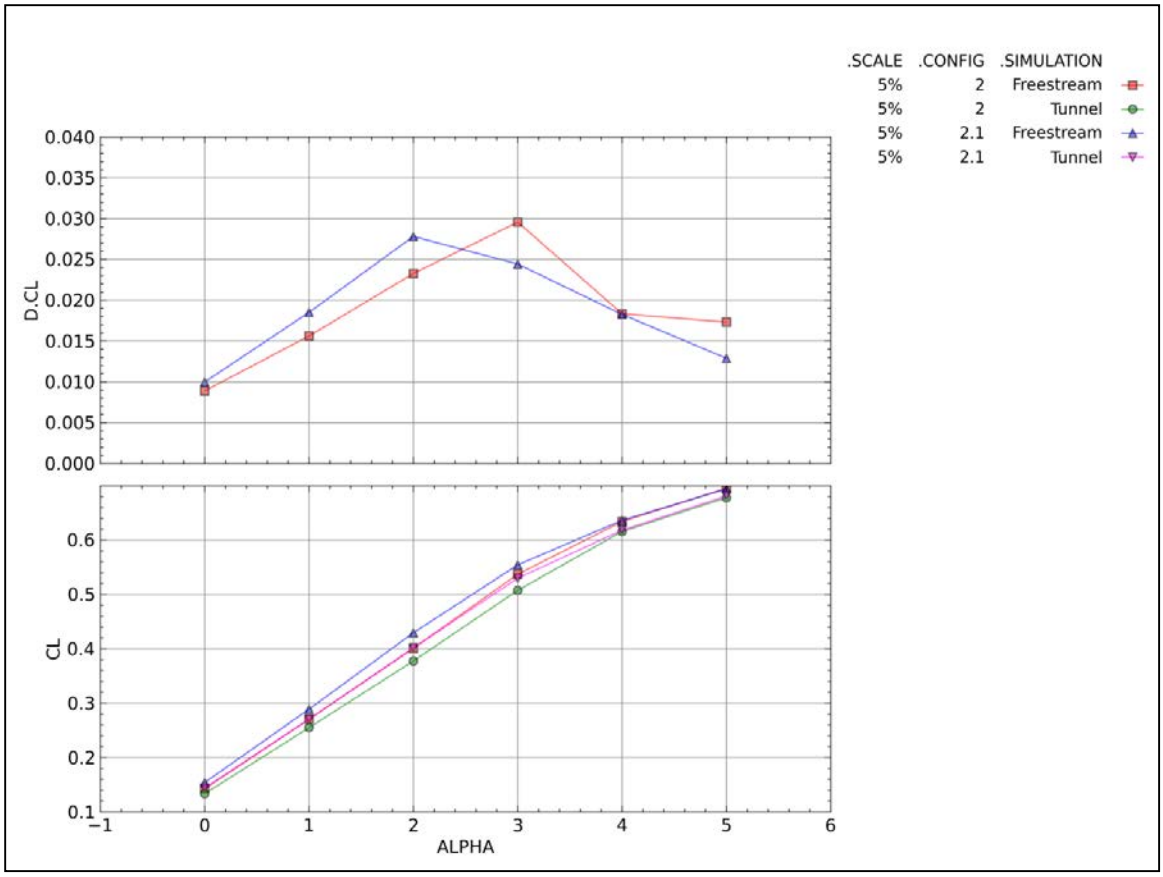

Figure 27. Free-stream and Wind Tunnel Simulation Lift Coefficient and Difference in Lift Coefficient as a Function of Angle of Attack for Configurations 2 and 2.1

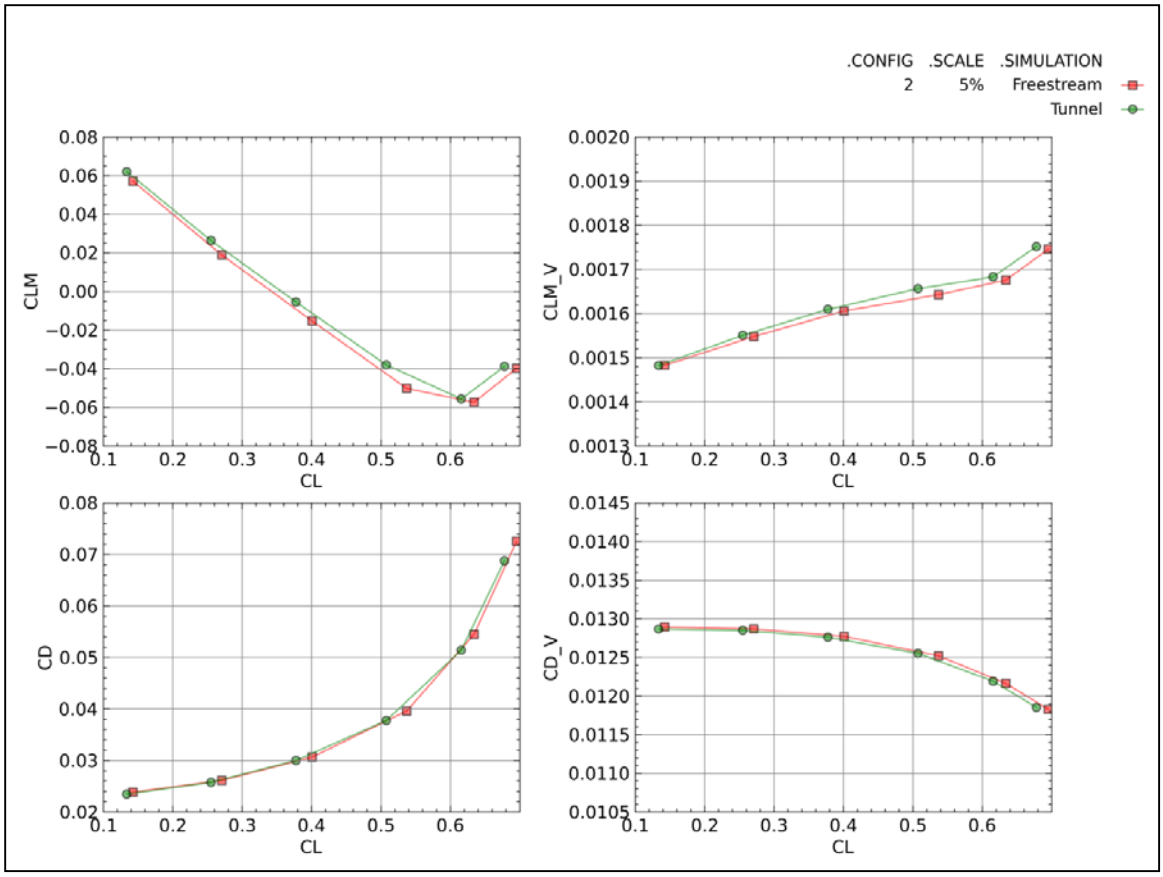

Figure 28. Free-stream and Wind Tunnel Simulation Total and Viscous Pitching Moment and Drag Coefficients for Configuration 2

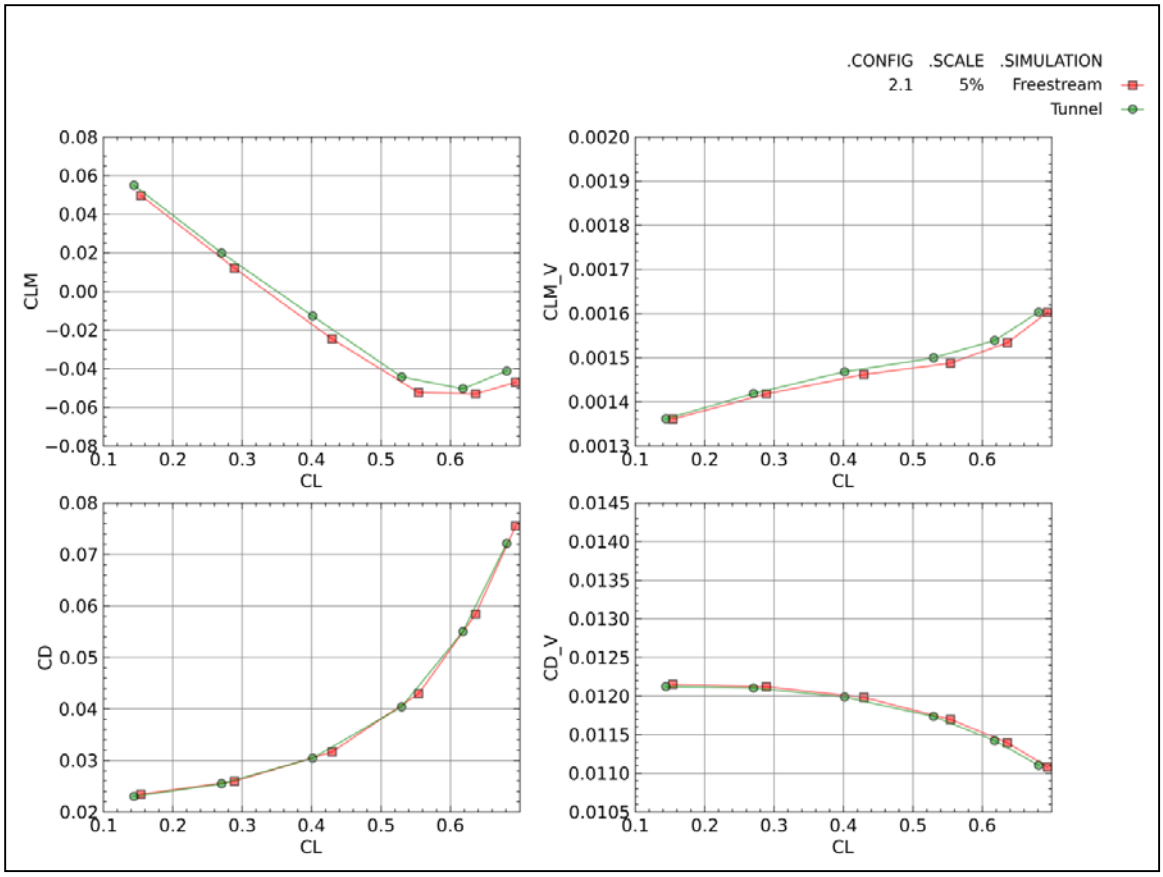

Figure 29. Free-stream and Wind Tunnel Simulation Total and Viscous Pitching Moment and Drag Coefficients for Configuration 2.1

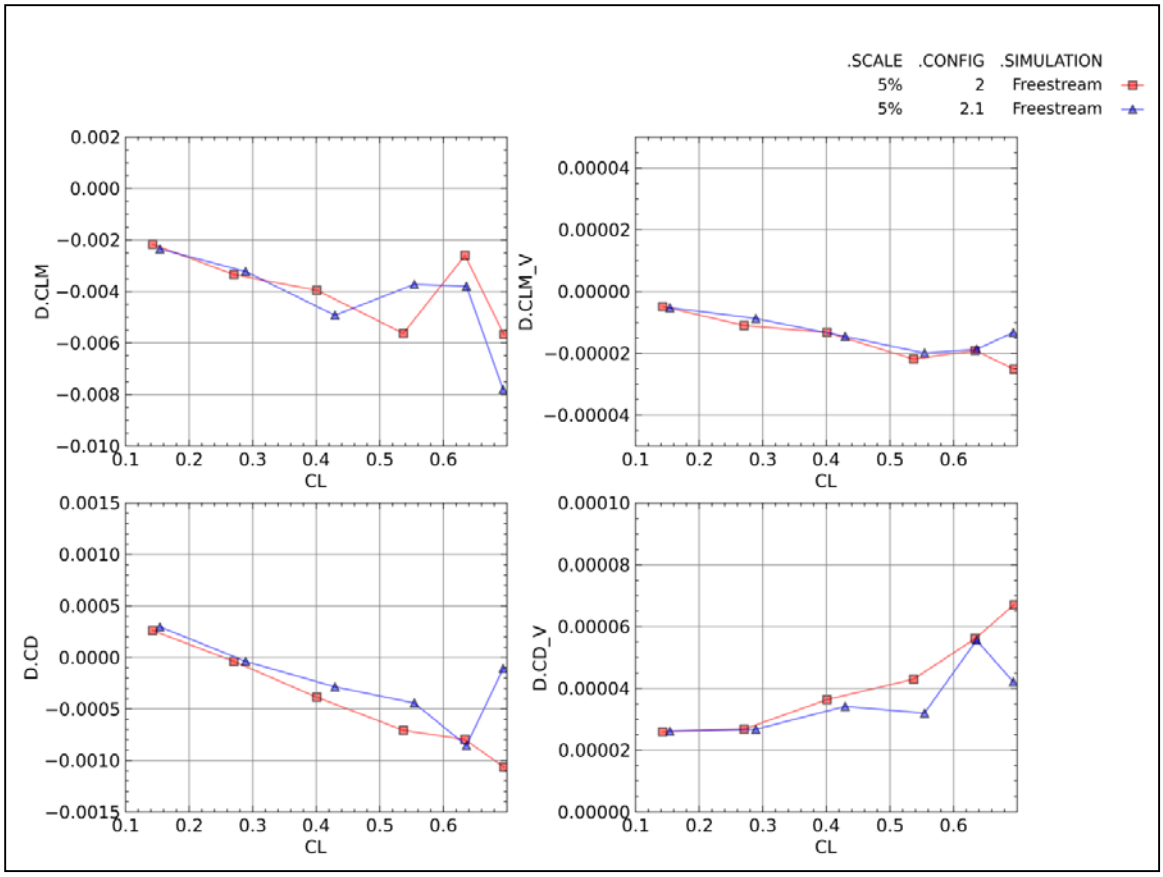

Figure 30. Differences in Free-stream and Wind Tunnel Simulation Total and Viscous Pitching Moment and Drag Coefficients for Configurations 2 and 2.1

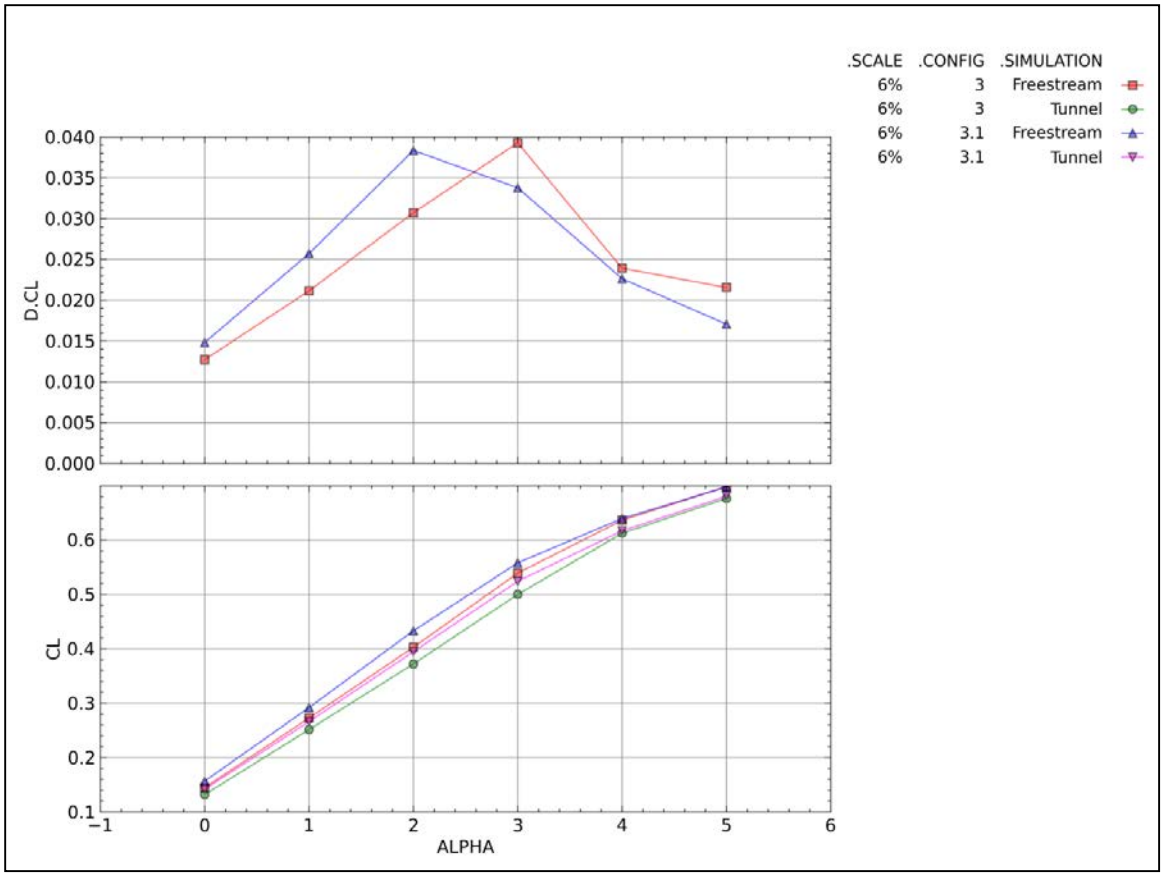

Figure 31. Free-stream and Wind Tunnel Simulation Lift Coefficient and Difference in Lift Coefficient as a Function of Angle of Attack for Configurations 3 and 3.1

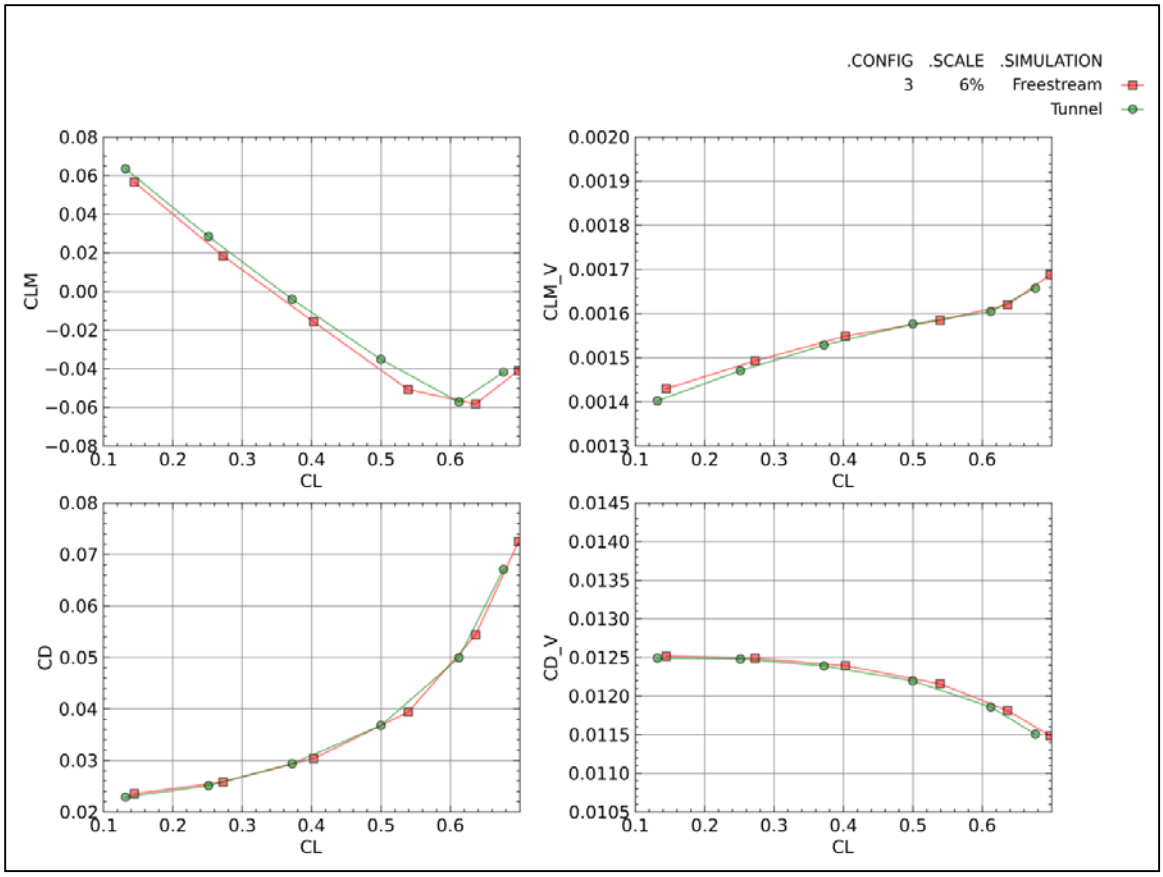

Figure 32. Free-stream and Wind Tunnel Simulation Total and Viscous Pitching Moment and Drag Coefficients for Configuration 3

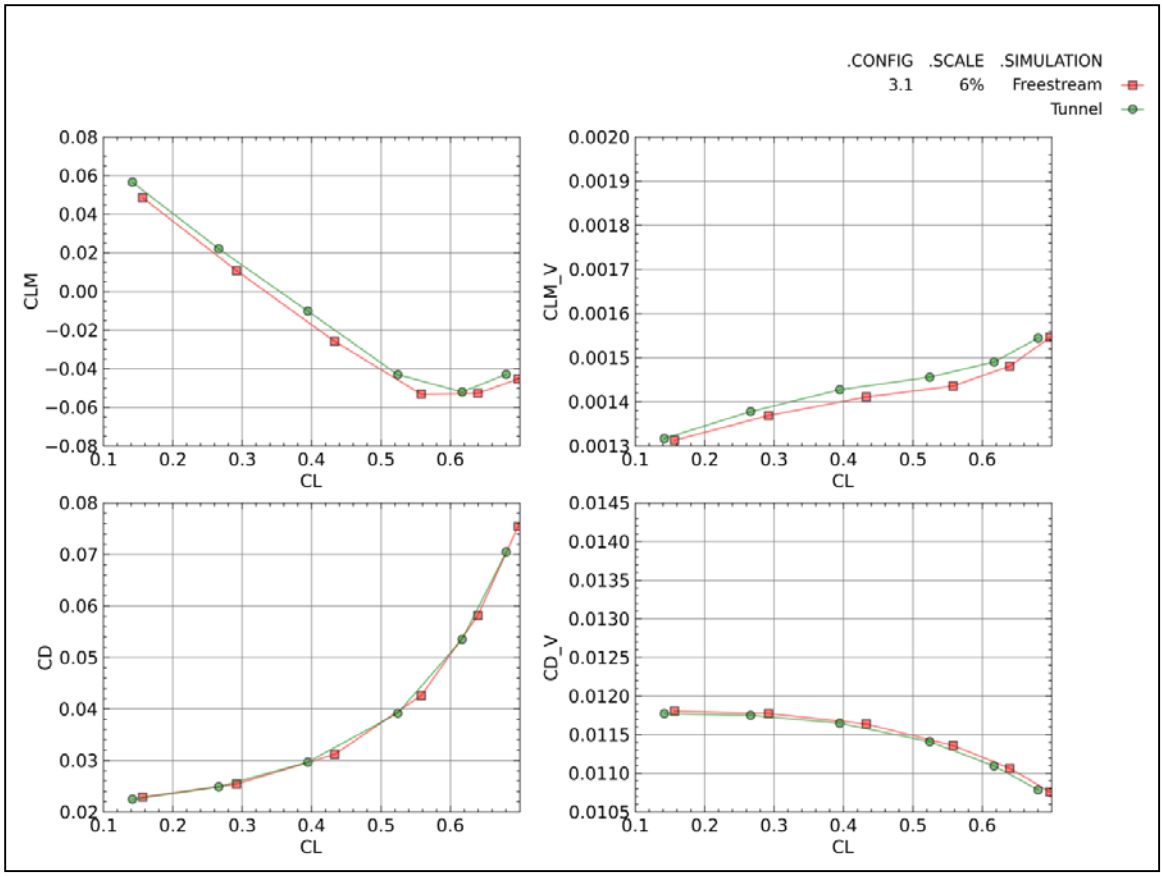

Figure 33. Free-stream and Wind Tunnel Simulation Total and Viscous Pitching Moment and Drag Coefficients for Configuration 3.1

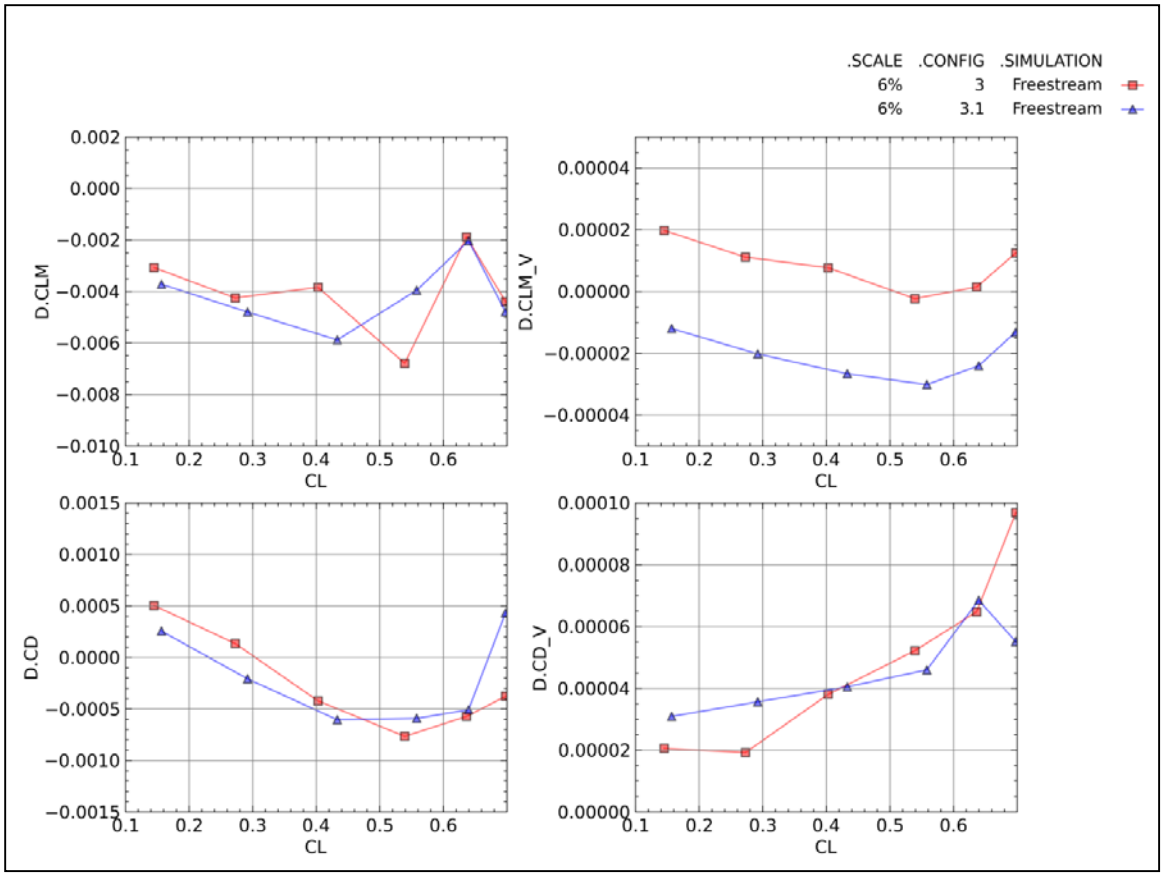

Figure 34. Differences in Free-stream and Wind Tunnel Simulation Total and Viscous Pitching Moment and Drag Coefficients for Configurations 3 and 3.1

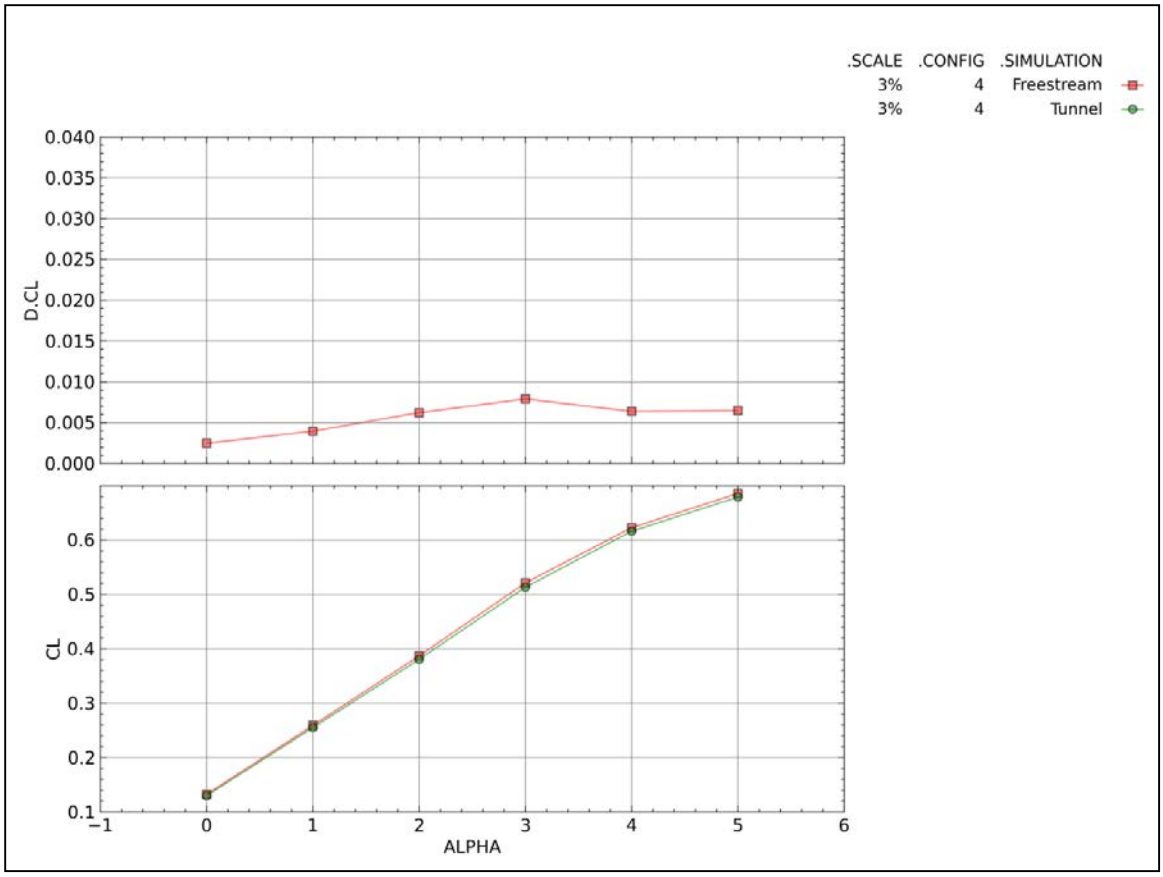

Figure 35. Free-stream and Wind Tunnel Simulation Lift Coefficient and Difference in Lift Coefficient as a Function of Angle of Attack for Configuration 4

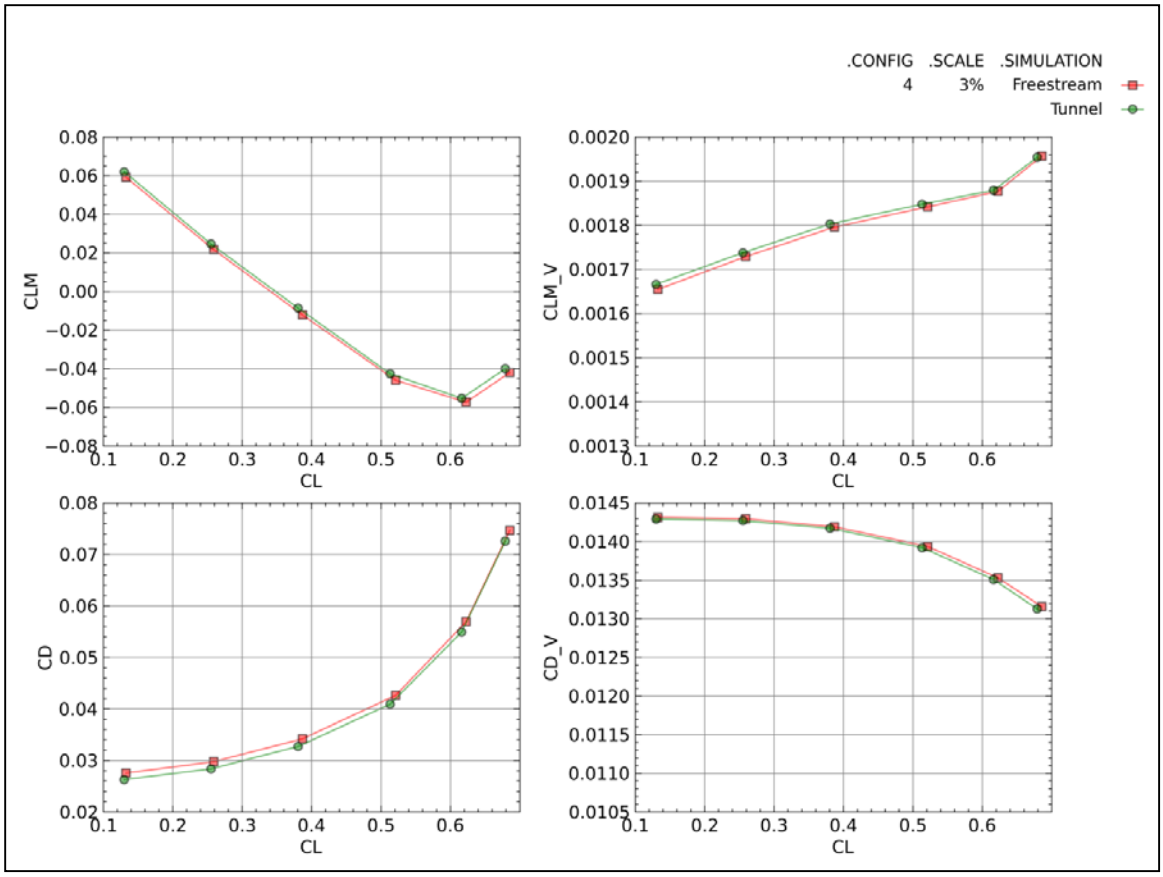

Figure 36. Free-stream and Wind Tunnel Simulation Total and Viscous Pitching Moment and Drag Coefficients for Configuration 4

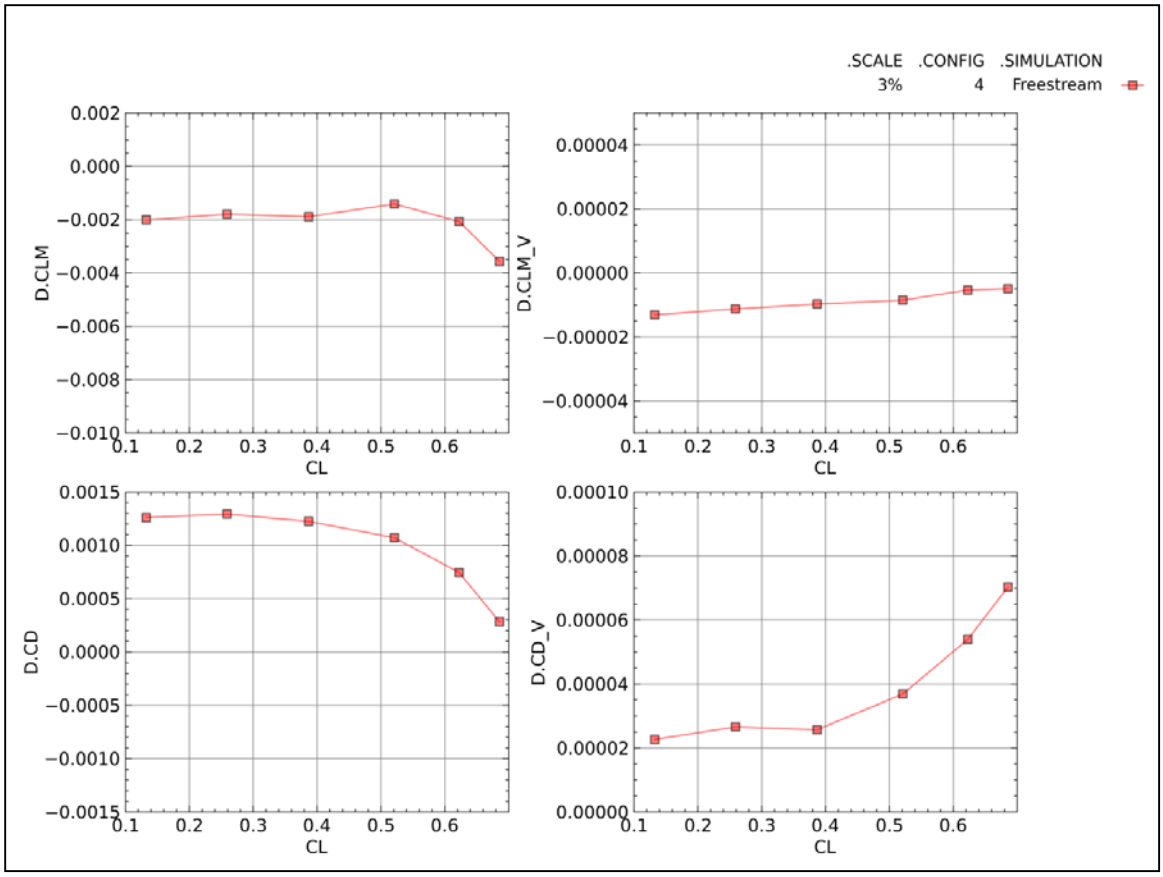

Figure 37. Differences in Free-stream and Wind Tunnel Simulation Total and Viscous Pitching Moment and Drag Coefficients for Configuration 4

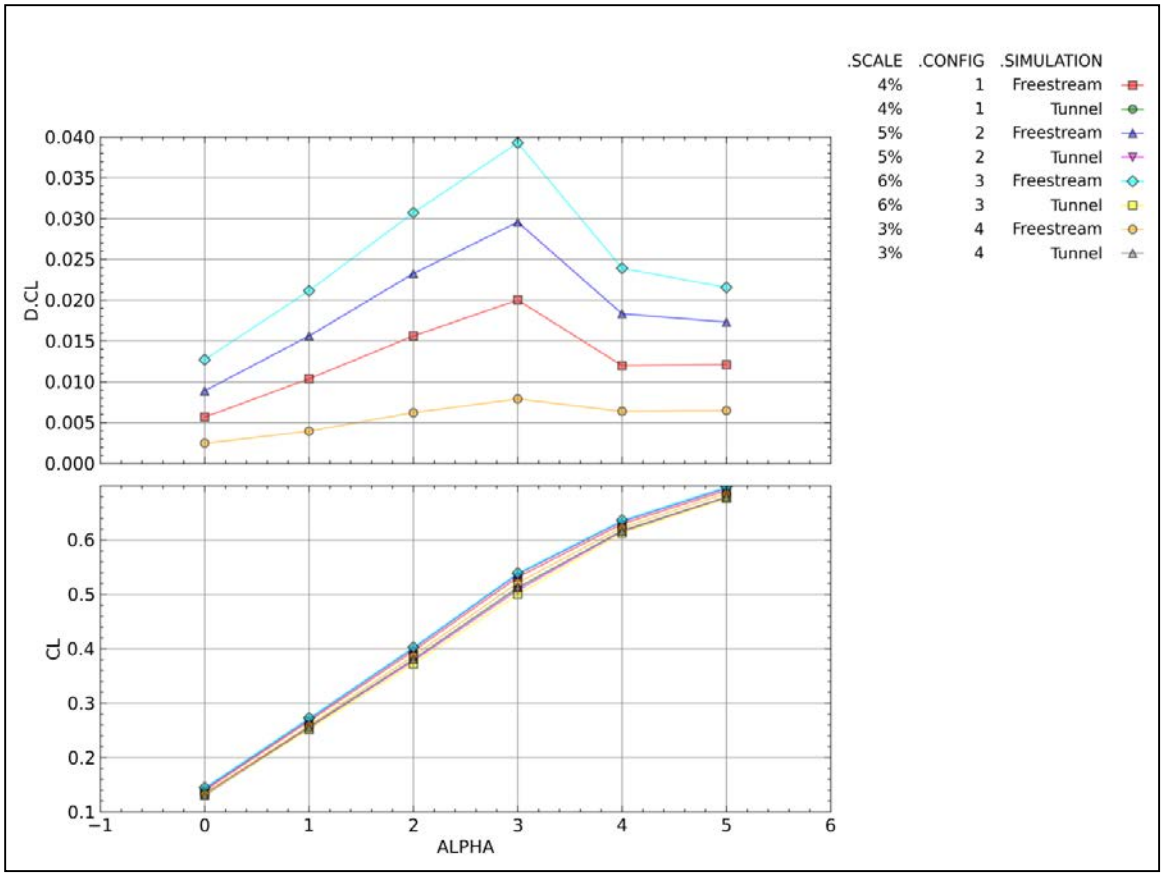

Figure 38. Free-stream and Wind Tunnel Simulation Lift Coefficient and Difference in Lift Coefficient as a Function of Angle of Attack for Configurations 1, 2, 3, and 4

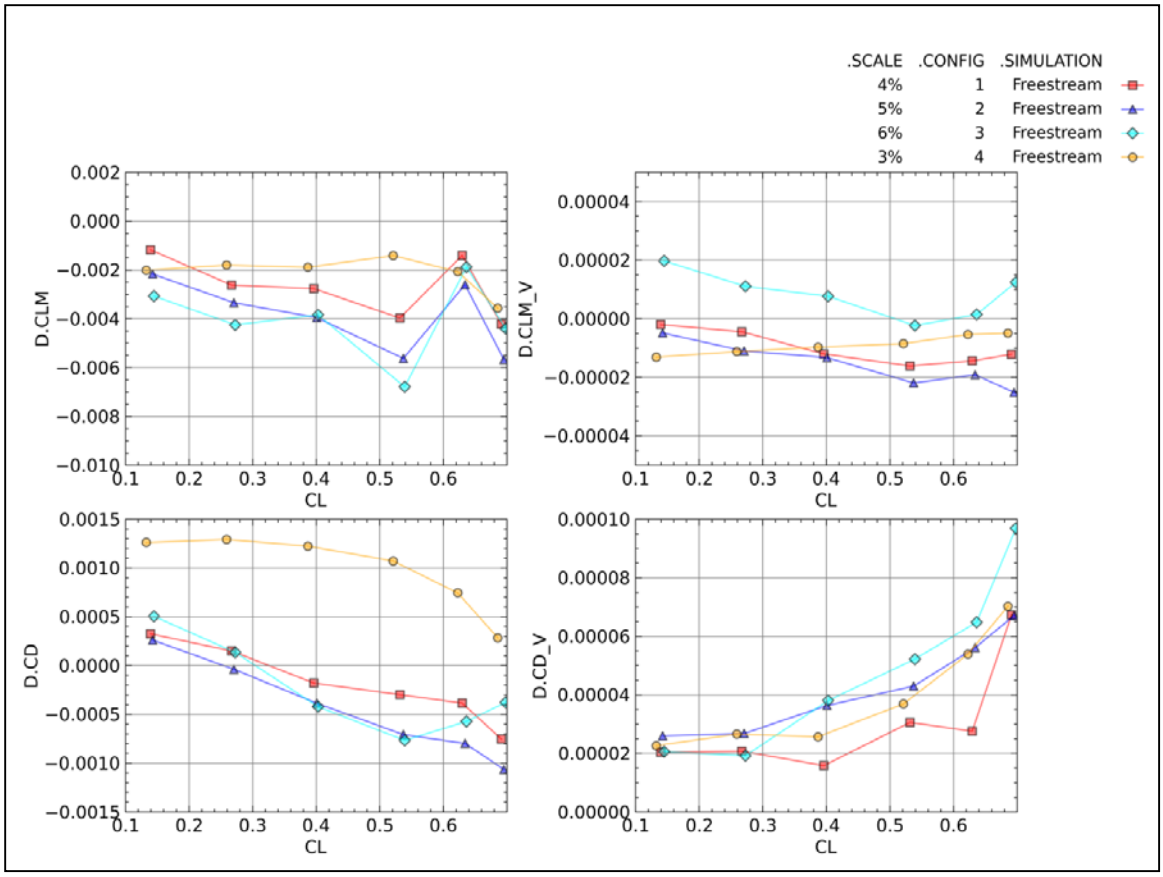

Figure 39. Differences in Free-stream and Wind Tunnel Simulation Total and Viscous Pitching Moment and Drag Coefficients for Configurations 1, 2, 3, and 4

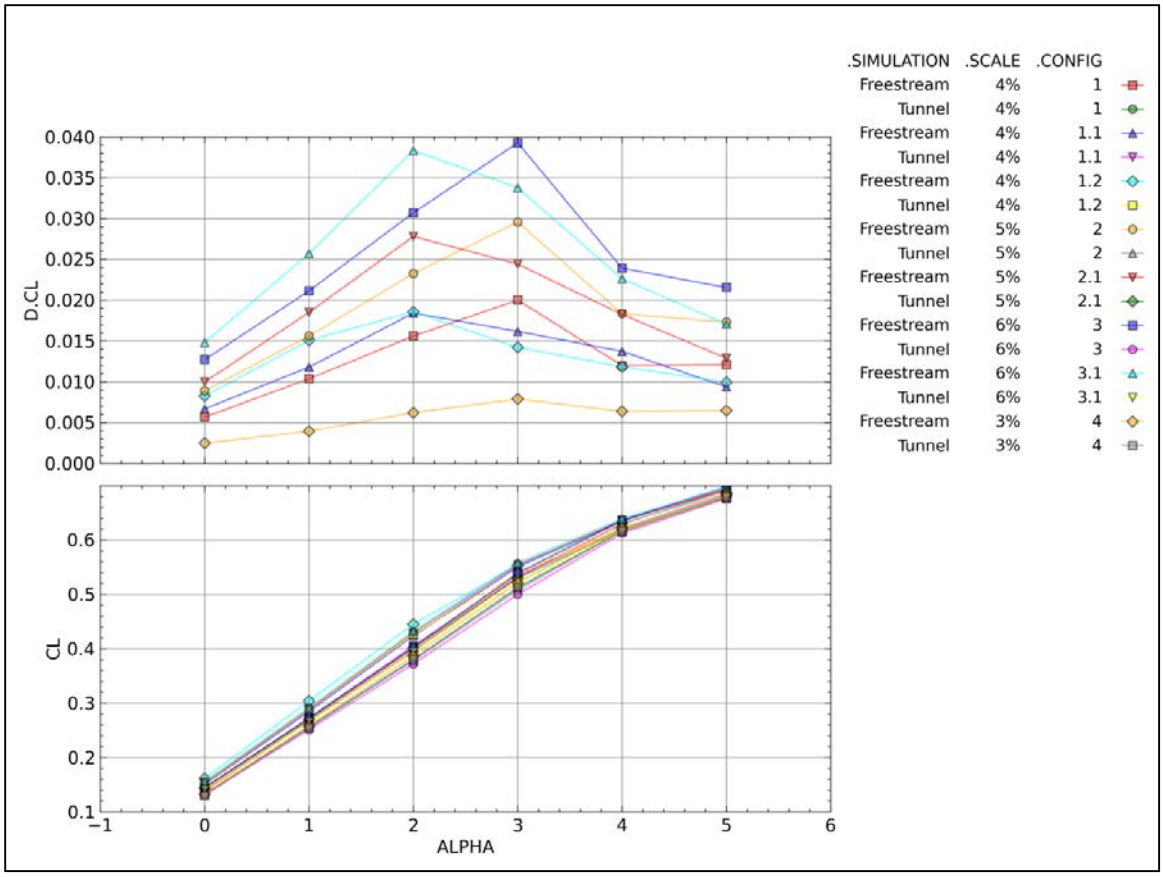

Figure 40. Lift Coefficient and Change in Lift Coefficient between Free-stream and Wind Tunnel Simulations for All Configurations Studied

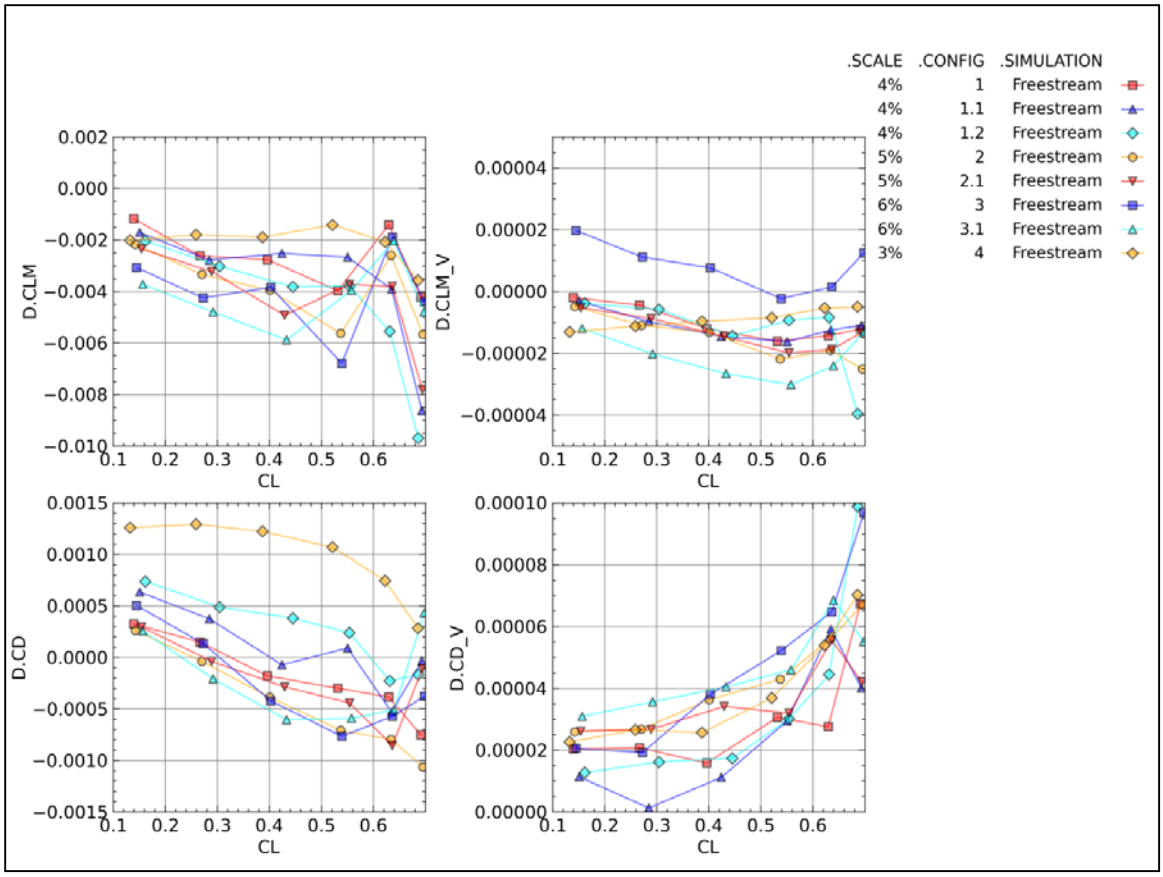

Figure 41. Differences in Free-stream and Wind Tunnel Simulation Total and Viscous Pitching Moment and Drag Coefficients for All Tested Configurations

Appendix 5: Differences in Pressure Coefficient Between Free-stream and Tunnel Simulations

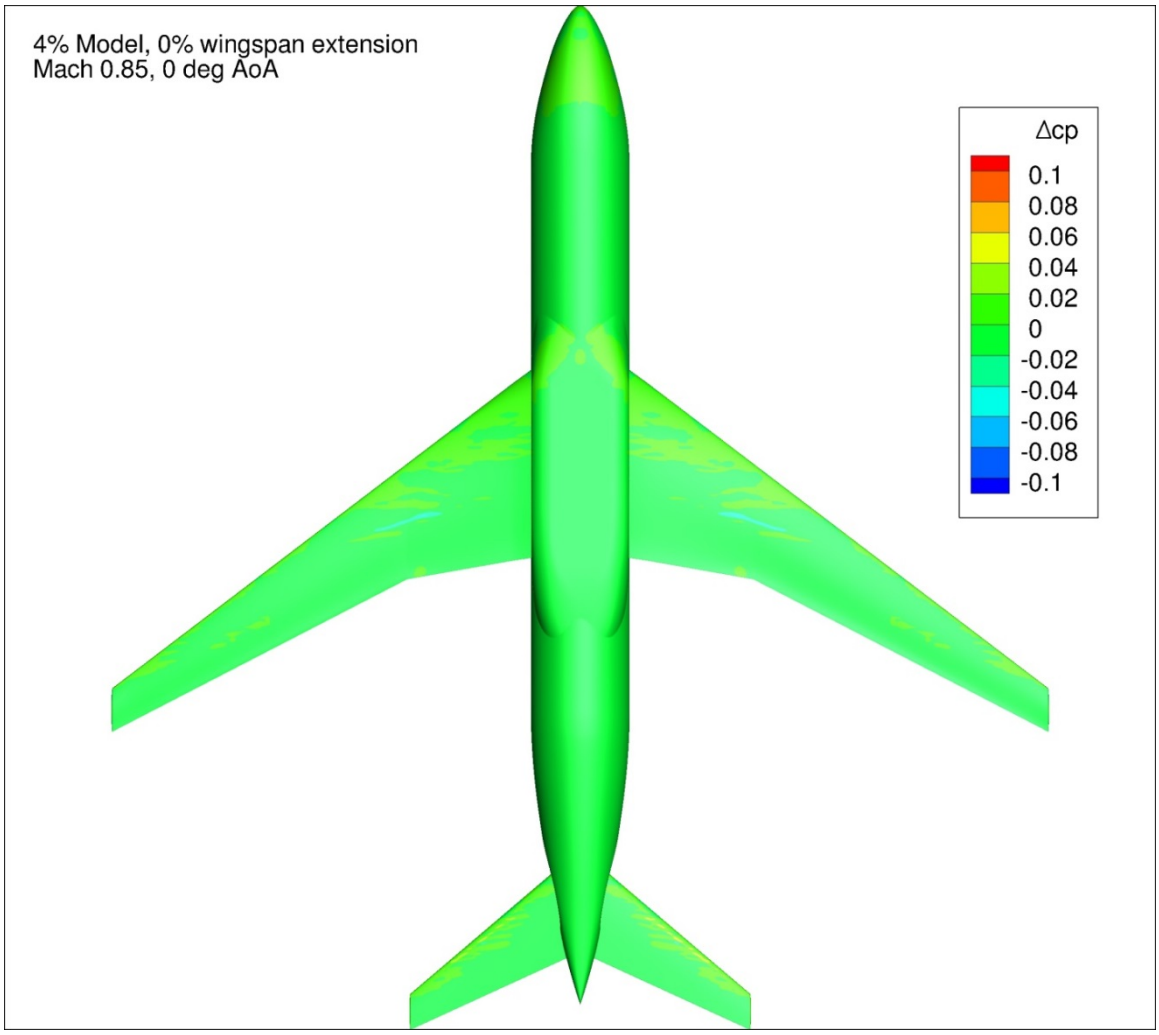

Figure 42. Configuration 1, Difference in Pressure Coefficient between Free-stream and Wind Tunnel Simulations, 0 deg Angle of Attack, Bottom View

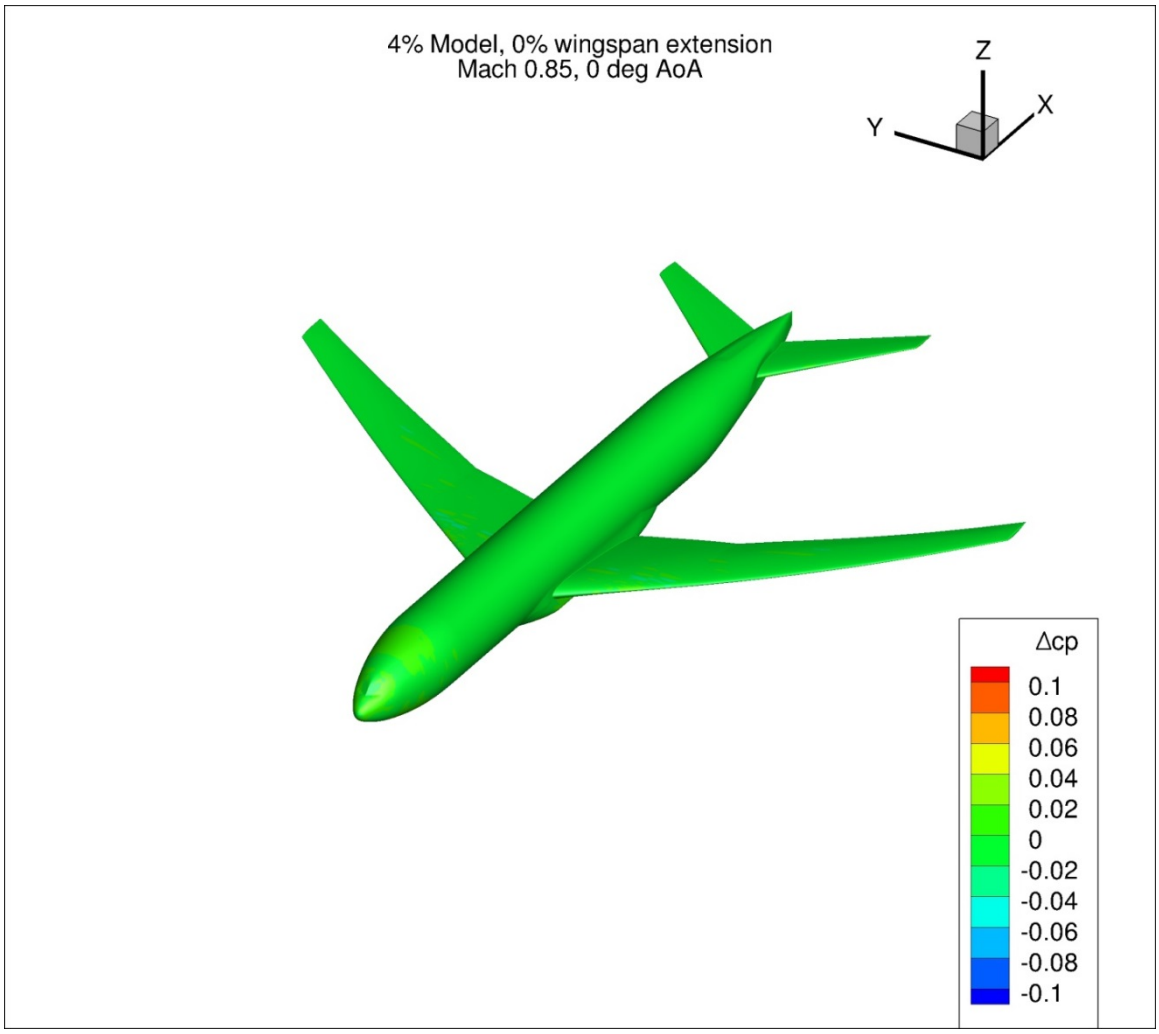

Figure 43. Configuration 1, Difference in Pressure Coefficient between Free-stream and Wind Tunnel Simulations, 0 deg Angle of Attack, Isometric View

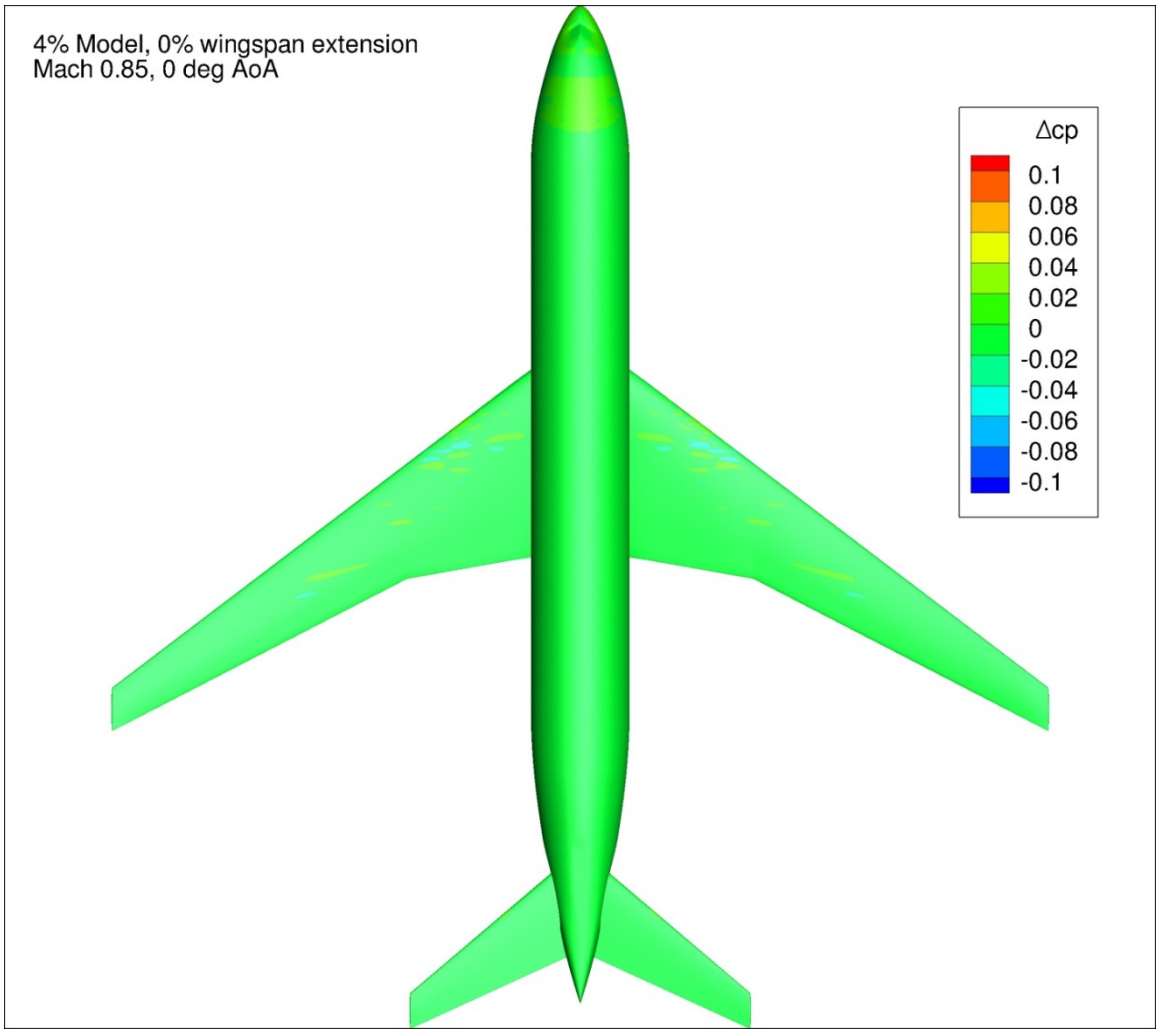

Figure 44. Configuration 1, Difference in Pressure Coefficient between Free-stream and Wind Tunnel Simulations, 0 deg Angle of Attack, Top View

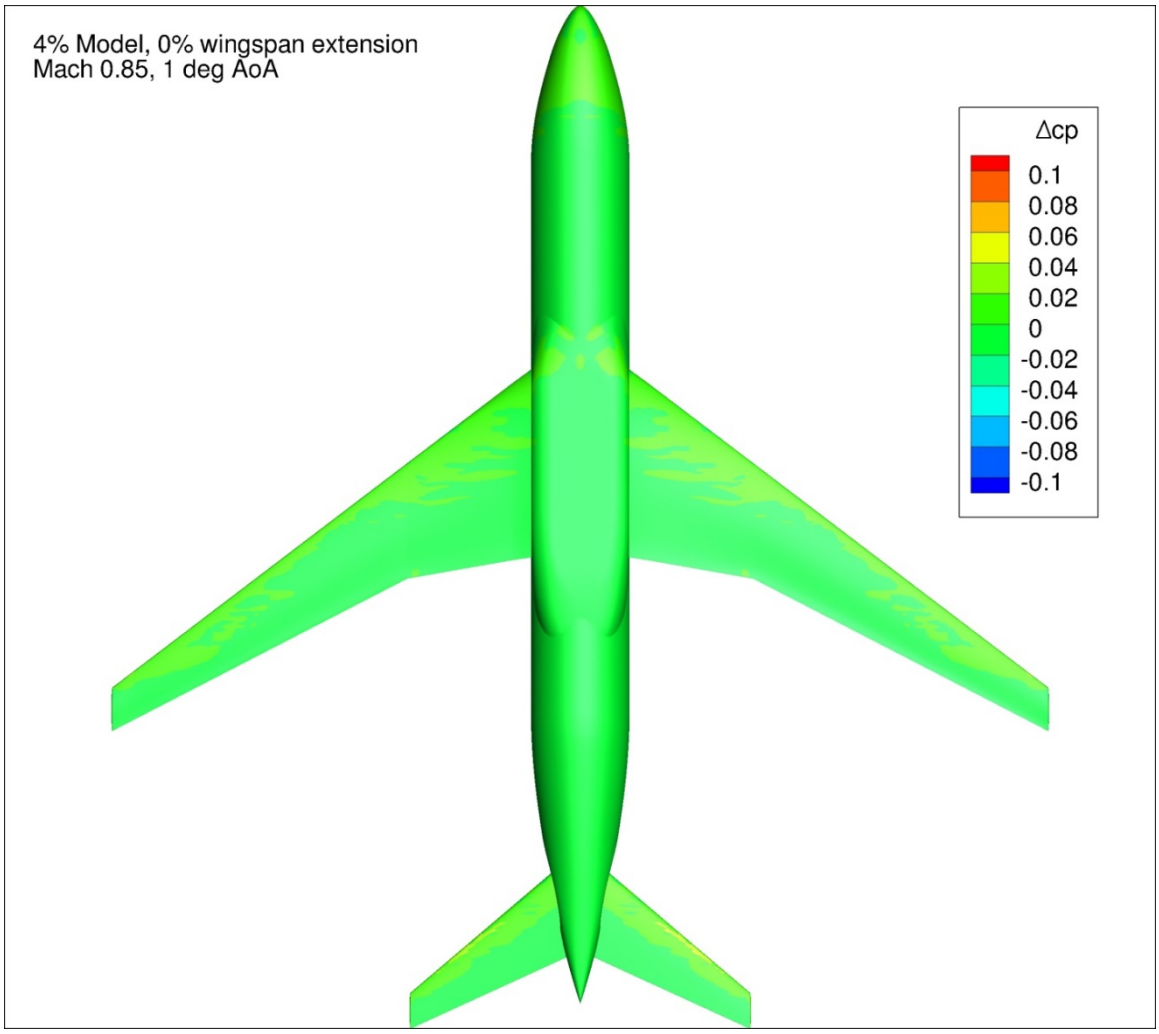

Figure 45. Configuration 1, Difference in Pressure Coefficient between Free-stream and Wind Tunnel Simulations, 1 deg Angle of Attack, Bottom View

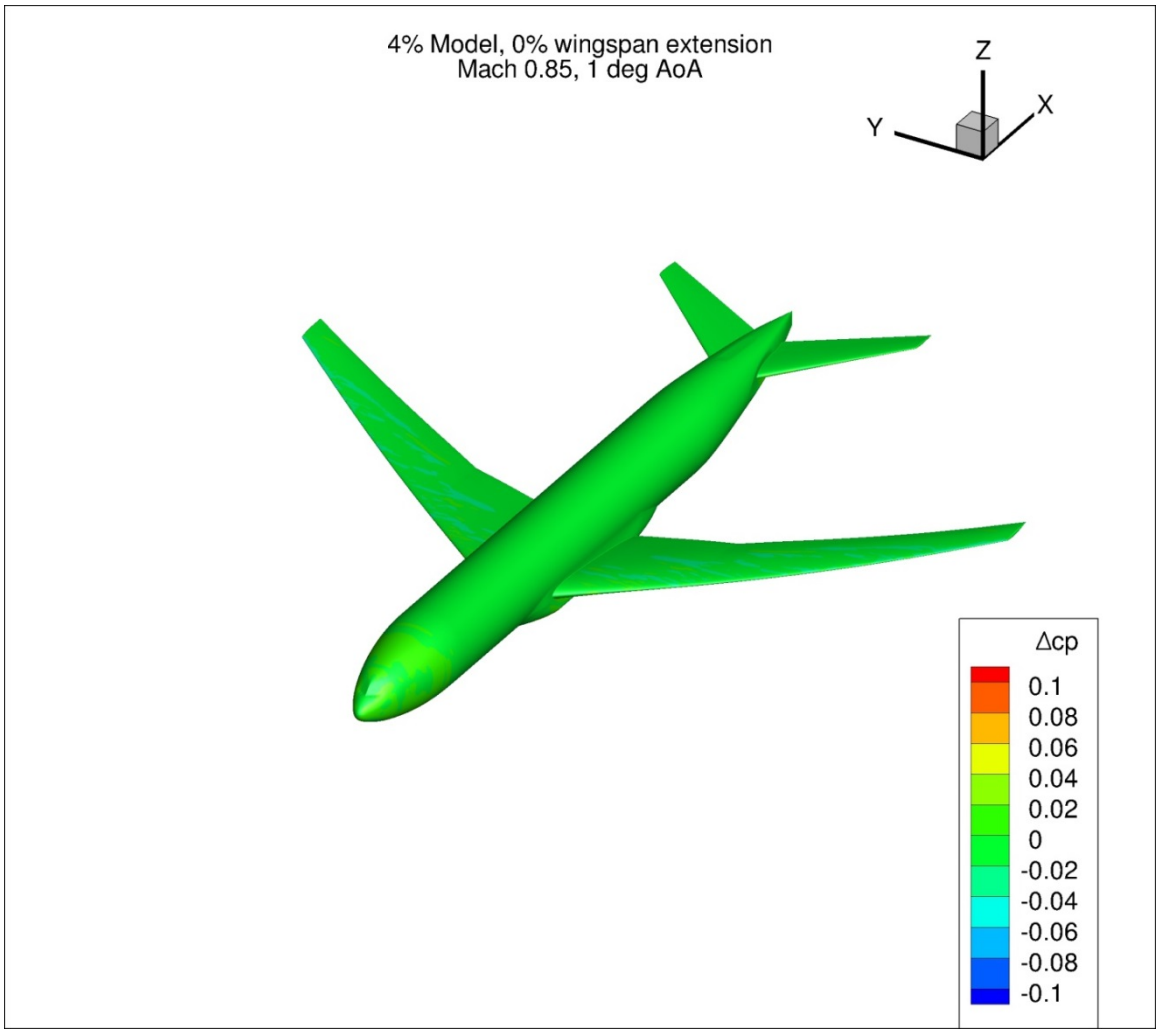

Figure 46. Configuration 1, Difference in Pressure Coefficient between Free-stream and Wind Tunnel Simulations, 1 deg Angle of Attack, Isometric View

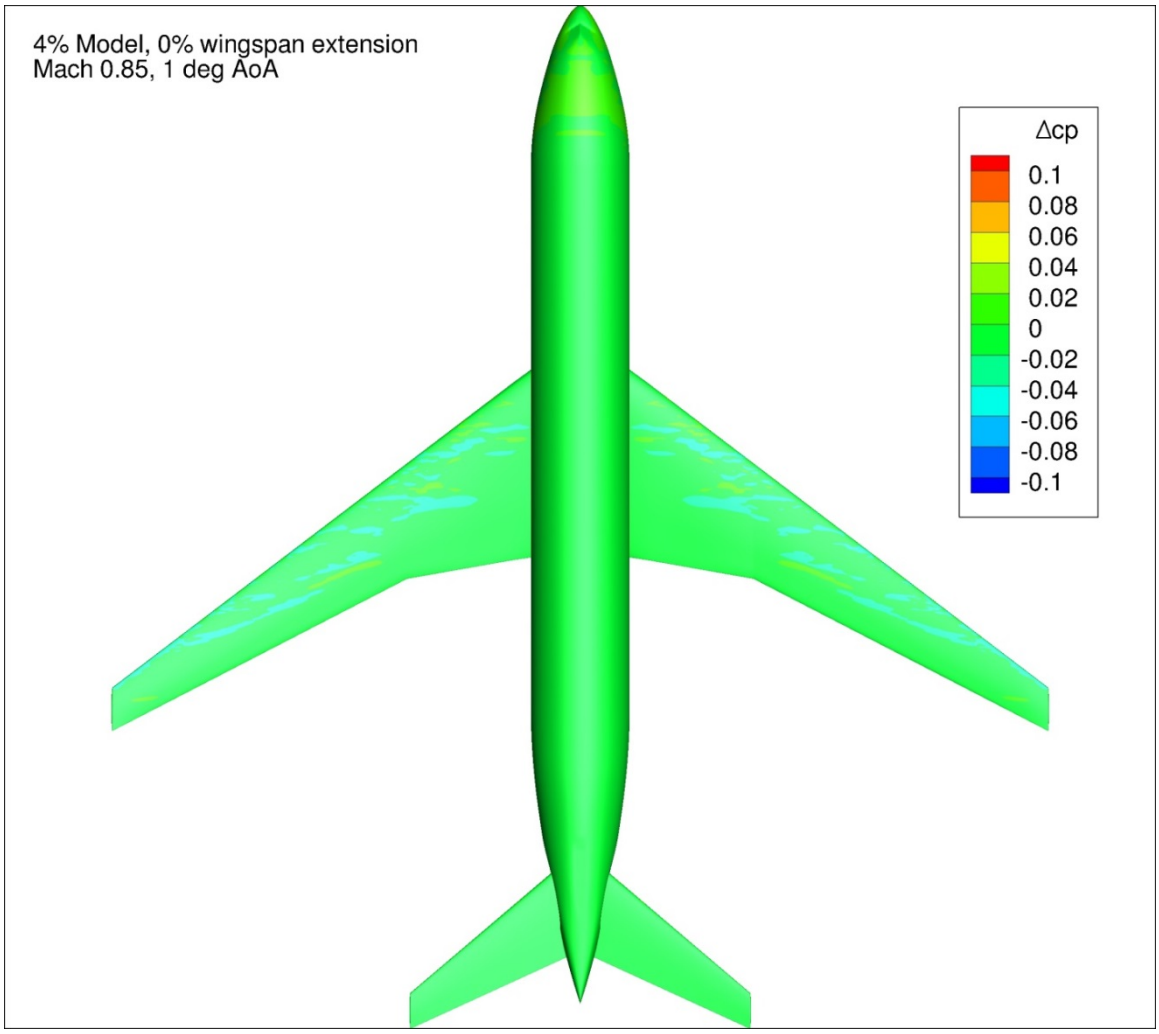

Figure 47. Configuration 1, Difference in Pressure Coefficient between Free-stream and Wind Tunnel Simulations, 1 deg Angle of Attack, Top View

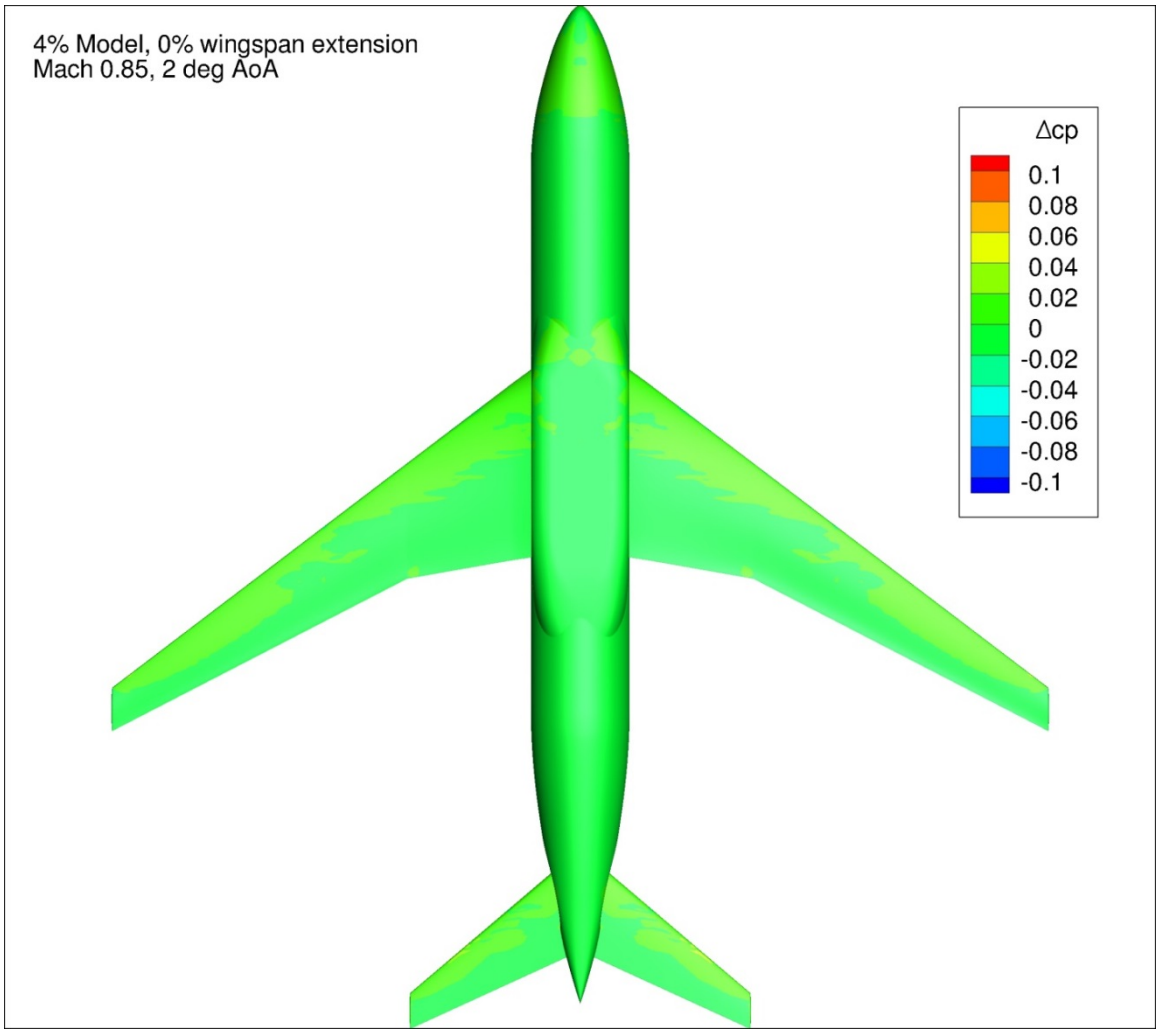

Figure 48. Configuration 1, Difference in Pressure Coefficient between Free-stream and Wind Tunnel Simulations, 2 deg Angle of Attack, Bottom View

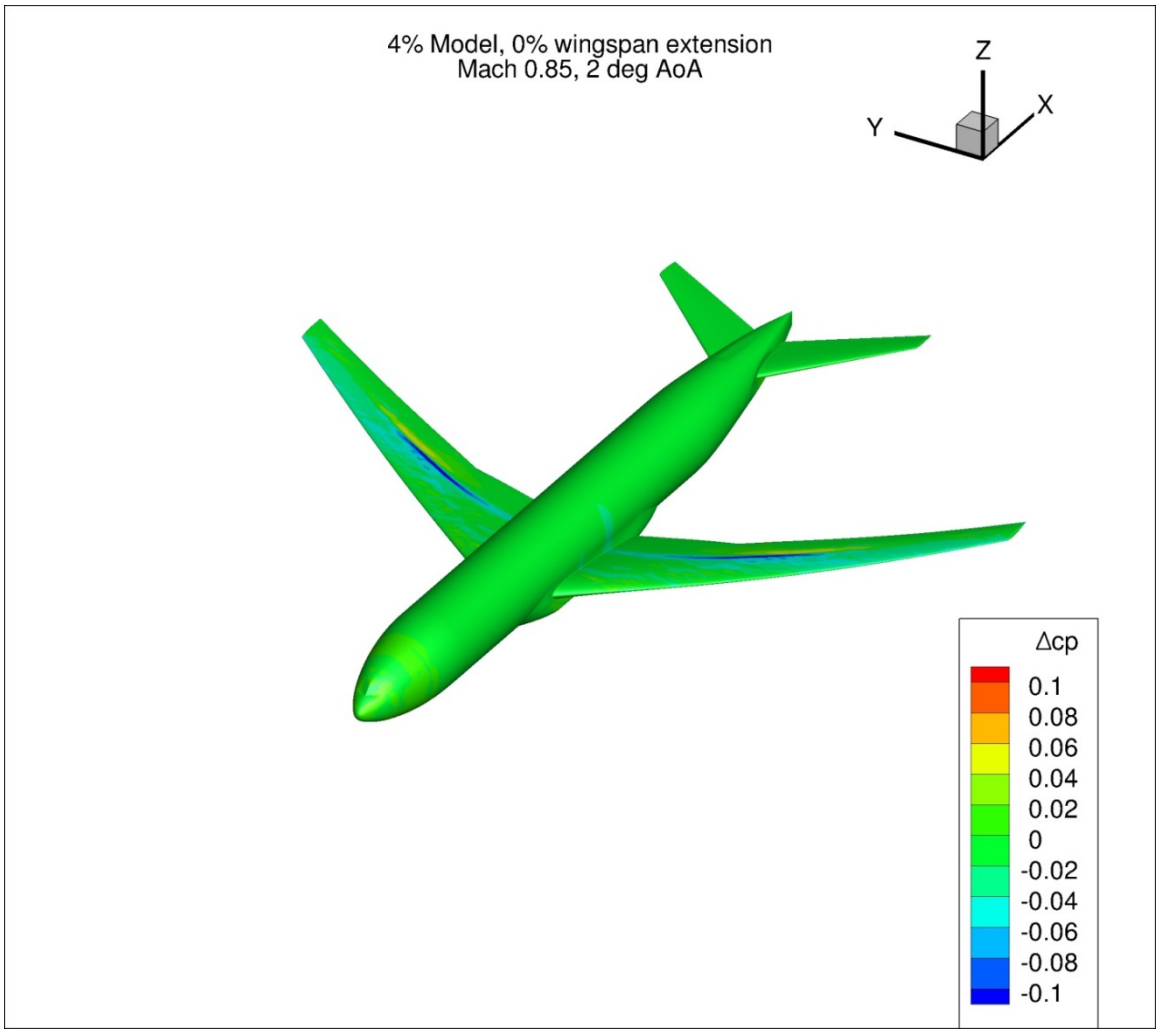

Figure 49. Configuration 1, Difference in Pressure Coefficient between Free-stream and Wind Tunnel Simulations, 2 deg Angle of Attack, Isometric View

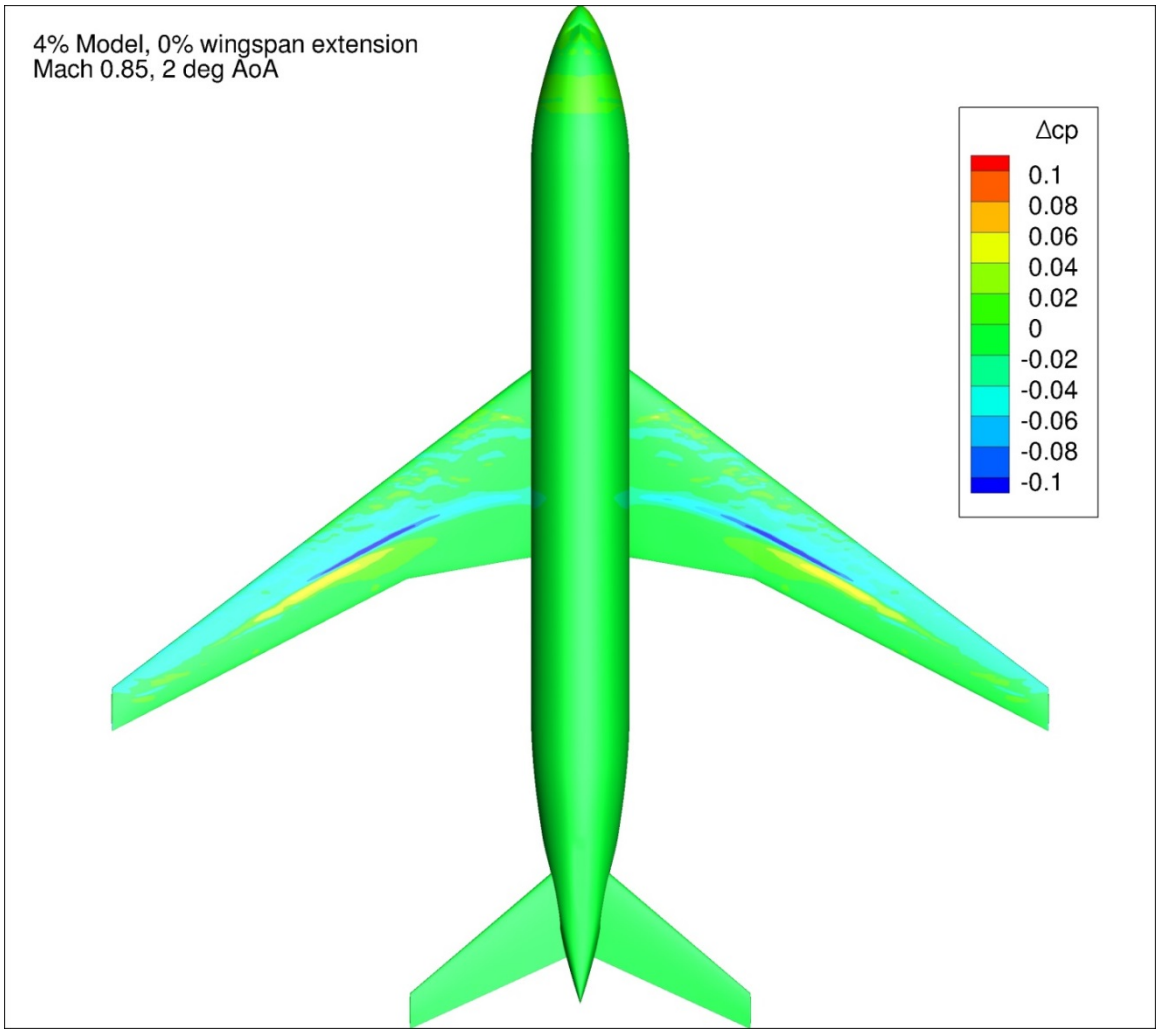

Figure 50. Configuration 1, Difference in Pressure Coefficient between Free-stream and Wind Tunnel Simulations, 2 deg Angle of Attack, Top View

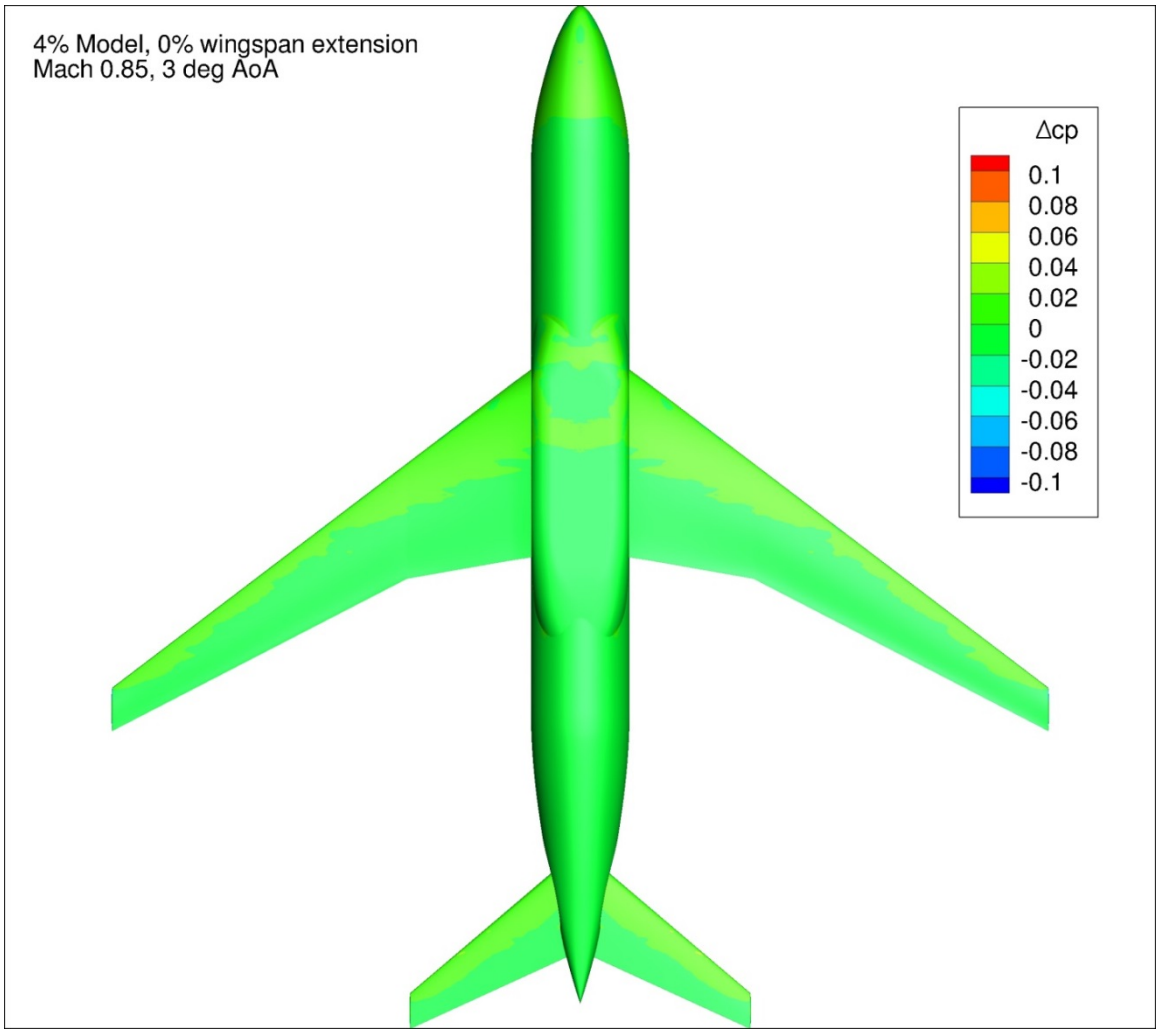

Figure 51. Configuration 1, Difference in Pressure Coefficient between Free-stream and Wind Tunnel Simulations, 3 deg Angle of Attack, Bottom View

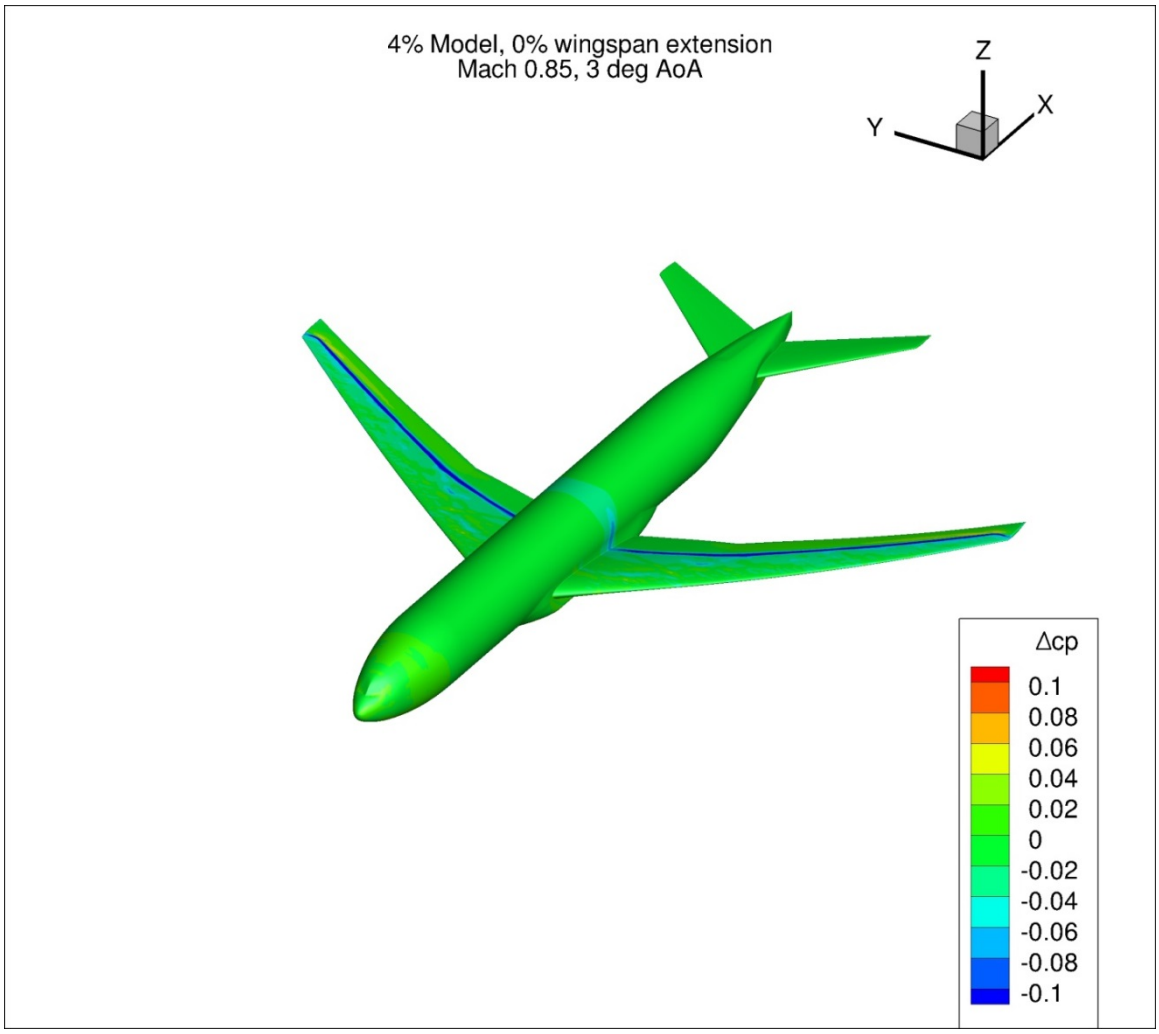

Figure 52. Configuration 1, Difference in Pressure Coefficient between Free-stream and Wind Tunnel Simulations, 3 deg Angle of Attack, Isometric View

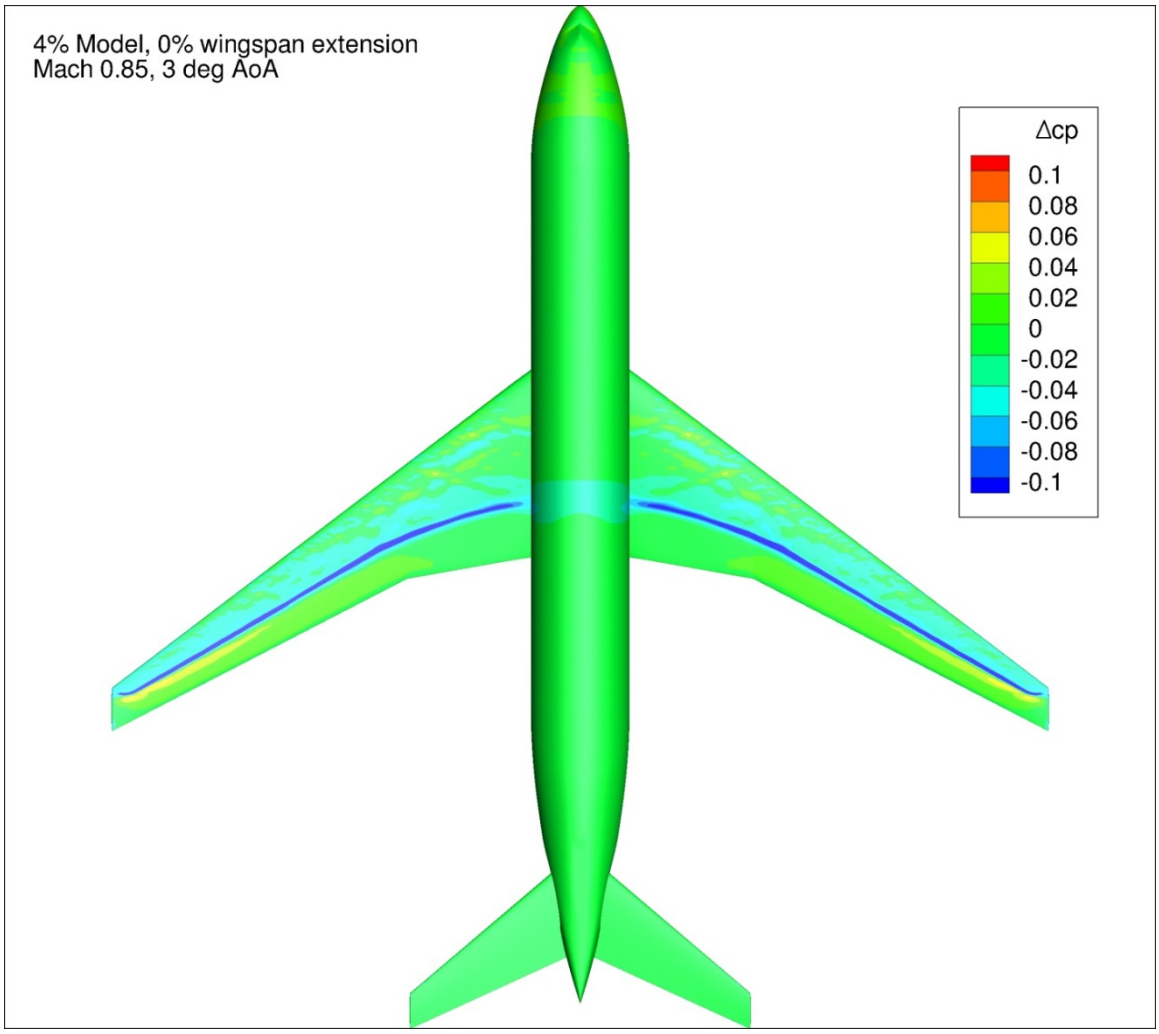

Figure 53. Configuration 1, Difference in Pressure Coefficient between Free-stream and Wind Tunnel Simulations, 3 deg Angle of Attack, Top View

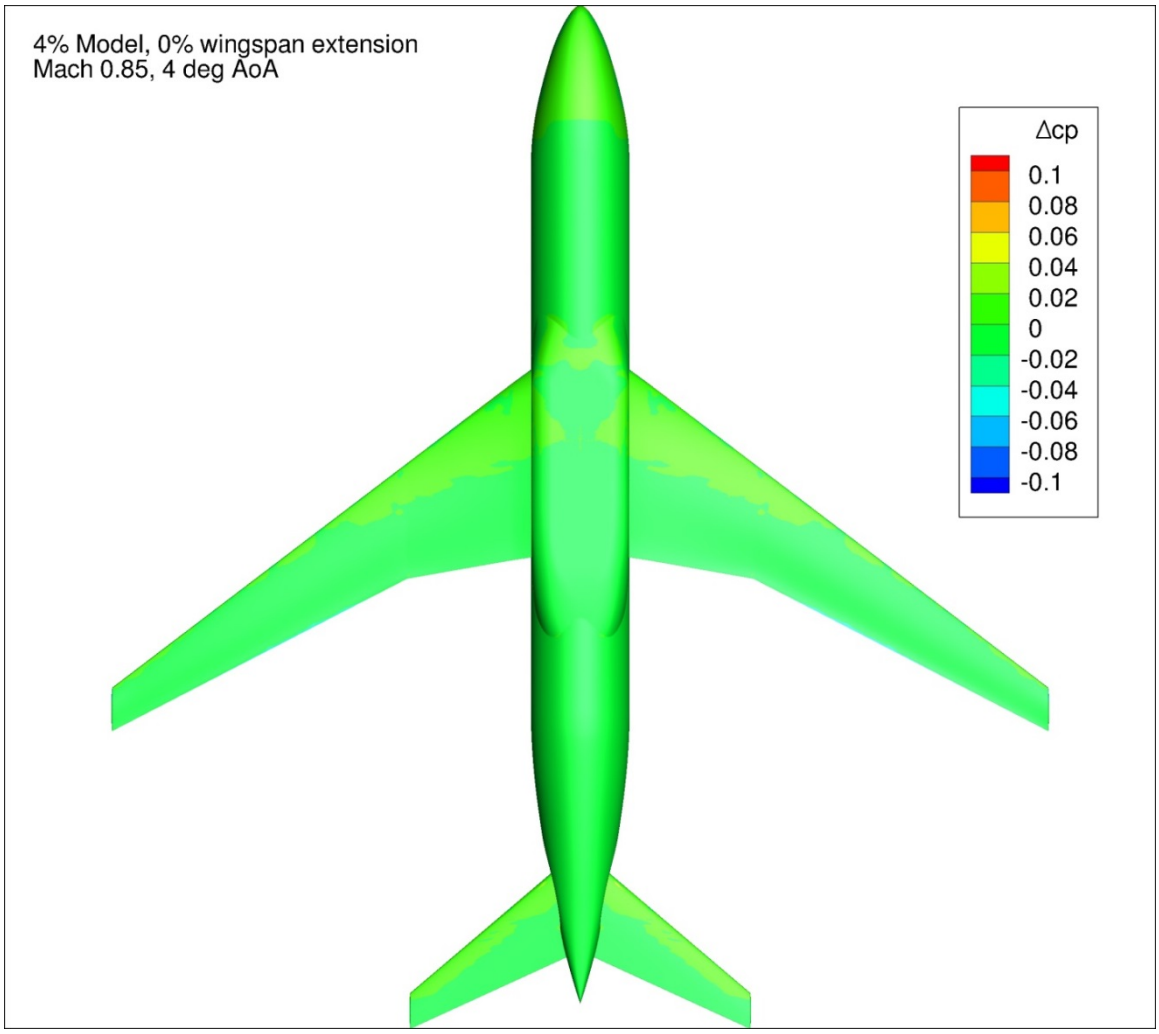

Figure 54. Configuration 1, Difference in Pressure Coefficient between Free-stream and Wind Tunnel Simulations, 4 deg Angle of Attack, Bottom View

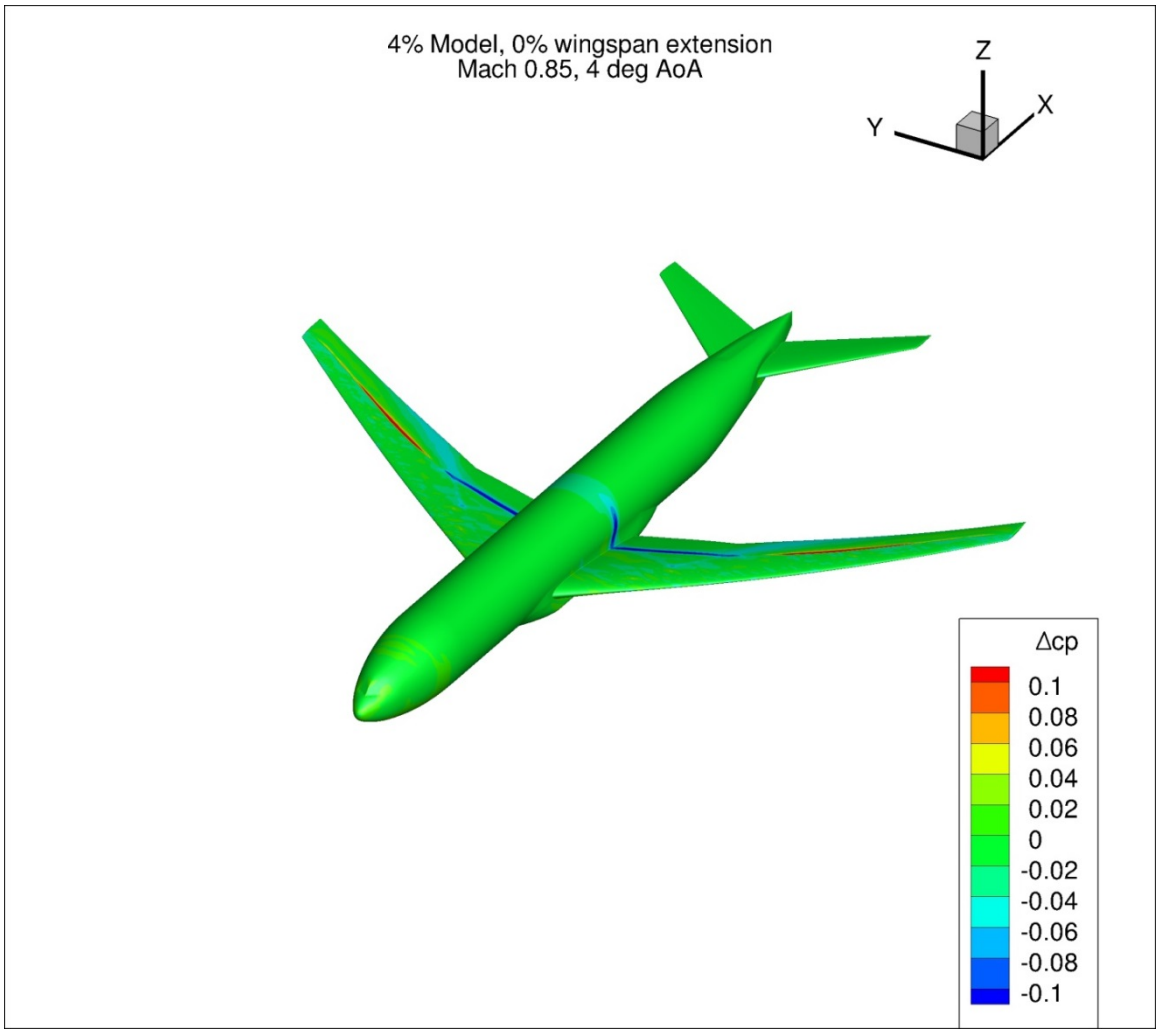

Figure 55. Configuration 1, Difference in Pressure Coefficient between Free-stream and Wind Tunnel Simulations, 4 deg Angle of Attack, Isometric View

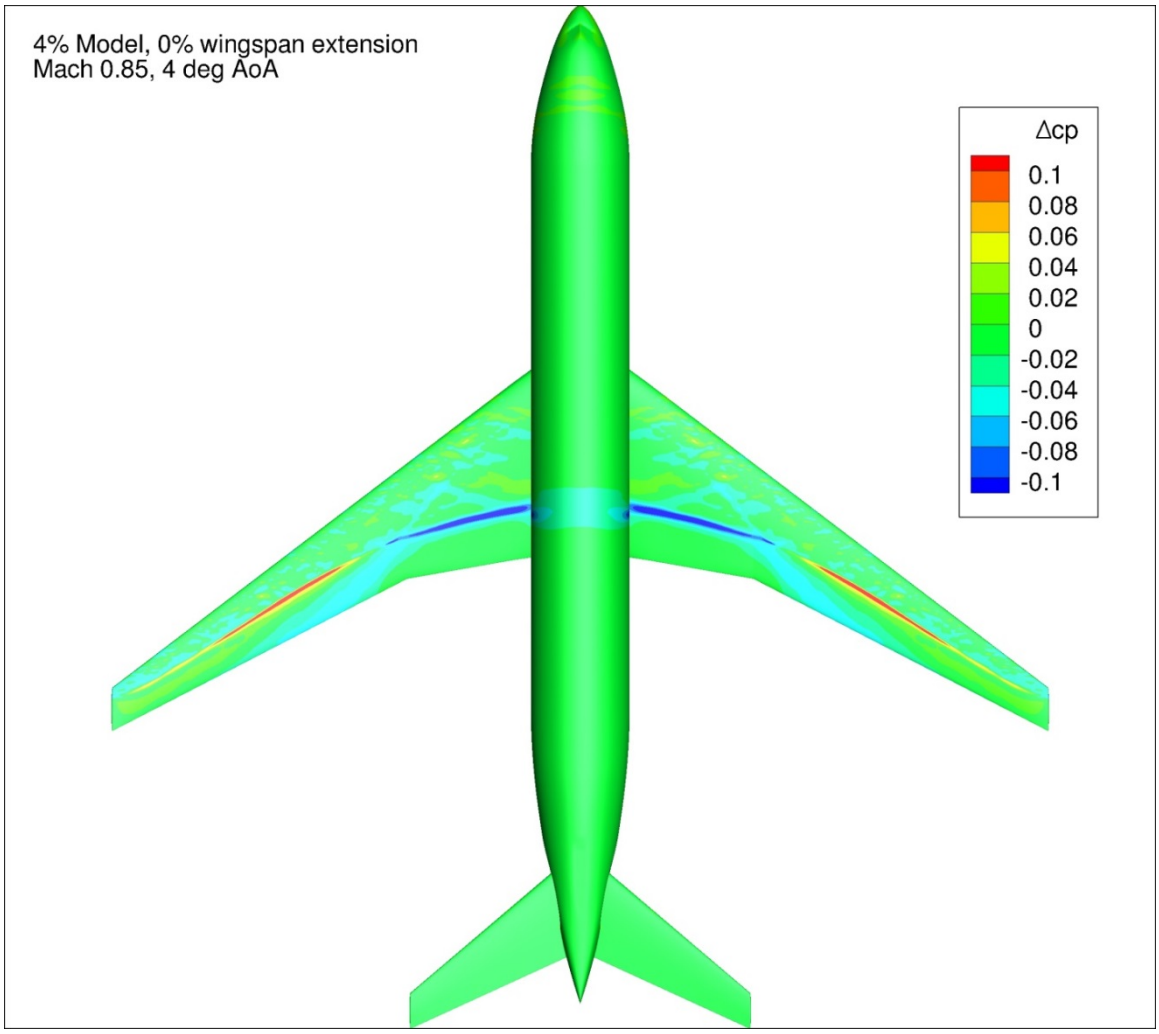

Figure 56. Configuration 1, Difference in Pressure Coefficient between Free-stream and Wind Tunnel Simulations, 4 deg Angle of Attack, Top View

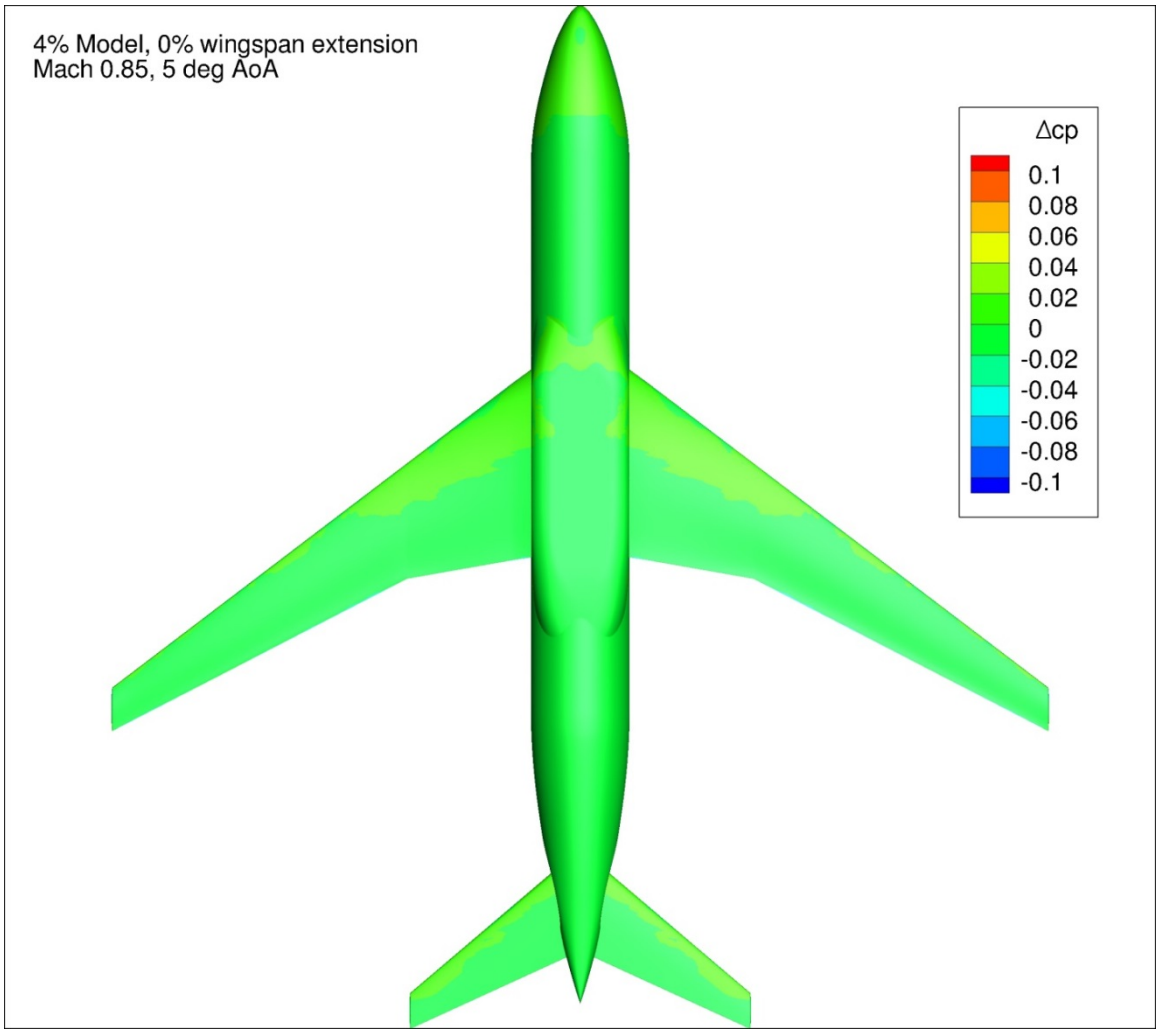

Figure 57. Configuration 1, Difference in Pressure Coefficient between Free-stream and Wind Tunnel Simulations, 5 deg Angle of Attack, Bottom View

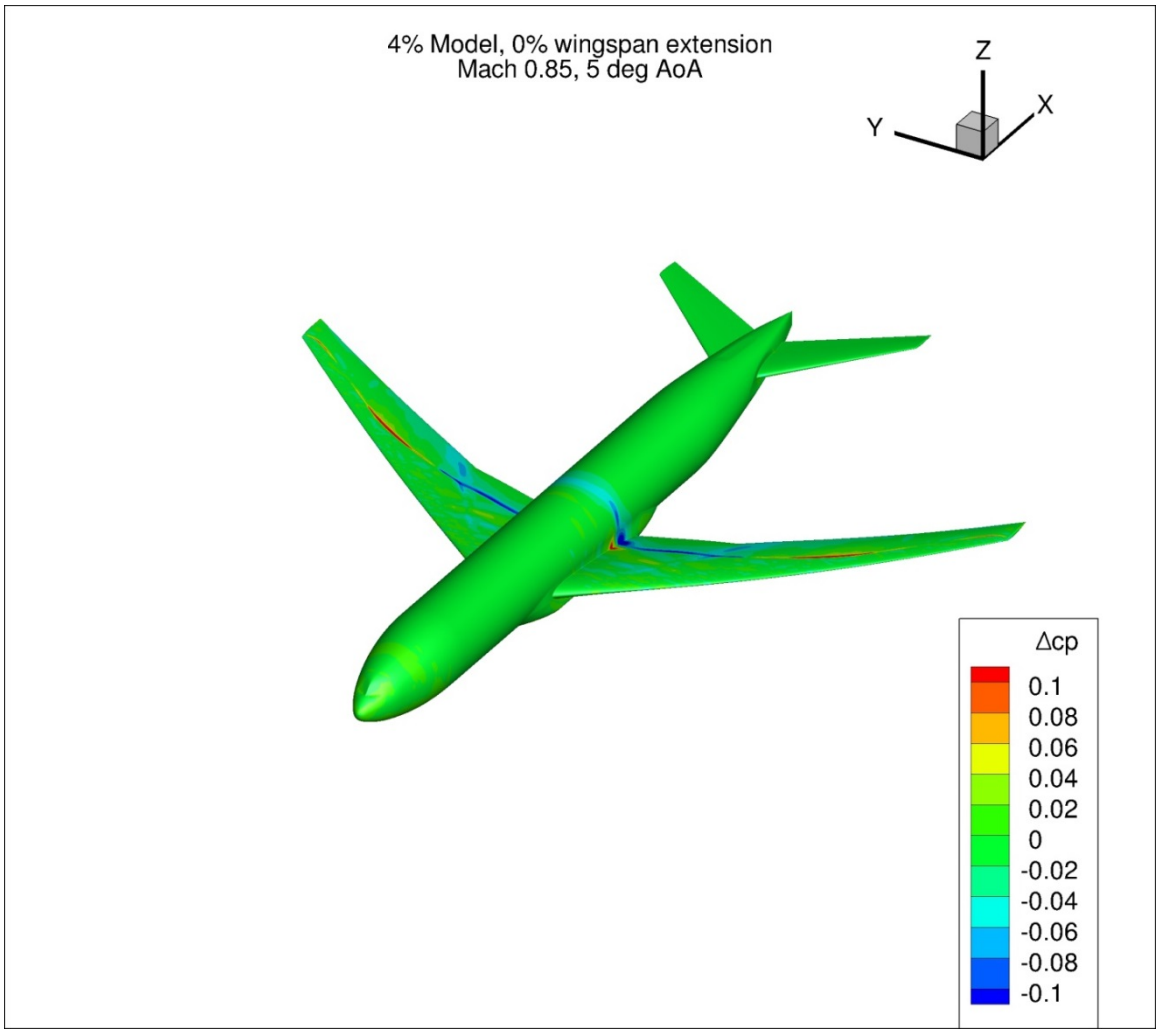

Figure 58. Configuration 1, Difference in Pressure Coefficient between Free-stream and Wind Tunnel Simulations, 5 deg Angle of Attack, Isometric View

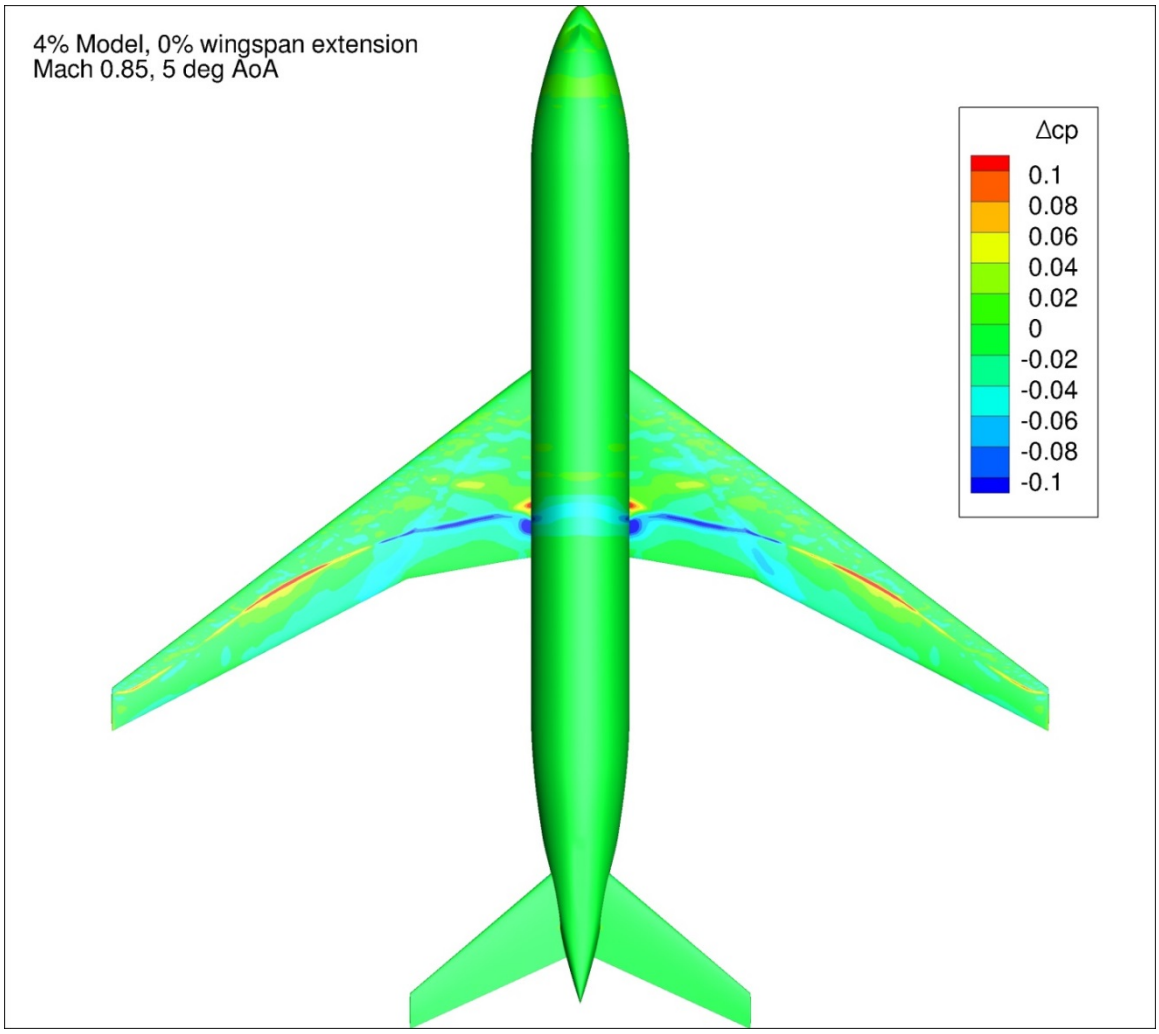

Figure 59. Configuration 1, Difference in Pressure Coefficient between Free-stream and Wind Tunnel Simulations, 5 deg Angle of Attack, Top View

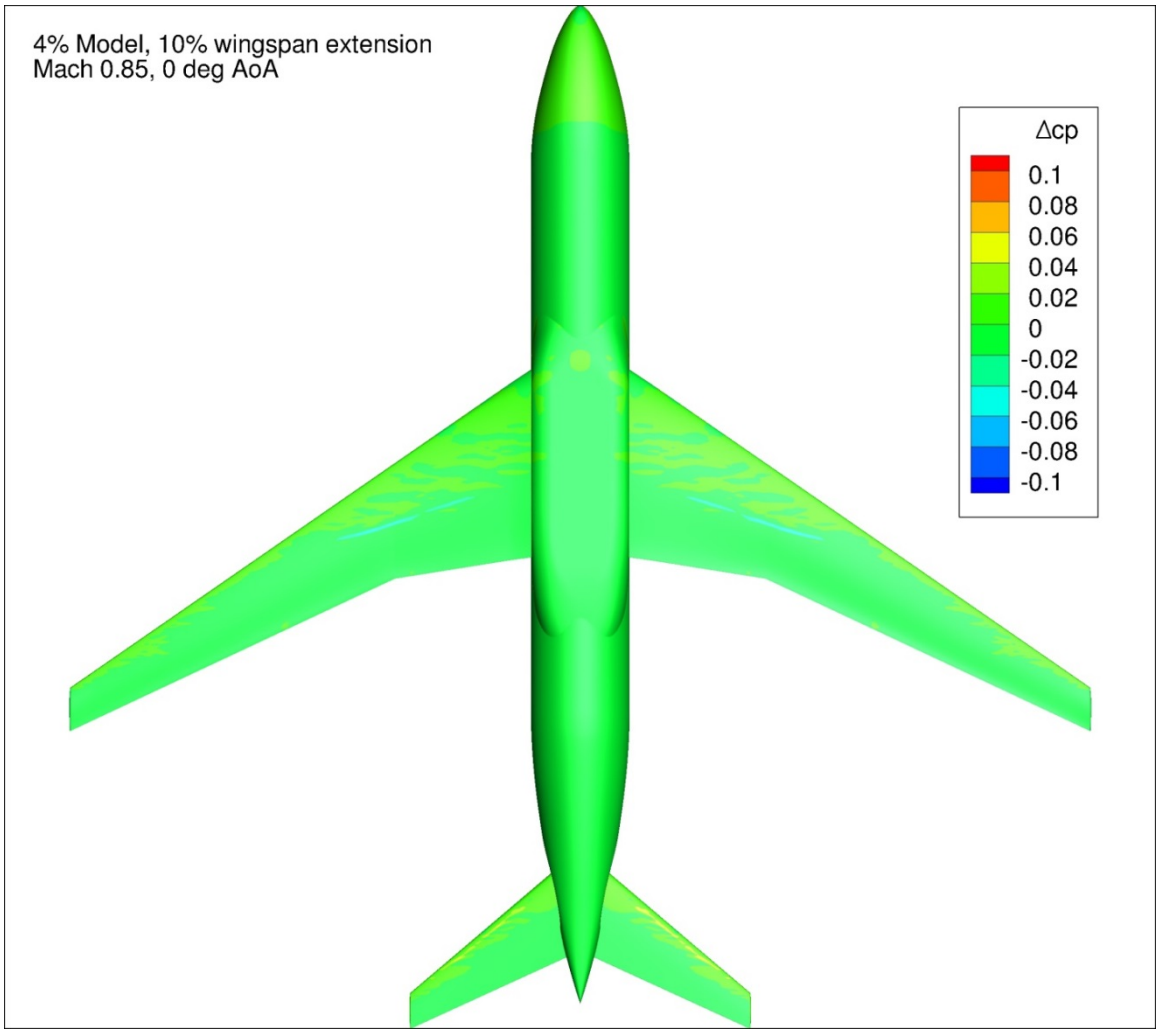

Figure 60. Configuration 1.1, Difference in Pressure Coefficient between Free-stream and Wind Tunnel Simulations, 0 deg Angle of Attack, Bottom View

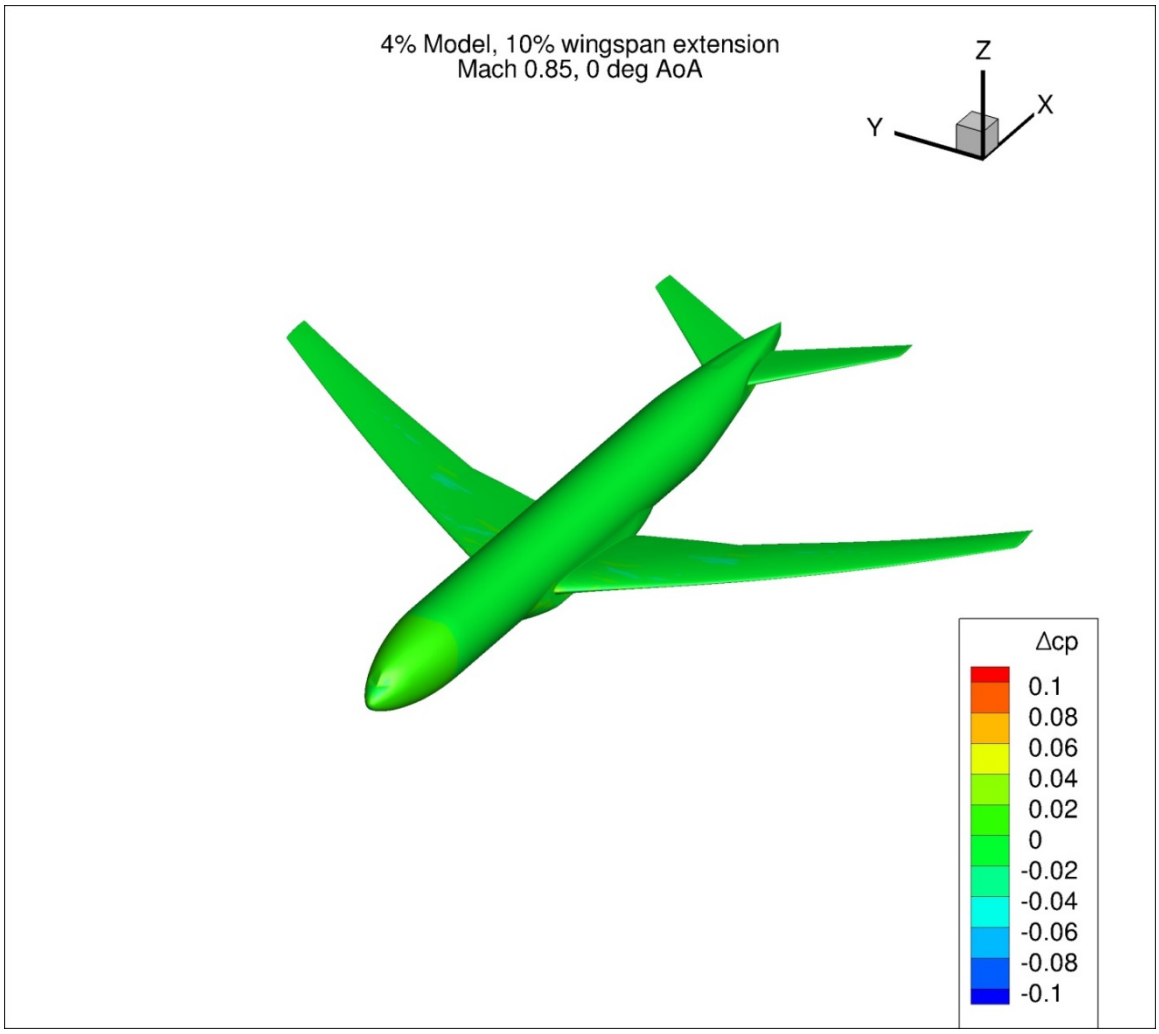

Figure 61. Configuration 1.1, Difference in Pressure Coefficient between Free-stream and Wind Tunnel Simulations, 0 deg Angle of Attack, Isometric View

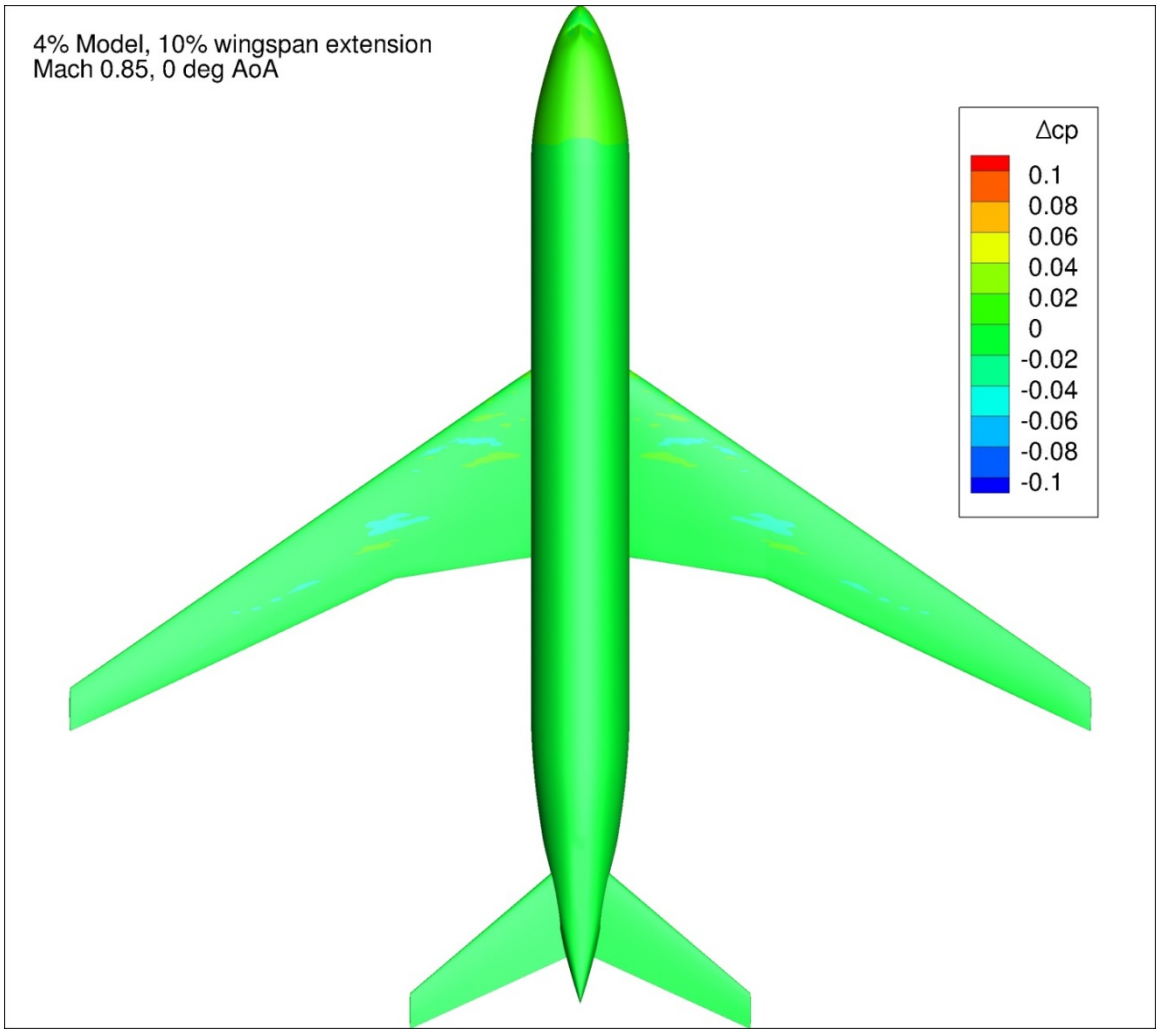

Figure 62. Configuration 1.1, Difference in Pressure Coefficient between Free-stream and Wind Tunnel Simulations, 0 deg Angle of Attack, Top View

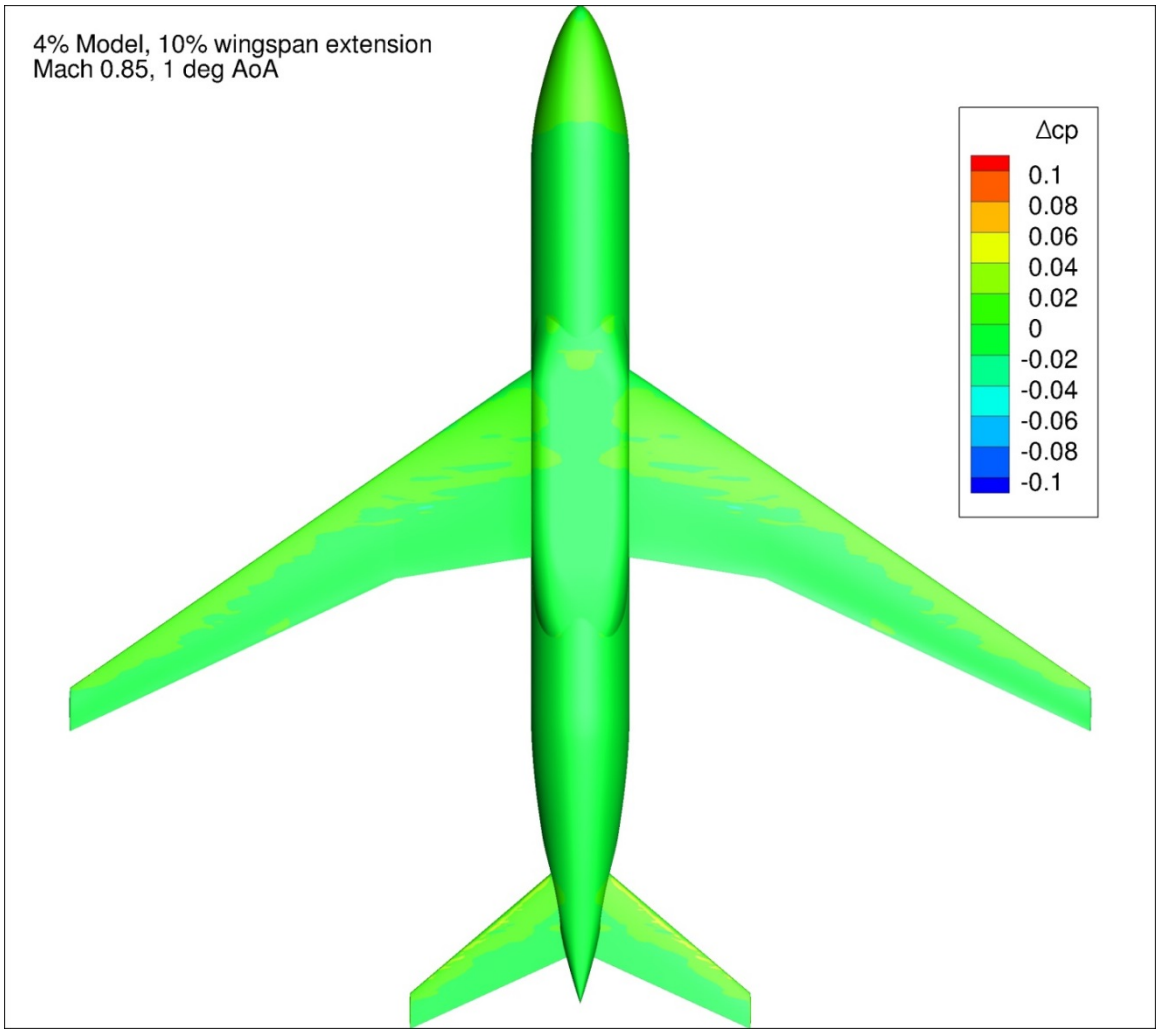

Figure 63. Configuration 1.1, Difference in Pressure Coefficient between Free-stream and Wind Tunnel Simulations, 1 deg Angle of Attack, Bottom View

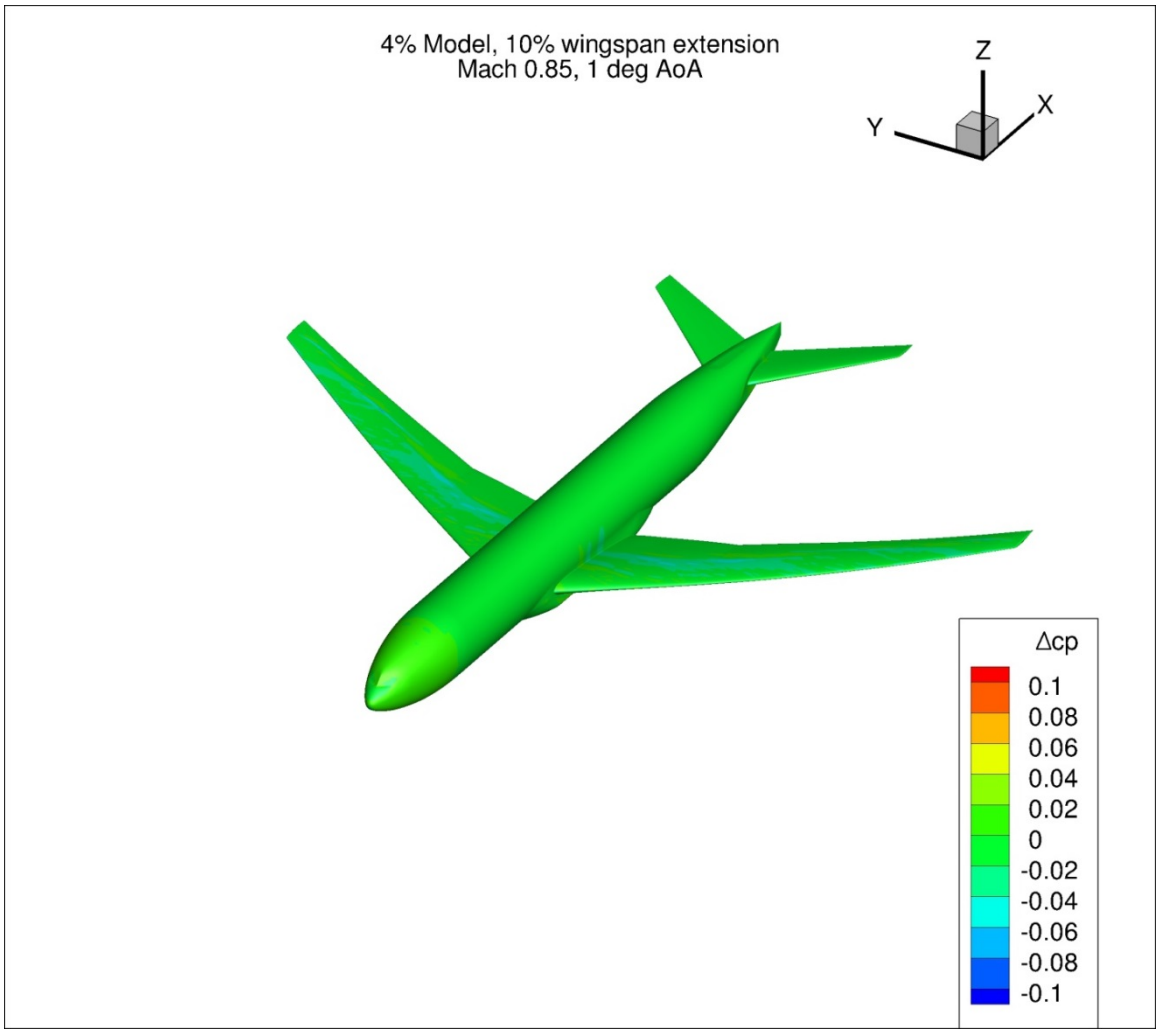

Figure 64. Configuration 1.1, Difference in Pressure Coefficient between Free-stream and Wind Tunnel Simulations, 1 deg Angle of Attack, Isometric View

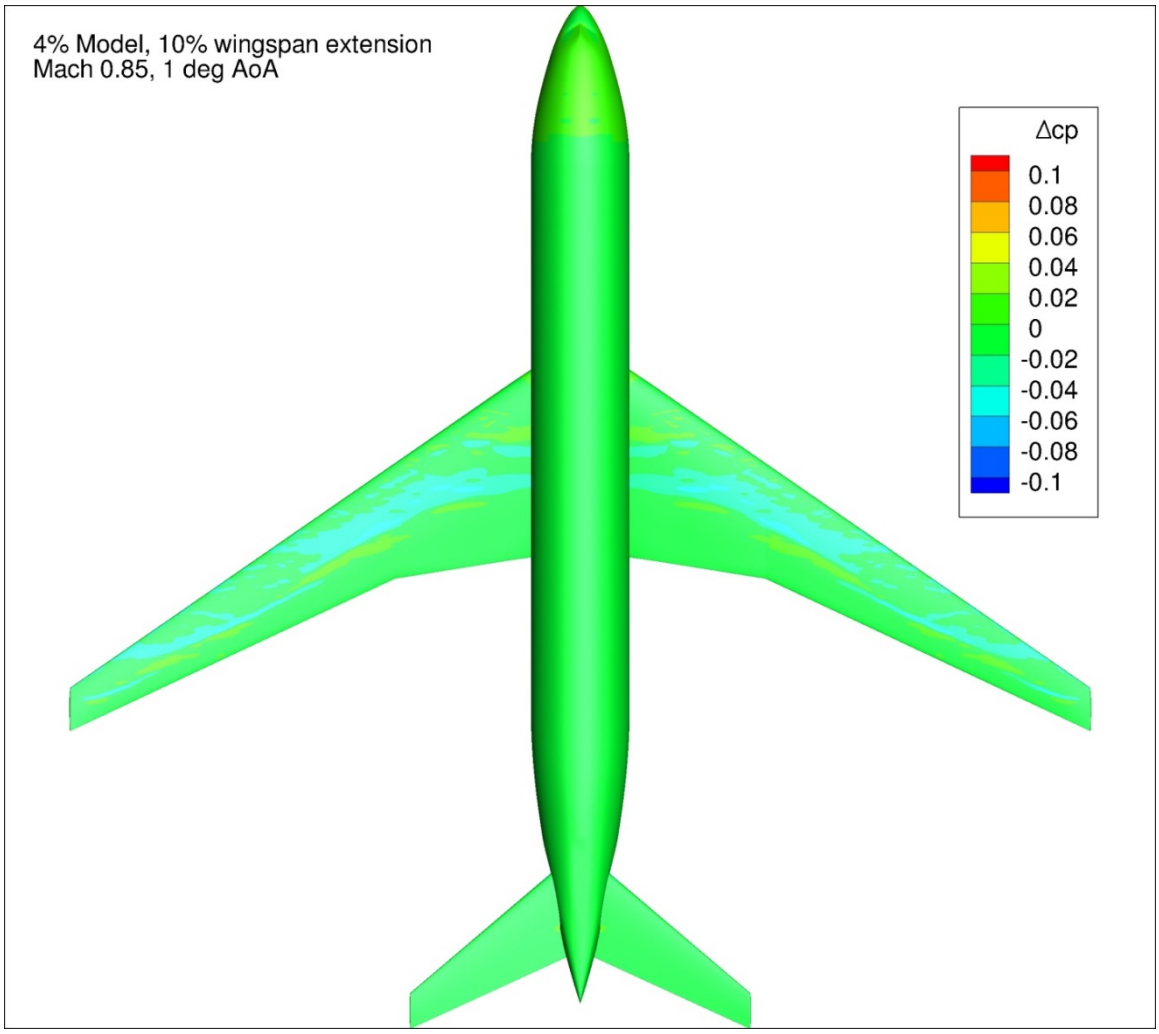

Figure 65. Configuration 1.1, Difference in Pressure Coefficient between Free-stream and Wind Tunnel Simulations, 1 deg Angle of Attack, Top View

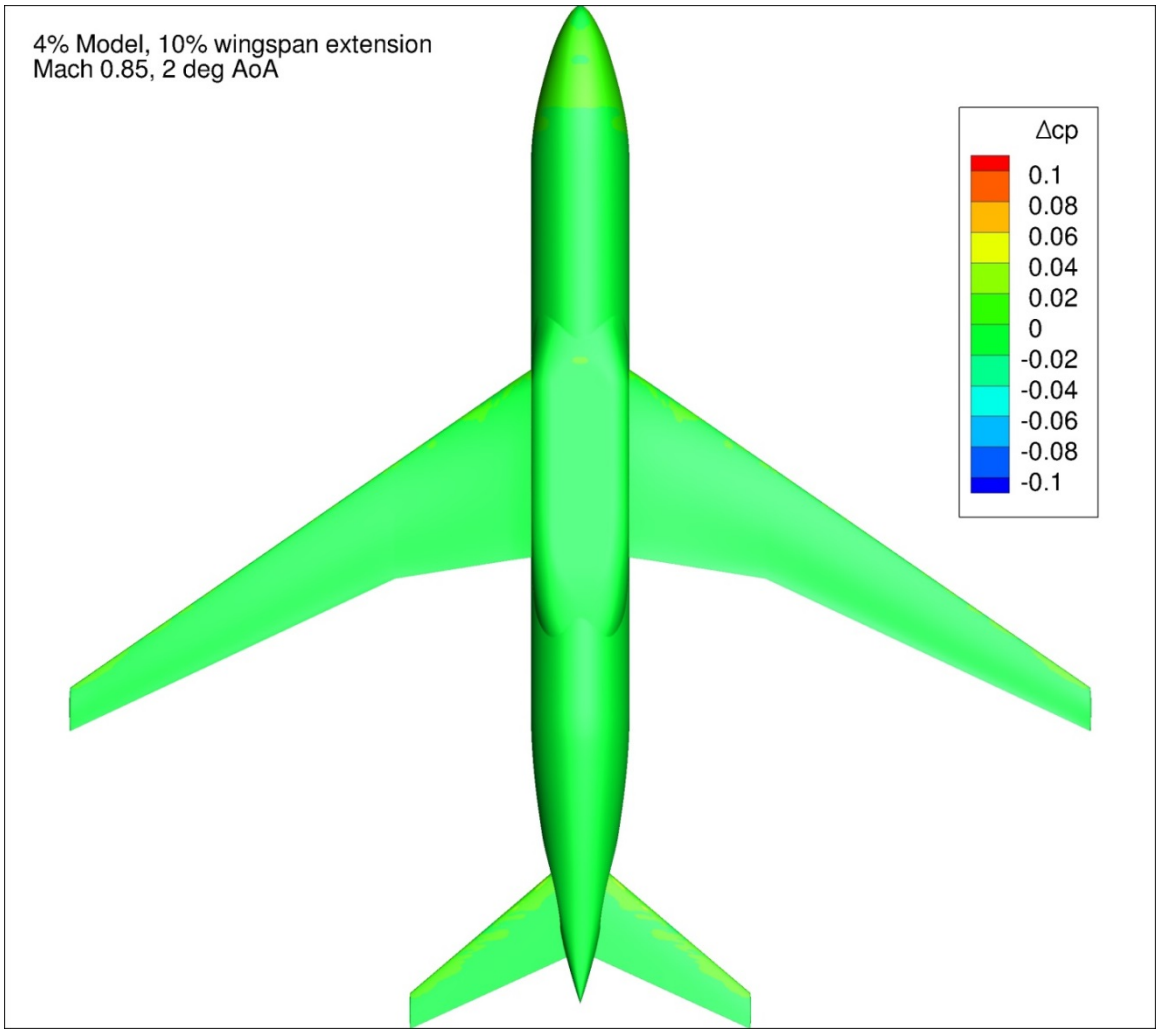

Figure 66. Configuration 1.1, Difference in Pressure Coefficient between Free-stream and Wind Tunnel Simulations, 2 deg Angle of Attack, Bottom View

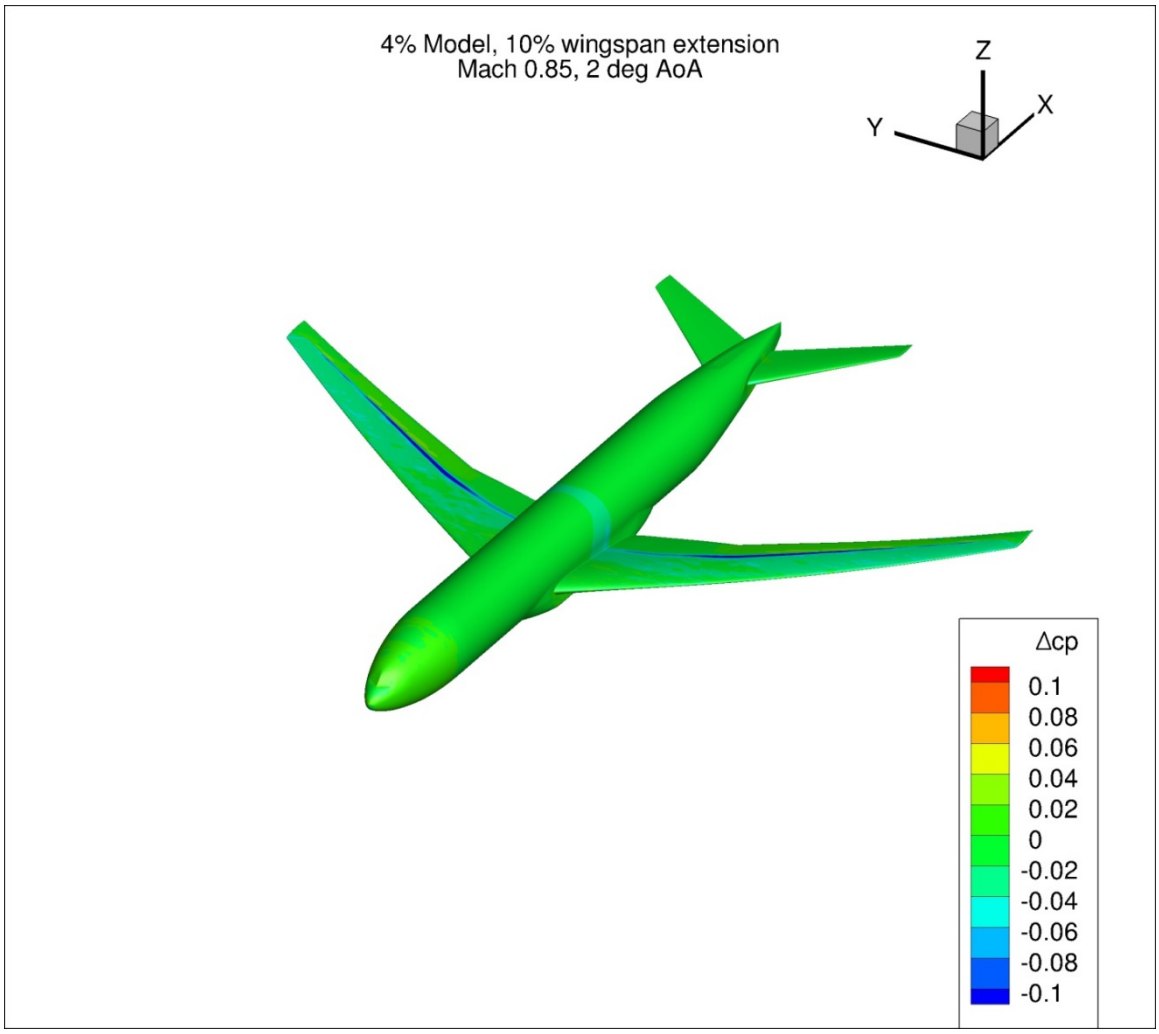

Figure 67. Configuration 1.1, Difference in Pressure Coefficient between Free-stream and Wind Tunnel Simulations, 2 deg Angle of Attack, Isometric View

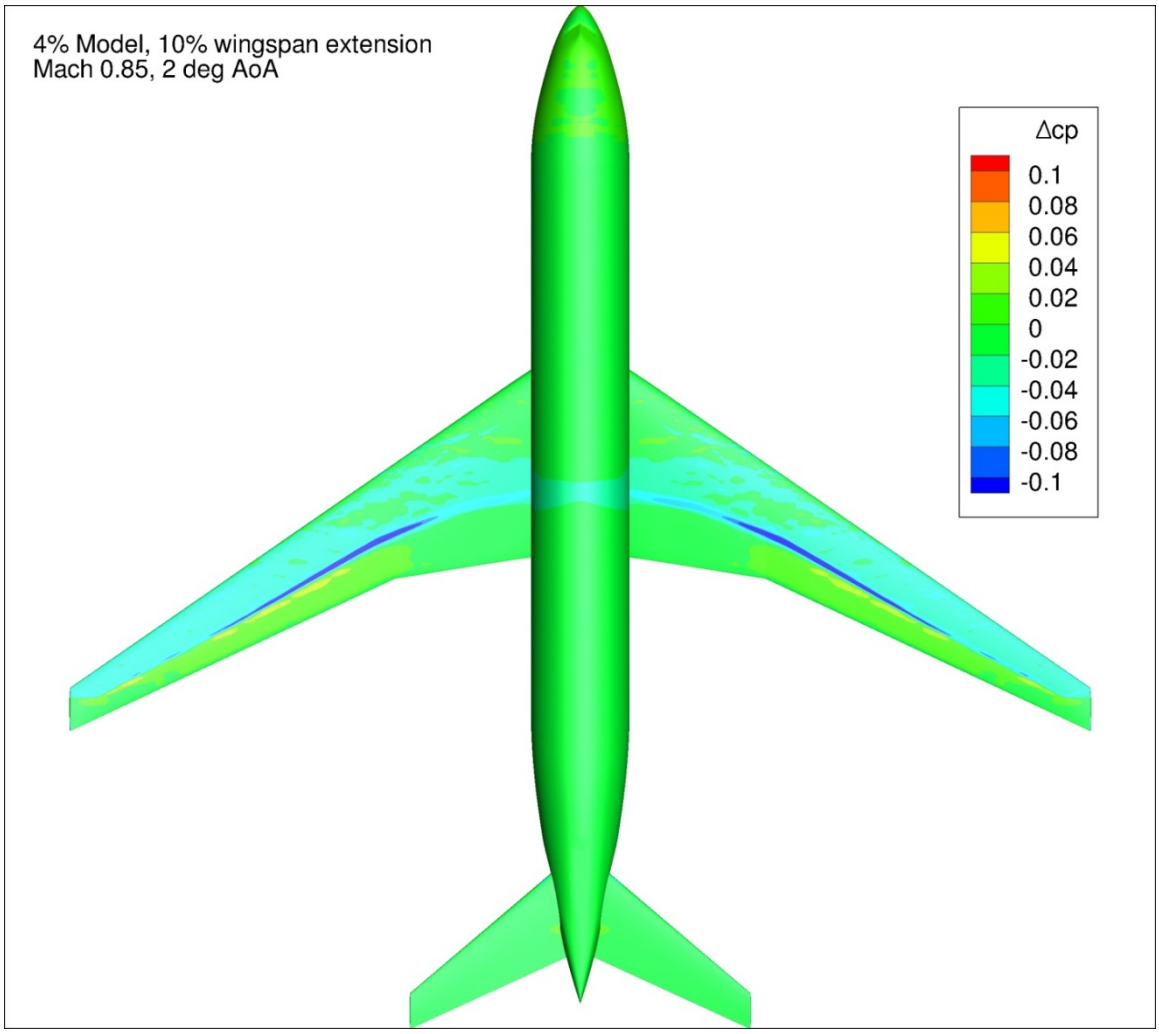

Figure 68. Configuration 1.1, Difference in Pressure Coefficient between Free-stream and Wind Tunnel Simulations, 2 deg Angle of Attack, Top View

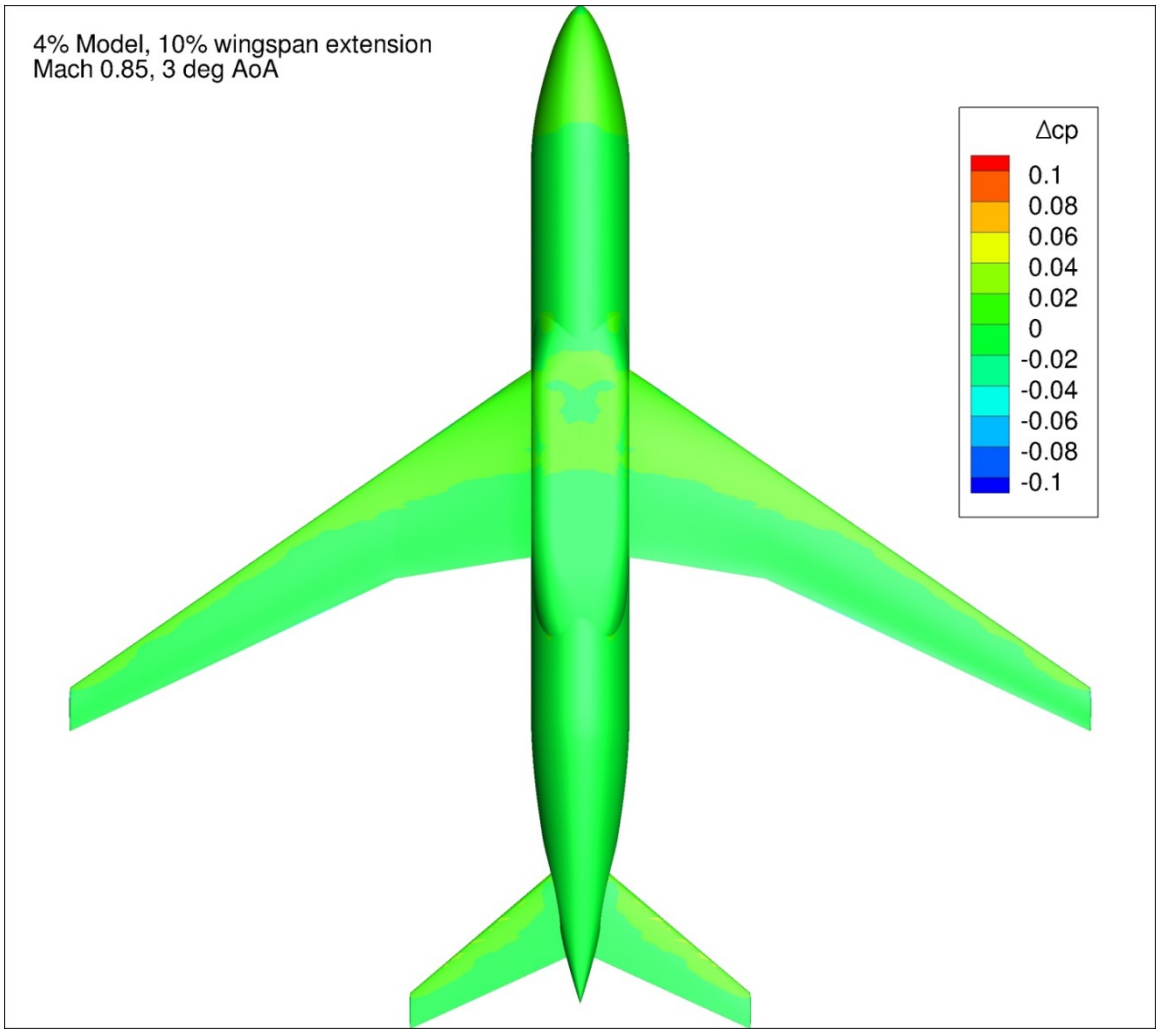

Figure 69. Configuration 1.1, Difference in Pressure Coefficient between Free-stream and Wind Tunnel Simulations, 3 deg Angle of Attack, Bottom View

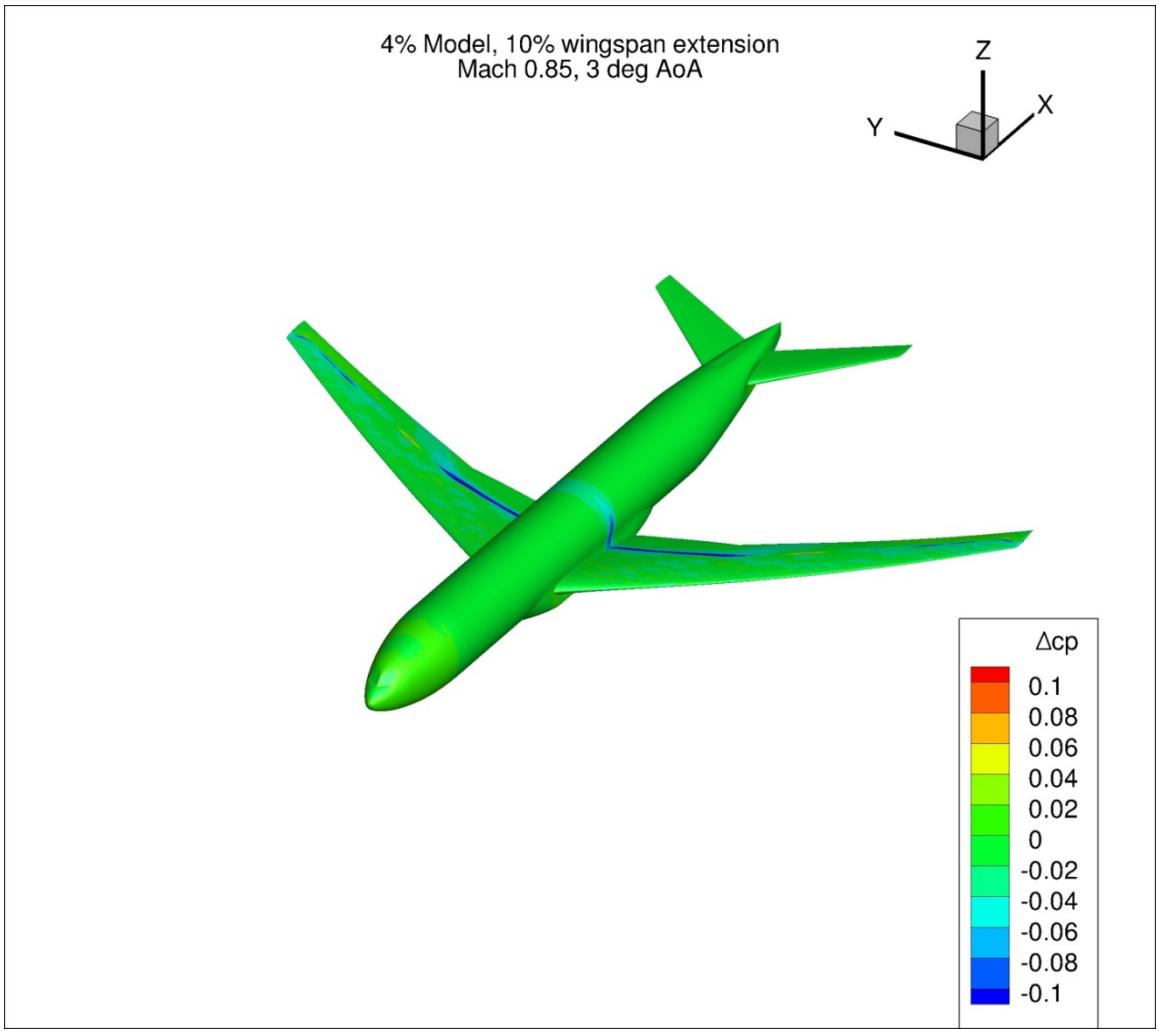

Figure 70. Configuration 1.1, Difference in Pressure Coefficient between Free-stream and Wind Tunnel Simulations, 3 deg Angle of Attack, Isometric View

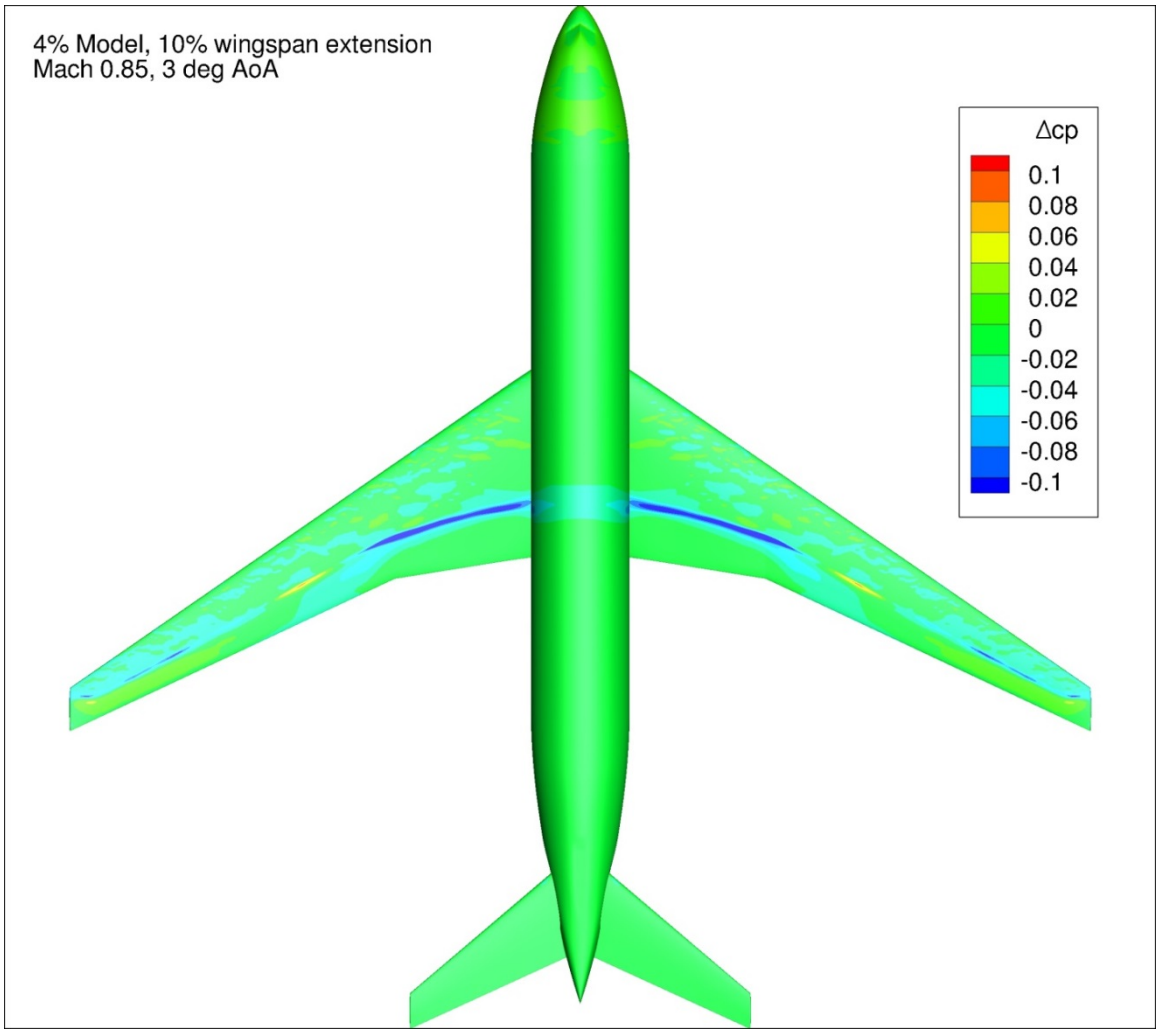

Figure 71. Configuration 1.1, Difference in Pressure Coefficient between Free-stream and Wind Tunnel Simulations, 3 deg Angle of Attack, Top View

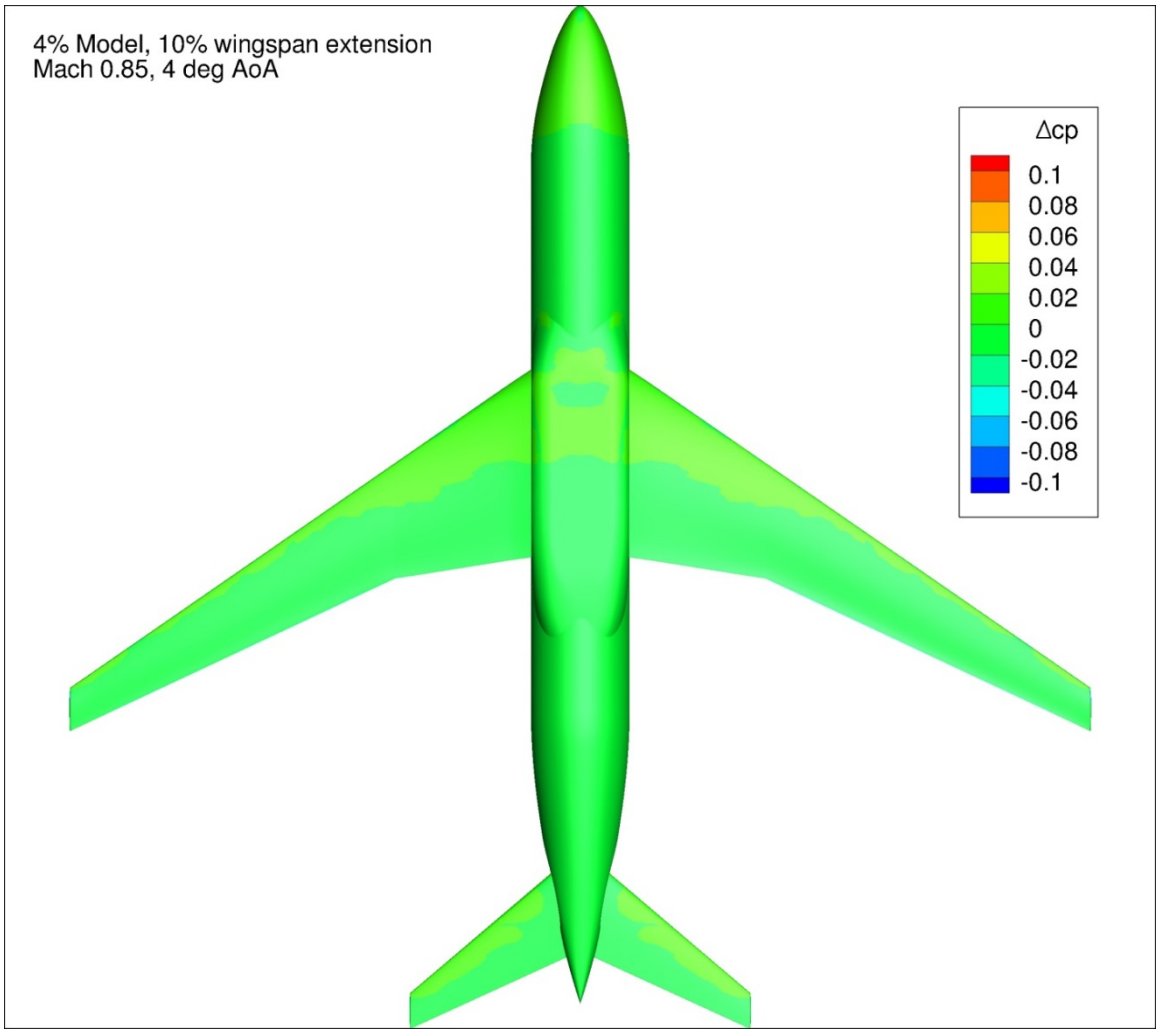

Figure 72. Configuration 1.1, Difference in Pressure Coefficient between Free-stream and Wind Tunnel Simulations, 4 deg Angle of Attack, Bottom View

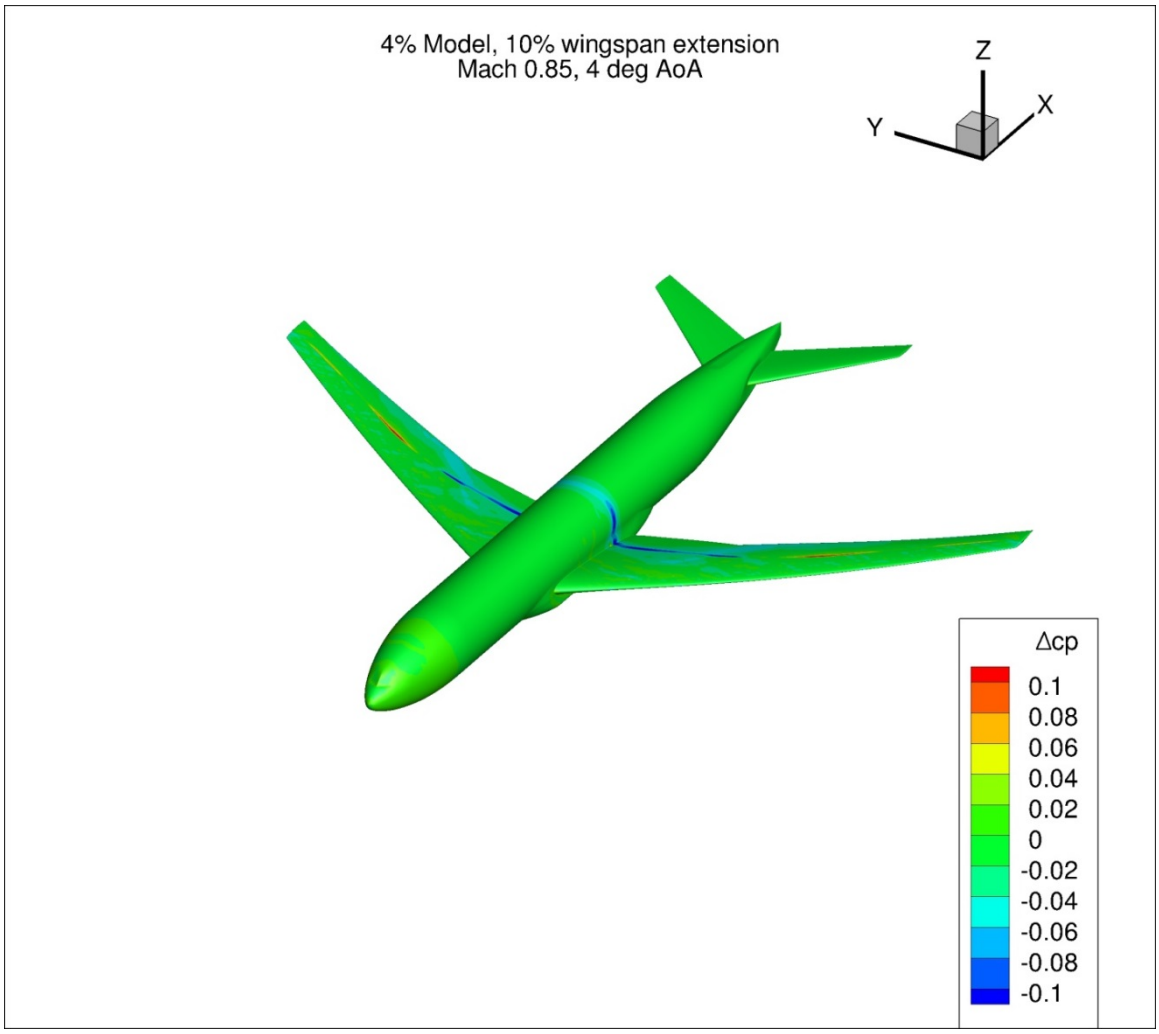

Figure 73. Configuration 1.1, Difference in Pressure Coefficient between Free-stream and Wind Tunnel Simulations, 4 deg Angle of Attack, Isometric View

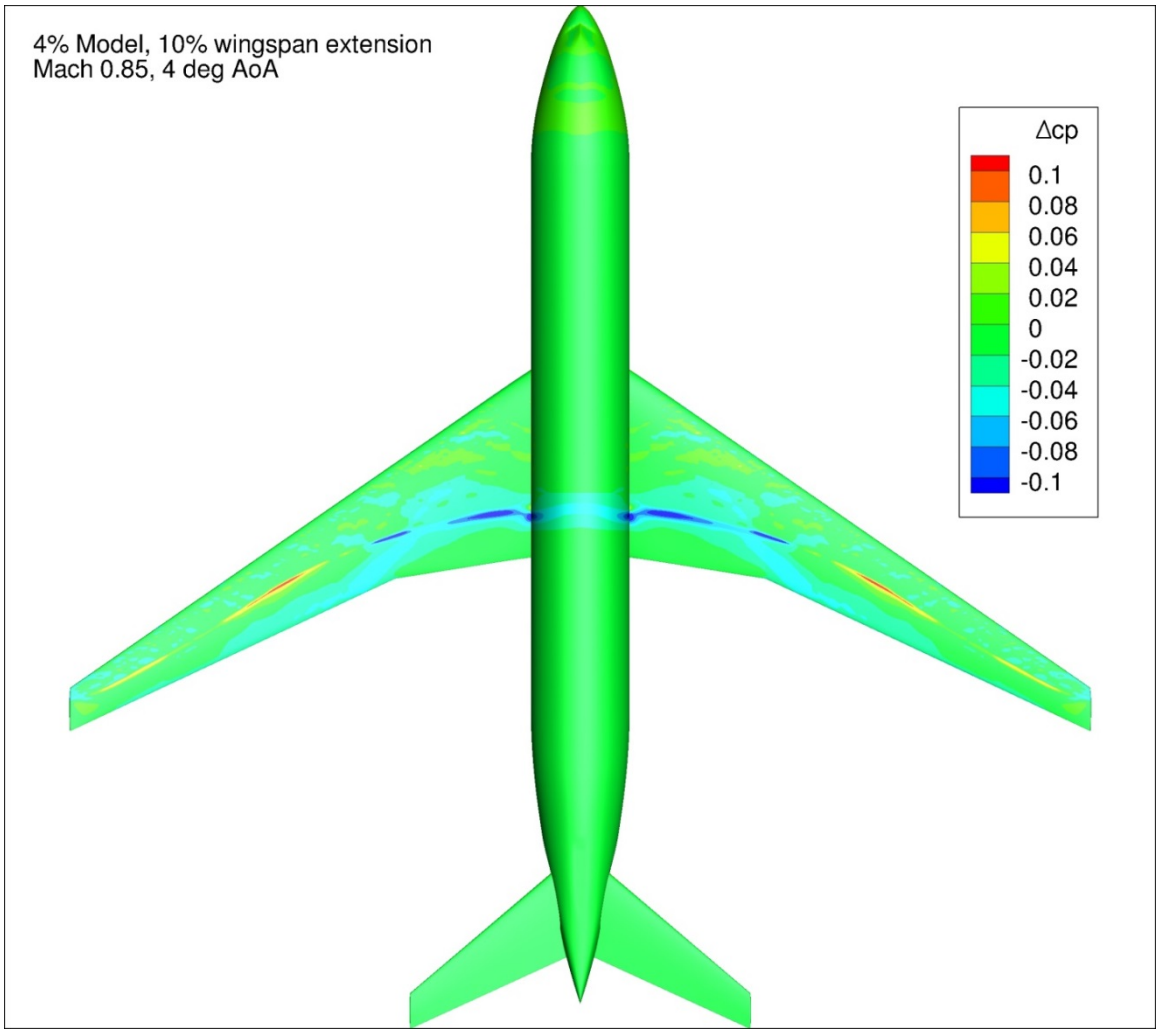

Figure 74. Configuration 1.1, Difference in Pressure Coefficient between Free-stream and Wind Tunnel Simulations, 4 deg Angle of Attack, Top View

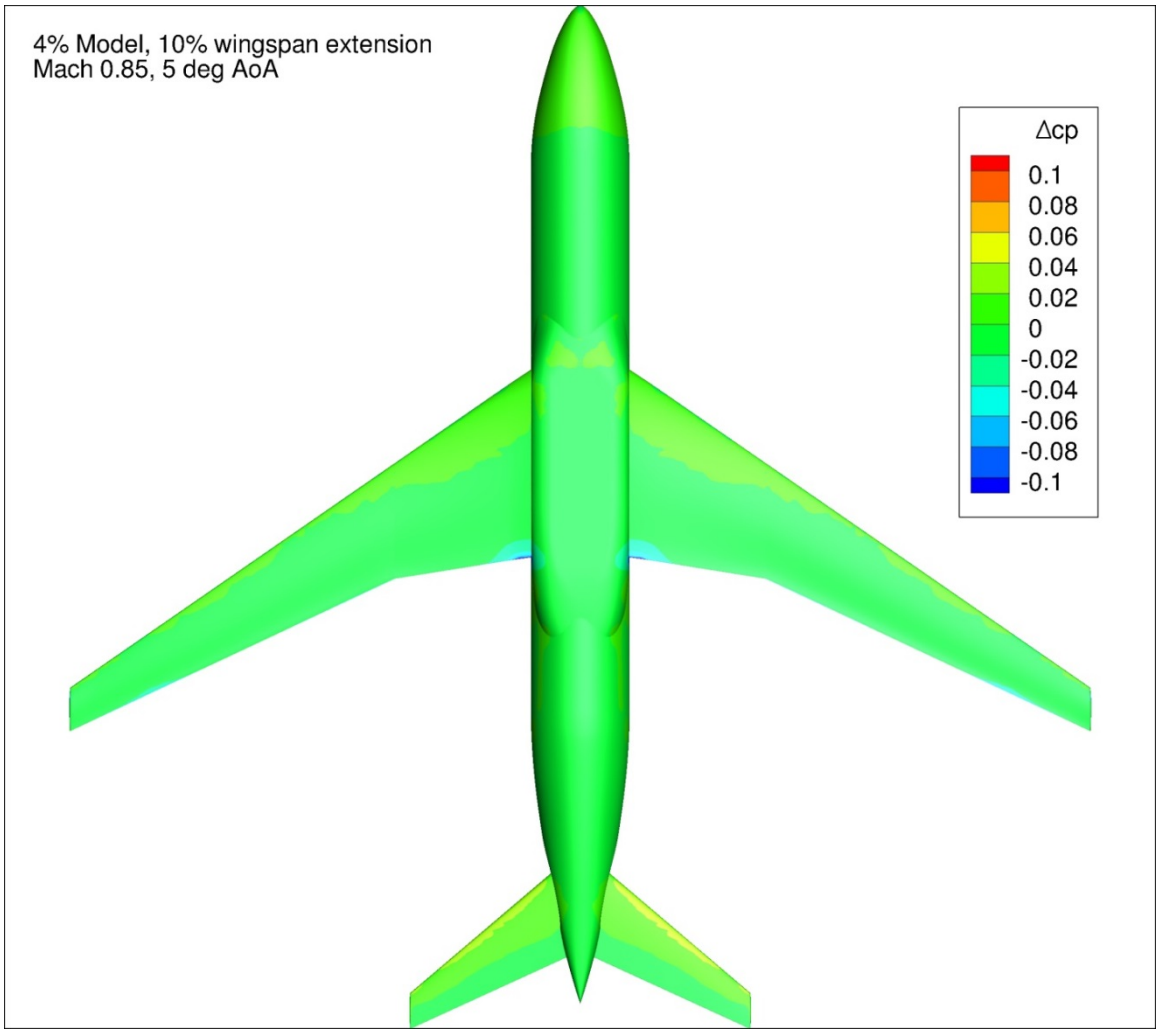

Figure 75. Configuration 1.1, Difference in Pressure Coefficient between Free-stream and Wind Tunnel Simulations, 5 deg Angle of Attack, Bottom View

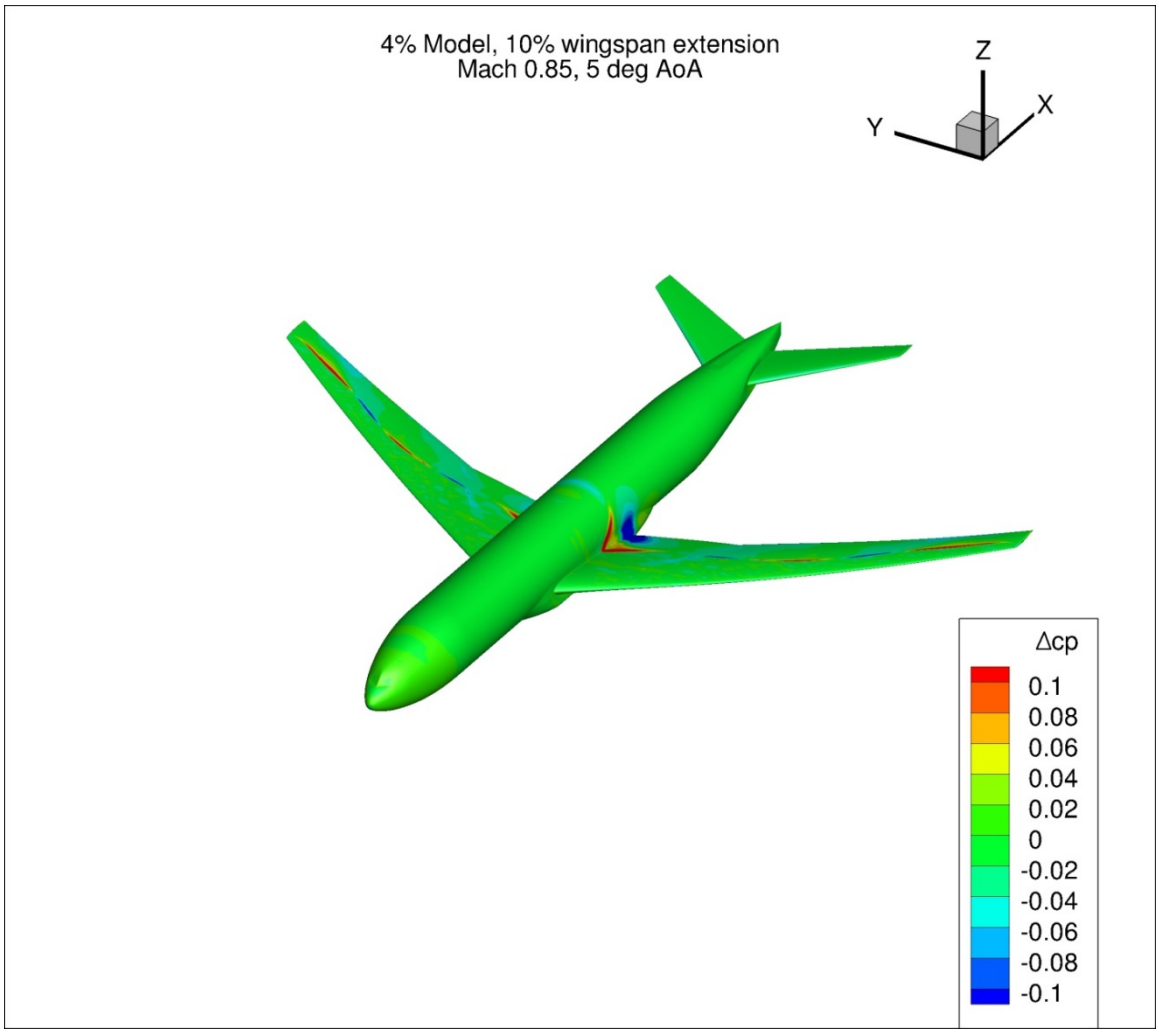

Figure 76. Configuration 1.1, Difference in Pressure Coefficient between Free-stream and Wind Tunnel Simulations, 5 deg Angle of Attack, Isometric View

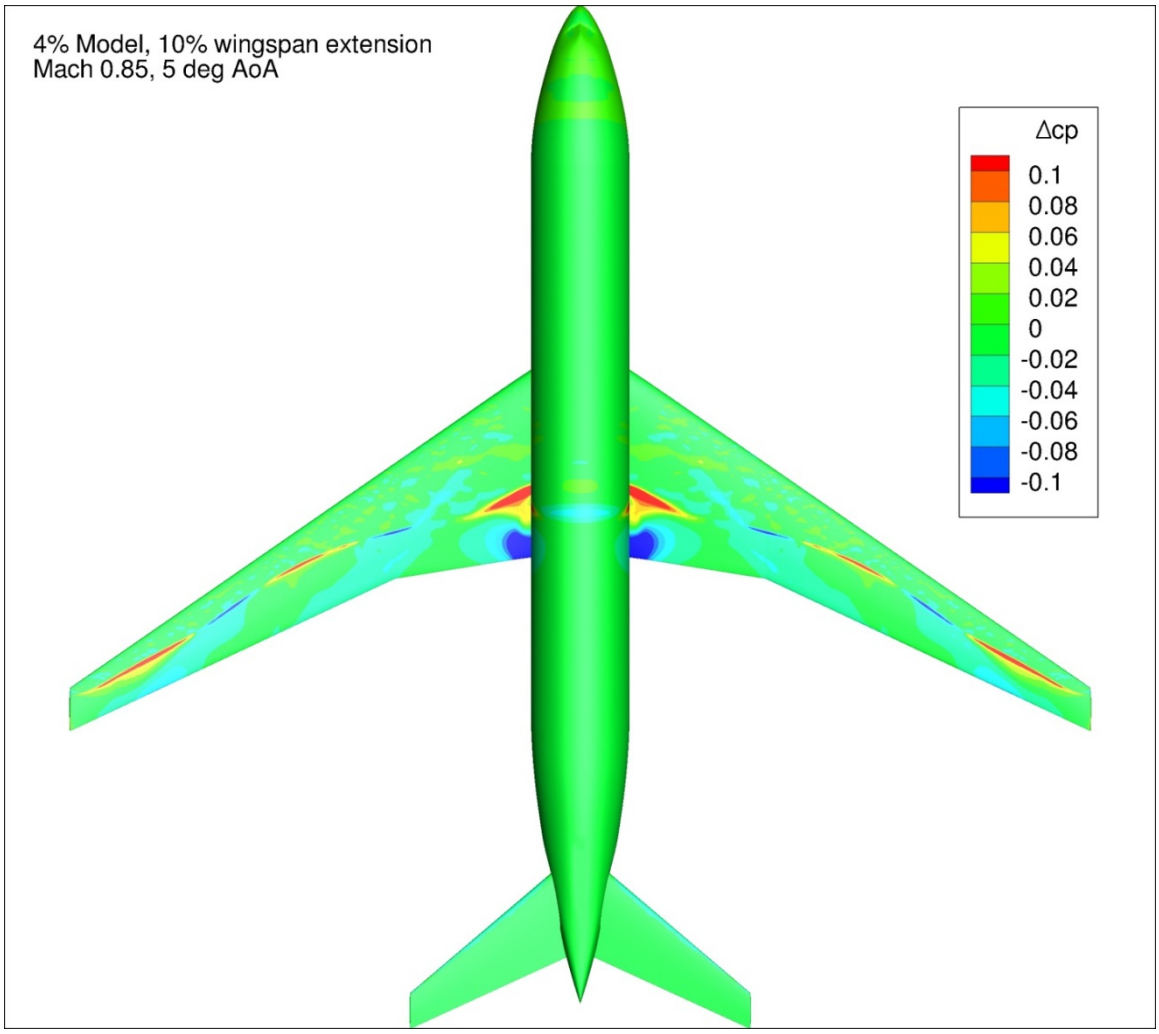

Figure 77. Configuration 1.1, Difference in Pressure Coefficient between Free-stream and Wind Tunnel Simulations, 5 deg Angle of Attack, Top View

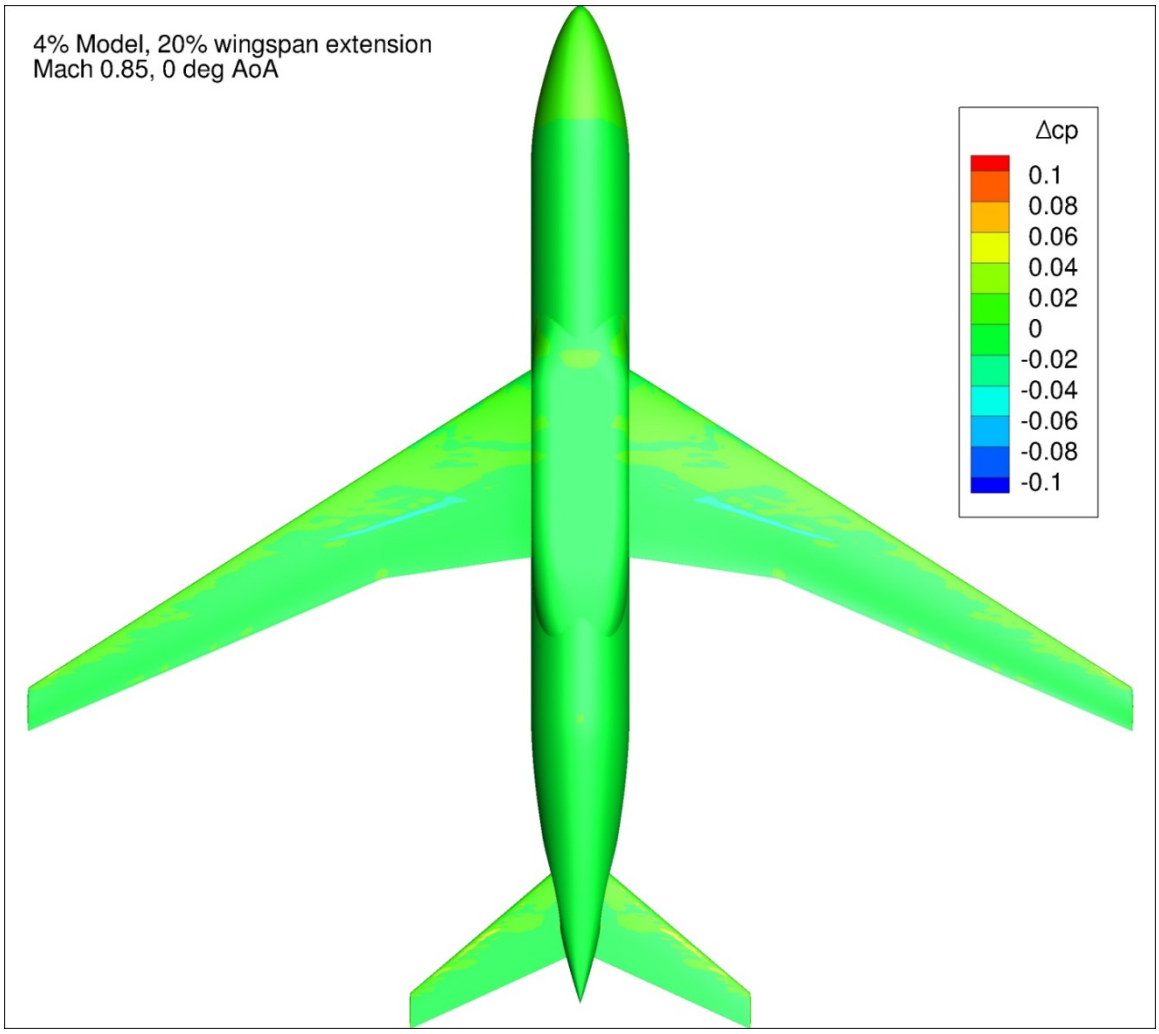

Figure 78. Configuration 1.2, Difference in Pressure Coefficient between Free-stream and Wind Tunnel Simulations, 0 deg Angle of Attack, Bottom View

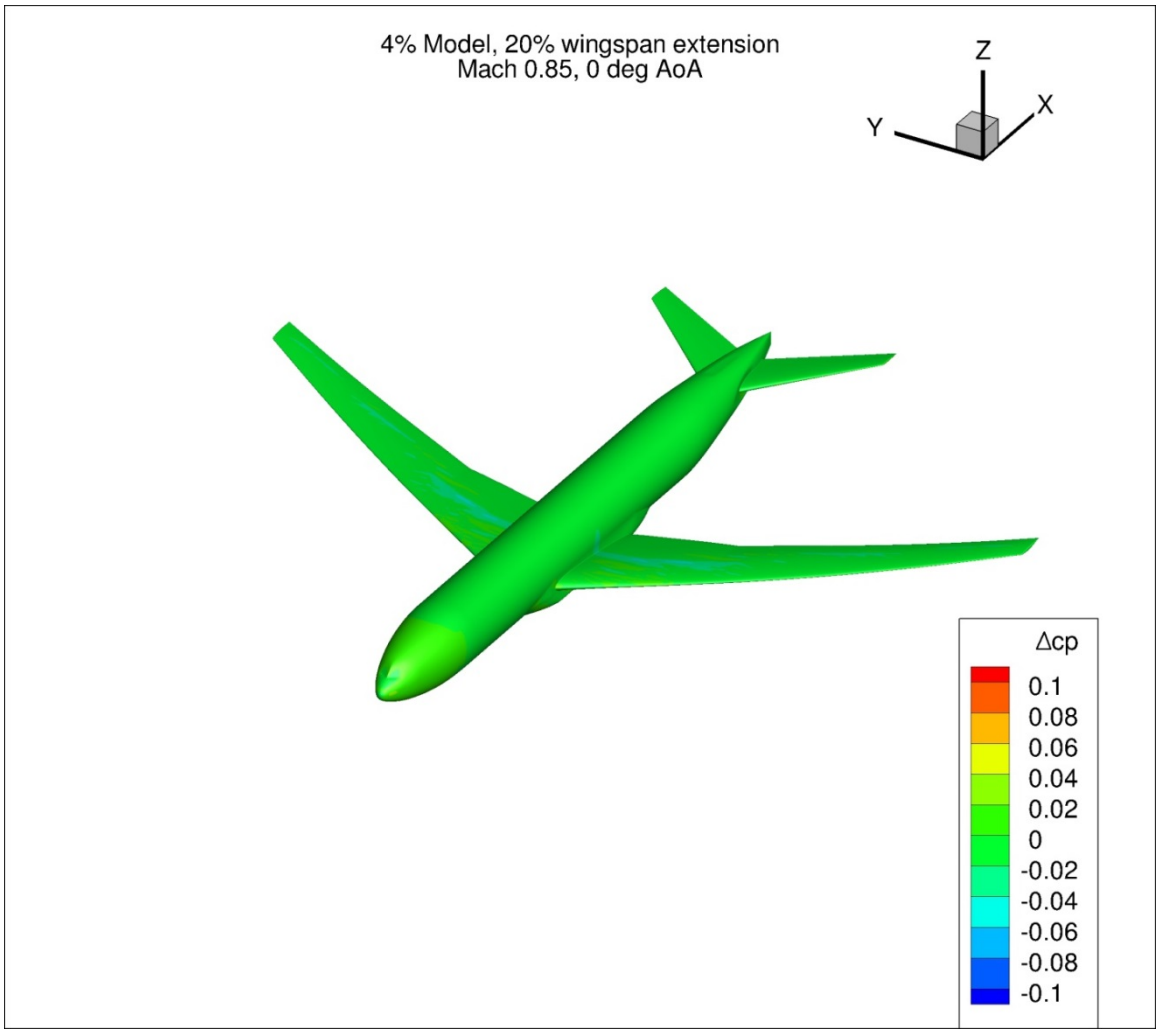

Figure 79. Configuration 1.2, Difference in Pressure Coefficient between Free-stream and Wind Tunnel Simulations, 0 deg Angle of Attack, Isometric View

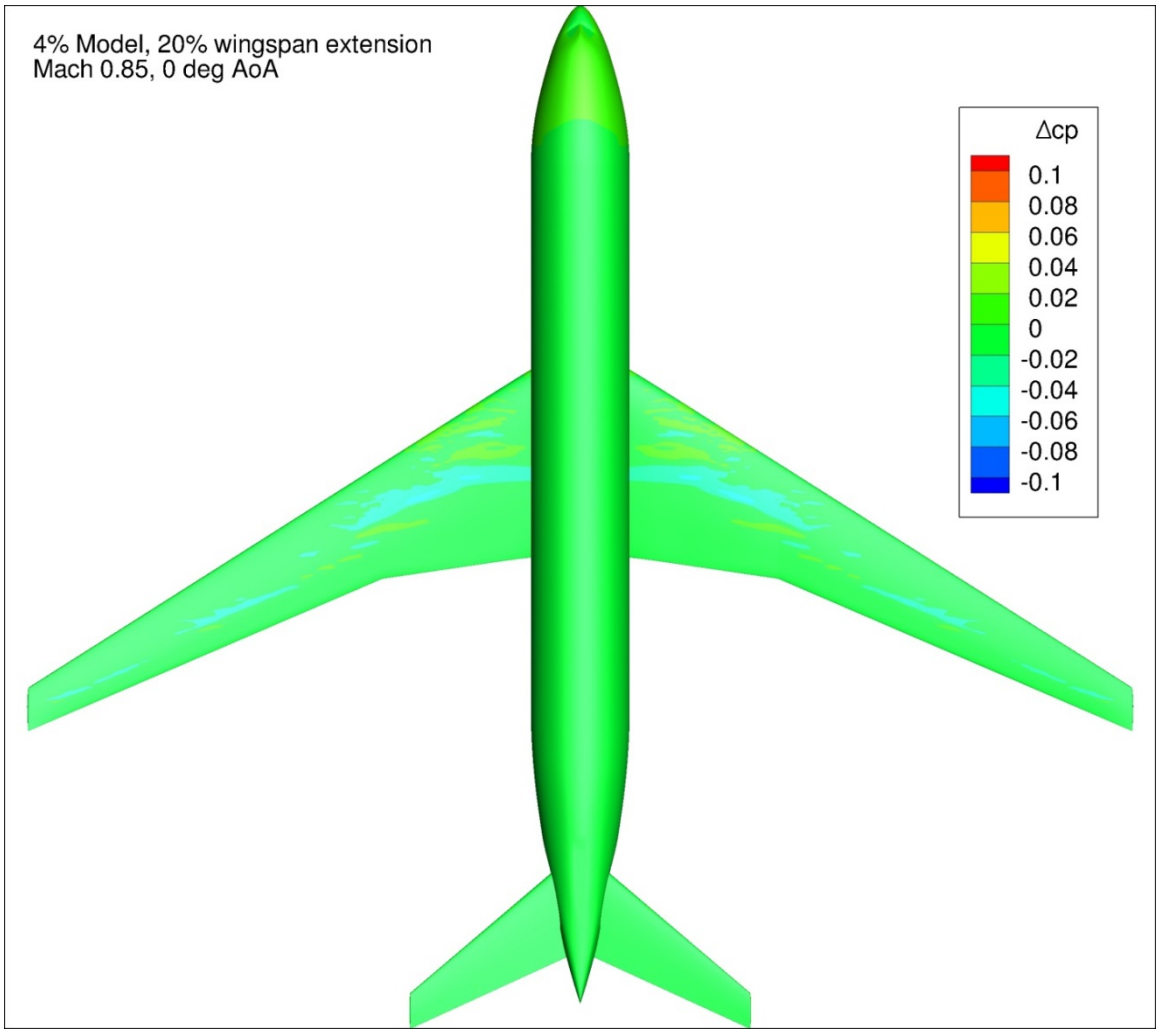

Figure 80. Configuration 1.2, Difference in Pressure Coefficient between Free-stream and Wind Tunnel Simulations, 0 deg Angle of Attack, Top View

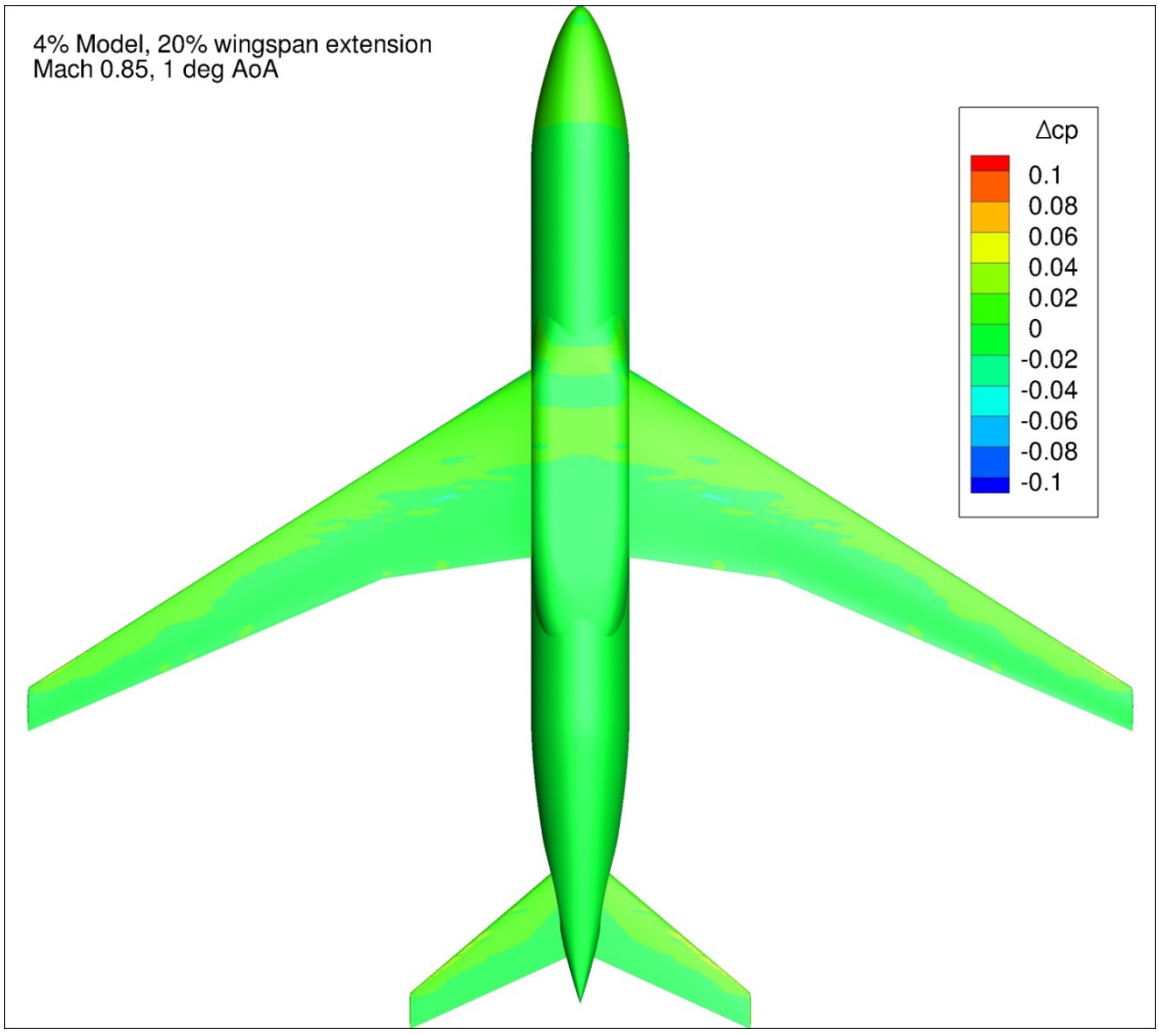

Figure 81. Configuration 1.2, Difference in Pressure Coefficient between Free-stream and Wind Tunnel Simulations, 1 deg Angle of Attack, Bottom View

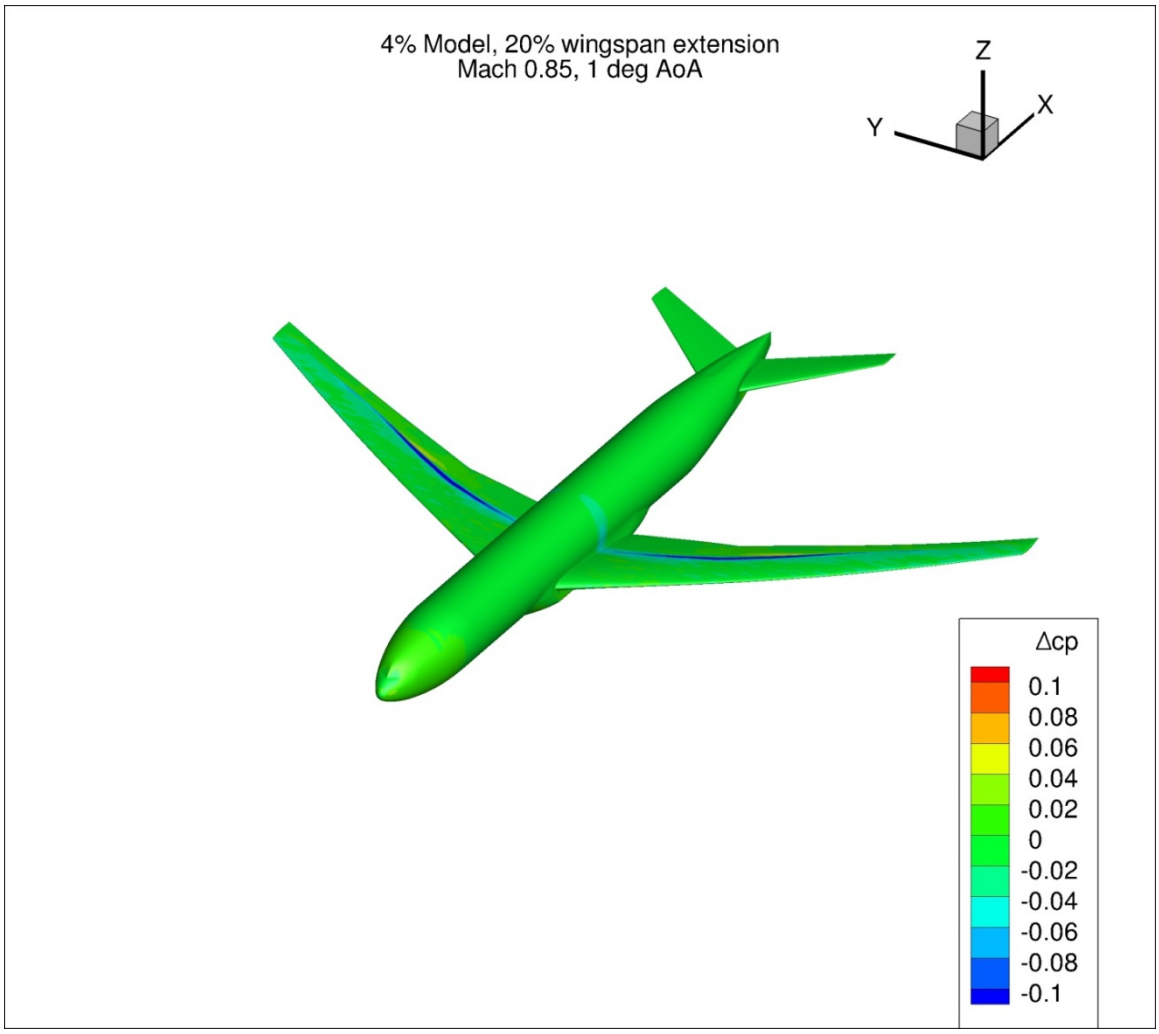

Figure 82. Configuration 1.2, Difference in Pressure Coefficient between Free-stream and Wind Tunnel Simulations, 1 deg Angle of Attack, Isometric View

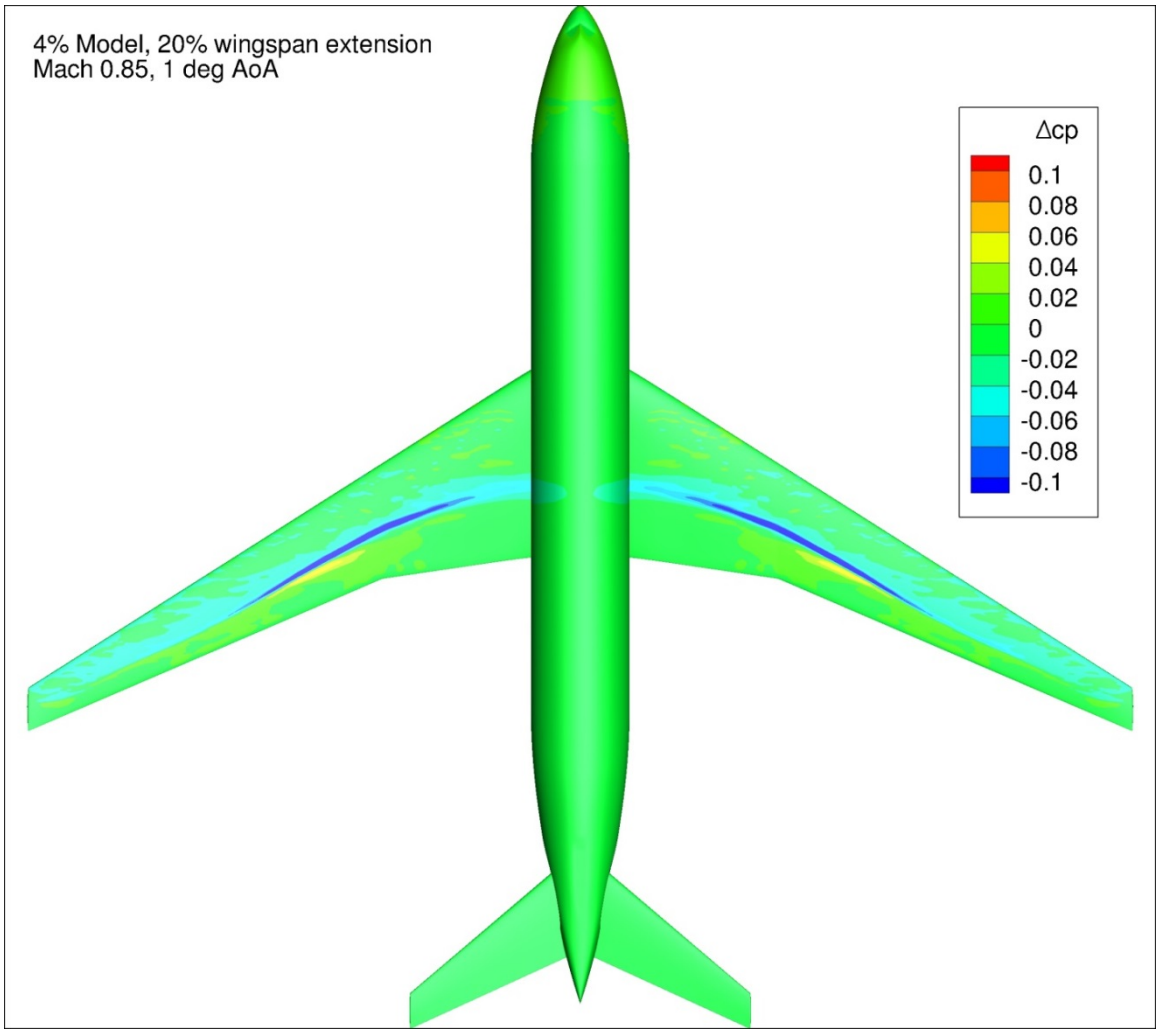

Figure 83. Configuration 1.2, Difference in Pressure Coefficient between Free-stream and Wind Tunnel Simulations, 1 deg Angle of Attack, Top View

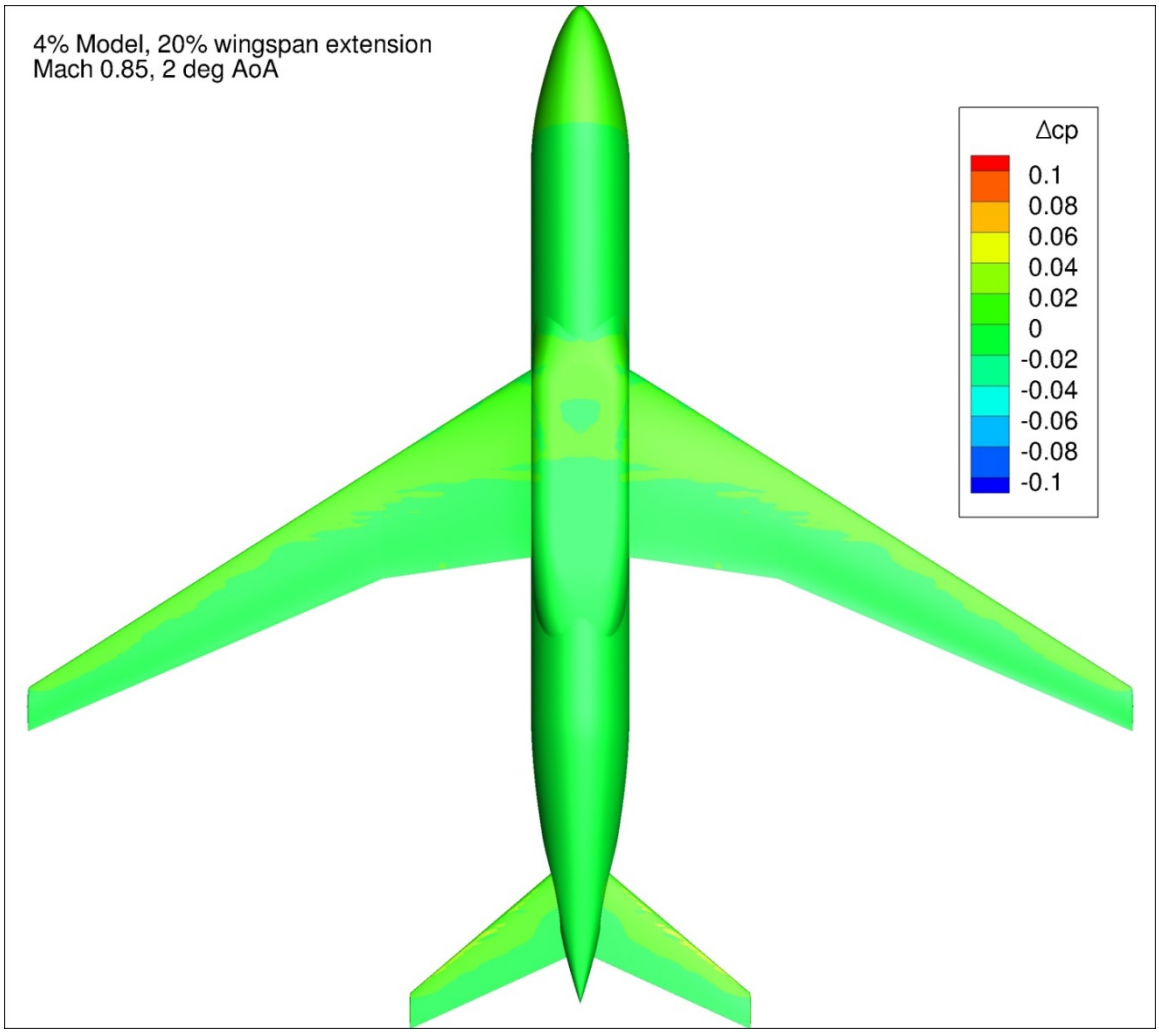

Figure 84. Configuration 1.2, Difference in Pressure Coefficient between Free-stream and Wind Tunnel Simulations, 2 deg Angle of Attack, Bottom View

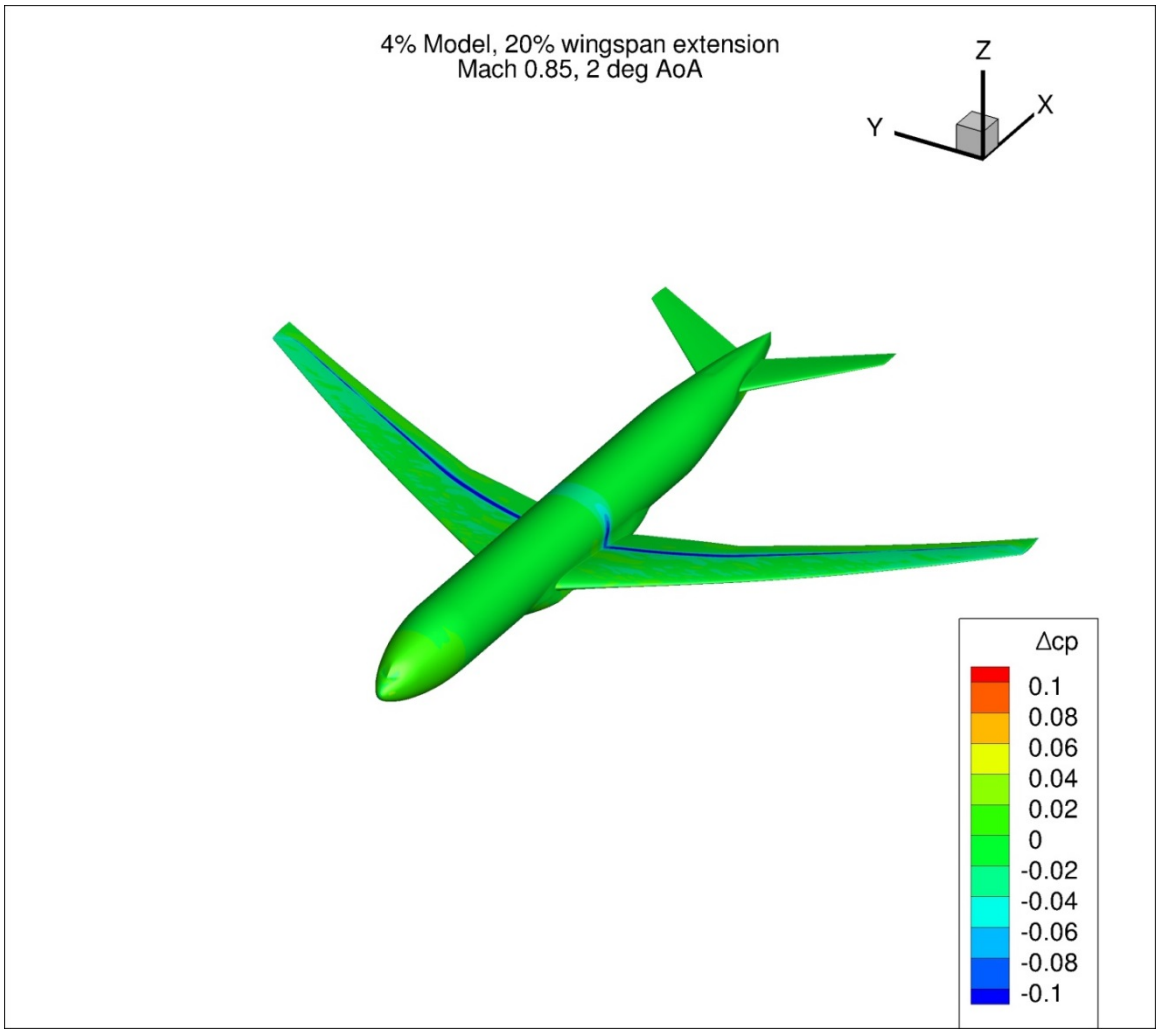

Figure 85. Configuration 1.2, Difference in Pressure Coefficient between Free-stream and Wind Tunnel Simulations, 2 deg Angle of Attack, Isometric View

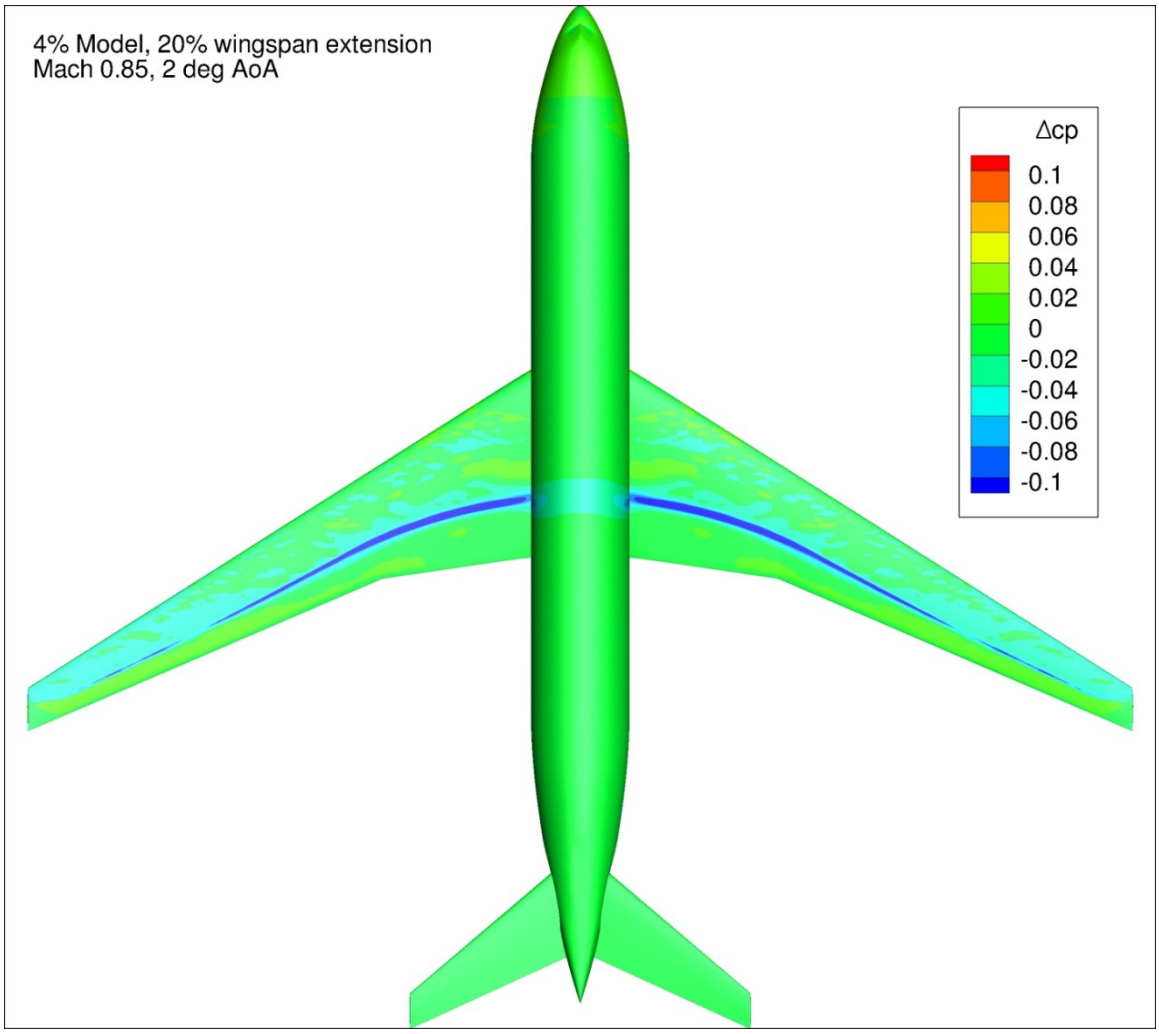

Figure 86. Configuration 1.2, Difference in Pressure Coefficient between Free-stream and Wind Tunnel Simulations, 2 deg Angle of Attack, Top View

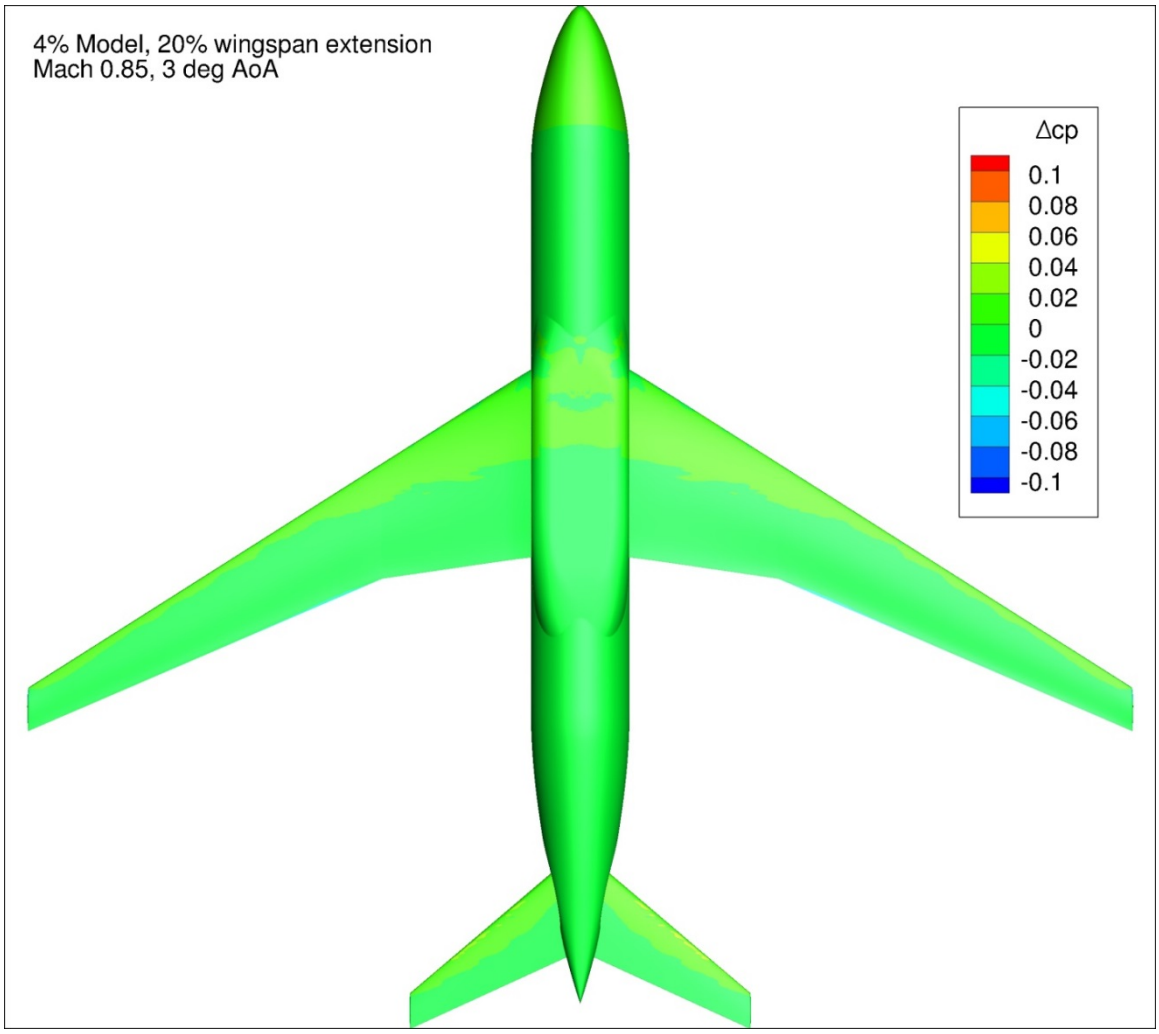

Figure 87. Configuration 1.2, Difference in Pressure Coefficient between Free-stream and Wind Tunnel Simulations, 3 deg Angle of Attack, Bottom View

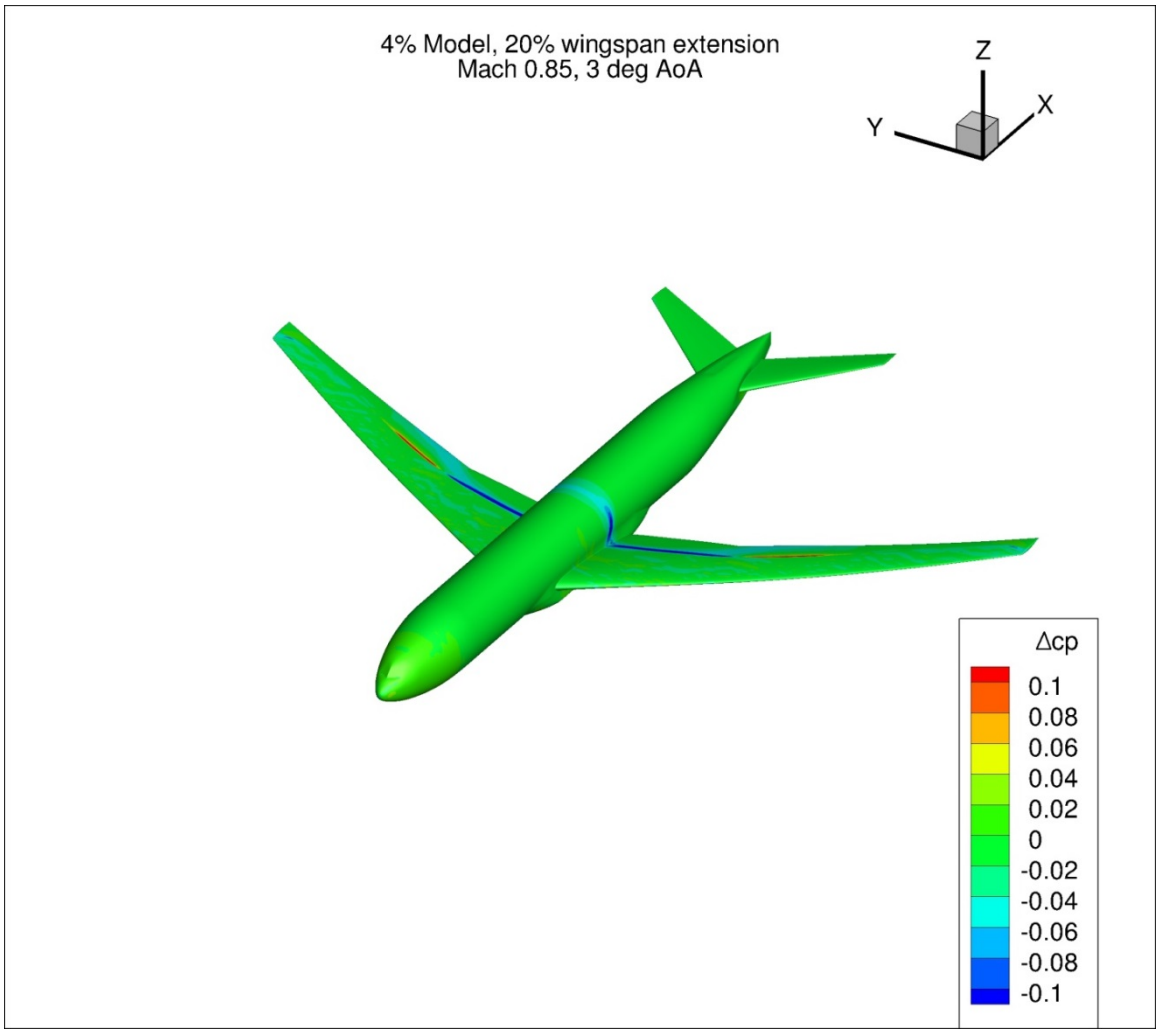

Figure 88. Configuration 1.2, Difference in Pressure Coefficient between Free-stream and Wind Tunnel Simulations, 3 deg Angle of Attack, Isometric View

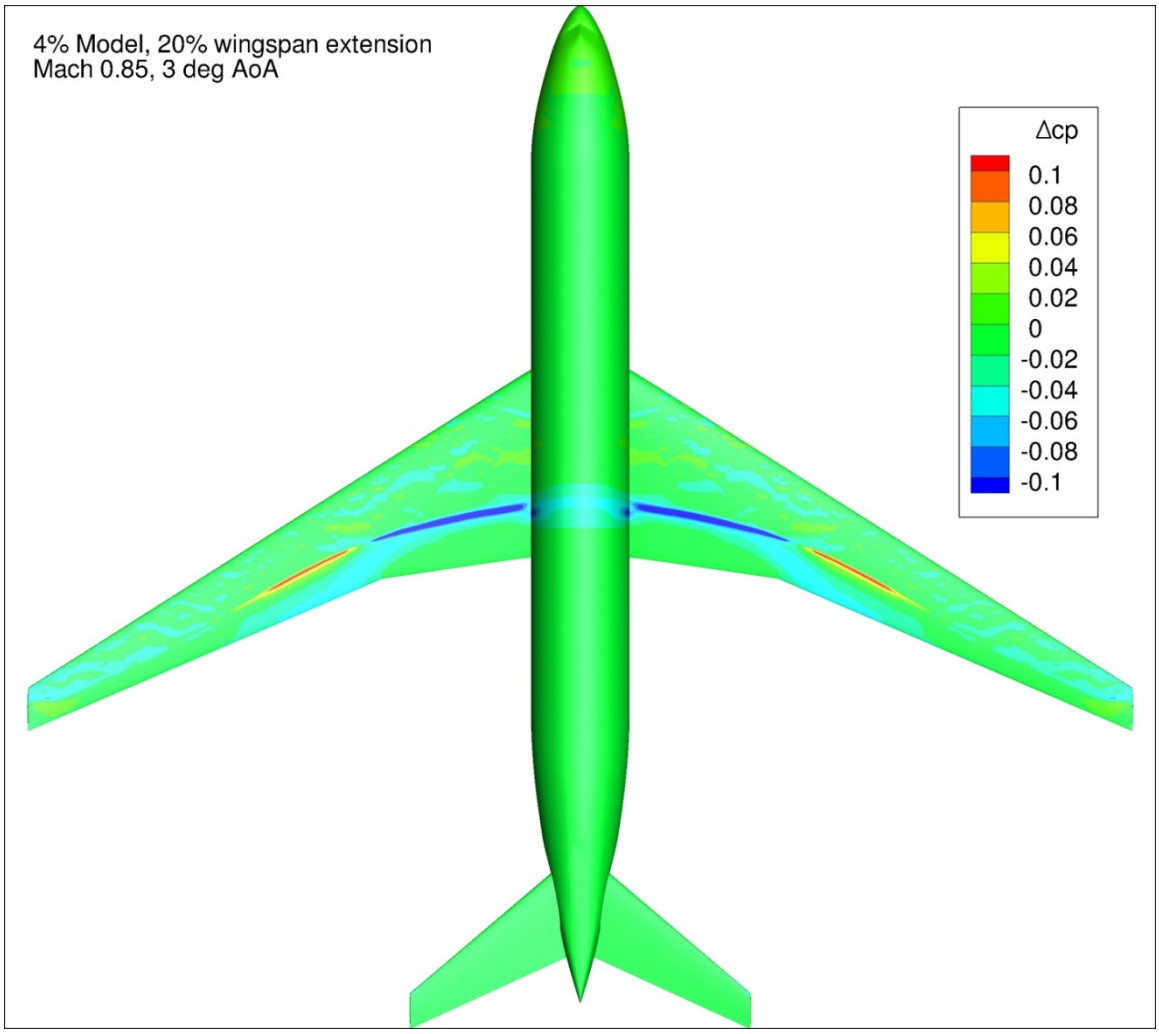

Figure 89. Configuration 1.2, Difference in Pressure Coefficient between Free-stream and Wind Tunnel Simulations, 3 deg Angle of Attack, Top View

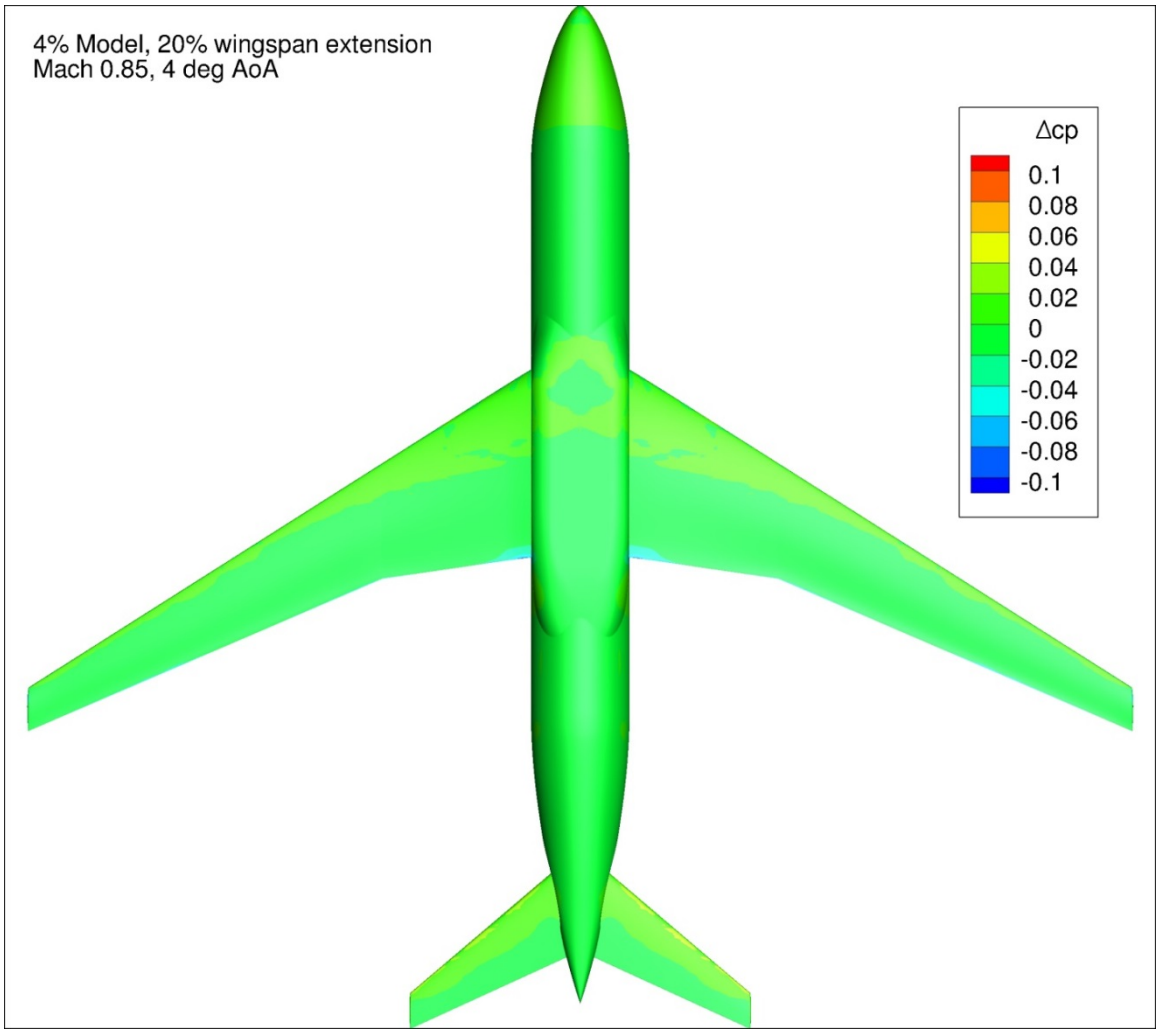

Figure 90. Configuration 1.2, Difference in Pressure Coefficient between Free-stream and Wind Tunnel Simulations, 4 deg Angle of Attack, Bottom View

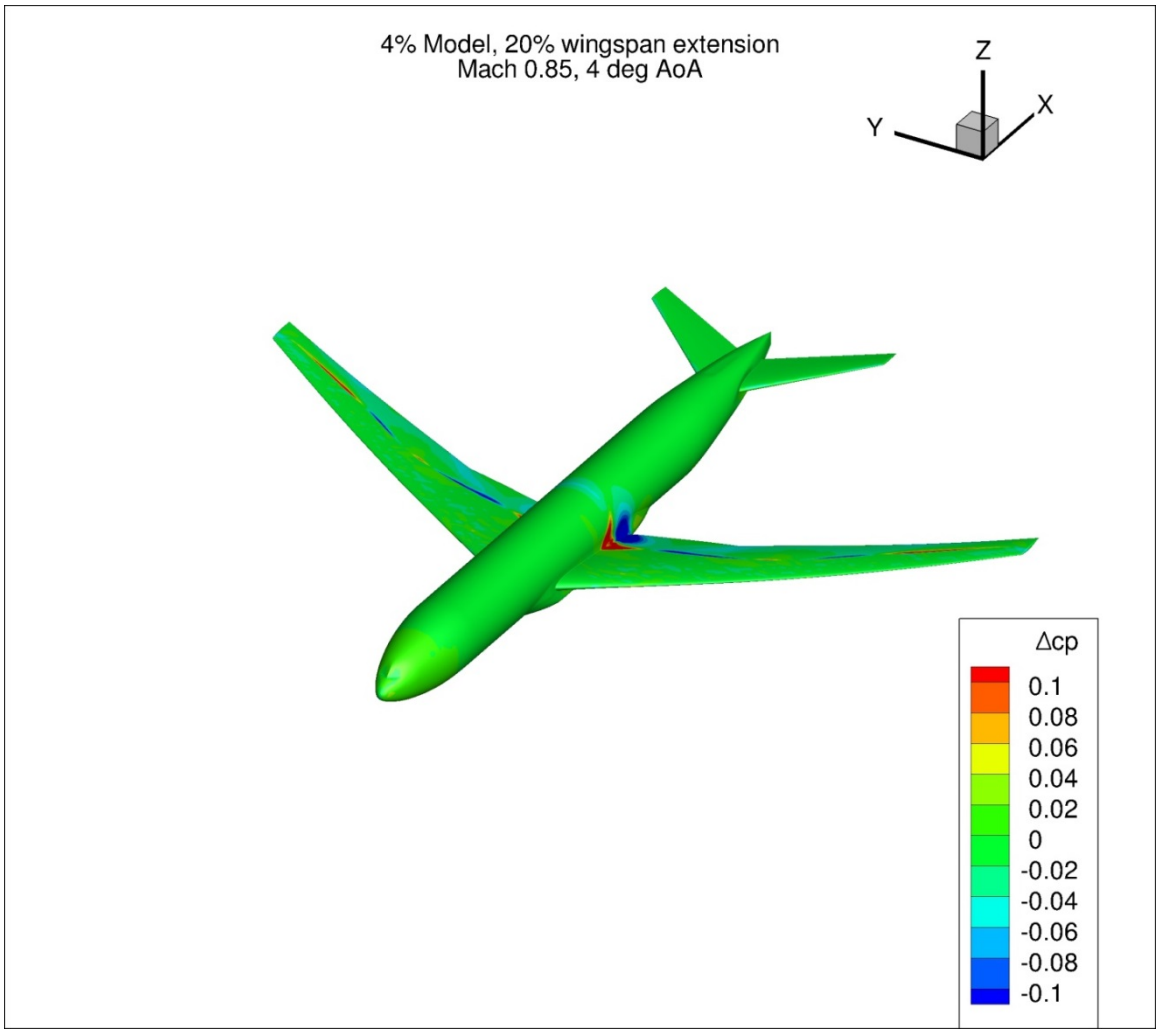

Figure 91. Configuration 1.2, Difference in Pressure Coefficient between Free-stream and Wind Tunnel Simulations, 4 deg Angle of Attack, Isometric View

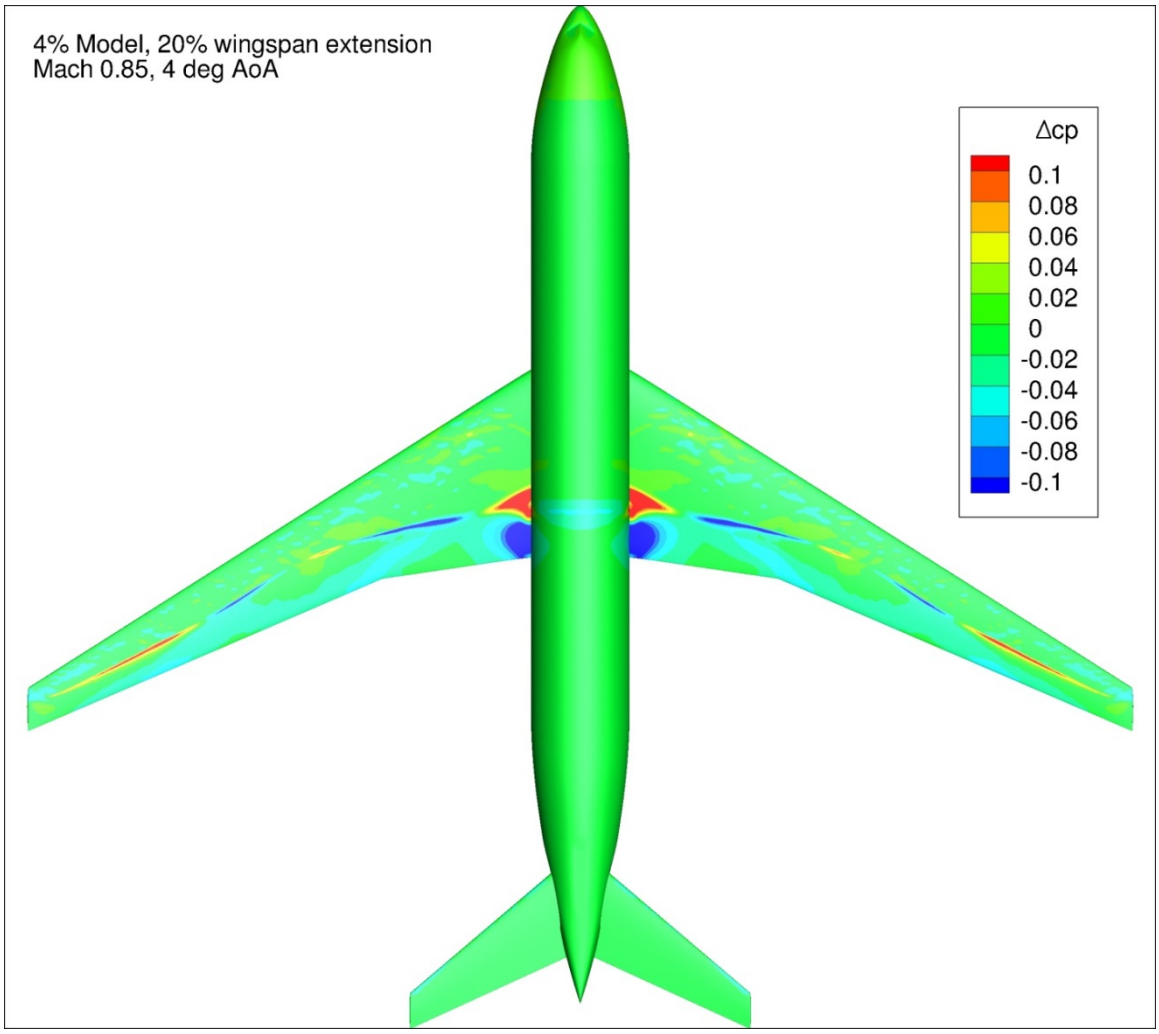

Figure 92. Configuration 1.2, Difference in Pressure Coefficient between Free-stream and Wind Tunnel Simulations, 4 deg Angle of Attack, Top View

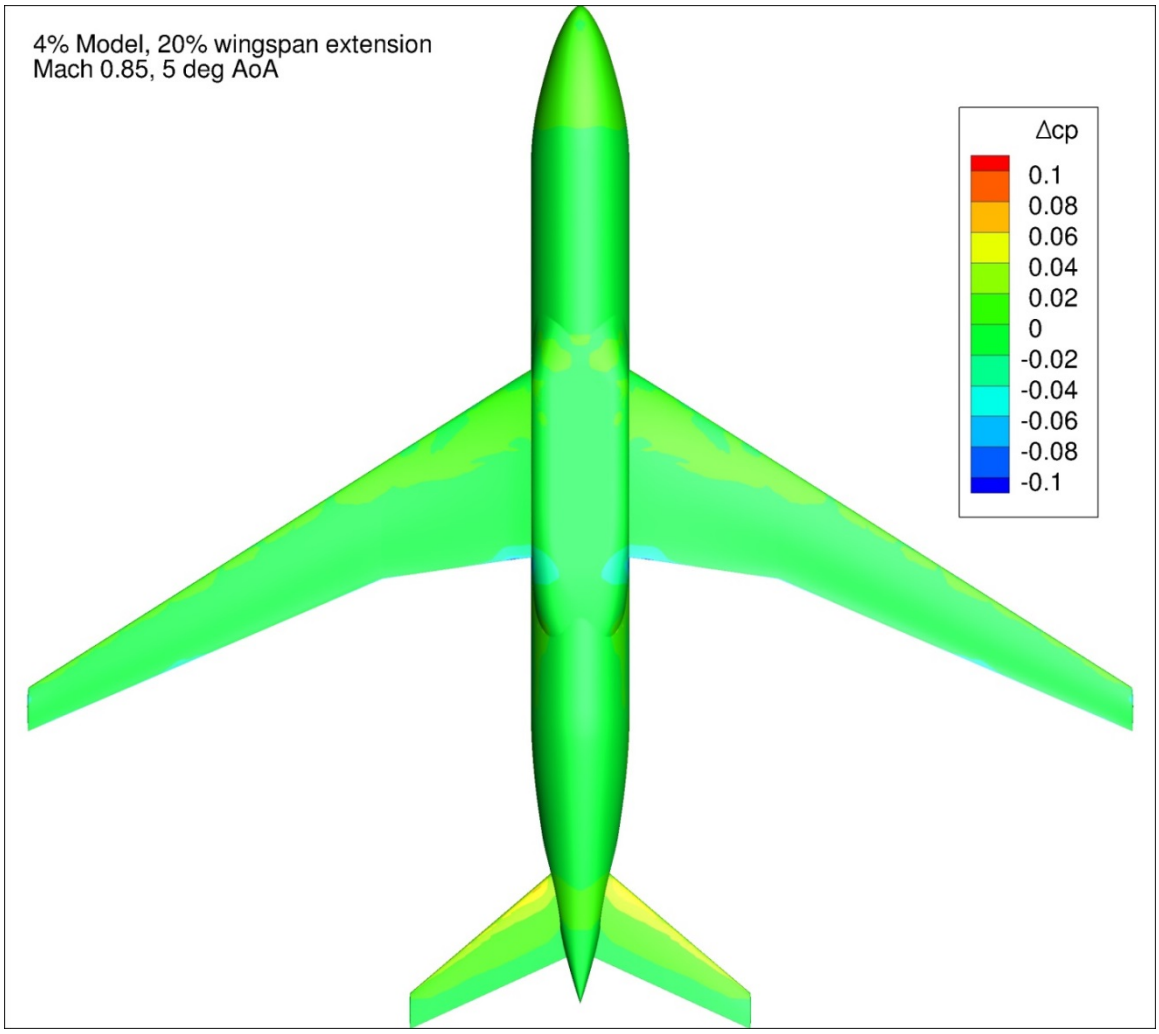

Figure 93. Configuration 1.2, Difference in Pressure Coefficient between Free-stream and Wind Tunnel Simulations, 5 deg Angle of Attack, Bottom View

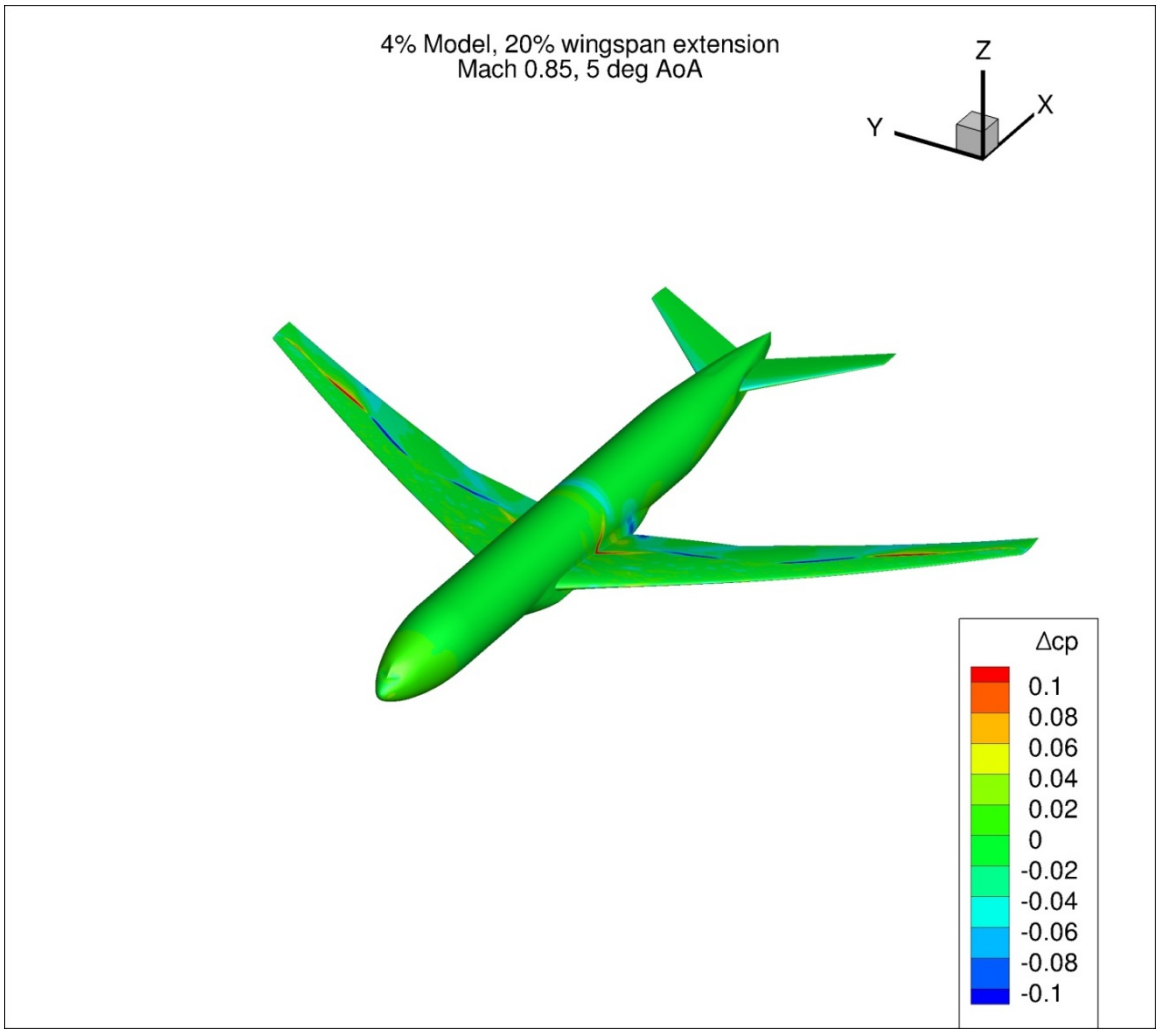

Figure 94. Configuration 1.2, Difference in Pressure Coefficient between Free-stream and Wind Tunnel Simulations, 5 deg Angle of Attack, Isometric View

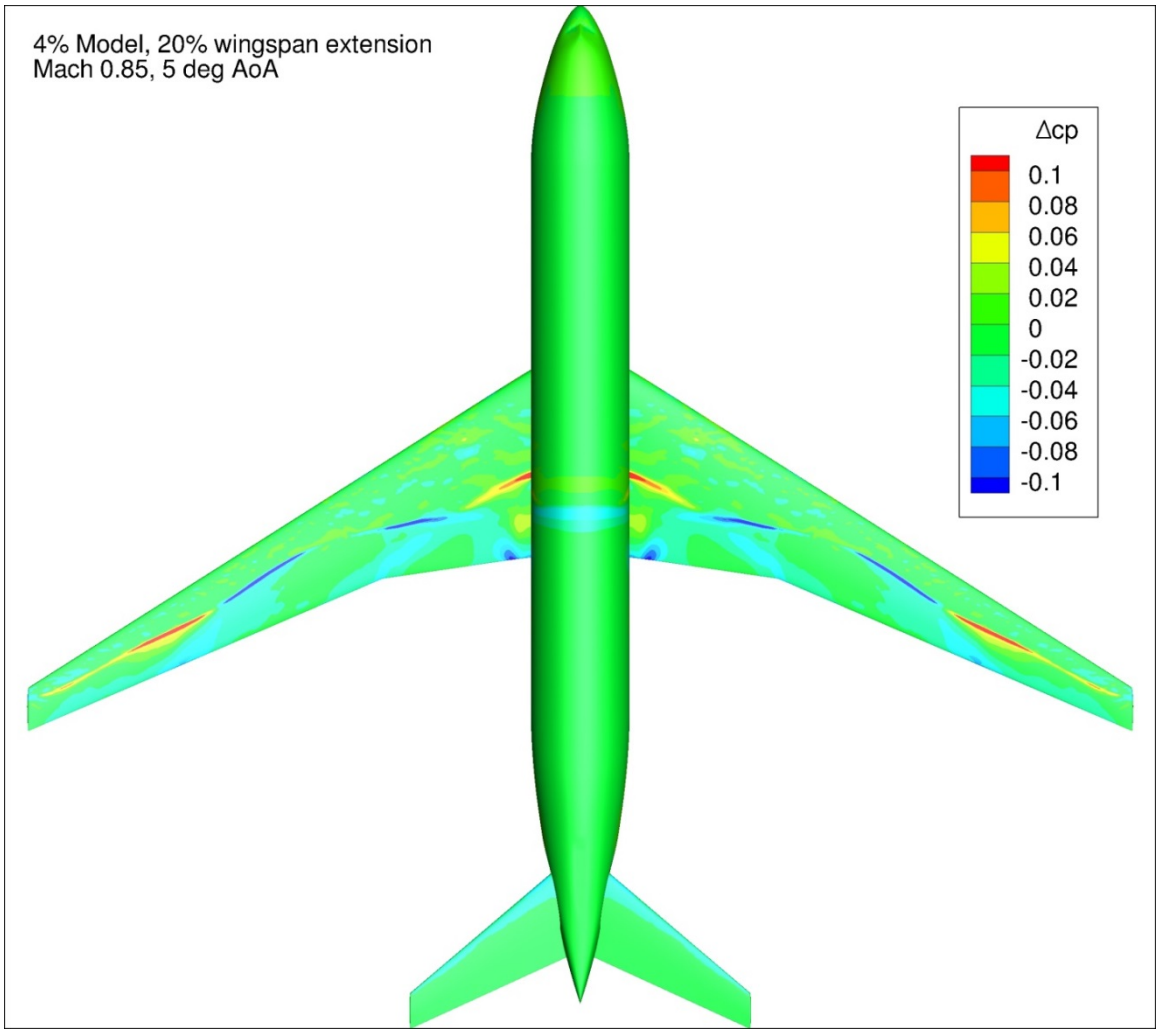

Figure 95. Configuration 1.2, Difference in Pressure Coefficient between Free-stream and Wind Tunnel Simulations, 5 deg Angle of Attack, Top View

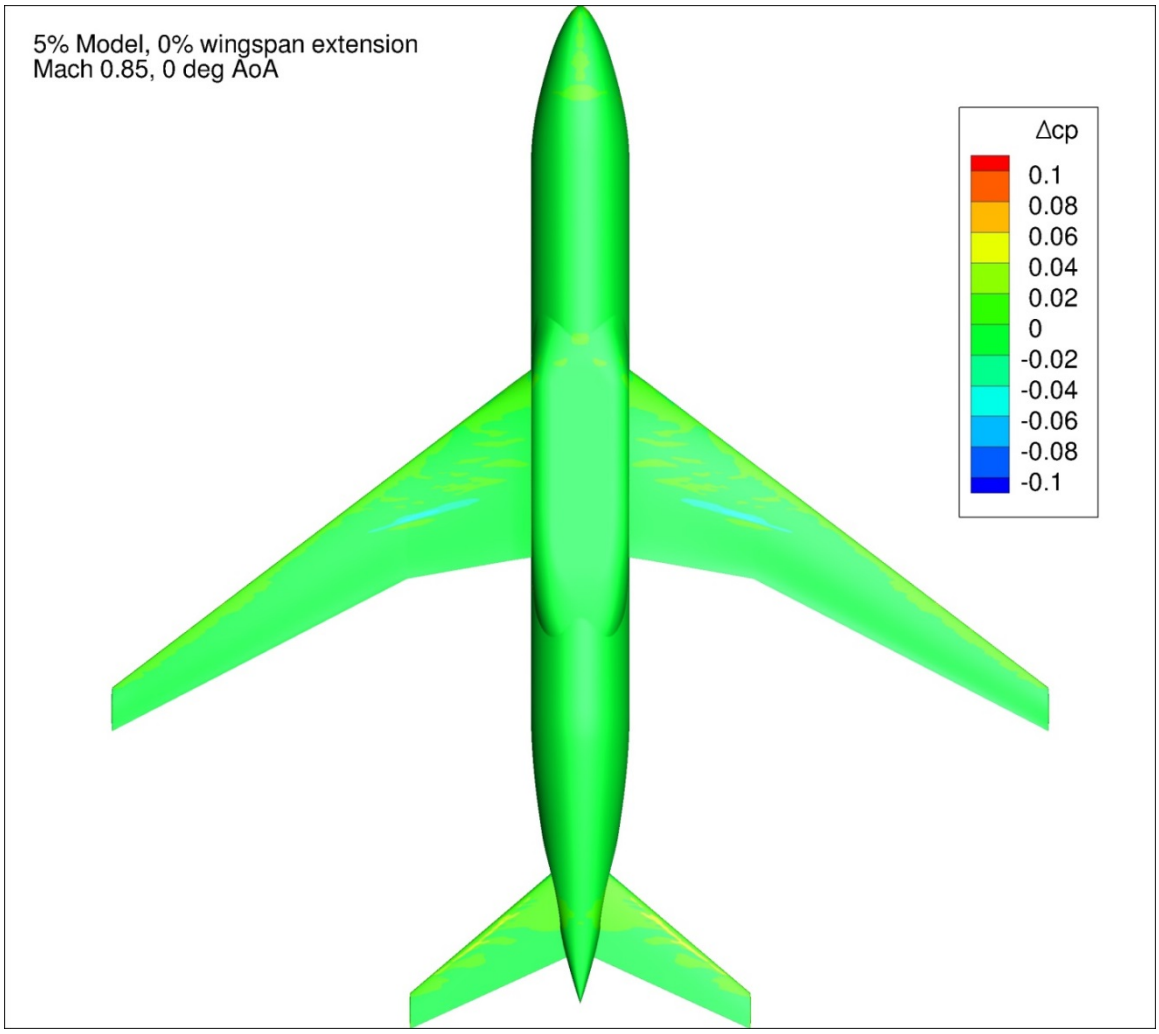

Figure 96. Configuration 2, Difference in Pressure Coefficient between Free-stream and Wind Tunnel Simulations, 0 deg Angle of Attack, Bottom View

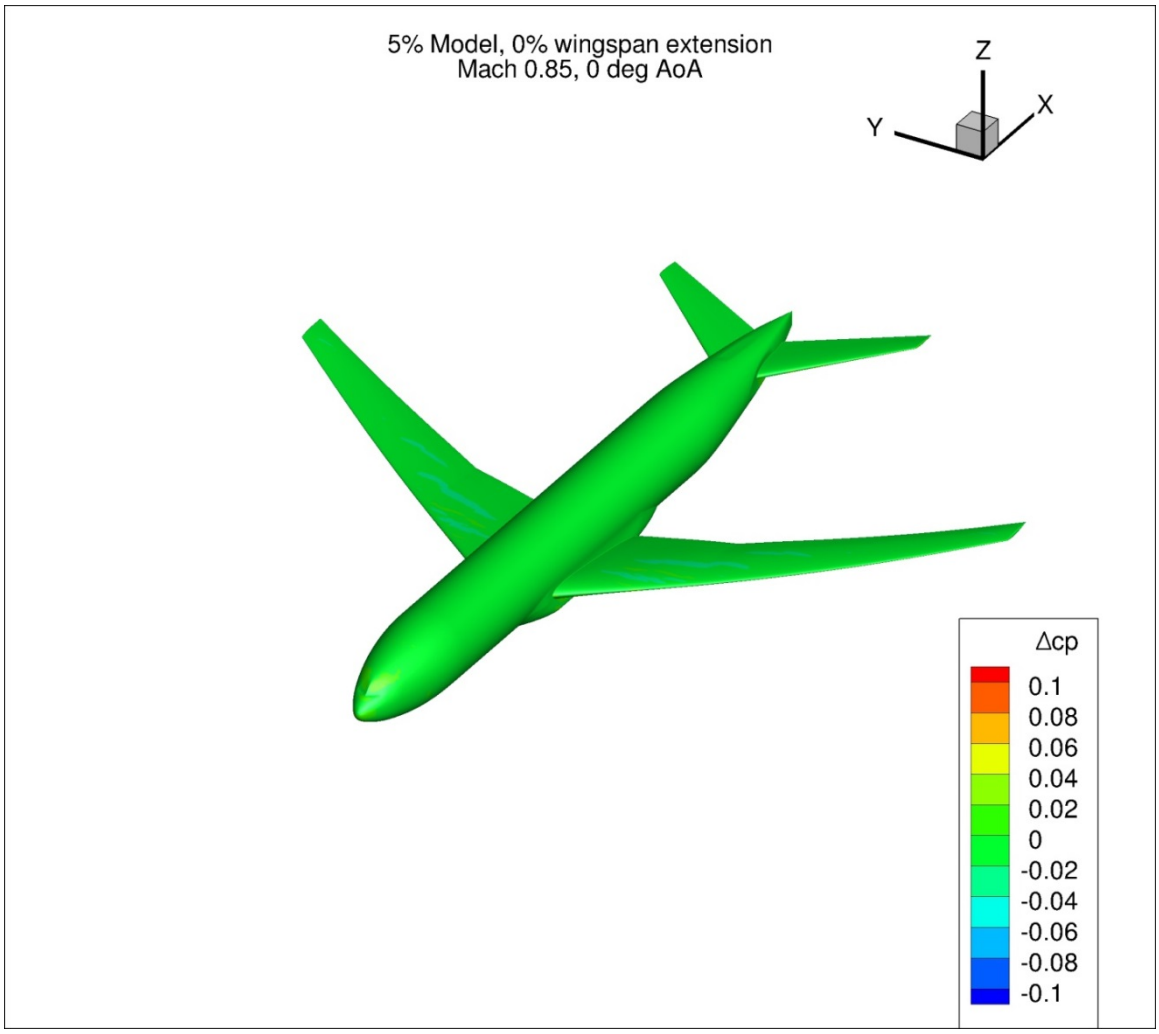

Figure 97. Configuration 2, Difference in Pressure Coefficient between Free-stream and Wind Tunnel Simulations, 0 deg Angle of Attack, Isometric View

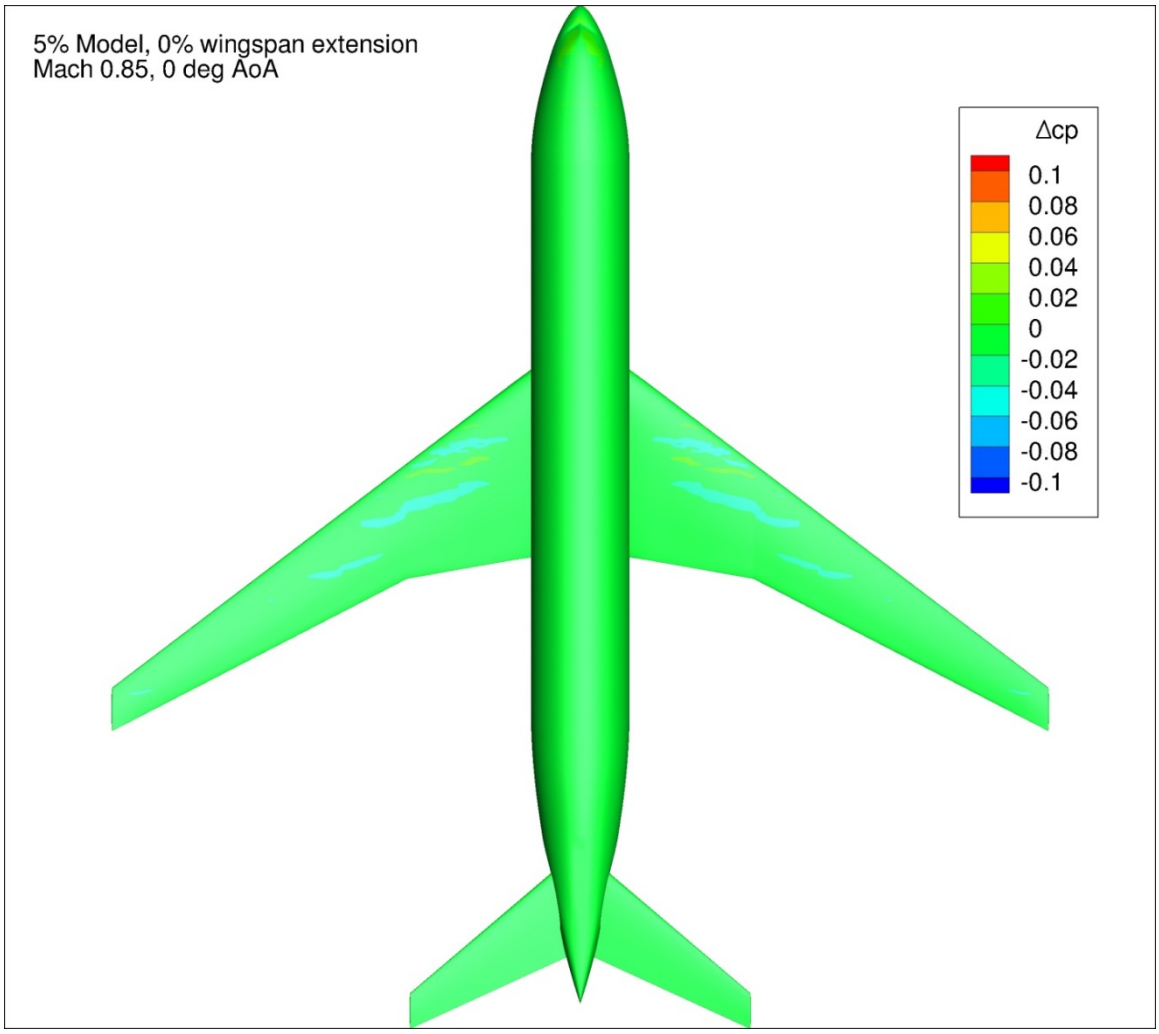

Figure 98. Configuration 2, Difference in Pressure Coefficient between Free-stream and Wind Tunnel Simulations, 0 deg Angle of Attack, Top View

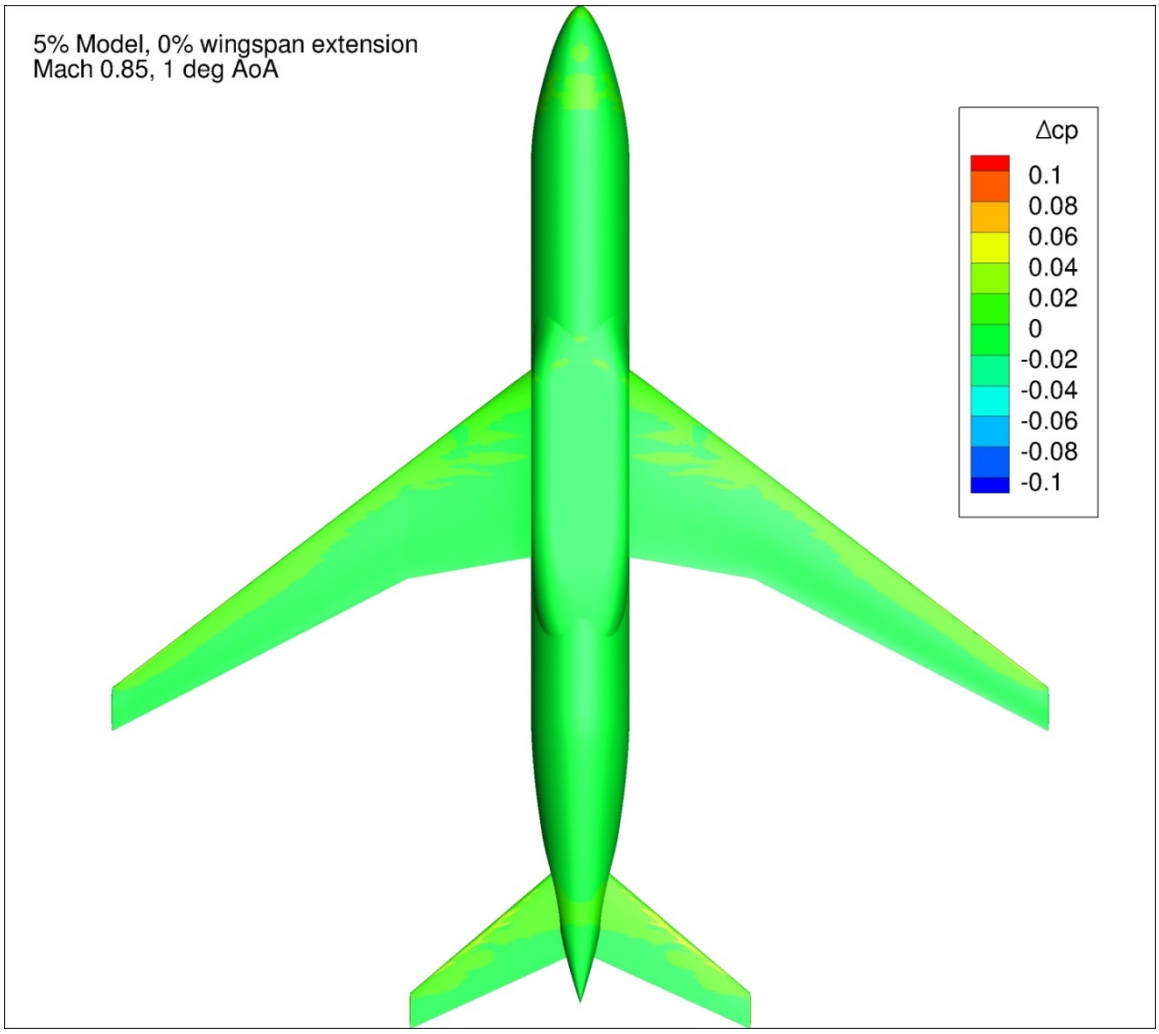

Figure 99. Configuration 2, Difference in Pressure Coefficient between Free-stream and Wind Tunnel Simulations, 1 deg Angle of Attack, Bottom View

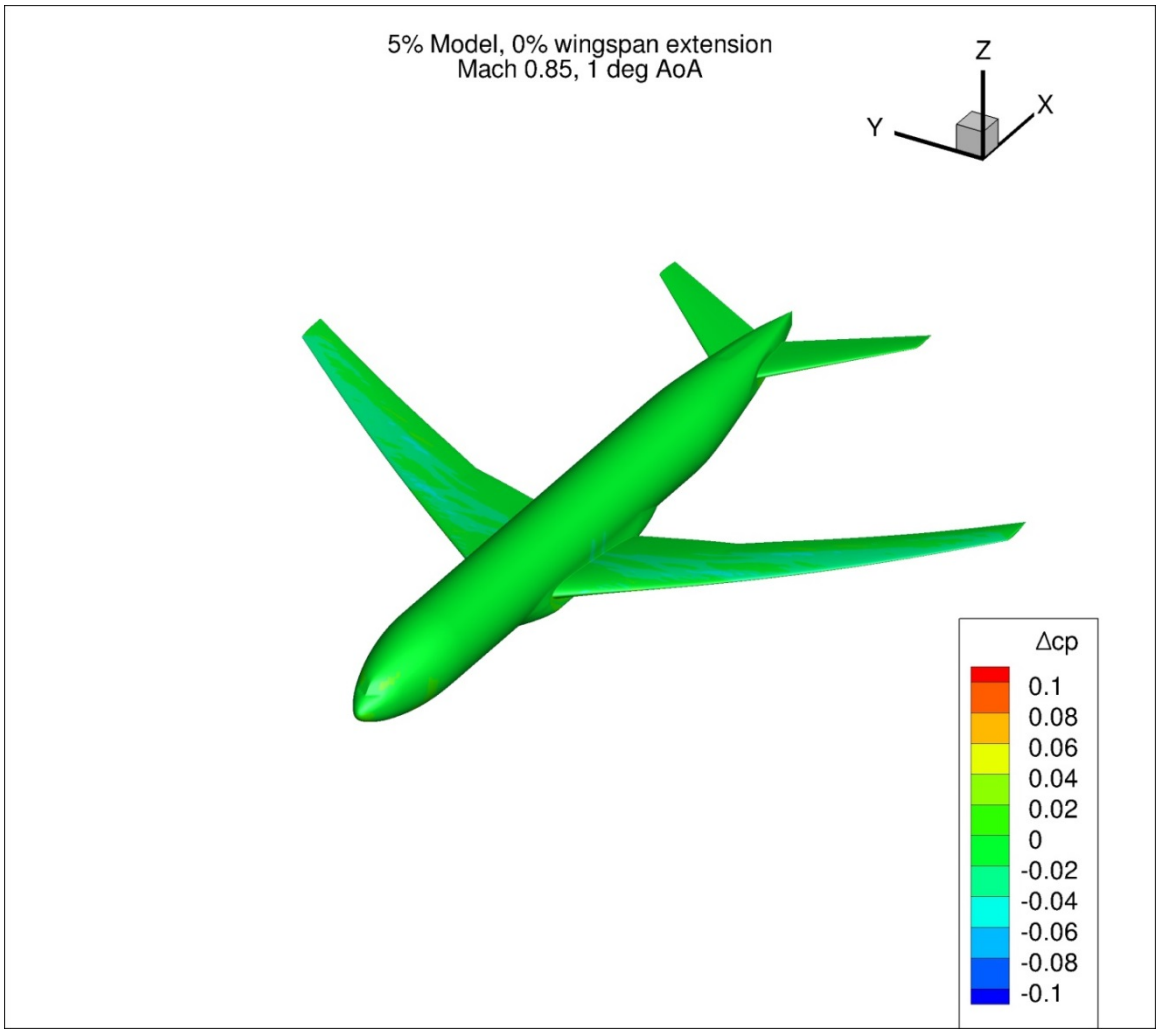

Figure 100. Configuration 2, Difference in Pressure Coefficient between Free-stream and Wind Tunnel Simulations, 1 deg Angle of Attack, Isometric View

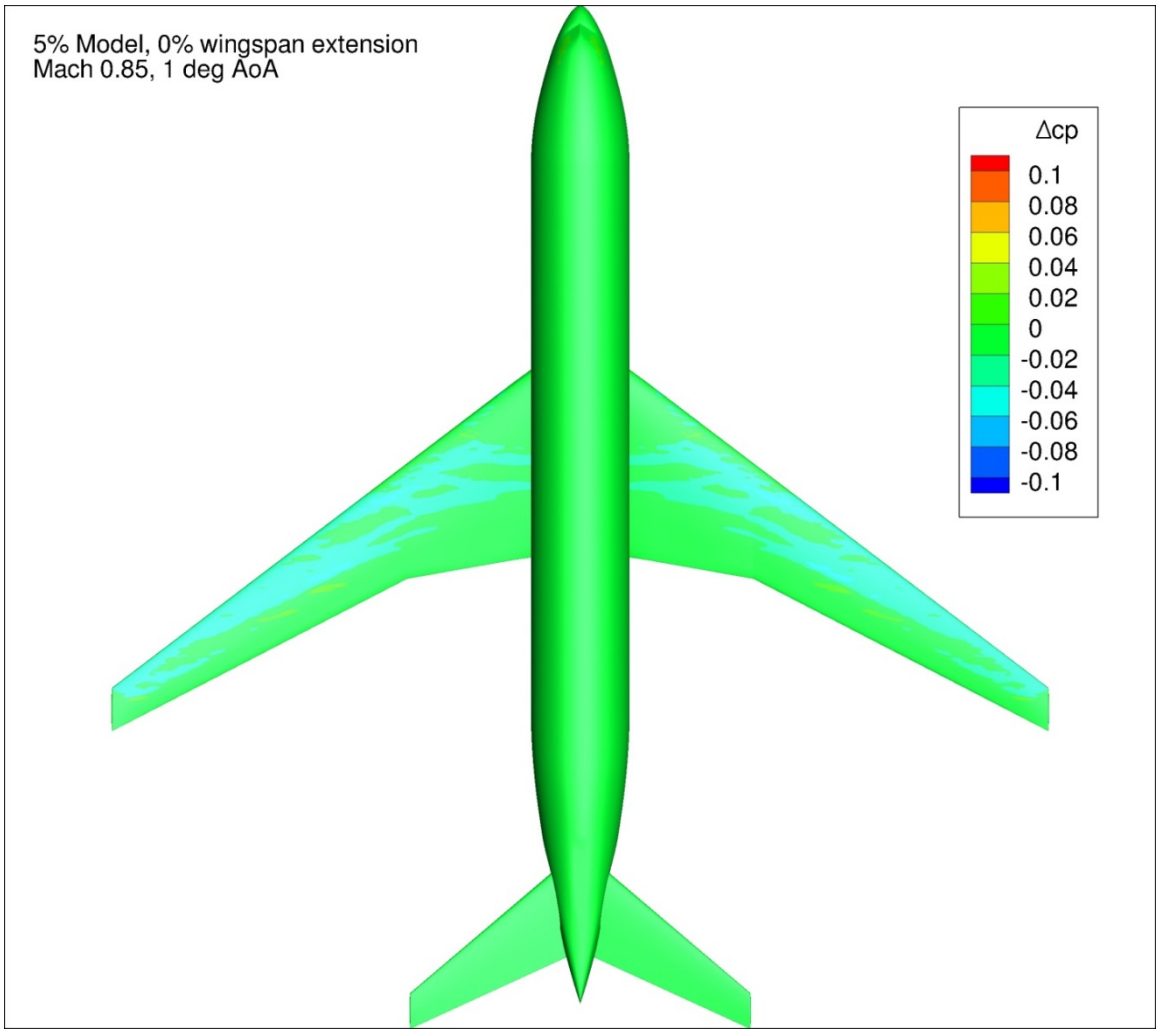

Figure 101. Configuration 2, Difference in Pressure Coefficient between Free-stream and Wind Tunnel Simulations, 1 deg Angle of Attack, Top View

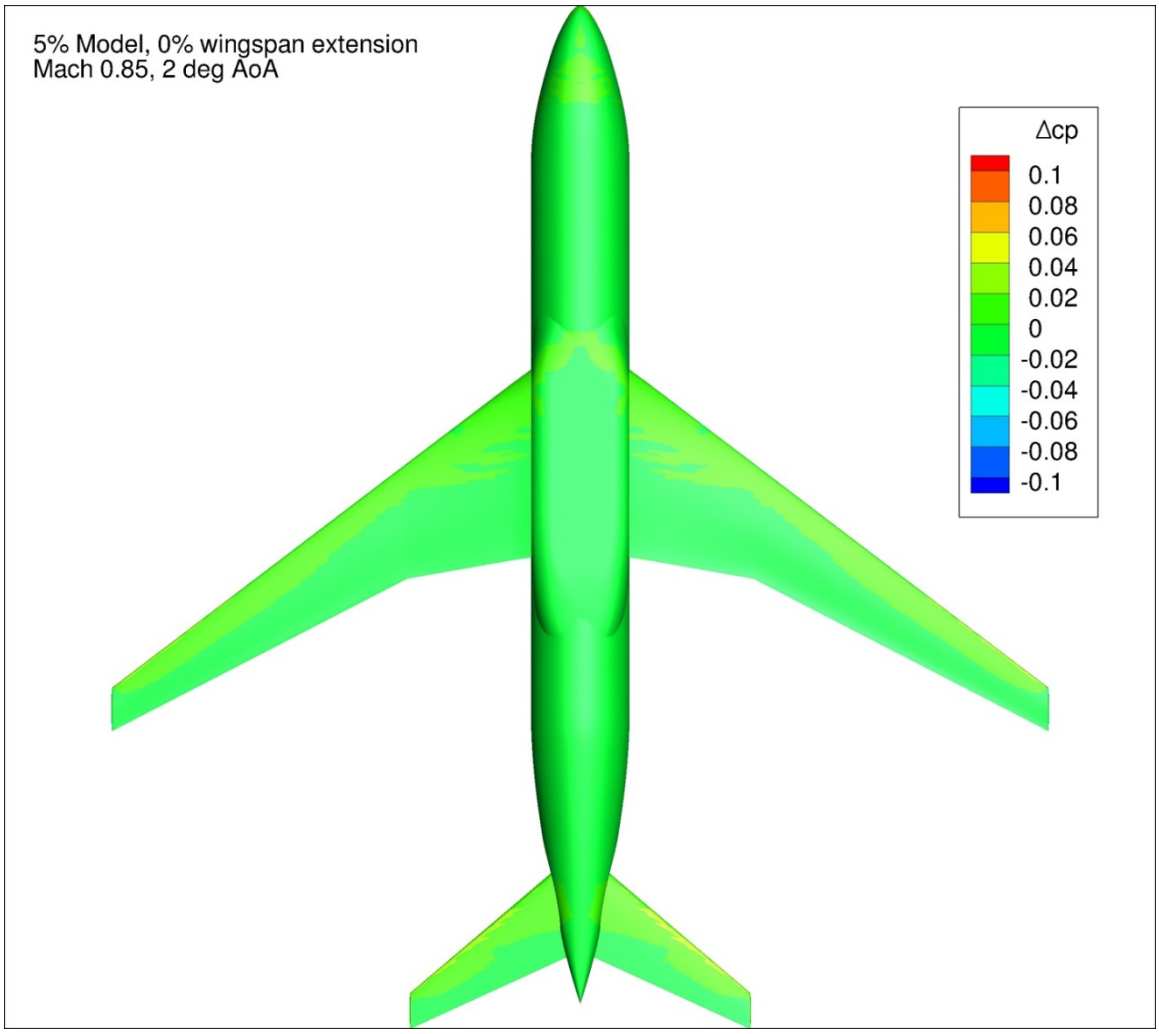

Figure 102. Configuration 2, Difference in Pressure Coefficient between Free-stream and Wind Tunnel Simulations, 2 deg Angle of Attack, Bottom View

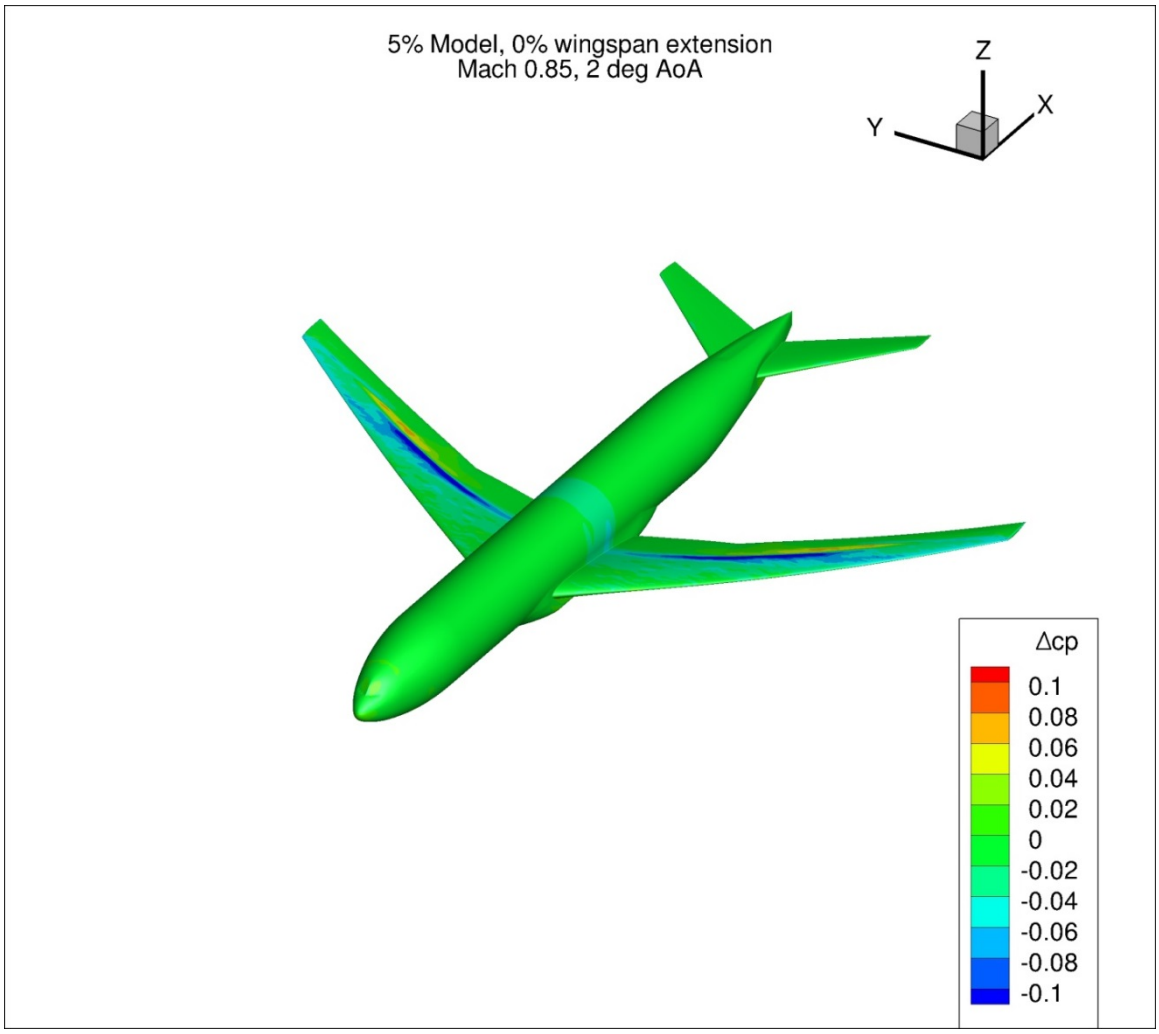

Figure 103. Configuration 2, Difference in Pressure Coefficient between Free-stream and Wind Tunnel Simulations, 2 deg Angle of Attack, Isometric View

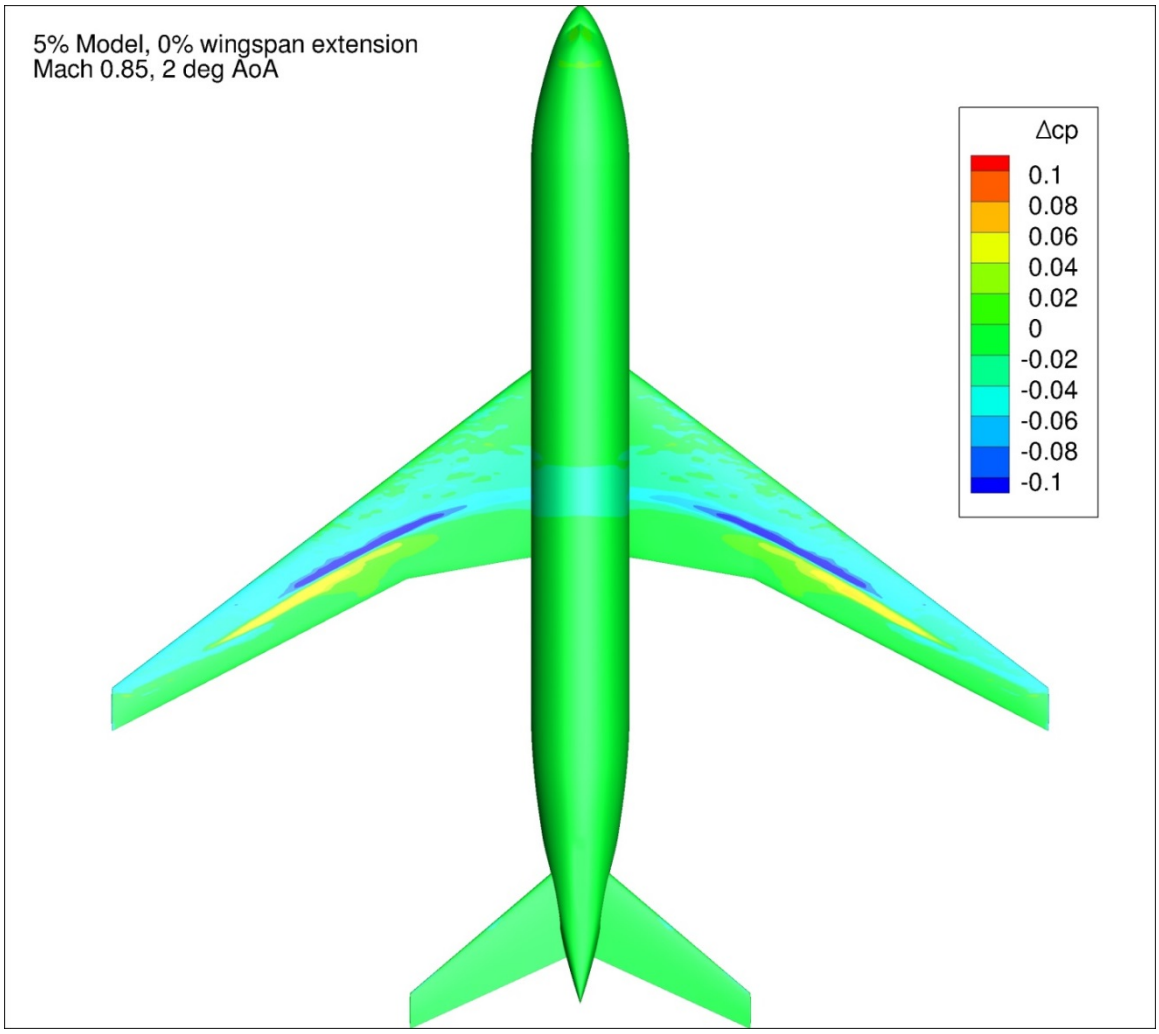

Figure 104. Configuration 2, Difference in Pressure Coefficient between Free-stream and Wind Tunnel Simulations, 2 deg Angle of Attack, Top View

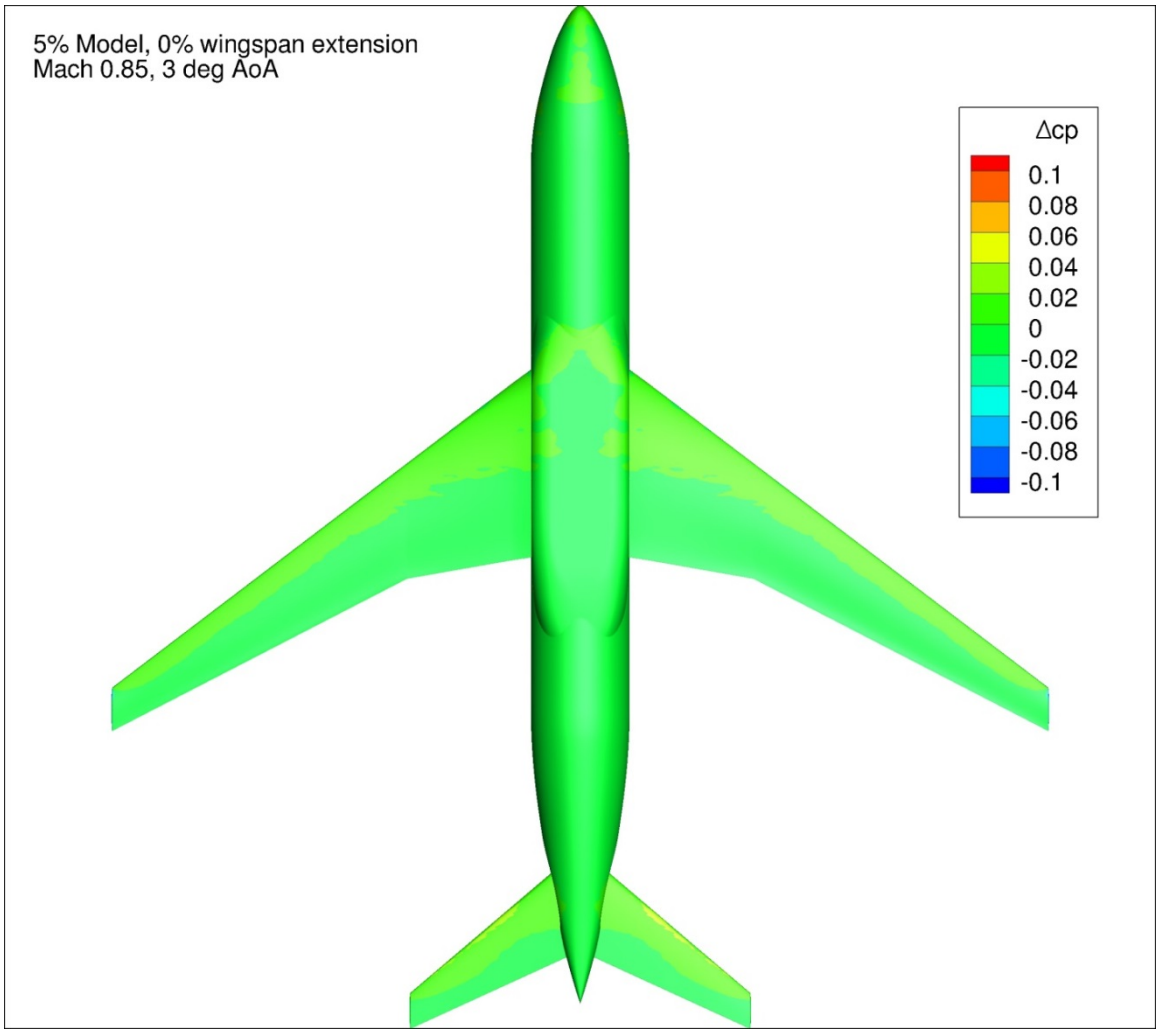

Figure 105. Configuration 2, Difference in Pressure Coefficient between Free-stream and Wind Tunnel Simulations, 3 deg Angle of Attack, Bottom View

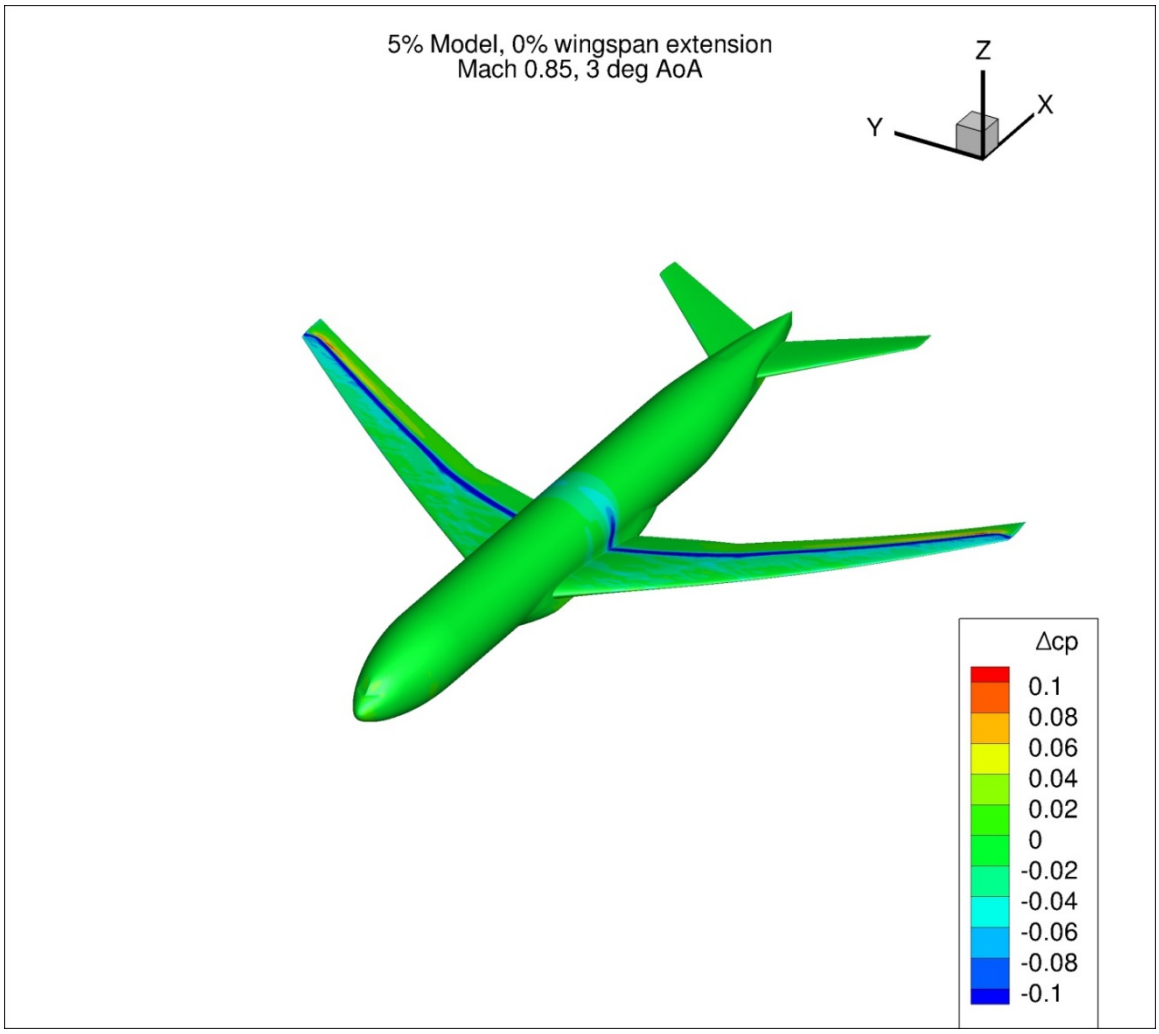

Figure 106. Configuration 2, Difference in Pressure Coefficient between Free-stream and Wind Tunnel Simulations, 3 deg Angle of Attack, Isometric View

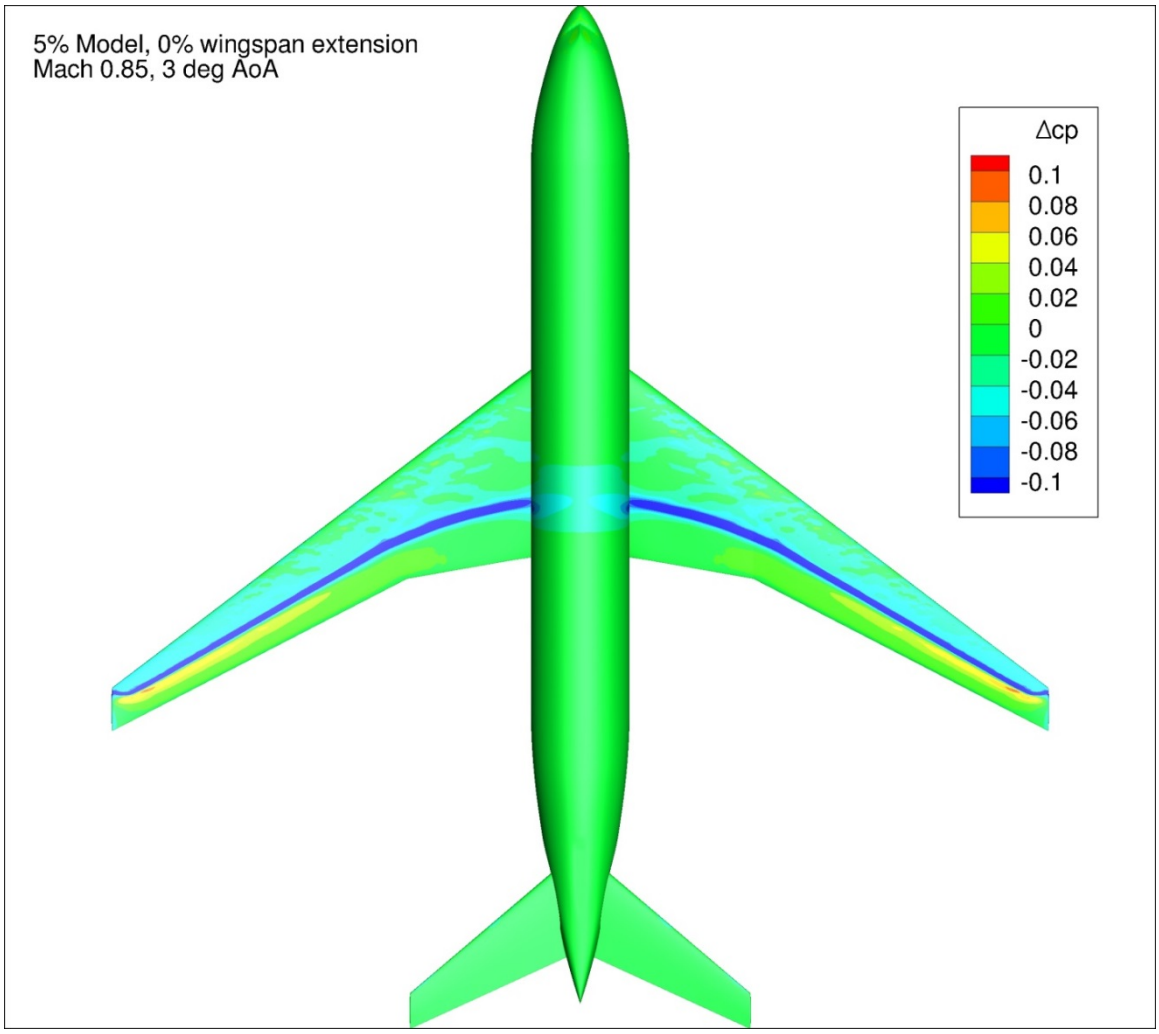

Figure 107. Configuration 2, Difference in Pressure Coefficient between Free-stream and Wind Tunnel Simulations, 3 deg Angle of Attack, Top View

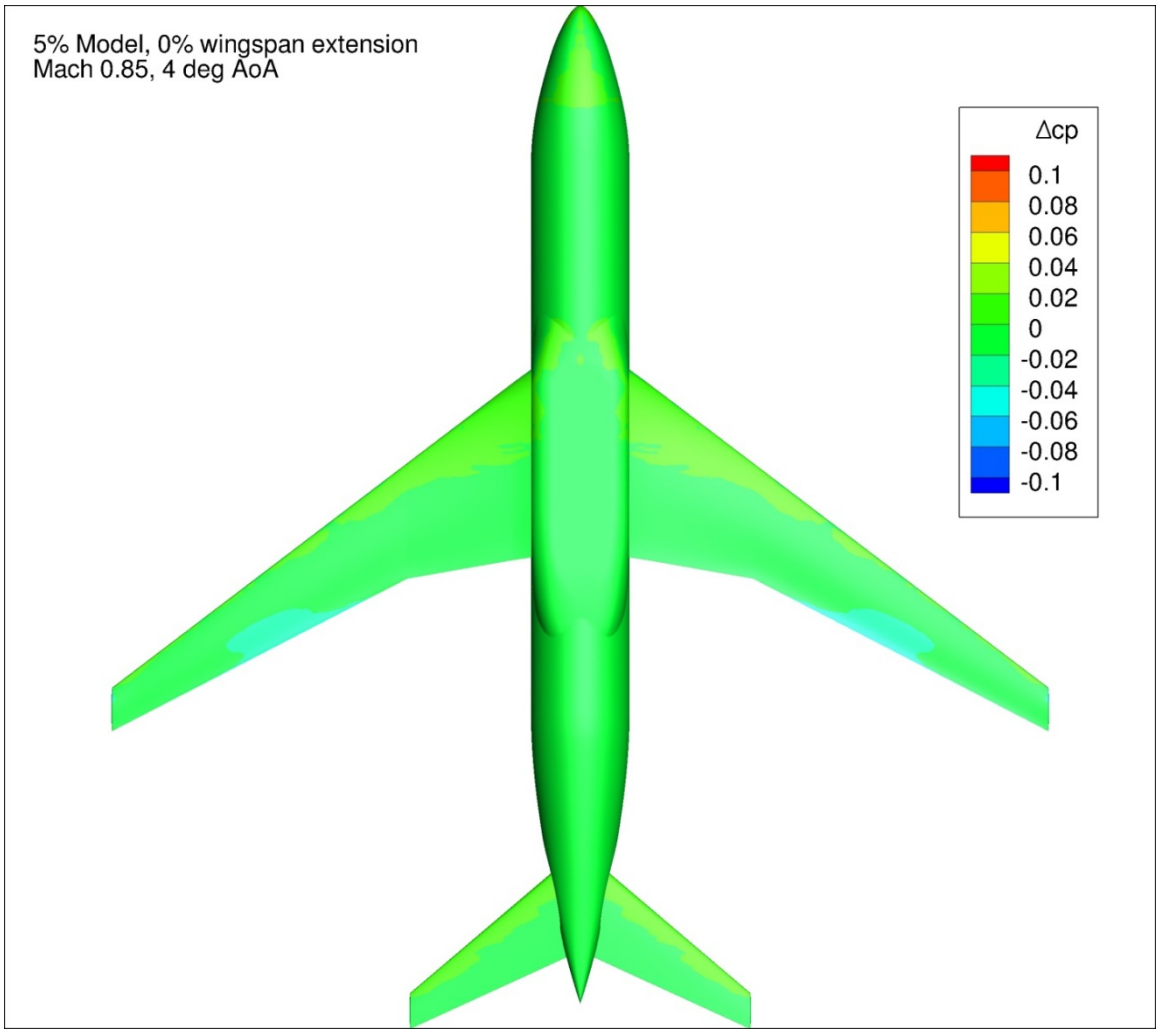

Figure 108. Configuration 2, Difference in Pressure Coefficient between Free-stream and Wind Tunnel Simulations, 4 deg Angle of Attack, Bottom View

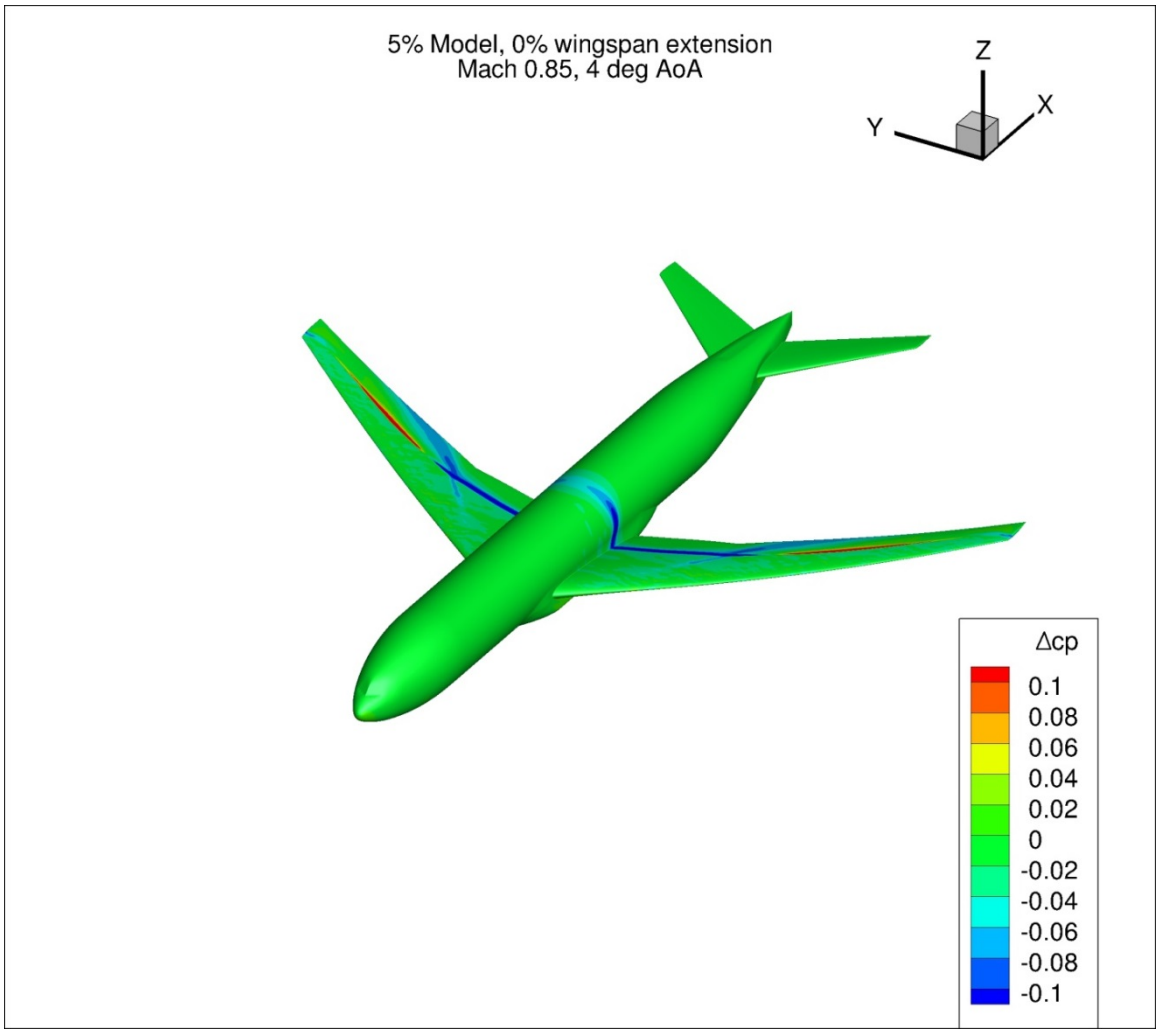

Figure 109. Configuration 2, Difference in Pressure Coefficient between Free-stream and Wind Tunnel Simulations, 4 deg Angle of Attack, Isometric View

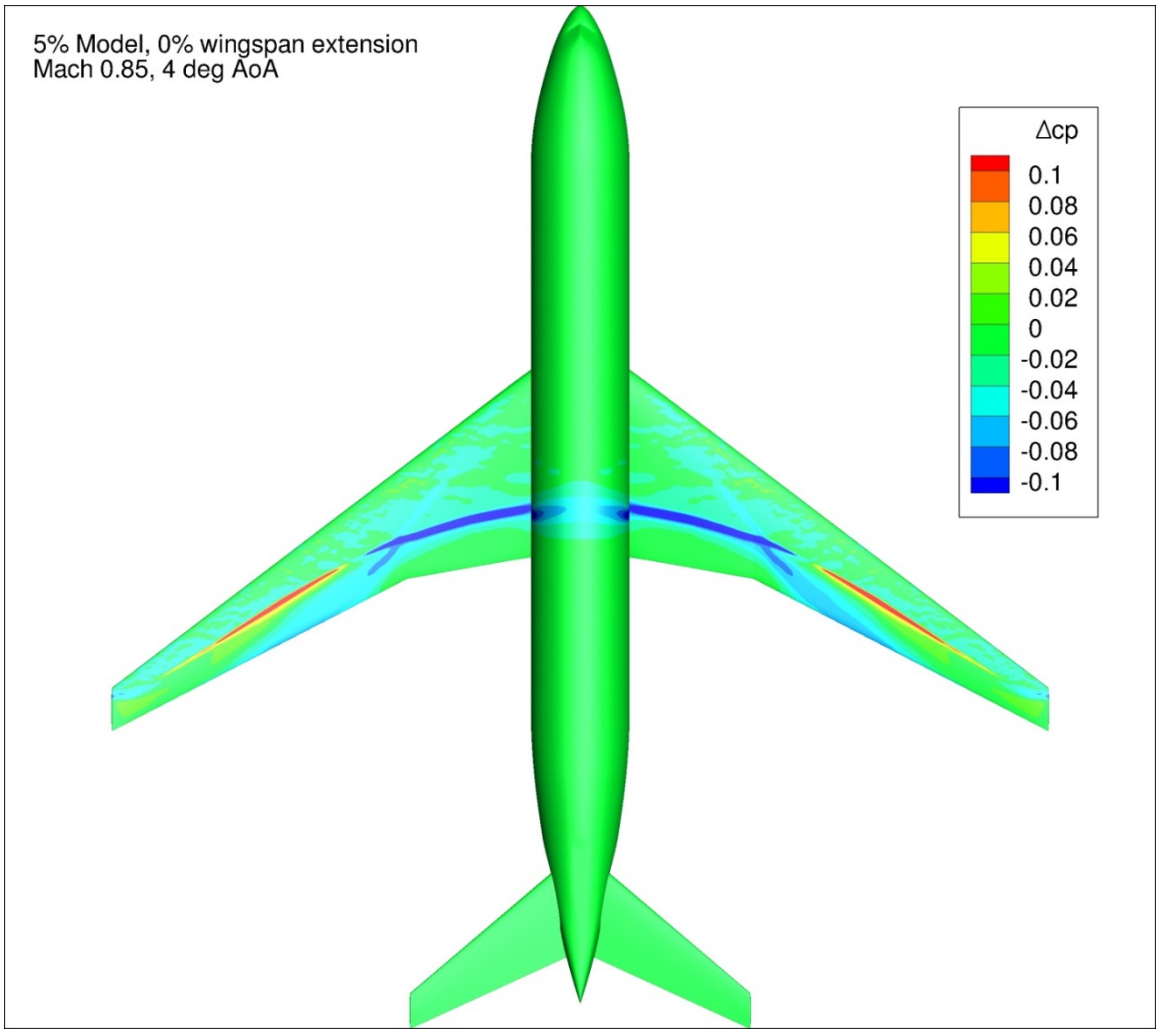

Figure 110. Configuration 2, Difference in Pressure Coefficient between Free-stream and Wind Tunnel Simulations, 4 deg Angle of Attack, Top View

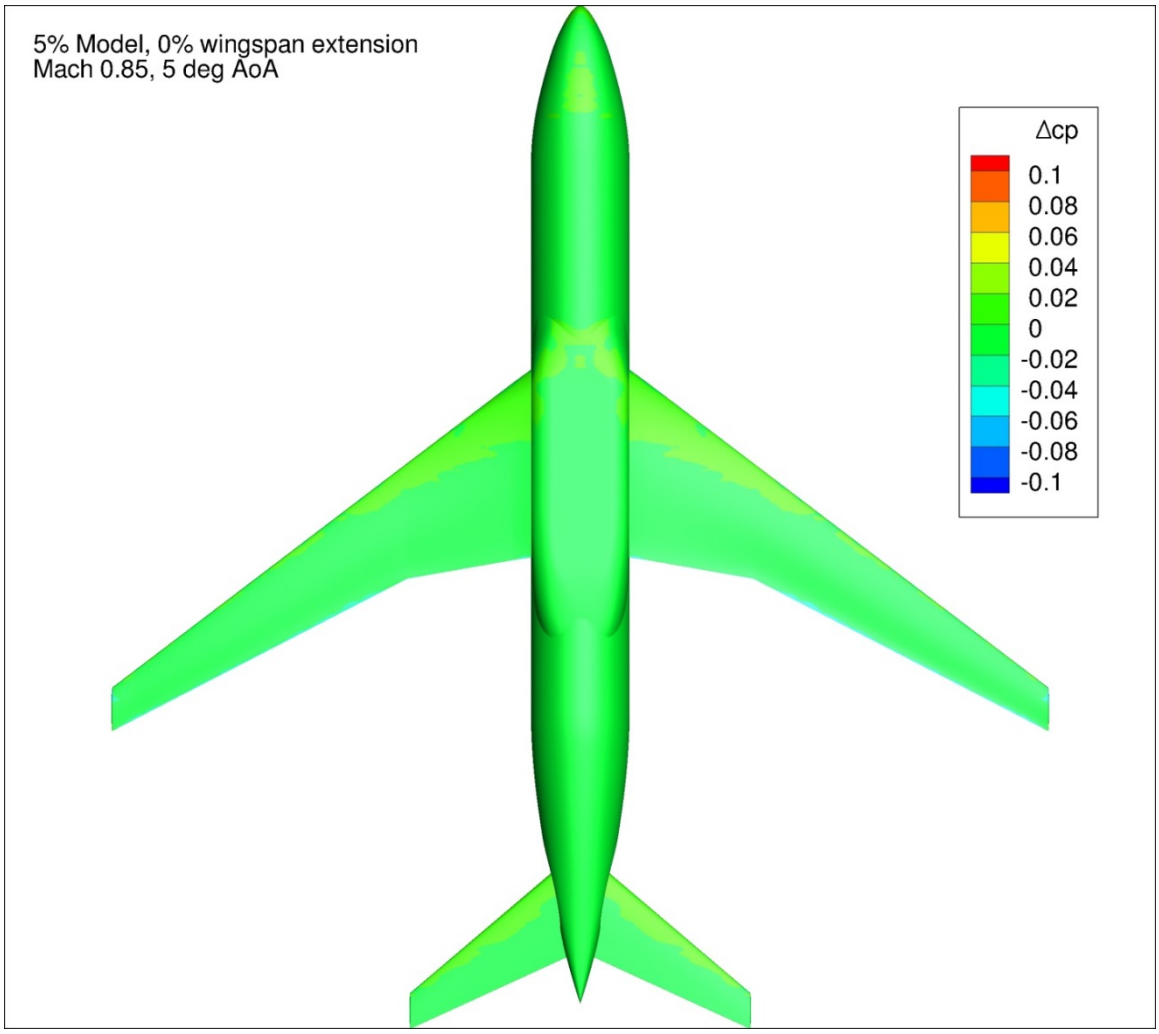

Figure 111. Configuration 2, Difference in Pressure Coefficient between Free-stream and Wind Tunnel Simulations, 5 deg Angle of Attack, Bottom View

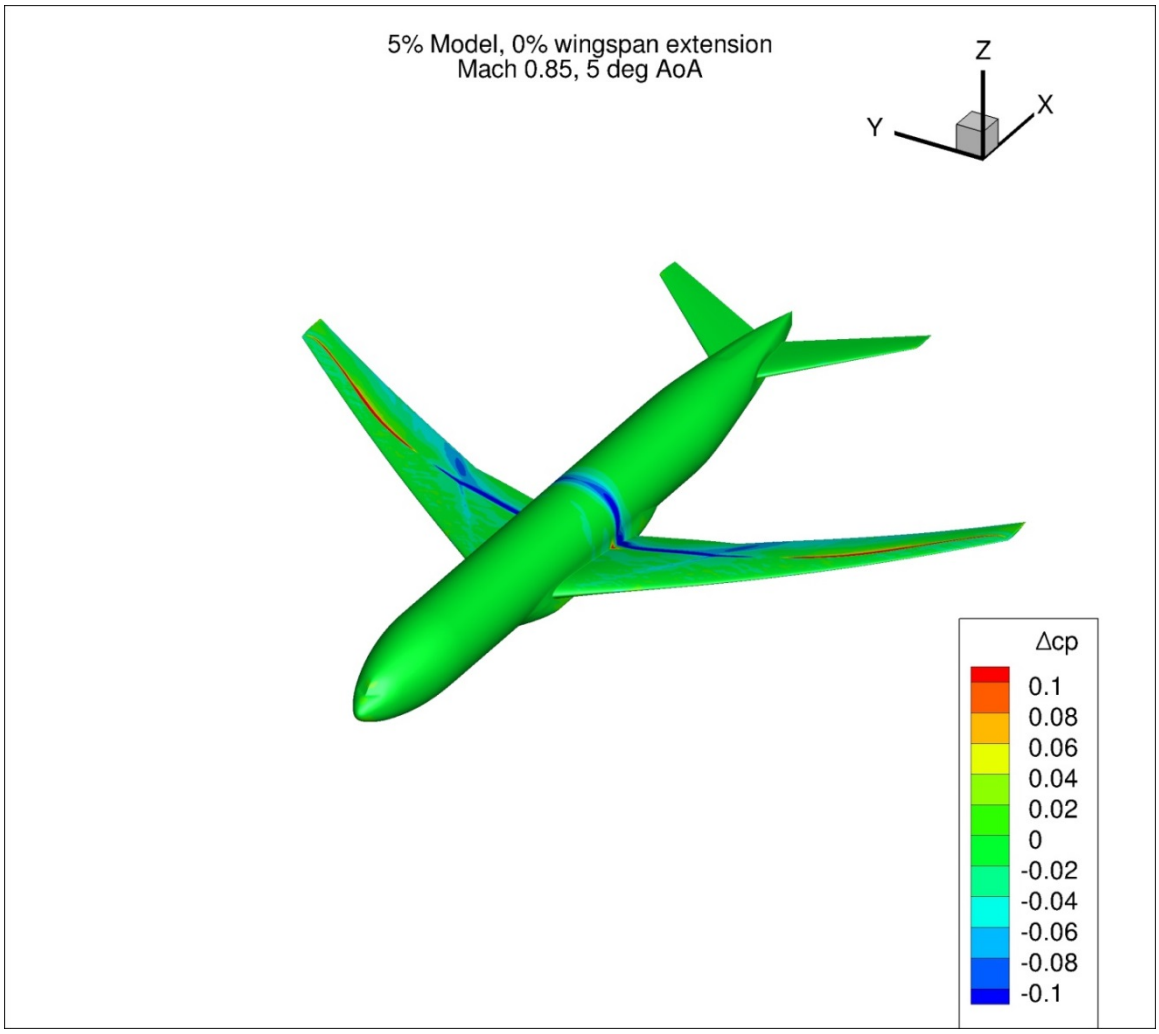

Figure 112. Configuration 2, Difference in Pressure Coefficient between Free-stream and Wind Tunnel Simulations, 5 deg Angle of Attack, Isometric View

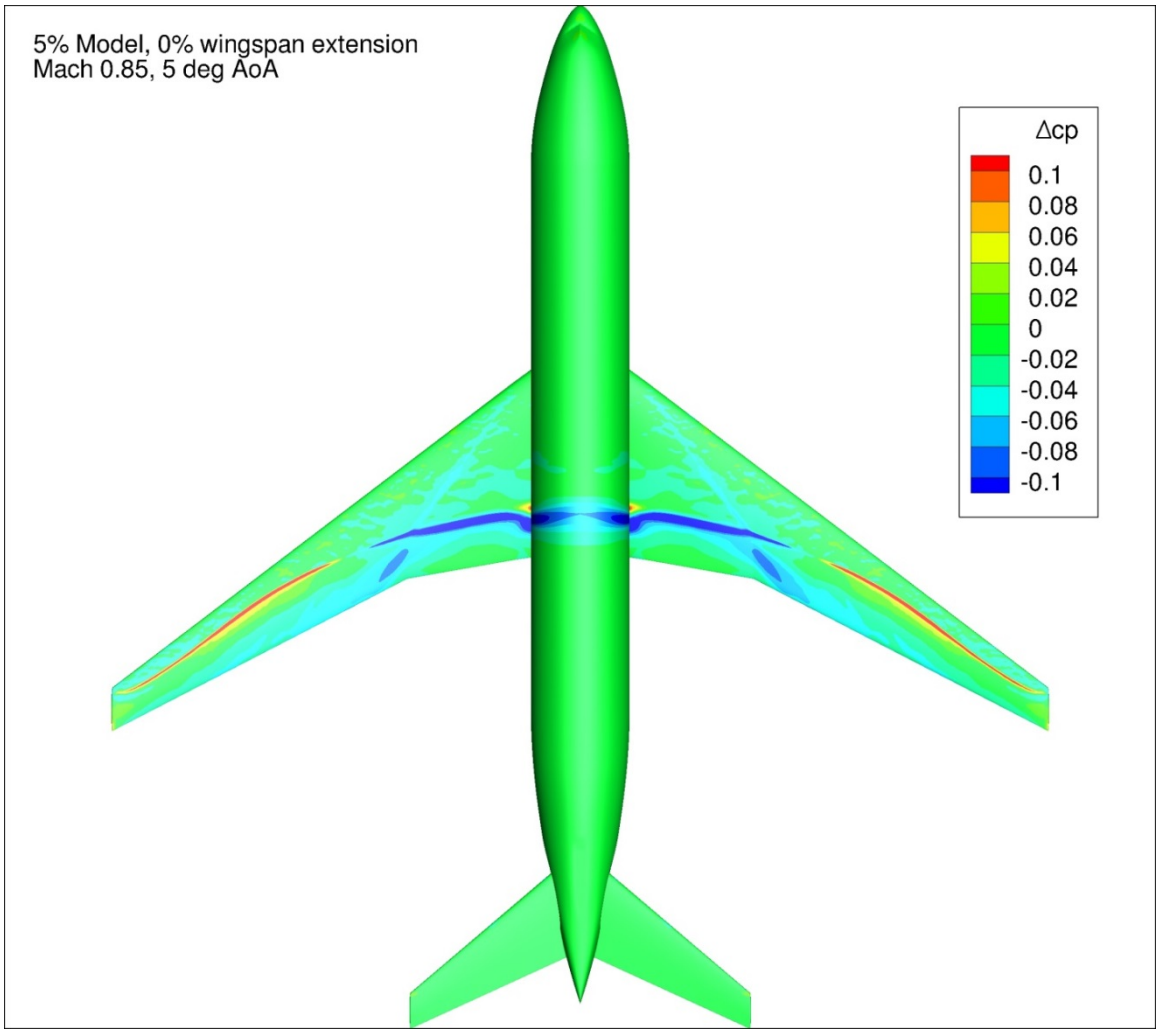

Figure 113. Configuration 2, Difference in Pressure Coefficient between Free-stream and Wind Tunnel Simulations, 5 deg Angle of Attack, Top View

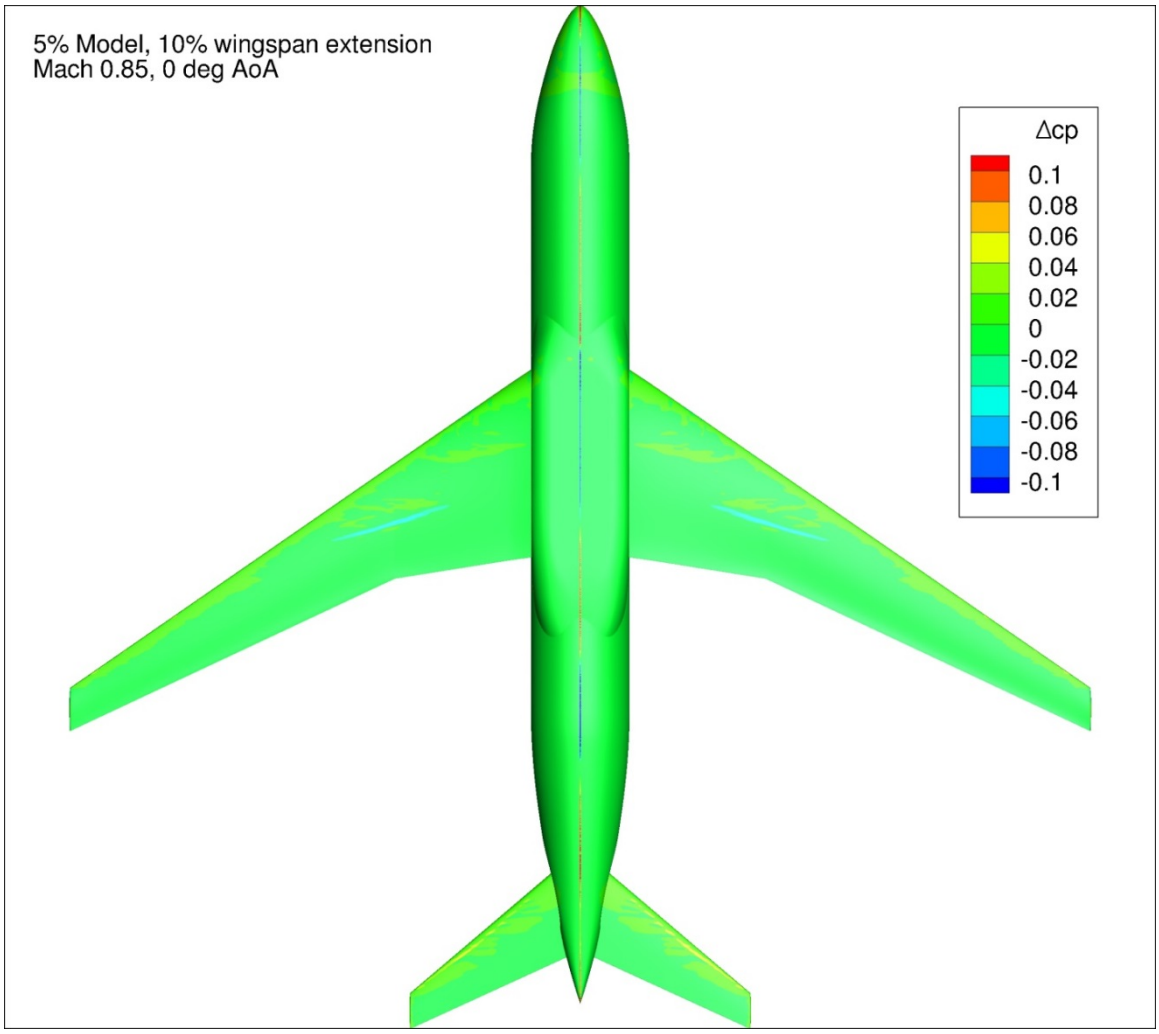

Figure 114. Configuration 2.1, Difference in Pressure Coefficient between Free-stream and Wind Tunnel Simulations, 0 deg Angle of Attack, Bottom View

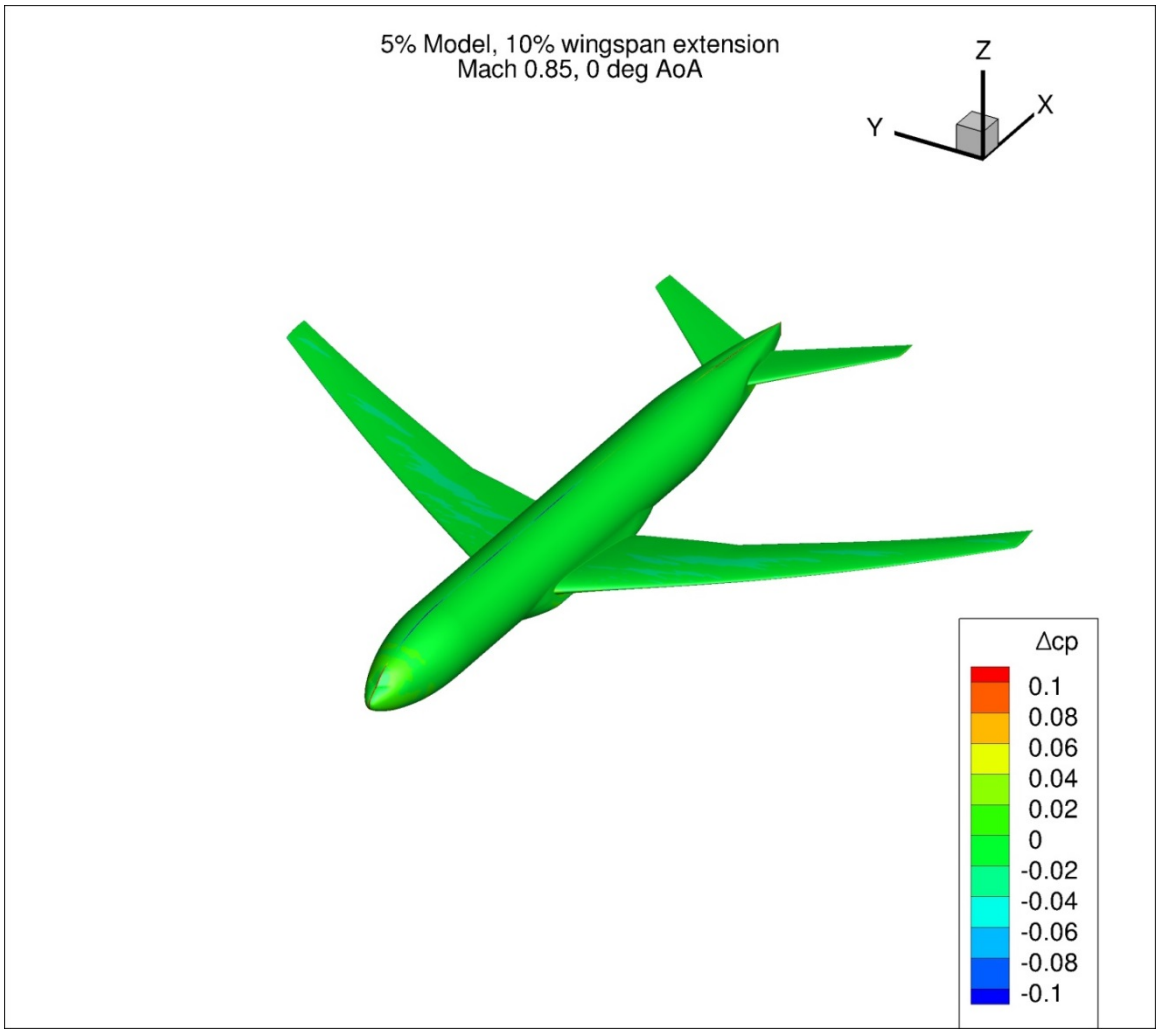

Figure 115. Configuration 2.1, Difference in Pressure Coefficient between Free-stream and Wind Tunnel Simulations, 0 deg Angle of Attack, Isometric View

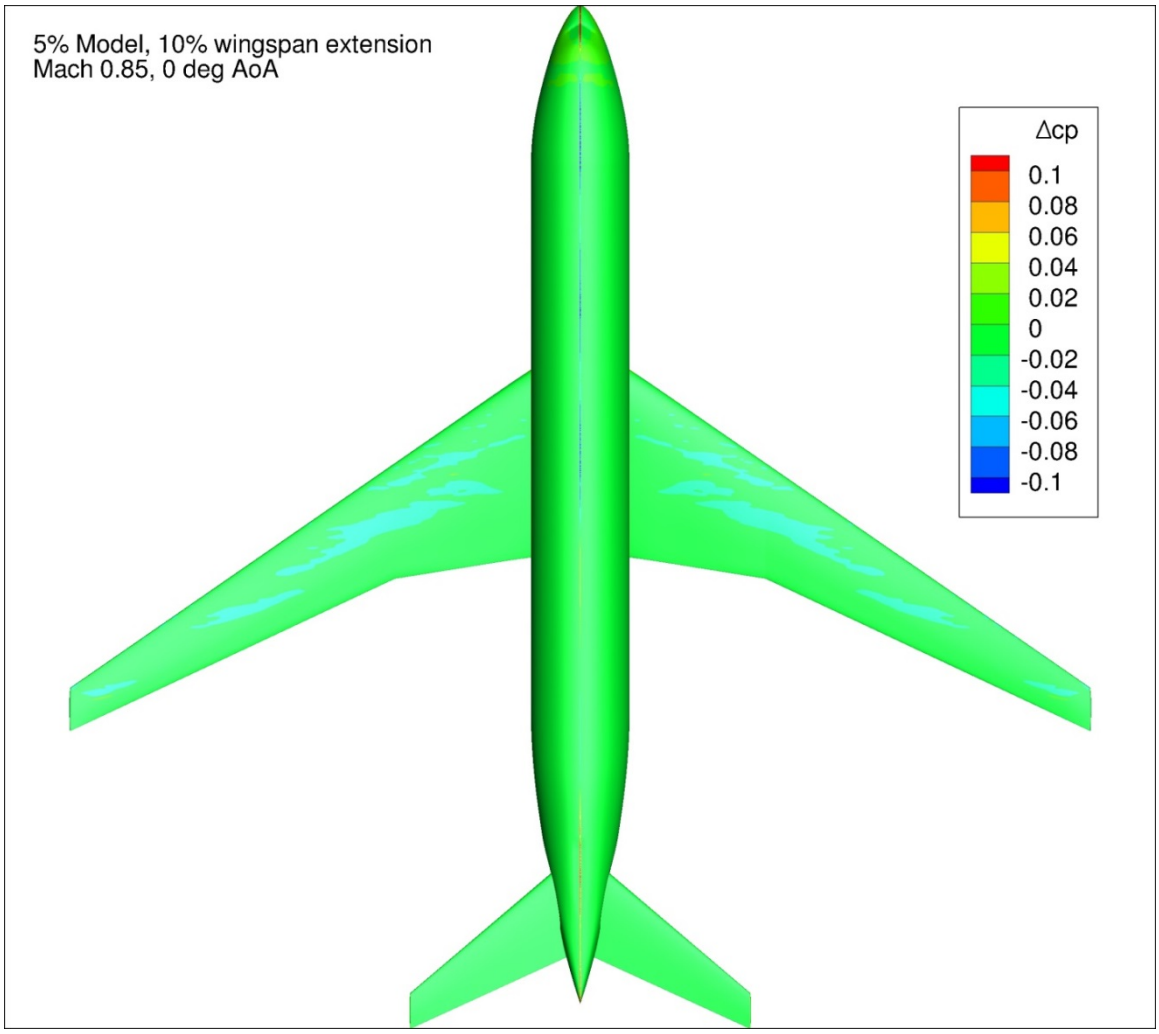

Figure 116. Configuration 2.1, Difference in Pressure Coefficient between Free-stream and Wind Tunnel Simulations, 0 deg Angle of Attack, Top View

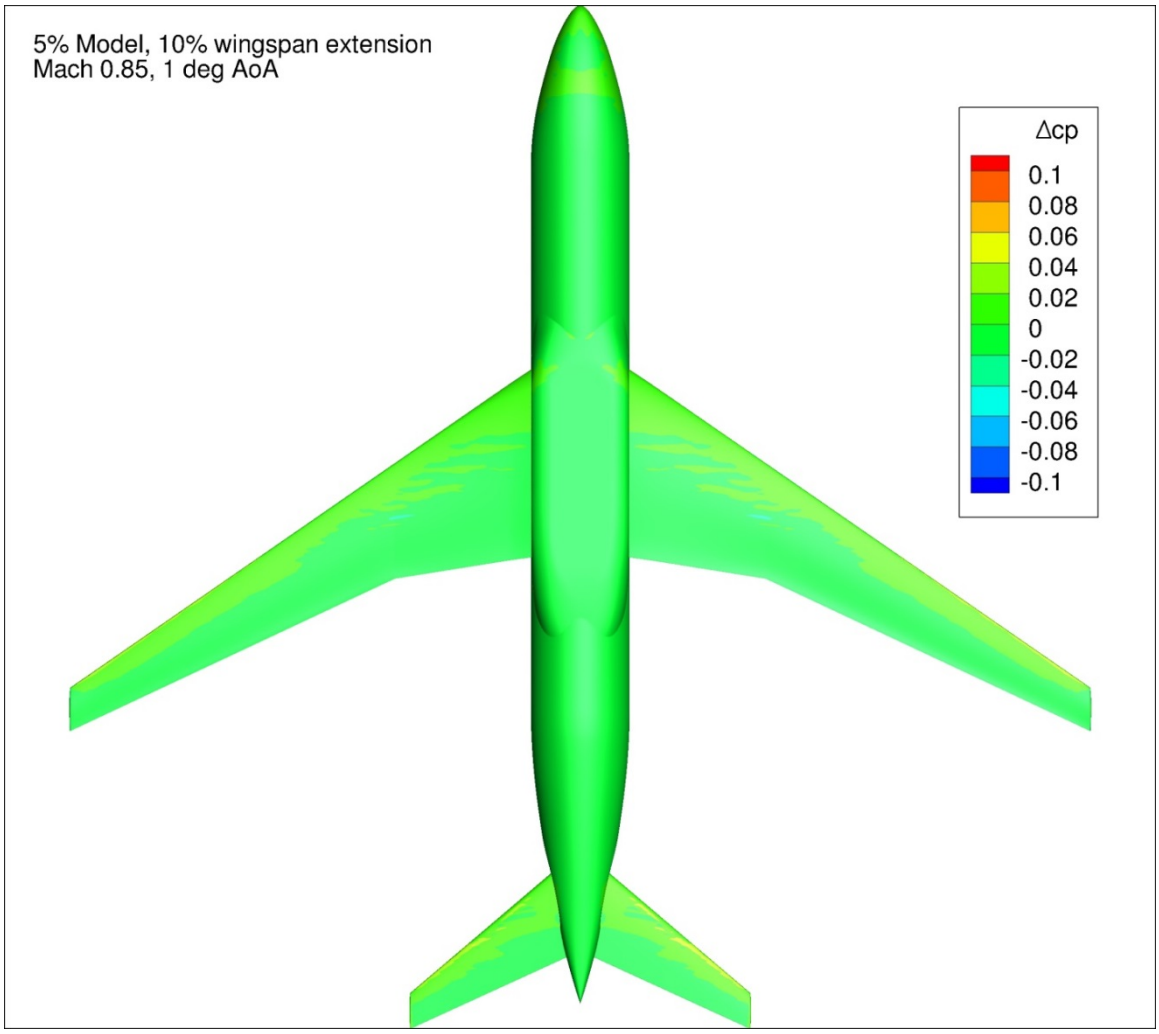

Figure 117. Configuration 2.1, Difference in Pressure Coefficient between Free-stream and Wind Tunnel Simulations, 1 deg Angle of Attack, Bottom View

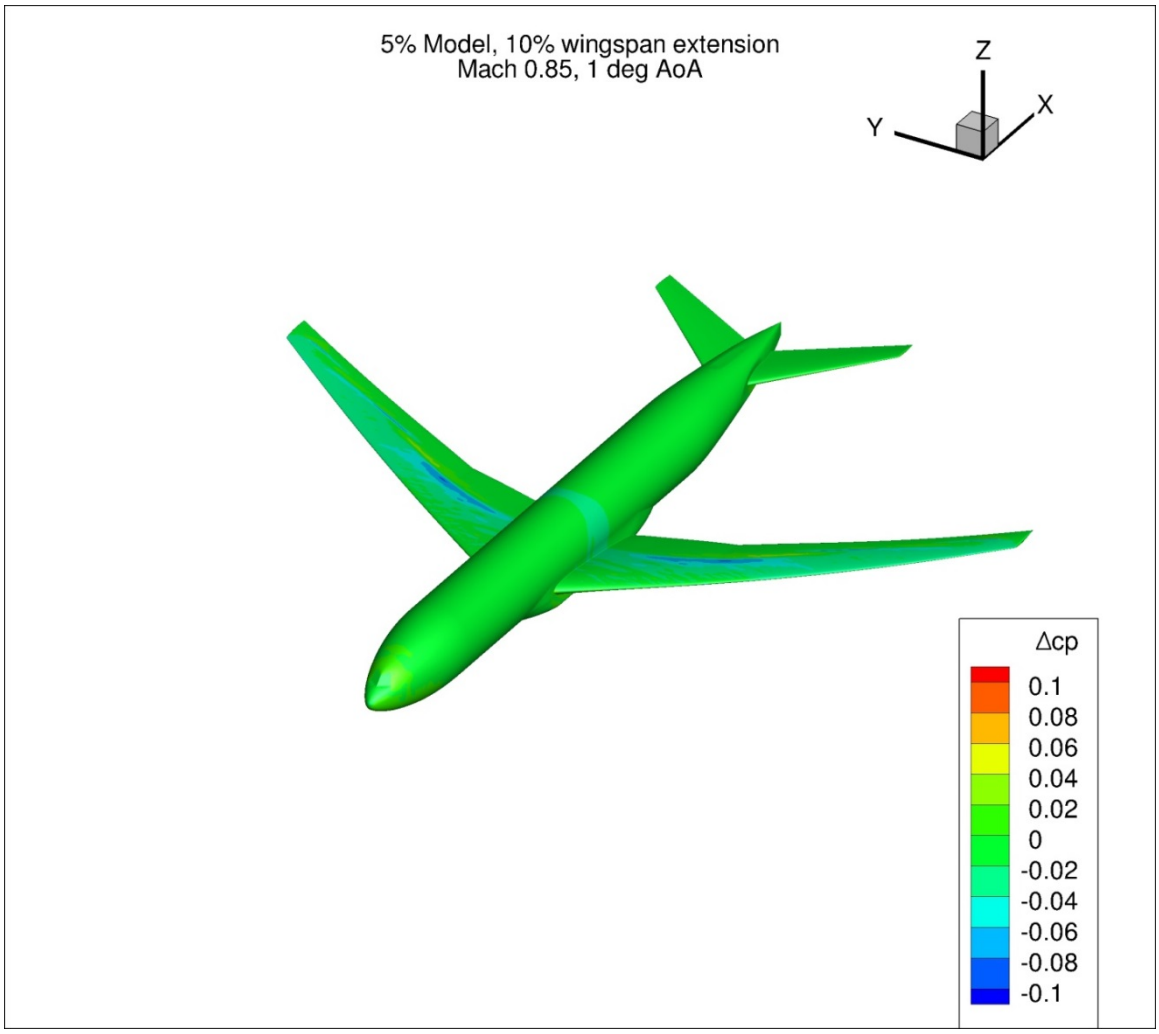

Figure 118. Configuration 2.1, Difference in Pressure Coefficient between Free-stream and Wind Tunnel Simulations, 1 deg Angle of Attack, Isometric View

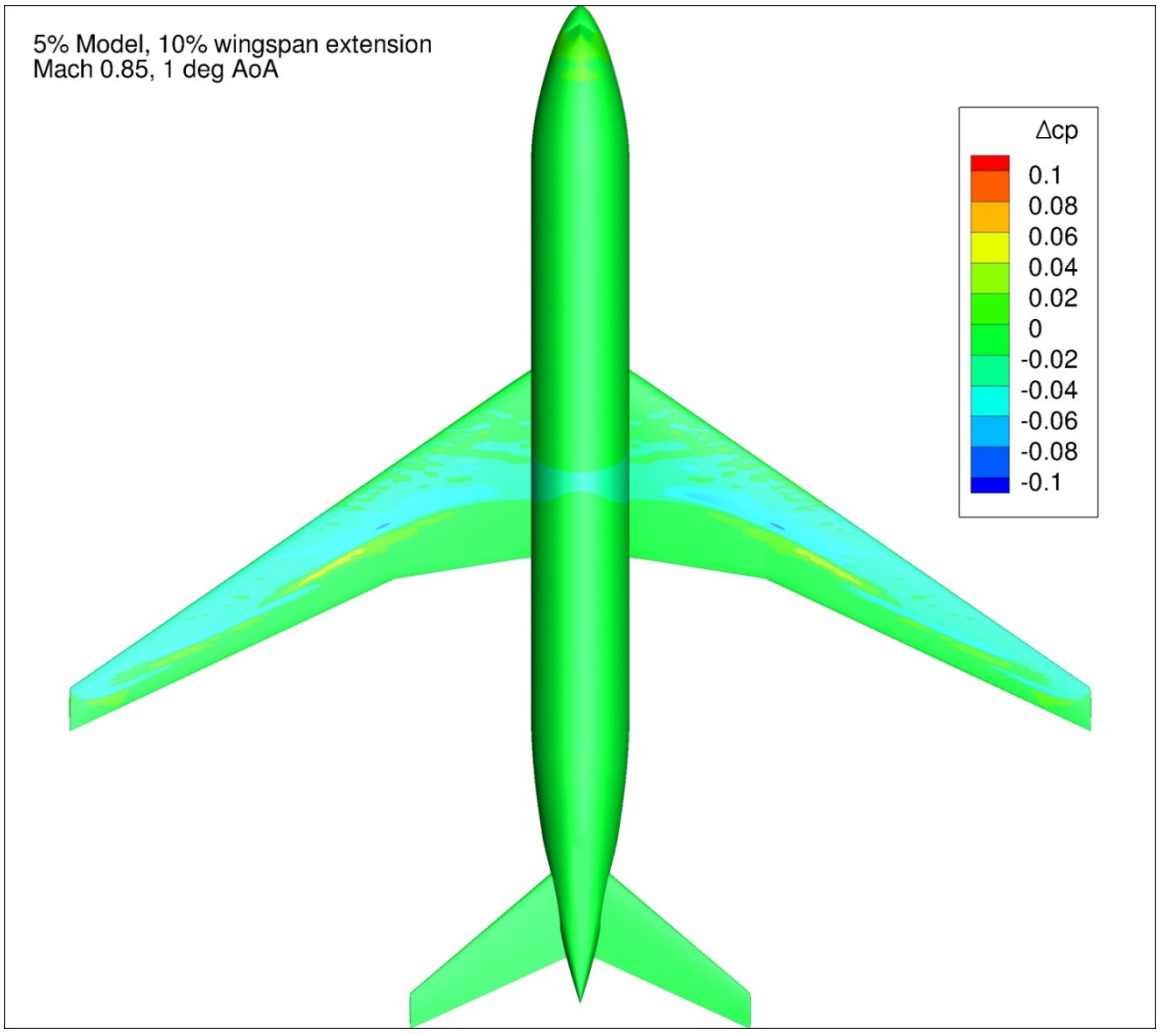

Figure 119. Configuration 2.1, Difference in Pressure Coefficient between Free-stream and Wind Tunnel Simulations, 1 deg Angle of Attack, Top View

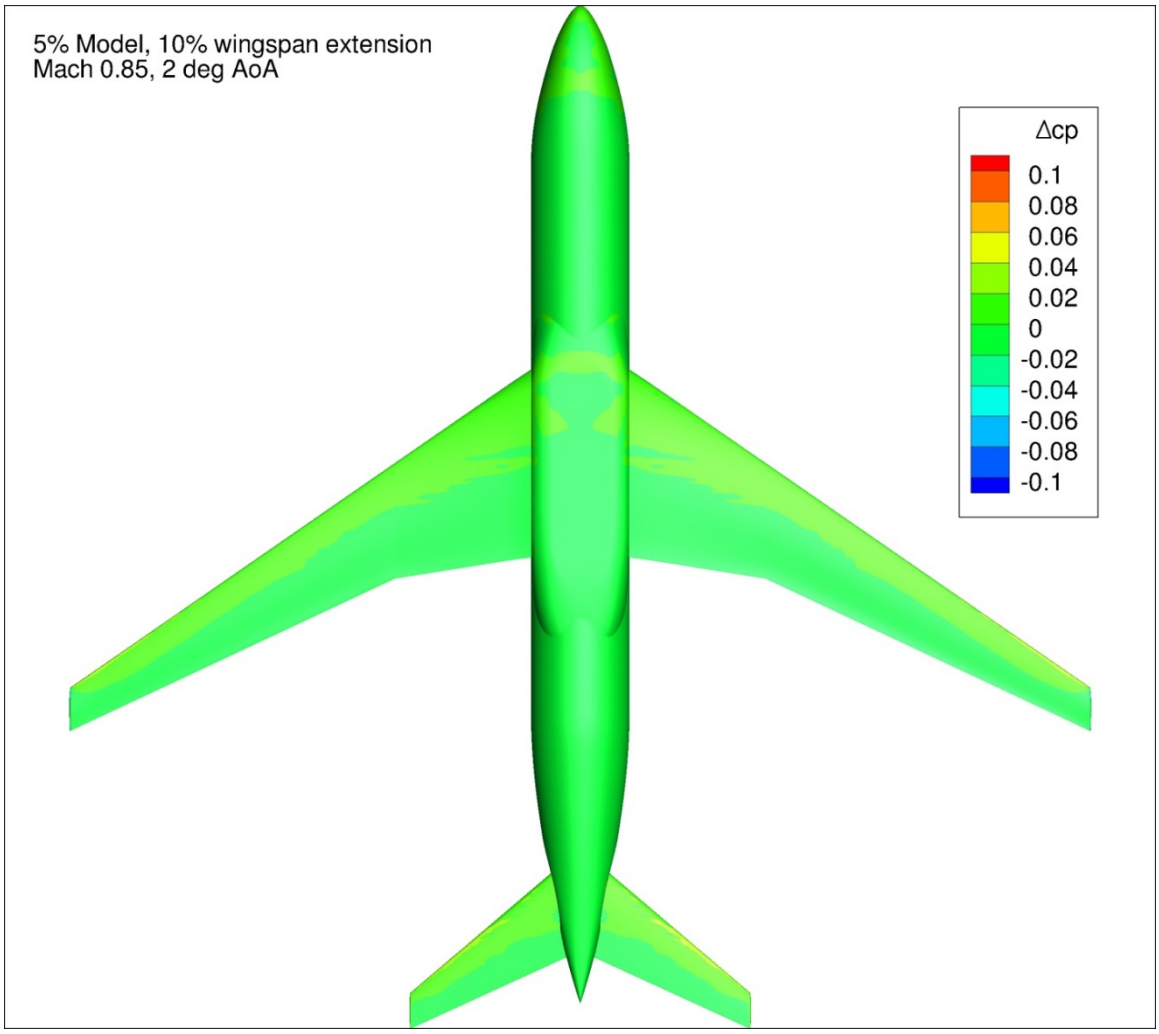

Figure 120. Configuration 2.1, Difference in Pressure Coefficient between Free-stream and Wind Tunnel Simulations, 2 deg Angle of Attack, Bottom View

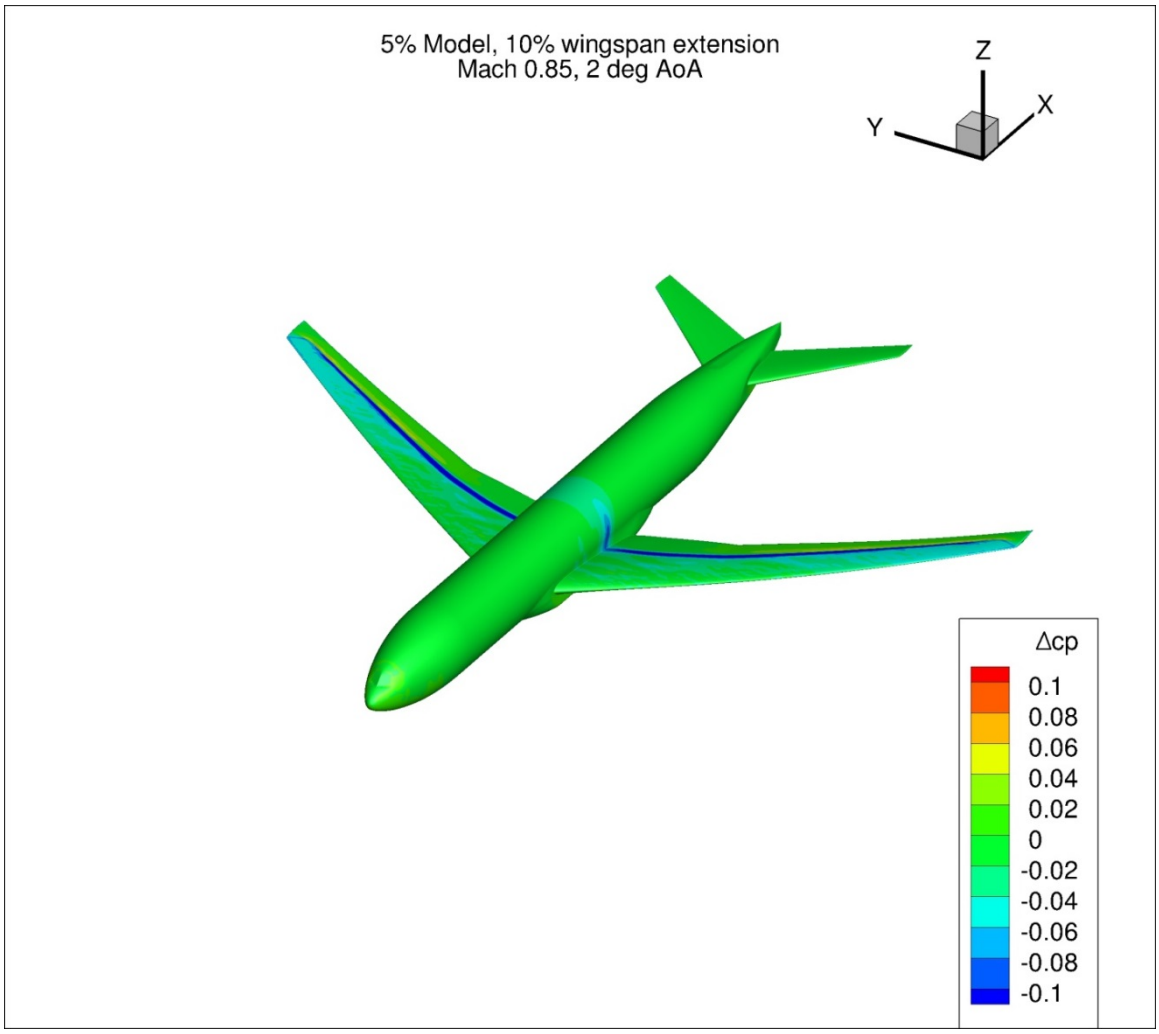

Figure 121. Configuration 2.1, Difference in Pressure Coefficient between Free-stream and Wind Tunnel Simulations, 2 deg Angle of Attack, Isometric View

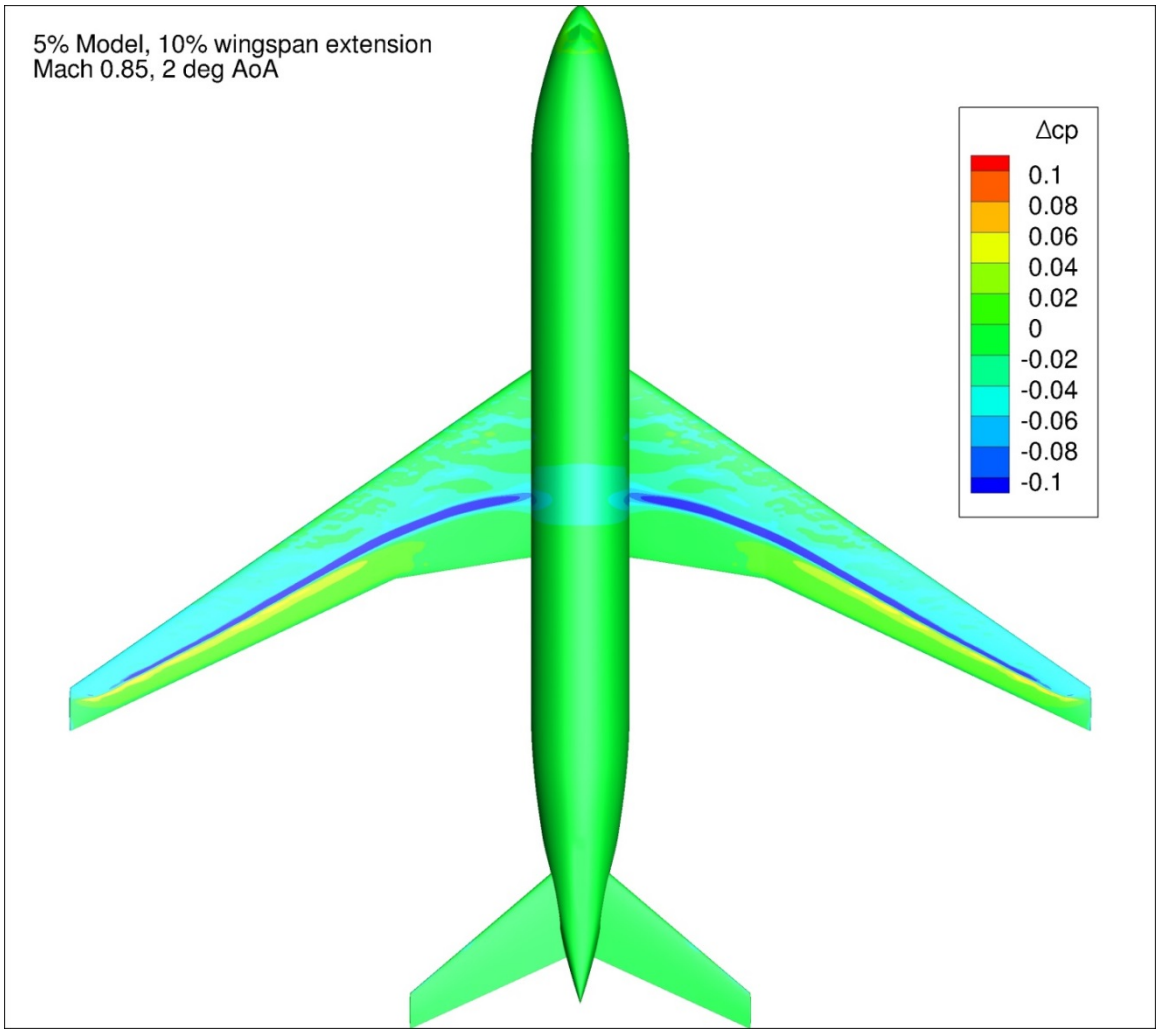

Figure 122. Configuration 2.1, Difference in Pressure Coefficient between Free-stream and Wind Tunnel Simulations, 2 deg Angle of Attack, Top View

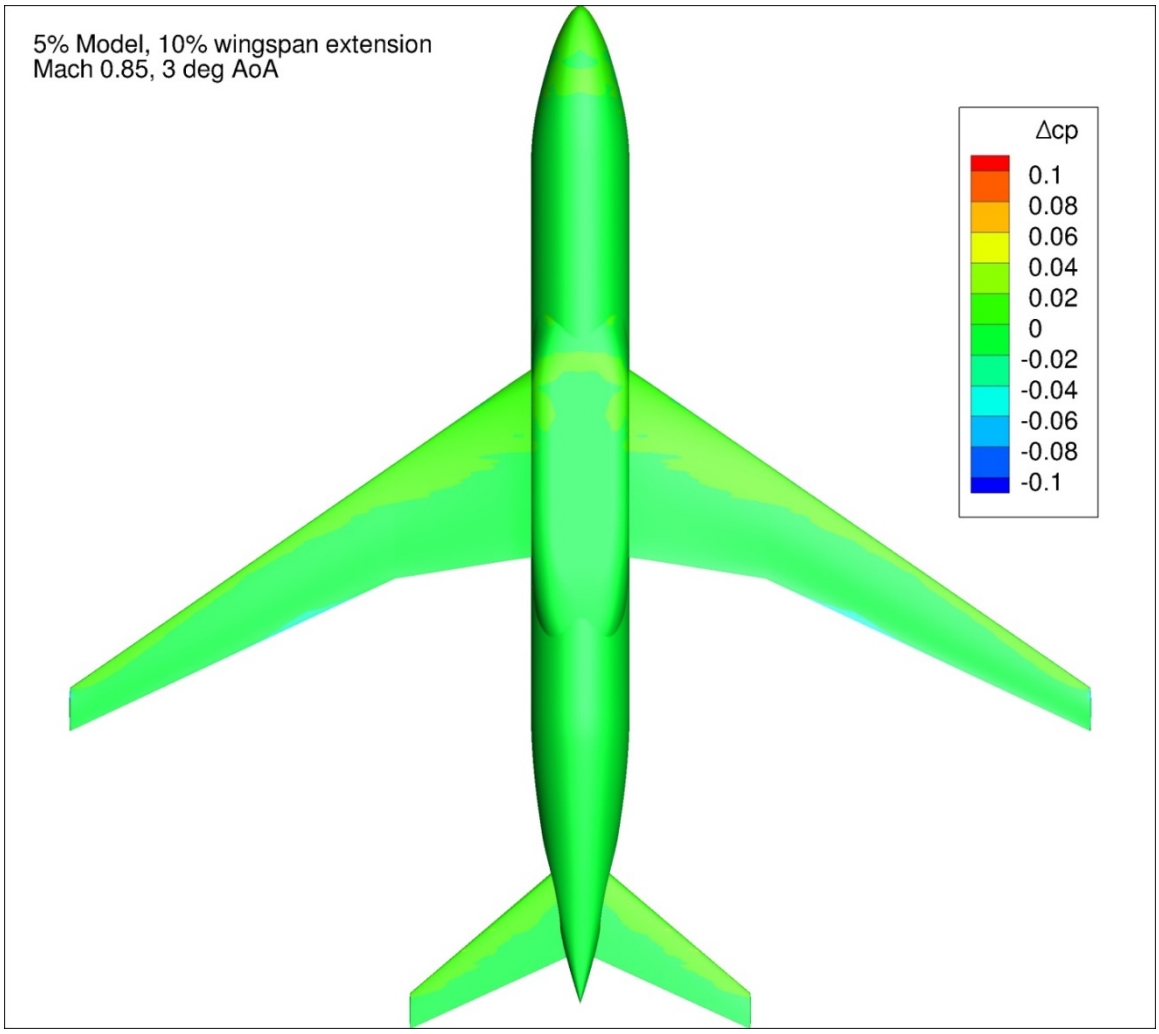

Figure 123. Configuration 2.1, Difference in Pressure Coefficient between Free-stream and Wind Tunnel Simulations, 3 deg Angle of Attack, Bottom View

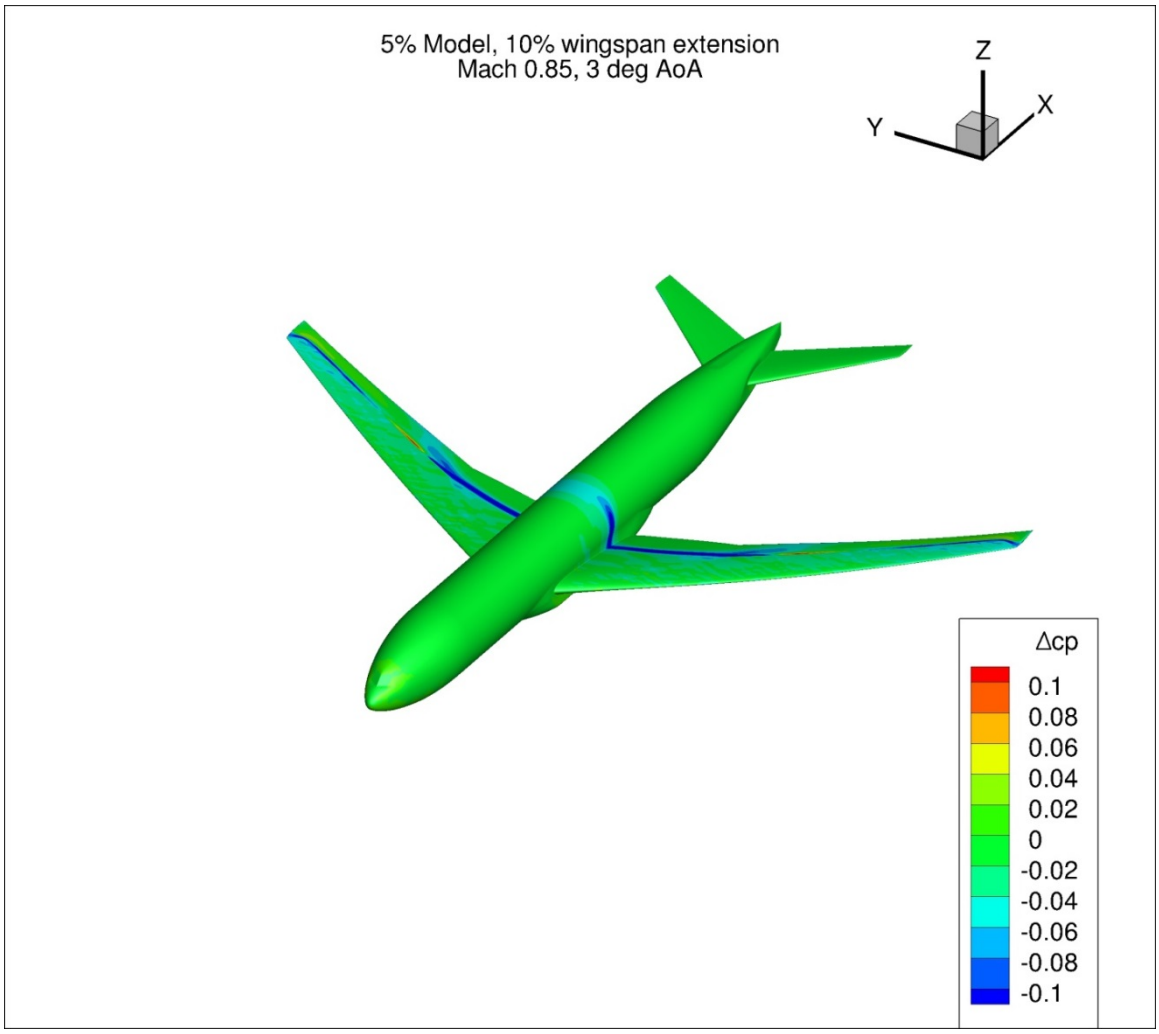

Figure 124. Configuration 2.1, Difference in Pressure Coefficient between Free-stream and Wind Tunnel Simulations, 3 deg Angle of Attack, Isometric View

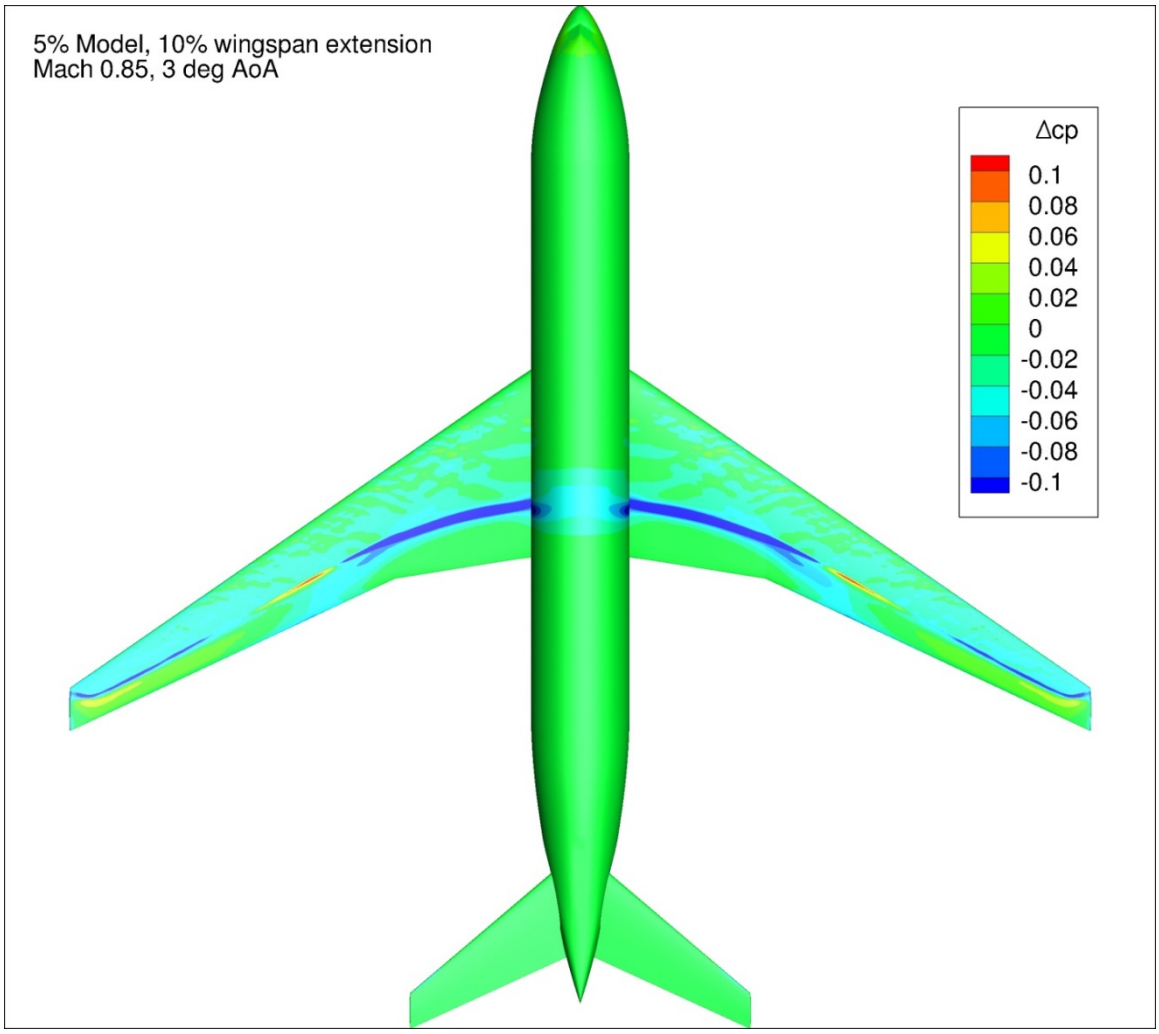

Figure 125. Configuration 2.1, Difference in Pressure Coefficient between Free-stream and Wind Tunnel Simulations, 3 deg Angle of Attack, Top View

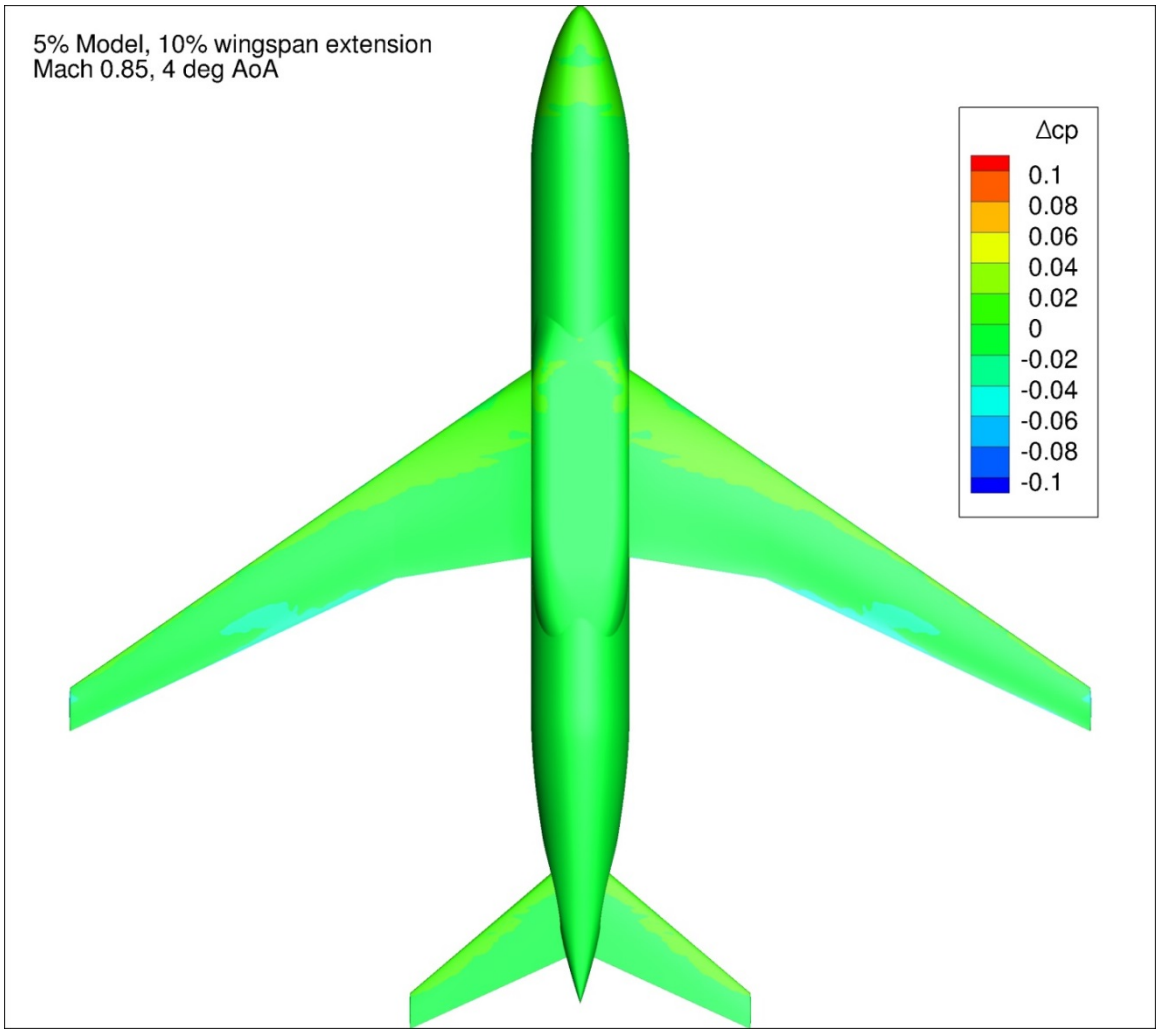

Figure 126. Configuration 2.1, Difference in Pressure Coefficient between Free-stream and Wind Tunnel Simulations, 4 deg Angle of Attack, Bottom View

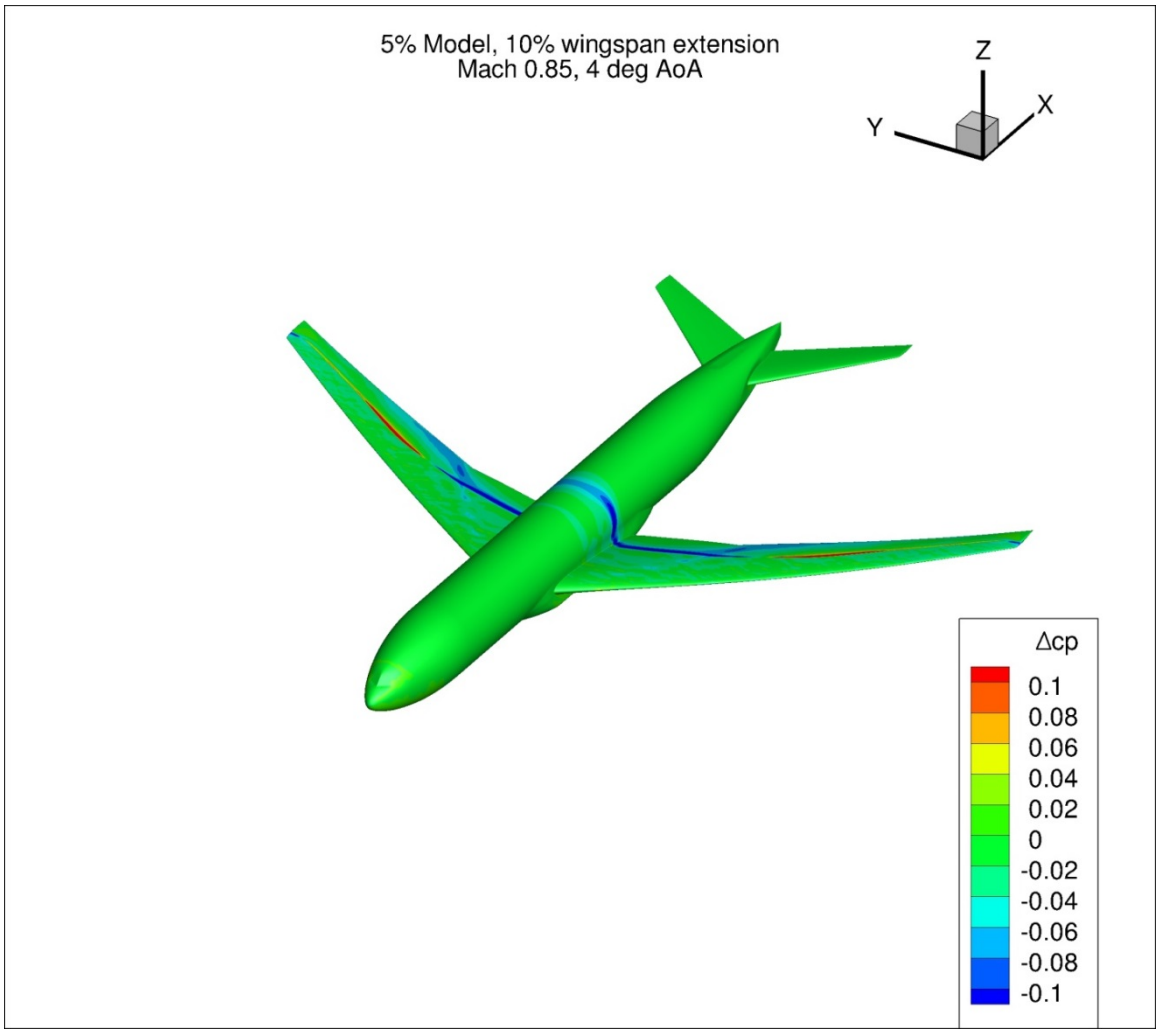

Figure 127. Configuration 2.1, Difference in Pressure Coefficient between Free-stream and Wind Tunnel Simulations, 4 deg Angle of Attack, Isometric View

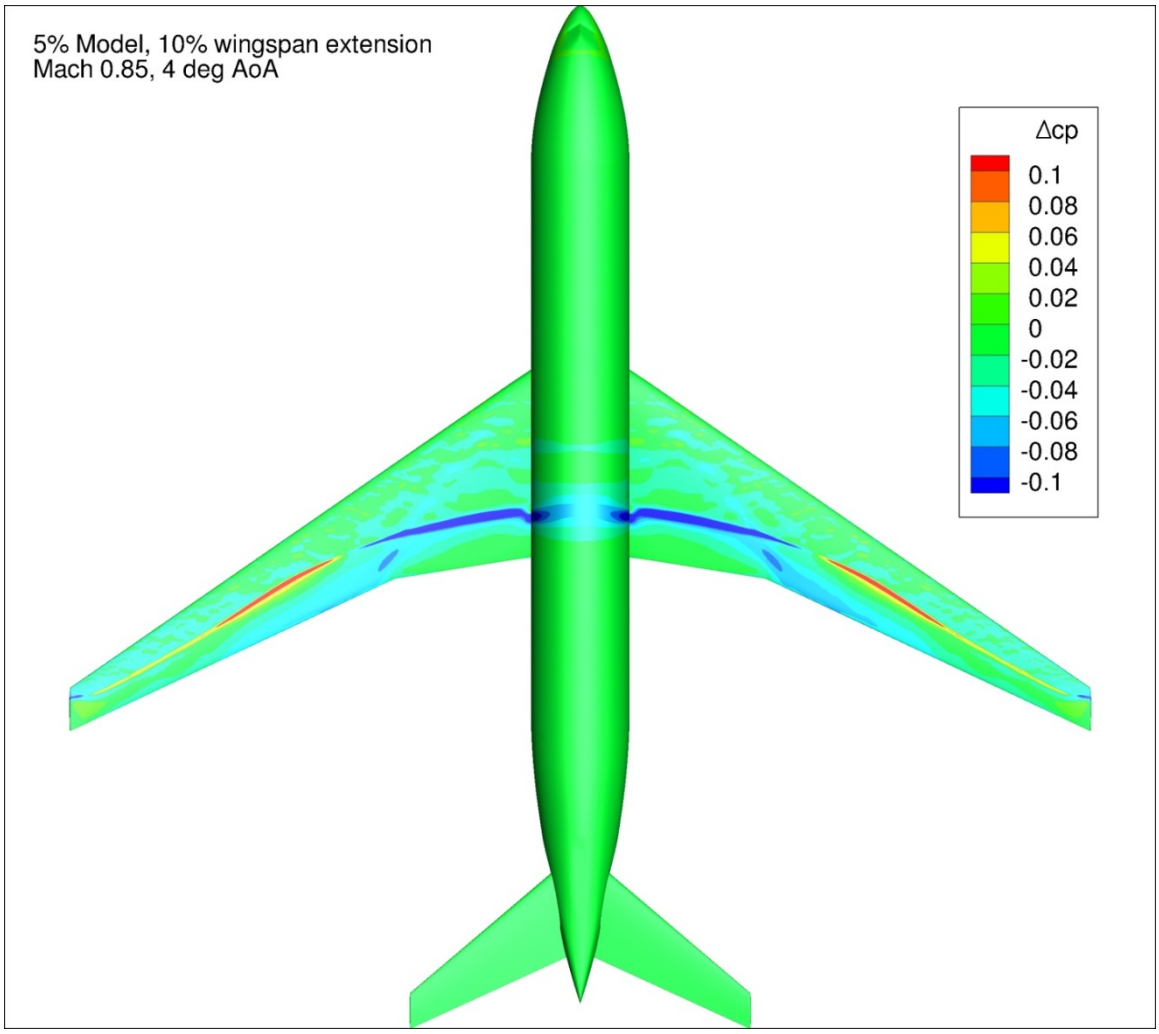

Figure 128. Configuration 2.1, Difference in Pressure Coefficient between Free-stream and Wind Tunnel Simulations, 4 deg Angle of Attack, Top View

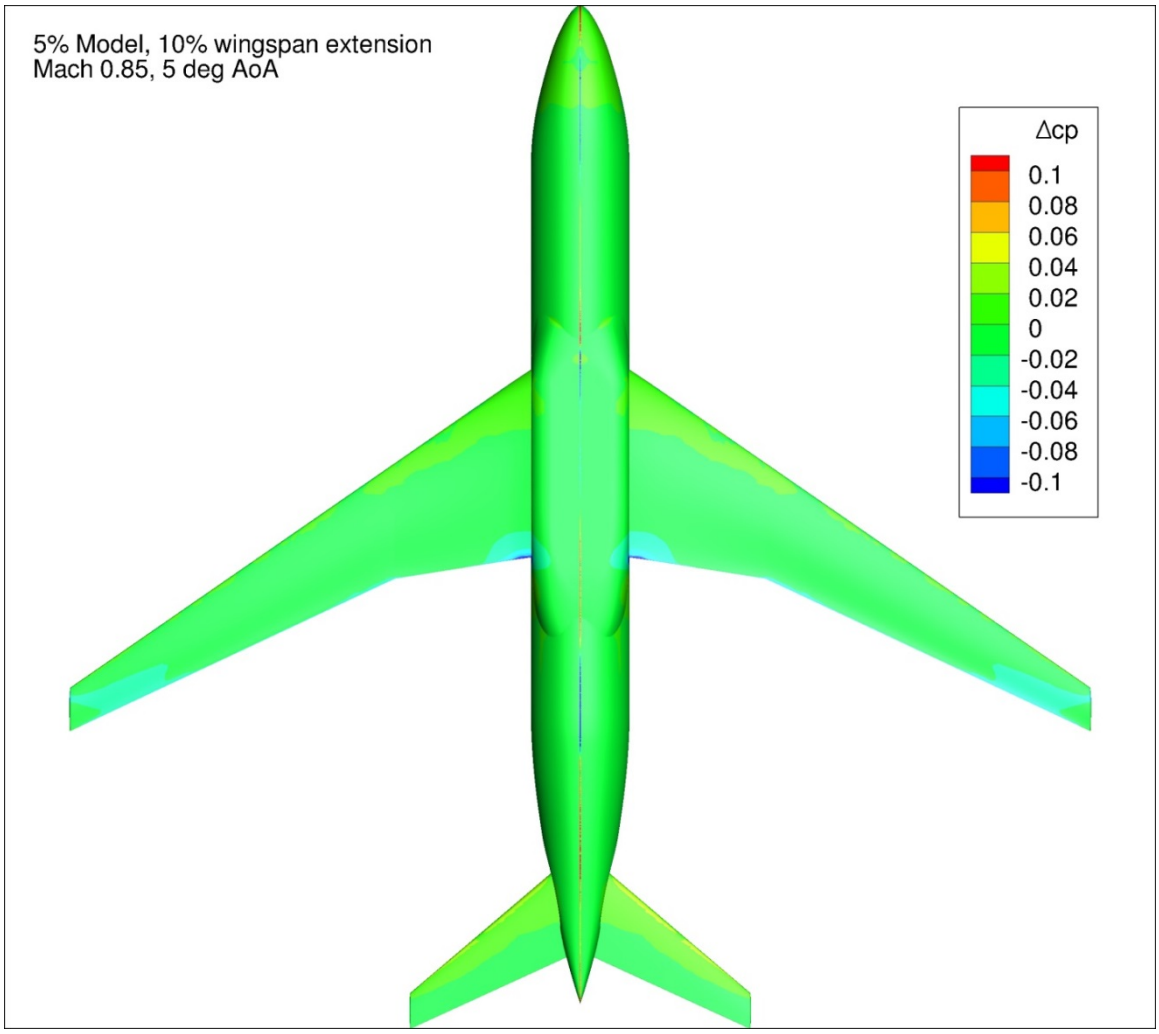

Figure 129. Configuration 2.1, Difference in Pressure Coefficient between Free-stream and Wind Tunnel Simulations, 5 deg Angle of Attack, Bottom View

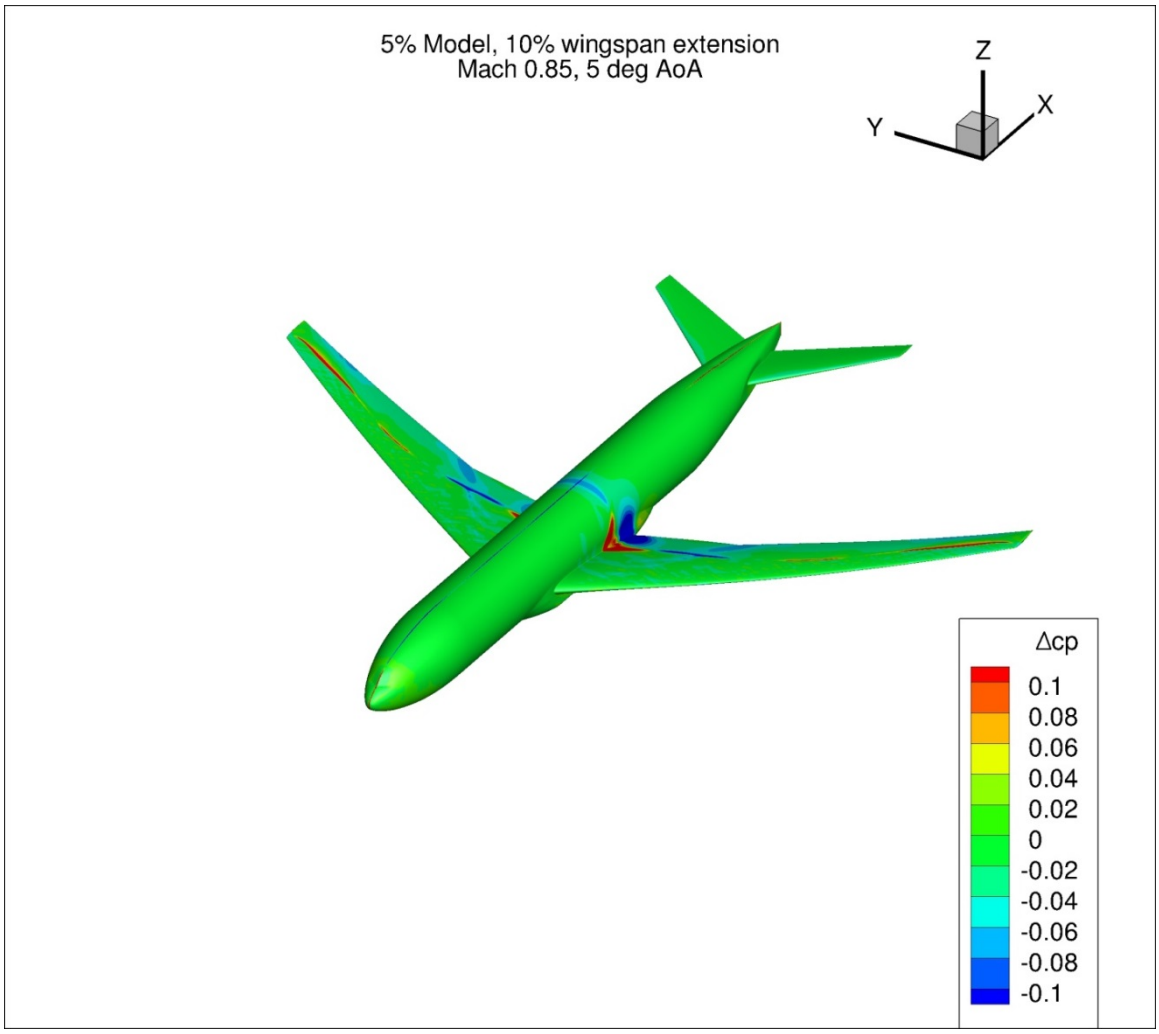

Figure 130. Configuration 2.1, Difference in Pressure Coefficient between Free-stream and Wind Tunnel Simulations, 5 deg Angle of Attack, Isometric View

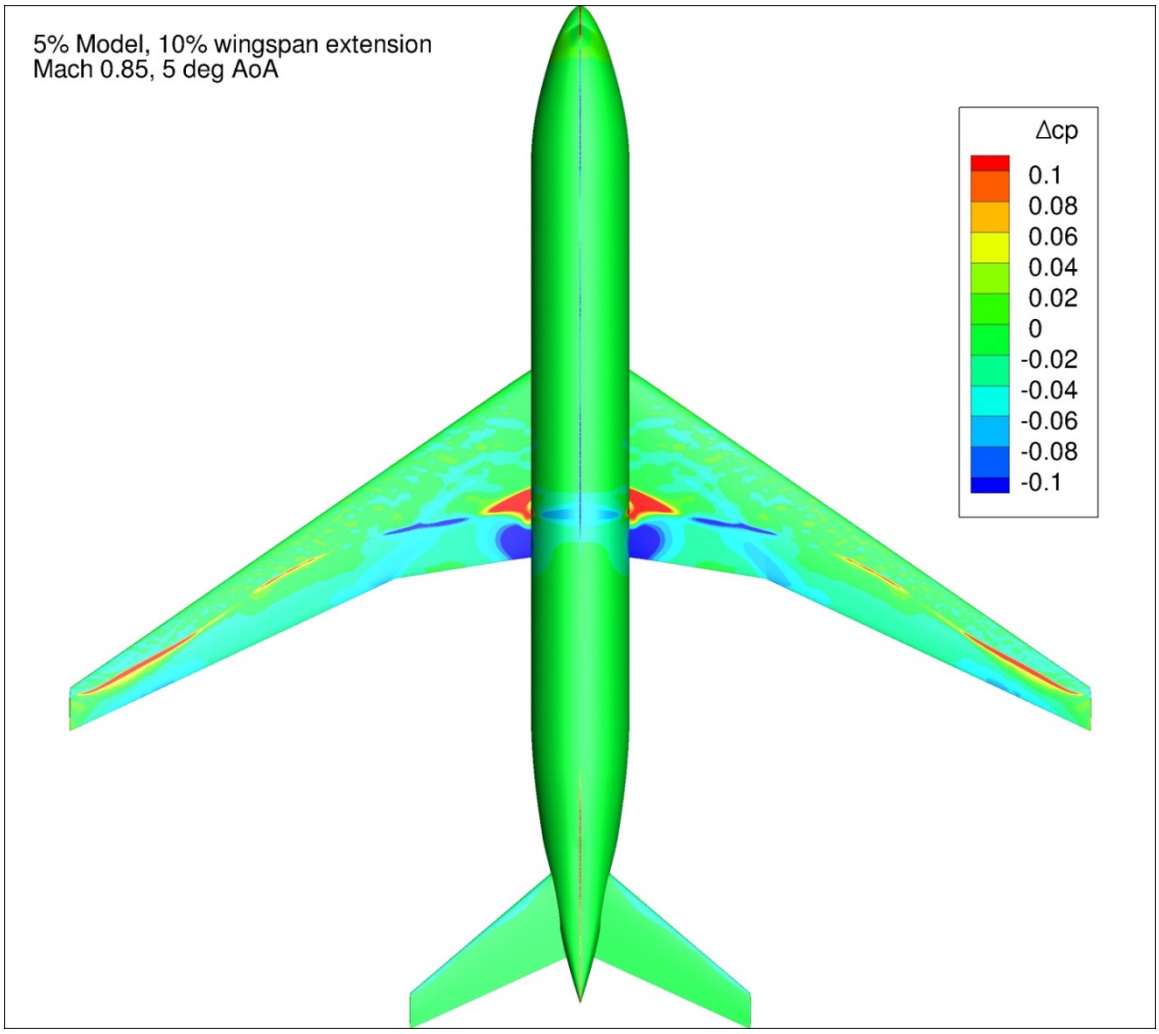

Figure 131. Configuration 2.1, Difference in Pressure Coefficient between Free-stream and Wind Tunnel Simulations, 5 deg Angle of Attack, Top View

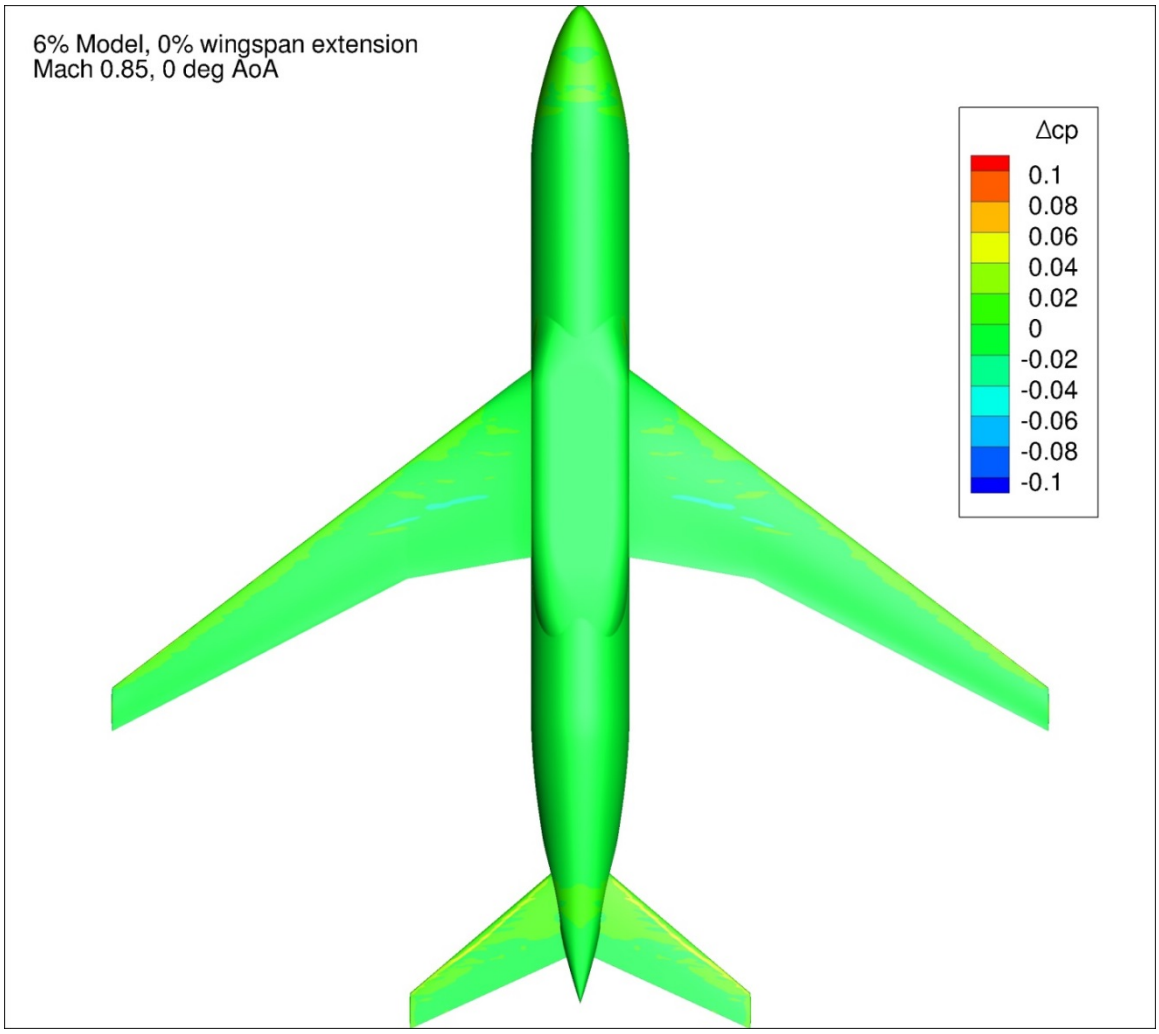

Figure 132. Configuration 3, Difference in Pressure Coefficient between Free-stream and Wind Tunnel Simulations, 0 deg Angle of Attack, Bottom View

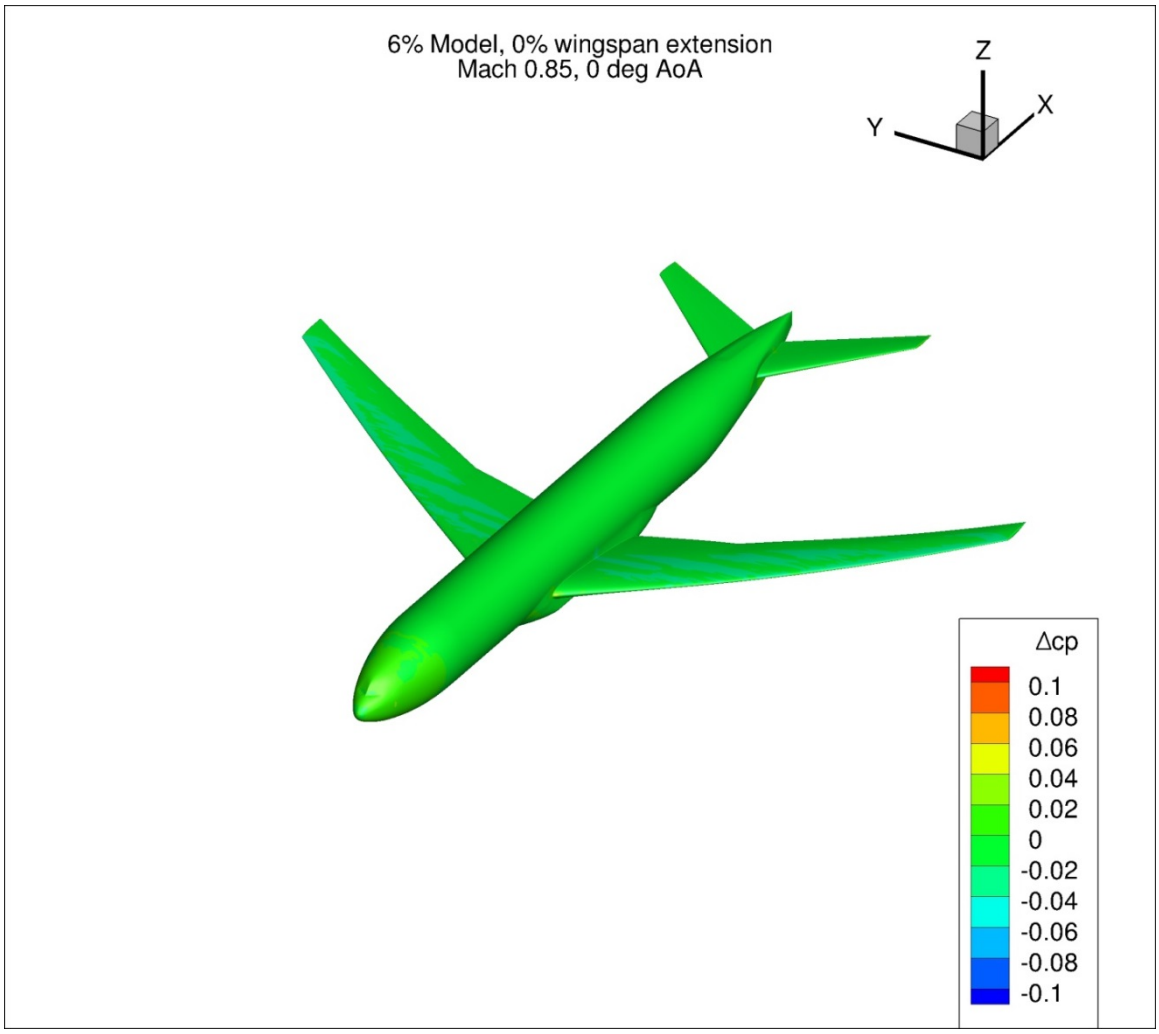

Figure 133. Configuration 3, Difference in Pressure Coefficient between Free-stream and Wind Tunnel Simulations, 0 deg Angle of Attack, Isometric View

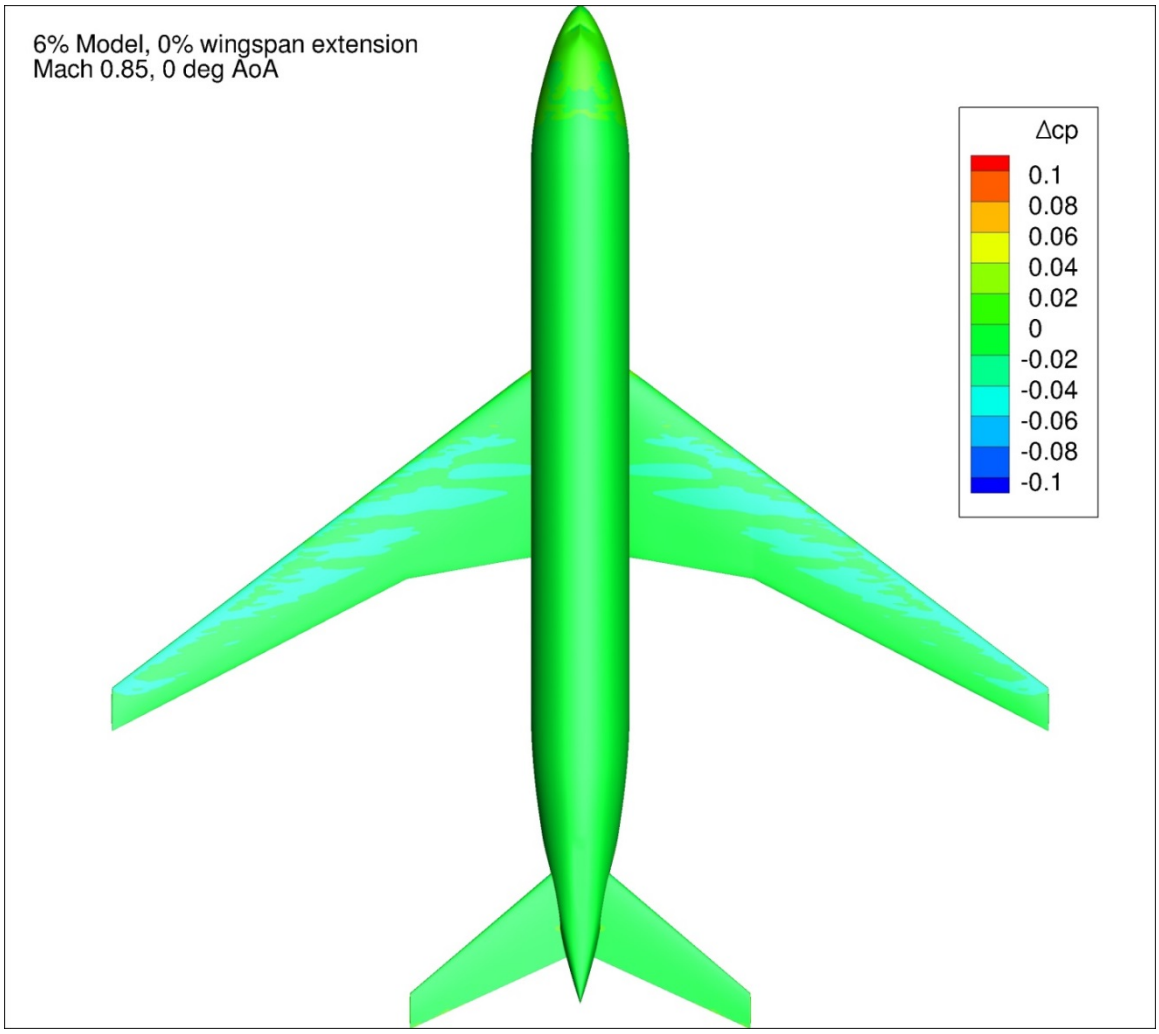

Figure 134. Configuration 3, Difference in Pressure Coefficient between Free-stream and Wind Tunnel Simulations, 0 deg Angle of Attack, Top View

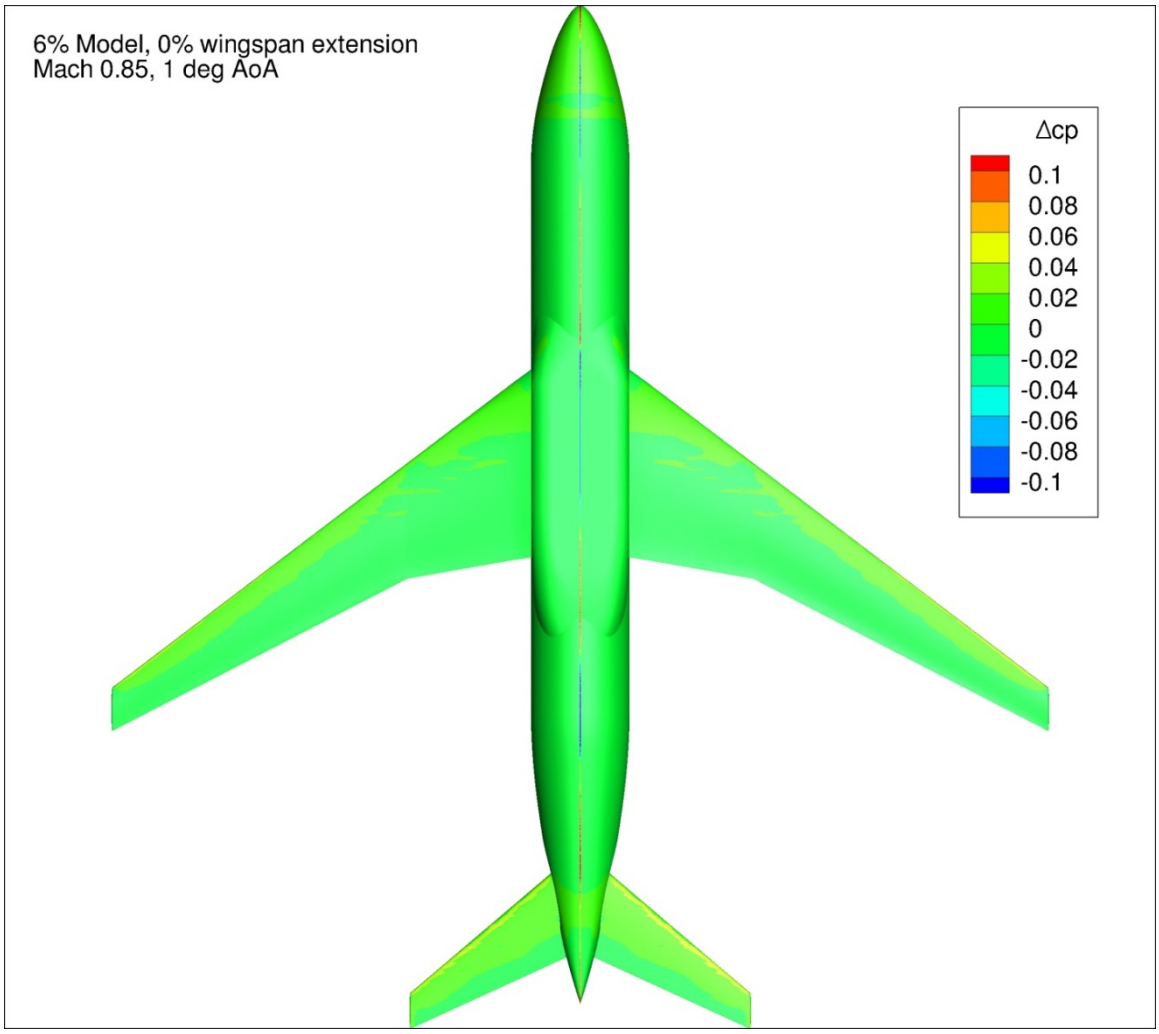

Figure 135. Configuration 3, Difference in Pressure Coefficient between Free-stream and Wind Tunnel Simulations, 1 deg Angle of Attack, Bottom View

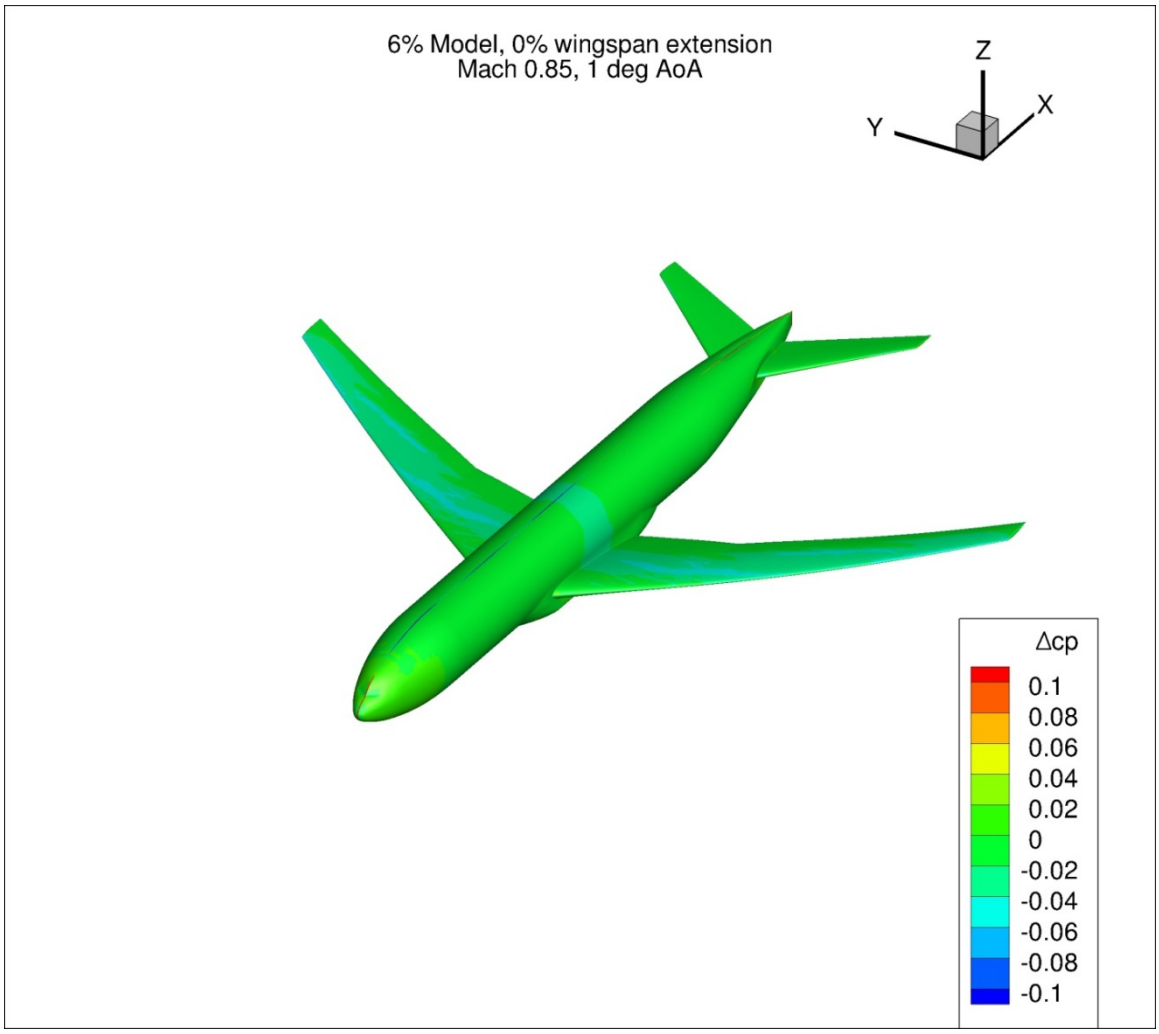

Figure 136. Configuration 3, Difference in Pressure Coefficient between Free-stream and Wind Tunnel Simulations, 1 deg Angle of Attack, Isometric View

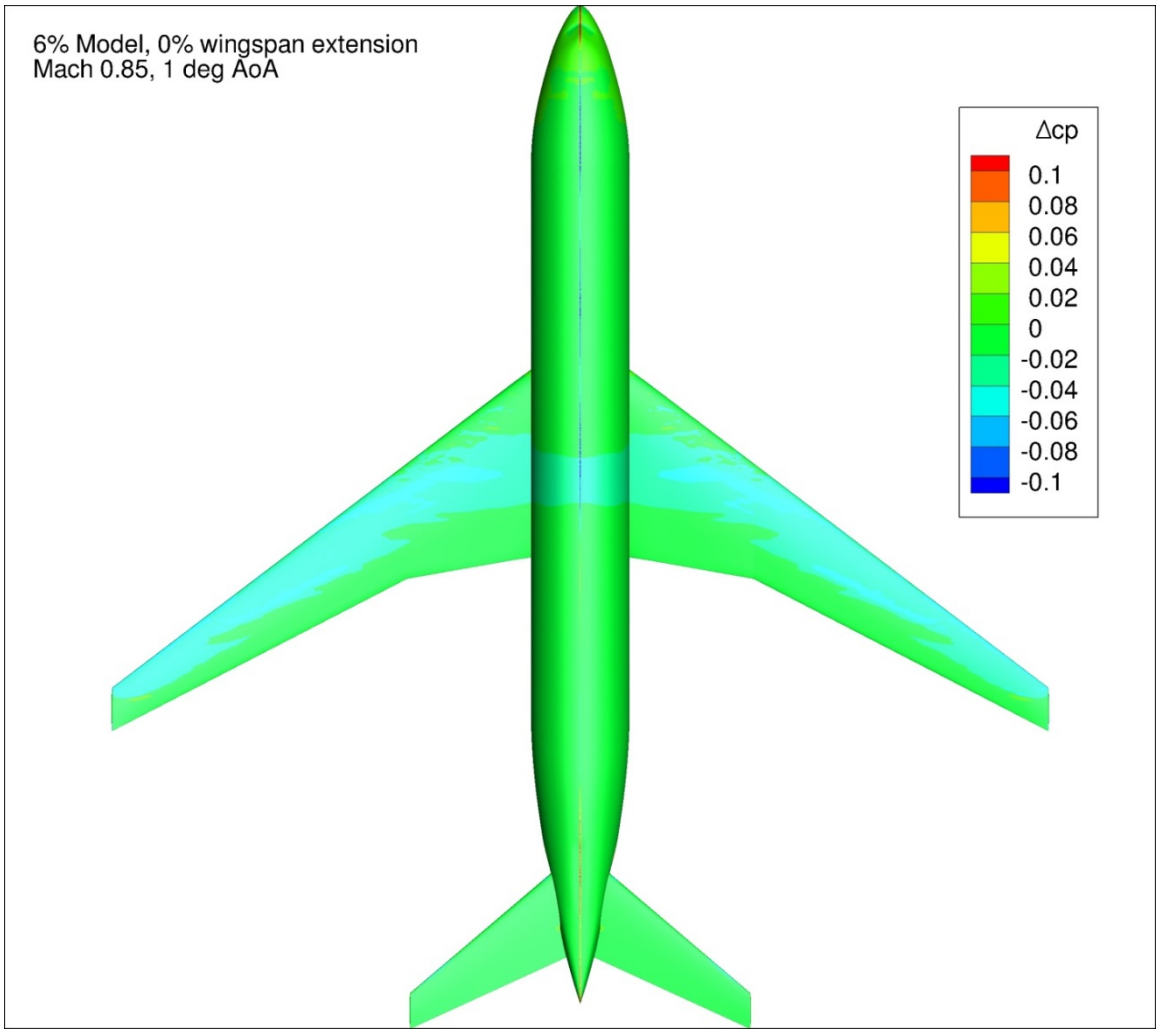

Figure 137. Configuration 3, Difference in Pressure Coefficient between Free-stream and Wind Tunnel Simulations, 1 deg Angle of Attack, Top View

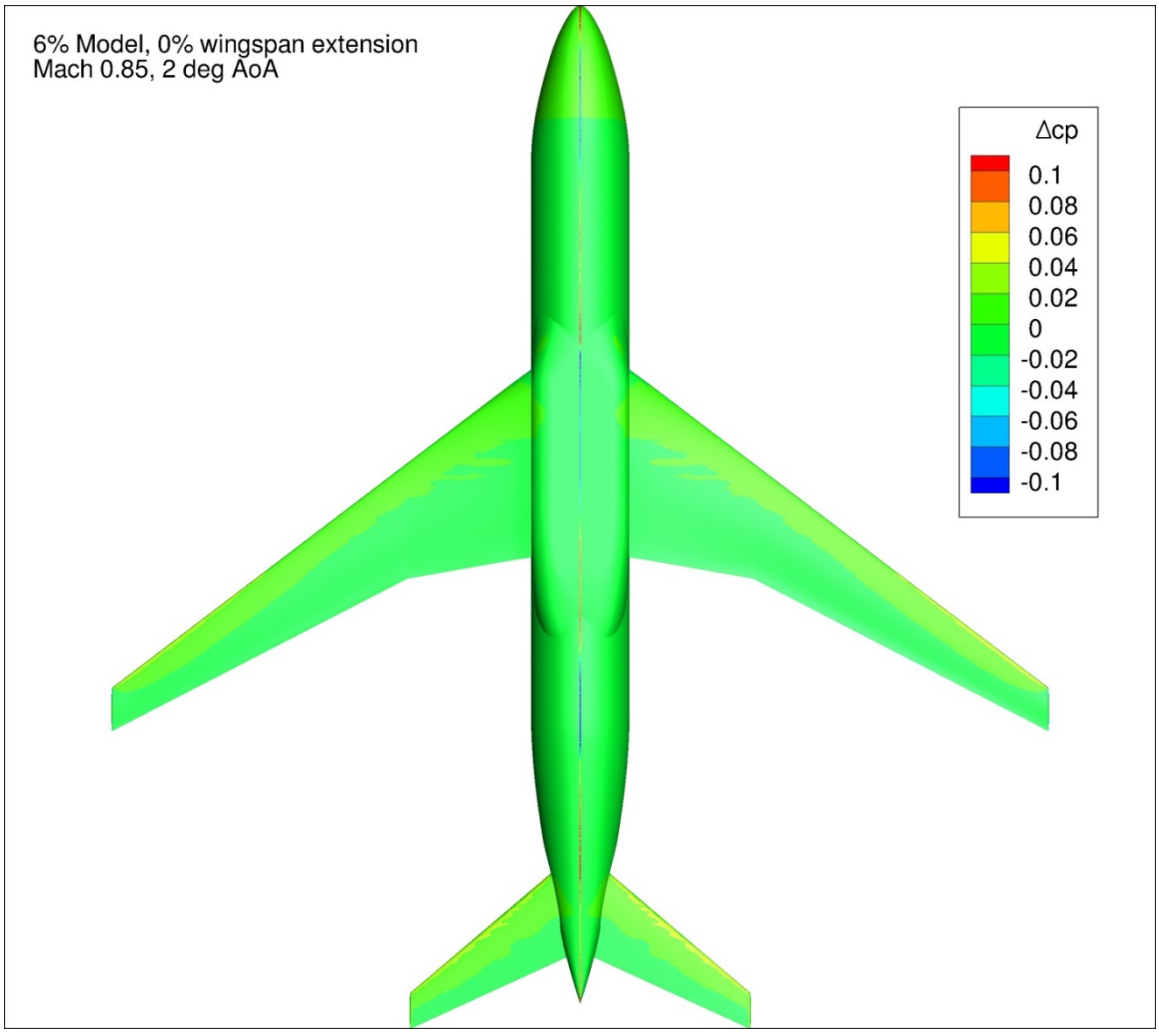

Figure 138. Configuration 3, Difference in Pressure Coefficient between Free-stream and Wind Tunnel Simulations, 2 deg Angle of Attack, Bottom View

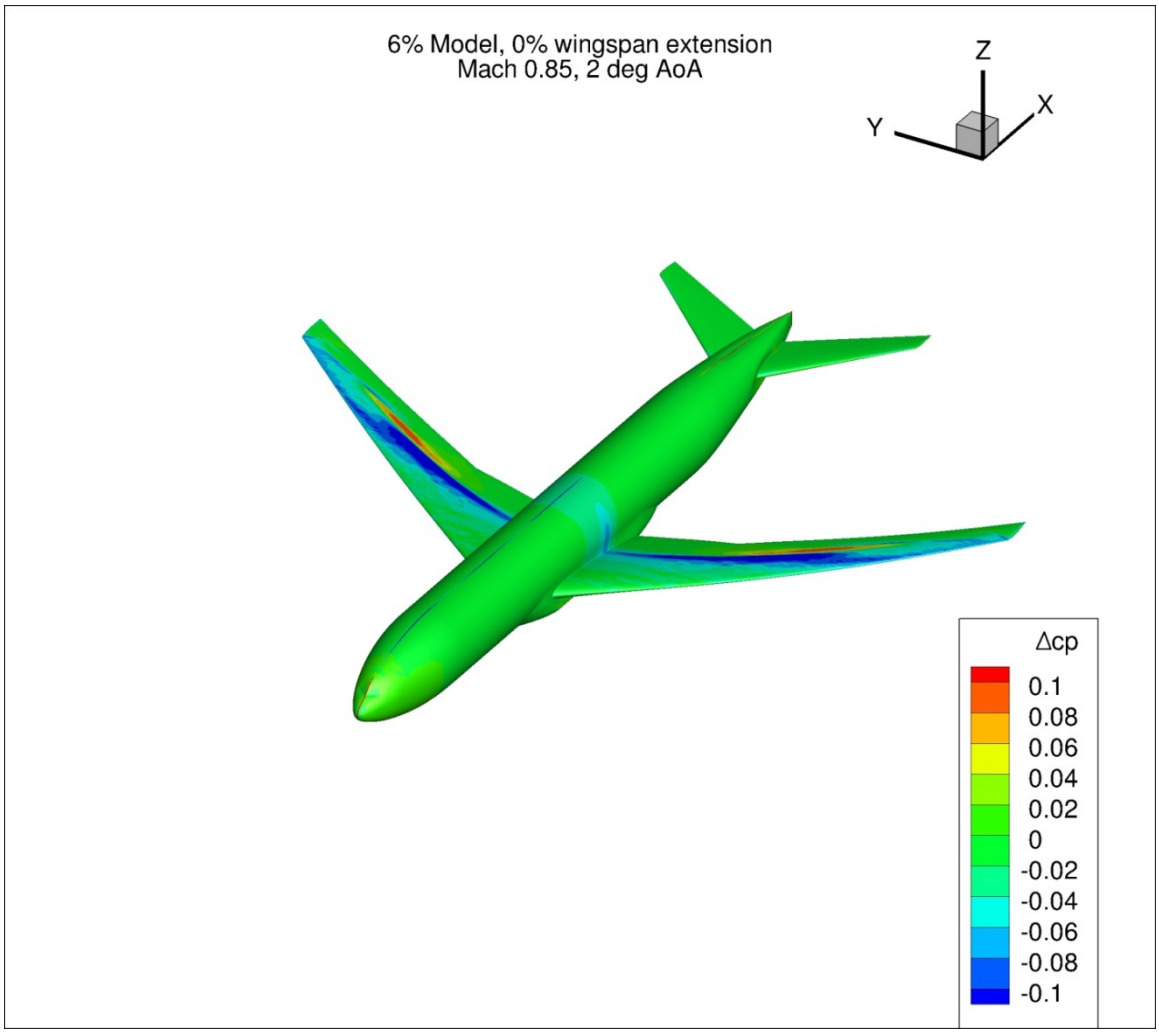

Figure 139. Configuration 3, Difference in Pressure Coefficient between Free-stream and Wind Tunnel Simulations, 2 deg Angle of Attack, Isometric View

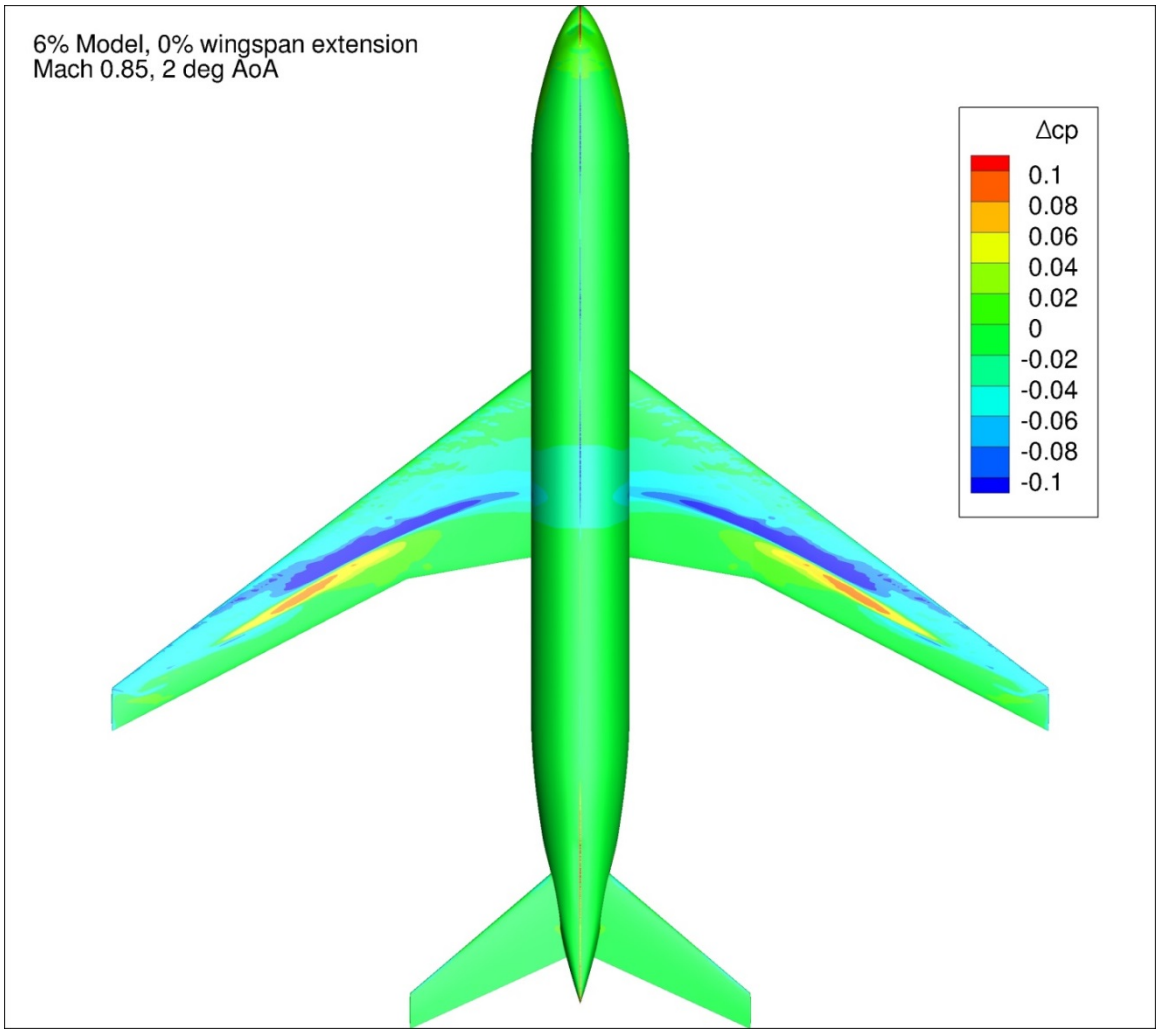

Figure 140. Configuration 3, Difference in Pressure Coefficient between Free-stream and Wind Tunnel Simulations, 2 deg Angle of Attack, Top View

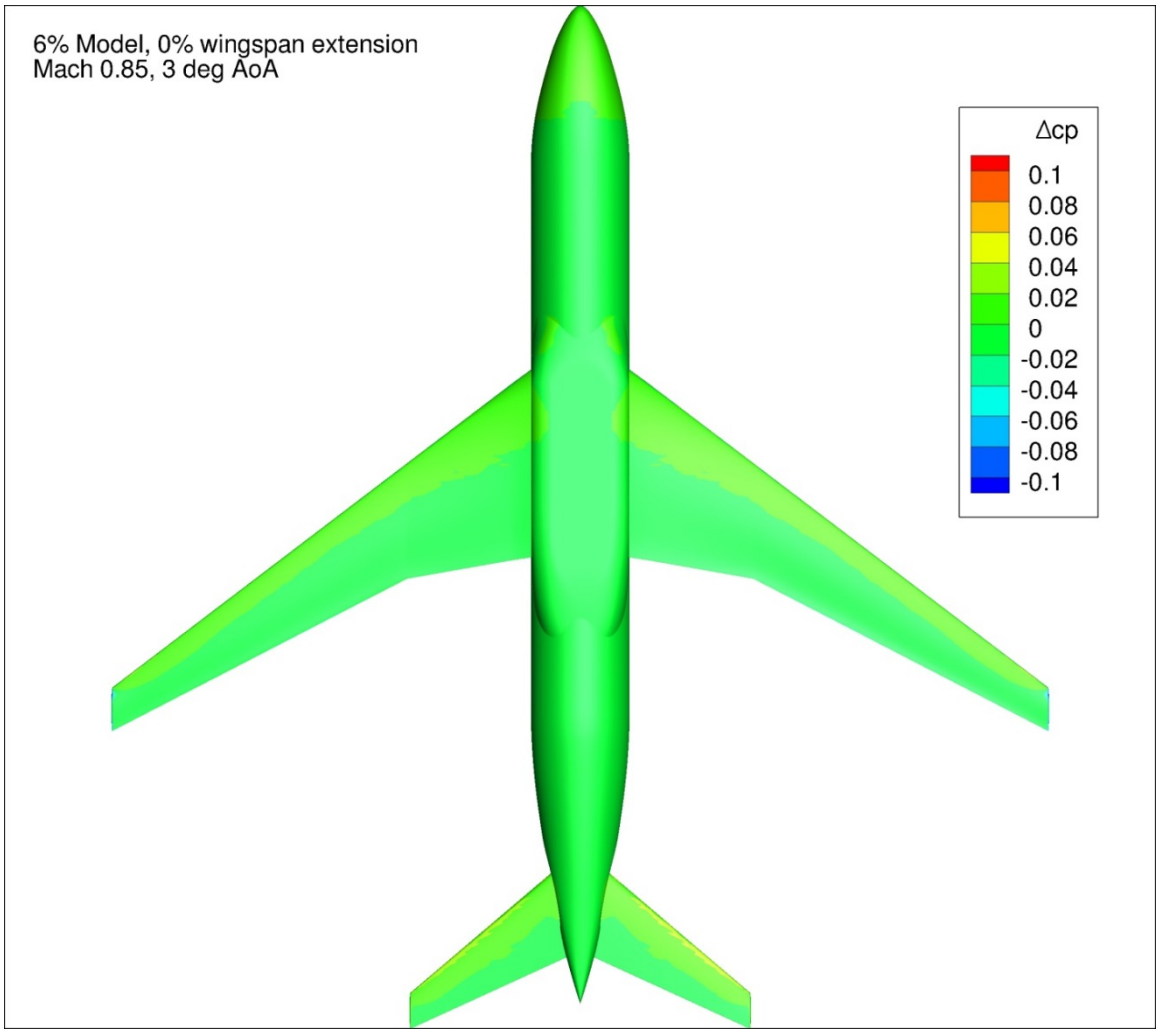

Figure 141. Configuration 3, Difference in Pressure Coefficient between Free-stream and Wind Tunnel Simulations, 3 deg Angle of Attack, Bottom View

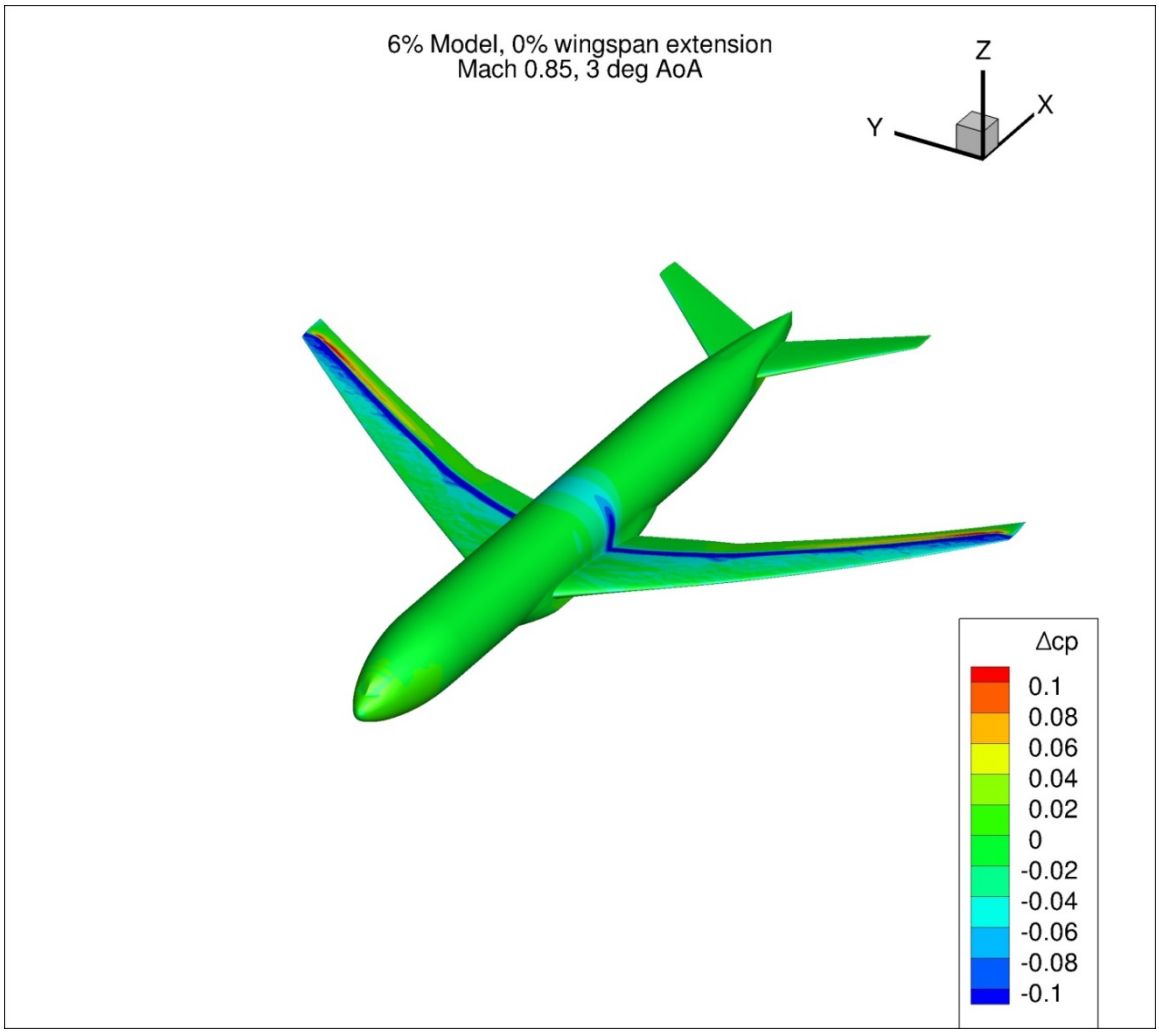

Figure 142. Configuration 3, Difference in Pressure Coefficient between Free-stream and Wind Tunnel Simulations, 3 deg Angle of Attack, Isometric View

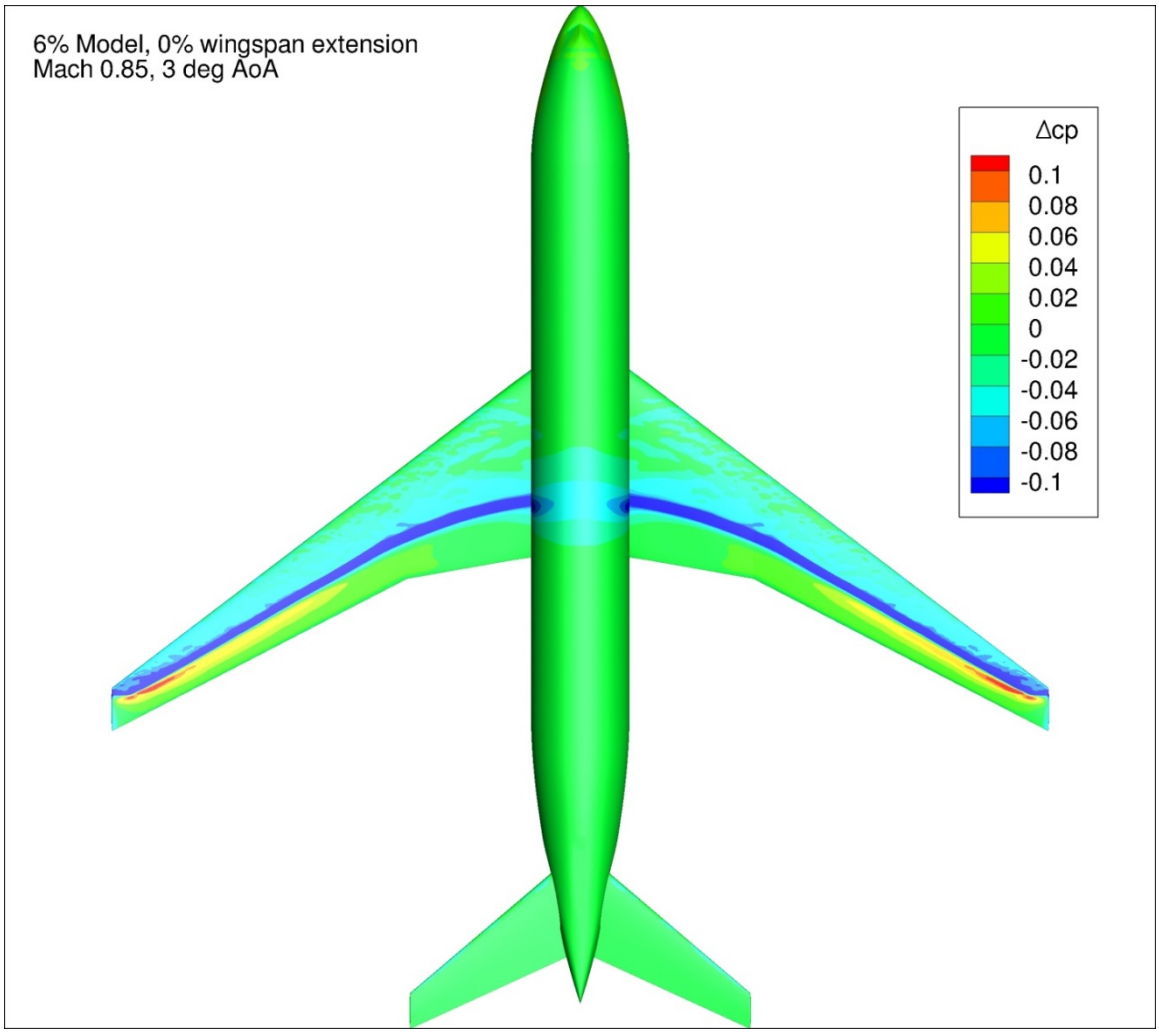

Figure 143. Configuration 3, Difference in Pressure Coefficient between Free-stream and Wind Tunnel Simulations, 3 deg Angle of Attack, Top View

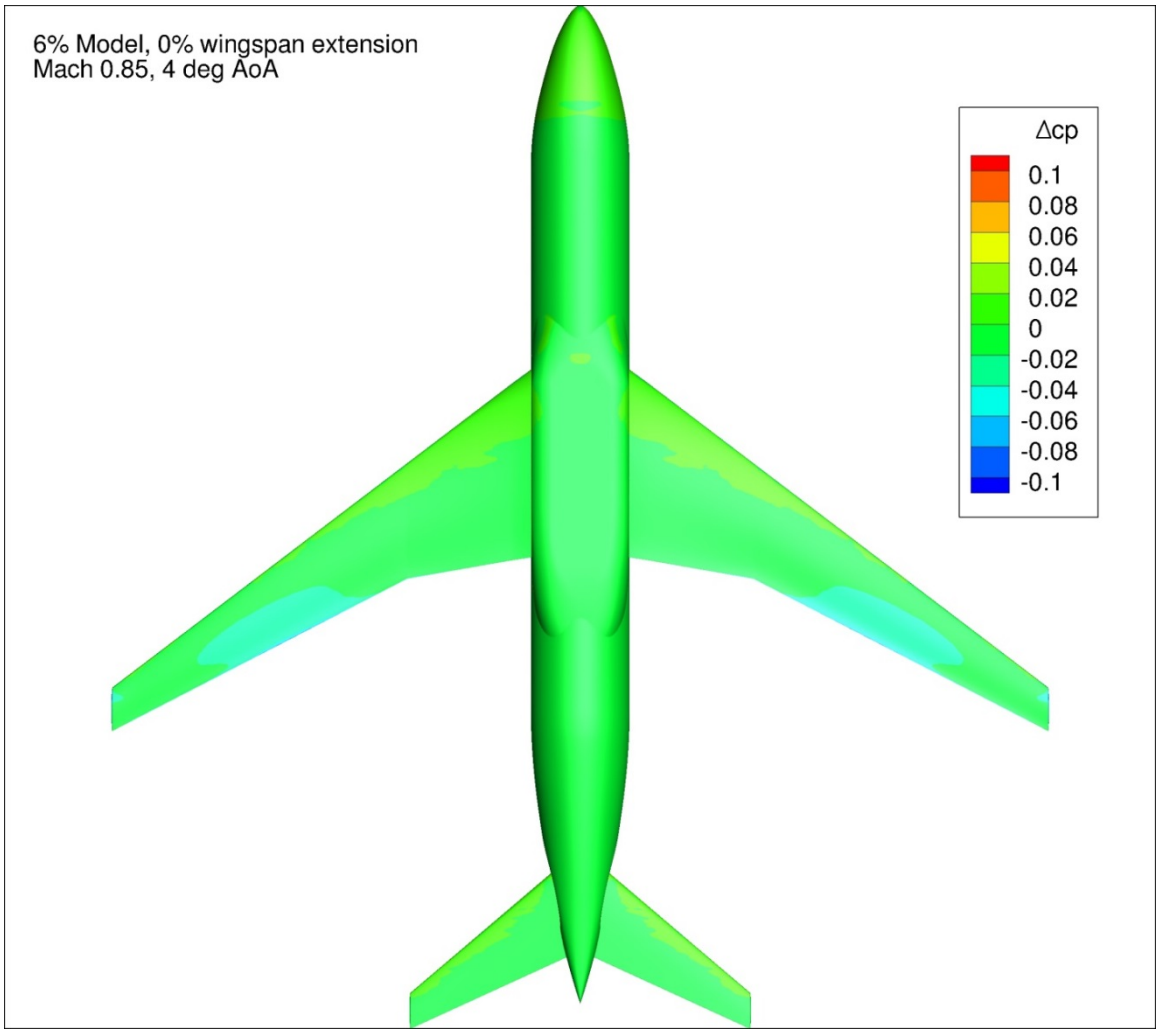

Figure 144. Configuration 3, Difference in Pressure Coefficient between Free-stream and Wind Tunnel Simulations, 4 deg Angle of Attack, Bottom View

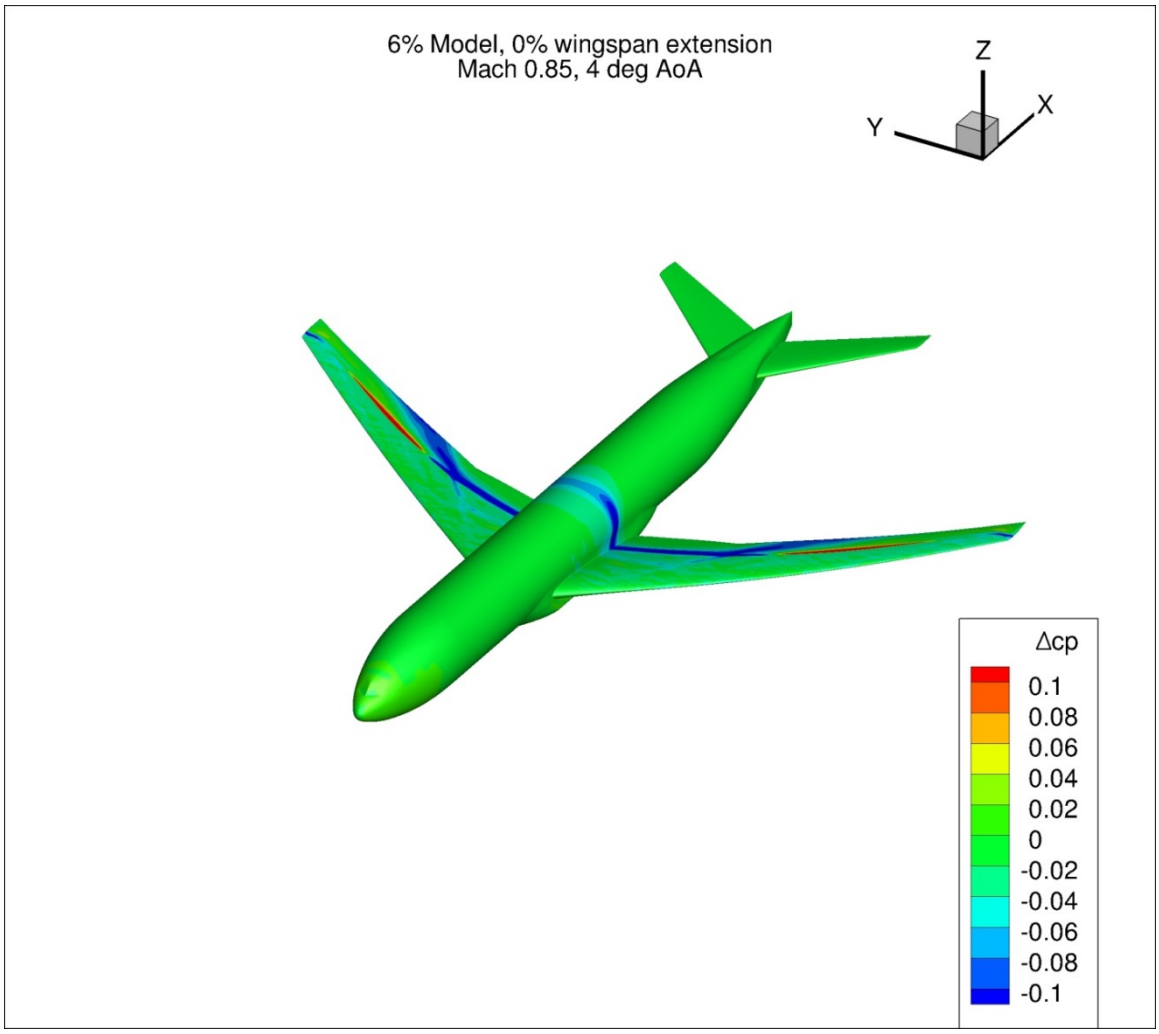

Figure 145. Configuration 3, Difference in Pressure Coefficient between Free-stream and Wind Tunnel Simulations, 4 deg Angle of Attack, Isometric View

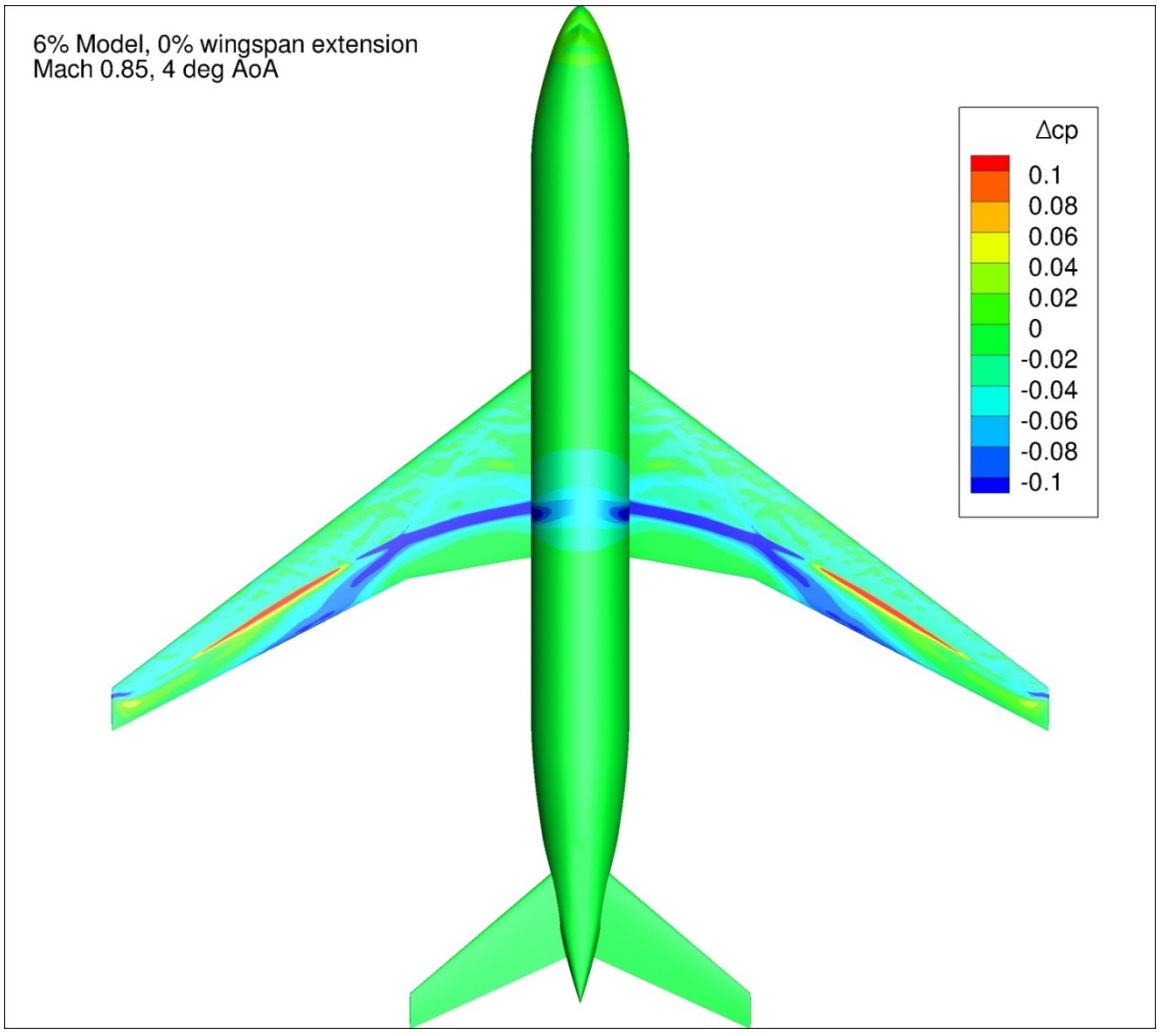

Figure 146. Configuration 3, Difference in Pressure Coefficient between Free-stream and Wind Tunnel Simulations, 4 deg Angle of Attack, Top View

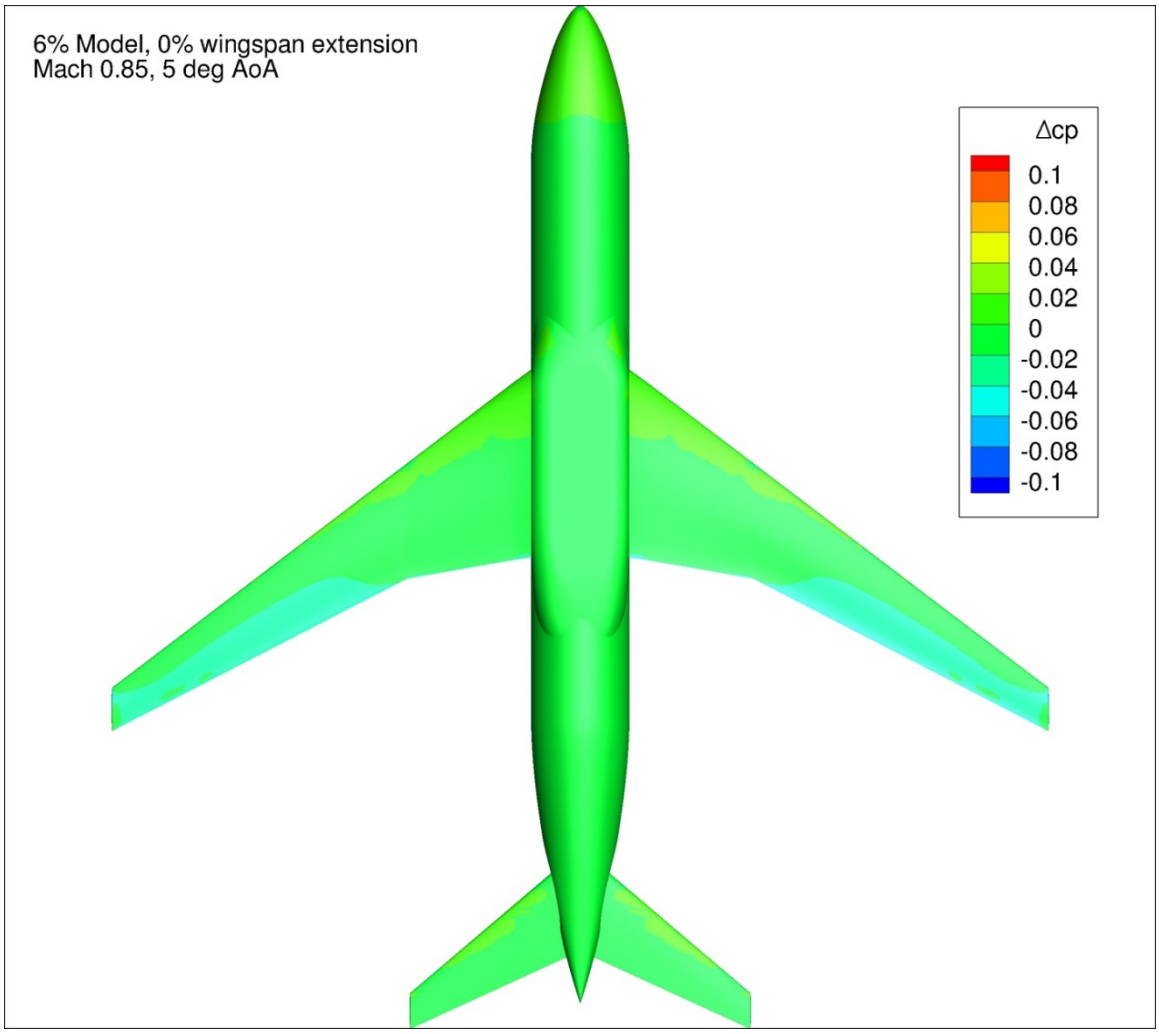

Figure 147. Configuration 3, Difference in Pressure Coefficient between Free-stream and Wind Tunnel Simulations, 5 deg Angle of Attack, Bottom View

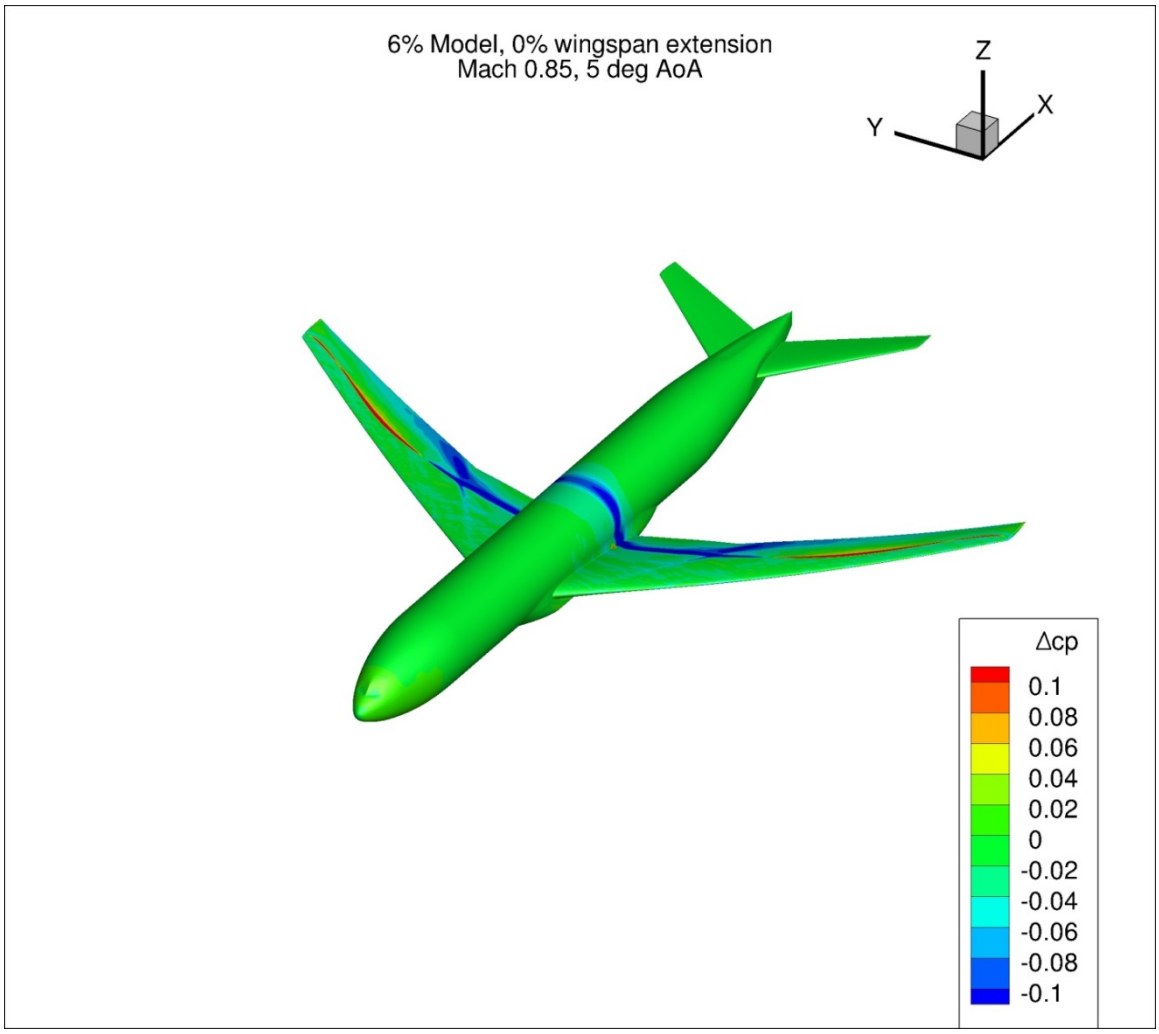

Figure 148. Configuration 3, Difference in Pressure Coefficient between Free-stream and Wind Tunnel Simulations, 5 deg Angle of Attack, Isometric View

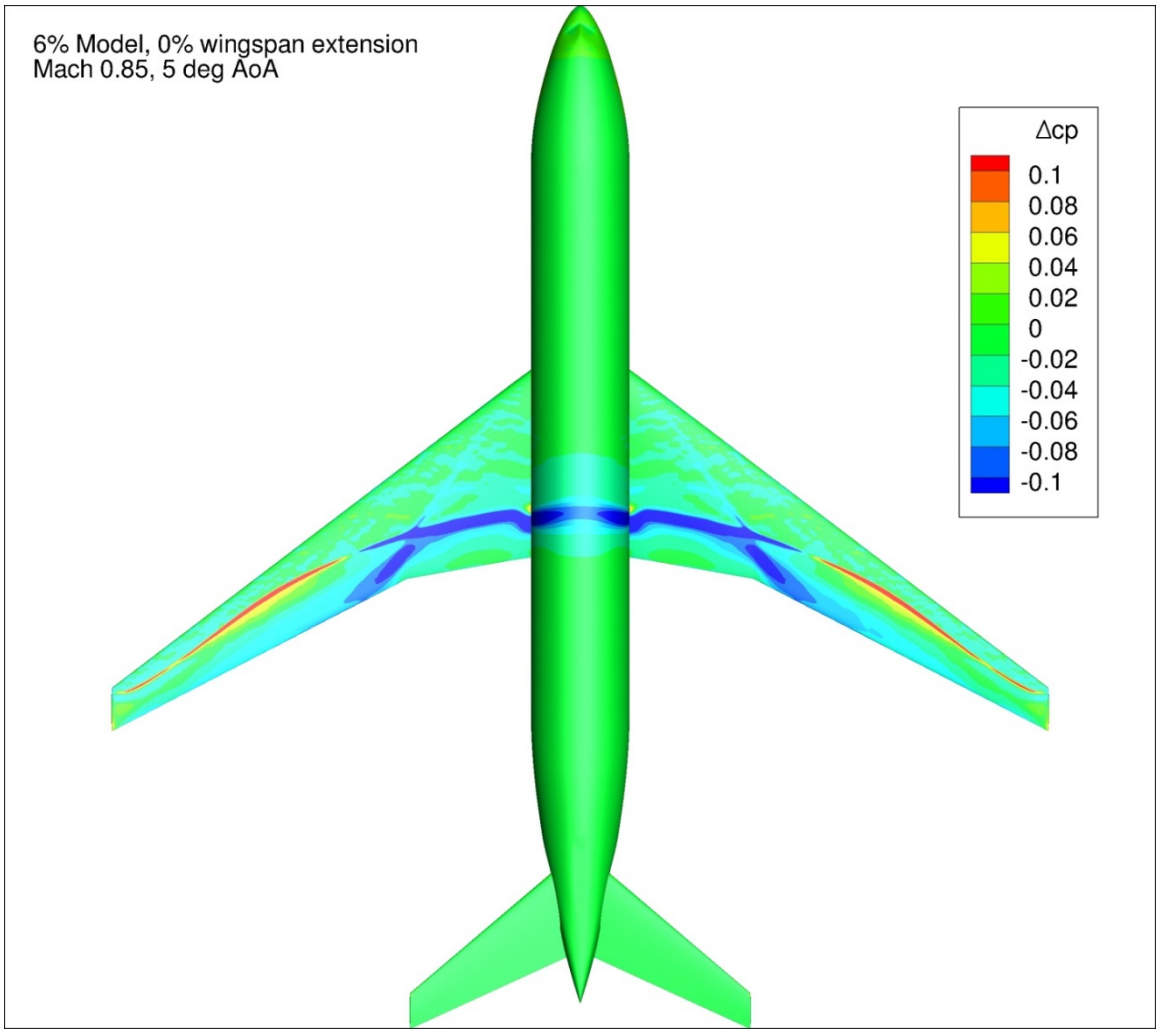

Figure 149. Configuration 3, Difference in Pressure Coefficient between Free-stream and Wind Tunnel Simulations, 5 deg Angle of Attack, Top View

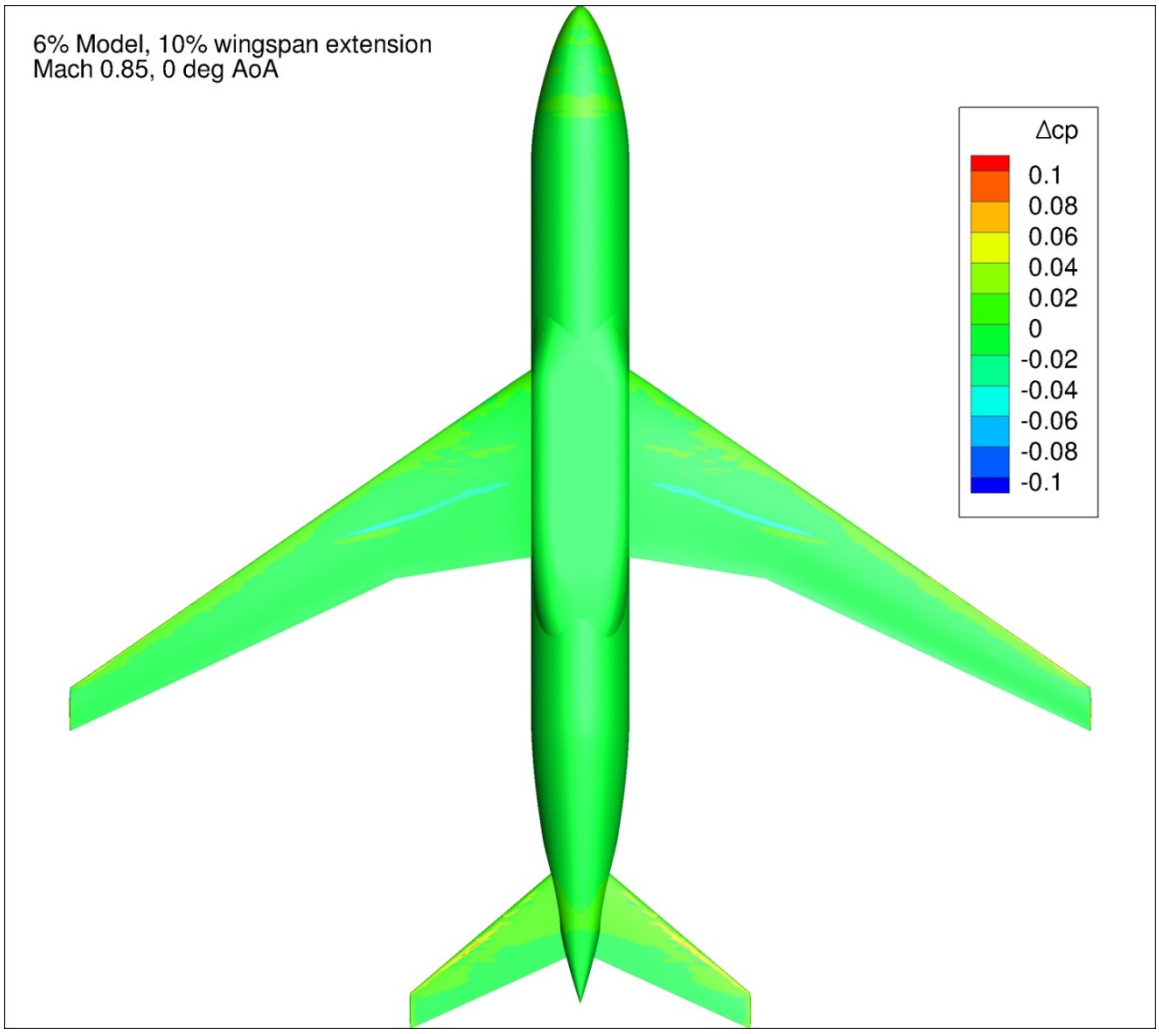

Figure 150. Configuration 3.1, Difference in Pressure Coefficient between Free-stream and Wind Tunnel Simulations, 0 deg Angle of Attack, Bottom View

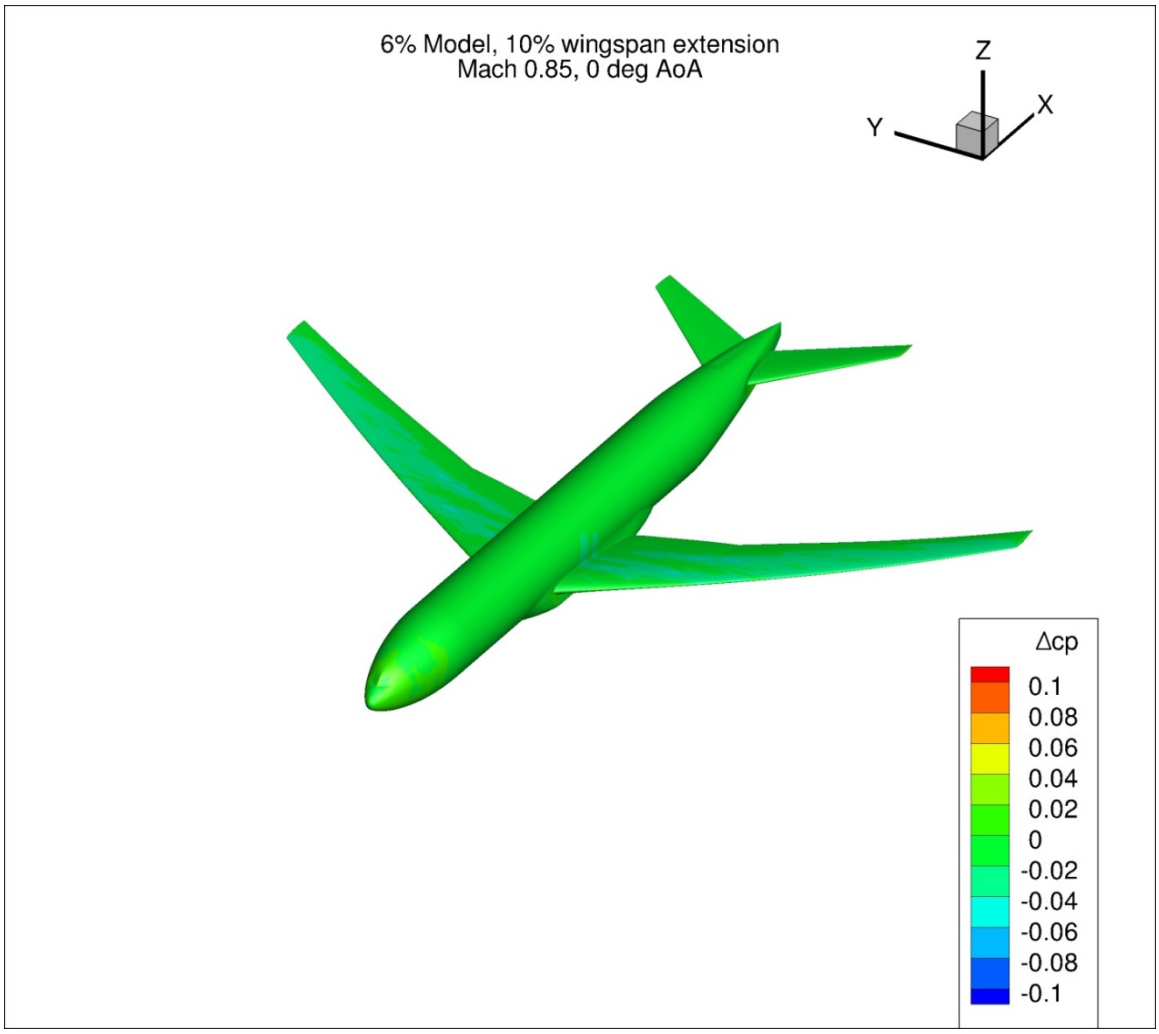

Figure 151. Configuration 3.1, Difference in Pressure Coefficient between Free-stream and Wind Tunnel Simulations, 0 deg Angle of Attack, Isometric View

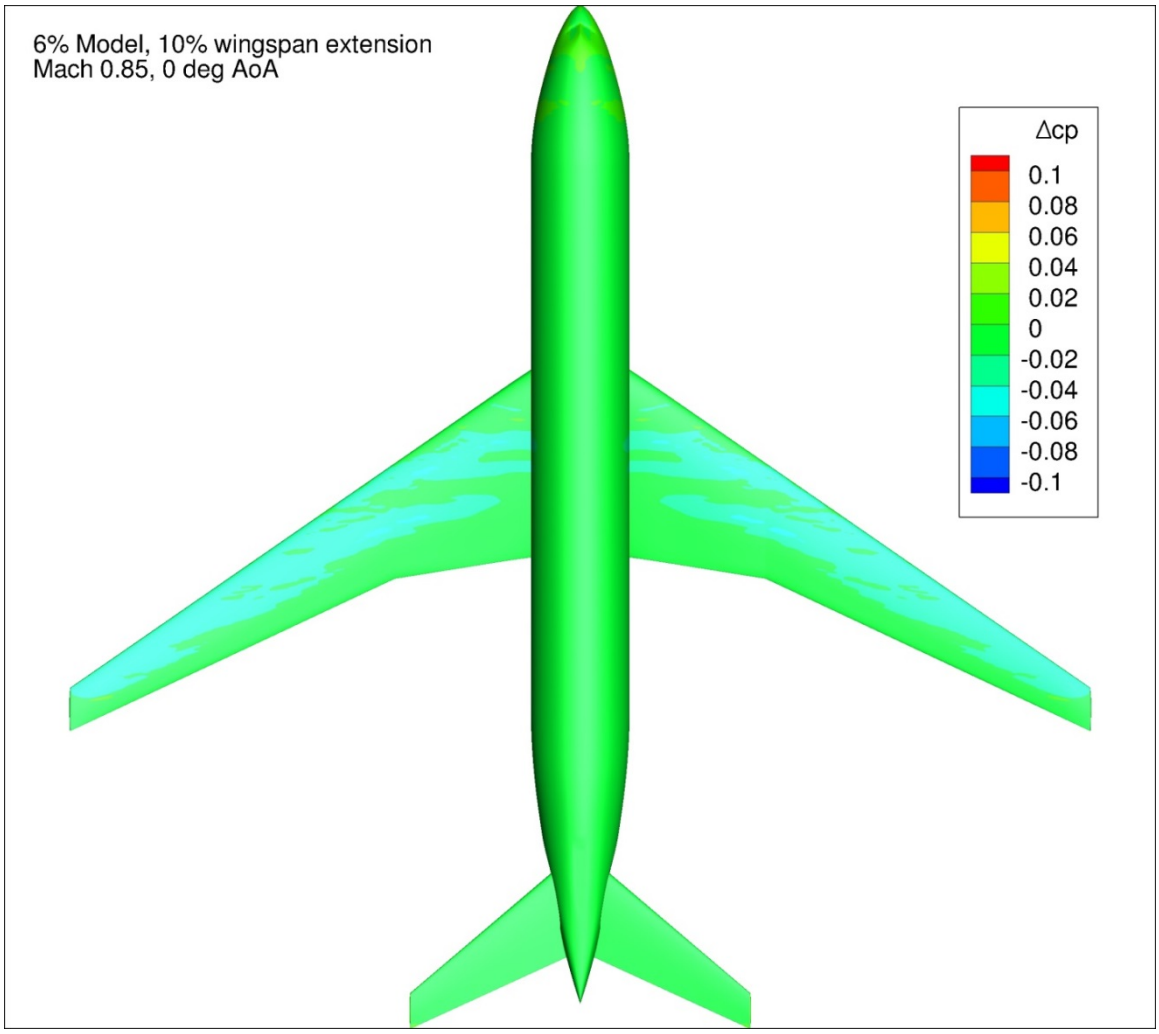

Figure 152. Configuration 3.1, Difference in Pressure Coefficient between Free-stream and Wind Tunnel Simulations, 0 deg Angle of Attack, Top View

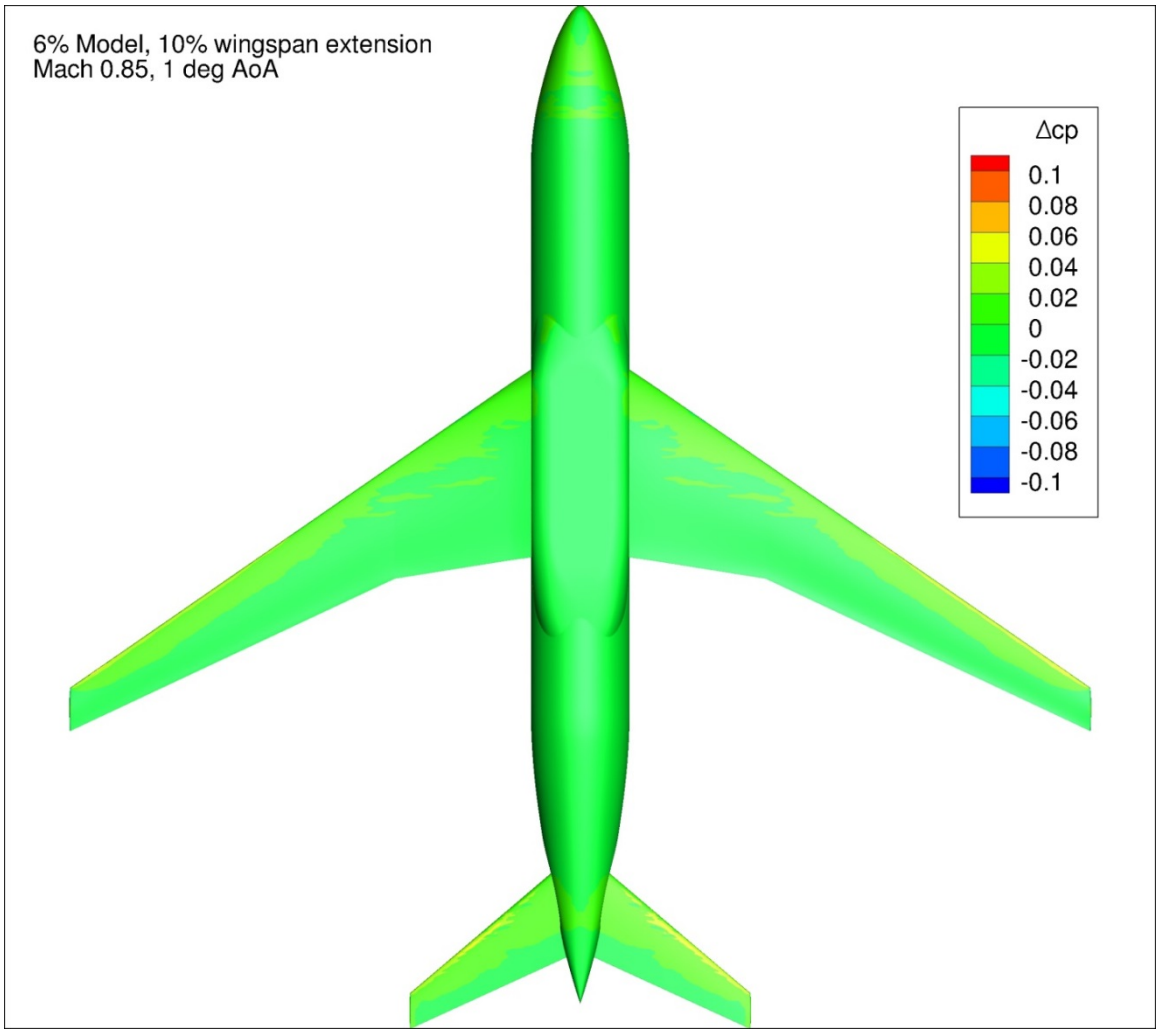

Figure 153. Configuration 3.1, Difference in Pressure Coefficient between Free-stream and Wind Tunnel Simulations, 1 deg Angle of Attack, Bottom View

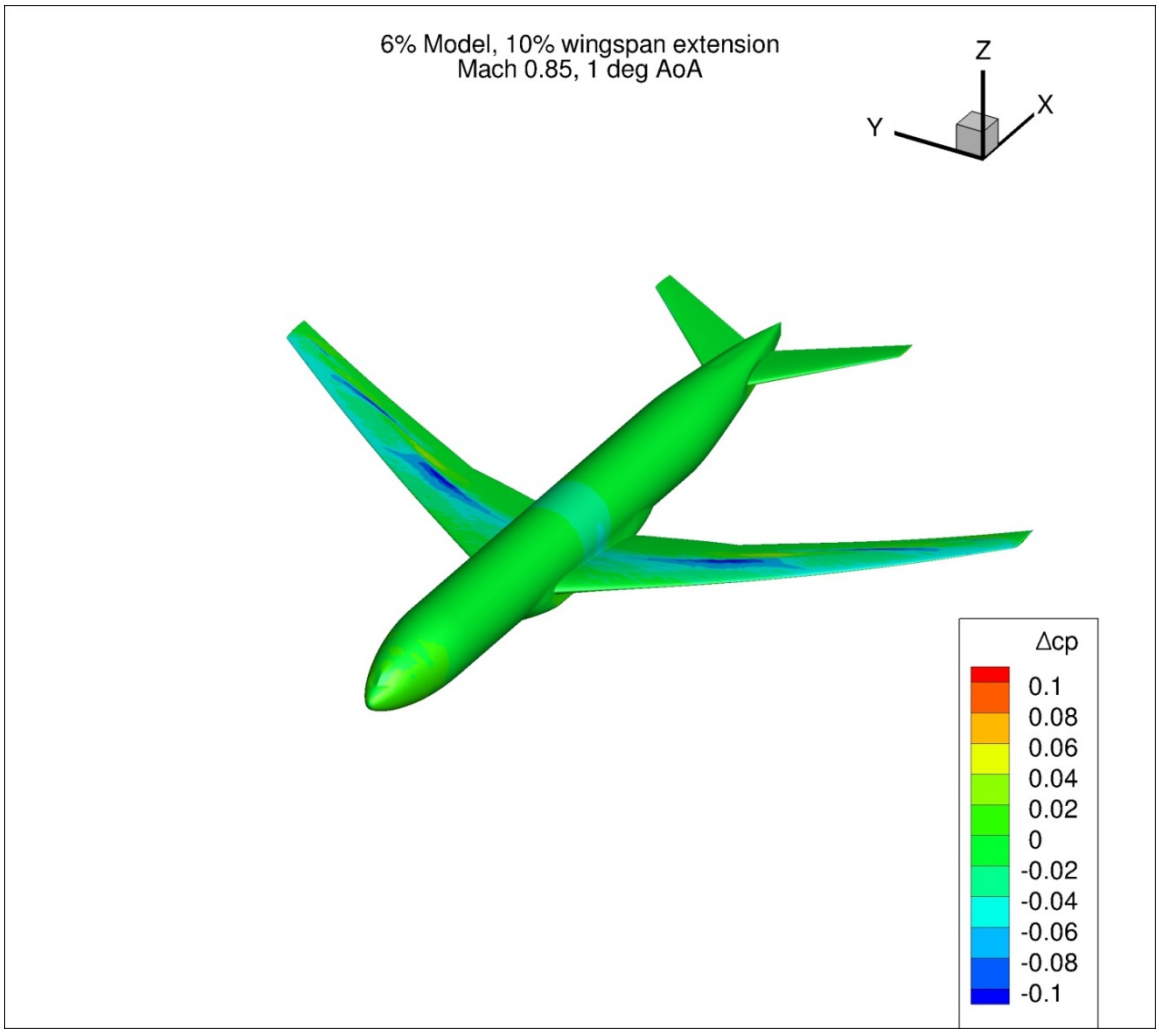

Figure 154. Configuration 3.1, Difference in Pressure Coefficient between Free-stream and Wind Tunnel Simulations, 1 deg Angle of Attack, Isometric View

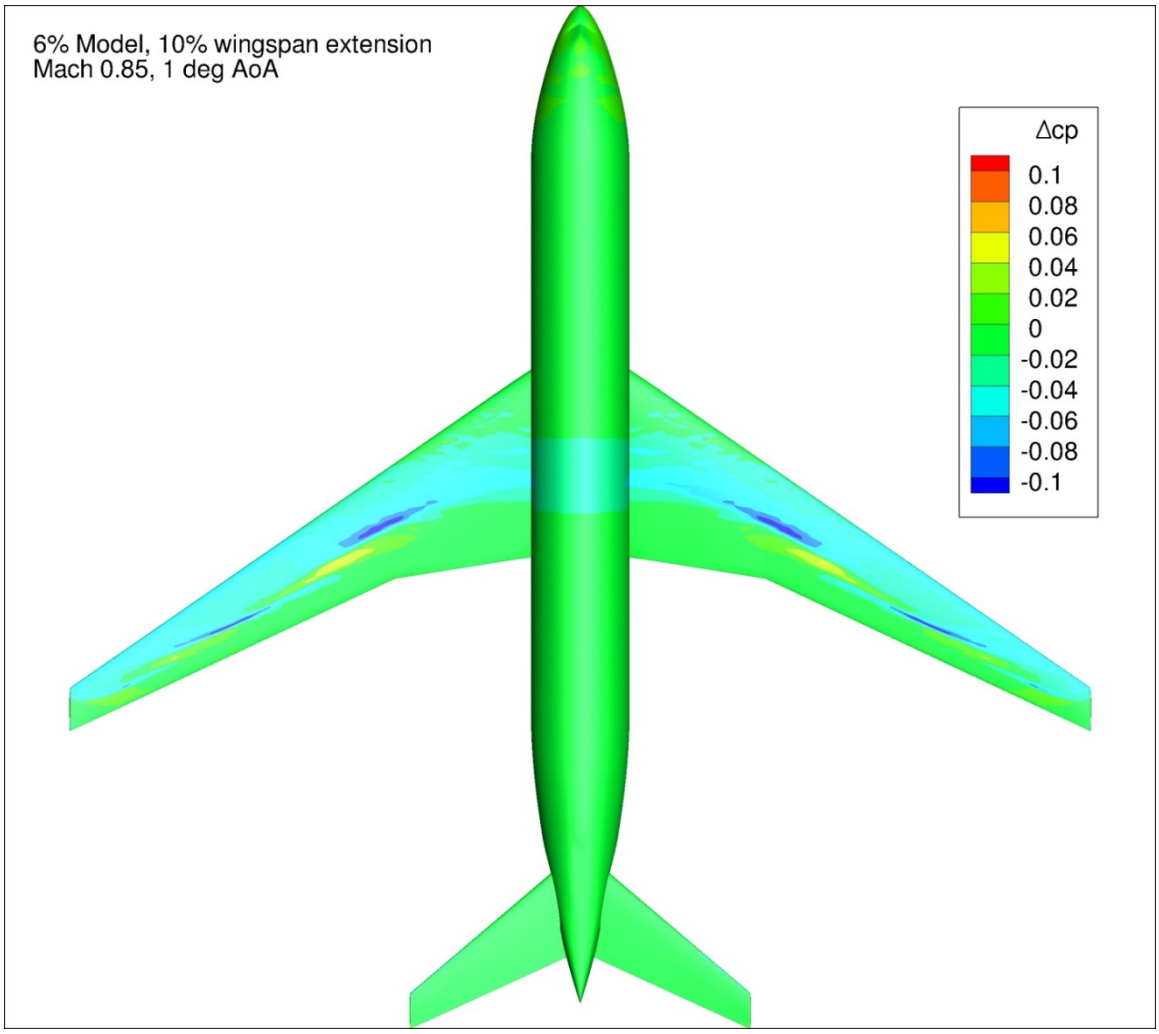

Figure 155. Configuration 3.1, Difference in Pressure Coefficient between Free-stream and Wind Tunnel Simulations, 1 deg Angle of Attack, Top View

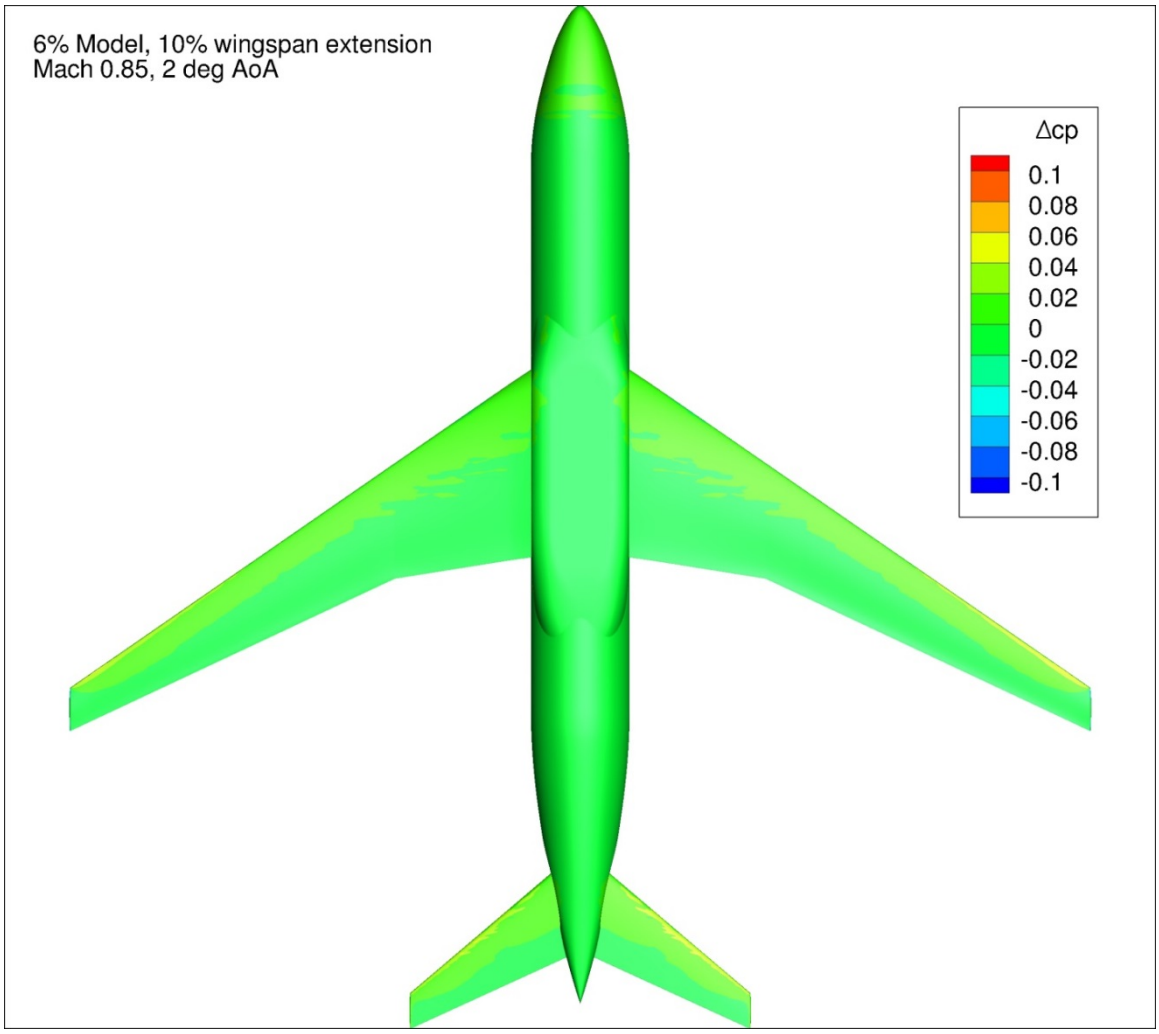

Figure 156. Configuration 3.1, Difference in Pressure Coefficient between Free-stream and Wind Tunnel Simulations, 2 deg Angle of Attack, Bottom View

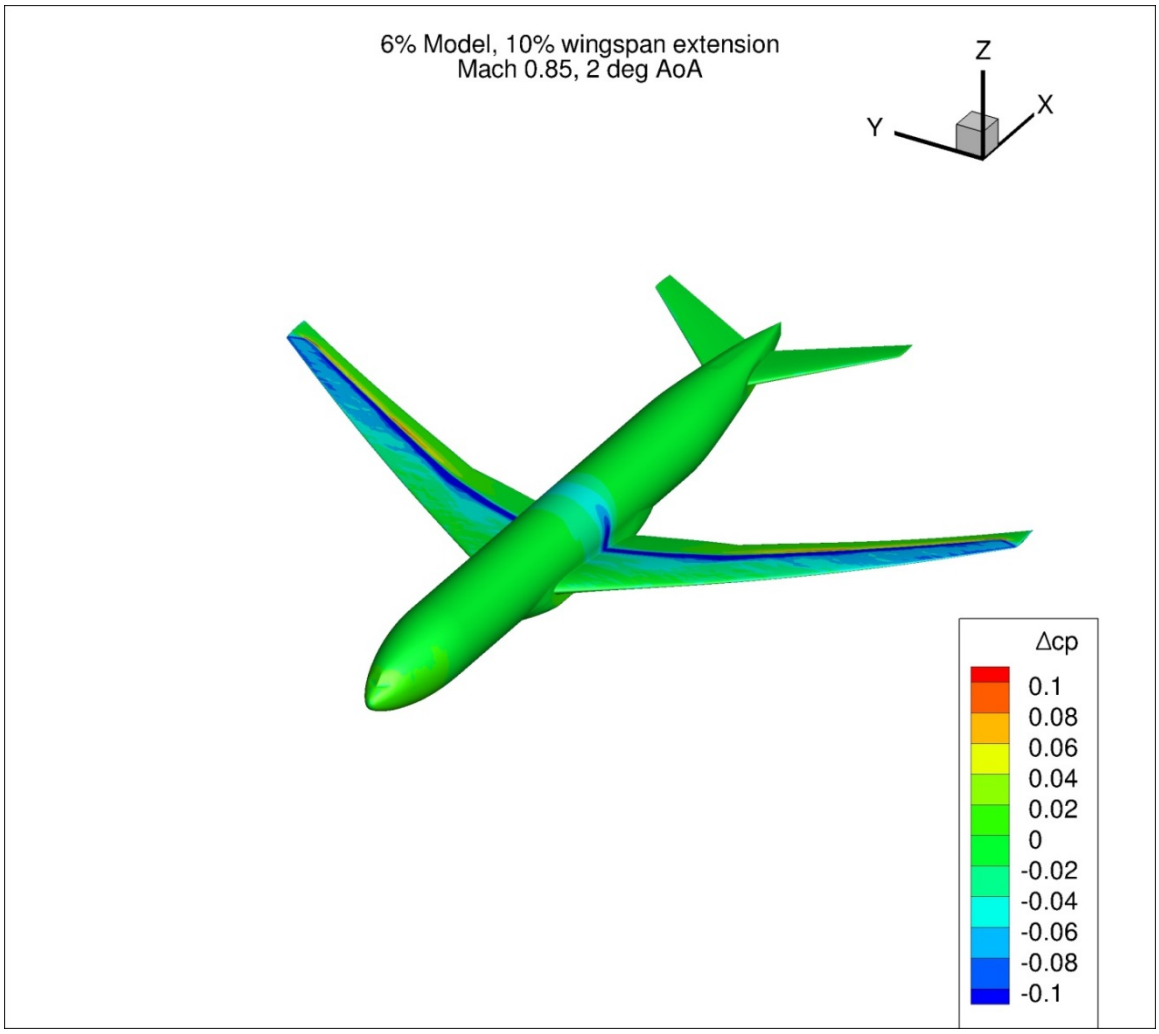

Figure 157. Configuration 3.1, Difference in Pressure Coefficient between Free-stream and Wind Tunnel Simulations, 2 deg Angle of Attack, Isometric View

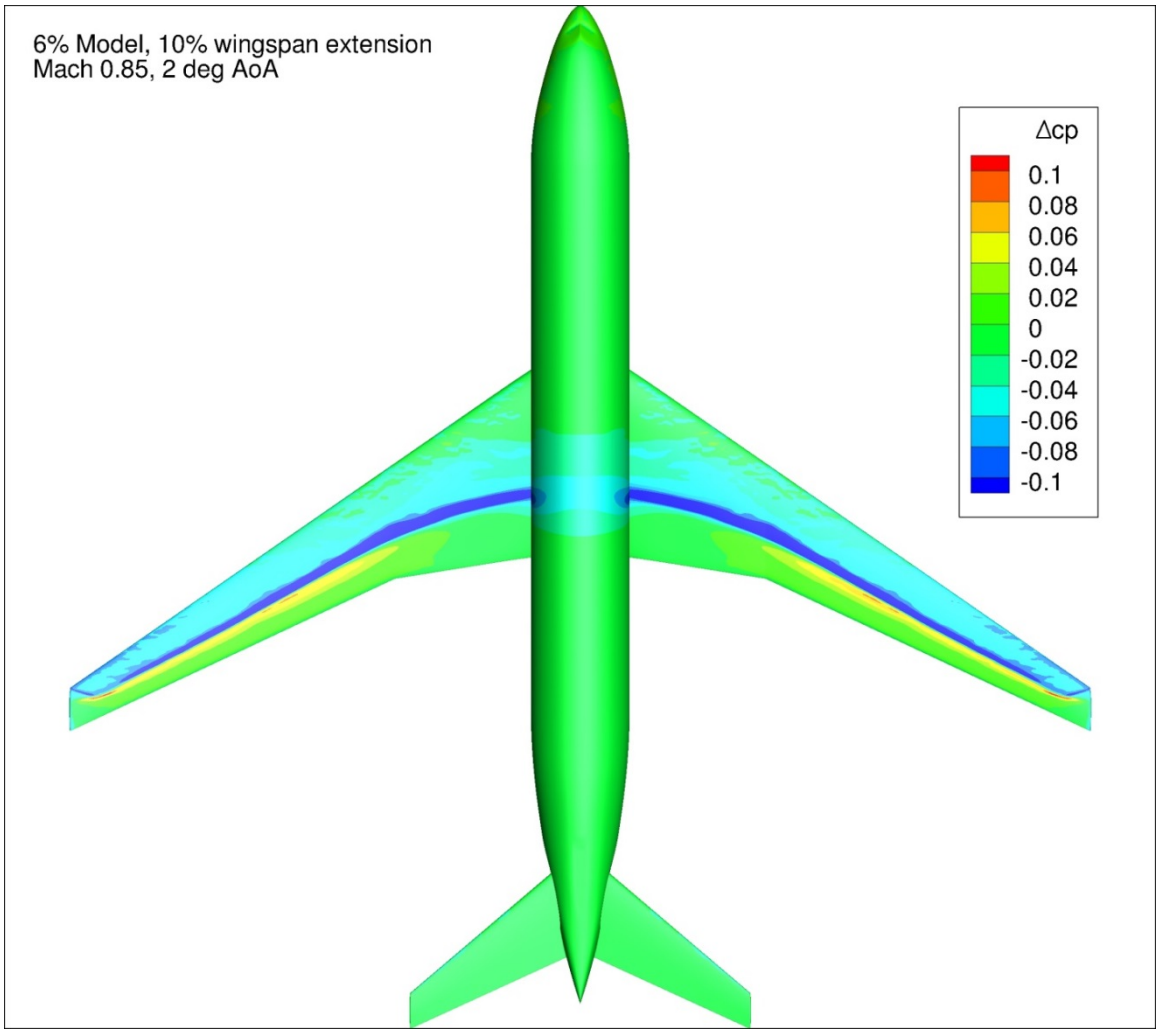

Figure 158. Configuration 3.1, Difference in Pressure Coefficient between Free-stream and Wind Tunnel Simulations, 2 deg Angle of Attack, Top View

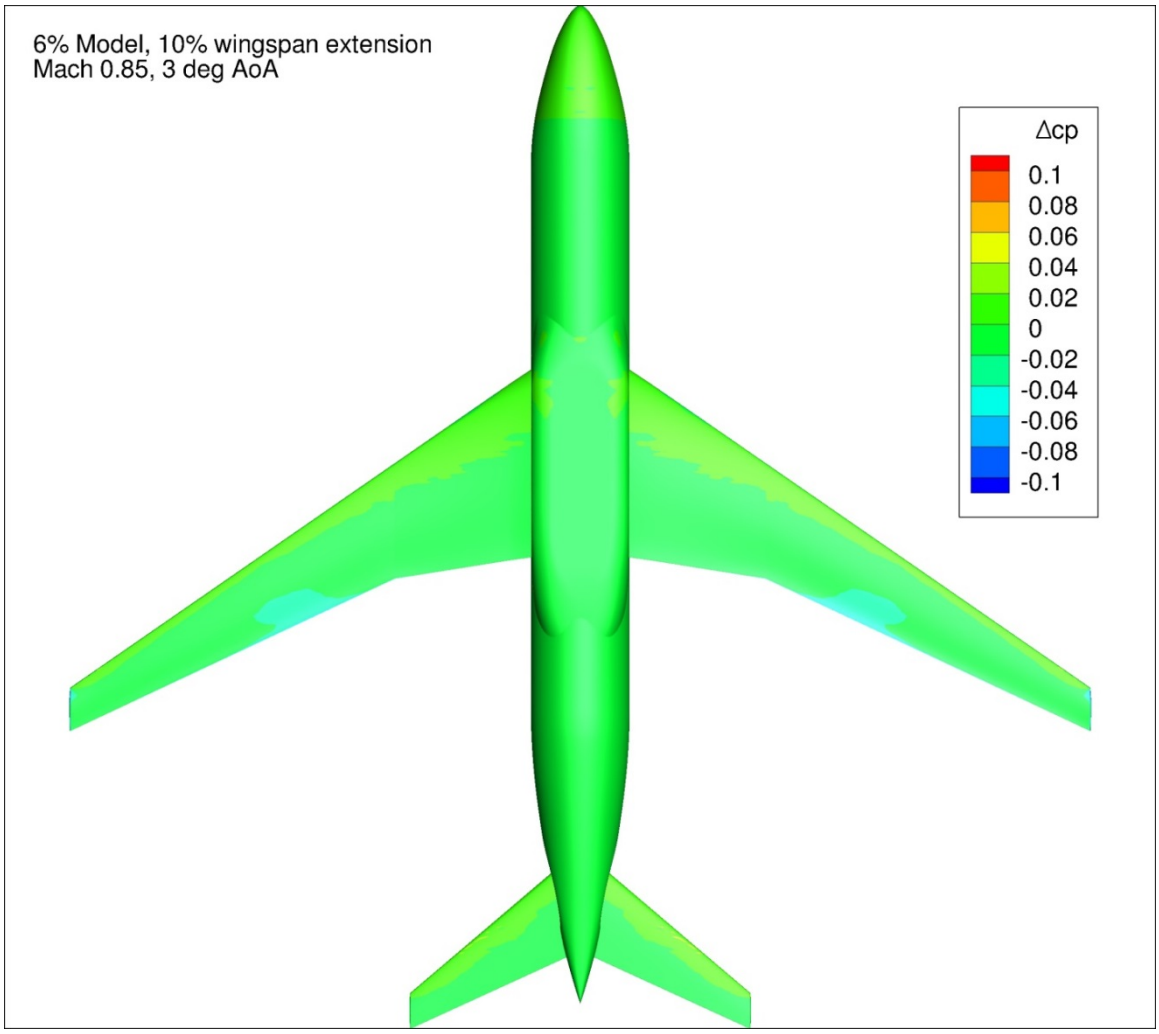

Figure 159. Configuration 3.1, Difference in Pressure Coefficient between Free-stream and Wind Tunnel Simulations, 3 deg Angle of Attack, Bottom View

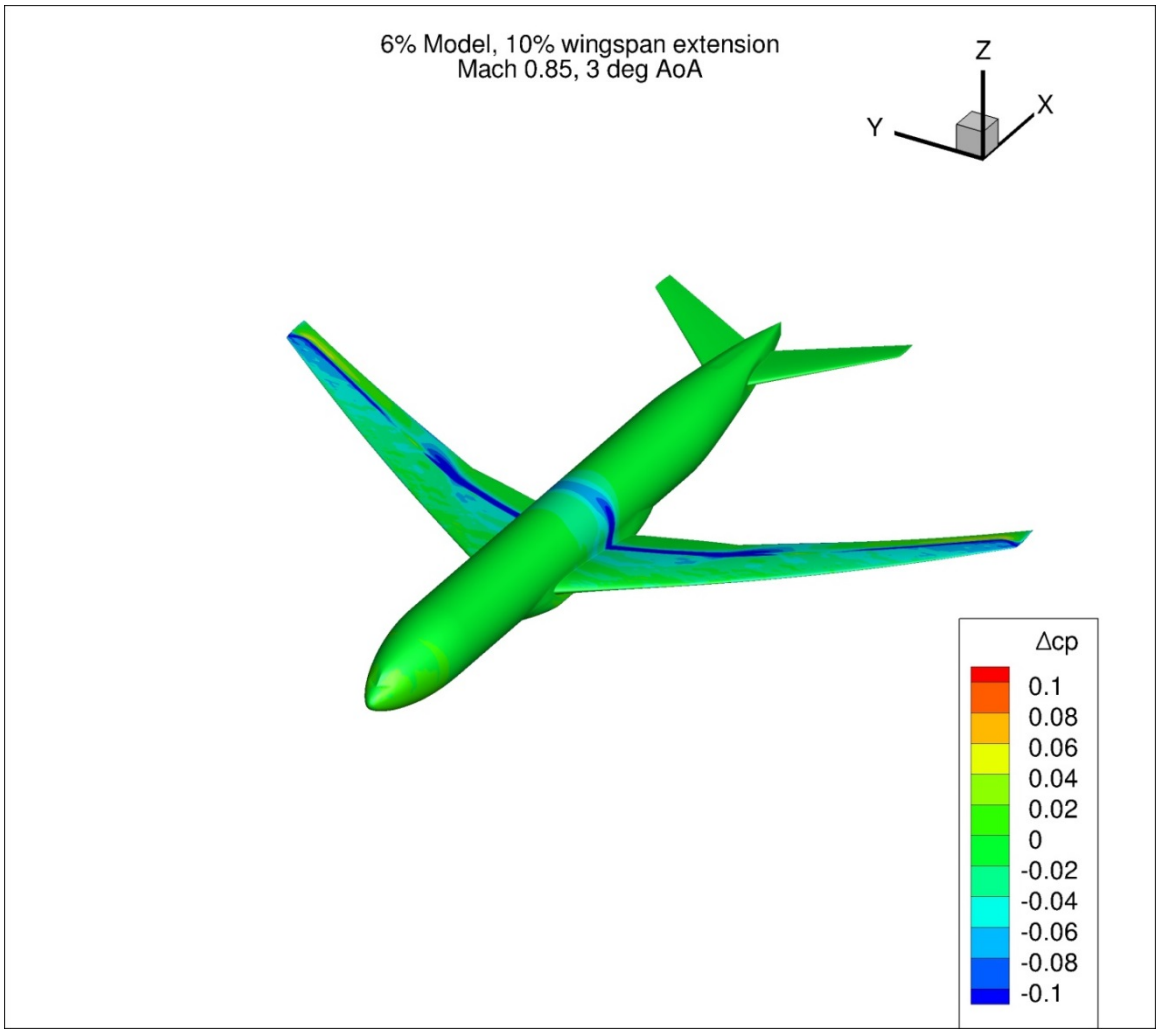

Figure 160. Configuration 3.1, Difference in Pressure Coefficient between Free-stream and Wind Tunnel Simulations, 3 deg Angle of Attack, Isometric View

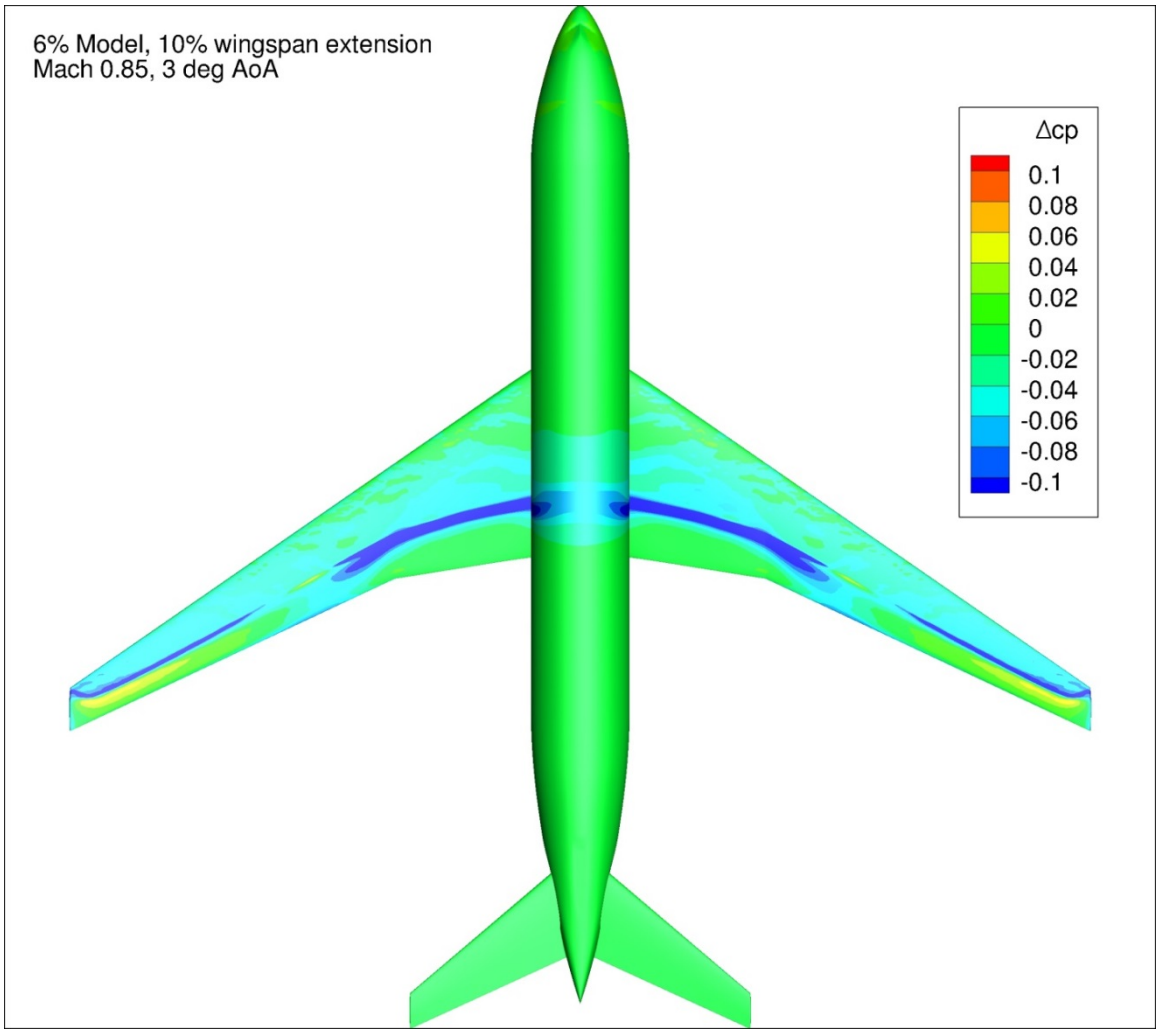

Figure 161. Configuration 3.1, Difference in Pressure Coefficient between Free-stream and Wind Tunnel Simulations, 3 deg Angle of Attack, Top View

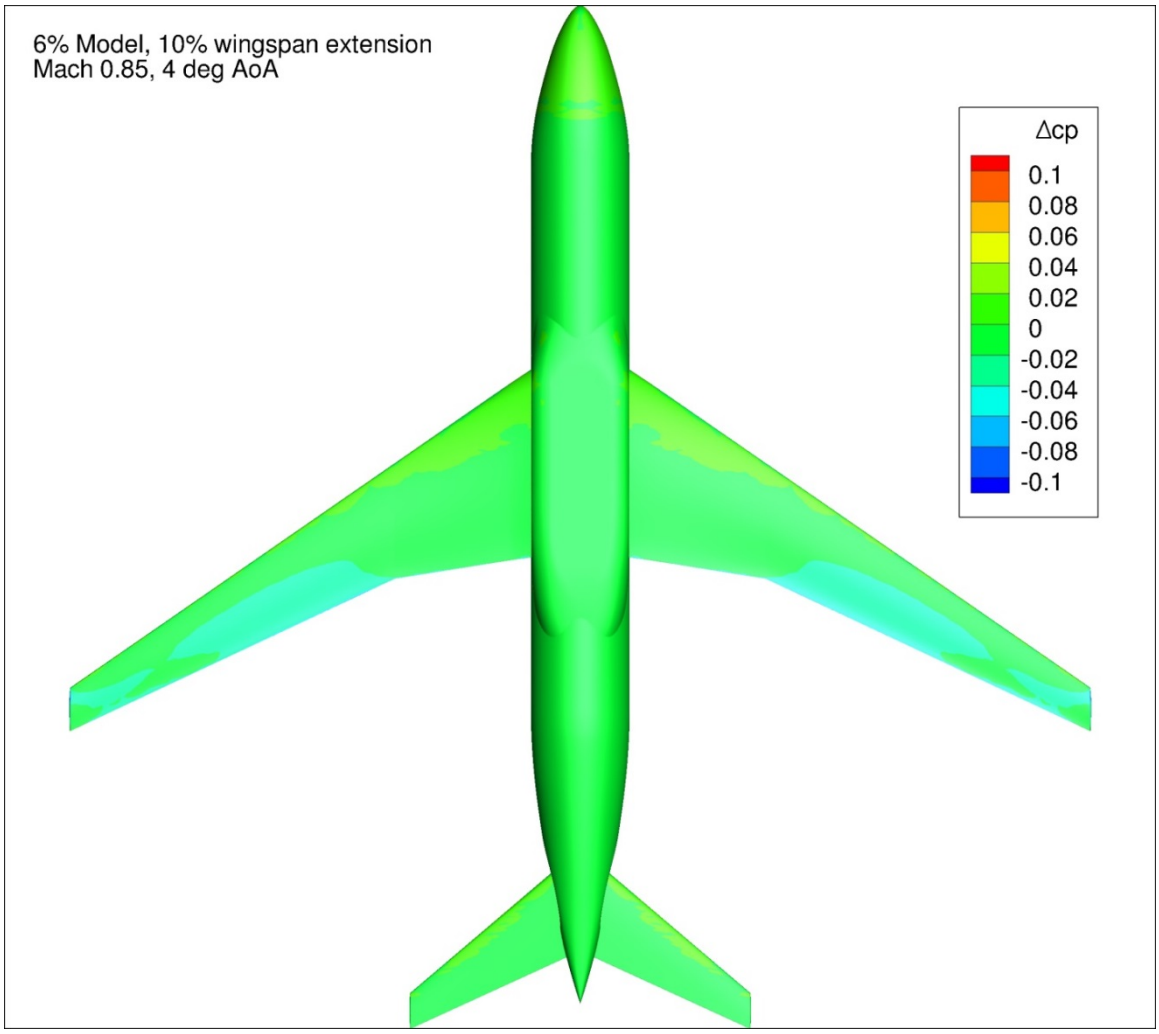

Figure 162. Configuration 3.1, Difference in Pressure Coefficient between Free-stream and Wind Tunnel Simulations, 4 deg Angle of Attack, Bottom View

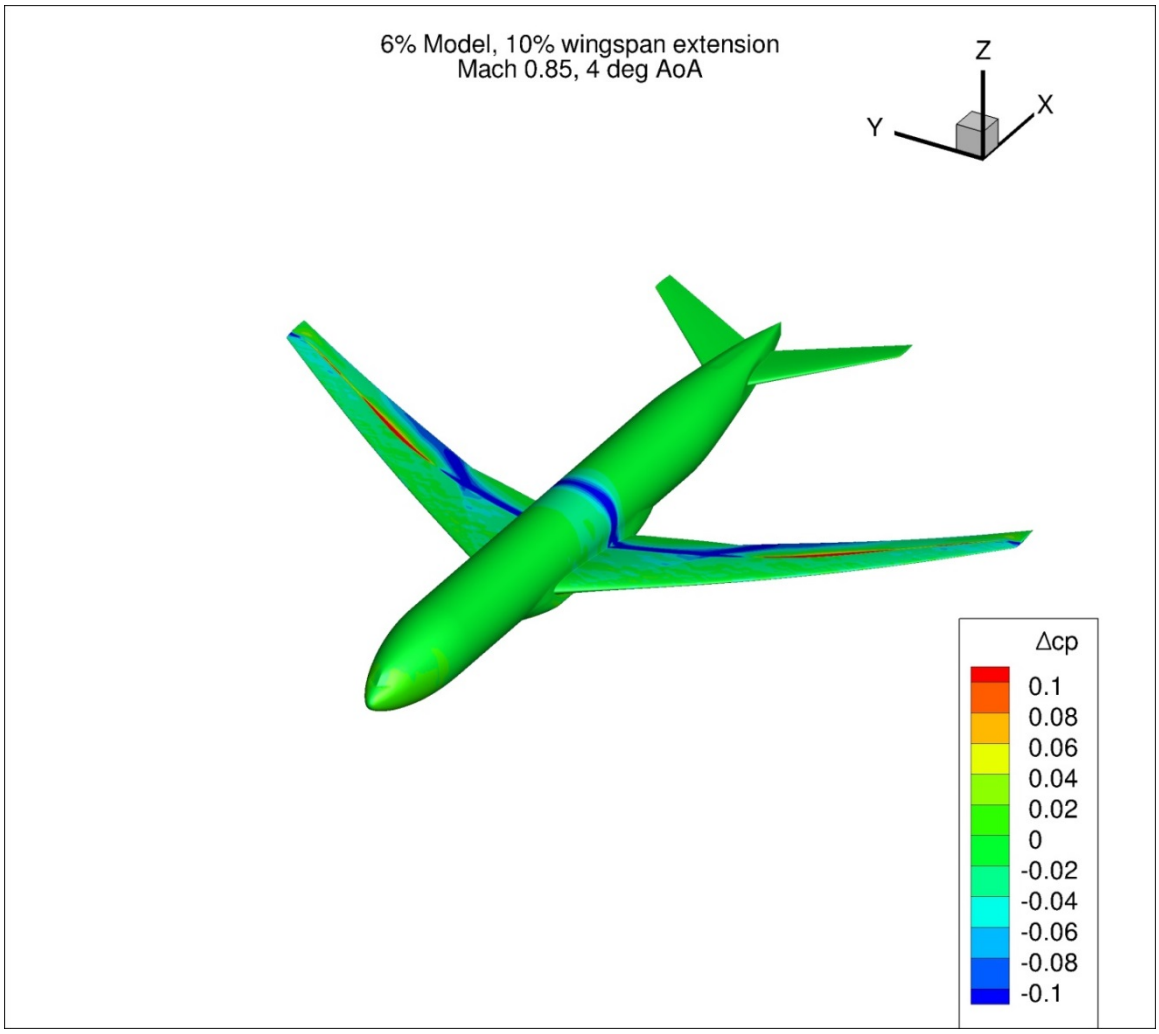

Figure 163. Configuration 3.1, Difference in Pressure Coefficient between Free-stream and Wind Tunnel Simulations, 4 deg Angle of Attack, Isometric View

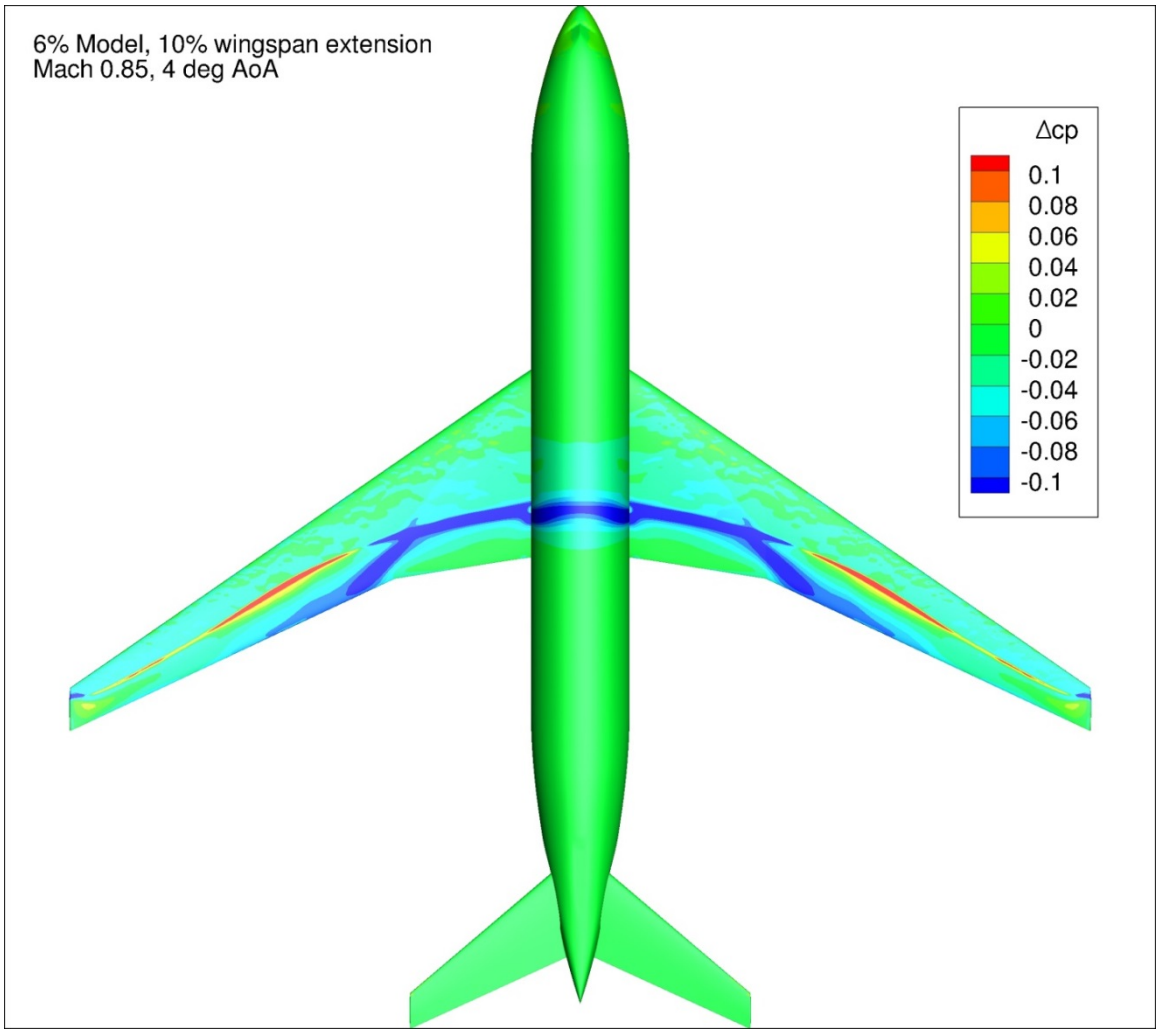

Figure 164. Configuration 3.1, Difference in Pressure Coefficient between Free-stream and Wind Tunnel Simulations, 4 deg Angle of Attack, Top View

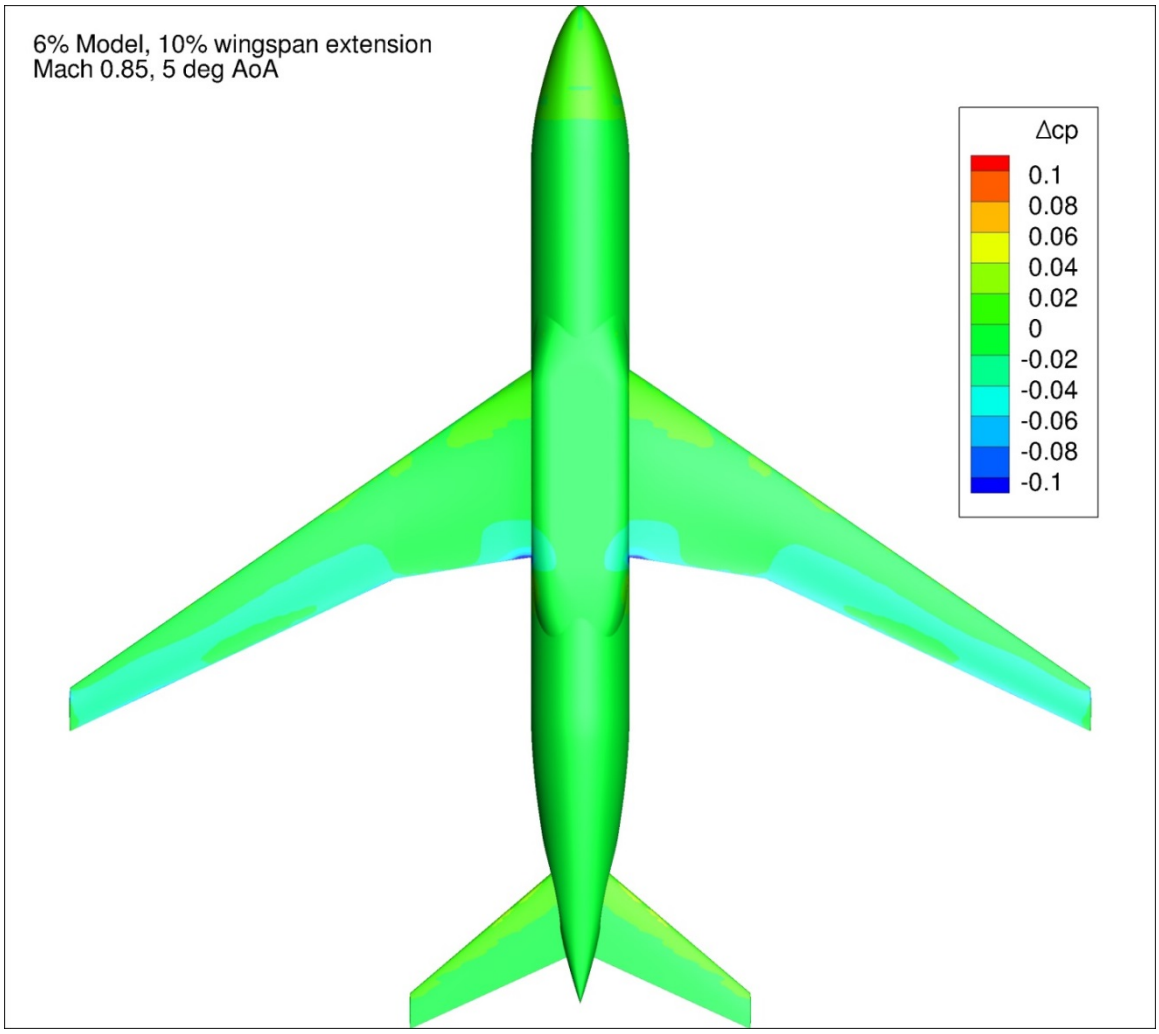

Figure 165. Configuration 3.1, Difference in Pressure Coefficient between Free-stream and Wind Tunnel Simulations, 5 deg Angle of Attack, Bottom View

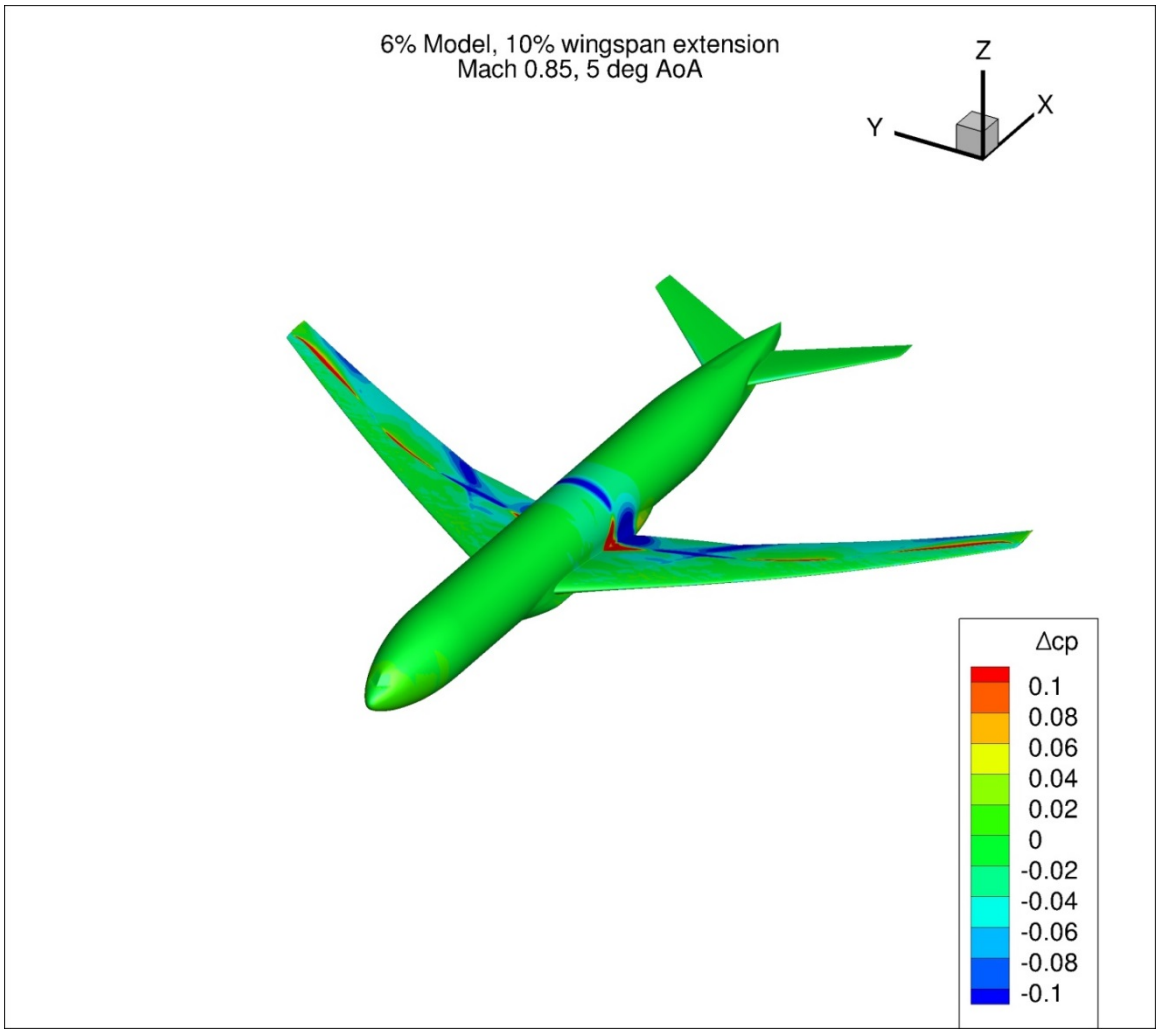

Figure 166. Configuration 3.1, Difference in Pressure Coefficient between Free-stream and Wind Tunnel Simulations, 5 deg Angle of Attack, Isometric View

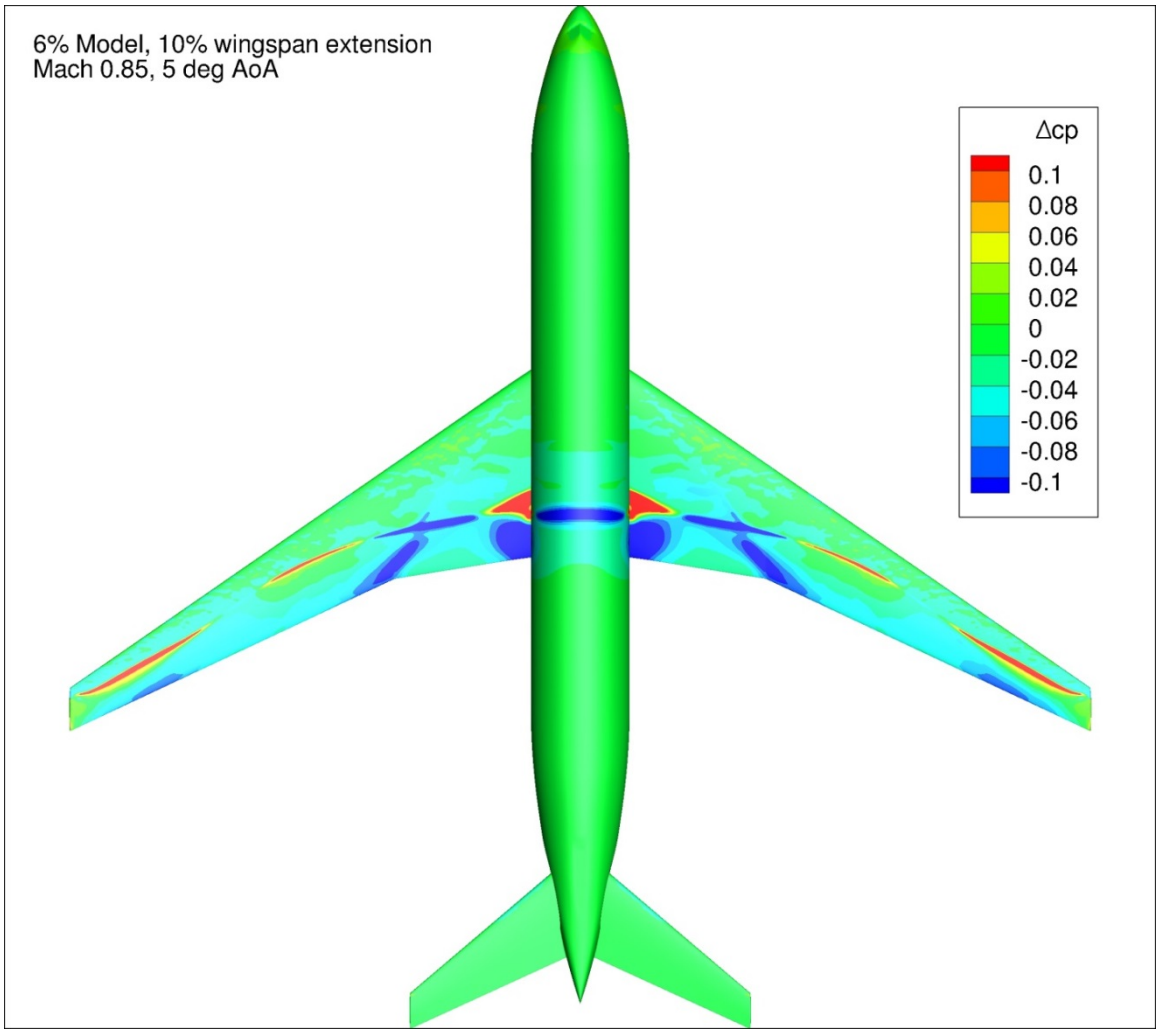

Figure 167. Configuration 3.1, Difference in Pressure Coefficient between Free-stream and Wind Tunnel Simulations, 5 deg Angle of Attack, Top View

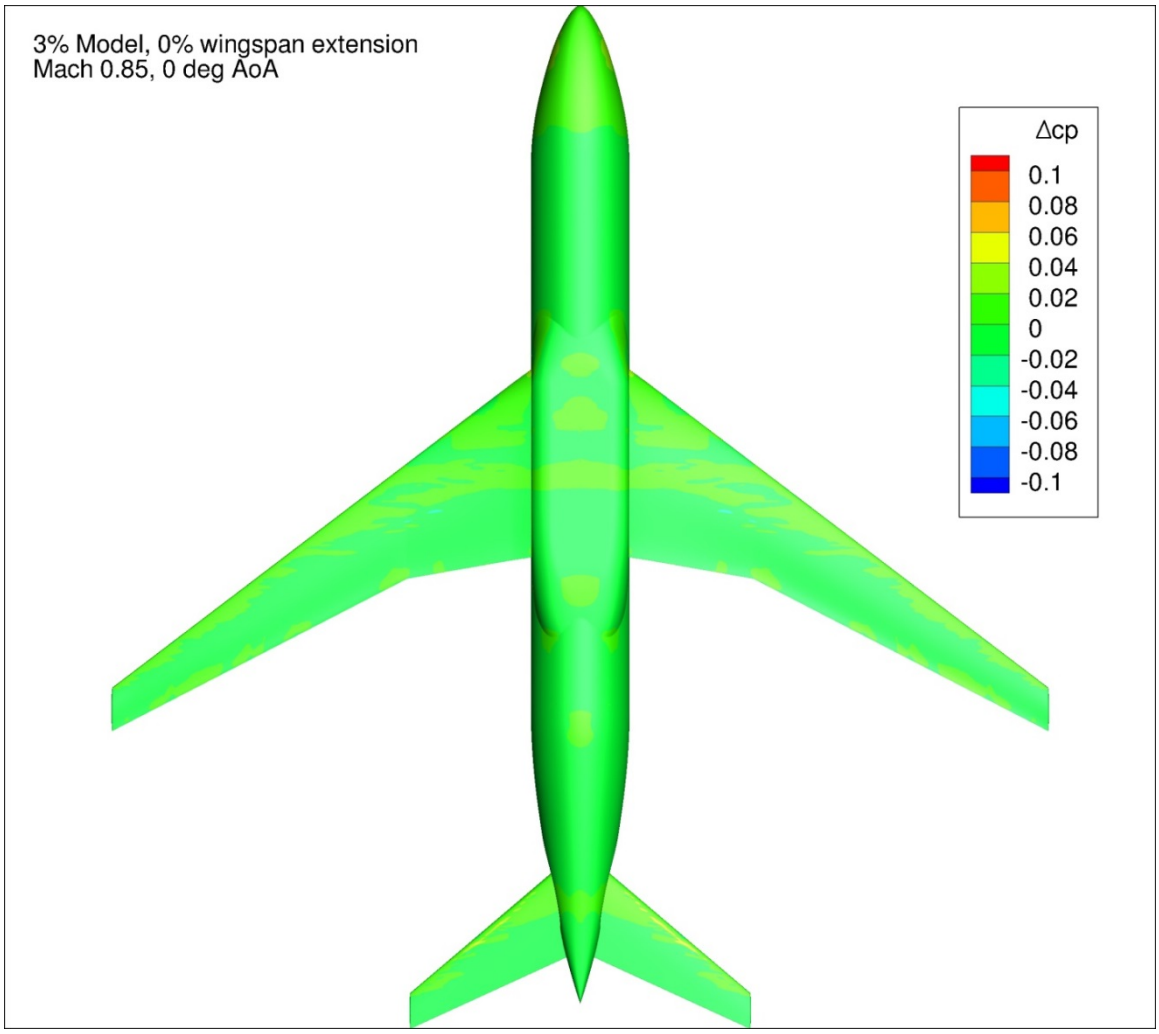

Figure 168. Configuration 4, Difference in Pressure Coefficient between Free-stream and Wind Tunnel Simulations, 0 deg Angle of Attack, Bottom View

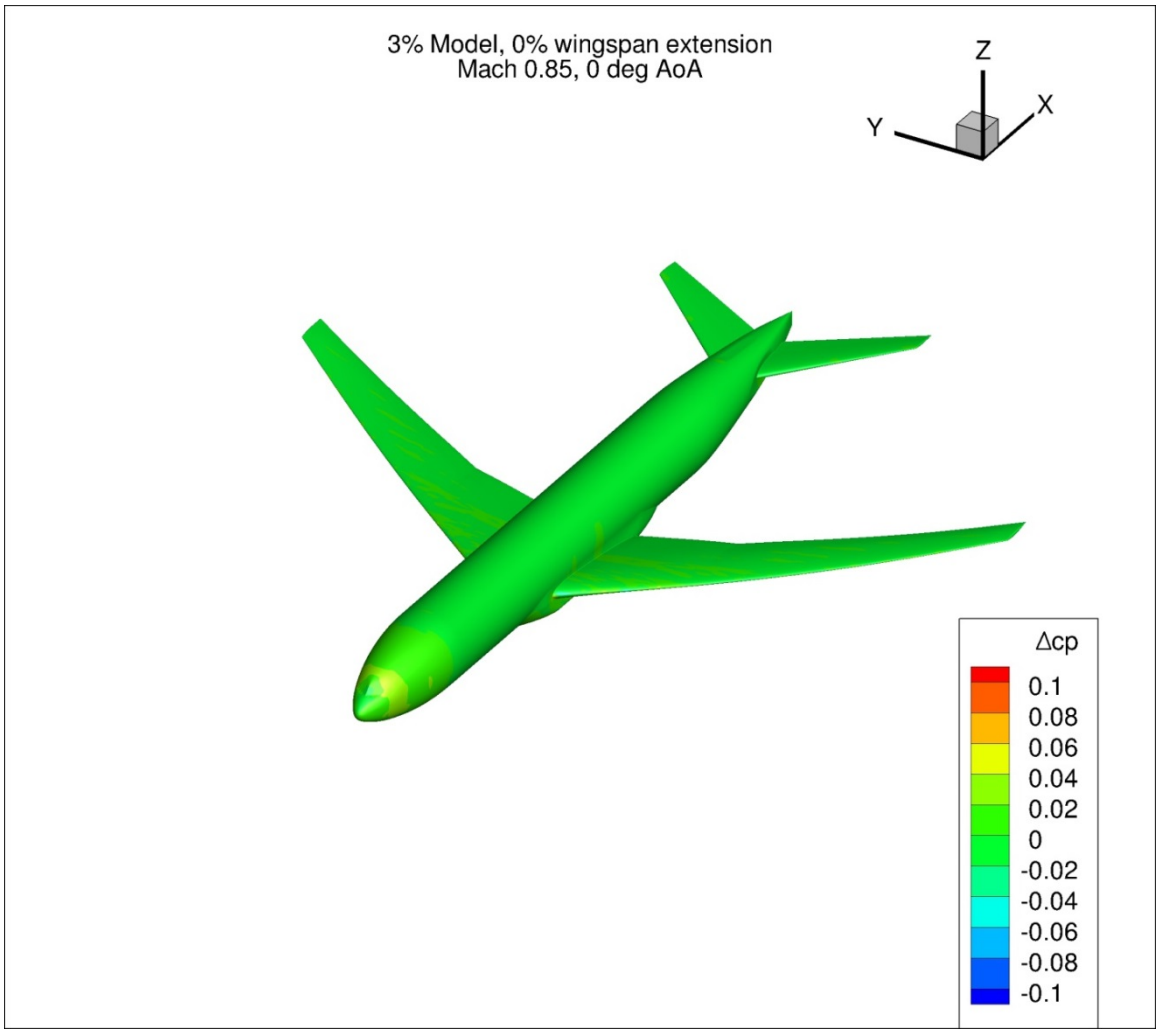

Figure 169. Configuration 4, Difference in Pressure Coefficient between Free-stream and Wind Tunnel Simulations, 0 deg Angle of Attack, Isometric View

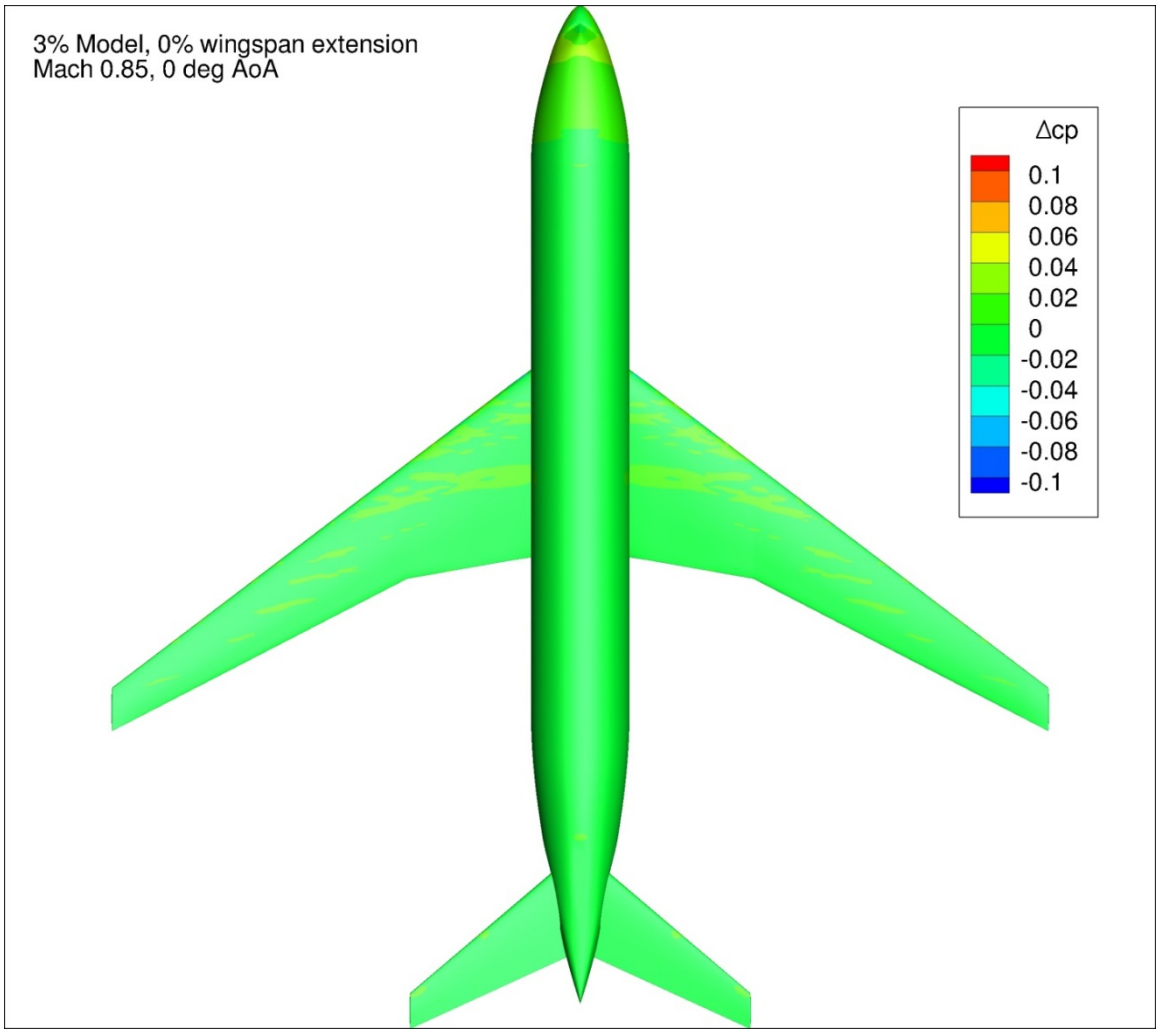

Figure 170. Configuration 4, Difference in Pressure Coefficient between Free-stream and Wind Tunnel Simulations, 0 deg Angle of Attack, Top View

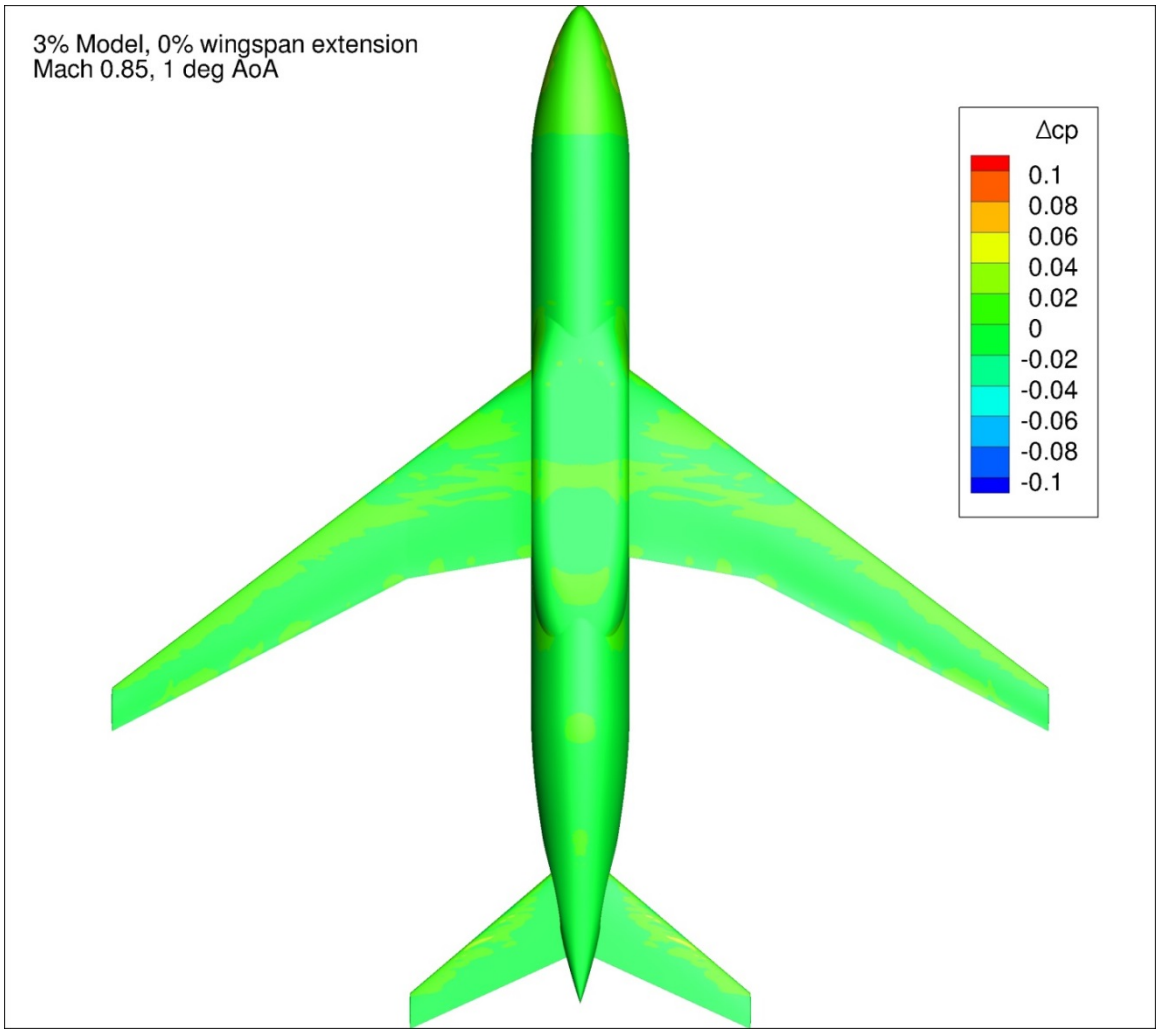

Figure 171. Configuration 4, Difference in Pressure Coefficient between Free-stream and Wind Tunnel Simulations, 1 deg Angle of Attack, Bottom View

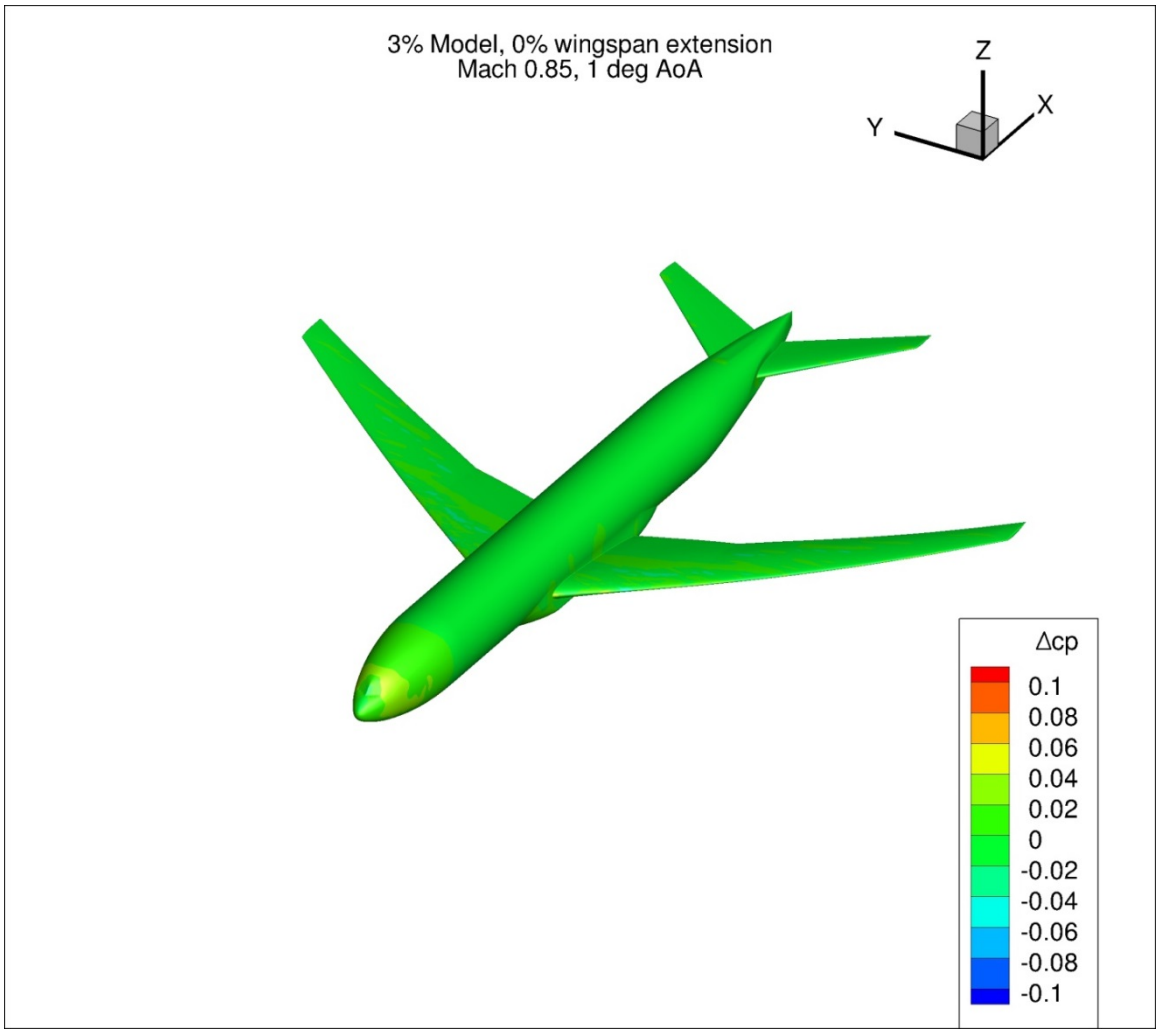

Figure 172. Configuration 4, Difference in Pressure Coefficient between Free-stream and Wind Tunnel Simulations, 1 deg Angle of Attack, Isometric View

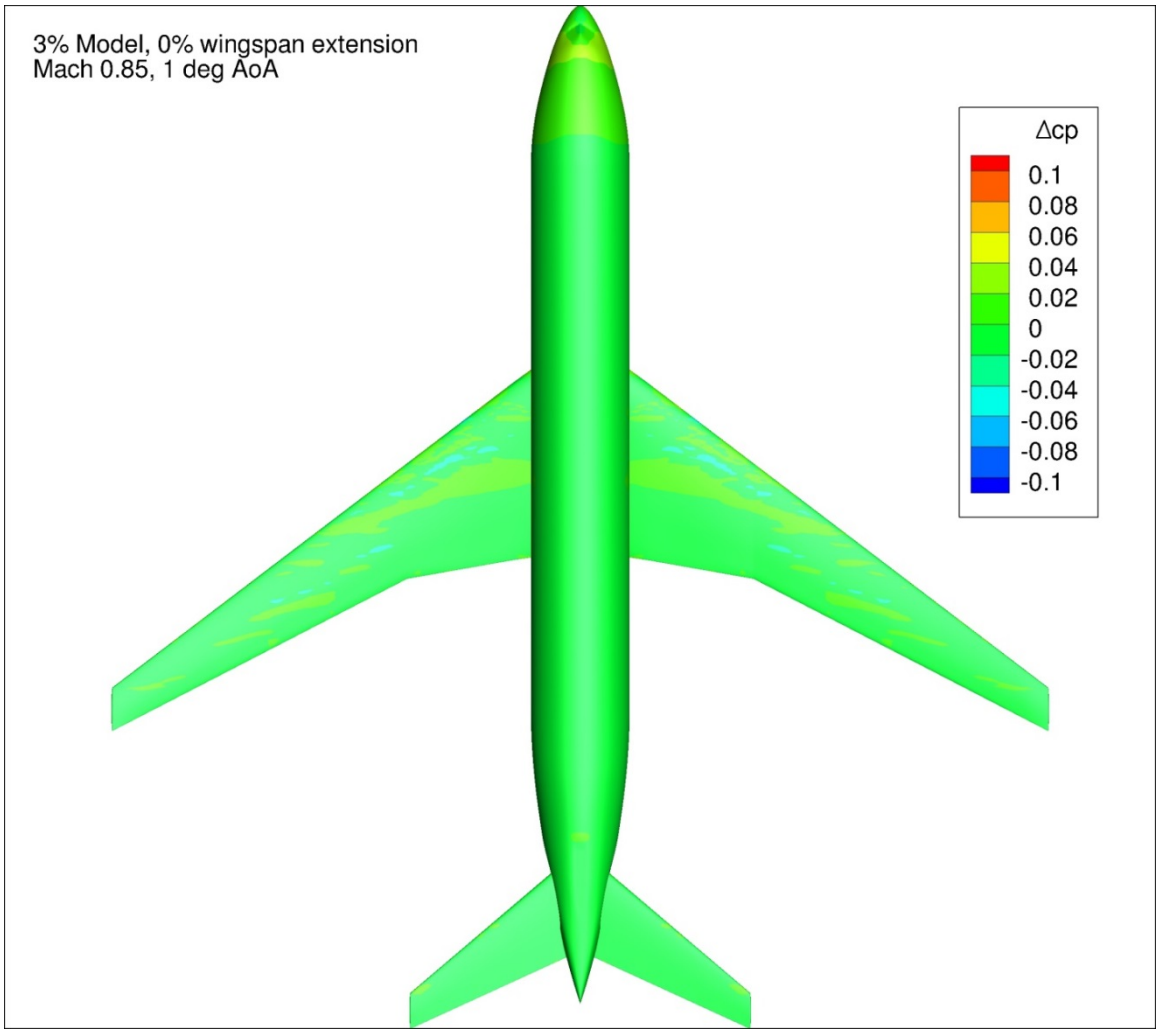

Figure 173. Configuration 4, Difference in Pressure Coefficient between Free-stream and Wind Tunnel Simulations, 1 deg Angle of Attack, Top View

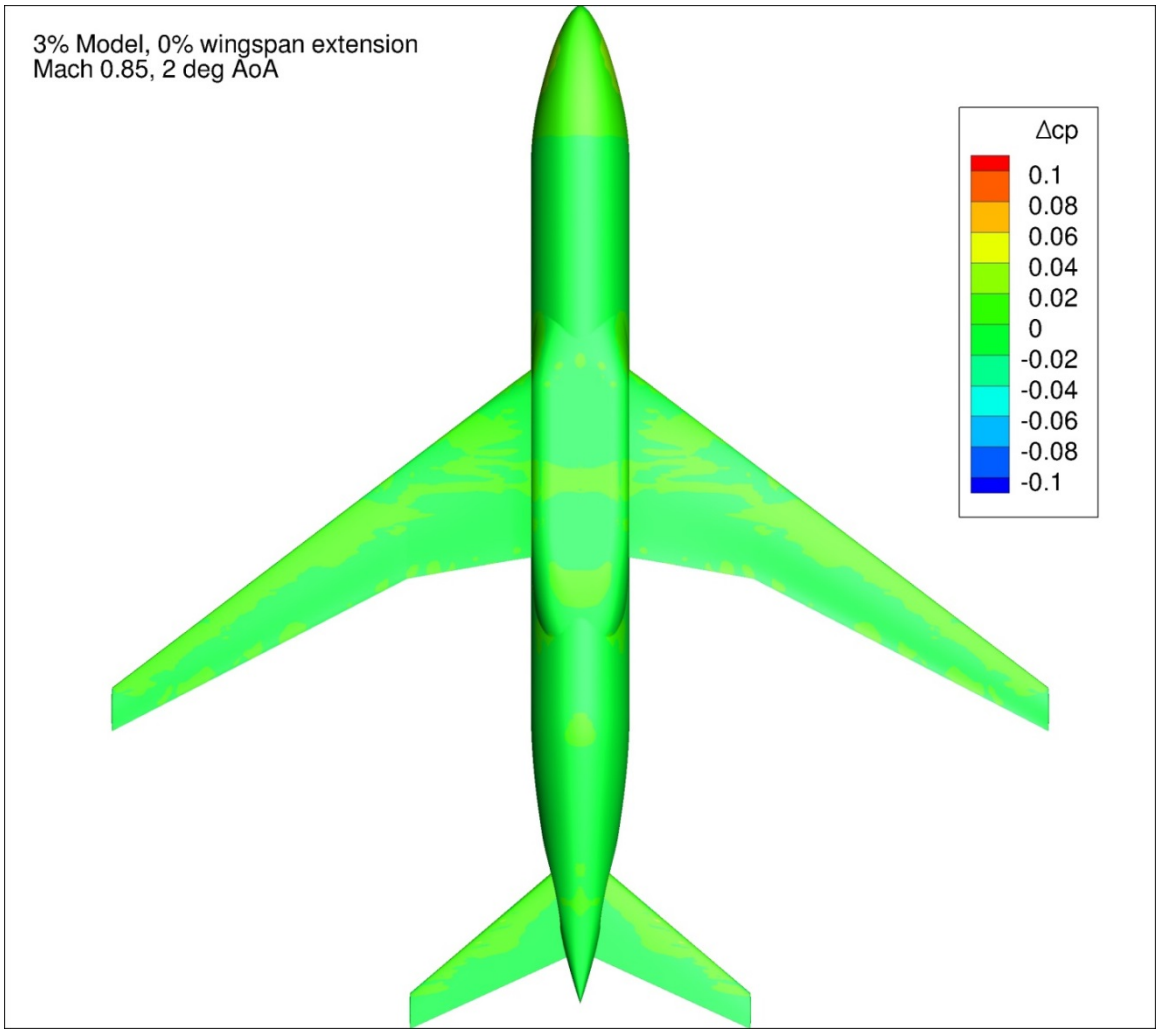

Figure 174. Configuration 4, Difference in Pressure Coefficient between Free-stream and Wind Tunnel Simulations, 2 deg Angle of Attack, Bottom View

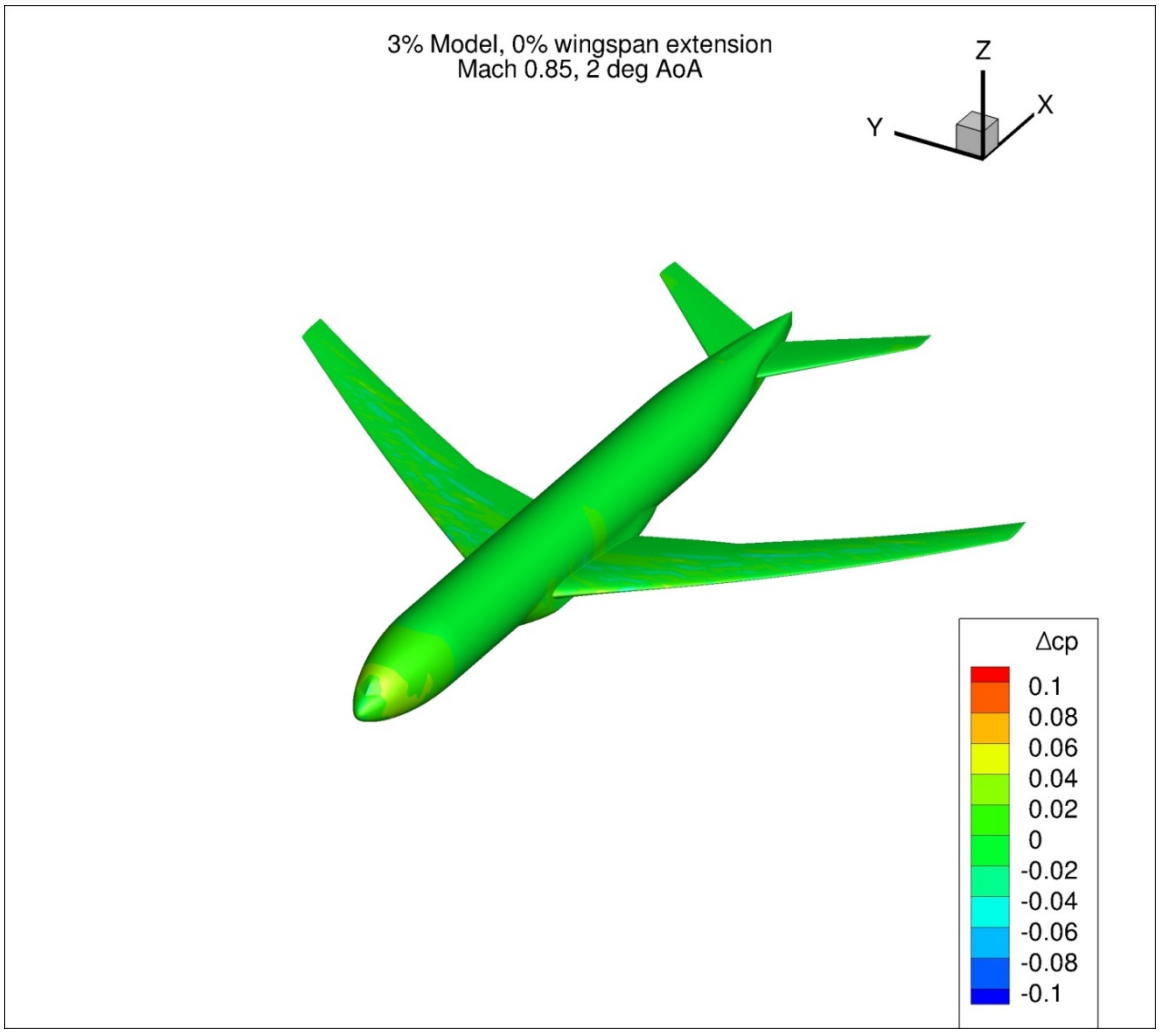

Figure 175. Configuration 4, Difference in Pressure Coefficient between Free-stream and Wind Tunnel Simulations, 2 deg Angle of Attack, Isometric View

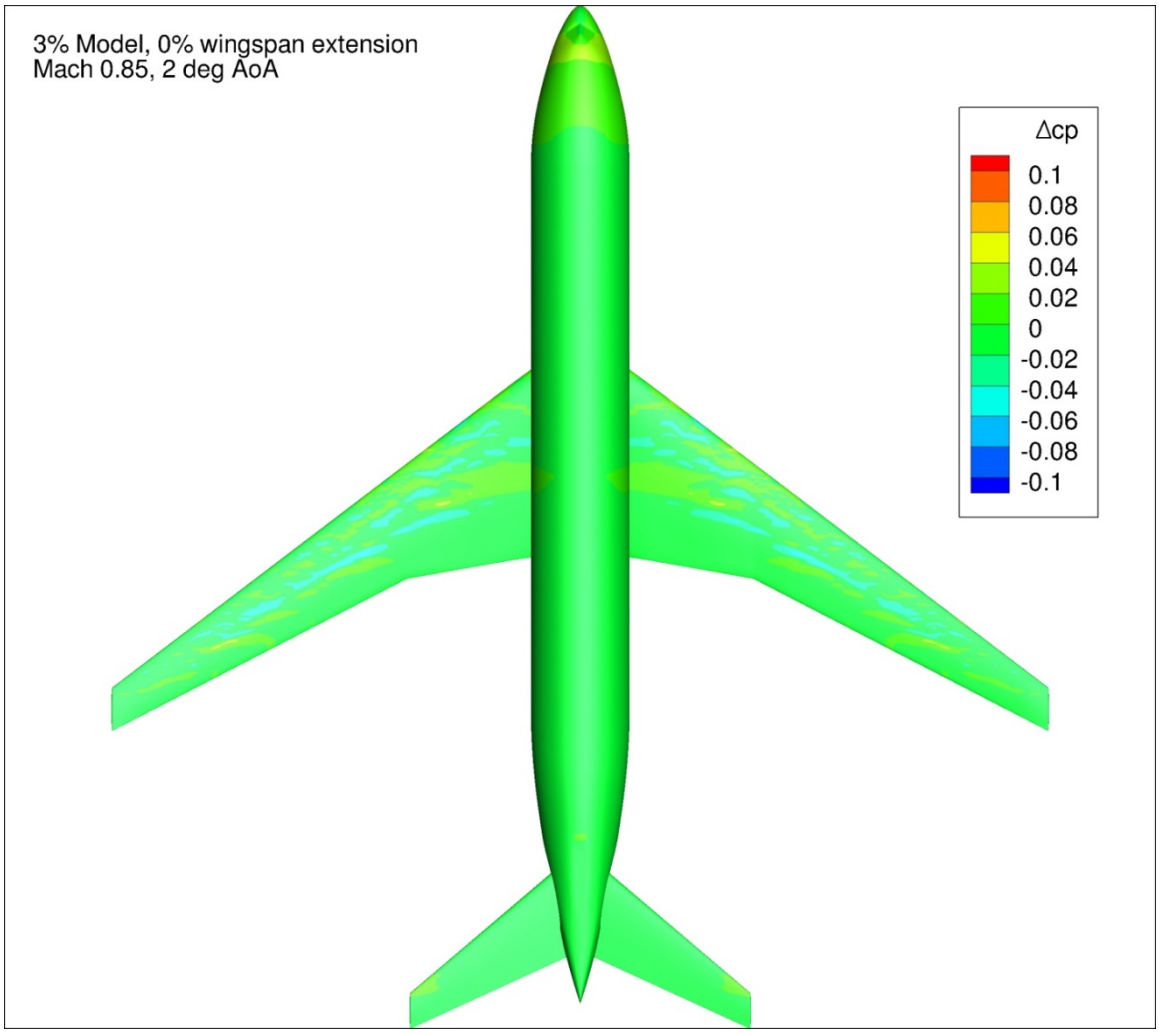

Figure 176. Configuration 4, Difference in Pressure Coefficient between Free-stream and Wind Tunnel Simulations, 2 deg Angle of Attack, Top View

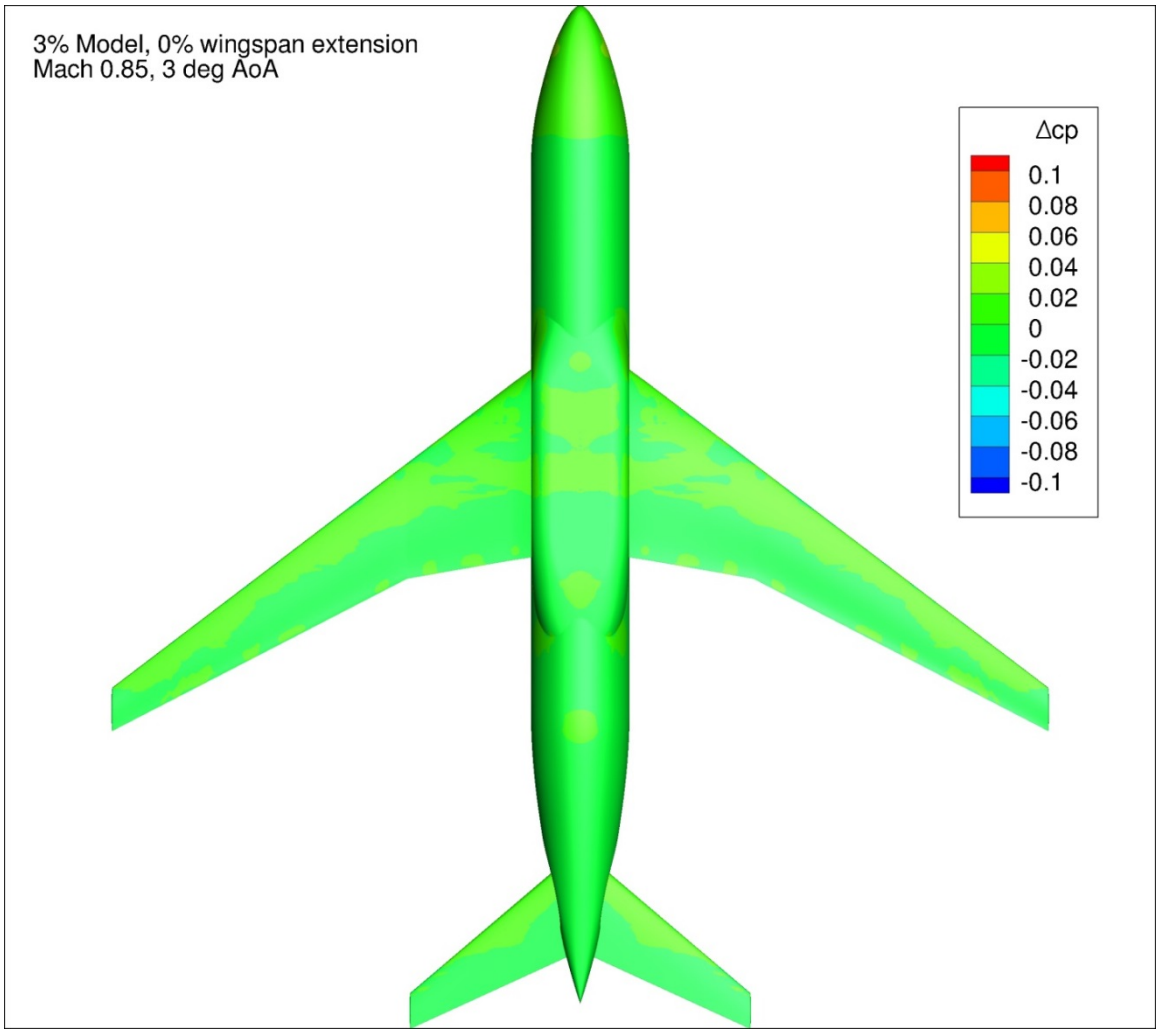

Figure 177. Configuration 4, Difference in Pressure Coefficient between Free-stream and Wind Tunnel Simulations, 3 deg Angle of Attack, Bottom View

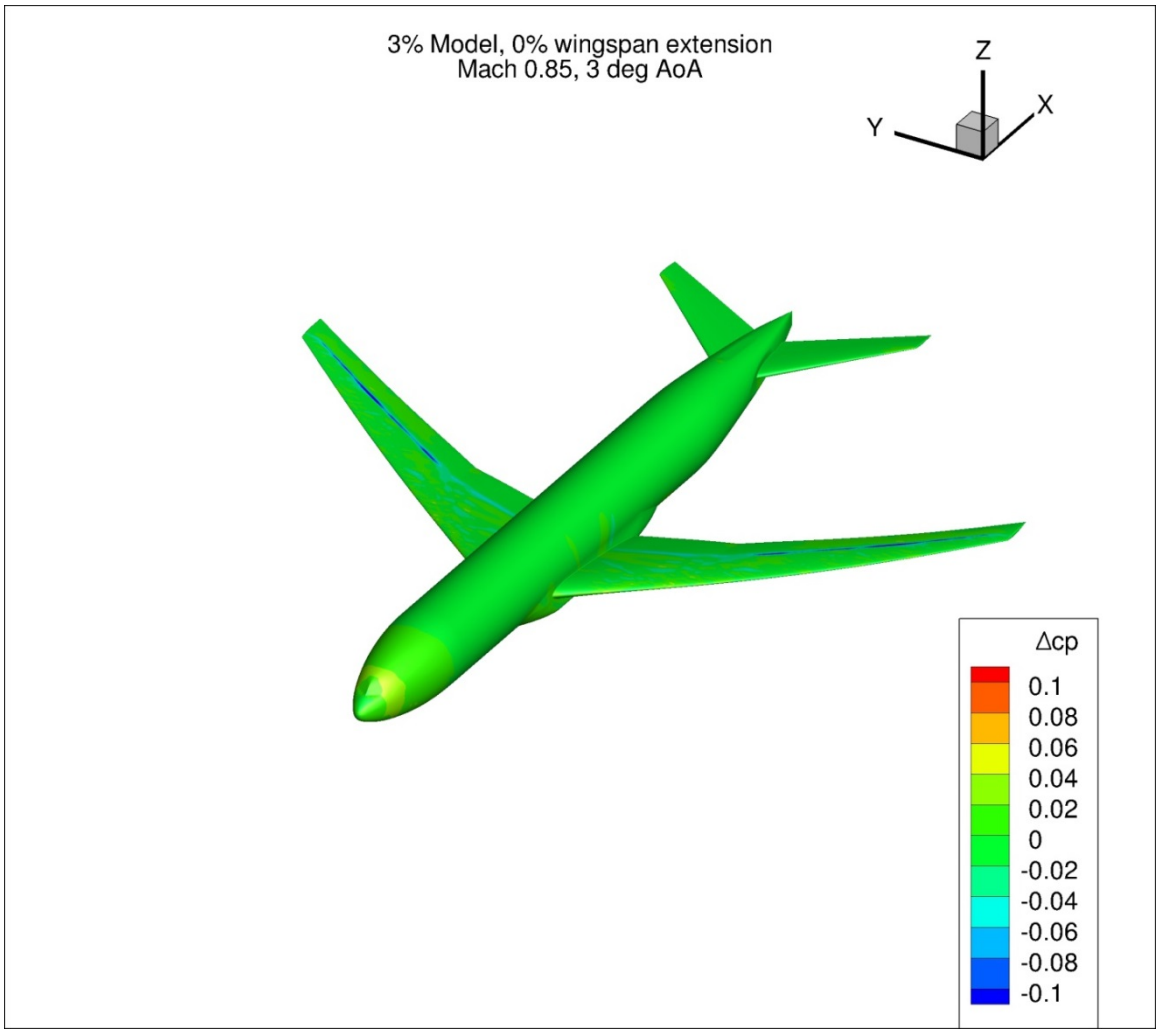

Figure 178. Configuration 4, Difference in Pressure Coefficient between Free-stream and Wind Tunnel Simulations, 3 deg Angle of Attack, Isometric View

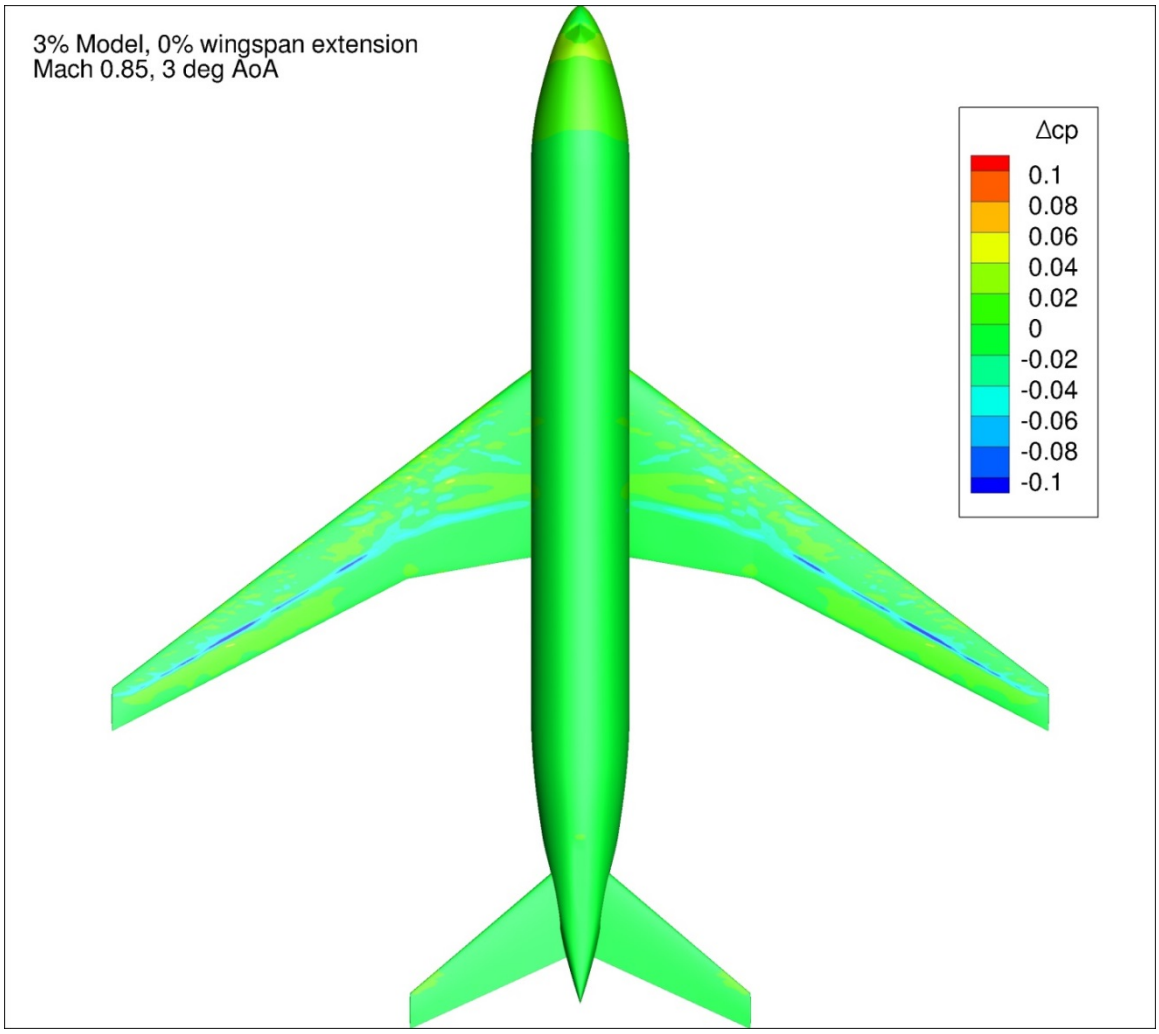

Figure 179. Configuration 4, Difference in Pressure Coefficient between Free-stream and Wind Tunnel Simulations, 3 deg Angle of Attack, Top View

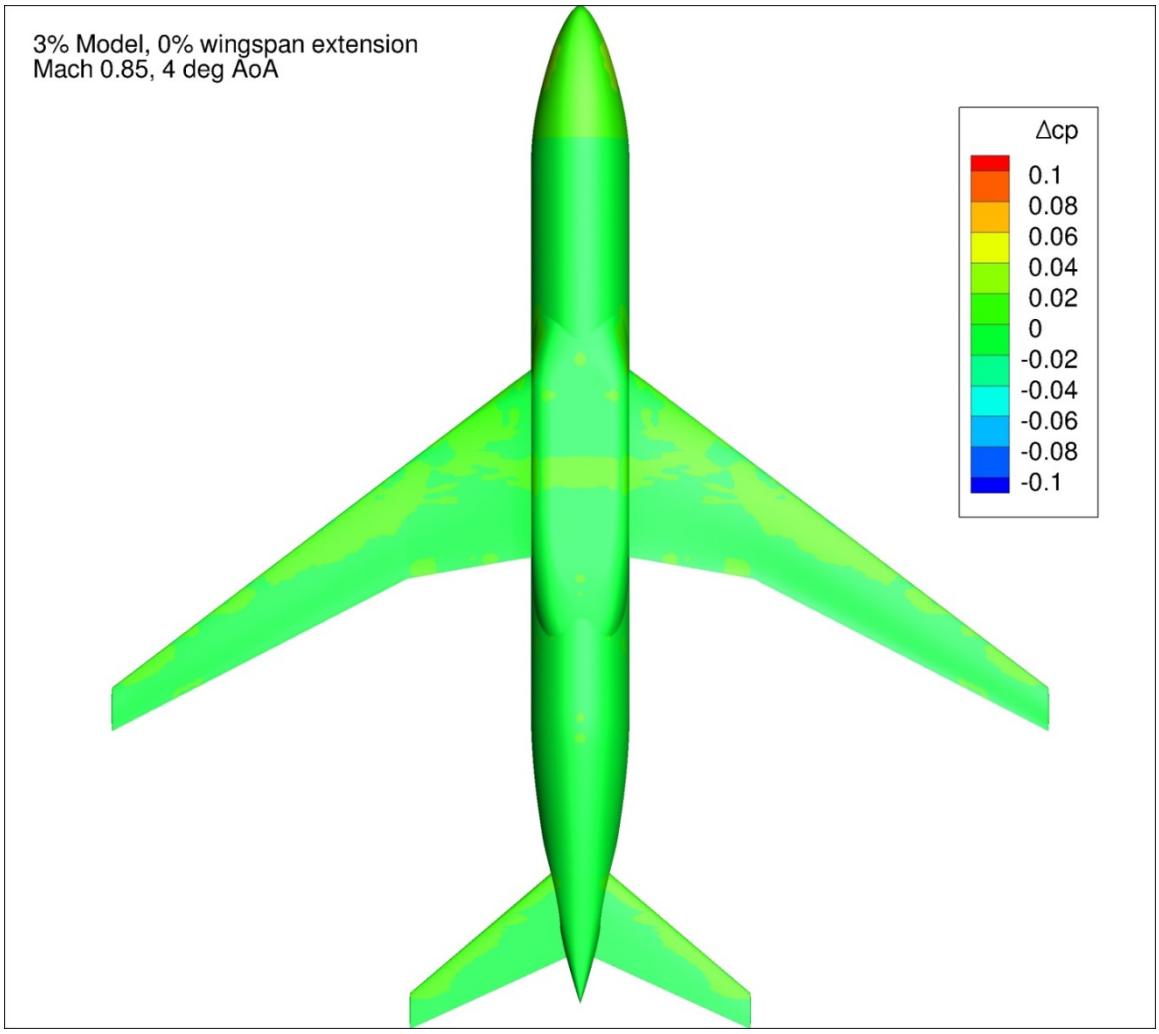

Figure 180. Configuration 4, Difference in Pressure Coefficient between Free-stream and Wind Tunnel Simulations, 4 deg Angle of Attack, Bottom View

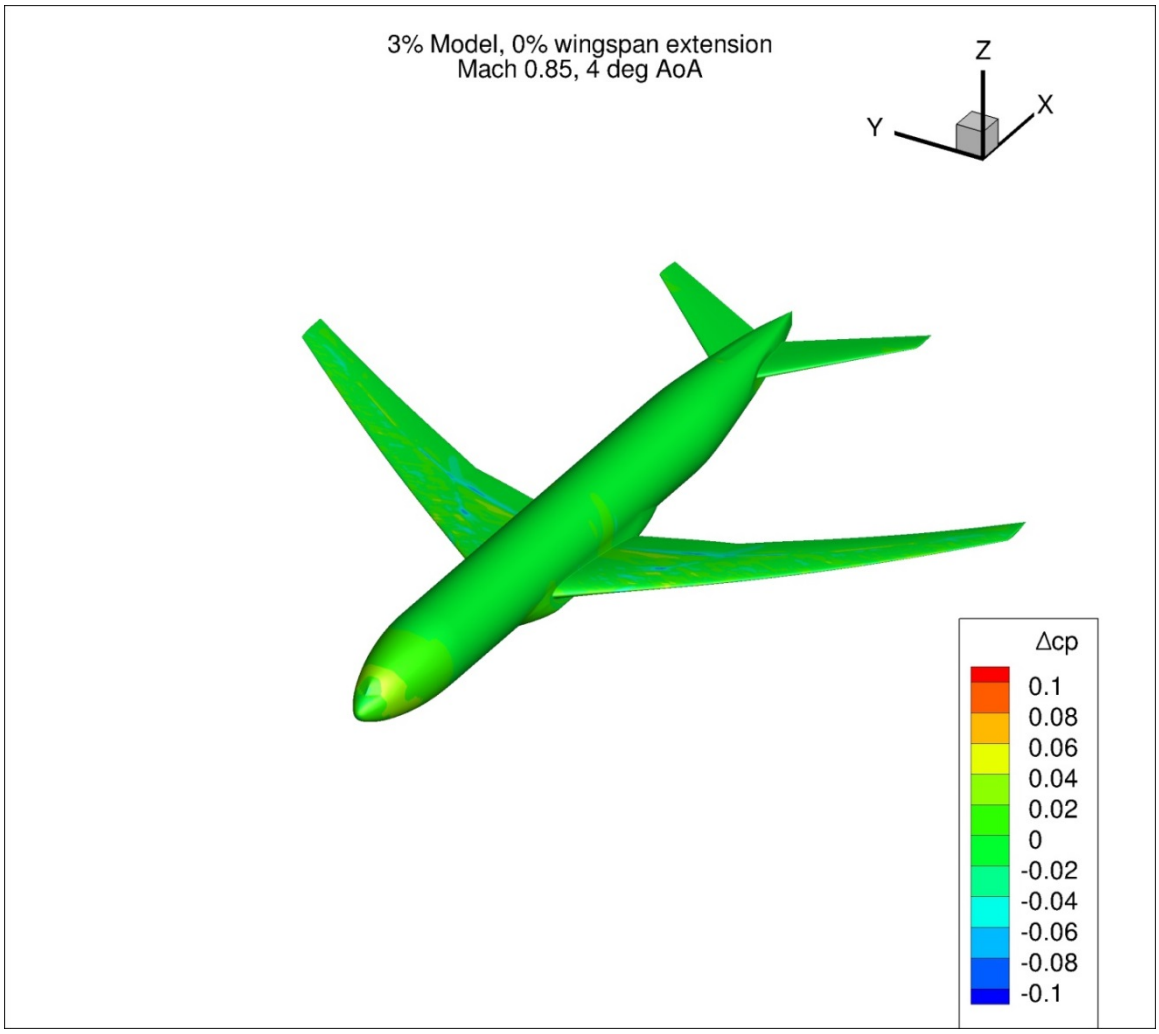

Figure 181. Configuration 4, Difference in Pressure Coefficient between Free-stream and Wind Tunnel Simulations, 4 deg Angle of Attack, Isometric View

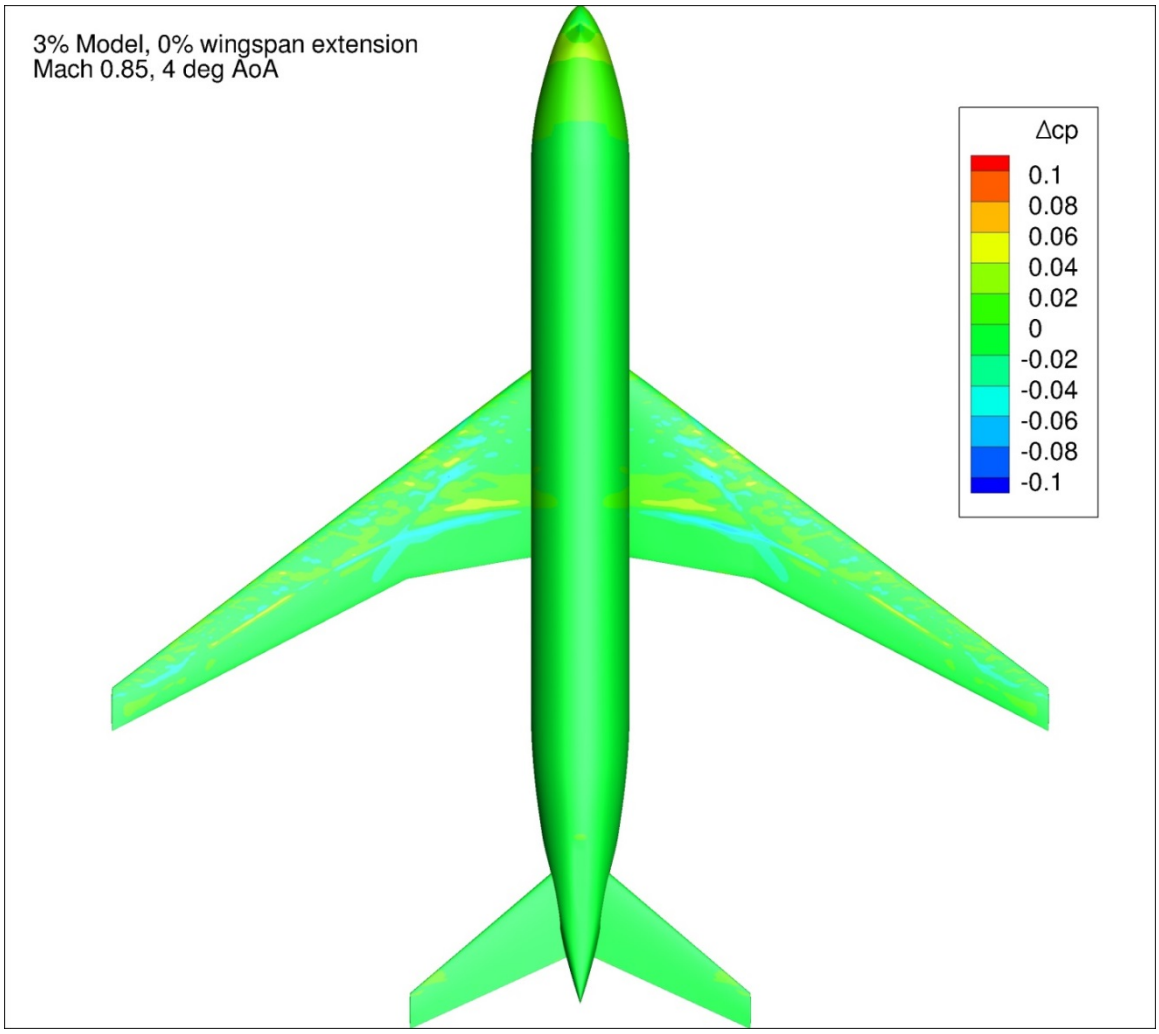

Figure 182. Configuration 4, Difference in Pressure Coefficient between Free-stream and Wind Tunnel Simulations, 4 deg Angle of Attack, Top View

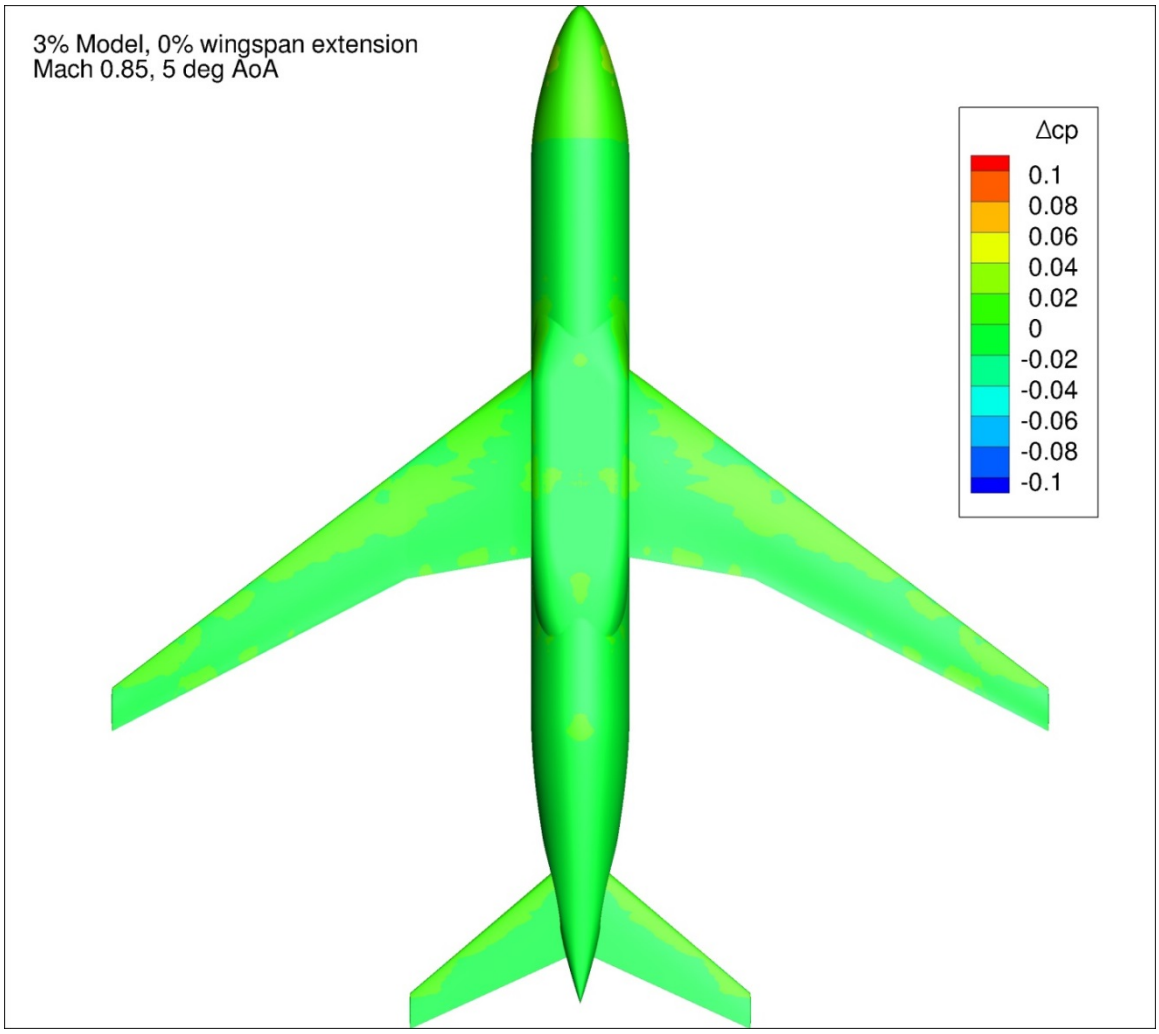

Figure 183. Configuration 4, Difference in Pressure Coefficient between Free-stream and Wind Tunnel Simulations, 5 deg Angle of Attack, Bottom View

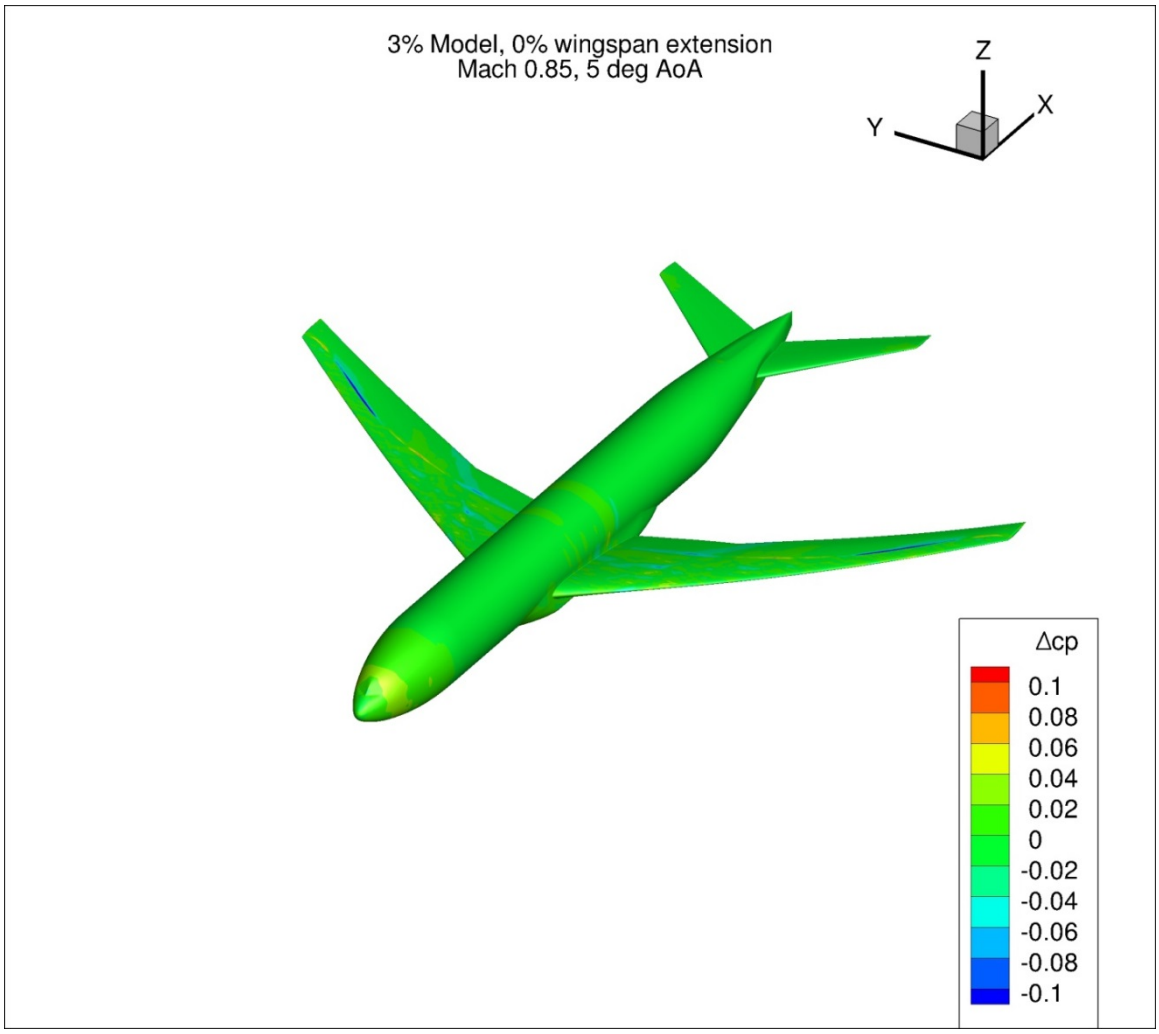

Figure 184. Configuration 4, Difference in Pressure Coefficient between Free-stream and Wind Tunnel Simulations, 5 deg Angle of Attack, Isometric View

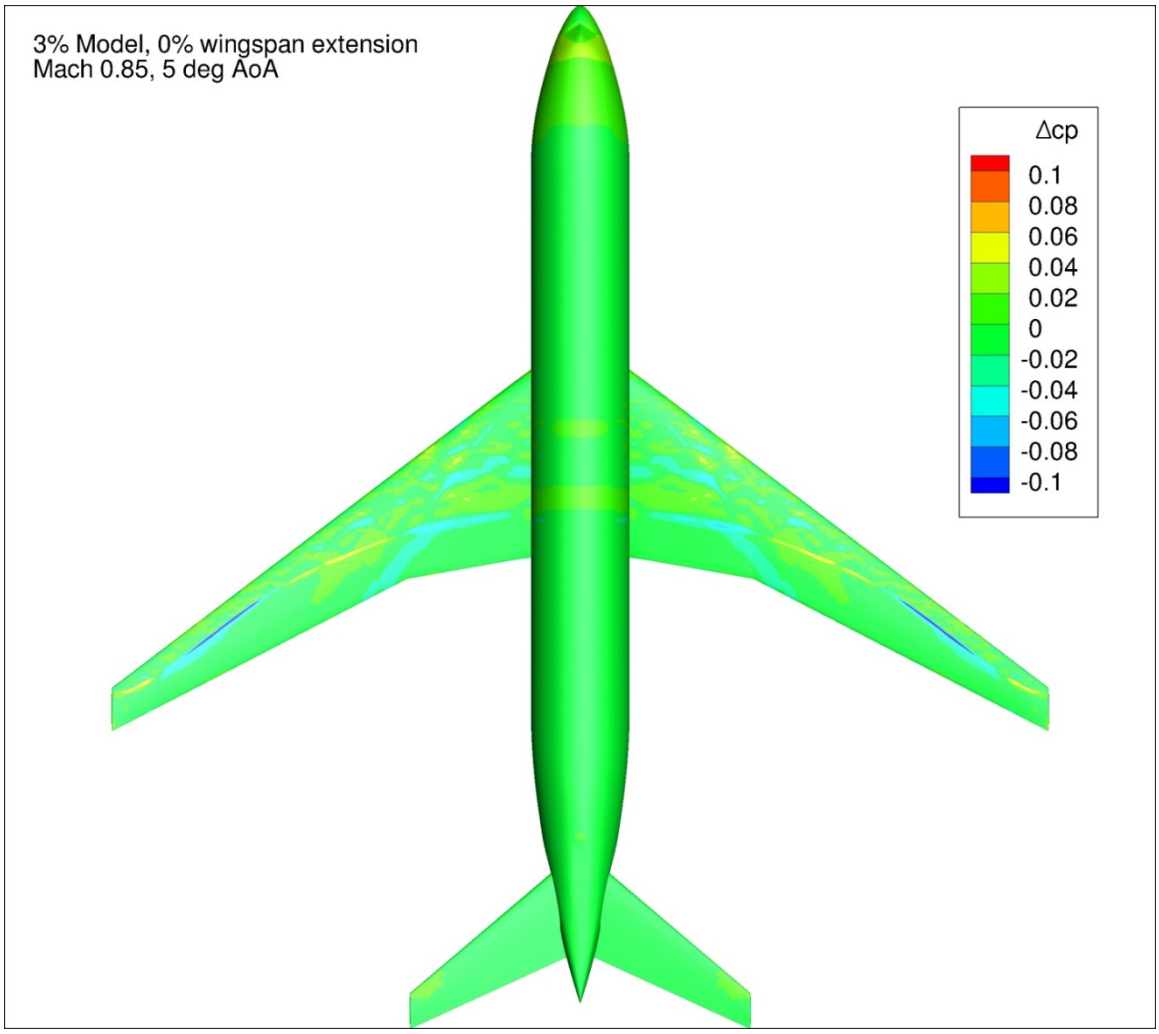

Figure 185. Configuration 4, Difference in Pressure Coefficient between Free-stream and Wind Tunnel Simulations, 5 deg Angle of Attack, Top View

Appendix 6: Pressure Coefficient Profile Plots for Free-stream and Wind Tunnel Simulations

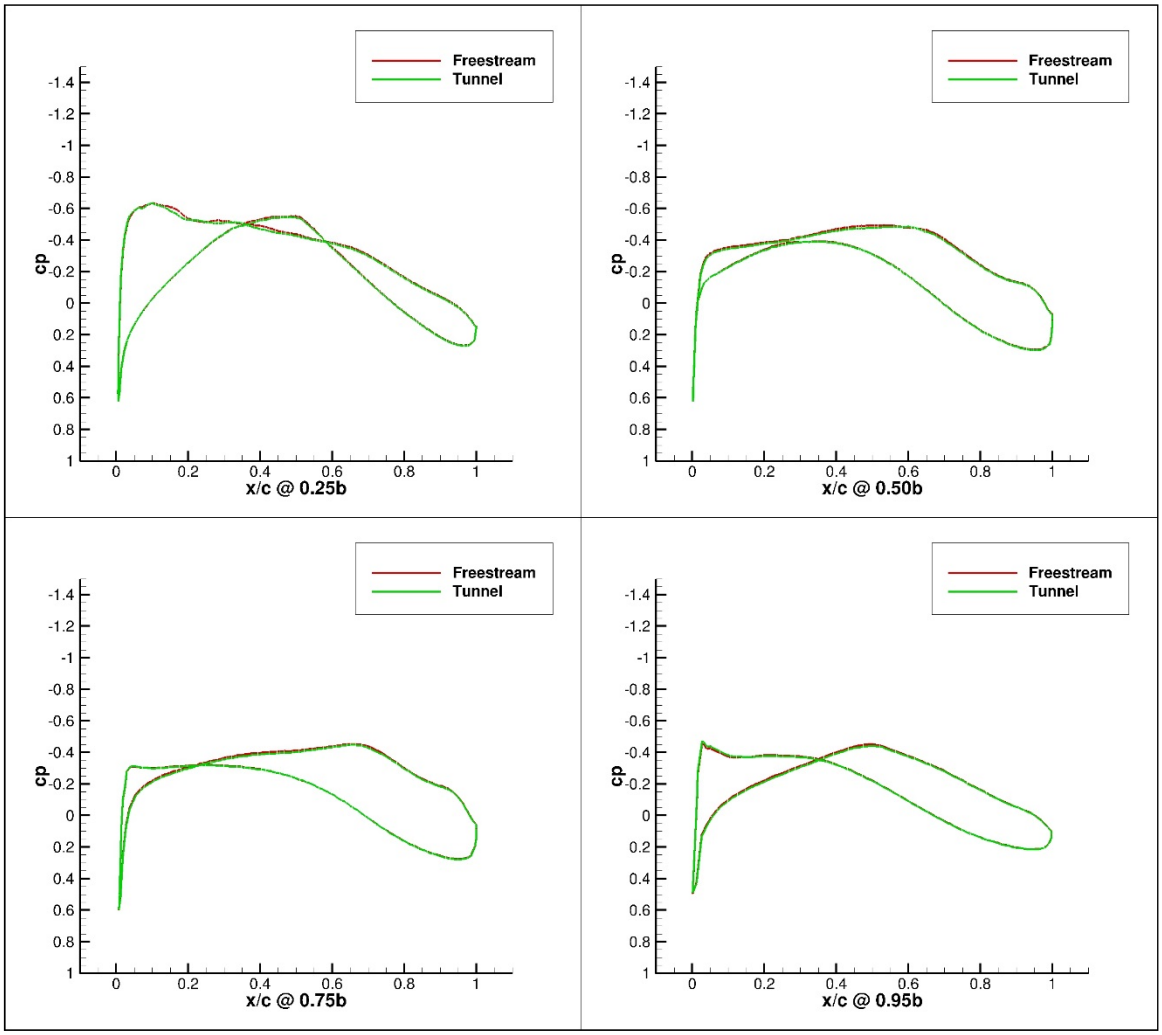

Figure 186. Configuration 1, 0 deg Angle of Attack Pressure Coefficient Contours for Free-stream and Wind Tunnel Simulations

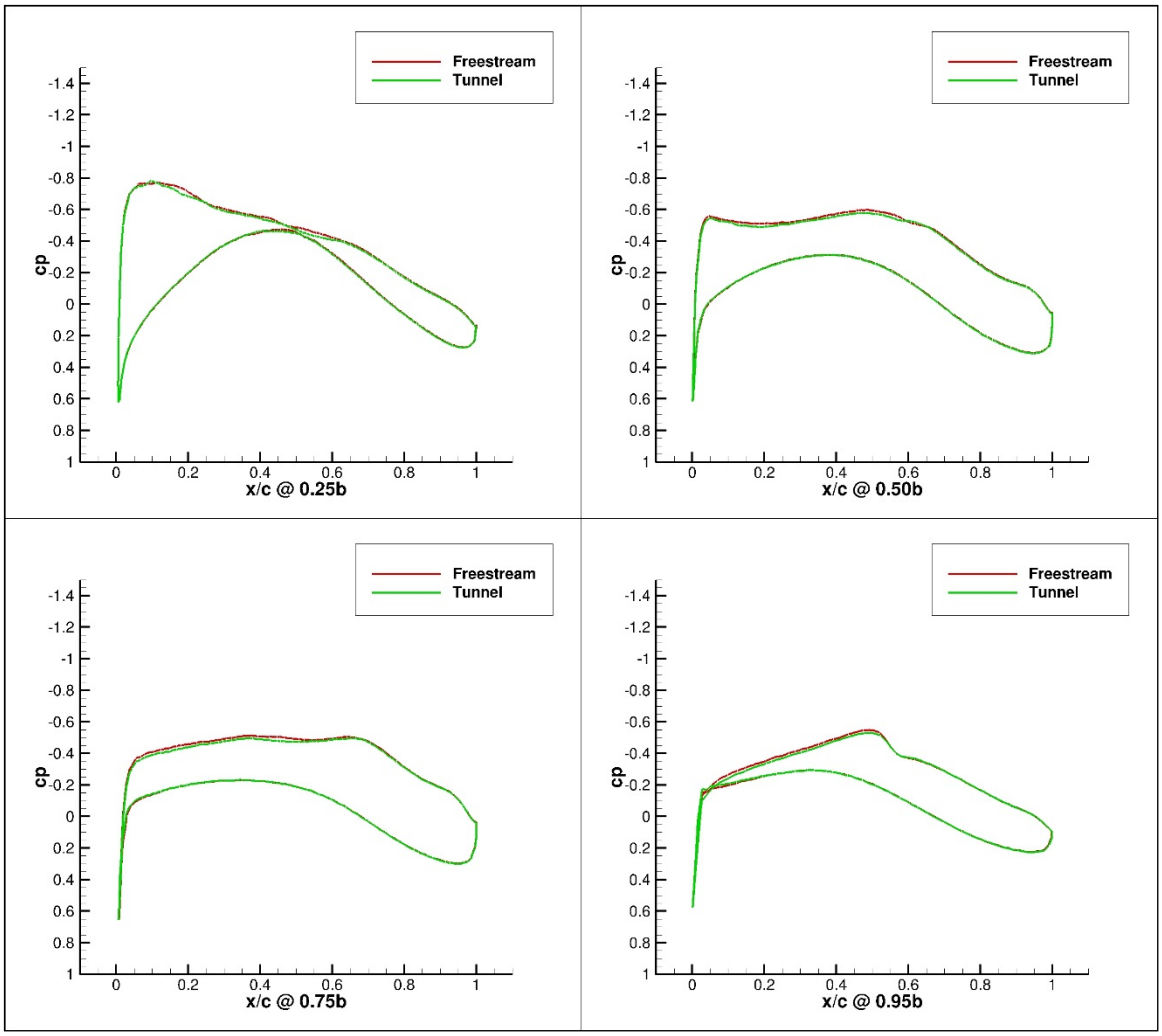

Figure 187. Configuration 1,1 deg Angle of Attack Pressure Coefficient Contours for Free-stream and Wind Tunnel Simulations

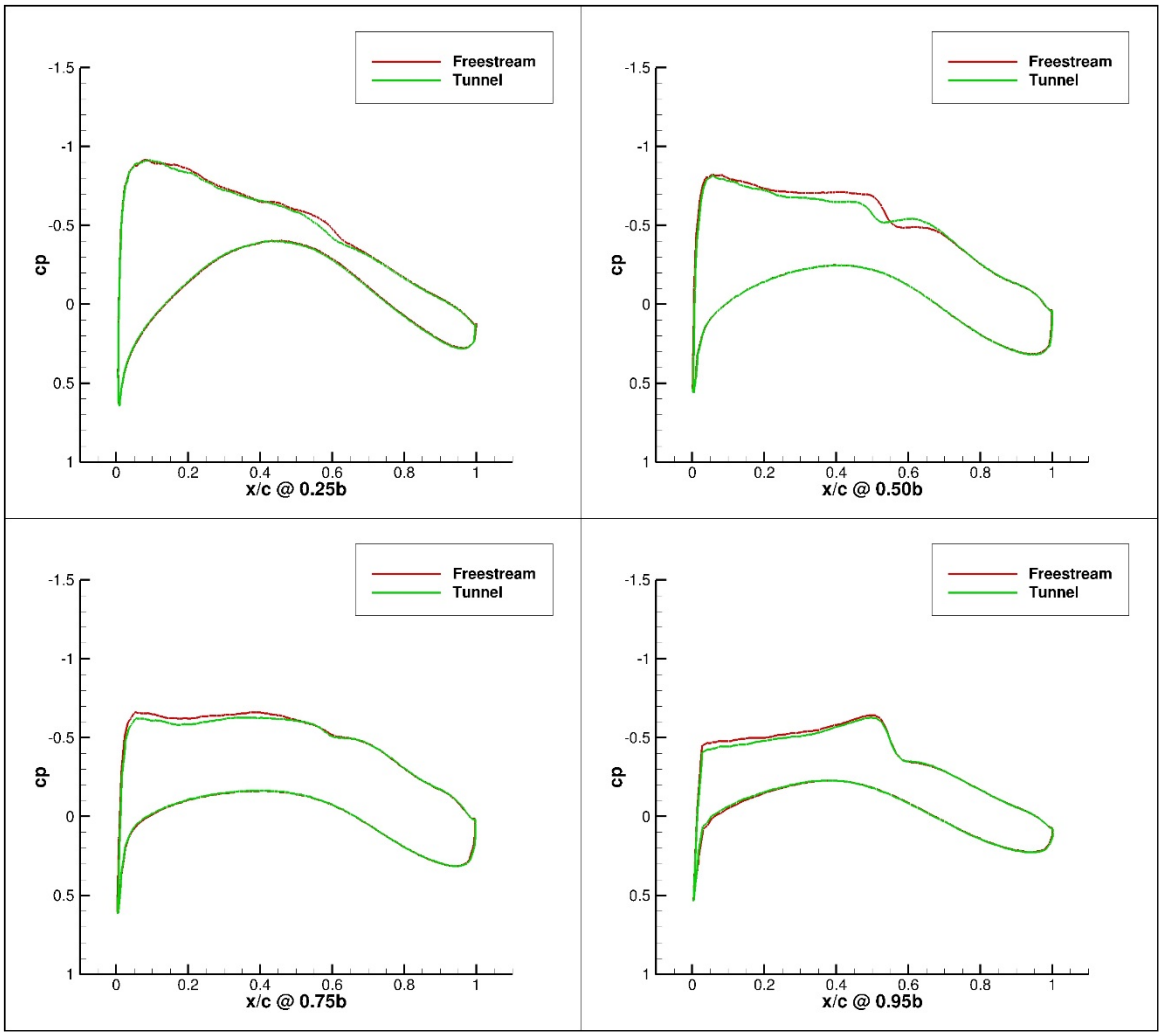

Figure 188. Configuration 1, 2 deg Angle of Attack Pressure Coefficient Contours for Free-stream and Wind Tunnel Simulations

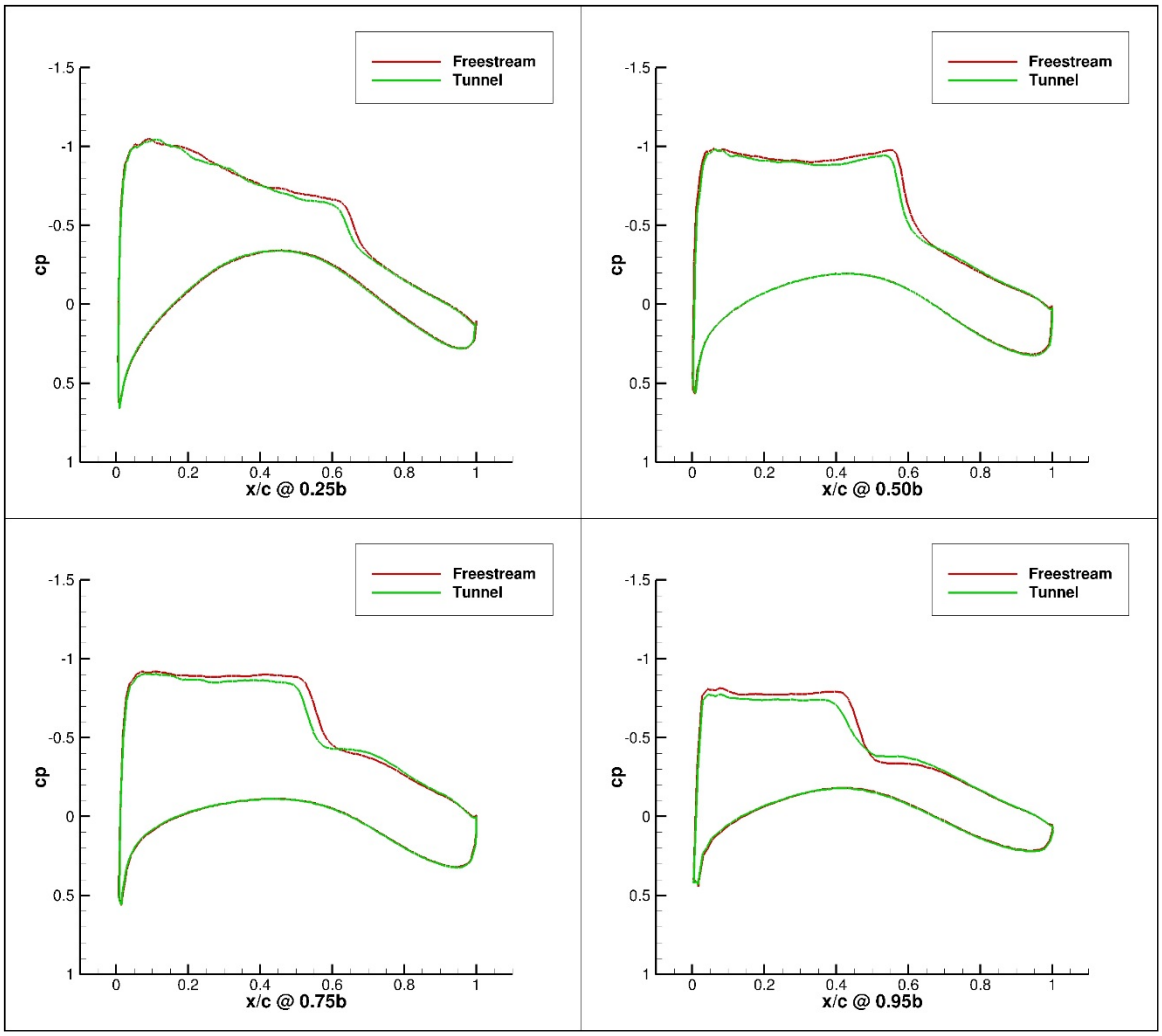

Figure 189. Configuration 1, 3 deg Angle of Attack Pressure Coefficient Contours for Free-stream and Wind Tunnel Simulations

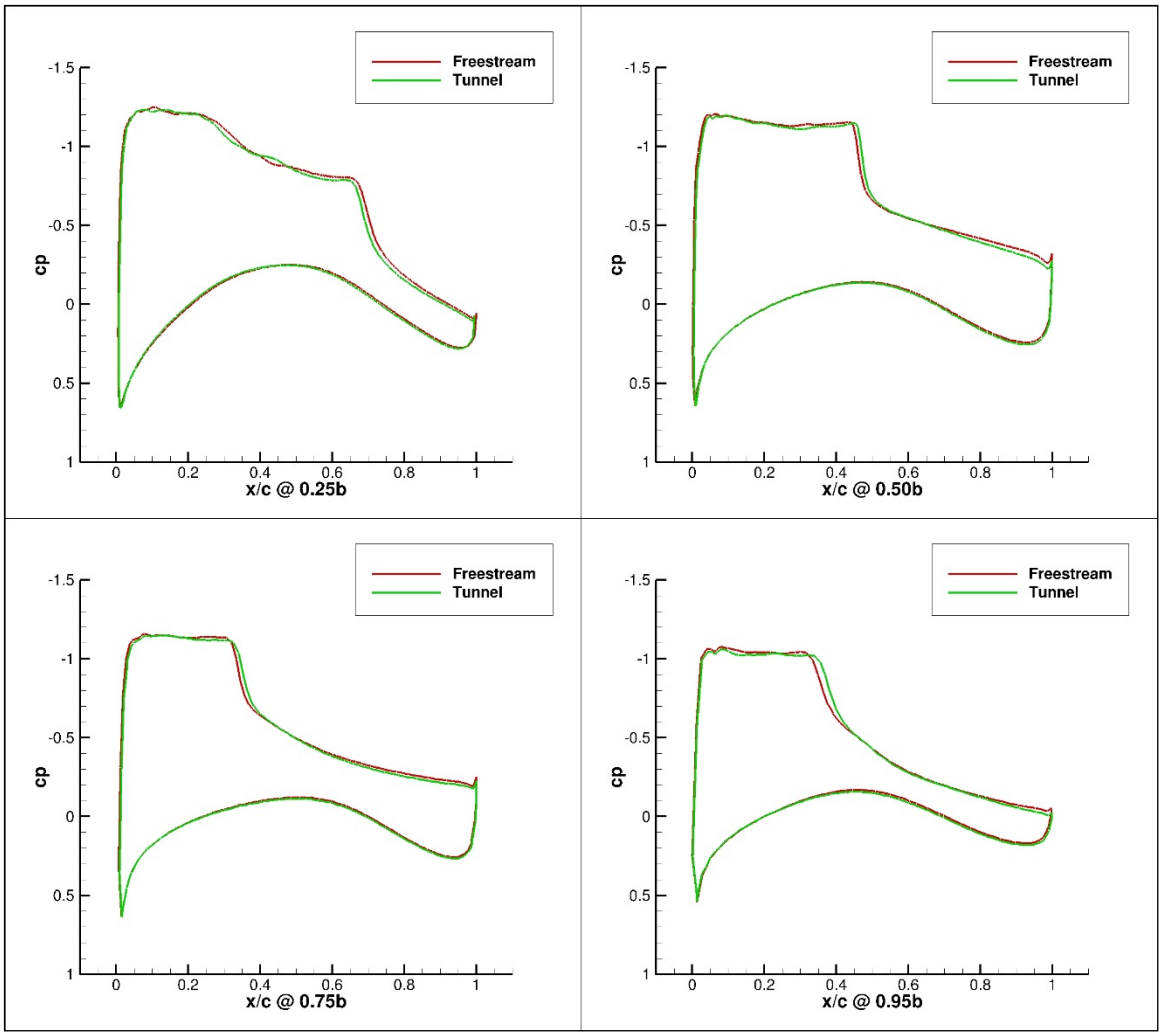

Figure 190. Configuration 1, 4 deg Angle of Attack Pressure Coefficient Contours for Free-stream and Wind Tunnel Simulations

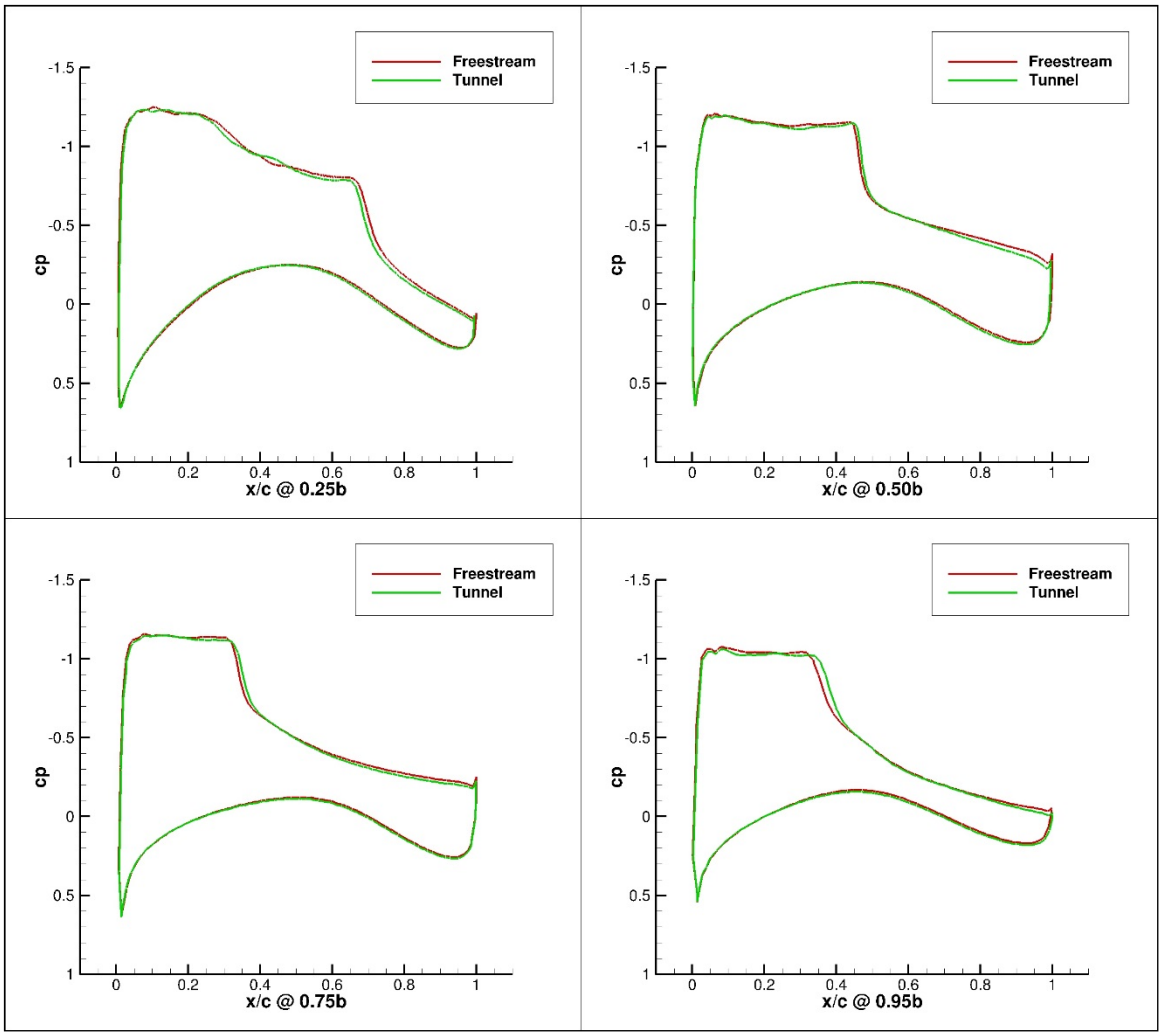

Figure 191. Configuration 1, 5 deg Angle of Attack Pressure Coefficient Contours for Free-stream and Wind Tunnel Simulations

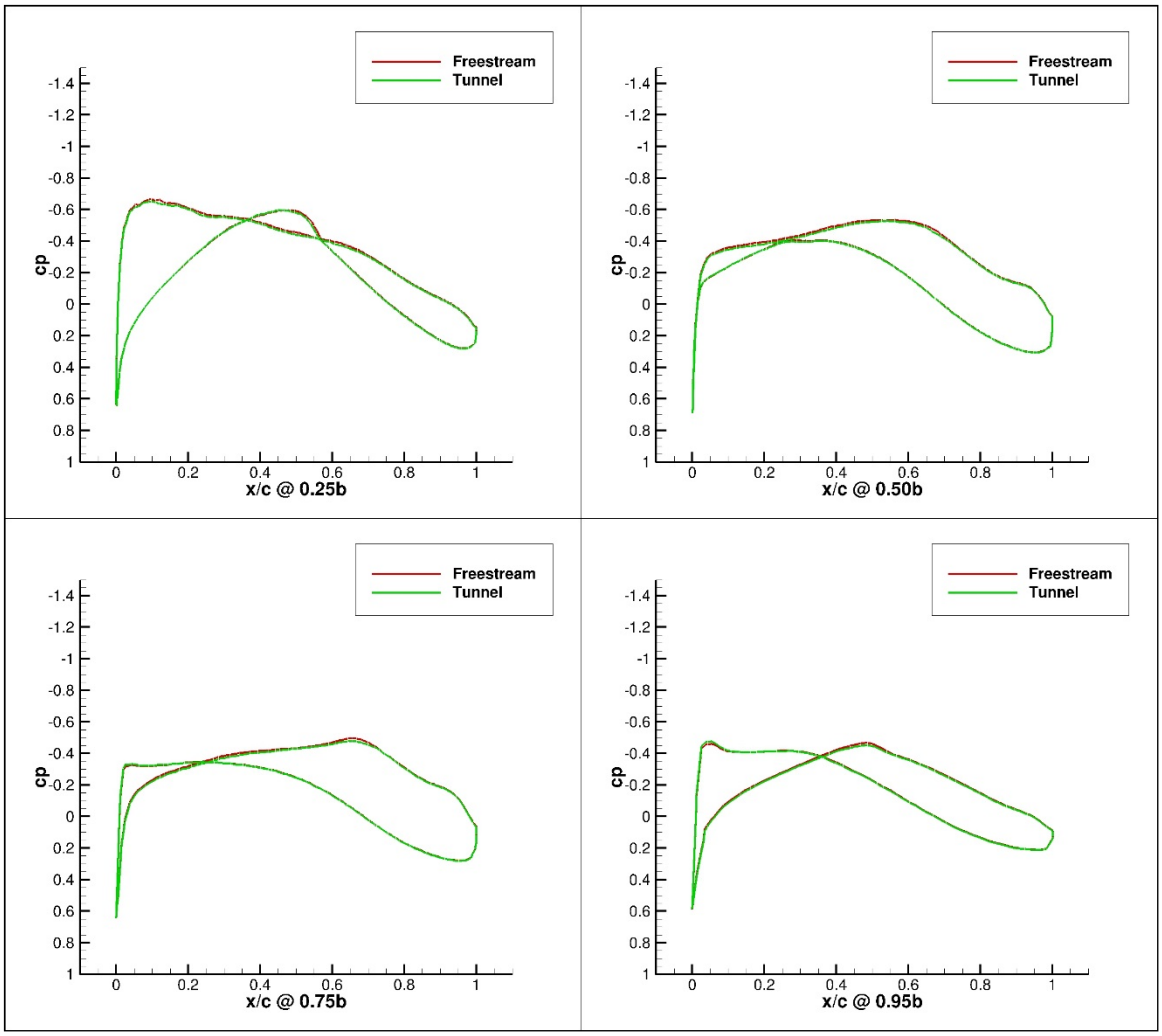

Figure 192. Configuration 1.1, 0 deg Angle of Attack Pressure Coefficient Contours for Free-stream and Wind Tunnel Simulations

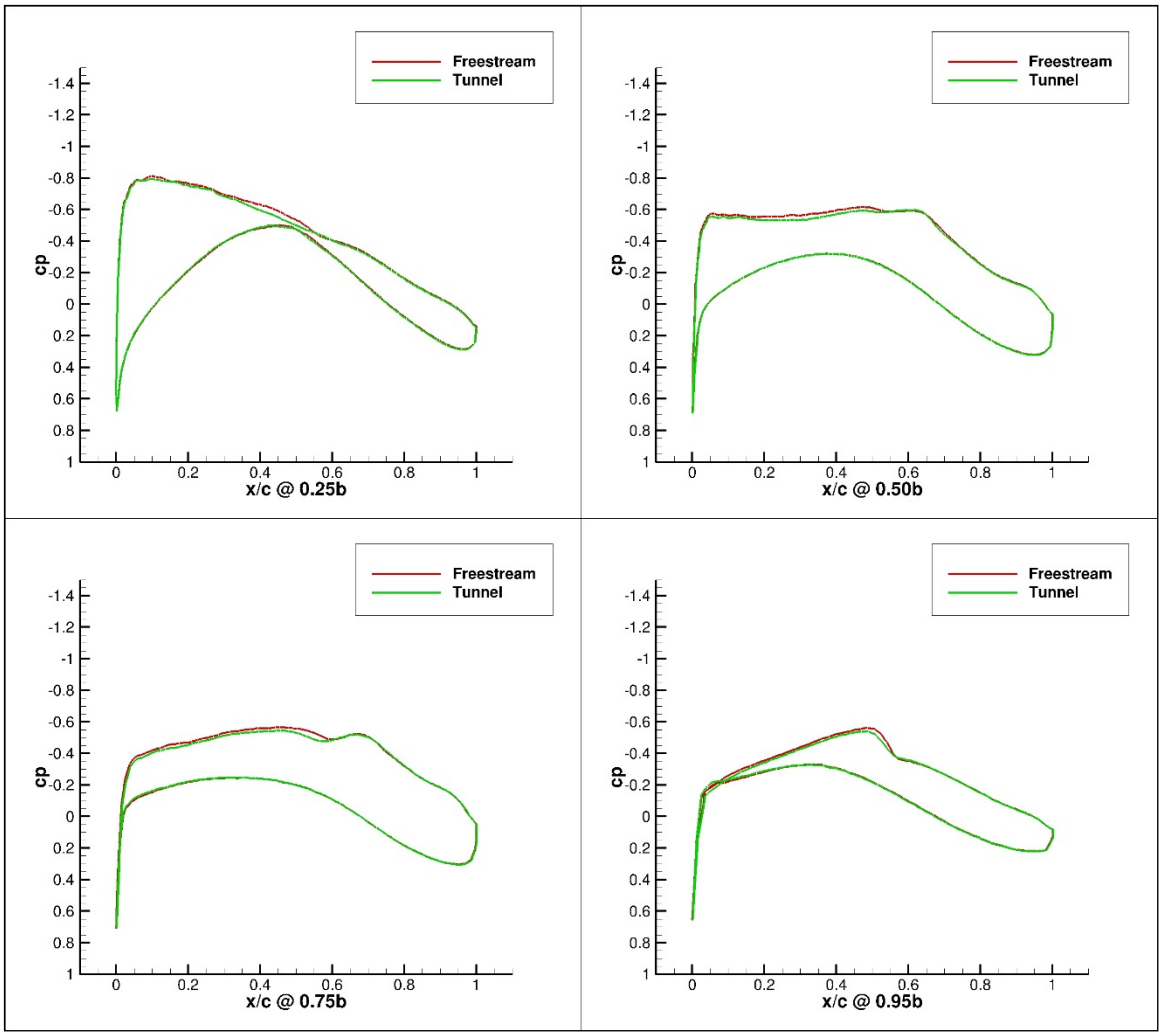

Figure 193. Configuration 1.1, 1 deg Angle of Attack Pressure Coefficient Contours for Free-stream and Wind Tunnel Simulations

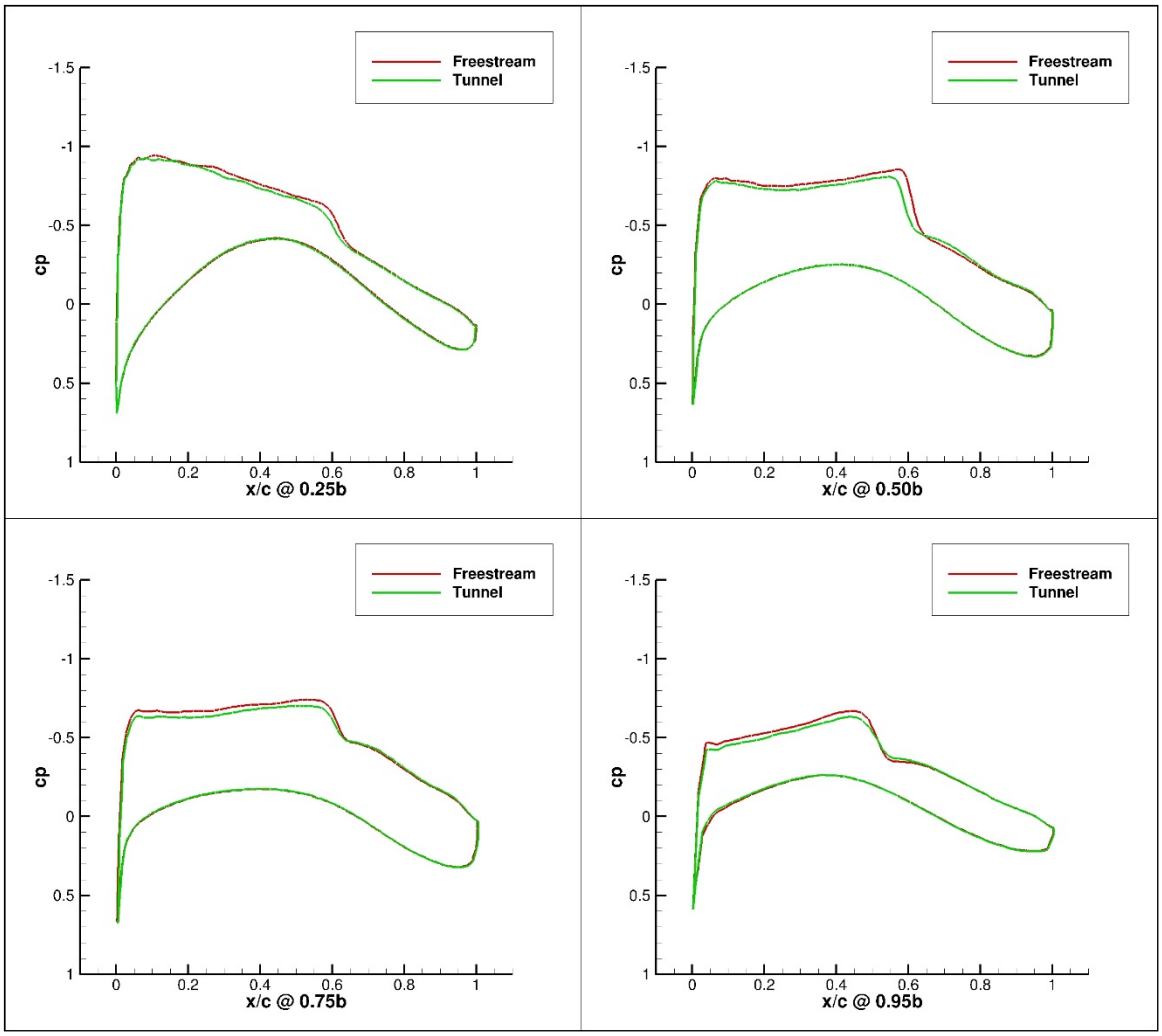

Figure 194. Configuration 1.1, 2 deg Angle of Attack Pressure Coefficient Contours for Free-stream and Wind Tunnel Simulations

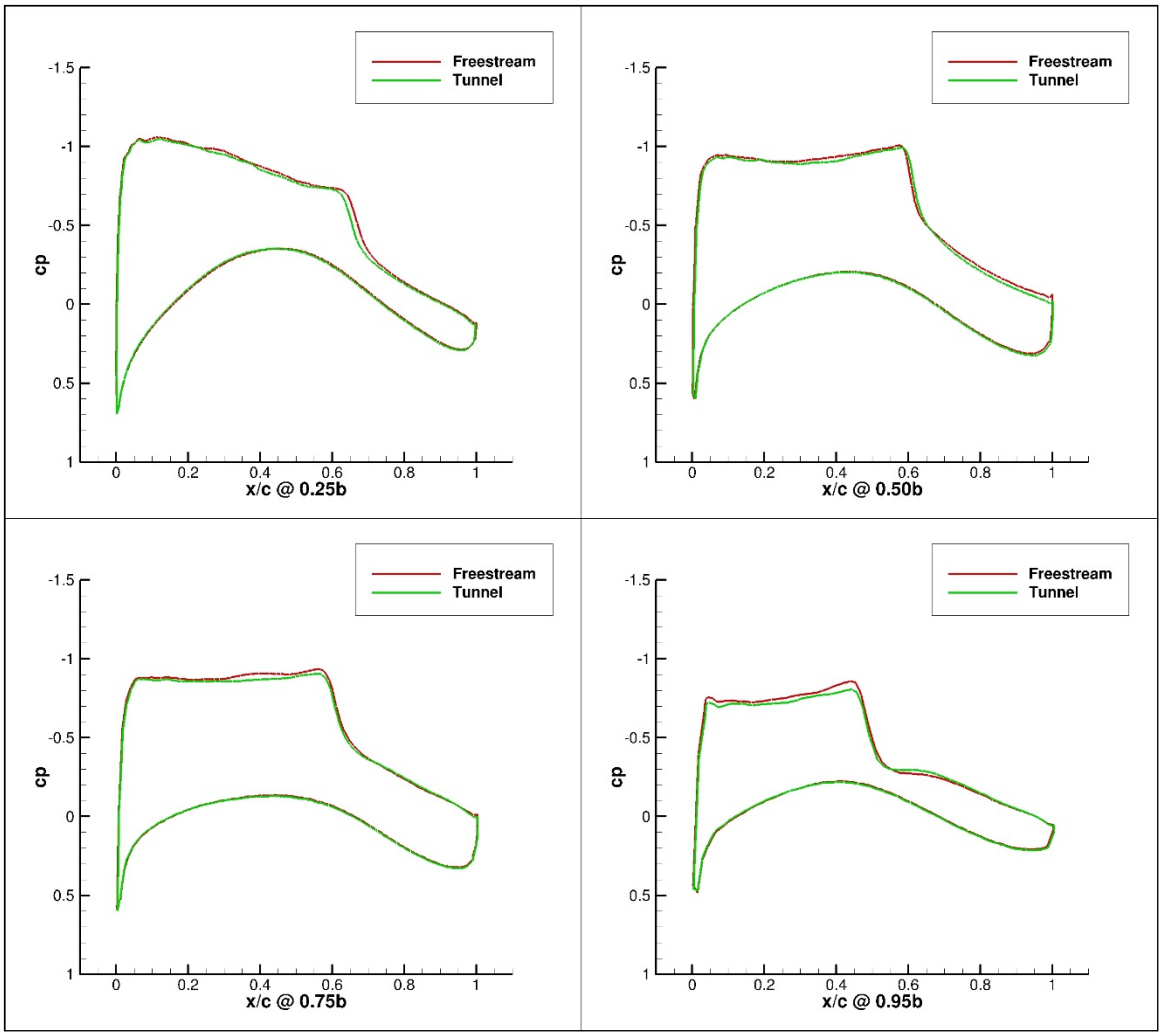

Figure 195. Configuration 1.1, 3 deg Angle of Attack Pressure Coefficient Contours for Free-stream and Wind Tunnel Simulations

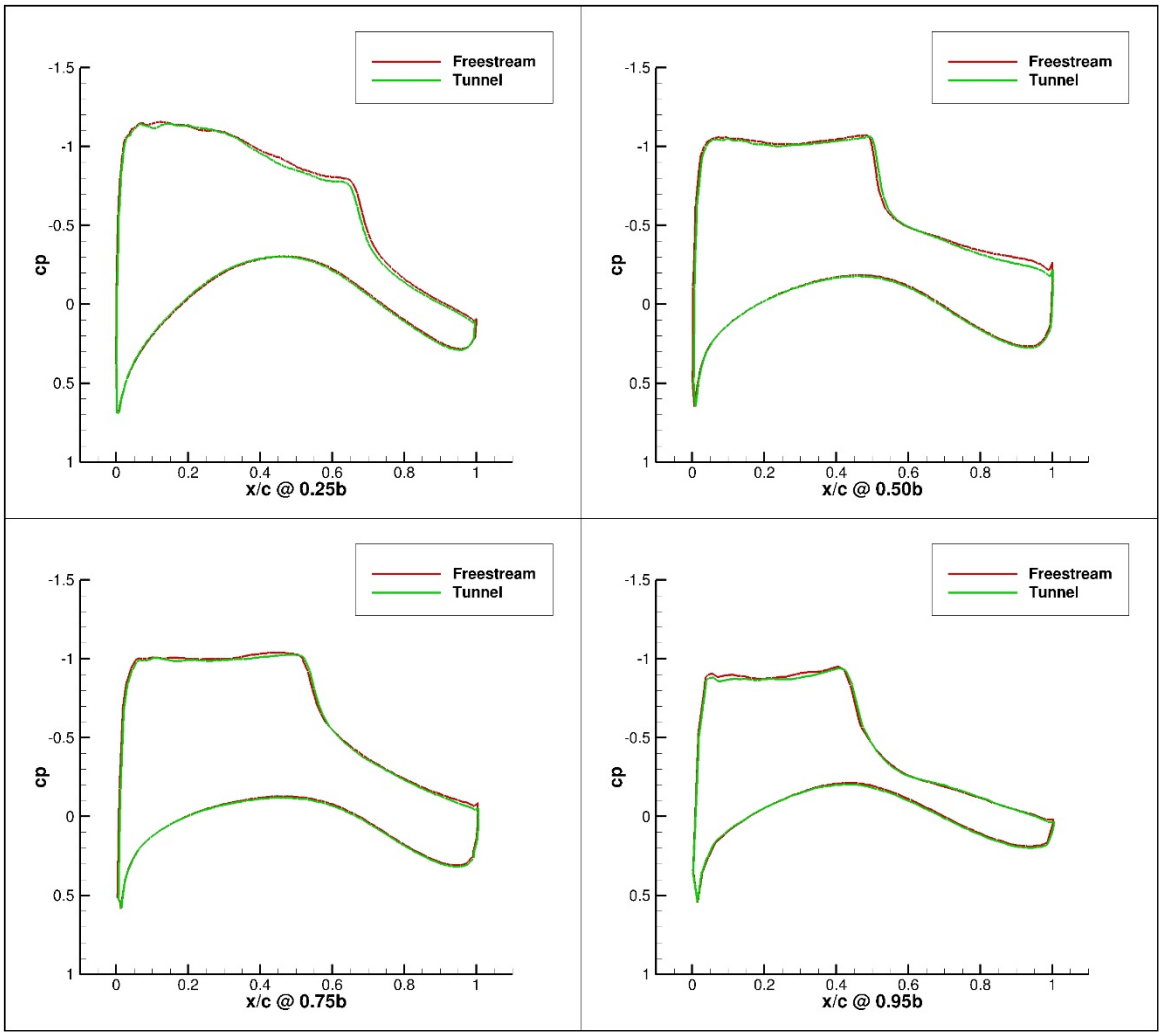

Figure 196. Configuration 1.1, 4 deg Angle of Attack Pressure Coefficient Contours for Free-stream and Wind Tunnel Simulations

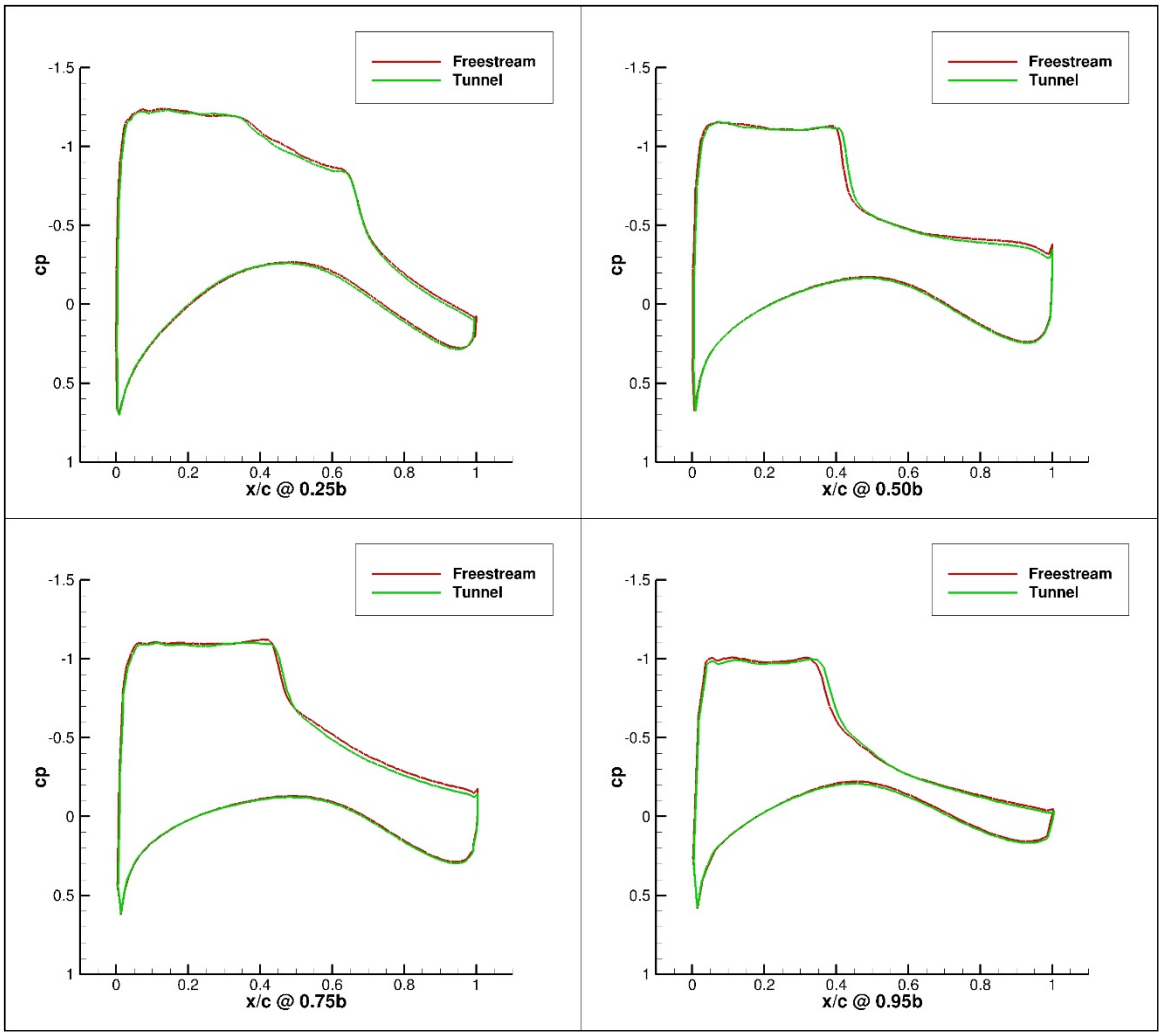

Figure 197. Configuration 1.1, 5 deg Angle of Attack Pressure Coefficient Contours for Free-stream and Wind Tunnel Simulations

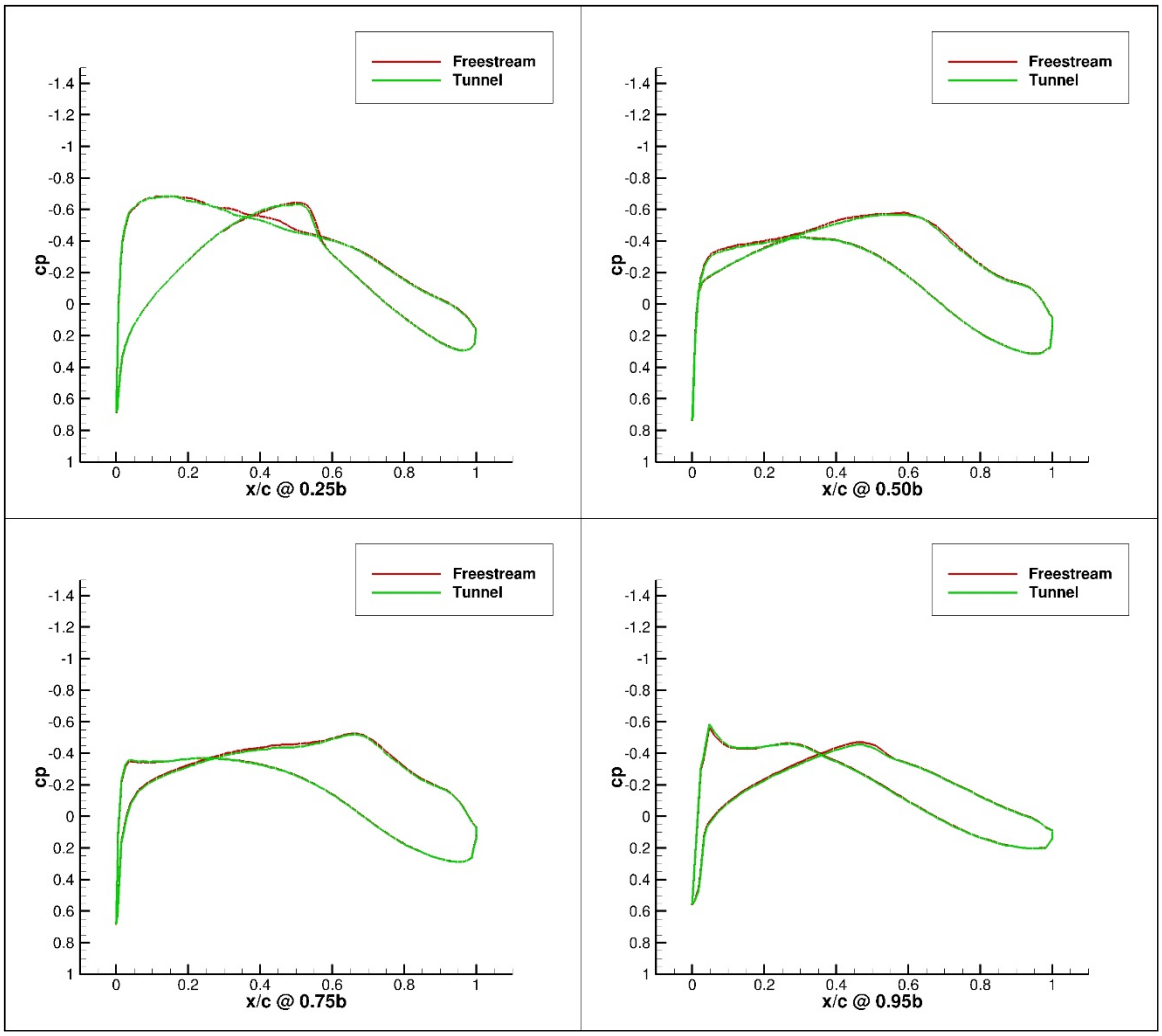

Figure 198. Configuration 1.2, 0 deg Angle of Attack Pressure Coefficient Contours for Free-stream and Wind Tunnel Simulations

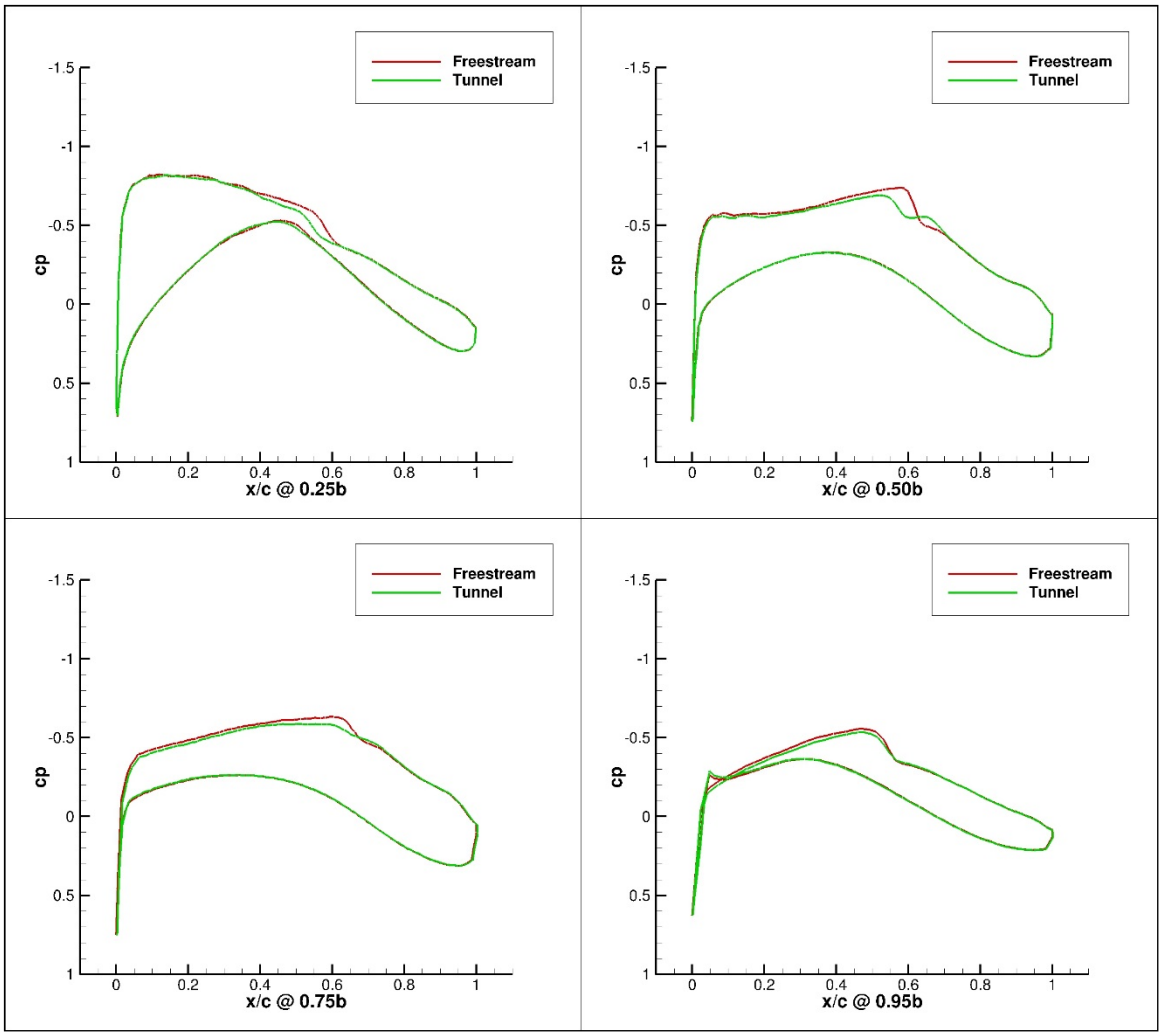

Figure 199. Configuration 1.2, 1 deg Angle of Attack Pressure Coefficient Contours for Free-stream and Wind Tunnel Simulations

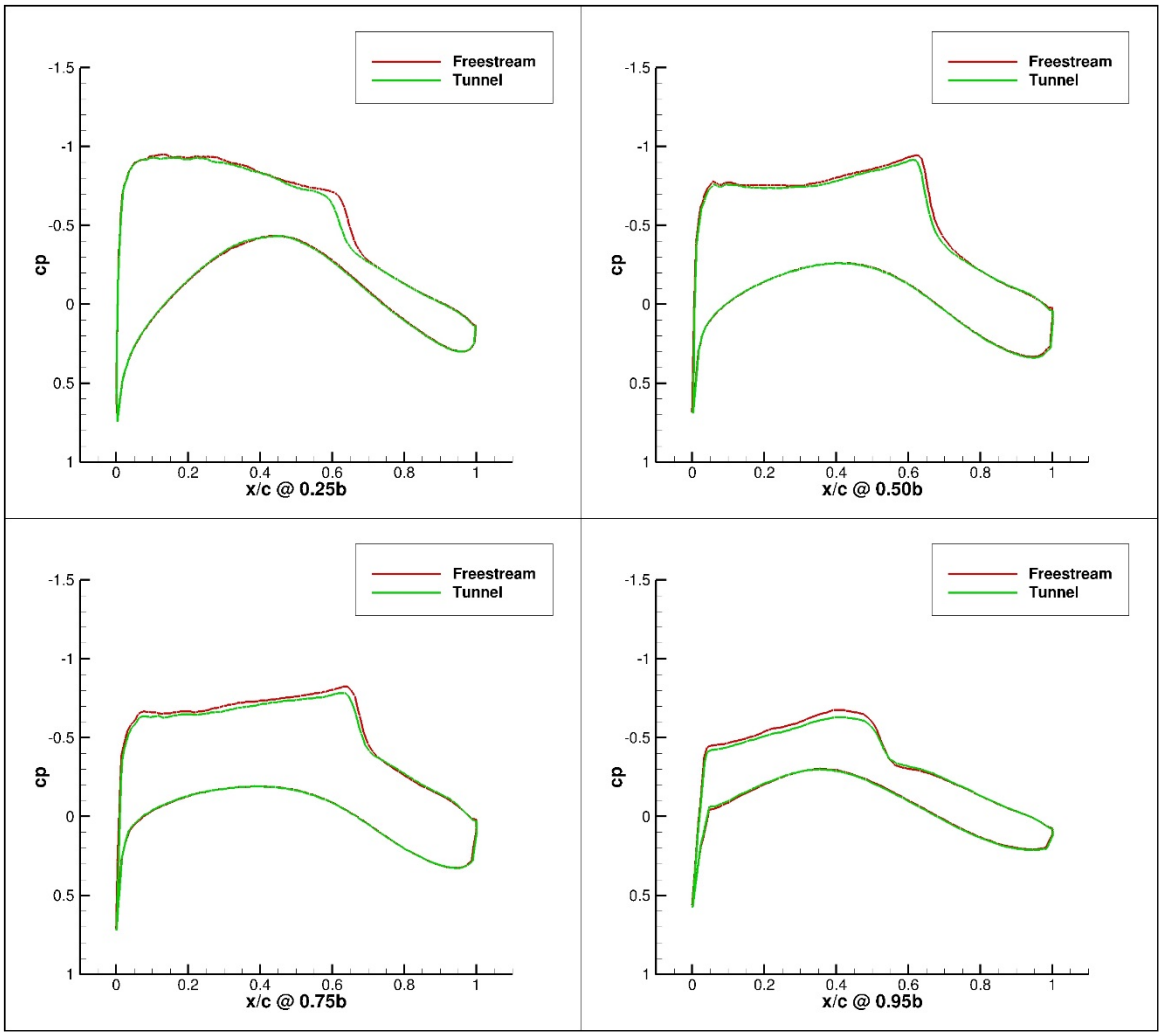

Figure 200. Configuration 1.2, 2 deg Angle of Attack Pressure Coefficient Contours for Free-stream and Wind Tunnel Simulations

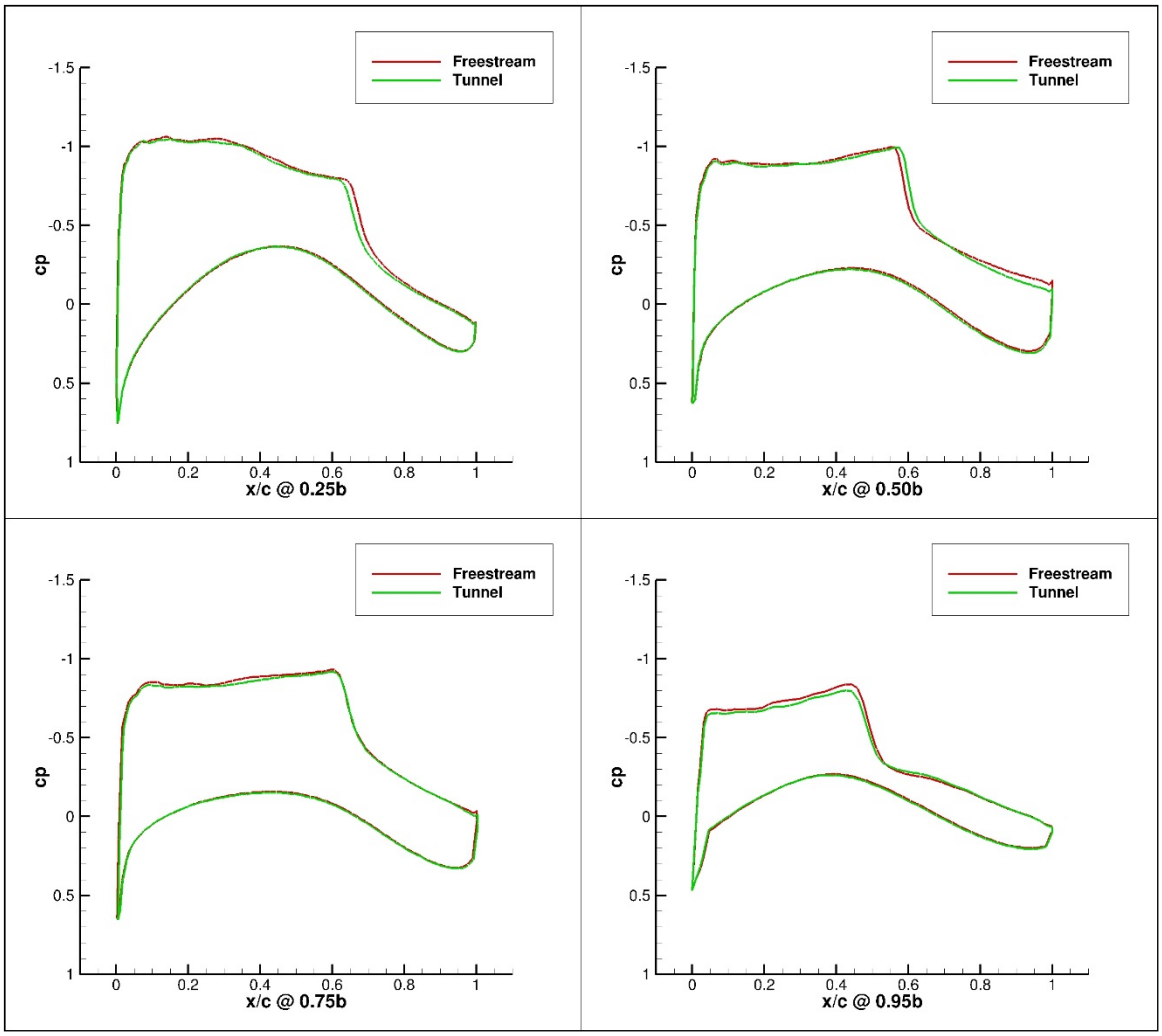

Figure 201. Configuration 1.2, 3 deg Angle of Attack Pressure Coefficient Contours for Free-stream and Wind Tunnel Simulations

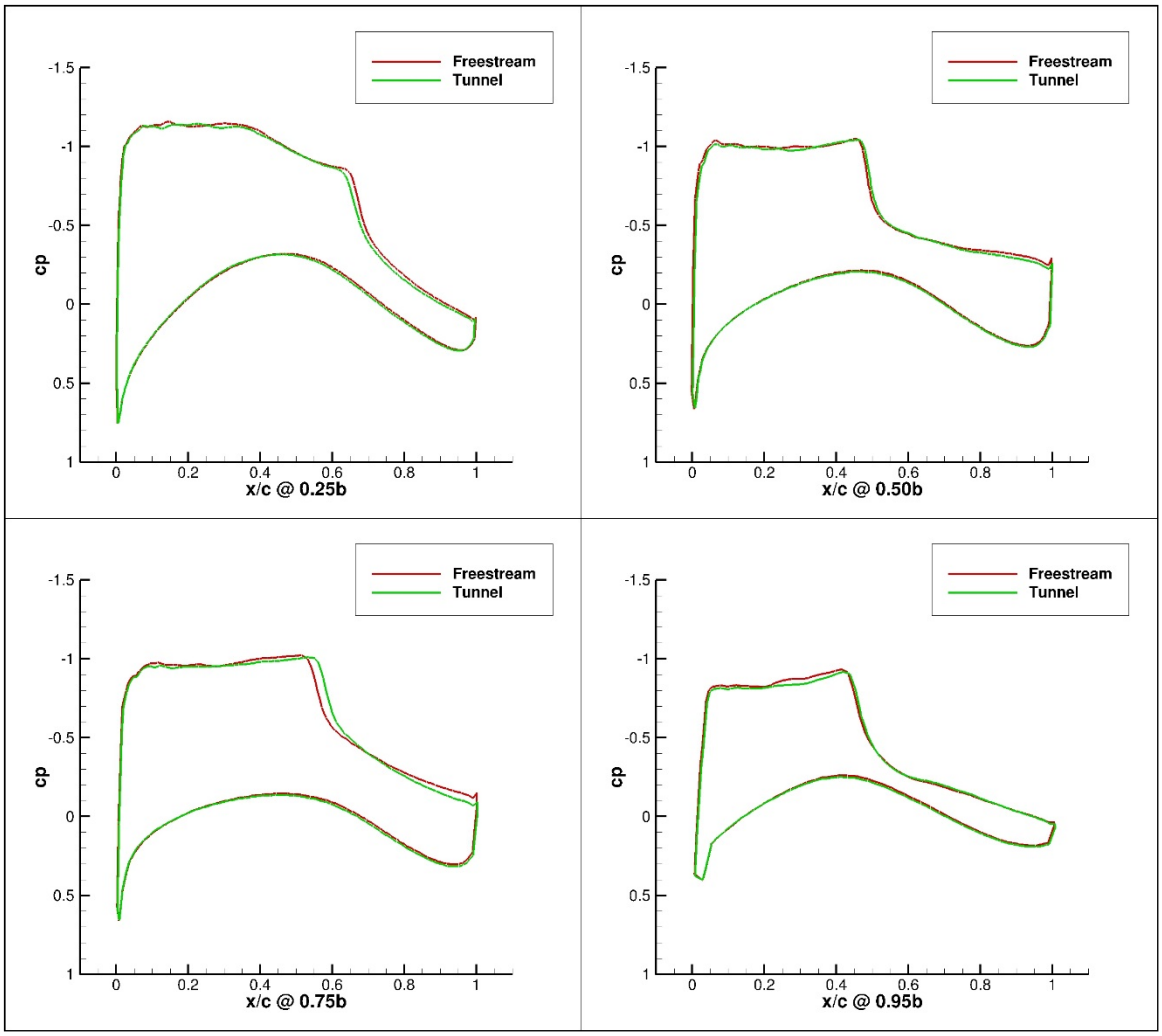

Figure 202. Configuration 1.2, 4 deg Angle of Attack Pressure Coefficient Contours for Free-stream and Wind Tunnel Simulations

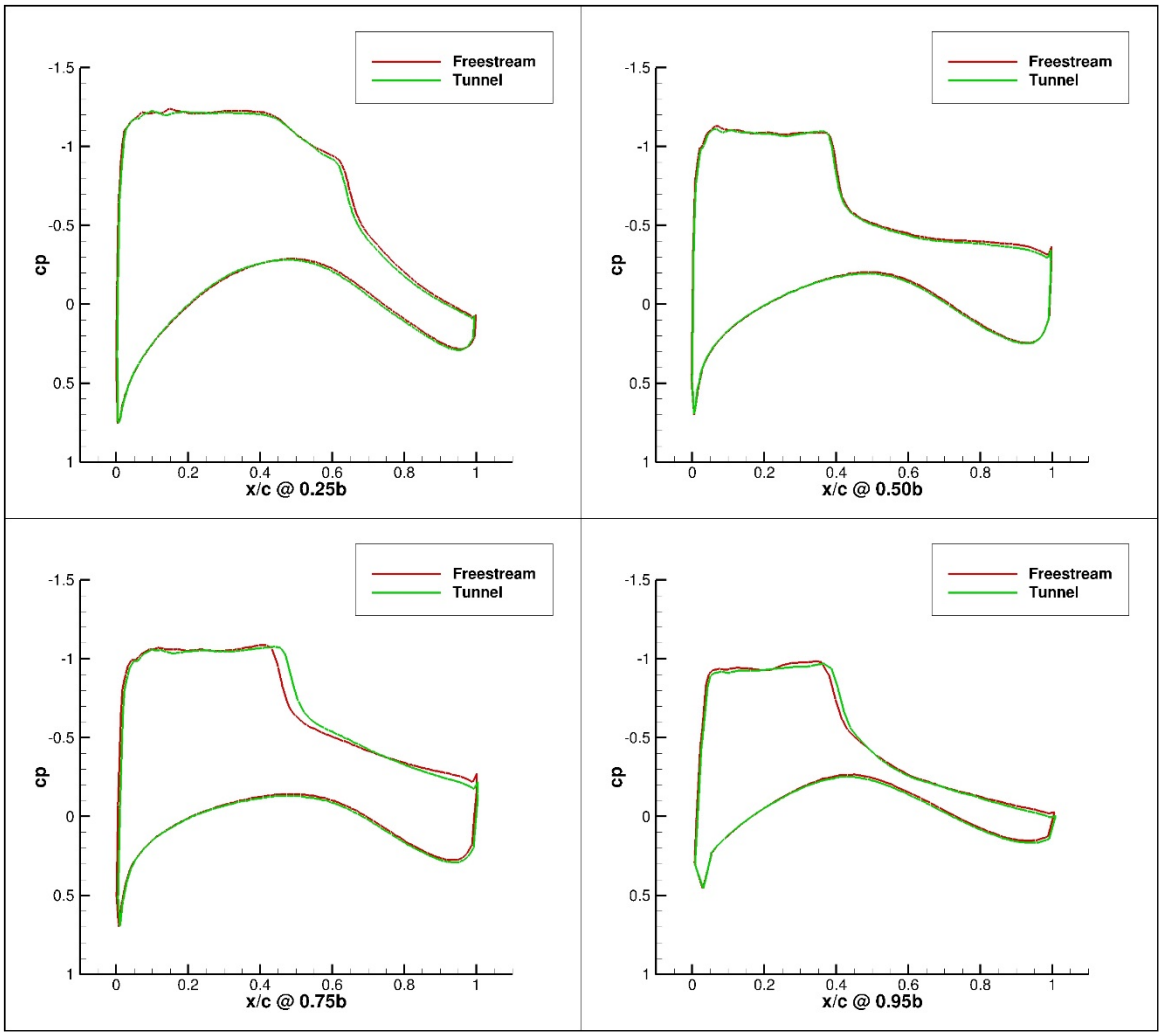

Figure 203. Configuration 1.2, 5 deg Angle of Attack Pressure Coefficient Contours for Free-stream and Wind Tunnel Simulations

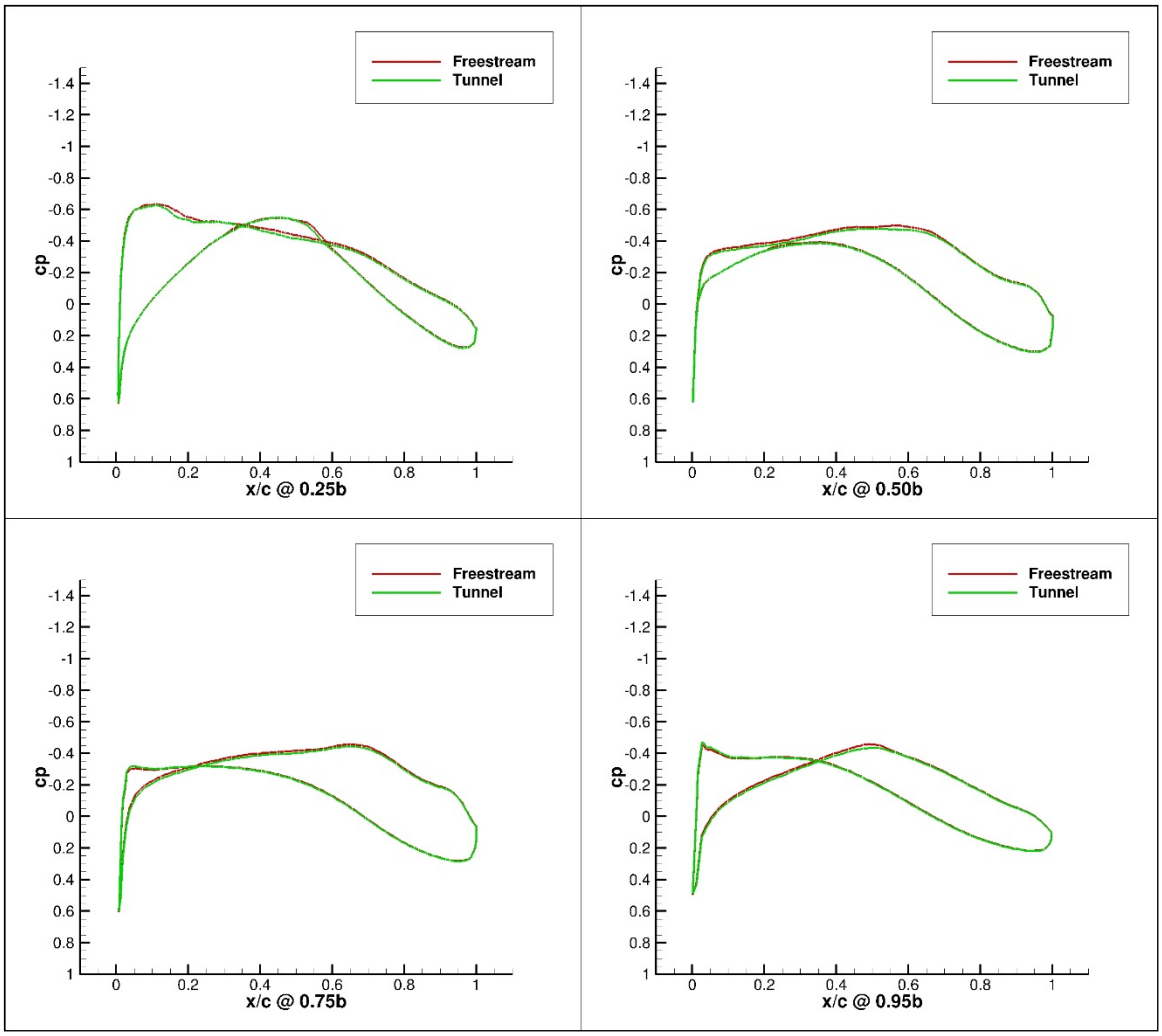

Figure 204. Configuration 2, 0 deg Angle of Attack Pressure Coefficient Contours for Free-stream and Wind Tunnel Simulations

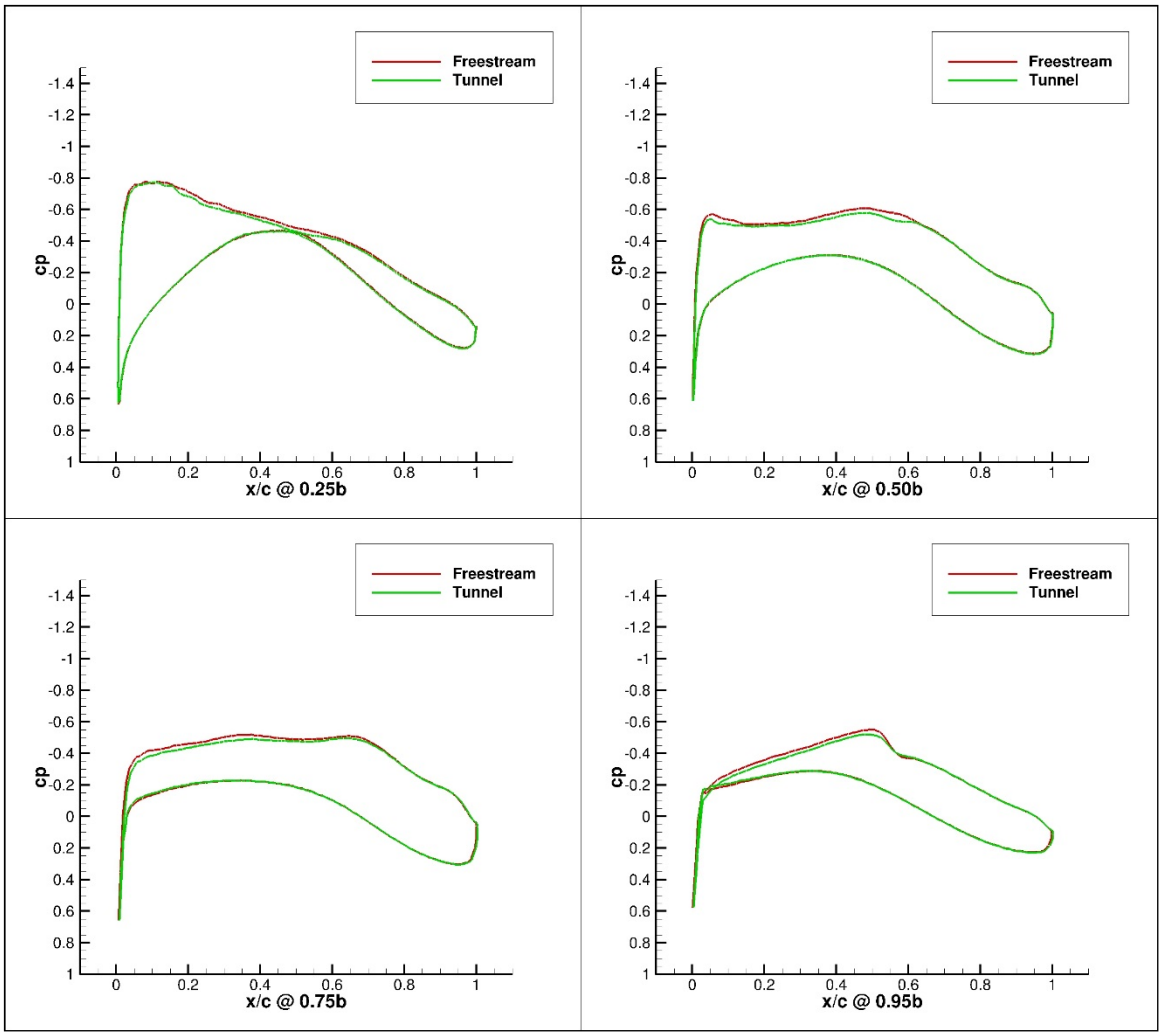

Figure 205. Configuration 2, 1 deg Angle of Attack Pressure Coefficient Contours for Free-stream and Wind Tunnel Simulations

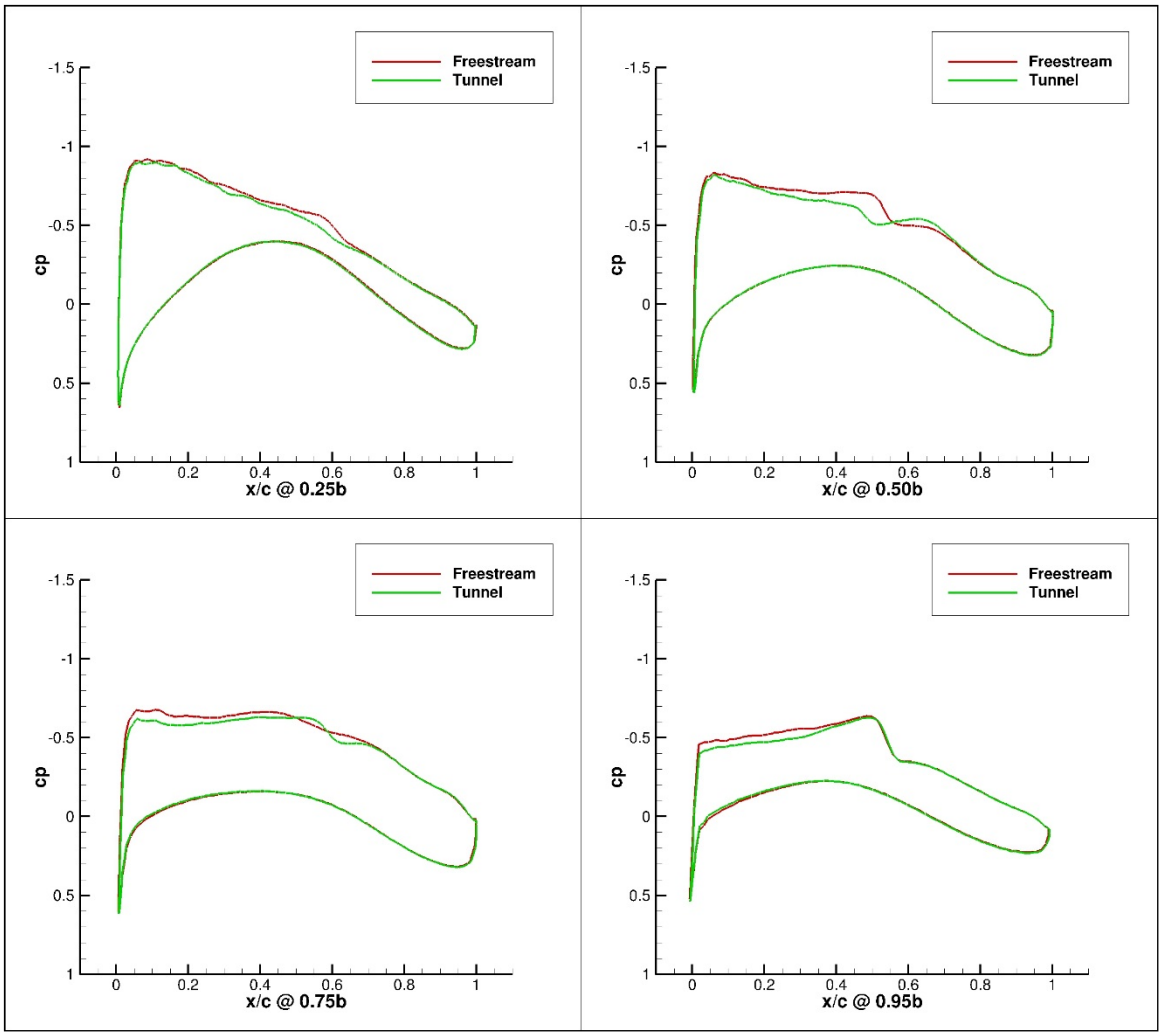

Figure 206. Configuration 2, 2 deg Angle of Attack Pressure Coefficient Contours for Free-stream and Wind Tunnel Simulations

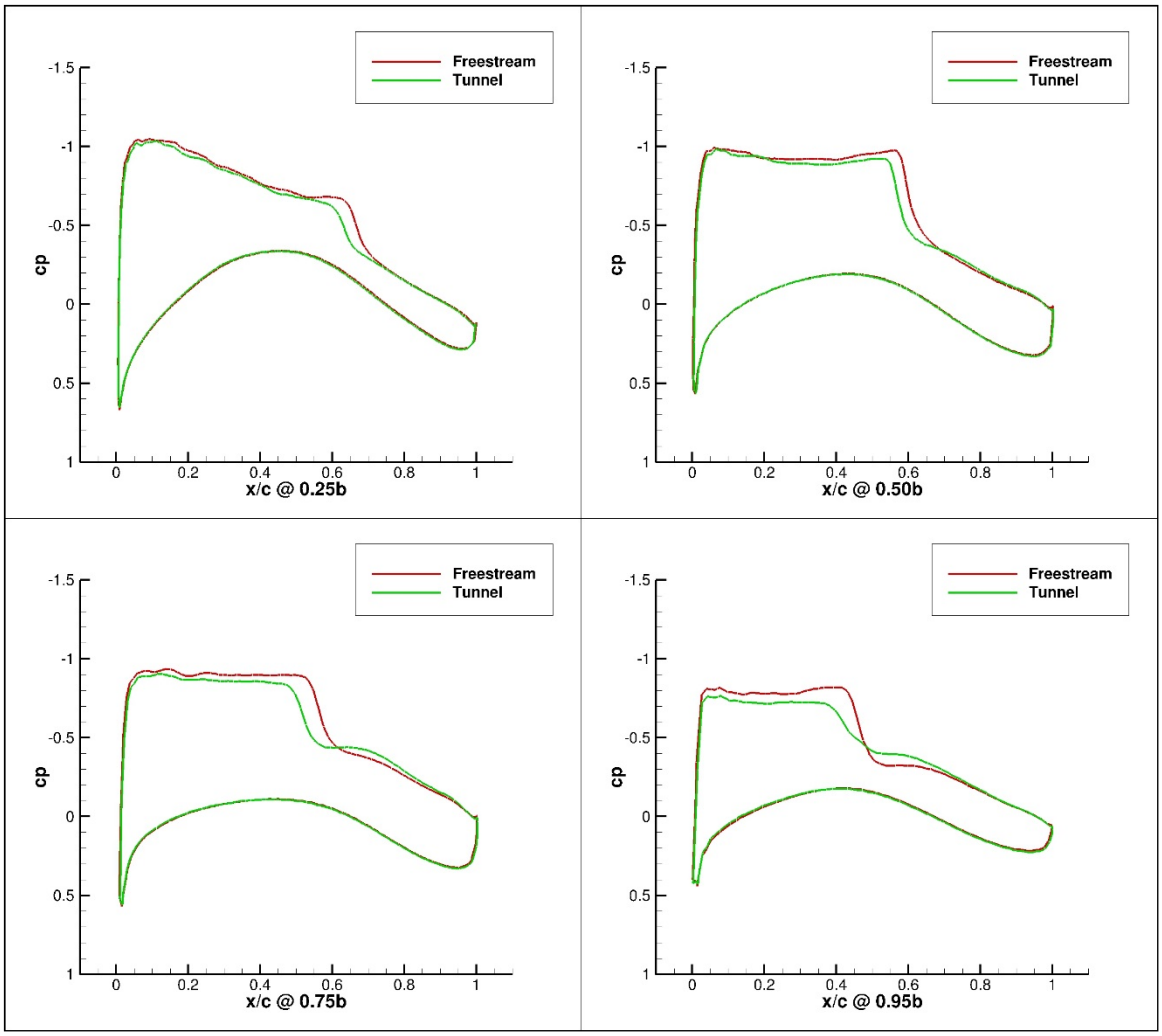

Figure 207. Configuration 2, 3 deg Angle of Attack Pressure Coefficient Contours for Free-stream and Wind Tunnel Simulations

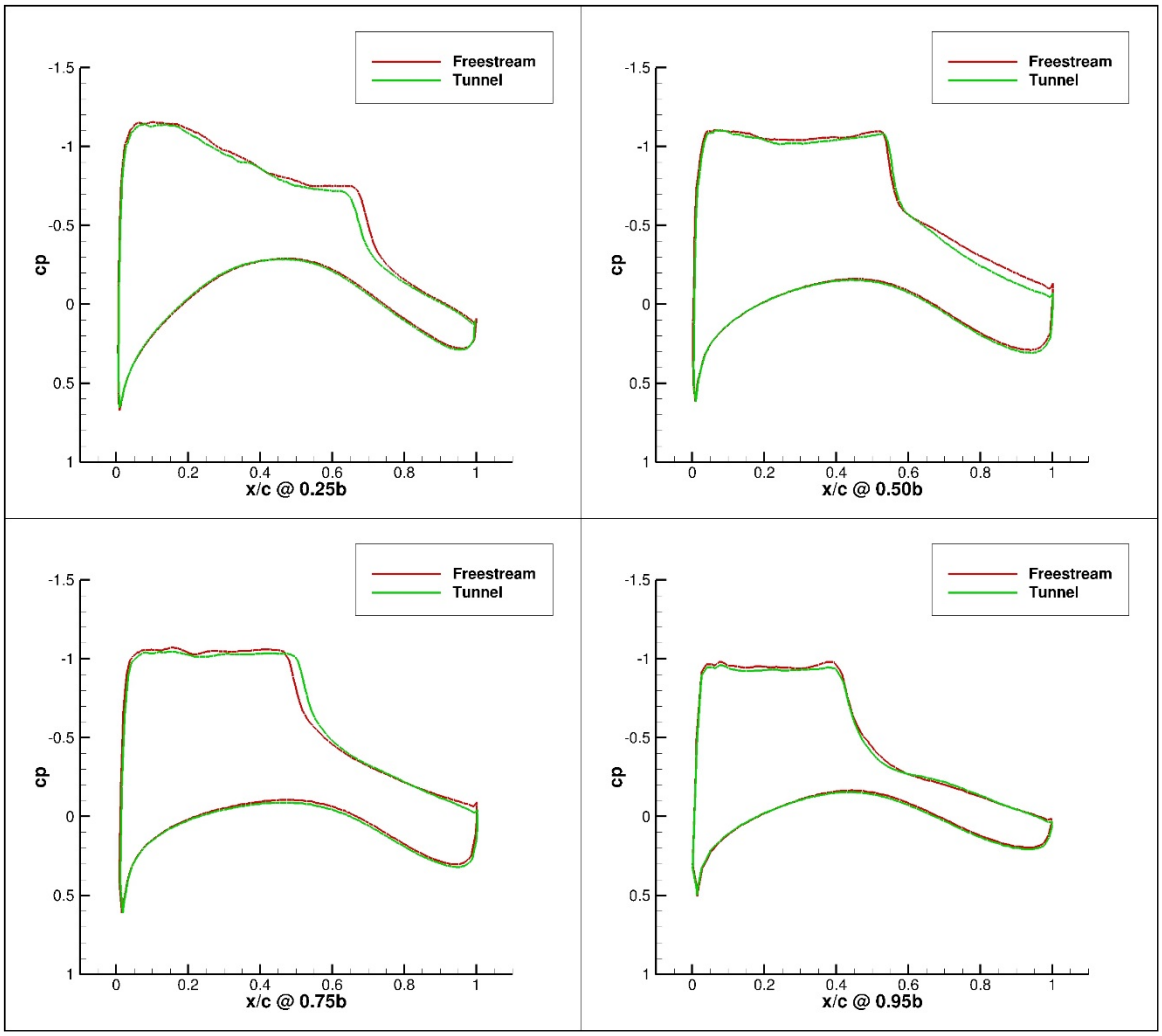

Figure 208. Configuration 2, 4 deg Angle of Attack Pressure Coefficient Contours for Free-stream and Wind Tunnel Simulations

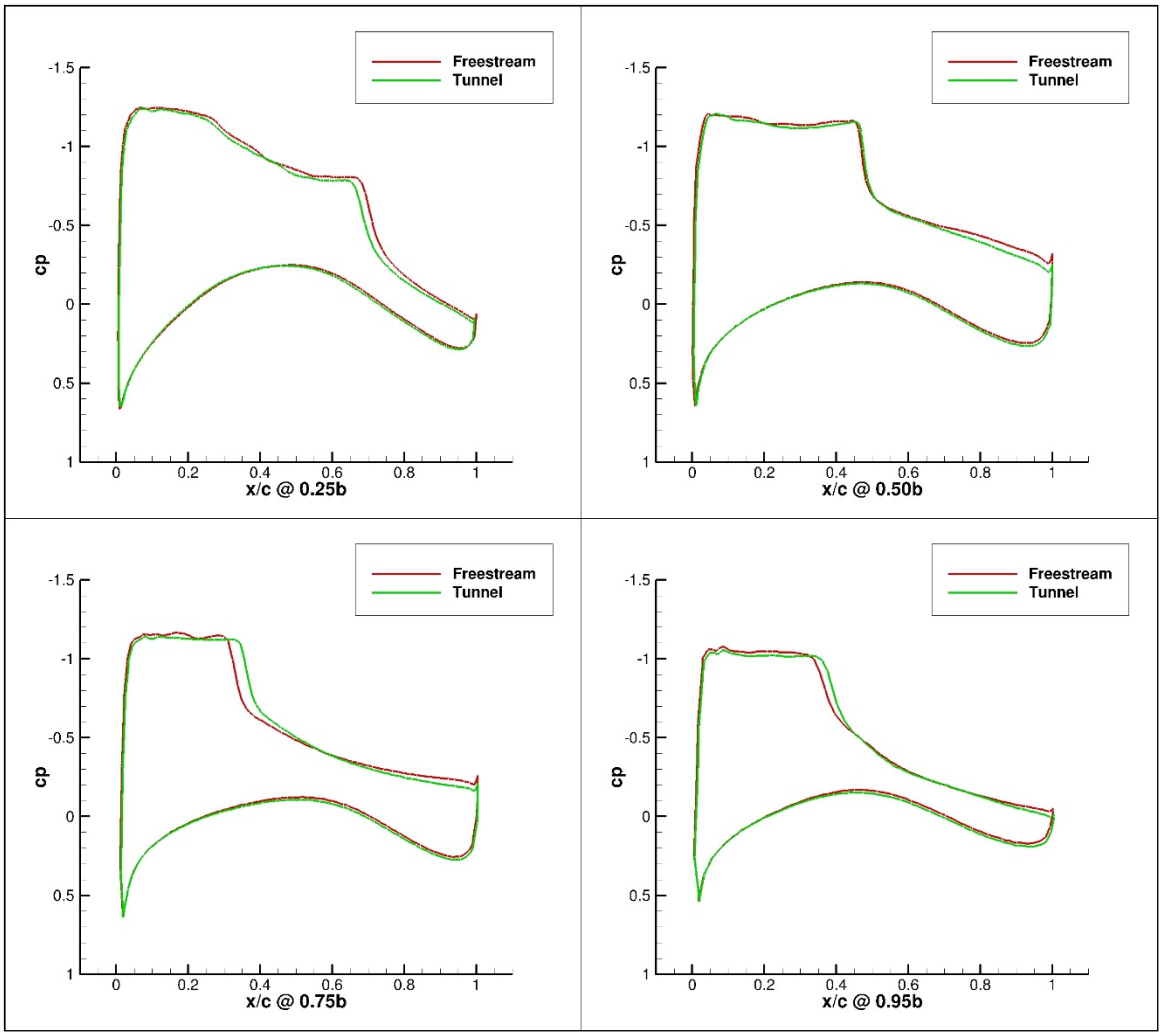

Figure 209. Configuration 2, 5 deg Angle of Attack Pressure Coefficient Contours for Free-stream and Wind Tunnel Simulations

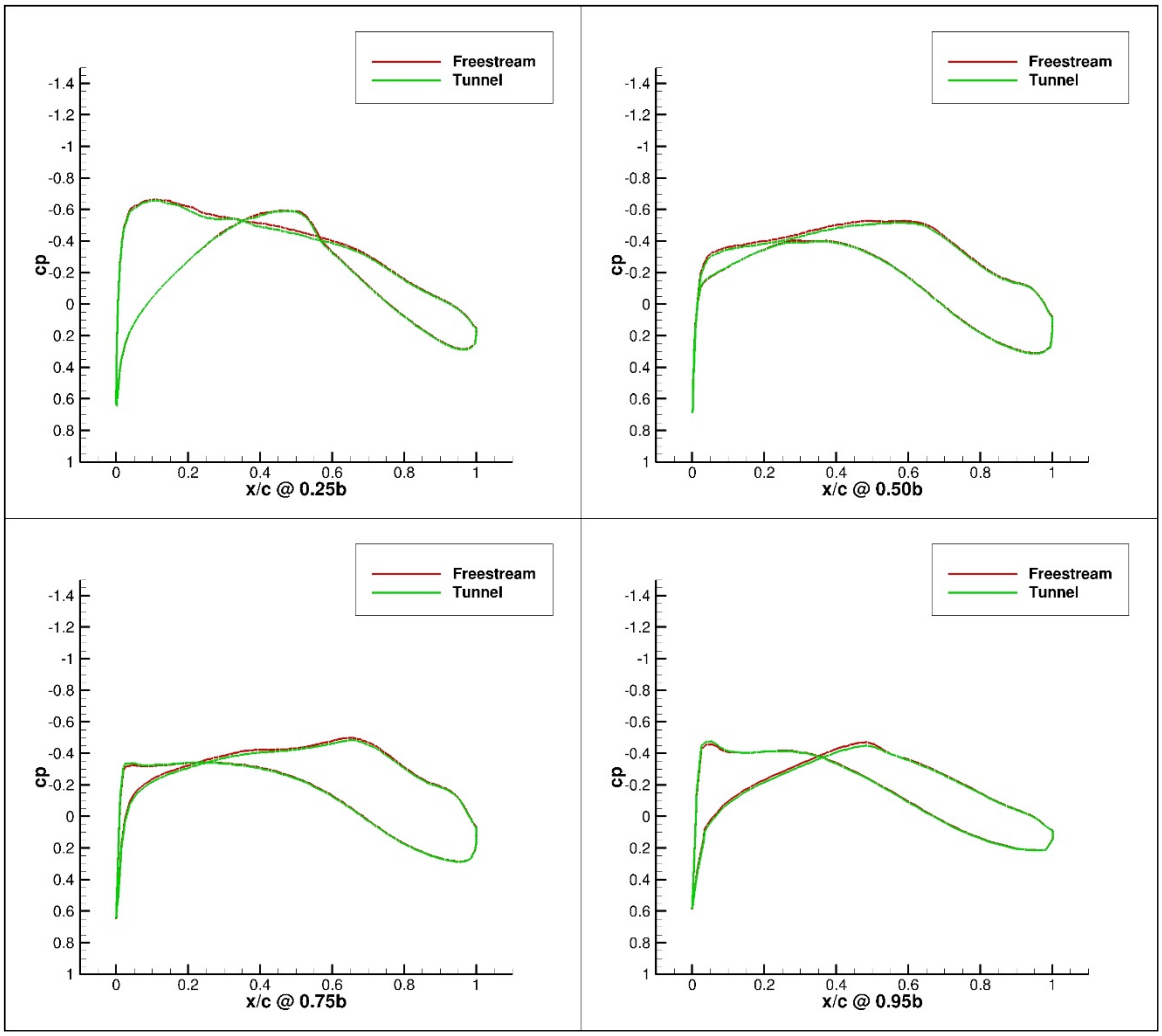

Figure 210. Configuration 2.1, 0 deg Angle of Attack Pressure Coefficient Contours for Free-stream and Wind Tunnel Simulations

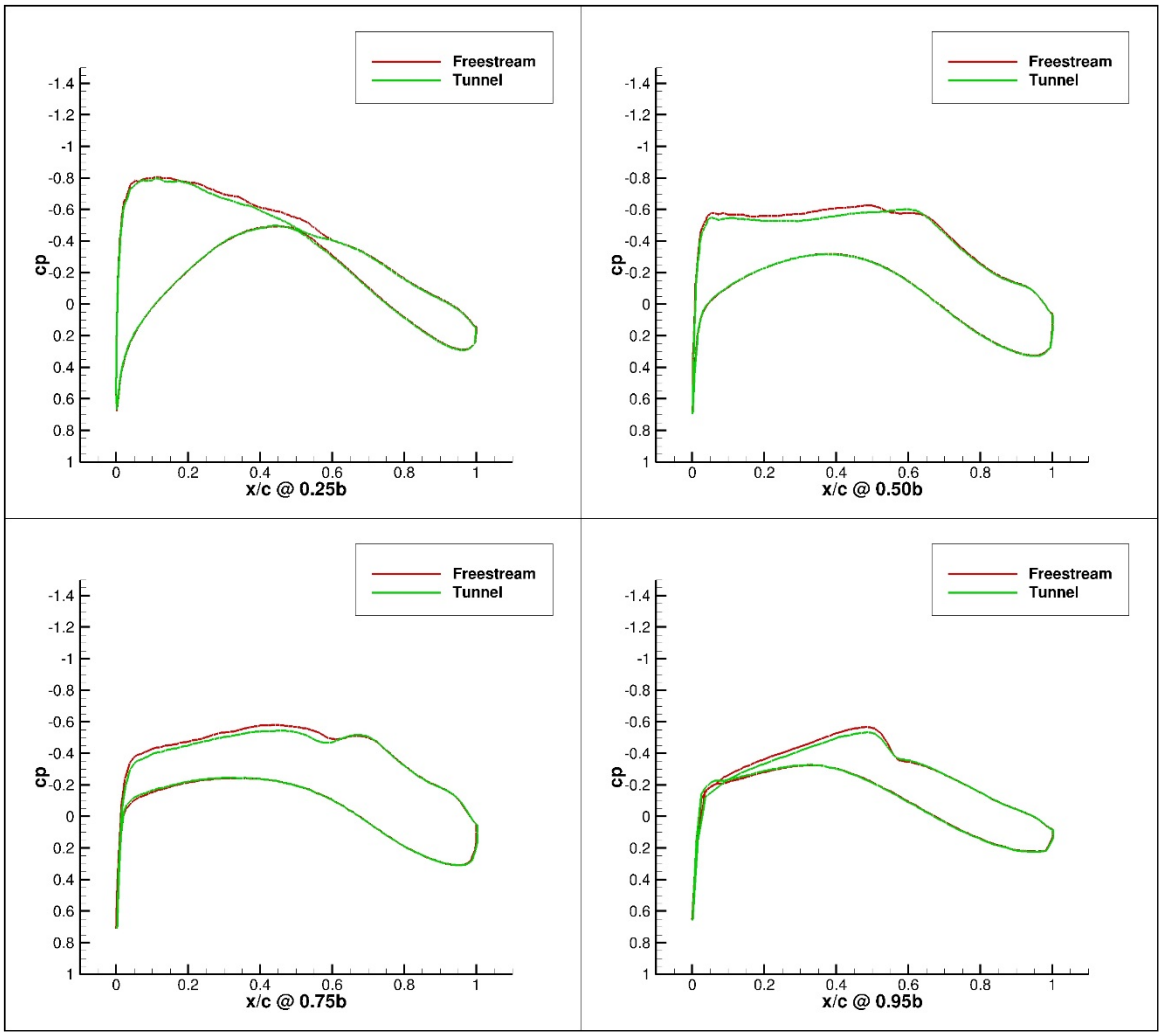

Figure 211. Configuration 2.1, 1 deg Angle of Attack Pressure Coefficient Contours for Free-stream and Wind Tunnel Simulations

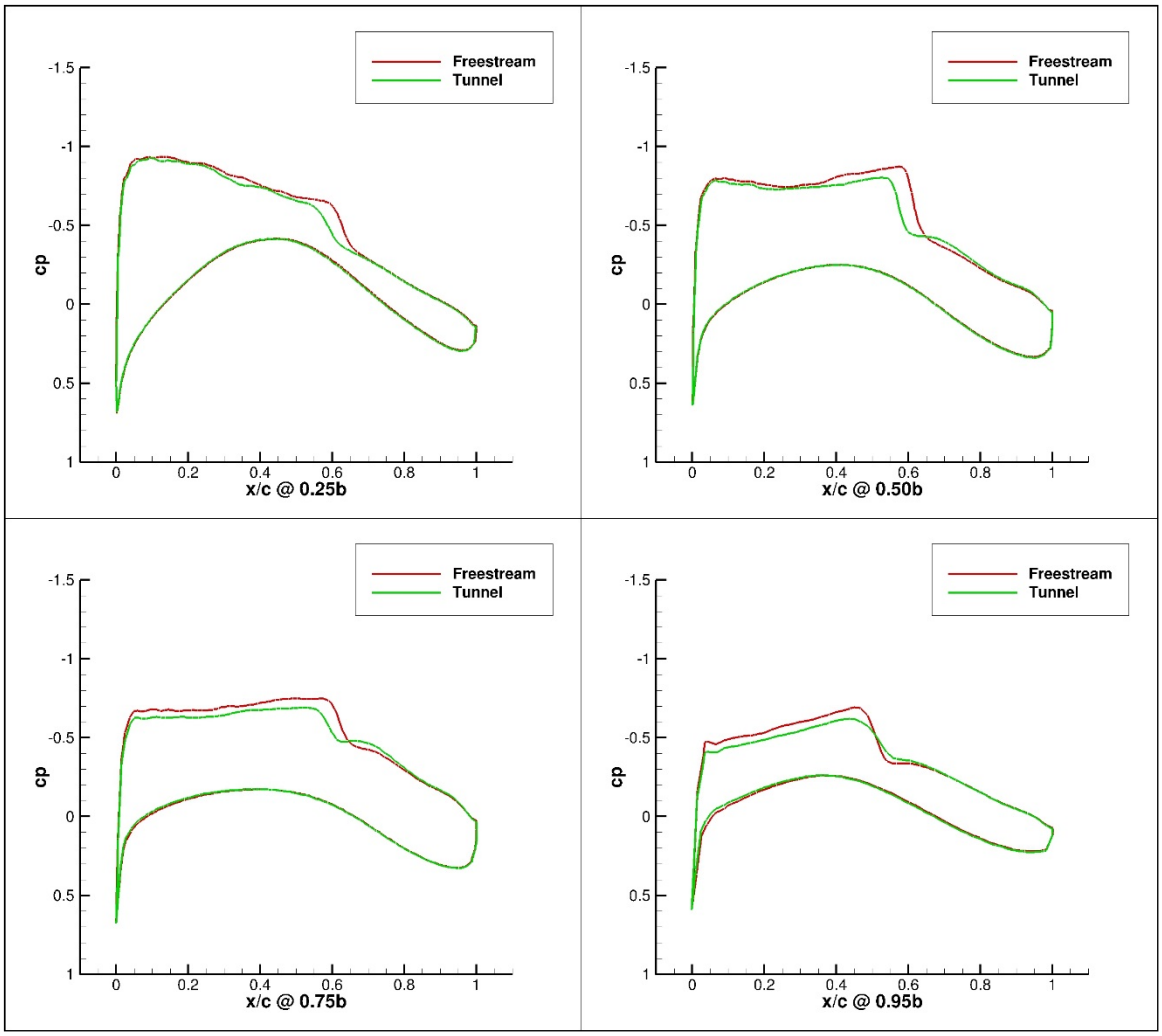

Figure 212. Configuration 2.1, 2 deg Angle of Attack Pressure Coefficient Contours for Free-stream and Wind Tunnel Simulations

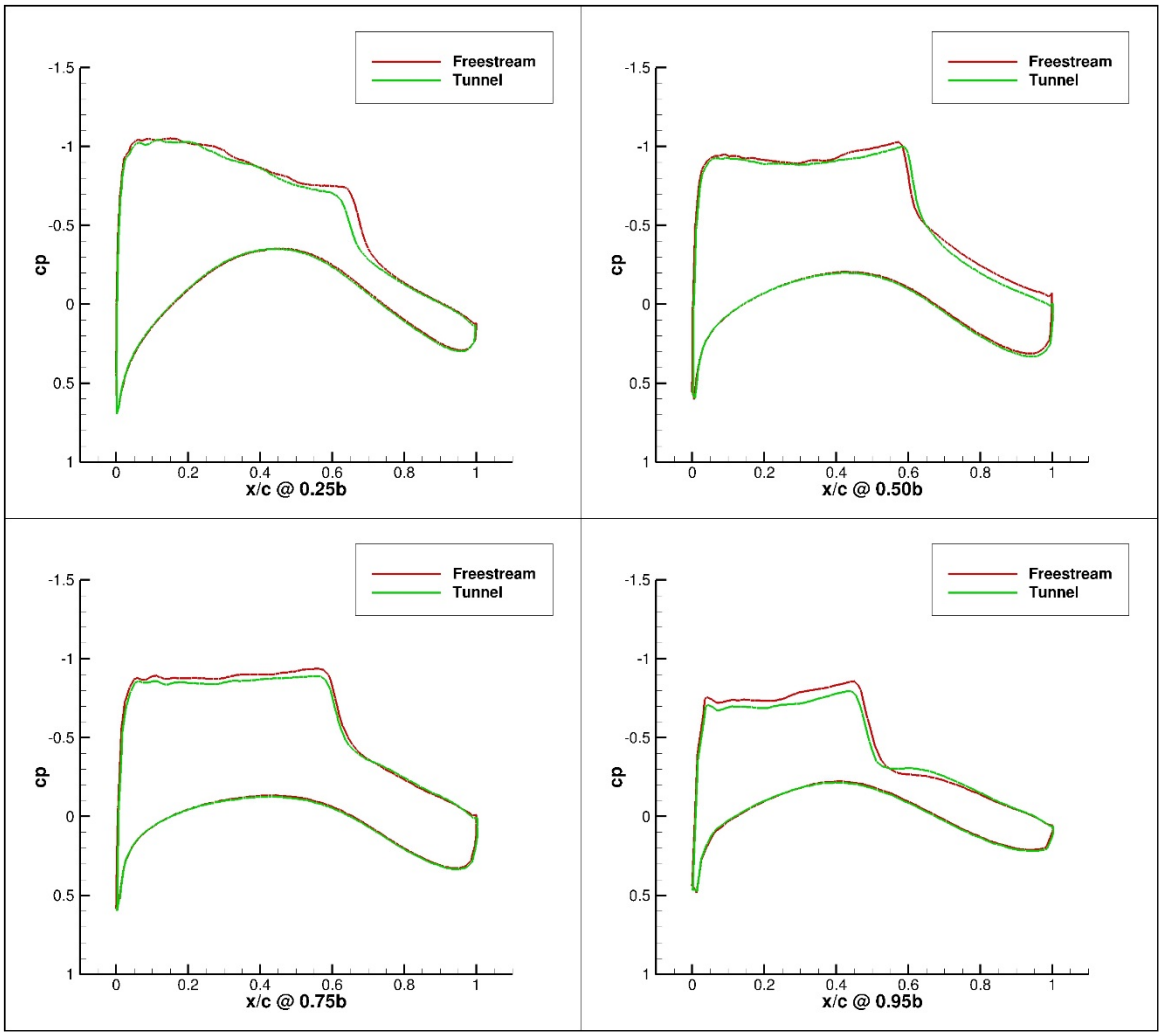

Figure 213. Configuration 2.1, 3 deg Angle of Attack Pressure Coefficient Contours for Free-stream and Wind Tunnel Simulations

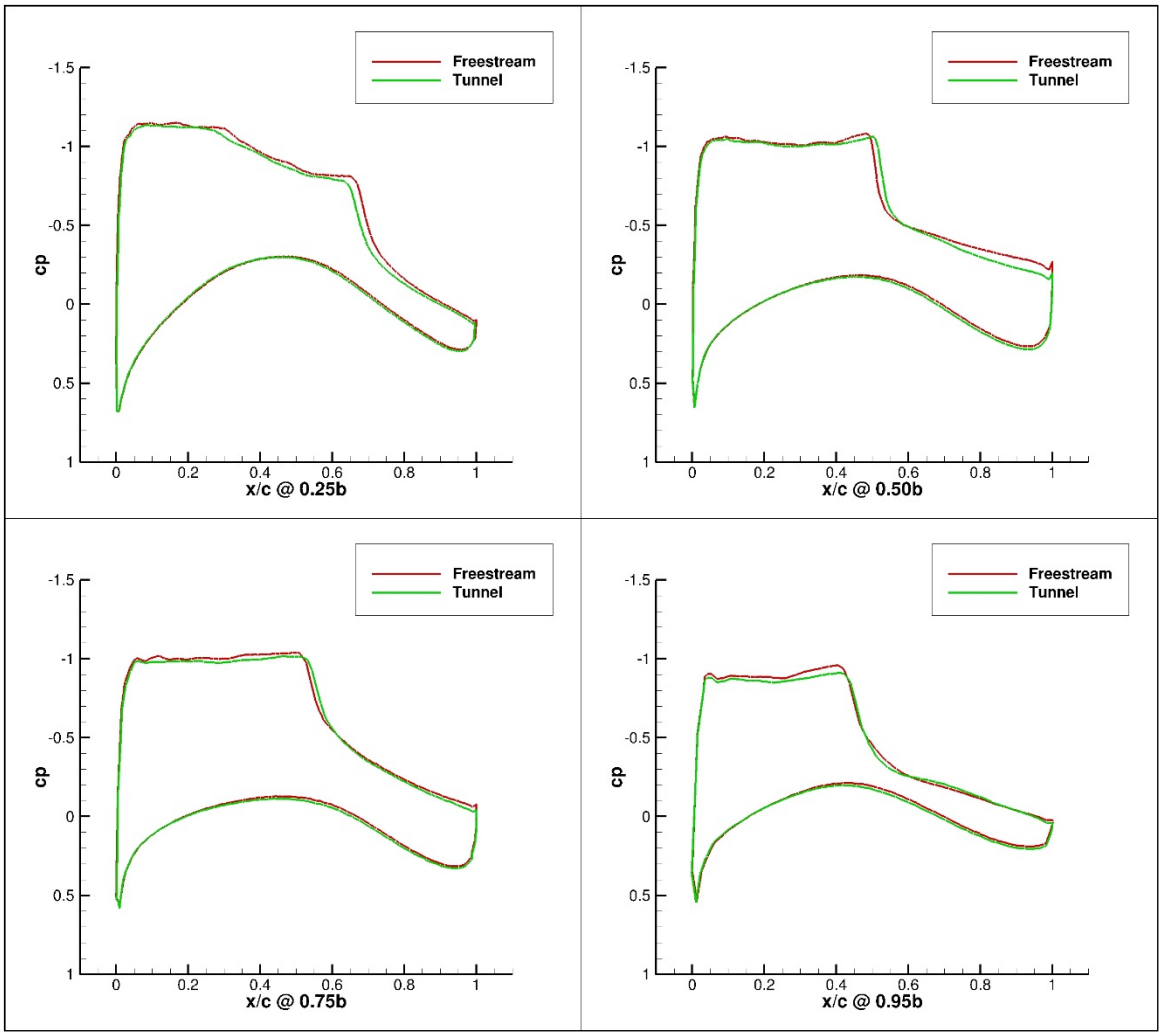

Figure 214. Configuration 2.1, 4 deg Angle of Attack Pressure Coefficient Contours for Free-stream and Wind Tunnel Simulations

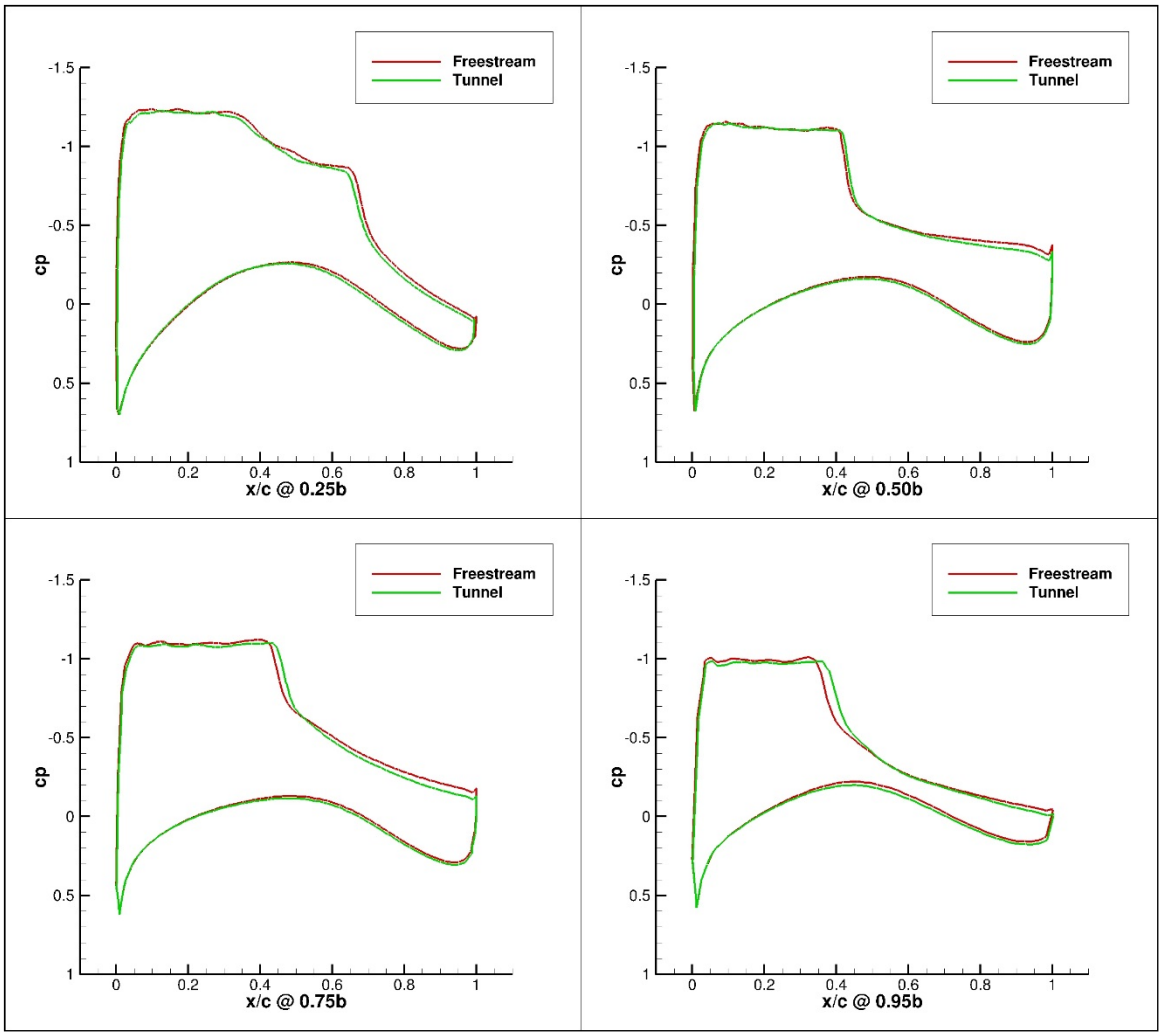

Figure 215. Configuration 2.1, 5 deg Angle of Attack Pressure Coefficient Contours for Free-stream and Wind Tunnel Simulations

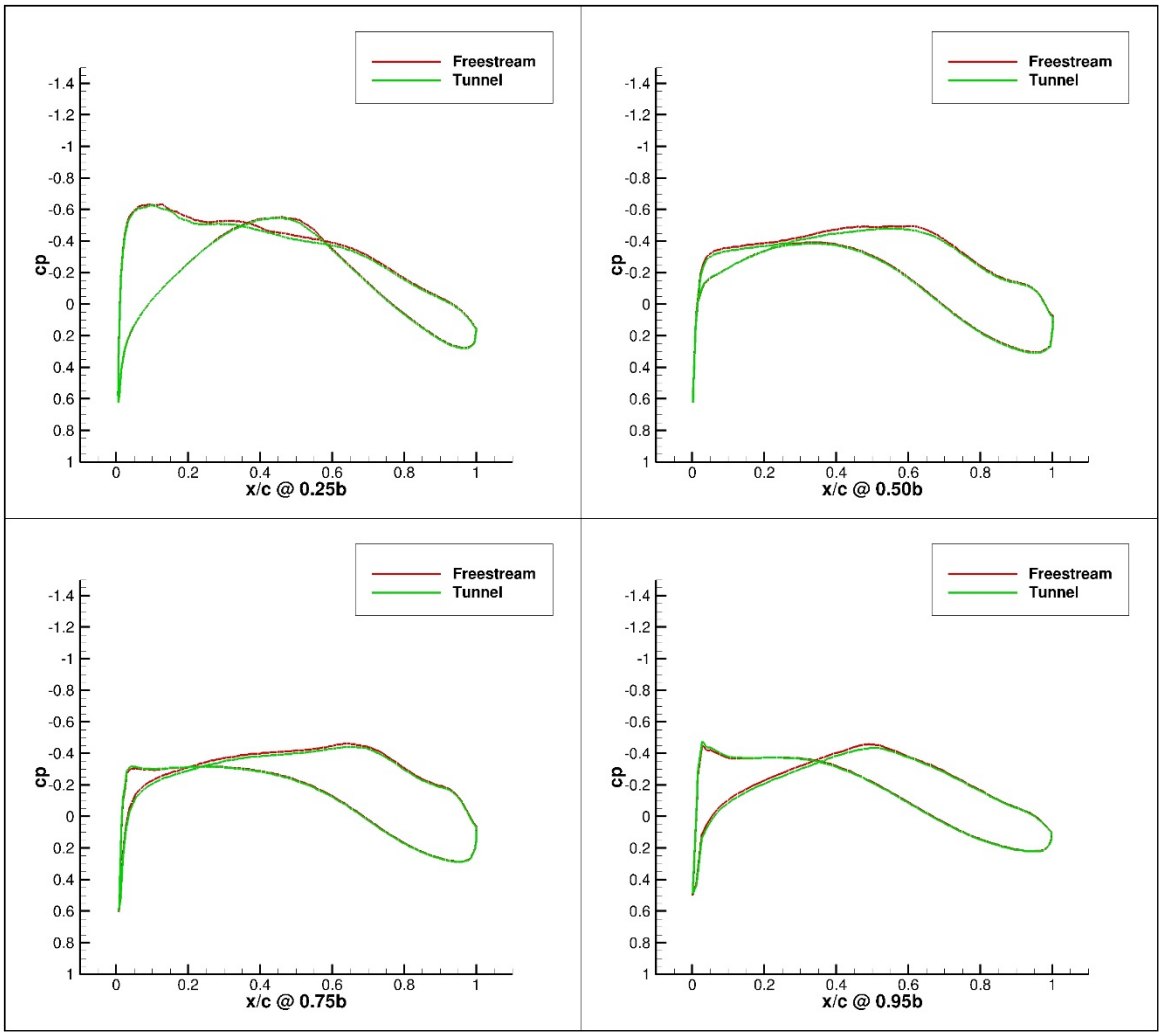

Figure 216. Configuration 3, 0 deg Angle of Attack Pressure Coefficient Contours for Free-stream and Wind Tunnel Simulations

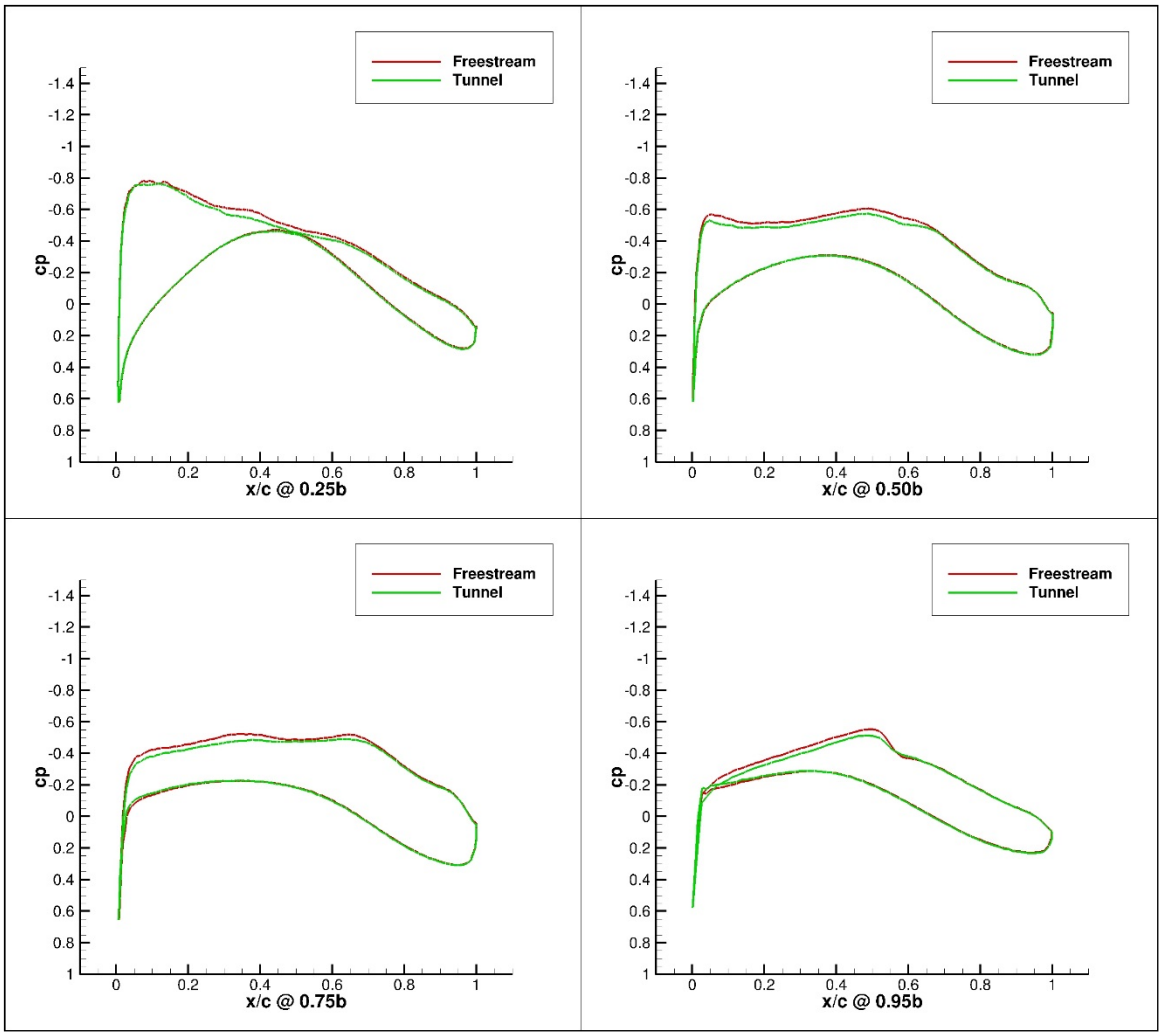

Figure 217. Configuration 3, 1 deg Angle of Attack Pressure Coefficient Contours for Free-stream and Wind Tunnel Simulations

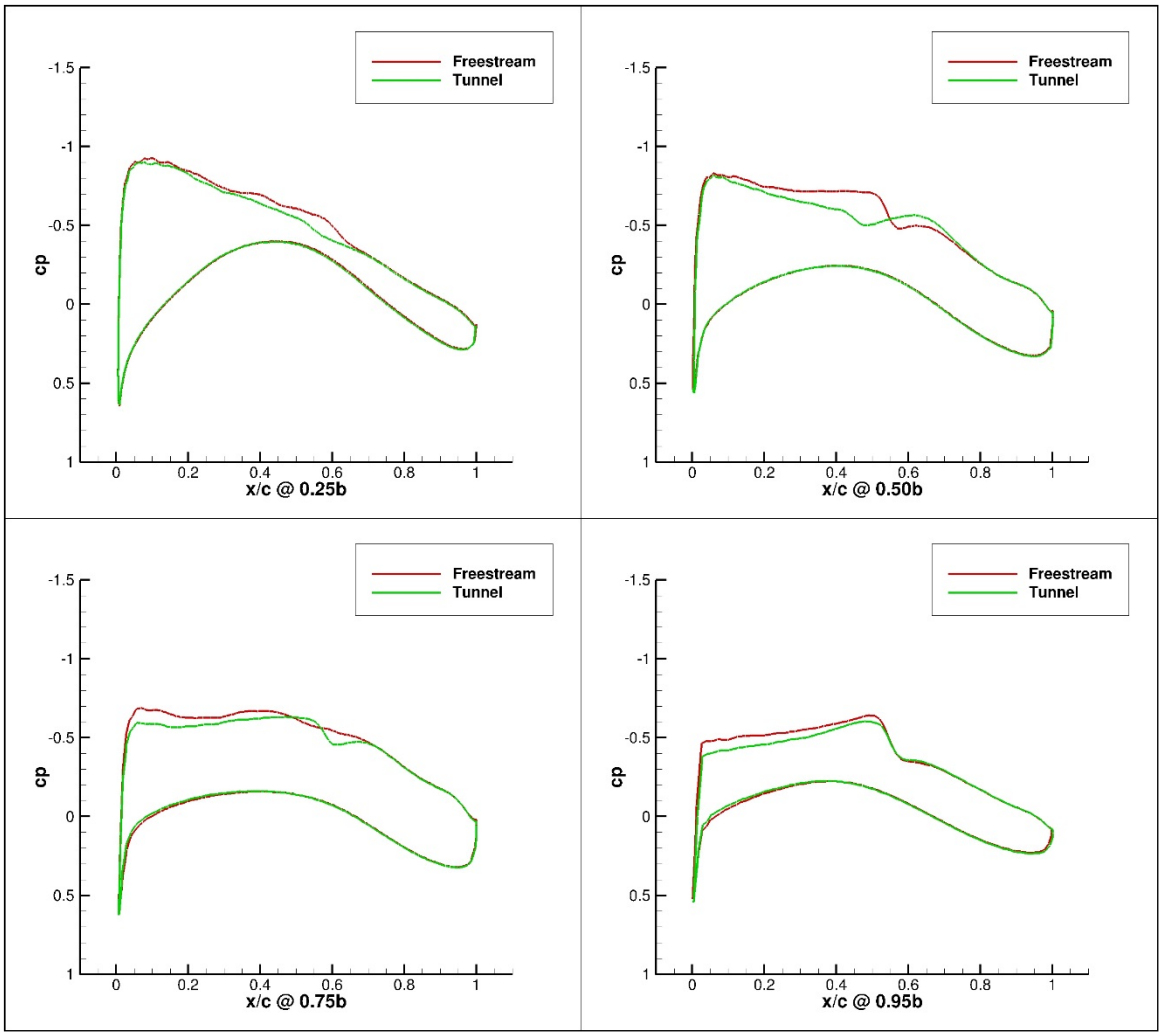

Figure 218. Configuration 3, 2 deg Angle of Attack Pressure Coefficient Contours for Free-stream and Wind Tunnel Simulations

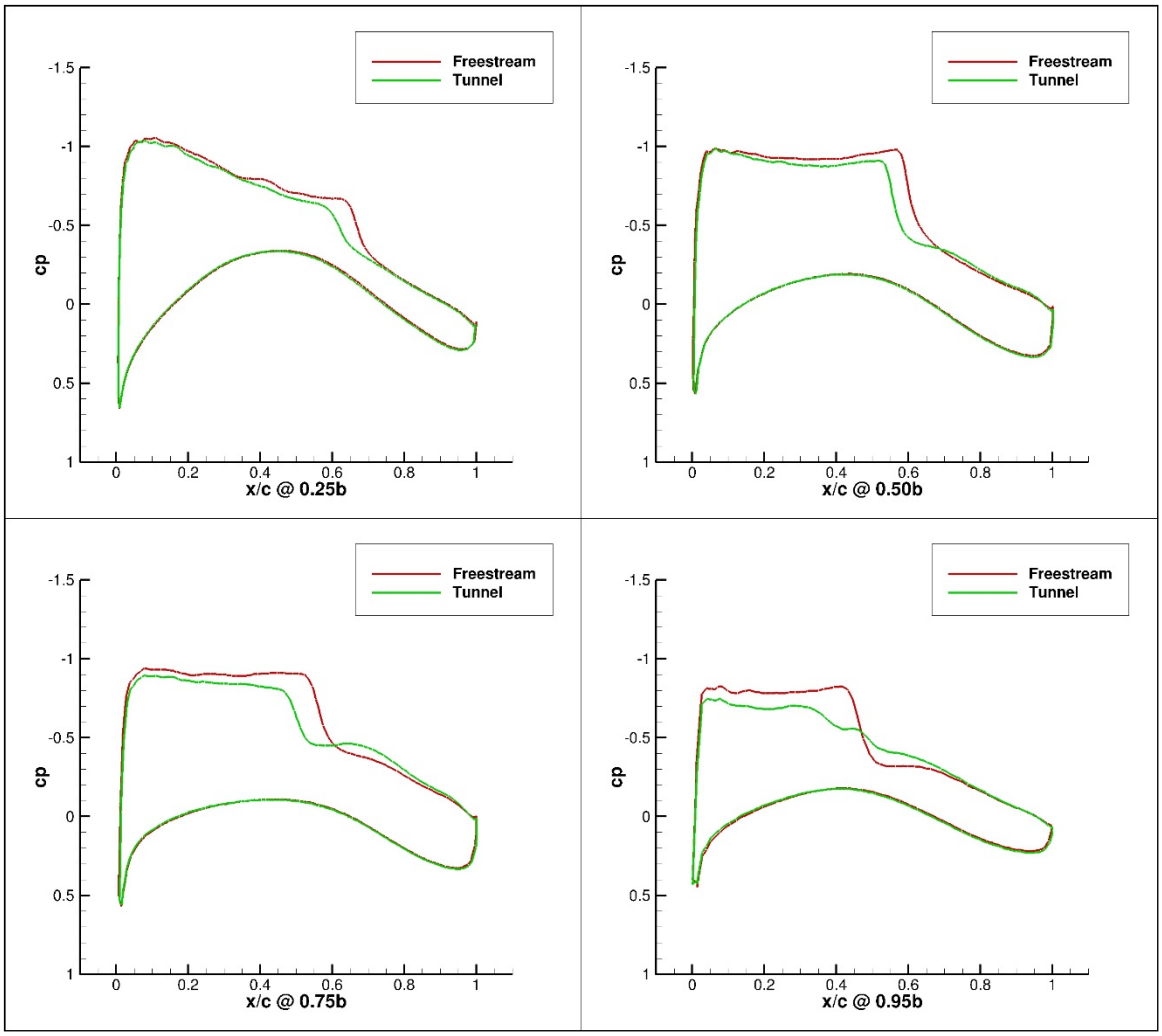

Figure 219. Configuration 3,3 deg Angle of Attack Pressure Coefficient Contours for Free-stream and Wind Tunnel Simulations

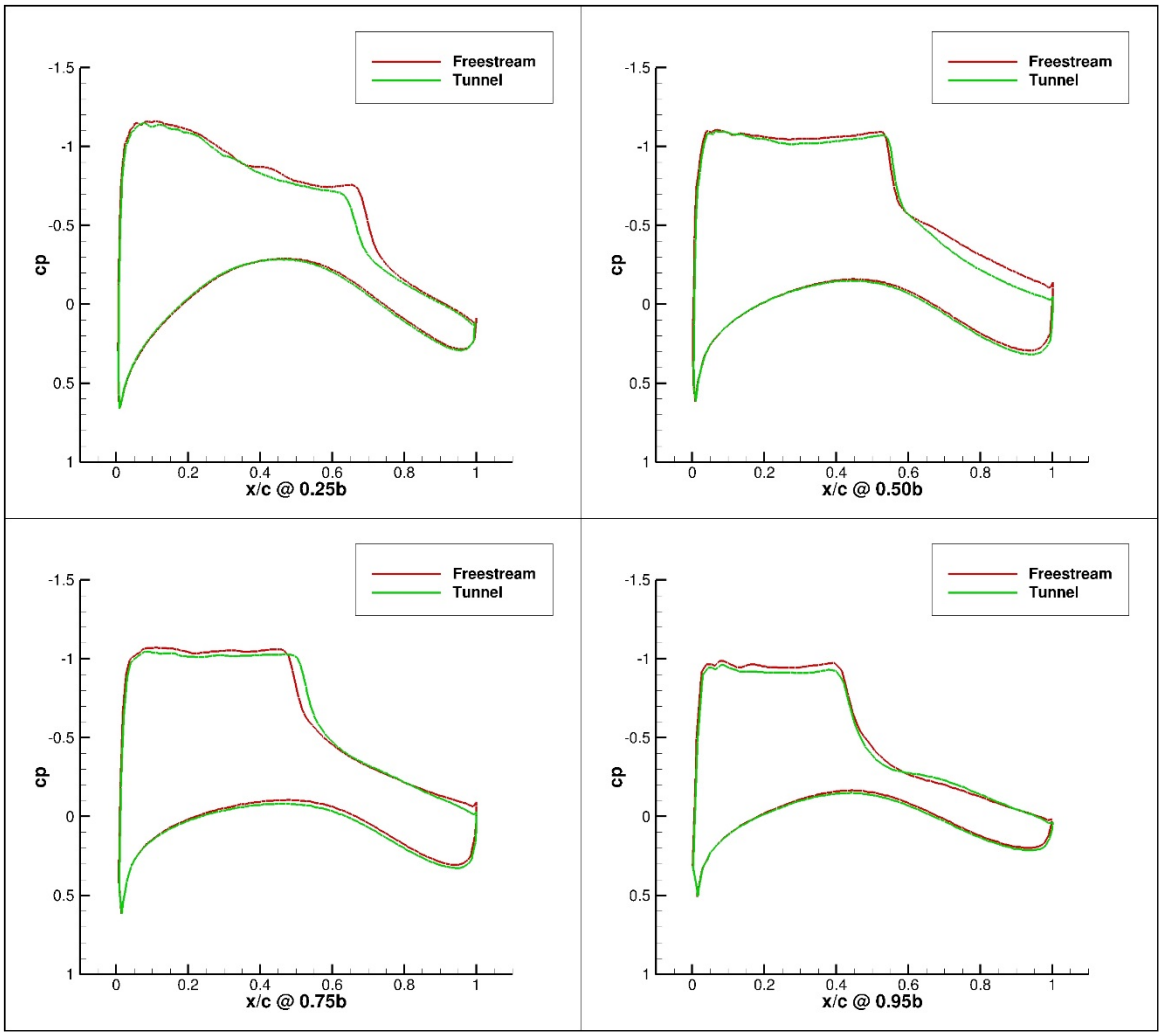

Figure 220. Configuration 3, 4 deg Angle of Attack Pressure Coefficient Contours for Free-stream and Wind Tunnel Simulations

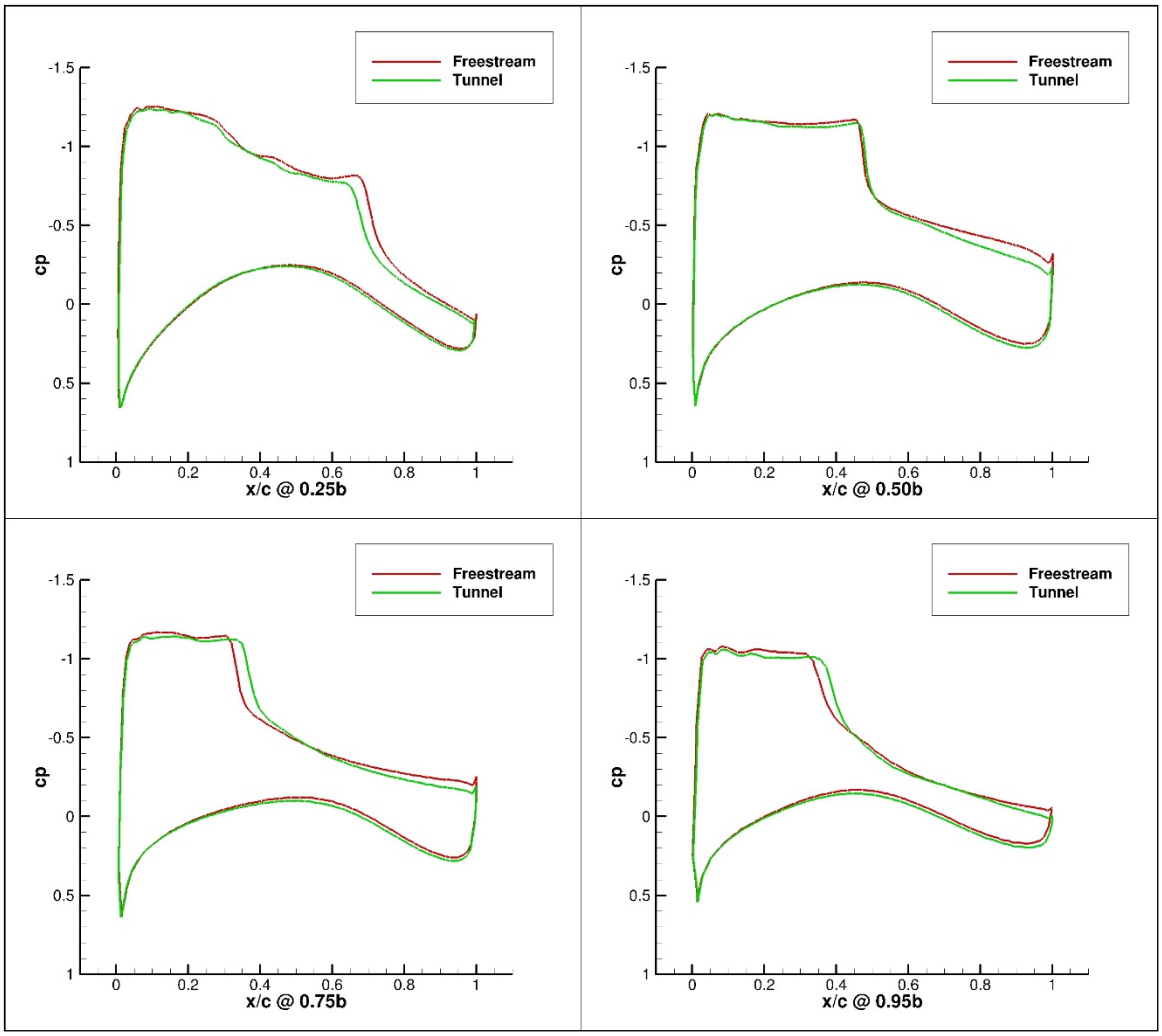

Figure 221. Configuration 3, 5 deg Angle of Attack Pressure Coefficient Contours for Free-stream and Wind Tunnel Simulations

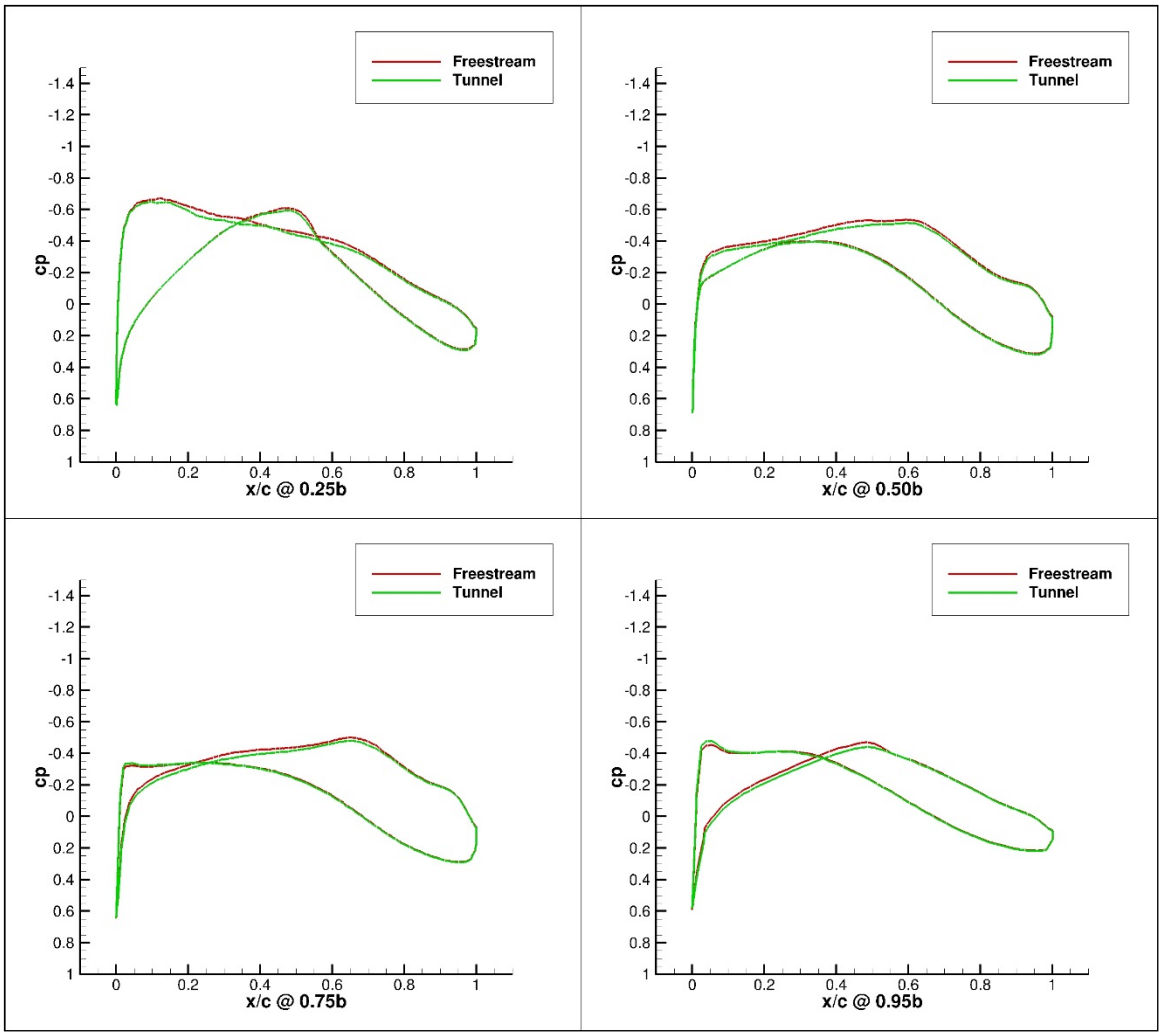

Figure 222. Configuration 3.1, 0 deg Angle of Attack Pressure Coefficient Contours for Free-stream and Wind Tunnel Simulations

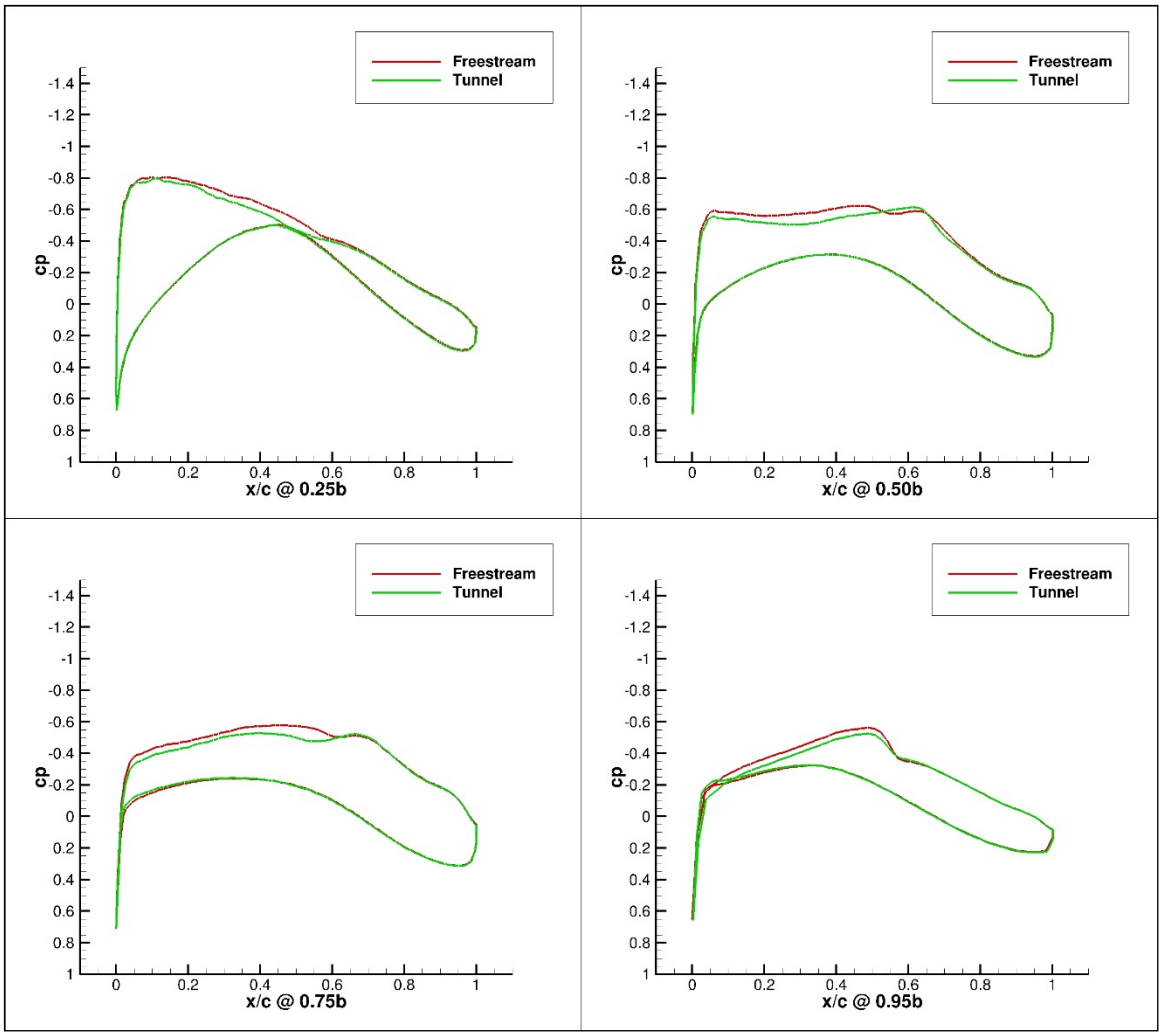

Figure 223. Configuration 3.1, 1 deg Angle of Attack Pressure Coefficient Contours for Free-stream and Wind Tunnel Simulations

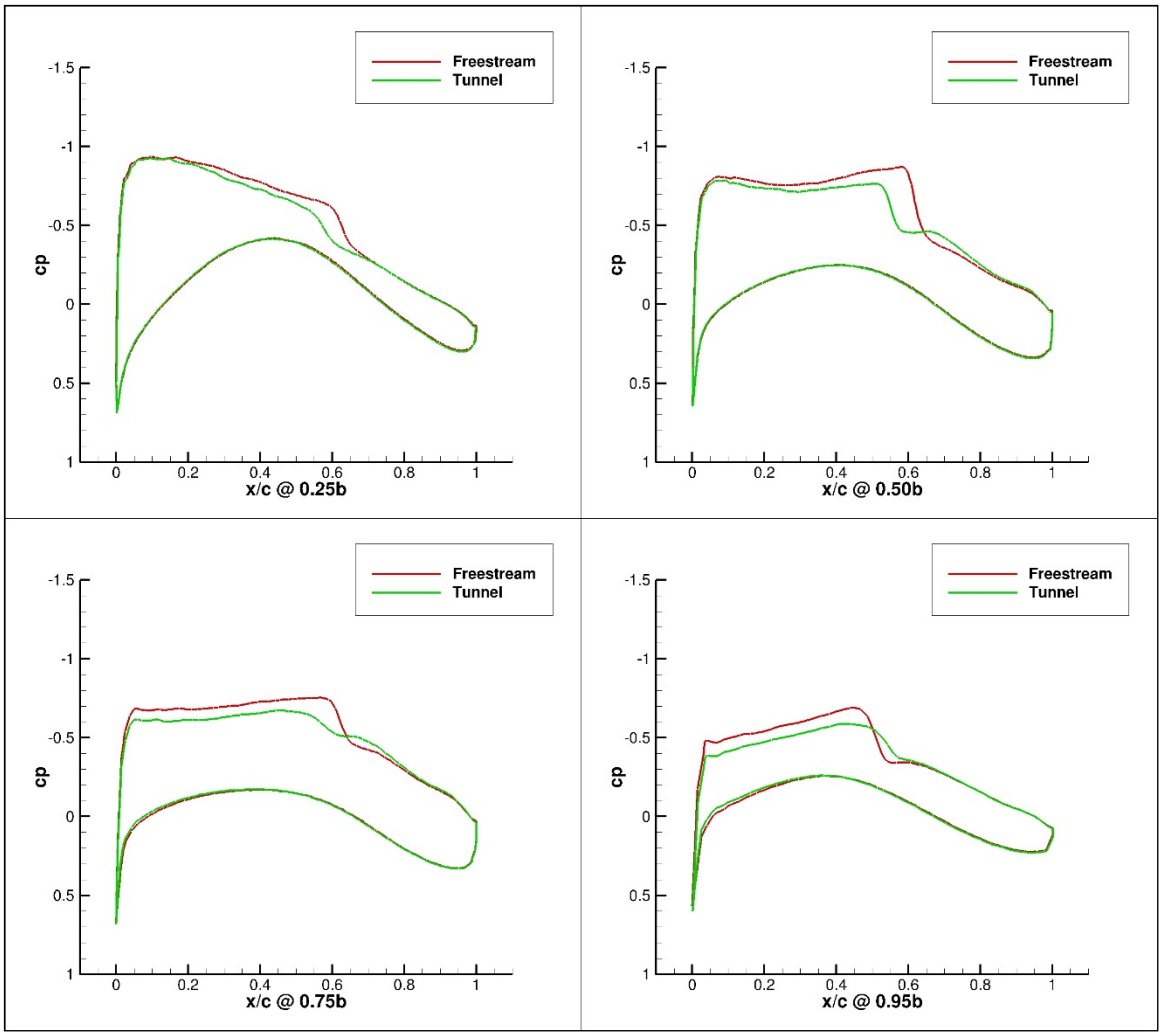

Figure 224. Configuration 3.1, 2 deg Angle of Attack Pressure Coefficient Contours for Free-stream and Wind Tunnel Simulations

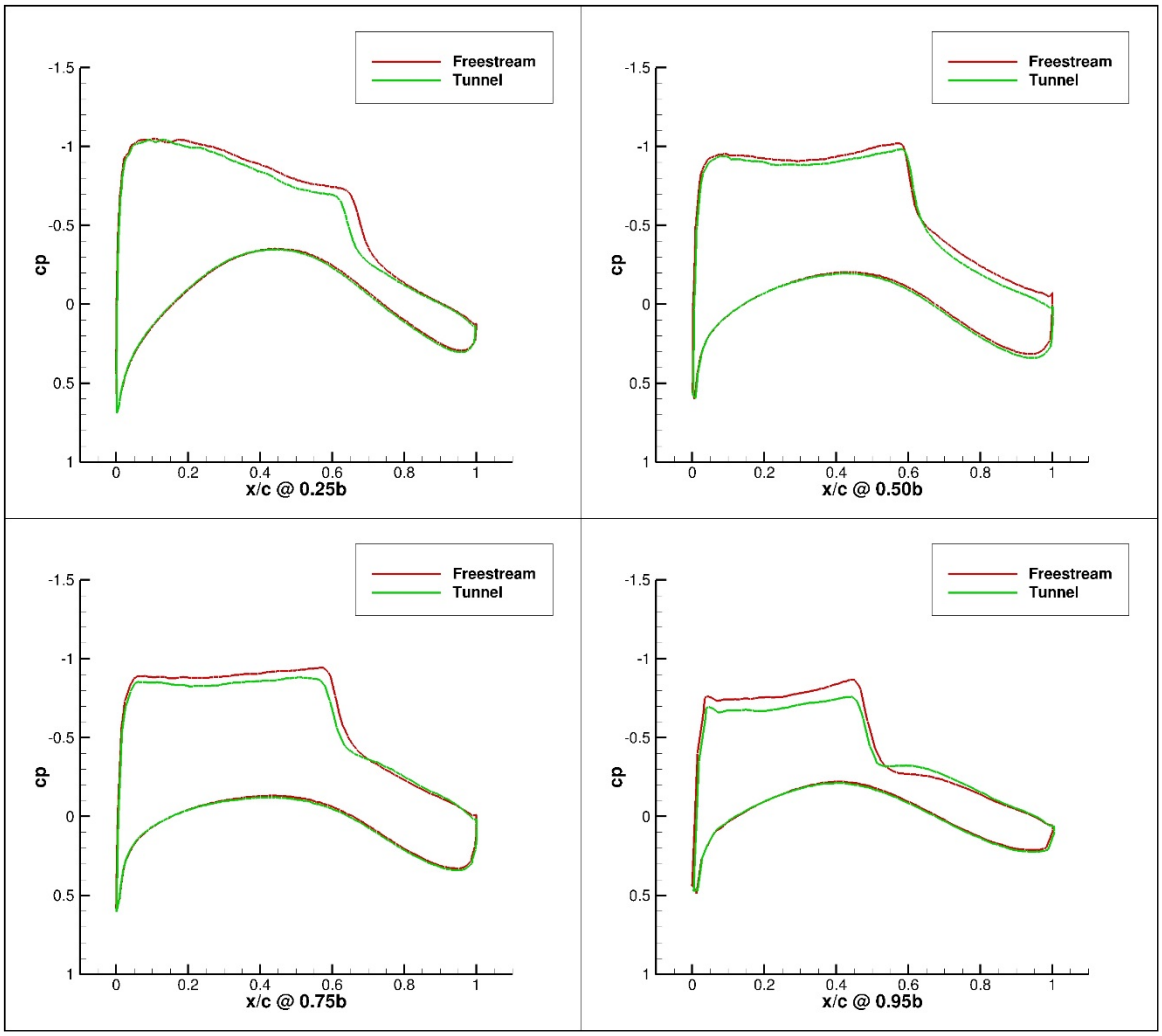

Figure 225. Configuration 3.1, 3 deg Angle of Attack Pressure Coefficient Contours for Free-stream and Wind Tunnel Simulations

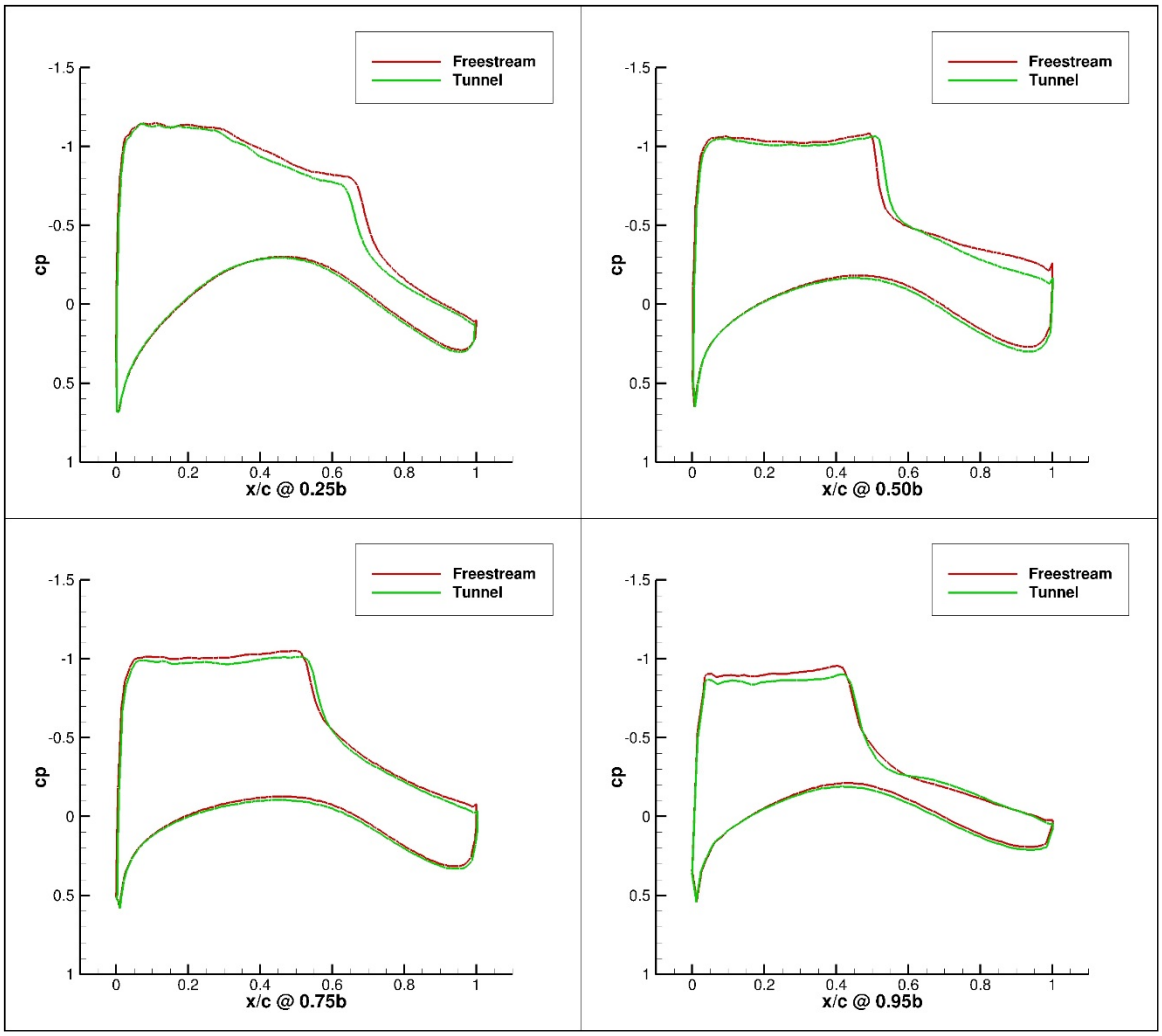

Figure 226. Configuration 3.1, 4 deg Angle of Attack Pressure Coefficient Contours for Free-stream and Wind Tunnel Simulations

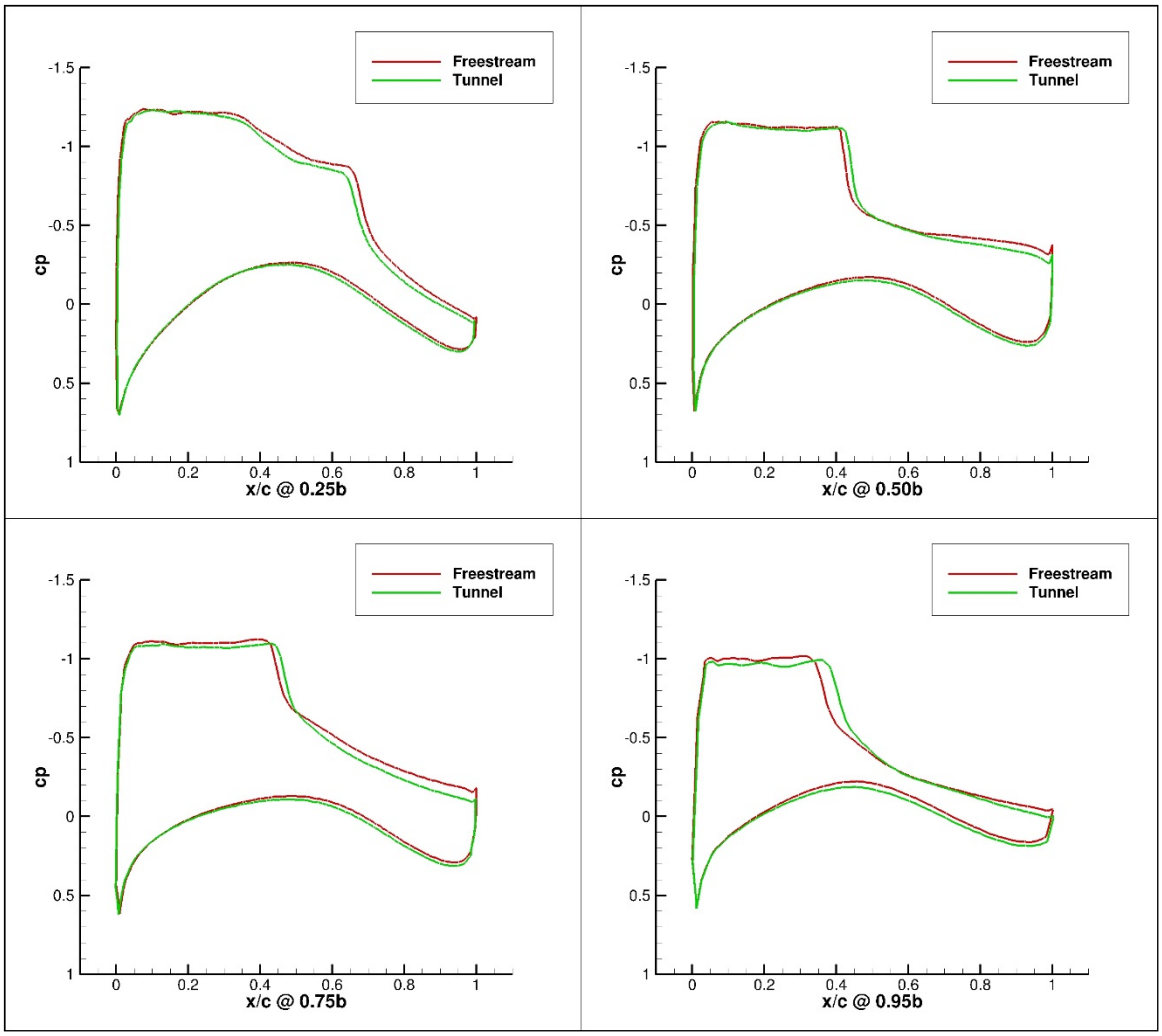

Figure 227. Configuration 3.1, 5 deg Angle of Attack Pressure Coefficient Contours for Free-stream and Wind Tunnel Simulations

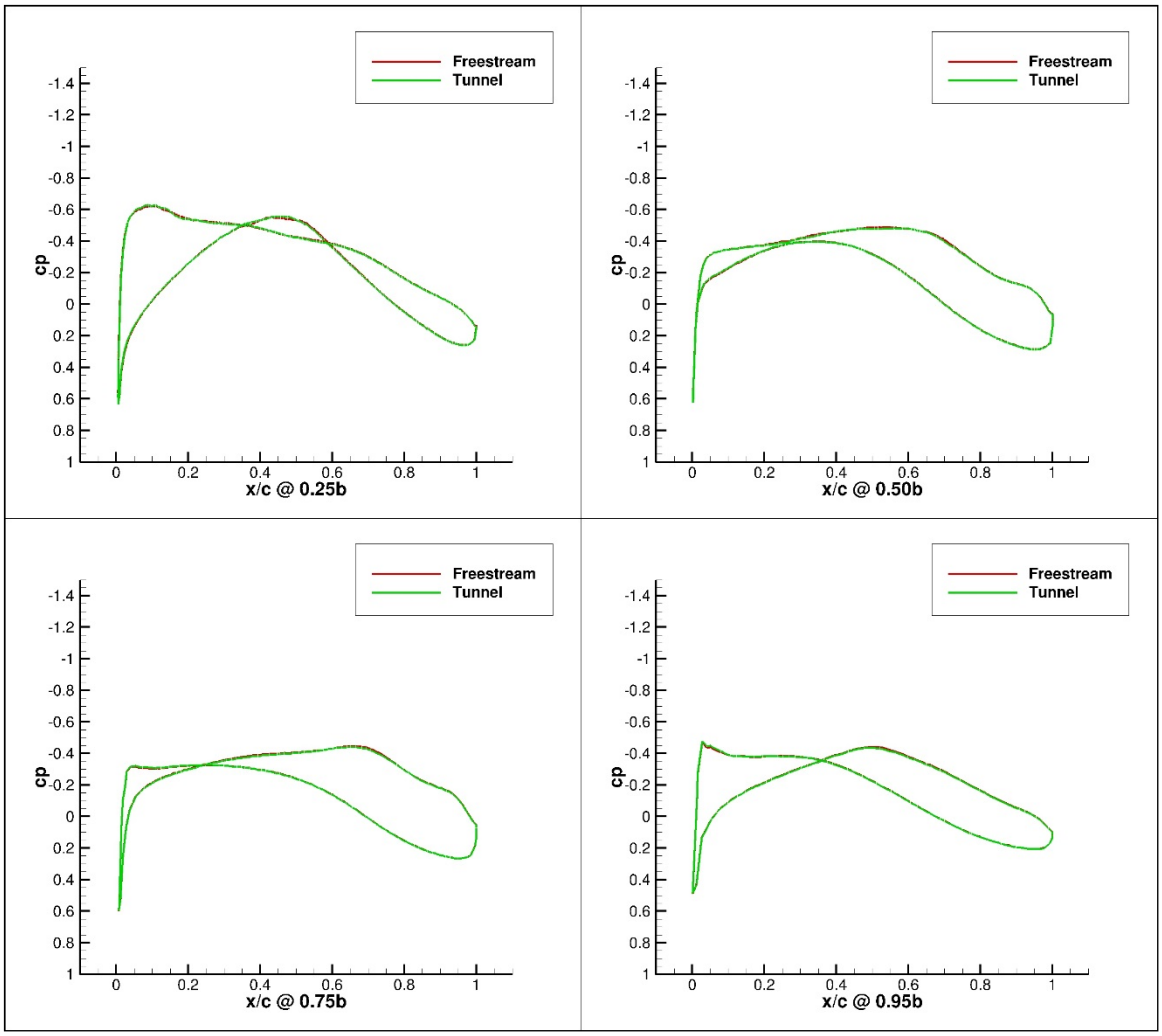

Figure 228. Configuration 4, 0 deg Angle of Attack Pressure Coefficient Contours for Free-stream and Wind Tunnel Simulations

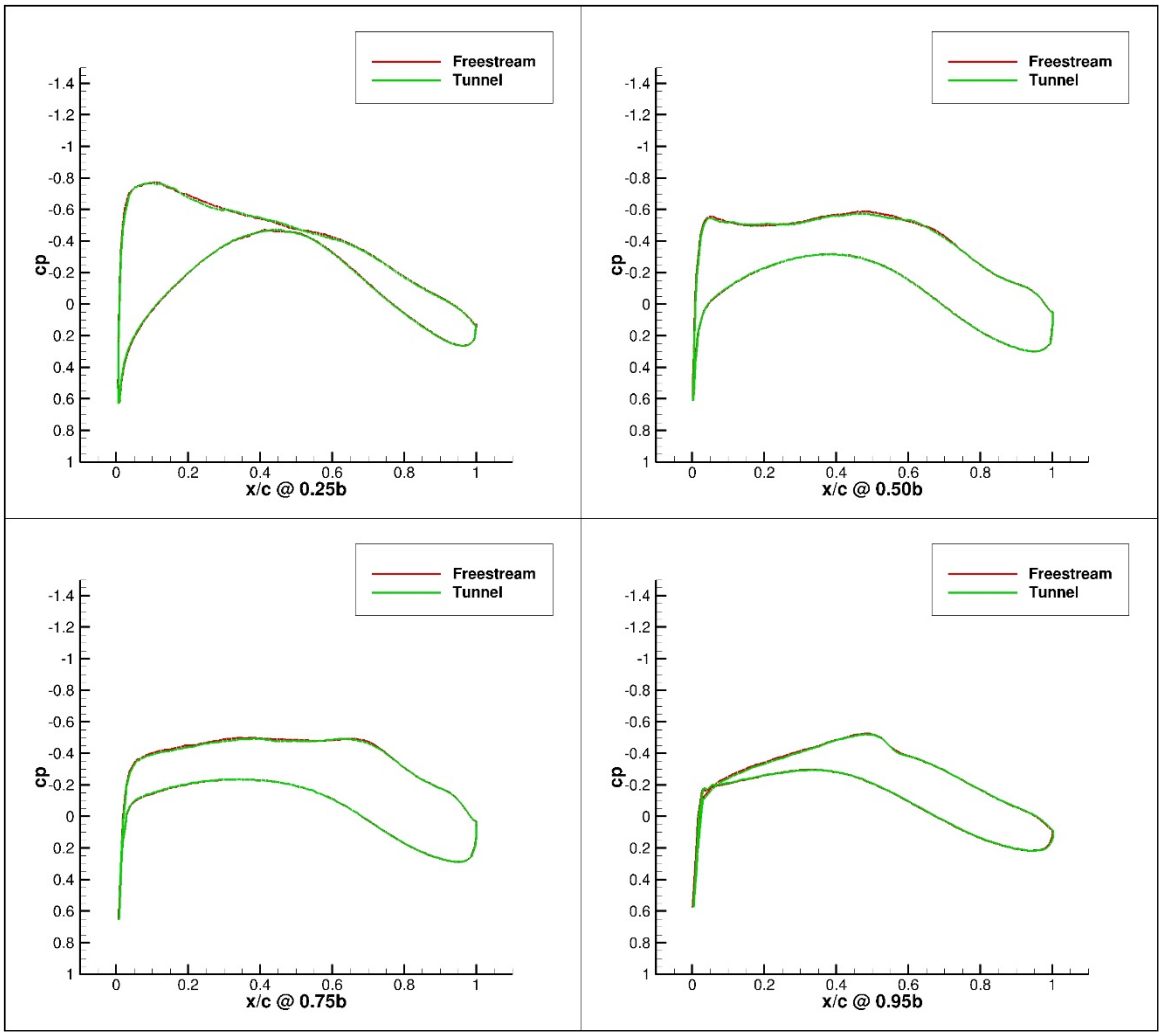

Figure 229. Configuration 4, 1 deg Angle of Attack Pressure Coefficient Contours for Free-stream and Wind Tunnel Simulations

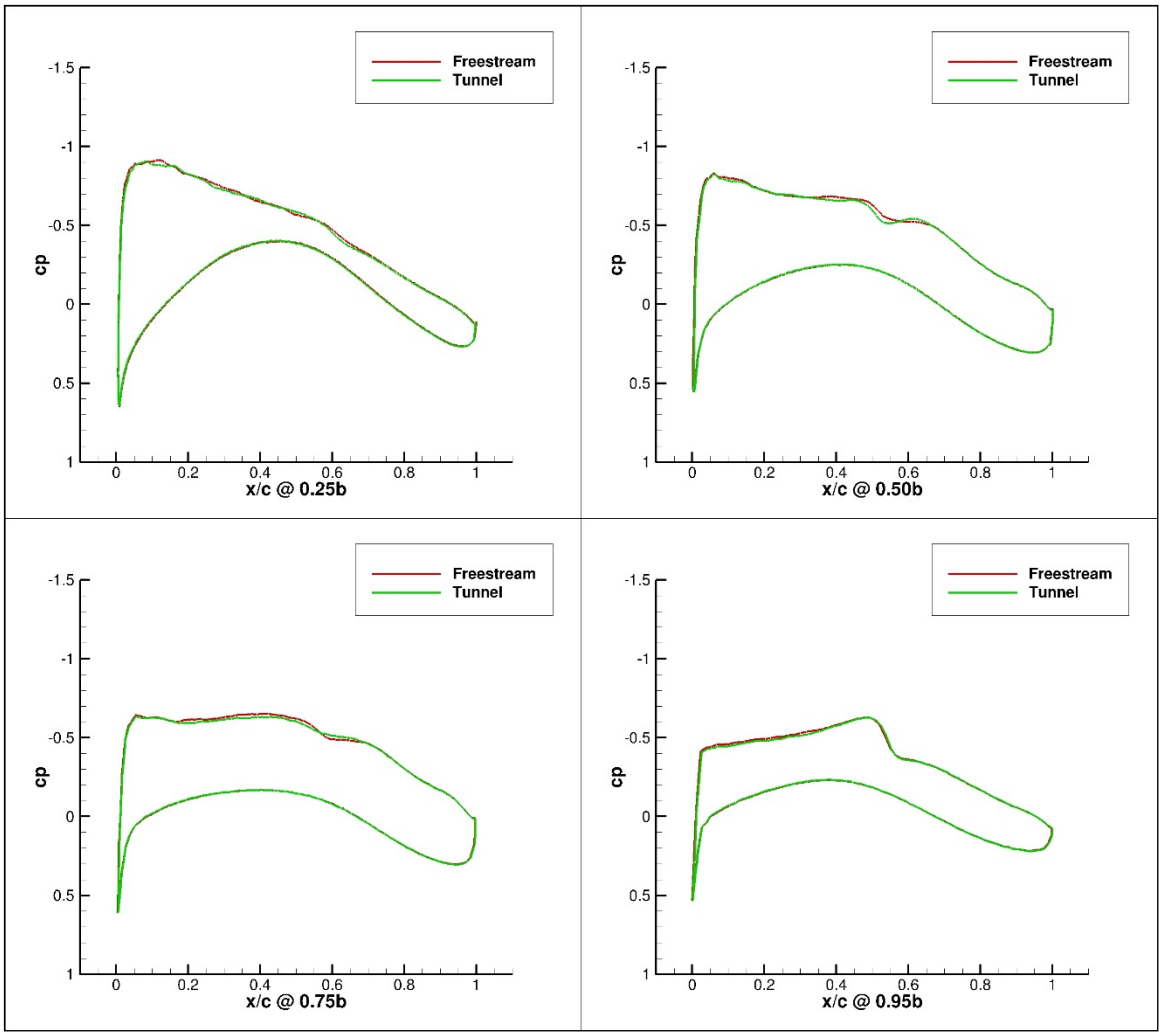

Figure 230. Configuration 4, 2 deg Angle of Attack Pressure Coefficient Contours for Free-stream and Wind Tunnel Simulations

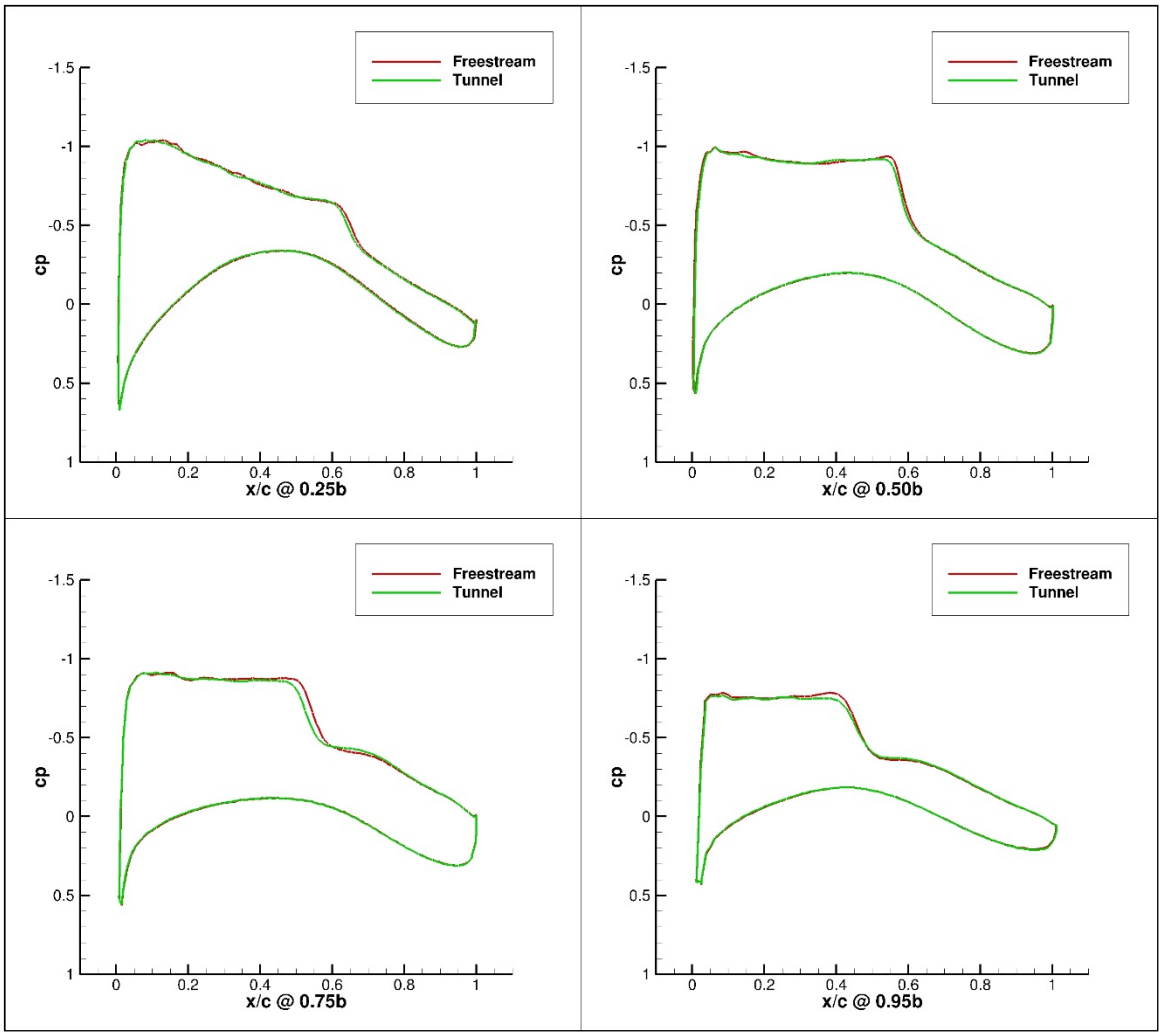

Figure 231. Configuration 4, 3 deg Angle of Attack Pressure Coefficient Contours for Free-stream and Wind Tunnel Simulations

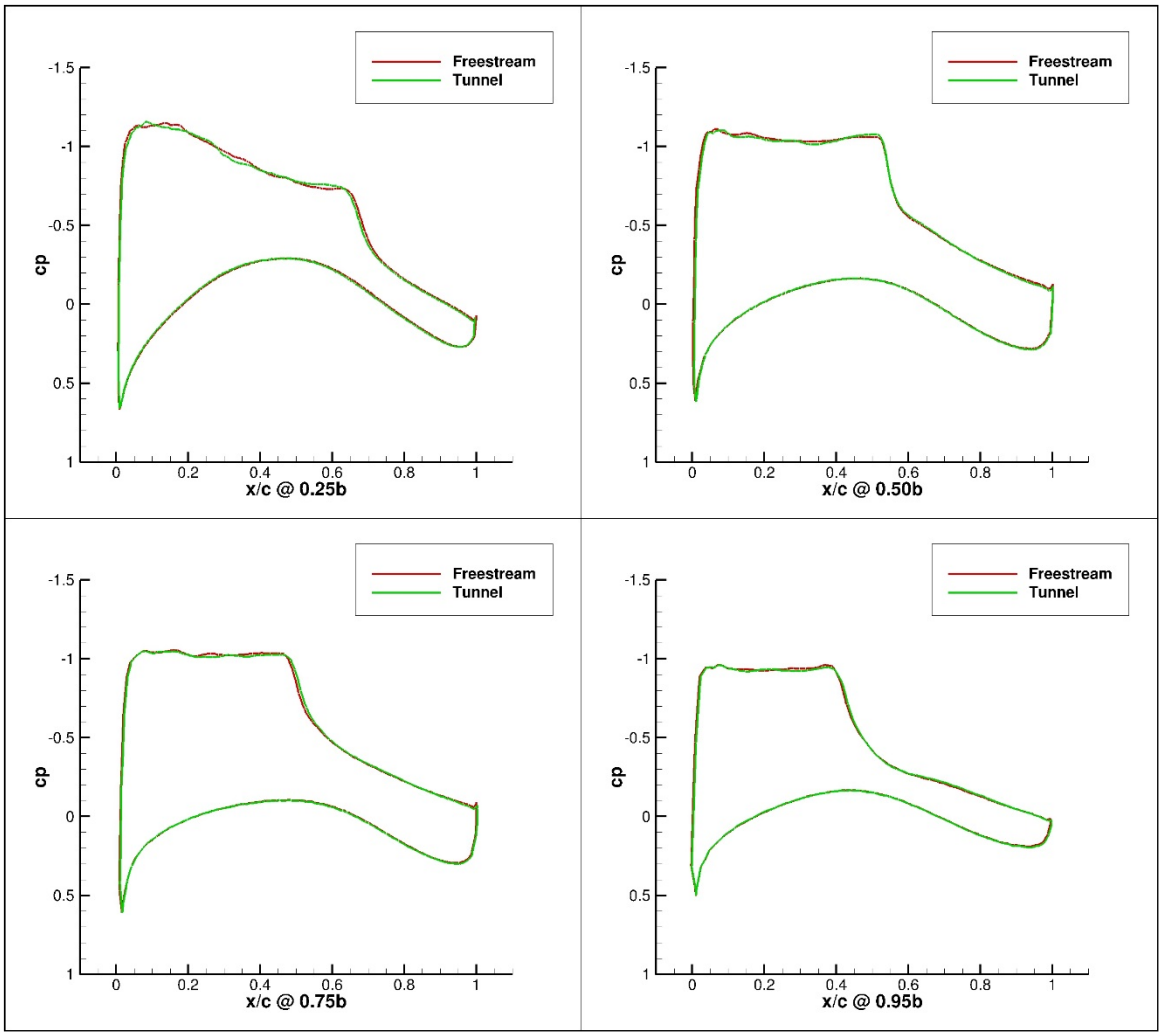

Figure 232. Configuration 4, 4 deg Angle of Attack Pressure Coefficient Contours for Free-stream and Wind Tunnel Simulations

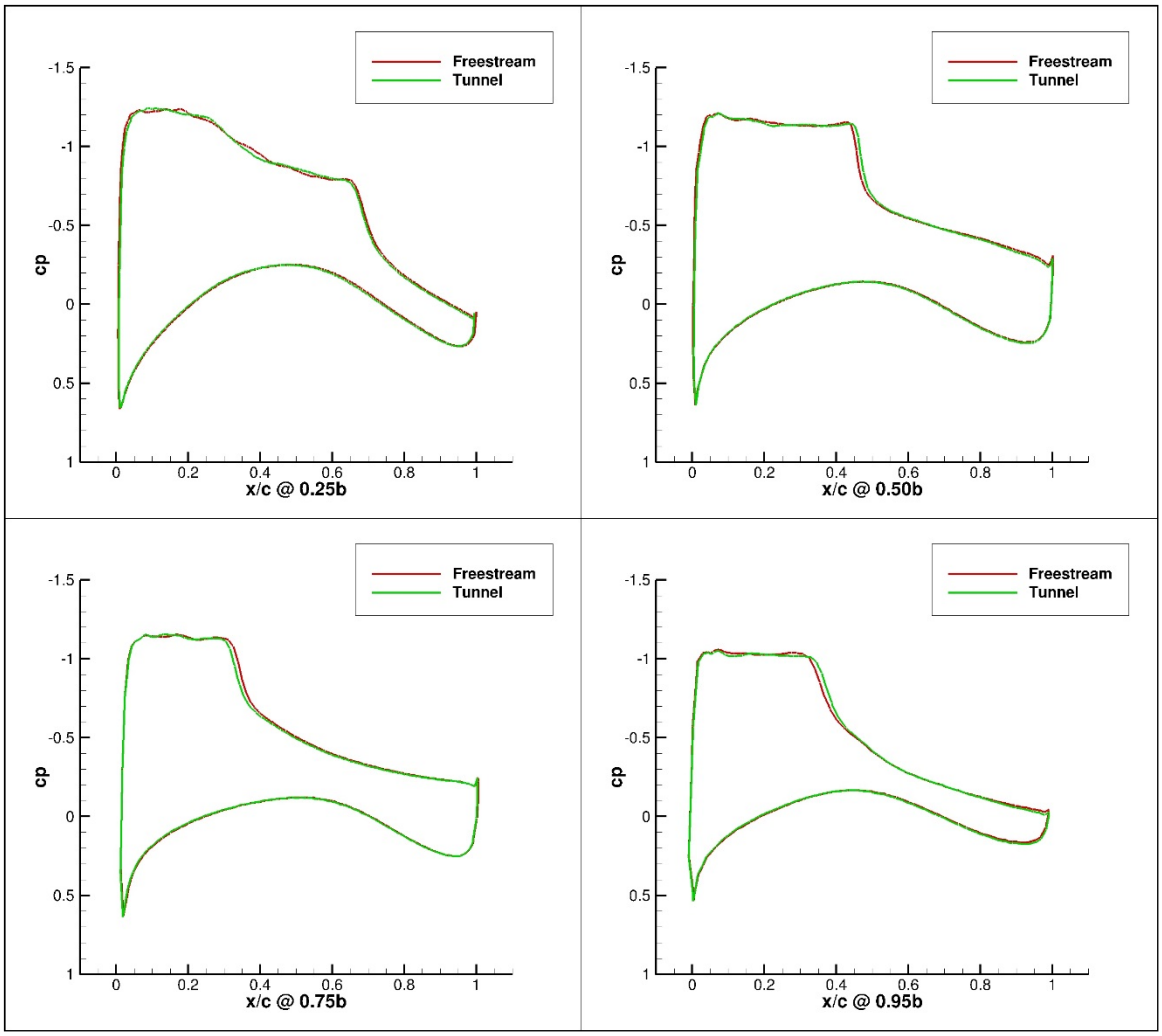

Figure 233. Configuration 4, 5 deg Angle of Attack Pressure Coefficient Contours for Free-stream and Wind Tunnel Simulations

VITA

William Calain Schuman was born in Nashville, TN. After graduating from McEwen High School, he pursued an undergraduate degree at the University of Tennessee, Knoxville. He received a Bachelor of Science in Aerospace Engineering from the University of Tennessee Knoxville in May 2010. Starting in August 2010 he was employed as an aerospace engineer at Arnold Engineering Development Complex, where he continues to work today as a Flight Systems data analyst. He began graduate work at the University of Tennessee Space Institute August 2011.